

12 April 2013 | \$10


Science



Australopithecus sediba


What can RabMAbs[®] do for you?

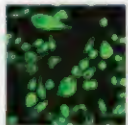
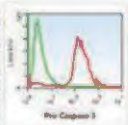


abcam[®]
discover more

Rabbit Monoclonal Antibodies
( **RabMAbs**) offer multiple advantages to bring you the highest quality antibody possible.



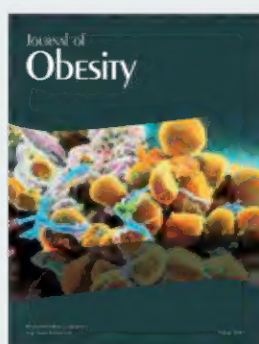
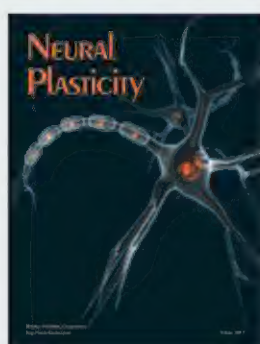
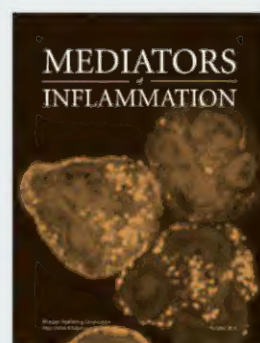
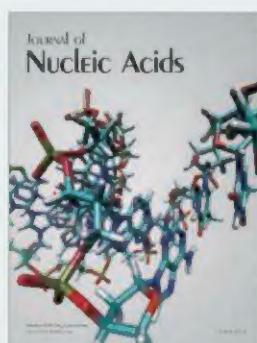
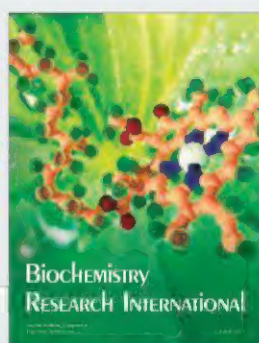
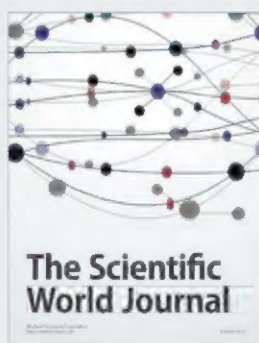
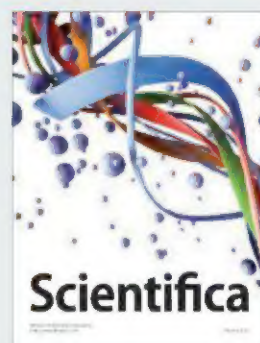
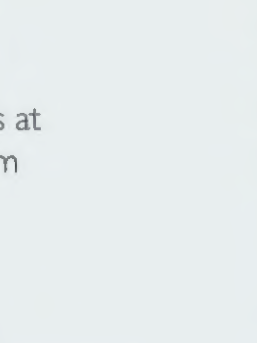
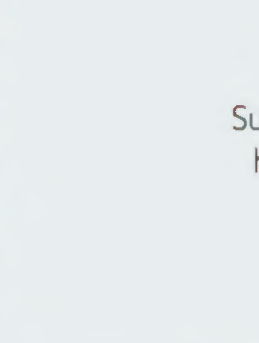
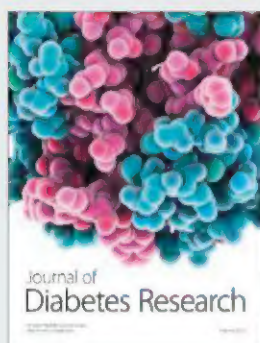
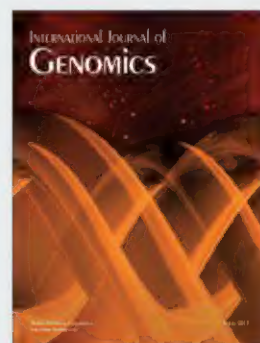
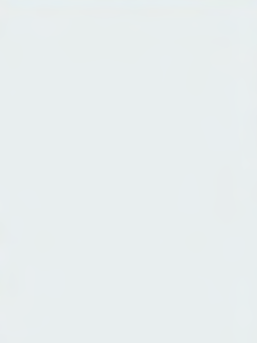
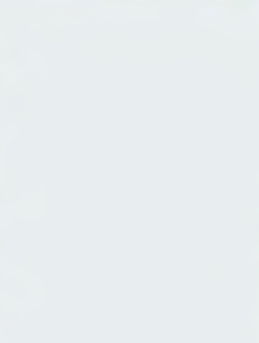
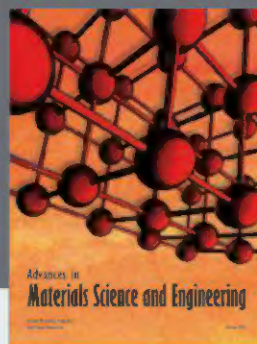
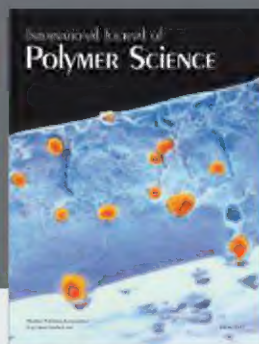
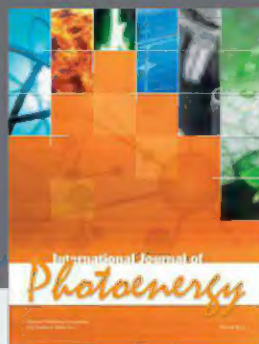
#6	Novel Epitopes
#7	Multiple Applications
#8	Ideal for use on mouse model
#1	Low Background

 **RabMAbs[®]** are tested in multiple applications (WB, IHC, ICC/IF, IP and FACS) and multiple species (Human, Mouse and Rat) before release.



Validation data for Caspase-3 (Pro) RabMAb (ab32150) in A) WB on HeLa cell lysate, B) IHC on FFPE cervical carcinoma tissue, C) FACS on Jurkat cells and D) ICC on HeLa cells.

Try a RabMAb and discover more at **abcam.com/rabmabs**



Hindawi

Submit your manuscripts at
<http://www.hindawi.com>

Make ends meet.



Gibson Assembly[™] Cloning Kit

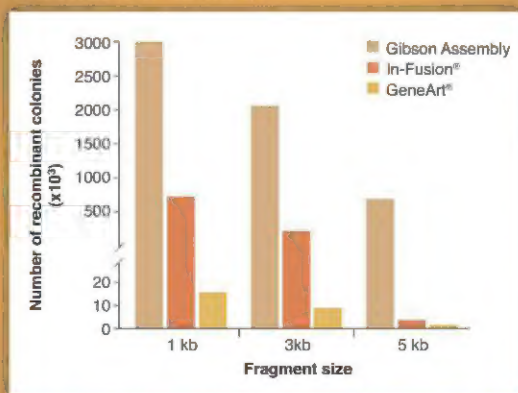
New England Biolabs has revolutionized your laboratory's standard cloning methodology. The Gibson Assembly Cloning Kit combines the power of the Gibson Assembly Master Mix with NEB 5-alpha Competent *E. coli*, enabling fragment assembly and transformation in just under two hours. Save time, without sacrificing efficiency.

Making ends meet is now quicker and easier than ever before, with the Gibson Assembly Cloning Kit from NEB.

NEBuilder[™]
for Gibson Assembly

Visit NEBGibson.com to view the latest tutorials and to try our primer design tool.

Gibson Assembly Cloning Kit provides robust transformation efficiencies



Assembly reactions containing 25 ng of linear pUC19 vector and 0.04 pmol of each fragment were performed following individual suppliers' recommended protocols and using the competent cells provided with the kit. The total number of recombinant colonies was calculated per 25 ng of linear pUC19 vector added to the assembly reaction.

SPECIAL SECTION

Australopithecus sediba

INTRODUCTION

- 163 The Mosaic Nature of *Australopithecus sediba*
L. R. Berger

ABSTRACTS

REPORTS

- 164 Dental Morphology and the Phylogenetic "Place" of *Australopithecus sediba*
J. D. Irish et al.
Mandibular Remains Support Taxonomic Validity of *Australopithecus sediba*
D. J. de Ruiter et al.

RESEARCH ARTICLES

- 164 The Upper Limb of *Australopithecus sediba*
S. E. Churchill et al.
Mosaic Morphology in the Thorax of *Australopithecus sediba*
P. Schmid et al.
The Vertebral Column of *Australopithecus sediba*
S. A. Williams et al.
The Lower Limb and Mechanics of Walking in *Australopithecus sediba*
J. M. DeSilva et al.
>> Science Podcast

>> News story p. 132, for full text:
www.sciencemag.org/extra/sediba

EDITORIAL

- 119 An Important Anniversary
Ralph J. Cicerone

NEWS OF THE WEEK

- 126 A roundup of the week's top stories

NEWS & ANALYSIS

- 129 New Flu Virus in China Worries and Confuses
A Decade After SARS, China's Flu Response Wins Cautious Praise
131 Tissue Imaging Method Makes Everything Clear
132 A Human Smile and Funny Walk for *Australopithecus sediba*
>> *Australopithecus sediba* section p. 163
135 Two-Billion-Dollar Cosmic Ray Detector Sees Signs of Something
>> Science Podcast

NEWS FOCUS

- 136 From Cosmic Dawn to Milkmeda, and Beyond
138 Lunar and Planetary Science Conference
The Mystery of Our Moon's Gravitational Bumps Solved?
Pesky Perchlorates All Over Mars
More Support for an Ocean in Enceladus
Snapshots From the Meeting

LETTERS

- 141 Drawbacks to Natural Gas
S. Souther
Biosecurity's Weakest Link
P. E. Hulme
China's Nuclear Power Goals Surge Ahead
X. J. Yang et al.

CORRECTIONS AND CLARIFICATIONS

TECHNICAL COMMENT ABSTRACTS

BOOKS ET AL.

- 145 Nature's Oracle
U. Segerstrale, reviewed by J. J. Boomsma
146 Studying Human Behavior
H. E. Longino, reviewed by E. L. Milam



page 136

POLICY FORUMS

- 147 Right-Sizing Stem-Rust Research
P. G. Pardey et al.
149 Latin America's Nitrogen Challenge
A. T. Austin et al.

PERSPECTIVES

- 150 Self-Medication in Animals
J. C. de Roode et al.
>> Science Podcast
152 Pactamycin Made Easy
J. A. Codelli and S. E. Reisman
>> Report p. 180
153 The Complete Quantum Hall Trio
S. Oh
>> Report p. 167
154 Lifting the Veil on an Old Mystery
L. Vereecken
>> Reports pp. 174 and 177
155 An Interferon Paradox
P. M. Odorizzi and E. J. Wherry
>> Reports pp. 202 and 207

CONTENTS continued >>

ON THE WEB THIS WEEK

>> **Science Express**
Read Reports on self-assembling peptide cages, explaining a missing spleen, and more.

DEPARTMENTS

- 117 This Week in Science
121 Editors' Choice
124 Science Staff
223 New Products
224 Science Careers



COVER

Reconstruction of a ~2-million-year-old *Australopithecus sediba* skeleton (height: ~1.3 meters) based on fossils from the Malapa Hominin 1 (MH1), MH2, and MH4 specimens from Malapa, Gauteng, South Africa. Brown indicates discovered fossils. *Au. sediba* exhibits a mosaic morphology distinct from that of other australopithecines and early *Homo*. See pages 132 and 163, as well as www.sciencemag.org/extra/sediba.

Reconstruction: Peter Schmid and casting technicians at the University of the Witwatersrand's Evolutionary Studies Institute; Photo: Brett Eloff, courtesy of Lee R. Berger and the University of the Witwatersrand

DESIGN

THE PROTEIN PURIFICATION SYSTEM
YOU'VE BEEN DREAMING OF.

(AND IF YOUR NEEDS CHANGE, SO CAN YOUR SYSTEM.)



NGC™ Chromatography System

Reinvent your approach to protein purification with the NGC Chromatography Systems. Position pumps, valves, detectors, and columns wherever you need them. Expand vertically by adding additional tiers over time. Maximize your bench space and minimize your hold up volumes with the NGC system's unique Tier Rotate™ architecture. The NGC platform and your custom design come together to turn your dreams into reality.

Dream big. Design your own NGC system today at bio-rad.com/ad/ngcsystems

BIO-RAD

REVIEW

- 157 **Deep Homology of Arthropod Central Complex and Vertebrate Basal Ganglia**
N. J. Strausfeld and F. Hirth

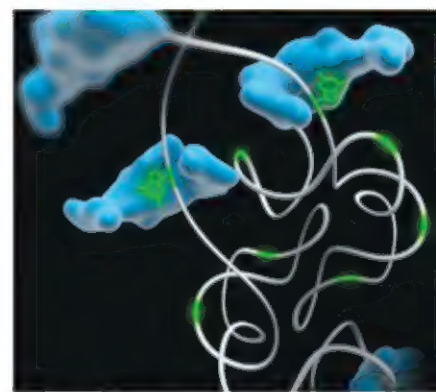
REPORTS

- 167 **Experimental Observation of the Quantum Anomalous Hall Effect in a Magnetic Topological Insulator**
C.-Z. Chang et al.
An elusive effect emerges in thin films of a bismuth-antimony-telluride topological insulator doped with magnetic chromium.
>> *Perspective p. 153*
- 170 **Evidence for Two Distinct Populations of Type Ia Supernovae**
X. Wang et al.
The spectral diversity of a particular type of stellar explosion is tied to the stellar environment.
- 174 **Infrared Absorption Spectrum of the Simplest Criegee Intermediate CH_2OO**
Y.-T. Su et al.
The vibrational spectrum of an intermediate involved in ozone chemistry may facilitate its direct study in the atmosphere.
- 177 **Direct Measurements of Conformer-Dependent Reactivity of the Criegee Intermediate CH_3CHOO**
C. A. Taatjes et al.
The reaction kinetics of an intermediate implicated in atmospheric ozone chemistry has been measured in the laboratory.
>> *Perspective p. 154*
- 180 **Enantioselective Synthesis of Pactamycin, a Complex Antitumor Antibiotic**
J. T. Malinowski et al.
A synthetic route to a complex natural product could foster preparation of analogs for exploratory medicinal chemistry.
>> *Perspective p. 152*
- 183 **Speleothems Reveal 500,000-Year History of Siberian Permafrost**
A. Vaks et al.
Siberian caves recorded the history of permafrost occurrence during the past 450,000 years.
- 186 **A Long-Lived Relativistic Electron Storage Ring Embedded in Earth's Outer Van Allen Belt**
D. N. Baker et al.
NASA's Van Allen Probes revealed an additional, dynamic belt of relativistic particles surrounding Earth.

- 190 **A Guanosine-Centric Mechanism for RNA Chaperone Function**
J. K. Grohman et al.
RNA chaperones promote assembly of complex RNA structures by binding to and "neutralizing" guanosine bases.
- 195 **A Histone Acetylation Switch Regulates H2A.Z Deposition by the SWR-C Remodeling Enzyme**
S. Watanabe et al.
A modification on histone H3 in a nucleosome favors the swapping out of one type of H2A histone for another.
- 199 **Latency-Associated Degradation of the MRP1 Drug Transporter During Latent Human Cytomegalovirus Infection**
M. P. Weekes et al.
A virally encoded protein eliminates a cell surface drug transporter, promoting latent human cytomegalovirus infection.
- 202 **Blockade of Chronic Type I Interferon Signaling to Control Persistent LCMV Infection**
E. B. Wilson et al.
- 207 **Persistent LCMV Infection Is Controlled by Blockade of Type I Interferon Signaling**
J. R. Teijaro et al.
Blockade of type I interferons leads to better control of persistent lymphocytic choriomeningitis virus infection.
>> *Perspective p. 155*
- 211 **Injectable, Cellular-Scale Optoelectronics with Applications for Wireless Optogenetics**
T. Kim et al.
Miniaturized and implantable light-emitting diodes offer precise and flexible control of neurons, when used in combination with optogenetics.
- 216 **Interactions Between the Nucleus Accumbens and Auditory Cortices Predict Music Reward Value**
V. N. Salimpoor et al.
Activity in the mesolimbic striatum and its interaction with the auditory cortices determines the hedonic response to new music.



page 145



page 190

SCIENCE (ISSN 0036-8075) is published weekly on Friday, except the last week in December, by the American Association for the Advancement of Science, 1200 New York Avenue, NW, Washington, DC 20005. Periodicals Mail postage (publication No. 484460) paid at Washington, DC, and additional mailing offices. Copyright © 2013 by the American Association for the Advancement of Science. The title SCIENCE is a registered trademark of the AAAS. Domestic individual membership and subscription (S1 issues): \$149 (\$74 allocated to subscription). Domestic institutional subscription (S1 issues): \$990; Foreign postage extra: Mexico, Caribbean (surface mail) \$55; other countries (air assist delivery) \$85. First class, airmail, student, and emeritus rates on request. Canadian rates with GST available upon request, GST #1254 88122. Publications Mail Agreement Number 1069624. Printed in the U.S.A.

Change of address: Allow 4 weeks, giving old and new addresses and 8-digit account number. **Postmaster:** Send change of address to AAAS, P.O. Box 96178, Washington, DC 20090-6178. **Single-copy sales:** \$10.00 current issue, \$15.00 back issue prepaid includes surface postage; bulk rates on request. **Authorization to photocopy** material for internal or personal use under circumstances not falling within the fair use provisions of the Copyright Act is granted by AAAS to libraries and other users registered with the Copyright Clearance Center (CCC) Transactional Reporting Service, provided that \$30.00 per article is paid directly to CCC, 222 Rosewood Drive, Danvers, MA 01923. The identification code for Science is 0036-8075. Science is indexed in the Reader's Guide to Periodical Literature and in several specialized indexes.



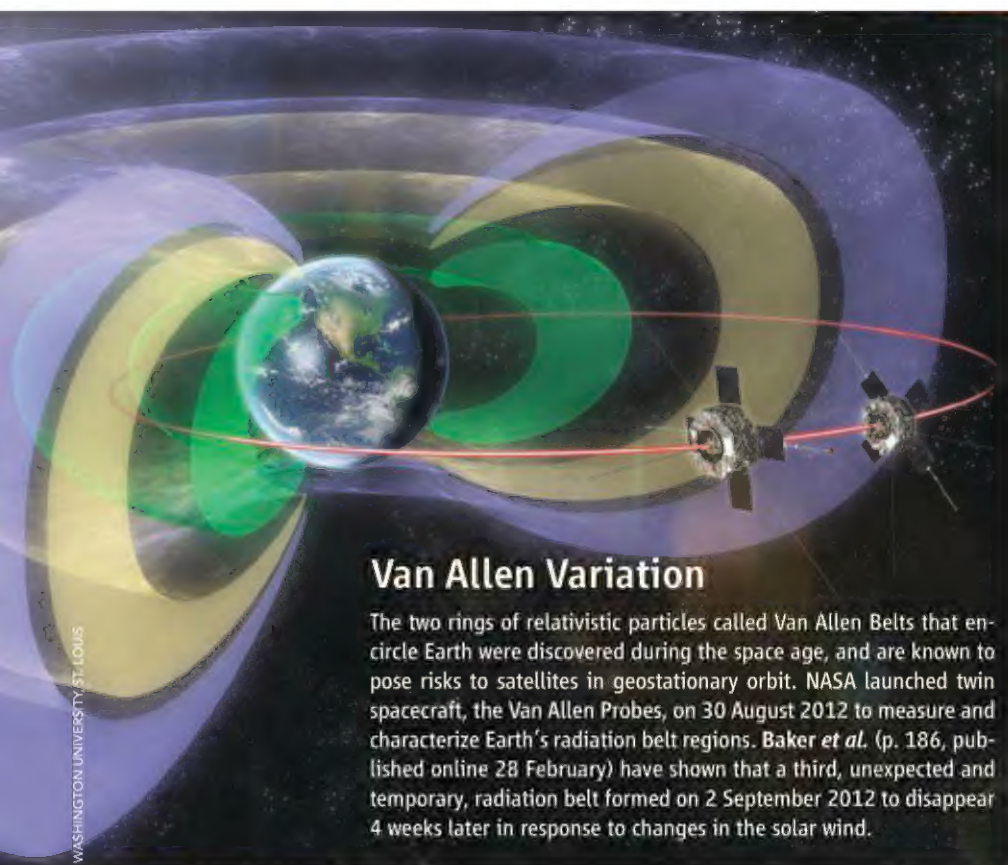
Always had a global view?

MAKE GREAT THINGS HAPPEN

Opportunities for research scientists and professionals: Looking beyond borders has been your dream since childhood days. EMD offers extraordinary global career perspectives for scientists in our Research & Development hubs in Greater Boston (USA), Greater Frankfurt (Germany), Beijing (China) or Tokio (Japan). Contribute to

challenging research projects aimed at fighting disease worldwide. Join us and take part in shaping our diversified bio pharma business. Ready for an exploration journey?

come2emd.com



Van Allen Variation

The two rings of relativistic particles called Van Allen Belts that encircle Earth were discovered during the space age, and are known to pose risks to satellites in geostationary orbit. NASA launched twin spacecraft, the Van Allen Probes, on 30 August 2012 to measure and characterize Earth's radiation belt regions. **Baker et al.** (p. 186, published online 28 February) have shown that a third, unexpected and temporary, radiation belt formed on 2 September 2012 to disappear 4 weeks later in response to changes in the solar wind.

Of Flies and Men

Similarities of brain structure, function, and behavior are usually ascribed to convergent evolution. In their review, **Strausfeld and Hirth** (p. 157) identify multiple commonalities shared by vertebrate basal ganglia and a system of forebrain centers in arthropods called the central complex. The authors conclude that circuits essential to behavioral choice originated very early across phyla.

Fast and Young

Type Ia supernovae are thought to result from the thermonuclear explosion of a white dwarf star accreting material from a companion star in a binary system. Their adoption as cosmic yardsticks has led to the discovery of the accelerated expansion of the universe. **Wang et al.** (p. 170, published online 7 March) show that supernovae with higher expansion velocities are located in the central, brighter regions of their host galaxies and are found in larger, more luminous galaxies, suggesting that they are associated with younger stellar populations.

Preparing Pactamycin

Microbially derived organic compounds often have remarkably intricate structures that confer striking bioactivity, but such complexity may

become an impediment to drug development. Pactamycin is one such case—a potent antibiotic used to probe ribosome structure and function that in its native form is too cytotoxic for therapeutic application. **Malinowski et al.** (p. 180; see the Perspective by **Codelli and Reisman**) present a 15-step laboratory-scale synthesis of this molecule that offers prospects for the generation of structural analogs that could facilitate further exploratory medicinal research.

Hide-and-Seek Virus

Human cytomegalovirus (HCMV) establishes latent infection in human progenitor dendritic cells, causing significant morbidity and mortality on reactivation, which may occur in transplantation patients who are immunosuppressed. Neither detection nor selective removal of rare latent HCMV-infected cells has been possible. **Weekes et al.** (p. 199) have found that the multidrug-resistant ABC transporter, multidrug resistance-associated protein-1 (MRP1) is down-regulated during latent HCMV infection. Consequently, cytotoxic MRP1-specific substrates are not exported from HCMV-infected cells and accumulate—leading to cell death, which could potentially provide a mechanism for eliminating infected cells prior to transplantation.

Permafrost Thaw Predictions

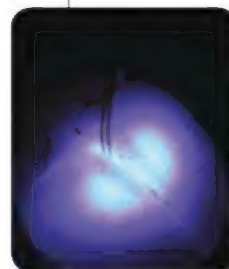
Permafrost contains twice as much carbon as the atmosphere which could have serious consequences if it were to be released by widespread thawing. **Vaks et al.** (p. 183, published online 21 February) present a 450,000 year-long record of speleothem growth at selected locations in Siberia, which traces changes in the extent of permafrost over that time period. The authors conclude that conditions only slightly warmer than those of today would cause widespread thawing of continuous permafrost as far north as 60°N.

Simply Folding

RNA chaperones simplify what would otherwise be complex and slow RNA folding events. **Grohman et al.** (p. 190, published online 7 March) show that the Moloney murine leukemia virus (MuLV) nucleocapsid (NC) protein, which chaperones MuLV RNA dimerization promotes MuLV RNA folding by binding to exposed guanosine bases and destabilizing strong guanosine interactions. With base-pairs being rendered roughly of the same energy, RNA assembly pathways are simplified, promoting proper folding.

The Smaller, the Better

New semiconductor device technology enables injection of light-emitting diodes, silicon devices, actuators, and sensors at precisely controlled locations within biological tissues, such as the brain. **Kim et al.** (p. 211) show how wireless control of animal models using these technologies and the techniques of optogenetics provide new insights into basic behavioral neuroscience.



Music Was My First Love

Why do human beings enjoy music? **Salimpoor et al.** (p. 216) combined behavioral economics with brain scanning to explore how a piece of music is considered rewarding to an individual when it is heard for the first time. They discovered that neural activity in the mesolimbic striatum during listening to a novel piece of music was the best predictor of the money listeners were willing to spend on buying the piece. These observations implicate sensory cortical areas in reward processing, which the authors attribute to the aesthetic nature of the judgment.

AS WE SEE IT, OUR JOB IS TO SIMPLIFY YOURS.

PRODUCTIVITY—WE UNDERSTAND.



Optimizing efficiency in your lab is about to get a little easier with the latest innovations from Tecan. From cutting-edge instrumentation to a better way to train, we know what it takes to help you streamline workflows and boost productivity.

TouchTools™ 3.0

Enjoy simple workflow programming and an easier user experience through a next generation touchscreen interface.

Tecan Academy

Get users up to speed faster and ensure consistent instrument operation with on-demand online training and certification.

Infinite® 200 PRO Multimode Reader With Integrated Incubator

Enhance throughput in cell-based assays with an integrated system that controls sample conditions with a built-in Gas Control Module (GCM™).

Tecan. No matter what your everyday challenges or the goals for your lab ... we understand.

www.tecan.com

The Americas: +1 919 361 5200 **Europe:** +49 79 5194 170 **Asia:** +81 44 556 7311
info@tecan.com





Ralph J. Cicerone is president of the U.S. National Academy of Sciences, Washington, DC. E-mail: naspresident@nas.edu.

An Important Anniversary

ONE HUNDRED FIFTY YEARS AGO, ON 22 APRIL 1863, THE U.S. NATIONAL ACADEMY OF SCIENCES (NAS) held its first meeting. The founding of the academy was but one of an impressive array of federal actions that would prepare the United States of America for a bright future. During the dark days of 1862 and 1863, mired in a bloody and intense Civil War, Congress passed, and President Lincoln signed, the Morrill Act, creating a system of Land Grant Colleges. The Act greatly enhanced access to higher education for Americans and promoted scientific and technical research in the coming generations. In the same period, Congress authorized the completion of the Transcontinental Railroad, and President Lincoln issued the Emancipation Proclamation. Only a few months later, President Lincoln and Congress took another major step to advance the young nation by creating NAS, a bold way to elevate American science and to incorporate science into the U.S. future. This was a remarkable set of government actions during very tough times.

NAS was created as a private nonprofit organization, and yet it was directed to provide scientific analysis and advice to the U.S. government* and to plan new federal agencies whose capabilities would be needed by the government. It is rare for any government to create and respect such an external organization that is independent and not subject to government control. NAS works closely with the National Academy of Engineering (NAE, created in 1964) and the Institute of Medicine (IOM, created in 1970), and their responses to government requests are provided through the jointly governed National Research Council (NRC, created in 1916). These organizations are nonpartisan, and their reports are subjected to rigorous peer review. Receiving no annual appropriations from the federal government, the costs of each project conducted for the federal government are reimbursed one by one. NAS has a very broad mission that includes validating scientific excellence, enhancing the vitality of the scientific enterprise, guiding public policy with science, and communicating the nature, values, and judgments of science to government and the public.† In addition, there are increasingly global roles for the NAS and other science academies.*

The close partnership of NAS, NAE, IOM, and NRC provides a large positive advantage in providing advice and analysis for the government, inasmuch as many questions of public policy require expertise that is much broader than that provided by individual scientific disciplines. In many other nations, the academies of science, engineering, and medicine are completely separate, which makes it more difficult for them to collaborate in addressing critical national issues.

Academy members contribute greatly to the writing of NRC reports, and they also help to identify other excellent researchers to work on these projects. Over 5000 such individuals, most of whom are not members of NAS, NAE, and IOM, serve in these important roles, pro bono, each year. Additionally, nearly 2000 individuals from across science and engineering disciplines serve as independent peer reviewers for the more than 200 reports produced annually. This enormous volunteer resource derives from the creation of NAS in 1863, and these generous contributions of thousands of experts enable and energize the entire enterprise. Looking ahead, I can foresee many further roles for such efforts, as the world confronts and solves science-based problems that involve multiple disciplines.

Today, science and engineering enable society to select major goals and provide the collective wherewithal to achieve them. Sustained efforts are often required to select and achieve such goals. The pro bono contributions of thousands of researchers to NAS's projects deserve great appreciation and respect, as do the parallel efforts of scientists on behalf of many other scientific organizations and educational institutions.

Let us salute the contributions of these individuals and institutions to progress through science.

— Ralph J. Cicerone

10.1126/science.1238209

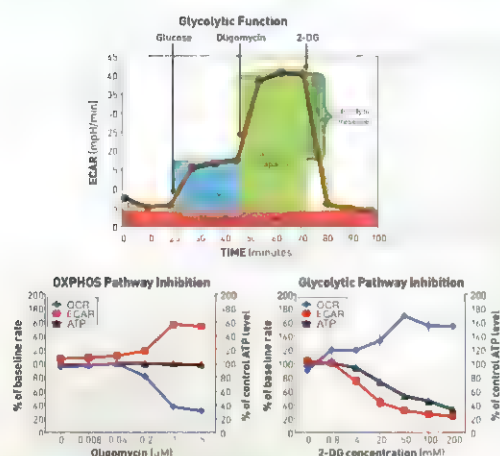


“ WE’RE BRINGING A NEW PERSPECTIVE TO
cancer metabolism research

FIRST WE MADE IT POSSIBLE – NOW WE’VE MADE IT EASY.

XF technology provides the easiest and most comprehensive assessment of cancer cell metabolism, measuring glucose and glutamine metabolism, and fatty acid oxidation of cancer cells in a microplate, in real-time! ”

— David Ferrick, PhD,
CSO, Seahorse Bioscience



The Seahorse XF® Extracellular Flux Analyzer

Measurements of cellular glycolysis are essential to understanding cancer, immune response, stem cell differentiation, aging, and cardiovascular and neurodegenerative diseases. The XF® Analyzer and XF Glycolysis Stress Test Kit make it easy to measure the three key parameters of cellular glycolysis in a microplate: glycolysis, glycolytic capacity, and glycolytic reserve, revealing critical information not evident in mitochondrial respiration measurements alone.



See what's possible.

Scan this QR code to view videos and see what the XF Analyzer can achieve. Visit www.seahorsebio.com/science for more information!

Seahorse Bioscience

MATERIALS SCIENCE

Surfactants on Double Duty

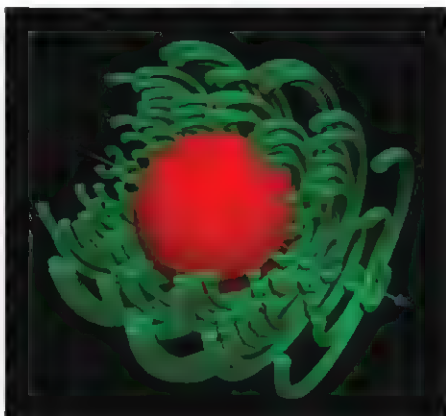
In an emulsion, droplets of one liquid are kept stable within an immiscible second liquid through the use of surfactants; oil-and-water-based salad dressings are a well-known example. Multiple emulsions, comprising multiple shells of the two liquids, are of increasing interest for applications to drug delivery as well as food and cosmetics. However, these emulsions typically need both hydrophobic and hydrophilic surfactants to stabilize the two interfaces. Besnard *et al.* show that a single polymer can be used to modify the curvature of the oil/water interface and thereby promote the phase inversion required to create a multiple emulsion. The material is a diblock copolymer with blocks of polystyrene and a random polymer of styrene and 2-(dimethylamino)ethylmethacrylate monomers (DMAEMA). A change in temperature alters the hydrogen bonds between DMAEMA and water, and thus the hydrophobicity of the polymer. A second phase inversion can also be induced by varying the acidity of the solution within a narrow pH window. Several mixing methods and polymers with different chain lengths were used to generate the emulsions, and in all cases the emulsions showed stability for at least several months. — MSL

Adv. Mater. **25**, 10.1002/adma.201204496 (2013).

PHYSICS

Cloaked in Silence

The daily commute can be a trudge. On top of that, you often have to share, involuntarily, in the irritating noise coming out of the headphones of someone intent on going deaf prematurely. Of course, there are also the more serious safety aspects of protection from sudden and loud noise, as well as the peace and quiet provided by good sound insulation. The ideas developed over the past decade in cloaking



MICROBIOLOGY

Not Just a Human Zoo

Human beings are stewpots of microorganisms influenced by a variety of environmental perturbations to the detriment or enhancement of our health. Humans have penetrated and disturbed nearly all habitats on the planet and in their turn influence the symbioses and pathogens in the wild animals they encounter. For example, Amato *et al.* have discovered that the diversity, richness, and composition of the microbiota of Mexican black howler monkeys correlate with the quality of the habitat they inhabit (and eat). Monkeys living in habitats degraded by human activity have simplified microbiomes displaying fewer genes for butyrate production, implying an impact on the monkeys' overall health. In another example of an anthropogenic perturbation, the health of zoo elephants has been compromised by an emerging, fatal, haemorrhagic herpesvirus disease, which Zachariah *et al.* report also affects working elephants in southern India. It seems that in this case the virus is endemic to Asia and has spread from this focus as humans have spread elephants around the world's zoos. — CA

ISME J. **7**, 10.1038/ismaj.2013.16 (2013); *J. Wildl. Dis.* **49**, 10.7589/2012-07-193 (2013)

an object from view using metamaterials and transformational optics can also be carried to other waveforms, including acoustics. Using such ideas, Sanchis *et al.* have designed and fabricated a three-dimensional (3D) acoustic cloak for airborne sound. Their cloak consists of a series of concentric tori that surround a sphere about 8 cm in diameter. Designed by an optimization algorithm and using a 3D printing method to fabricate the directional cloak, initial characterization shows that they can reduce the scattering cross section of the sphere for sound of 8.55 kHz by some 90%. A design modification should be possible to make the cloak omnidirectional. Perhaps it won't be too long before such a cloak can be incorporated into headphone design to stop sound leaking out. — ISO

Phys. Rev. Lett. **110**, 124301 (2013).

GENETICS

Relying on Our Ancestors

Human populations exhibit differences in linkage disequilibrium, the loss of association between alleles that are located close together on the same chromosome. These differences result in genome-wide association tests—which look for genetic markers associated with a phenotypic trait—finding few significant variants and requiring very large sample sizes. Diversity among linked alleles, such as in people of African descent who on average exhibit more genetic diversity than other populations, helps pinpoint genetic variants associated with traits. Wu *et al.* investigated the genetic architecture of loci as-

Continued on page 123

Rethink Western blotting. Take protein detection to new dimensions.

Biology isn't flat—neither are your Westerns.

Meet the fast, versatile SNAP i.d.® 2.0 system, to fully exploit three-dimensional reagent distribution. Unlike conventional Western blotting, where diffusion is the primary means of reagent transport, the SNAP i.d.® 2.0 system applies a vacuum to actively drive antibodies and buffers right through the membrane. This advanced technology promotes antigen binding and thorough washing, enabling you to better optimize your Western blotting conditions.

www.emdmillipore.com/SNAP



EMD Millipore is a division of Merck KGaA, Darmstadt, Germany

Continued from page 121

sociated with lipids in people of African, Asian, and European descent to elucidate functional variants in lipids among and between populations. Sequential conditional analyses identified complex patterns of variation in previously identified loci within and among populations, as well as novel genotypes associated with lipid levels. Thus, utilizing population structure helps identify the genetic underpinnings of human phenotypic variation. — LMZ

PLoS Genet. 9, e1003379 (2013).

CLIMATE SCIENCE

Where's Warming?

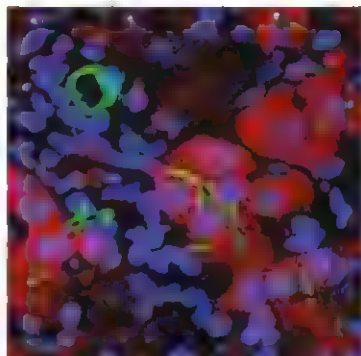
The addition of greenhouse gases to the atmosphere caused by fossil fuel burning and other anthropogenic activity has caused temperatures at the surface of Earth to increase significantly over the past century and a half, and rapidly during the interval from around 1975 until the early years of the 21st century. However, sea surface and surface-air temperatures have not risen over most of the past decade, encouraging some to question the continued reality of global warming, despite the fact that similar variability also can be seen in the instrumental records of the past century. The real question, then, is not whether climate warming has stopped, but where in the earth system the heat resides that would have caused the expected warming? Naturally, the first place to look is in the ocean, because that is where most of the heat taken up due to global warming is stored. Accordingly, Balmaseda *et al.* conducted a reanalysis of changes in the global ocean heat content from 1958 through 2009 and found that much of the warming has occurred below depths of 700 m, rather than in the surface ocean, and that much of that redistribution is due to changes in surface winds over that period. This helps to explain why air temperatures have not reflected this heating and shows that global warming is continuing, but out of our daily reach. — HJS

Geophys. Res. Lett. 10.1002/grl.50382 (2013).

DEVELOPMENT

Following a New Program

As illustrated in Greek mythology, in which an eagle feeds on Prometheus' liver each day, the amazing regenerative properties of the liver have long been known. An intriguing feature of liver regeneration is that it is context-specific: Excising part of the liver results in the growth or proliferation of existing cells, whereas exposure to



toxic agents drives the accumulation of cells that have a biliary phenotype. Yanger *et al.* sought to determine whether cellular plasticity plays a role during liver response to injury and found that indeed it does. Toxin-induced injury of mouse hepatocytes generated cells that had the morpho-

logical, structural, and molecular features of normal biliary epithelial cells (BECs). Similar to BEC development, Notch signaling was required. Normal hepatocytes are binucleated; likewise, so were the BEC-like cells that were generated in response to injury,

which suggests a hepatocyte origin. As cells went through the hepatocyte-to-BEC-like cell transition, they displayed an intermediate state where they co-expressed transcription factors of both cell types. The conversion of adult hepatocytes to BECs may find applicability in treatment of conditions with loss of these cells in humans. — BAP

Genes Dev. 27, 10.1101/gad.207803.112 (2013).

IMMUNOLOGY

Type 2 for Tissue Regeneration

Although we classically think of the immune system as important for warding off foreign invaders, once the invaders are squashed, it sticks around to help pick up the pieces. The specific mechanisms by which the immune system supports tissue repair can differ from tissue to tissue and overall are not very well understood. Heredia *et al.* investigate this in the context of skeletal muscle injury and specifically look at the role of type 2 immunity, which has previously been implicated in tissue repair. The signature type 2 cytokines interleukin (IL)-4 and -13 were up-regulated in response to skeletal muscle injury in mice, and the use of genetically modified mice demonstrated that signaling through the IL-4 receptor was required for muscle repair. Surprisingly, the primary source of IL-4 was eosinophils, not macrophages, which had been shown previously to infiltrate damaged tissue and make IL-4. Within damaged tissues, fibro/adipogenic progenitor cells, which have the potential to give rise to either fibroblasts or adipocytes, responded to IL-4 and were induced to support myogenesis rather than differentiating into adipocytes. Moreover, they were necessary for the clearance of necrotic debris. — KLM

Cell 10.1016/j.cell.2013.02.053 (2013).



At Atlas Antibodies we have a very singular focus. It's the complete human.

From our facilities in Stockholm, Sweden, we manufacture and distribute highly characterized antibodies targeting all human proteins. All of our antibodies are manufactured using a standardized production process to ensure the most rigorous levels of quality.

Working in close partnership with the Human Protein Atlas project, we are looking to complete the systematic exploration of the human proteome using antibodies. Of the possible 20,000 protein coding genes in the human body we already have over 15,000 antibodies covering 13,000 gene products. This is of course supported by millions of images available on our websites.

So, if you're interested in some human dialogue, why not talk with us.

atlasantibodies.com/totallyhuman

ATLAS ANTIBODIES
Totally human

Atlas Antibodies AB Stockholm, Sweden
atlasantibodies.com, proteinatlas.org

**1200 New York Avenue, NW
Washington, DC 20005**

Editorial: 202-326-6550, FAX 202-289-7562
News: 202-326-6591, FAX 202-371-9227

Bateman House, 82-88 Hills Road

Bateman House, 82-88 Hills Road

Bateman House, 82-88 Hills Road

Bateman House, 82-88 Hills Road

Cambridge, UK CB2 1LQ
+44 (0) 1223 326500. FAX +44 (0) 1223 326501

SUBSCRIPTION SERVICES For change of address, missing issues, new orders and renewals, and payment questions: 866 434 AAAS (2227) or 202-326-6417, FAX 202-842-1065. Mailing addresses: AAAS, P.O. Box 96178, Washington, DC 20090 6178 or AAAS Member Services, 1200 New York Avenue, NW, Washington, DC 20005

INSTITUTIONAL SITE LICENSES please call 202-326-6755 for any questions or information

REPRINTS: Author Inquiries 800-635-7181

Commercial Inquiries 803-359-4578

PERMISSIONS 202-326-7074, FAX 202-682-0816

MEMBER BENEFITS AAAS Travels: Betchart Expeditions 800-252-4910; Apple Store www.store.apple.com/us/go/epstore/aaas; NASA Federal 1-888-NASA-FCU (1-888-627-2328) or www.nasa.gov. com; Cold Spring Harbor Laboratory Press Publications www.cshlpress.com/affiliates/aaas.htm; GEICO Auto Insurance www.geico.com/landingpage/go51.htm?logo=17624;Hsd 800-654-2200 CDP#334357; Office Depot <https://bsd.officedepot.com/porta/login.do>; Seabury & Smith Life Insurance 800-424-9883; Subaru VIP Program 202-326-6417, VIP Moving Services www.vipmayflower.com/domestic/index.html; Other Benefits: AAAS Member Services 202-326-6417 or www.aaasmember.org.

science_editors@aaas.org (for general editorial queries)

science_letters@aaas.org
(for queries about letters)

science_reviews@aaas.org (for returning manuscript reviews)

science_bookrevs@aaas.org
(for book review queries)

Published by the American Association for the Advancement of Science (AAAS), *Science* serves its readers as a forum for the presentation and discussion of important issues related to the advancement of science, including the presentation of minority or conflicting points of view, rather than by publishing only material on which a consensus has been reached. Accordingly, all articles published in *Science*—including editorials, news and comment, and book reviews—are signed and reflect the individual views of the authors and not official points of view adopted by AAAS or the institutions with which the authors are affiliated.

AAAS was founded in 1848 and incorporated in 1874. Its mission is to advance science, engineering, and innovation throughout the world for the benefit of all people. The goals of the association are to: enhance communication among scientists, engineers, and the public; promote and defend the integrity of science and its use; strengthen support for the science and technology enterprise; provide a voice for science on societal issues; promote the responsible use of science in public policy; strengthen and diversify the science and technology workforce; foster education in science and technology for everyone; increase public engagement with science and technology; and advance international cooperation in science.

INFORMATION FOR AUTHORS

See pages 716 and 717 of the 8 February 2013 issue or
access www.sciencemag.org/about/authors

SENIOR EDITORIAL BOARD

A. Paul Alivisatos, Lawrence Berkeley Nat'l. Laboratory
Cori Bargmann, The Rockefeller Univ.
Ernst Fehr, Univ. of Zurich
Erin O'Shea, Harvard Univ.
Michael S. Turner, University of Chicago

BOARD OF REVIEWING EDITORS

Adriano Aguzzi, Univ. Hospital Zürich
Takuzo Aida, Univ. of Tokyo
Leslie Aiello, Wenner-Gren Foundation
Sonia Altieri, Univ. of Georgia
Sebastian Amigorena, Institut Curie
Angelika Amos, MPI
Kathryn Anderson, Memorial Sloan-Kettering Cancer Center
Siv G. E. Andersson, Uppsala Univ.
Peter Andolfatto, Princeton Univ.
Meinrat D. Andreae, Max Planck Inst., Mainz
Pao Ariotta, Harvard Univ.
Johann Auerer, EPR
David Awechselblom, Univ. of California Santa Barbara
Ben Barres, Stanford Medical School
Jordi Bascompte, Estación Biológica de Doñana, CSIC
Facundo Batista, London Research Inst.
R. H. Baughman, Univ. of Texas, Dallas
David Baum, Univ. of Wisconsin
Mark Bear, Massachusetts Inst. of Technology
Yasmine Belkaid, NIAID, NIH
Philip Benfey, Duke Univ.
Stephen J. Benke, Penn State State Univ.
Christophe Bernard, Aix-Marseille Univ.
Gregory C. Beroza, Stanford Univ.
Gabriele Bergers, Univ. of California, San Francisco
Peer Bork, EMBL
Bruno Branner, Ecole Normale Supérieure de Lyon
Chris Bowler, Ecole Normale Supérieure
Ian Boyd, Univ. of St. Andrews
Christian Büchel, Universitätsklinikum Hamburg-Eppendorf
Joseph A. Burns, Cornell Univ.
William L. Butz, Population Reference Bureau
Gyöngyi Buzsáki, Harvard Univ., School of Medicine
Miles Carlsson, Univ. of Oslo
Mildred Chao, Stanford Univ.
David Clapham, Children's Hospital, Boston
David Clary, Univ. of Oxford
Jonathan D. Cohen, Princeton Univ.
Robert Cook-Deegan, Duke Univ.
Jane Collins, Boston Univ.
Alan Cowman, Walter & Eliza Hall Inst.
James H. Crabtree, Yale Univ.
Wolfgang Croneck, Univ. of North Carolina
Jeff L. Dapkin, Univ. of North Carolina

Tom Daniel, *Univ. of Washington*
Frans de Waal, *Emory Univ.*
Stanislav Dehaene, *Collège de France*
Robert Desimone, *MIT*
Claude Desplan, *New York Univ.*
Ap Dijksterhuis, *Radboud Univ. of Nijmegen*
Detlev Fischer, *Univ. of Pennsylvania*
Gerald W. Dorn II, *Washington Univ. School of Medicine*
Jennifer A. Doudna, *Univ. of California, Berkeley*
Julian Downward, *Cancer Research UK*
Bruce Dunn, *Univ. of California, Los Angeles*
Christopher Dye, *WHO*
David Ehrhardt, *Carnegie Inst. of Washington*
Tim Elston, *Univ. of North Carolina at Chapel Hill*
Gerhard Ertl, *Fritz-Haber-Institut, Berlin*
Barry Everitt, *Univ. of Cambridge*
Paul C. Falkowski, *Rutgers Univ.*
Ernst Fehr, *Univ. of Zurich*
Tom Fenchel, *Univ. of Copenhagen*
Michael Fehr, *The George Washington Univ.*
Alain Fischer, *INSERM*
Simon Fiske, *Princeton Univ.*
Anne C. Ferguson-Smith, *Univ. of Cambridge*
Peter Fratzl, *Max Planck Inst.*
Elena Fuchs, *Rockefeller Univ.*
Ulfrum Gerstner, *EPFL Lausanne*
Andrew Gewirth, *Univ. of Illinois*
Karl-Herz Glassmeier, *70 Braunschweig*
Elizabeth Grove, *Univ. of Chicago*
Kip Guy, *St. Jude's Children's Research Hospital*
Takuyuki Han, *Univ. of Illinois at Urbana-Champaign*
Christian Haas, *Ludwig Maximilians Univ.*
Stefan Hanebeck, *Fred Hutchinson Cancer Research Center*
Gregory I. Hannos, *Cold Spring Harbor Lab.*
Martin Heilmann, *Max Planck Inst., Jena*
Ysa Helariutta, *Univ. of Finland*
Isaac Held, *NCAR*
James A. Hendler, *Rensselaer Polytechnic Inst.*
Janet G. Hering, *Swiss Fed. Inst. of Aquatic Science & Technology*
Ray Hiborn, *Univ. of Washington*
Michael E. Himmel, *National Renewable Energy Lab.*
Klaus Hinrichs, *Univ. of Bremen*
Kiel Hirose, *Tokyo Inst. of Technology*
David Hodell, *Univ. of Cambridge*
David Holden, *Imperial College*
Lora Hoopes, *UT Southwestern Medical Ctr at Dallas*
Jens Hübner, *EPFL Lausanne*
Thomas Hudson, *Ontario Inst. for Cancer Research*
Ray Huey, *Univ. of Washington*
Steven Jacobsen, *Univ. of California, Los Angeles*
Kai Johnson, *EPFL Lausanne*
Peter Jonas, *Universität Zürich*
Matth. Karleberlein, *Univ. of Washington*

William Kaelin Jr., Dana-Farber Cancer Inst.
Daniel Kahne, Harvard Univ.
Daniel Kammien, Univ. of California, Berkeley
Joel Kingsolver, Univ. of North Carolina at Chapel Hill
Robert Kingston, Harvard Medical School
Robert Kolter, Harvard Medical School
Alberto R. Kornblum, Universidad de Buenos Aires
Leonid Kruglyak, Princeton Univ.
Thomas Langer, Univ. of Cologne
Mitchell A. Lazar, Univ. of Pennsylvania
David Lazer, Harvard Univ.
Virginia Lee, Univ. of Pennsylvania
Ottoline Leyser, Cambridge Univ.
Marcia C. Linn, Univ. of California, Berkeley
Jiangsu Liu, Michigan State Univ.
Luis Lis-Marzan, CIB DiomaGUNE
Jonathan Lissac, Harvard Univ.
Ke Lu, Chinese Acad. of Sciences
Christian Lüscher, Univ. of Geneva
Laura Mackesy, CRUK Beaton Inst. for Cancer Research
Anne Magurran, Univ. of St. Andrews
Olivier Martin, CIBC & Univ. of Toronto
Charles Marshall, Univ. of California, Berkeley
Chris Marshall, Inst. of Cancer Research
Martin M. Matzuk, Baylor College of Medicine
C. Robertson McClung, Dartmouth College
Graham Medley, Univ. of Warwick
Yasushi Miyasita, Univ. of Tokyo
Richard Morris, Univ. of Edinburgh
Edvard Moser, Norwegian Univ. of Science and Technology
Seun Munro, MRC Lab. of Molecular Biology
Thomas Murray, The Hastings Center
Wito Nagasawa, Univ. of Tokyo
James Nelson, Stanford Univ. School of Med.
Daniel Neumark, Univ. of California, Berkeley
Stuart Newman, New York Medical College
Timothy W. Nilsen, Case Western Reserve Univ.
Pär Nordlund, Karolinska Univ. Hospital
Helga Nowotny, European Research Advisory Board
Luke O'Neill, Trinity College, Dublin
Stuart Newman, New York Medical College
N. Phuan Ong, Princeton Univ.
Joe Orantze, Univ. of California, Berkeley & Lawrence
Berkeley National Lab.
Harry Orr, Univ. of Minnesota
Andrew Oswald, Univ. of Warwick
Steve Palombi, Stanford Univ.
John Parker, MRC Centre for Plant Breeding Research
Donald R. Paul, Univ. of Texas at Austin
P. David Pearson, Univ. of California, Berkeley
John H. J. Petrini, Memorial Sloan-Kettering Cancer Center
Simon Philpott, Univ. of Florida
Joshua Plotkin, Univ. of Pennsylvania
Phillippe Pollet, CNRS

Colin Renner, *Univ. of Cambridge*
 Trevor Robbins, *Univ. of Cambridge*
 Jim Roberts, *Fred Hutchinson Cancer Research Ctr*
 Barbara A. Romanowicz, *Univ. of California, Berkeley*
 Jens Rosendorp-Nielsen, *Haldor Tøpsoe*
 Miles Ryan, *Univ. of Texas, MD Anderson*
 Shimon Sakaguchi, *Kyoto Univ.*
 Miguel Salmeron, *Lawrence C Berkeley National Lab*
 Jürgen Sandkühler, *Medical Univ. of Vienna*
 Alexander Schier, *Harvard Univ.*
 Ramon Seeley, *Univ. of Cincinnati*
 Vladimir Shalaev, *Purdue Univ.*
 Joseph Silk, *Institut d'Astrophysique de Paris*
 Denis Simon, *Arizona State Univ.*
 Alison Smith, *John Innes Centre*
 Doree Sofer, *State Univ. of Medical Biology, Singapore*
 Peter Sörger, *Harvard Medical School*
 John Speakman, *Univ. of Aberdeen*
 Allan C. Spradling, *Carnegie Institution of Washington*
 Jonathan Sprent, *Garnav Institute of Medical Research*
 Paul T. St. John, *State Univ. and National Bureau of Economic Research*
 Elveth Stern, *ETH Zürich*
 V. S. Subrahmanian, *Univ. of Maryland*
 Ira Tabas, *Columbia Univ.*
 Yoshiko Takahashi, *Kyoto University*
 Sarah Teichmann, *Cambridge Univ.*
 John Thomas, *Duke Univ.*
 Herbert Virsik, *Washington Univ.*
 Bert Vogelstein, *Johns Hopkins Univ.*
 Cynthia Volkert, *Univ. of Göttingen*
 Bruce D. Walker, *Harvard Medical School*
 Douglas Wallace, *Dalhousie Univ.*
 Ian Walmsey, *Univ. of Oxford*
 David Wardle, *State Univ. of Agric Sciences*
 David Waxman, *Fudan Univ.*
 Jonathan Weissman, *Univ. of California, San Francisco*
 Kathy Willis, *Oxford Univ.*
 Ian A. Wilson, *The Scripps Res. Inst.*
 Timothy D. Wilson, *Univ. of Virginia*
 Rosemary Wyse, *Johns Hopkins Univ.*
 Jan Zaenen, *Leiden Univ.*
 Kenneth Zaret, *Univ. of Penn. School of Medicine*
 Jonathan Zehr, *Univ. of California, Santa Cruz*

BOOK REVIEW BOARD

BOOK REVIEW BOARD
John Aldrich, *Duke Univ.*
David Bloom, *Harvard Univ.*
Angela Creager, *Princeton Univ.*
Richard Swedner, *Univ. of Chicago*
Ed Wasserman, *DuPont*
Lewis Wolcott, *Univ. College London*

FULFILLMENT SYSTEMS AND OPERATIONS (membership@aaas.org), CUSTOMER SERVICE SUPERVISOR Pat Butler; SPECIALISTS LaToya Casteel, Michelle Ofordire, April Marshall; MANAGER, DATA ENTRY Mickie Napoleoni; DATA ENTRY SPECIALISTS Il Regan, Jaimee Wise, Fiona Giblin

BUSINESS OPERATIONS AND ADMINISTRATION DIRECTOR Deborah Rivera Wienhold.
BUSINESS SYSTEMS AND FINANCIAL ANALYSIS DIRECTOR Randy Yi; **SYSTEMS ANALYST** Nicole Mehmedovich; **MANAGER, BUSINESS ANALYSIS** Eric Knott; **MANAGER, BUSINESS OPERATIONS** Jessica Tierney; **BUSINESS ANALYSTS** Cory Lipman, Celeste Troxler; **FINANCIAL ANALYST** Jeremy Clay; **RIGHTS AND PERMISSIONS:** wwwrights@emilias.com; Emilia.Rivera@emilias.com; Elisabeth.Sandberg@emilias.com

ADMINISTRATOR Emille Davis; ASSOCIATE Elizabeth Sandler; MARKETING DIRECTOR Ian King; MARKETING MANAGERS Alison Chandler, Julianne Wielga, Justin Sawyers; MARKETING ASSOCIATES Mary Ellen Crowley, Elizabeth Sattler, Rebecca Rifkin, SENIOR MARKETING EXECUTIVE Jennifer Reeves; DIRECTOR, SITE LICENSING Tom Ryan; DIRECTOR, CORPORATE RELATIONS Eileen Bernadette Moran; SENIOR PUBLISHER RELATIONS SPECIALIST Kiki Forsythe; PUBLISHER RELATIONS MANAGER Catherine Holland; PUBLISHER RELATIONS, EASTERN REGION Keith Layson, PUBLISHER RELATIONS, WESTERN REGION Ryan Rexroth; CUSTOMER RELATIONS MANAGER Iquo Edim; CUSTOMER RELATIONS ANALYSTS Simon Chong, Lana Guz; MARKETING MANAGER Christina Schlecht; MARKETING ASSOCIATES Paulina Curto, Mitchell Edmund; ELECTRONIC MEDIA DIRECTOR Lizabeth Harman; ASSISTANT MANAGER Lisa Stanford, PRODUCTION SPECIALISTS Antonette Hoda, Nichole Johnston, Lori Murphy, Kimberly Oster; WEB AND NEW MEDIA SENIOR PROJECT MANAGER Trista Smith, PROJECT LEADER Luke Johnson COMPUTER SPECIALISTS Walter Jones, Kan Zhang, WEB DEVELOPER Chris Coleman; PROGRAM DIRECTOR, AAAS MEMBER CENTRAL Peggy Mihelich

DIRECTOR, GLOBAL COLLABORATION, CUSTOM PUBLICATIONS, ADVERTISING Bill Moran
EDITOR, CUSTOM PUBLISHING Sean Sanders: 202-326-6430
ASSISTANT EDITOR, CUSTOM PUBLISHING Tianna Hicklin 202-326-6463
ASSOCIATE DIRECTOR, COLLABORATION, CUSTOM PUBLICATIONS/CHINA/TAIWAN/KOREA/
SINGAPORE Ruolei Wu +86-1367-101-5294

PRODUCT (science.dvtrtsing@aas.org), **MIDWEST** Rick Bongiovanni: 330-405-7080, FAX 330-405-7081; **EAST COAST/E.** CANADA Larry Faraday: 508-747-9395, FAX 617-507-8189; **SOUTH COAST/W.** CANADA Lynne Stickrod: 415-931-9782, FAX 415-920-6940; **UN EUROPE/ASIA** Roger Gonca-ve: TEL/FAX +41 43 243 1358; **JAPAN**, Makiko Hara +81 (3) 6802 4616, FAX +81 (3) 6802 4615; **ads@sciencemag.jp**, **CHINA/TAIWAN** R.Jolet Wu: +86 1367.1015.294 rwu@aas.org

WORLDWIDE ASSOCIATE DIRECTOR OF SCIENCE CAREERS Tracy Holmes: +44 (0) 1223 326525. FAX +44 (0) 1223 326532

CLASSIFIED (advertise@sciencecareers.org); U.S./CANADA/SOUTH AMERICA
Tina Burks: 202-326-6577; SALES ADMINISTRATOR Marci Gallun.

EUROPE/ROW SALES Lucy Nelson; SALES ASSISTANT Kelly Garg; JAPAN Yuki Kobayashi +81 (0)90-9110-1719; careerads@sciencemag.org;
CHINA/TAIWAN Ruolei Wu: +86 1367 1015 294 fwu@aaas.org;
ADVERTISING SUPPORT MANAGER Karen Foote. 202-326-6740; ADVERTISING
PRODUCTION OPERATIONS MANAGER Deborah Tompkins; SENIOR PRODUCTION
SPECIALIST/GRAPHIC DESIGNER Amy Hardcastle; PRODUCTION SPECIALIST
Yusef Lajrimumhup; SENIOR TRAFFIC ASSOCIATE Christine Hall; SALES
COORDINATOR Shirley Young; MARKETING MANAGER Allison Pritchard; MARKETING
ASSOCIATE Amee Aponte

AAAS BOARD OF DIRECTORS RETIRING PRESIDENT, CHAIR William H. Press; PRESIDENT Philip A. Sharp; PRESIDENT-ELECT Gerald R. Fink; TREASURER David Evans Shaw; CHIEF EXECUTIVE OFFICER Alan I. Leshner; BOARD Bonnie L. Bassler, May R. Berenbaum, Claire M. Fraser, Elizabeth Loftus, Stephen L. Mayo, Raymond Orbach, Sue V. Rosser, Inder M. Verma



Little Genius

A woman with curly brown hair, wearing a white lab coat over a black shirt and grey pants, stands against a yellow background. She is holding a small, white, rectangular device with a blue screen and a blue cap, which is the BLItz assay system. The device has the BLItz logo on it.

BLItz

BLItz brilliantly packs the power of Dip and Read™ label-free analysis into a personal assay system. Give BLItz a drop of your sample and it does the rest!

- Protein presence/absence in seconds
- Binding kinetics assays at your bench
- Protein quantitation in seconds
- Develop immunoassays in minutes
- Easily analyze crude samples

Cleverly priced under \$20K so you can have your own little genius.

Want to try BLItz in your lab? Visit BlitzMeNow.com or call 855.BLITZ.ME.

fortéBIO
A Division of **Pall Life Sciences**

PALL Life Sciences

AROUND THE WORLD



Washington, D.C. 1

Rallying Against Research Cuts

Thousands of scientists and patient advocates poured into a square in downtown Washington, D.C., earlier this week in what organizers called the largest-ever rally to call for more funding for biomedical research. The event, which drew many researchers who were in town for the annual meeting of the American Association for Cancer Research (AACR), highlighted the 5% cut to the National Institutes of Health's (NIH's) \$31 billion budget imposed by Congress last month through sequestration, as well as the flat growth of NIH's budget over the past decade.



AACR attendees and others from more than 200 supporting organizations chanted "more progress, more hope, more life" and listened for nearly 2 hours as members of Congress, patient advocates, and celebrities spoke in support of increasing NIH's budget. Emcee Cokie Roberts of ABC News and NPR declared that "it could not be a stupider time to cut back on funding for medical research." The event was "historic and really unprecedented," said AACR CEO Margaret Foti. For a while, she added, tweets with the

rally's tag #RallyMedRes were second to only tweets about former U.K. Prime Minister Margaret Thatcher's death.

Washington, D.C. 2

Next Up for NASA: Exoplanets And Neutron Stars

NASA's Astrophysics Explorer Program on 5 April announced it has selected two missions—an exoplanet-hunting satellite and an instrument to study neutron stars—for launch in 2017. The Transiting Exoplanet Survey Satellite (TESS) will use wide-field cameras to survey the brightest stars in the sun's neighborhood, searching

for gas giants and terrestrial planets, particularly those that are Earth-sized. Those planets, researchers hope, could be candidates for follow-up studies of their atmospheres by the James Webb Space Telescope, scheduled for launch in 2018.

The Neutron Star Interior Composition Explorer (NICER), which will be deployed on the International Space Station, will observe x-rays flashed by neutron stars, helping researchers understand the nature of matter contained in these dense, spinning objects that result from the collapse of massive stars. TESS will get up to \$200 million, and NICER will receive up to \$55 million.

Klamath River, California and Oregon 3

Klamath Dams Should Go, Interior Dept. Says

Remove four aging dams along the Klamath River in northern California and southern Oregon, the U.S. Department of the Interior advised in an environmental impact state-



Worth a dam. The Copco 1 Dam is one of four dams recommended for removal to restore salmon habitat.

ment (EIS) released last week. The dams, completed between 1918 and 1962, block salmon migration and raise water temperatures and algae levels, changes that also lower salmon survival.

Habitat restoration and sediment removal, together with the dams' demolition, would cost about \$1 billion. But that's cheaper than the other three options that the EIS panel considered, which leave some or all of the structures in place. If the dams remain, the operators will be required to pay for maintenance and upgrades, including installing expensive new fish ladders.

The EIS was carried out as part of the Klamath Hydroelectric Settlement Agreement (KHSAs), an agreement reached in 2010 by 40 stakeholder groups—including the states of California and Oregon as well as three Native American tribes—to determine

NOTED

>After years of pressure, Swiss drug company Roche says it will release all of its clinical trial data on Tamiflu, a controversial anti-influenza drug stockpiled by many nations despite some claims that there is not enough evidence of its efficacy. But some scientists remain skeptical, wondering what Roche might redact.

CREDITS (TOP TO BOTTOM): JEFF BARNARD/AP PHOTO; C. SMITH/SCIENCE

whether removing the dams would restore salmon fisheries. KHSA also requires authorization by Congress before the dams can be removed. But there is now little momentum for such legislation on Capitol Hill.

Ottawa 4

Canada to Investigate Alleged Muzzling of Scientists

Since Stephen Harper was sworn in as Canada's prime minister in February 2006, reporters and government scientists have bristled at the government's restrictions on communications with the press and public. On 27 March, Information Commissioner Suzanne Legault confirmed that she has opened an investigation into whether scientists in seven government departments are being muzzled by senior politicians.

The government's policy, which it says is to ensure that government employees speak with "one voice," requires federal civil servants and scientists to get permission for press interviews from their minister or the Privy Council Office (Harper's central shop) and that questions be submitted in advance. The Department of Fisheries and Oceans also recently required department scientists to get approval from senior officials before publishing papers.

Critics contend that these policies are tantamount to a gag order, and in February, two groups—the Environmental Law Centre at the University of Victoria and Democracy Watch, a nonpartisan group that advocates for government accountability—asked Legault to investigate. The timeline on Legault's investigation, or whether a final report will be submitted to Parliament, is unclear. <http://scim.ag/Canmuzz>

Abu Dhabi 5

Camel Connection To New Coronavirus?

Scientists in Germany are hoping that a camel owned by a man from the United Arab Emirates who died in Munich on 26 March will give them clues to the origins of a new coronavirus that has killed 11 people so far. The patient, a wealthy 73-year-old man from Abu Dhabi, was



Hump hypothesis. An nCoV patient from Abu Dhabi had been in close contact with a sick racing camel.

taken to the Klinikum Schwabing in Munich on 19 March and was confirmed to suffer from the new virus, nCoV, 4 days later (*Science*, 5 April, p. 17).

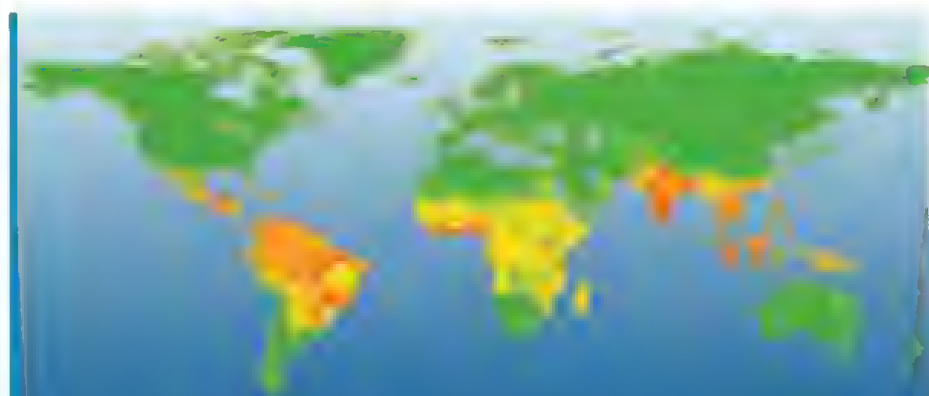
The patient owned racing camels and had been in close contact with a sick camel shortly before he fell ill, says Clemens Wendtner, a physician at the Munich hospital; a male relative also became sick after contact with the same camel. Researchers from the group of Christian Drosten, a viro-

THEY SAID IT

"[T]he secretary's action was politically motivated, scientifically unjustified, and contrary to agency precedent."

—Judge Edward Korman of the Eastern District of New York, slamming a 2011 decision by U.S. Department of Health and Human Services Secretary Kathleen Sebelius to prevent younger teenagers from accessing the emergency contraceptive Plan B without a prescription. Korman ruled last week that Plan B should be available over the counter to women of all ages.

ologist at the University of Bonn, are planning to travel to the United Arab Emirates to take samples from the camel, Wendtner says, to find out if it was infected with nCoV. Previous anecdotal reports had linked the virus to livestock, but so far, its origins remain a mystery. <http://scim.ag/CamelCor>



Dengue More Prevalent Than Thought

There is no current vaccine for dengue, a mosquito-borne viral disease so painful that it's sometimes called "breakbone fever." To keep it in check—through mosquito control and vaccination campaigns—planners have to know where the disease is. Now, a new study estimates that there are 390 million global cases of dengue (pictured)—several times the World Health Organization's estimates.

Jeremy Farrar, a clinician at the University of Oxford Clinical Research Unit in Ho Chi Minh City, Vietnam, and epidemiologist Simon Hay of the University of Oxford in the United Kingdom compiled 8300 reports of dengue infections and considered new evidence on risk factors, such as population growth in urban areas where the virus-carrying *Aedes aegypti* mosquito thrives. Using new modeling techniques, they concluded that in 2010, dengue sent 96 million people to clinics or caused them to miss school or work, while another 294 million had mild or asymptomatic infections, the researchers reported online on 7 April in *Nature*. <http://scim.ag/moredengue>

FINDINGS

On Twitter, #Antivaccination Goes Viral

When fear goes viral on the Internet, it can help spread viruses in the real world. Antivaccination tweets, researchers find, spread much faster than those supportive of vaccines.

Biologist and computer scientist Marcel Salathé and colleagues at Pennsylvania State University, University Park, collected almost half a million vaccine-related tweets during the 2009 influenza pandemic and categorized those relevant to flu as positive, negative, or neutral. (Undergrads rated the first 47,143 tweets; then an algorithm took over.) Negative tweets were often retweeted,

while positive ones generally weren't, the team reported in a paper published online on 4 April in *EPJ Data Science*. Instead, too much positive sentiment appeared to backfire: Twitter users who received many provaccine tweets sent out more negative messages themselves. Perhaps some held antivaccination views that they didn't express "until they were bombarded with positive messages," Salathé says.

"We are more compelled by fear than by rational thinking," says Paul Offit, director of the Vaccine Education Center at The Children's Hospital of Philadelphia in Pennsylvania. To reach the public, vaccine advocates may have to go negative themselves, he adds—for instance, by tapping into people's fear of losing a child.

Random Sample

Game of Habitable Zones

In the world of *Game of Thrones*, summer can last for years, winter for a generation. Fans have long debated the reason for these unpredictable seasons—and now astronomers at Johns Hopkins University in Baltimore, Maryland, offer a hypothesis: The show's setting may be a world that orbits two stars instead of one.

On this hypothetical planet, years last 700 days, and the two sunlike stars orbit each other every 100 days. This complicated dance results in erratic seasons, with winters that can last any-

where from 600 to 850 days. Because the orbit is a three-body problem, predicting the length of the seasons in advance would be impossible for the computerless maesters of Westeros. "With heavy hearts, we conclude that our attempts to provide the good folks of Westeros with a reliable weather forecast are inconclusive," the authors wrote in a paper posted on the arXiv server on 1 April.

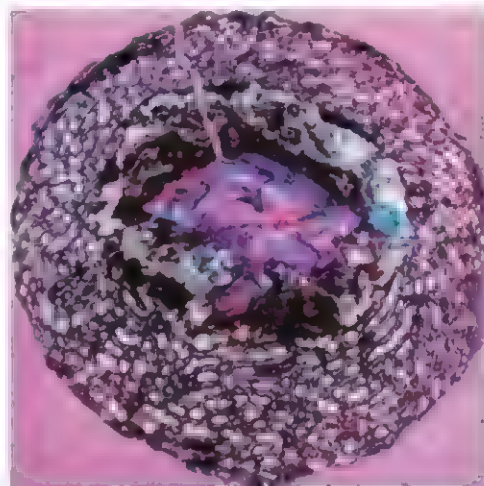
Other earth scientists are skeptical. The pattern of winters and summers plotted in the paper "doesn't quite seem chaotic enough" to cause the turmoil observed in Westeros, says Stephen Kane, an astronomer at the California Institute of Technology in Pasadena who has studied the habitable zones of exoplanets in such circumbinary orbits. He suggests injecting a bit more chaos by introducing a third star to the system or reimagining the planet as an exomoon orbiting a gas giant. Still, this paper "is on the right path to providing a purely physical explanation" of the Westerosi seasons, he says. "Of course, if there's magic involved, all bets are off."



Kit Harington as Jon Snow on *Game of Thrones*.

Tiny Bones, Giant Dinosaurs

Nearly 200 million years ago, one species of sauropodomorph—those long-necked, herbivorous dinosaurs known to grow to great sizes—nested its eggs at a site near what has become southern China's Yunnan Province. Periodically, the nests were destroyed by floods, washing away all but some of the eggs and the tiny bones they contained.



Today, this rare jumble of embryonic bones—some as thin as pencil lead—gives an unprecedented look at dinosaur embryos at various stages of development. Examining cross-sections of 24 different femurs from the species (probably of the genus *Lufengosaurus*), a team led by paleontologist Robert Reisz of the University of Toronto, Mississauga, in Canada observed a high proportion of vascular space inside the bones (pictured), indicating that these embryos grew extremely quickly—faster than any other known dinosaur and all living birds. This rapid embryonic development may have been the key to adult sauropodomorphs' towering physiques, the team reports online this week in *Nature*.

The bone bed is a "spectacular find," because it offers a look at how the species grew over time, something no single embryo can do, says Luis Chiappe, a vertebrate paleontologist at the Natural History Museum of Los Angeles County in California.

Science LIVE

Join us on Thursday, 18 April, at 3 p.m. EDT for a live chat on **genetic privacy**. How safe is your genome? <http://scim.ag/science-live>

CREDITS (TOP TO BOTTOM): A. LEBLANC, HELEN SLOAN/HBO



INFLUENZA

New Flu Virus in China Worries and Confuses

As many an influenza researcher has observed, the virus that they study is predictably unpredictable. But when a bird flu virus makes the jump to people, it's easy to predict how humans will react: Pandemic jitters will reverberate around the world, media will scrutinize the actions of public officials, and investigators will begin racing to answer questions about the virus's origins, spread, and potential threat.

The scenario unfolded again after China's National Health and Family Planning Commission announced on 31 March that a bird flu virus, designated H7N9, had infected three humans, killing two of them. But so far, researchers are guardedly optimistic: There is no persuasive evidence that the virus spreads between people, an ability it would need to set off the next flu pandemic. On 9 April, as *Science* went to press, a steady trickle of Chinese government reports had confirmed 28 cases and eight deaths.

The Chinese government has won praise for aggressively pursuing this outbreak and openly discussing its findings (see sidebar, p. 130). Chinese officials have monitored the health of more than 600 close contacts of confirmed cases—the earliest of whom became ill in mid-February—and have not found infections. “So far, there's no human-to-human transmission—that's the good news,”

says virologist Ab Osterhaus of Erasmus MC in Rotterdam, the Netherlands. “If it would have been there, you would probably have seen it by now.”

Part of the bad news is that it remains a mystery how the confirmed cases became infected. H7N9 influenza viruses are not often detected in birds, notes Robert Webster, an influenza researcher at St. Jude Children's Research Hospital in Memphis, Tennessee. “We rarely ever find the damn thing,” he says. In 2003, the Netherlands had an outbreak in humans of a related bird flu strain, H7N7; but that virus came to light because it readily killed chickens and then mainly caused mild eye problems, such as conjunctivitis, in humans. China has not reported any H7N9-related disease in commercial poultry. “The most important thing now is the Chinese have to do whatever they can to find the origin,” Osterhaus says.

On 5 April, China's Ministry of Agriculture reported that pigeon and chicken samples from two poultry markets in Shanghai, home to about half the confirmed cases, tested positive for H7N9. The National Avian Flu Reference Laboratory sequenced the virus's genome and said it was very similar to the sequences of human isolates. Officials culled some 98,000 poultry and subsequently stopped the sale of live birds at city markets.

Bird culls. Health officials killed nearly 100,000 poultry in Shanghai markets after finding H7N9-infected birds there.

Nanjing and Hangzhou, large cities a few hundred kilometers away affected by the outbreak, closed poultry markets, too. Some, but not all, of the human cases had known contact with poultry.

In early media reports, pigs had come under suspicion as a potential source. In March, bloggers revealed that thousands of dead pigs were washing up on the shores of the Huangpu River, which flows through Shanghai. Avian influenza viruses readily infect pigs, but the Shanghai Animal Disease Prevention and Control Center has reported that it tested 34 carcasses and none had the virus. Jürgen Richt, a swine flu researcher at Kansas State University, Manhattan, notes that 34 samples isn't very many and that influenza RNA may have become degraded during the trip downriver. “Pigs could be positive even if they test negative,” Richt says. Still, he thinks that the pig origin hypothesis is “highly speculative,” in part because other flu strains that are lethal in humans cause little disease in swine.

The clearest evidence so far about the origin of H7N9 comes from its genes. Richt's lab and several others began studying the sequences of H7N9 viruses from human cases immediately after China made them available. Type A influenza viruses like this one have a genome made up of eight RNA segments containing 11 genes coding for 11 proteins, including hemagglutinin and neuraminidase, which stick out from the viral surface. (They are the “H” and “N” in the names of influenza subtypes.) Comparisons with known influenza sequences show that all of the genes in the new virus closely resemble ones found in avian flu strains. But this H7N9 is a mashup, or “reassortant,” of several such strains.

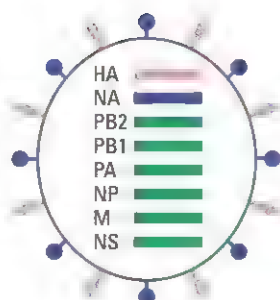
The genes that code for the proteins inside of the H7N9 virus closely match genes from H9N2 isolates recently found in chickens, pigeons, and bramblings (a type of finch) in China. H9N2 is a “totally benign virus,” Webster says, and “is in every big chicken house from China to Israel to Germany.” The H7, in contrast, appears similar to an H7N3 found in Chinese ducks 2 years ago, while the N9 has ties to H1N1 viruses found in ducks and wild birds in Europe and Asia.

Adding to the confusing backstory are mutations in H7N9 genes that suggest how the strain enters and sickens humans. Avian influenza typically doesn't affect humans because

receptors on our cells do not allow bird viruses to attach to them. But three of the first four human H7N9 isolates had mutations in what's known as H7's receptor binding site, allowing it to infect mammals, says Michael Shaw of the Centers for Disease Control and Prevention in

Atlanta. Researchers found another mutation in the *PB2* subunit of influenza's polymerase enzyme that's also known to help the virus thrive in mammals. In addition, H7N9 has a deletion in the neuraminidase gene that researchers typically find in domestic chickens and quail. "It looks like this virus has been in multiple hosts, and it's a real detective story to figure out which paths it has gone through to get to this point," Shaw says.

Richard Webby, another influenza researcher at St. Jude in Memphis, says a central mystery is whether humans became infected with H7N9s that had mammalian



HA: related to H7N3 viruses in ducks in China, 2011
 NA: related to H11N9 viruses in ducks and wild birds in Eurasia, 2010 and 2011
 Internal genes: related to H9N2 viruses found in China, 2011 and 2012

Origin clues. Sequences of eight RNA segments from human H7N9 isolates show close ties to different bird viruses.

adaptations—which would suggest the virus has been circulating in mammals for some time—or whether those variations occurred after the virus replicated in their bodies. "I don't think we've seen quite these many changes upon infection, but it is possible," Webby says. Either way, the changes are "worrying," he says.

The World Health Organization announced plans to work with partner countries to begin development of an H7N9 vaccine for humans, although whether that ever moves into large-scale production may depend on how readily the virus spreads. The

few known cases so far may be the tip of an iceberg: Researchers will have to screen for antibodies to H7N9 in large numbers of people, which might reveal that many had mild or no disease.

Richt says that he and his colleagues urgently need isolates of the virus to begin testing its effects in various species, including chickens, pigs, monkeys, and ferrets. Maybe the virus readily infects pigs and spreads between them, making swine an important reservoir. Maybe it reduces egg production in hens or weight in broilers, which would help identify infected flocks and rapidly contain spread. Animal studies can also clarify the likelihood of airborne transmission in mammals; Osterhaus and his colleagues last year caused an international ruckus when they published ferret experiments that showed how easily this could happen with a different bird flu virus that has jumped into humans (*Science*, 22 June 2012, p. 1494). "A lot of work needs to be done," Osterhaus says. "We have to take this seriously." —JON COHEN

With reporting by Kai Kupferschmidt and Mara Hvistendahl.

A Decade After SARS, China's Flu Response Wins Cautious Praise

SHANGHAI—Coming at the 10-year anniversary of the SARS outbreak, the Chinese government's announcement that a new influenza virus is killing people elicited suspicion from many Chinese. Why, some asked, did it take nearly 6 weeks after the first patient fell ill for the government to identify the H7N9 virus? And was there a connection to the thousands of dead pigs floating in Shanghai's Huangpu River?

But many scientists say that, while there are plenty of questions surrounding the new virus (see main story, p. 129), China has actually come a long way when it comes to monitoring health and has been forthcoming with the international health community—a sharp contrast with the SARS episode, when it was unable to identify the new pathogen and tried to sweep a deadly epidemic under the rug (*Science*, 15 March, p. 1264).

Reporting of the virus's initial discovery, and subsequent cases, appears to have been timely, says virologist Malik Peiris of the University of Hong Kong. "One should not underestimate the work and challenge" in identifying, confirming, and double-checking a new influenza strain, Peiris says. "The Chinese are getting out information as fast they can," adds virologist Robert Webster of St. Jude Children's Research Hospital in Memphis, Tennessee.

SARS was a turning point, says Yanzhong Huang, a global health fellow at the Council on Foreign Relations in New York City. "In the post-SARS era, the central health authorities have become more transparent in sharing disease-related informa-

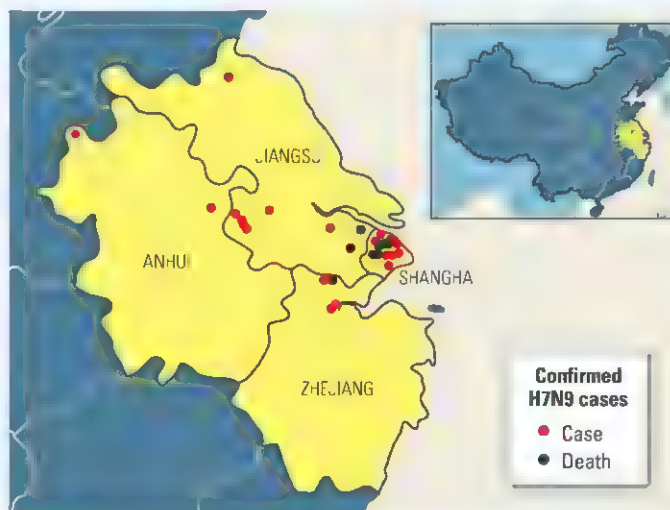
tion with the international community," Huang says. China has also boosted public health funding, set up a comprehensive disease prevention and control system, established a task force to combat avian influenza, and set up hundreds of monitoring stations for animal disease.

But China's Ministry of Agriculture—which will be critical in tracing H7N9's animal origins—remains a weak link. In 2006, the ministry was slow to share virus samples from poultry with the international community after researchers found a new strain of H5N1 in birds in six provinces (*Science*, 10 November 2006, p. 905). Now, there is again concern that the ministry "might not be very enthusiastic" to share with foreign labs, Huang says. Current regulations require Chinese scientists to get the ministry's permission to collect and study avian flu samples, effectively limiting research to three labs.

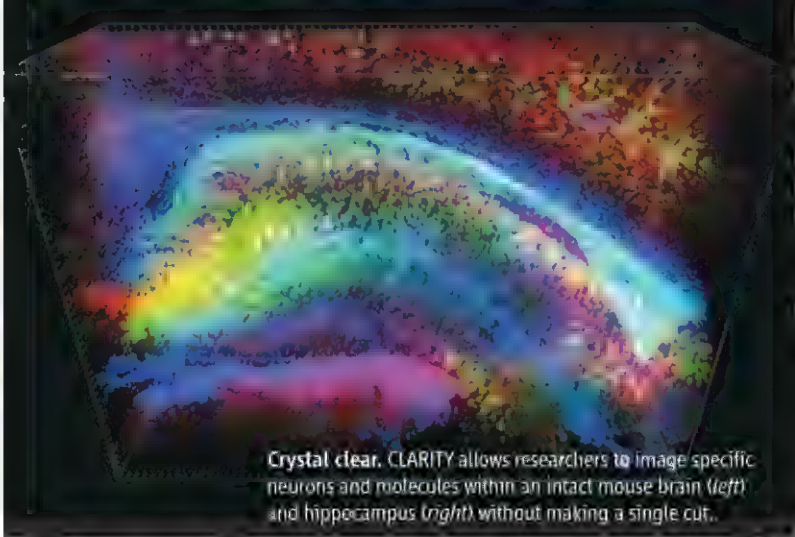
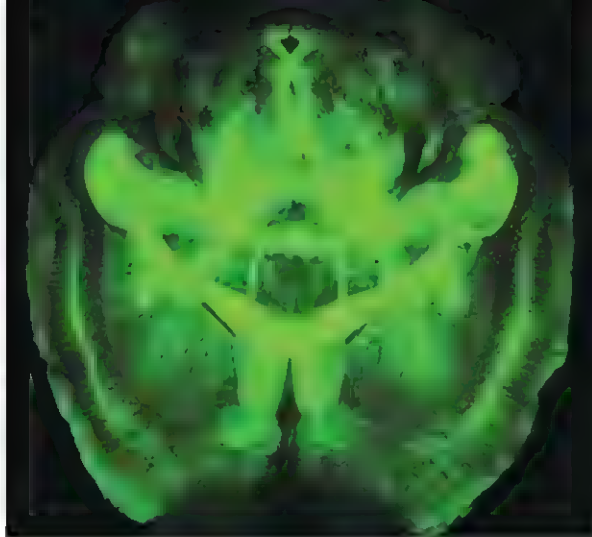
There are other reasons for concern. Many health labs are still not adequately equipped, Huang says: "Hospitals at the grassroots level probably are still unable to tell the difference among cold, annual flu, and avian influenza." The government has censored posts on Weibo, China's most popular microblog, about links to the dead pigs and alleged hidden cases. And in another sign that not everything has changed, some local disease centers have touted the traditional Chinese medicine banlangen as treatment for H7N9—the same unproven product that was trotted out 10 years ago as a remedy for SARS.

—MARA HVISTENDAHL

With reporting by Jon Cohen.



Limited spread. Ten days after reporting the first case of H7N9, Chinese officials had found only 27 others, all in Shanghai and surrounding provinces.



Crystal clear. CLARITY allows researchers to image specific neurons and molecules within an intact mouse brain (left) and hippocampus (right) without making a single cut.

NEUROSCIENCE

Tissue Imaging Method Makes Everything Clear

Karl Deisseroth is on a roll. In March, the neuroscientist-psychiatrist-engineer of Stanford University in Palo Alto, California, was awarded a share of the world's largest neuroscience prize for his work developing optogenetics, a tool which allows researchers to manipulate neuronal activity with light. Last week, he was appointed to advise President Barack Obama's new \$100 million brain research initiative. Now, this week in *Nature*, Deisseroth presents a new way of imaging the brain, which many researchers say will fundamentally change the way labs study the intricate organ.

"This is one of those singular events in the history of neuroscience," says Terrence Sejnowski, a neuroscientist at the Salk Institute for Biological Studies in San Diego, California, referring to CLARITY, Deisseroth's new method of rendering tissue transparent. Sejnowski compares the technique to the Golgi stain, which more than a century ago allowed scientists to trace specific neurons and their projections. "Until you actually see it, you don't quite appreciate how spectacular [CLARITY] is," he says. "You can see not just very detailed images of single neurons but whole populations of neurons, their projections, the inner structure of the brain. It's very revealing and has almost infinite potential to image anything that could be labeled."

The technique can be used to make any organ transparent, but it was the challenges of imaging the brain that motivated Deisseroth, who hopes to dissect psychiatric disorders such as schizophrenia and depression. Creating a 3D image of a brain today requires carving its tissue into hundreds or thousands of hair-thin slices, scanning an image of each slice in microscopic detail into a computer, and then painstakingly realigning the sections. Digitally stitching axons

back together—each roughly a hundredth the diameter of a human hair—not only takes a lot of computational time, but is also prone to significant error, says neuroscientist Arthur Toga of the University of California (UC), Los Angeles. After spending decades refining techniques for slicing and imaging brains, Toga says CLARITY may soon make that work irrelevant: "I'm gonna go up there and talk to these guys," he says, impressed.

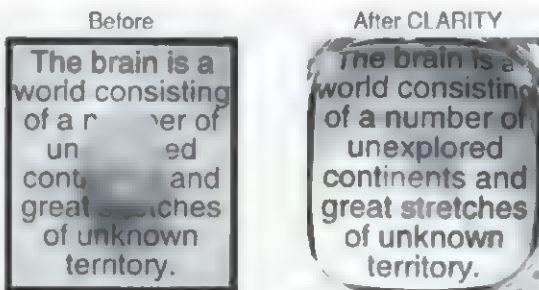
The CLARITY technique, which Deisseroth and colleagues have been working on for about 6 years, skips over slicing entirely and instead tackles the biggest obstacle to tra-

Deisseroth says. "Everything would just slosh around." Instead, CLARITY first replaces the lipids with a water-based gel by infusing a brain, or any other tissue, with single molecules of acrylamide—the same clear, jelly-like substance used to separate and analyze DNA molecules through electrophoresis. The fatty molecules are then flushed out with a combination of electrical current and detergent. For a roughly 4-mm-diameter mouse brain, the process takes about 9 days, Deisseroth says.

"This is a significant improvement" over previous methods of removing lipids from brain tissue, notes neurophysicist David Kleinfeld of UC San Diego. Although other labs have attempted to render the brain clear, he says, previous attempts have left the tissue far too fragile to work with. Kleinfeld says that he plans to use CLARITY to study the human brainstem, a region that is difficult to image because of all the lipid-packed myelin that surrounds neurons in that area. "We're pretty psyched."

One of the most exciting things about the technique is that it allows researchers to infiltrate the brain with labels for specific cell types, neurotransmitters, or proteins; wash them out; and image the brain again with different labels, Sejnowski says. "In one shot, you can look at every molecule in the brain that has that label." Digitizing the process will speed up by a hundredfold tasks such as counting all the neurons in a given brain region, he adds.

In the *Nature* paper, Deisseroth and colleagues describe using the technique to image



Disappearing act. CLARITY-treated mouse brain (right) reveals quote from famous neuroanatomist Santiago Ramón y Cajal.

ditional brain imaging: the fatty molecules, called lipids, that form the cellular membranes that keep neurons and other brain cells and organelles intact. Much as oil on sunlit water produces a rainbow sheen, these molecules scatter light in all directions, making it impossible to use light-based microscopy to see more than a few hundred microns deep into the brain. Lipids also repel many substances, such as antibodies, making it difficult to label specific types of cells without cutting the brain into sections.

Because lipids maintain the brain's structure, just getting rid of them isn't an option,

not only the mouse brain, but also small blocks of postmortem brain tissue from a person with autism. The experiment confirmed that the method works with brains preserved in formalin, a common fixative.

Will scientists ever be able to use CLARITY to look at an entire human brain? Although the notion is “not outrageous,” it would require building a much, much bigger microscope lens, Kleinfeld says. “We haven’t pushed that limit yet,” Deisseroth says. Now, existing microscopes can image up to only 6 to 8 mm in



On a roll. Karl Deisseroth wants to revolutionize neuroscience.

diameter of clarified brain tissue at a time—about the size of a whole adult mouse brain, he says. That’s convenient, Deisseroth says, because it’s about the size of what many researchers believe to be the core computational unit of the human cortex.

Although he agrees that CLARITY will lead to a “major advance” in tissue morphology, the technique may be dangerous and expensive for other labs to adopt, warns neuroimaging expert Hans Ulrich Dodt of the Vienna University of Technology, who has been explor-

ing other methods to render tissues transparent. For one thing, acrylamide is highly toxic and carcinogenic, “so it’s going to be a mess, and severe safety precautions have to be taken.” Deisseroth acknowledges the need for caution, but he expects that other labs will find the new technique easy to adopt. He has already run several workshops to share the method.

Nora Volkow, director of the National Institute on Drug Abuse in Bethesda, Maryland, and one of the reviewers of the National Institutes of Health Director’s Transformative Research Award that funded the experiment, describes CLARITY as “magnificent.” Deisseroth is an “extraordinary individual and extremely creative,” she says.

—EMILY UNDERWOOD

PALEOANTHROPOLOGY

A Human Smile and Funny Walk for *Australopithecus sediba*

If you happened to be in South Africa about 2 million years ago, you might have seen an odd sight: an older female hominin sashaying down a wooded slope, perhaps in search of water. She walked upright, but she wasn’t human, and she moved with what to our eyes would have looked like a distinctly strange gait. She was a member of *Australopithecus sediba*, and according to new analyses of fossils published online in *Science* this week (see p. 163), she may have twisted from side to side, rolling her feet inward with each step.

“*Sediba*’s got swag,” says paleoanthropologist Lee Berger of the University of the Witwatersrand in Johannesburg, South Africa. At least, she would have had swag until she fell into a death pit—a deep cave—at the site of Malapa, where she was buried with a youth and at least one other of her kind for nearly 2 million years before Berger and his son found them in 2008 (*Science*, 9 April 2010, p. 154).

The six new papers analyze two partial skeletons of *Au. sediba*, plus a shinbone of a third individual. They offer the most detailed picture yet of how this species moved and its relationship with other hominins, including our own ancestors. The remarkably complete skeletons reveal a strange creature with a small brain and primitive walk—but some surprisingly human teeth. “When you look at *Au. sediba* from head to toe, you get a package that’s very different from anything we’ve ever seen or predicted,” Berger

says. The analyses detail many traits shared with our genus *Homo*, in the spine, vertebral column, knee, teeth, and jaws, and Berger argues that *Au. sediba* could be the long-sought species that gave rise to *Homo*.

Few paleoanthropologists agree. But they say that at the very least, the new papers



Jaw dropper. *Au. sediba*’s skull shows a surprising mix of primitive features, such as a small brain, coupled with more human features in the jaw and teeth.

offer a detailed view of a novel way to be a member of the extended human family. They also show how evolution remodels the same body plan in diverse ways in different habitats. “If you look at the discoveries of hominins 2 to 3 million years ago, each one

seems to shuffle the deck [of traits] in different ways,” says paleoanthropologist William Kimbel of Arizona State University, Tempe. “It adds another subtle layer of information about the diversity of African hominins.”

The outlines of *Au. sediba* have been presented before, but the latest work brings this strange hominin into ever sharper focus. For example, ever since Berger’s team discussed a chimpanzee-like heel from one of the skeletons at a meeting last year (*Science*, 4 May 2012, p. 538), researchers have wondered how the species could walk upright. The bottom of the heel, preserved in the older female, is “exceptionally small,” twisted, and pointed as in a chimp, compared with the broad, flat base of a human heel bone, the authors write in *Science* (see image, p. 133). The narrow heel offers far less surface area on which to distribute weight when the foot strikes the ground, explains biological anthropologist Jeremy DeSilva of Boston University, first author of the foot and leg paper. (Chimps knuckle-walk, using their arms for added stability to support their skinny heels.)

In their analysis of bones from the female skeleton’s leg, DeSilva and his colleagues propose that *Au. sediba* had an arched foot that allowed it to put weight simultaneously on its heel and the outside of its midfoot. As it took each step, it must have pronated the foot, rolling it markedly inwards.

If modern humans try such a maneuver, they’ll quickly find that the hyperpronation puts torque on the foot, and also causes the lower leg and thigh to rotate excessively,

CREDITS (TOP TO BOTTOM): STEVE FISCUS/STANFORD UNIVERSITY; TY BRETTE ELOFF; COURTESY OF LEE R. BERGER AND THE UNIVERSITY OF THE WITWATERSRAND

straining the muscles that cross the knees and hips. Indeed, the new papers reveal signs of such strain in the ankle, knee, and hip, showing that *Au. sediba* compensated for the pronated walk. For example, the female's knee showed an "extreme" bony protrusion that may have helped to alleviate this stress and prevent the kneecap from dislocating, the authors write. Both partial skeletons also have flexible vertebral columns that have the curvature of the spine, or lordosis, that is considered a hallmark of upright walking.

Other researchers agree that despite the chimplike heel, the rest of the bones show that *Au. sediba* walked upright: "It's definitely a biped," says anatomist Bruce Latimer of Case Western Reserve University in Cleveland, Ohio. But it sure had an odd walk. "This particular hominid is walking in a different way than all earlier hominids," says paleoanthropologist Brian Richmond of George Washington University in Washington, D.C., who calls the team's reconstruction of the gait "provocative." He and others wonder if the older female's style of walking might have looked odd even to another *Au. sediba*, perhaps because of injury. "The key question is whether this was typical for the species."

The other new papers tackle different parts of the anatomy, such as the shoulder and arm, which are primitive and chimplike. This shoulder and the long arm show that *Au. sediba* was still spending a lot of time climbing trees or scrambling up rocky cliffsides, Berger says. Yet, an earlier analysis revealed a more humanlike hand.

The female skeleton's teeth, which are often considered useful for sorting out evolutionary relationships, also show an interesting mix of primitive and human traits. Bioarchaeologist Joel Irish of Liverpool John Moores University in the United Kingdom and collaborators compared *Au. sediba*'s teeth to those of more than 340 fossils of seven species of hominins to sort out how they are related to each other. Irish did a cladistic analysis of 22 inherited dental traits, such as small cusps or a shovel shape. Not surprisingly, the team found that *Au. sediba* is most closely related to *Au. africanus*, a species close to it in both space and time, living in South Africa roughly 3 million to 2 million years ago.



Twisted sister.

This composite of *Au. sediba* is partly based on a female skeleton that would have walked with a twist, because her heel (inset, center) was pointed like a chimp's (inset, left) rather than flat like a human's (inset, right).

method used by Irish doesn't include confidence intervals, showing which family trees are most reliable. "Without more information, I don't know whether this is something I want to bet \$5 on, \$50 on, or \$500 dollars on," Wood says.

Others point out that *Au. sediba* was alive after *Homo* came on the scene: The first fossil assigned to our genus is a lower jaw in Ethiopia dated to 2.4 million years ago. "*Sediba* is unique and very interesting, but *sediba* came too late to the party to be the ancestor of *Homo*," Richmond says. But Berger wonders if that jaw, which was found isolated, not connected to a skull or skeleton, is truly *Homo*. An isolated *Au. sediba* jaw would look a lot a *Homo* jaw, he notes.

However *Au. sediba* is related to us, what's exciting about this set of discoveries, Richmond says, is that the "fossils are complete enough that we're

starting to understand how these regions of anatomy are related to other regions of anatomy," connecting jaws to spines and feet.

Despite the wealth of fossils, researchers want more: They say another heel or more bones from the forefoot could "test the model" of how the species walked, Latimer says.

Comparisons with other australopithecines would also help, but the tiny bones of the foot are so rarely preserved that the *Au. sediba* foot bones don't overlap with the handful known for other ancient hominins. For example, the primitive foot of a still unnamed species of *Australopithecus* from Burtele, Ethiopia, has an opposable toe bone, but it's not clear if it's pronated, and those toe bones are missing for *Au. sediba*. An answer might come from the 2-million- to 3-million-year-old Little Foot skeleton—named for its many foot bones—found just 15 kilometers away at Sterkfontein Caves. But that skeleton is being excavated by a rival team of fossil hunters who have yet to publish in detail (*Science*, 9 September 2011, p. 1374).

More will be coming: The remainder of the defining type specimen of *Au. sediba* still lies inside a rock, waiting to be excavated. Berger's team plans to return to Malapa to begin digging for new fossils this summer.

—ANN GIBBONS

But the analysis also found that both of these species are more closely related to early *Homo* than they are to other members of *Australopithecus* from east Africa. This suggests, as Berger has argued for years, that the South African species may knock the queen of australopithecines, Lucy—a member of *Au. afarensis*—off her long-held perch as the most likely ancestor of *Homo*.

That's a radical view. Some paleoanthropologists critique the methodology of the dental analysis, which identifies inherited traits that vary among modern humans and are used to distinguish lineages within our species. It's unclear whether those traits are the best ones for sorting out relationships among hominins that lived millions of years ago. "These are minor differences in the crowns [of teeth]," Kimbel says. "To try to apply this to hominins that are millions of years old is fraught with difficulty." Paleoanthropologist Bernard Wood of George Washington University is concerned that the

advantage

New Promotion: April 1 – June 30, 2013



New Special Offers

Enhance your possibilities in long series dispensing with the new **Combitips advanced®**. Increase your performance: Start measuring small volumes ($\geq 1.5 \mu\text{L}$) of nucleic acids or proteins using the new **Eppendorf $\mu\text{Cuvette}^{\text{TM}}$ G1.0** with your Eppendorf BioPhotometer® or Eppendorf BioSpectrometer®.

Enhance your possibilities in long series dispensing with the new **Combitips advanced®**. These high-precision dispensing tips with improved product features bring a new level of application versatility to your lab.

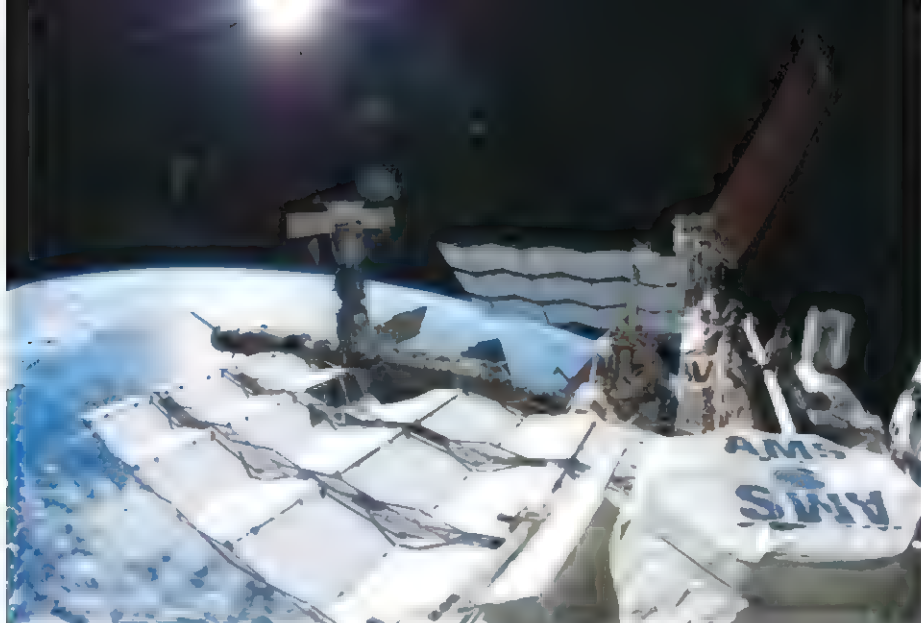
Increase your performance: Start measuring small volumes ($\geq 1.5 \mu\text{L}$) of nucleic acids or proteins using the new **Eppendorf $\mu\text{Cuvette}^{\text{TM}}$ G1.0** with your Eppendorf BioPhotometer® or Eppendorf BioSpectrometer®.



Check out our special offers online today.

www.eppendorf.com/advantage

Eppendorf®, the Eppendorf logo, Combitips advanced®, Eppendorf BioPhotometer® and Eppendorf BioSpectrometer® are registered trademarks of Eppendorf AG. Eppendorf $\mu\text{Cuvette}^{\text{TM}}$ and Eppendorf Advantage™ are trademarks of Eppendorf AG. Offers may vary by country. All rights reserved, including graphics and images. Copyright © 2012–2013 by Eppendorf AG.



PHYSICS

Two-Billion-Dollar Cosmic Ray Detector Sees Signs of *Something*

Don't scratch "discover what dark matter is" off your cosmological to-do list just yet. This week, physicists working with a \$2 billion cosmic ray detector aboard the International Space Station confirmed a previously reported excess of antiparticles from space that could emanate from dark matter, the mysterious stuff whose gravity binds the galaxies. If so, the observation could help scientists determine the nature of dark matter. But the excess measured by the 6.7-tonne Alpha Magnetic Spectrometer (AMS) could also be subatomic exhaust from a pulsar or some other mundane astronomical object. And determining which explanation is correct may require entirely different types of experiments and could take years.

"The question is, now what?" says Stéphane Coutu, a cosmic ray physicist at Pennsylvania State University, University Park, who does not work on AMS. "The answer is, that's a good question."

The brainchild of Samuel C. C. Ting, a 77-year-old Nobel Prize-winning particle physicist, AMS was bolted to the space station on 19 May 2011 after a long gestation in which the international project was killed and resurrected (*Science*, 22 April 2011, p. 408). Since then, he and the 347 members of the AMS collaboration have measured the ratio of antielectrons, or positrons, to the total number of electrons and positrons, as Ting reported in a talk on 3 April at the European particle physics laboratory, CERN, near Geneva, Switzerland. According to standard astrophysics, that "positron fraction" should be small and should fall as energy increases.

Instead, AMS found that the positron fraction increases from 5% at an energy of 10 giga-electron volts (GeV) to more than 15% at an energy 35 times as high, Ting reported.

The extra positrons could arise from dark matter. According to popular theories, dark matter could consist of weakly interacting massive particles, or WIMPs. When two WIMPs collide, they could annihilate each other to produce an electron-positron pair, bumping the positron fraction closer to 50%. Such an excess had been previously reported, but physicists questioned the reliability of those results. The AMS data prove that the excess is real, Coutu and others say.

But does it point to dark matter? The positrons could instead emanate from a spinning neutron star called a pulsar, if it were close enough to Earth. Ting and the AMS team acknowledge the point. In a paper in *Physical Review Letters*, they do not mention dark matter as the source of the excess but instead refer to "new physical phenomena."

AMS can ultimately determine the source on its own, Ting says. If the positrons come from the annihilation of dark matter particles, then their energy must be limited by the mass of those particles. So the positron fraction should plummet as energy increases beyond a distinct "cutoff." In contrast, an excess from an astrophysical source should ebb away with increasing energy, Ting says. "If we have a sharp drop-off, it is a very strong indication of dark-matter collisions," he says. The AMS data suggest that the positron fraction levels

One and only. AMS is the only major experiment on the International Space Station.

off at the highest energies analyzed so far, and additional data should reveal whether it goes over a cliff.

Not everyone buys it. An astrophysical source can crank out particles with a sharp energy cutoff, too, says Gregory Tarlé, a cosmic ray physicist at the University of Michigan, Ann Arbor. "It's very easy to put a cutoff into an astrophysical model," he explains. "All you have to do is limit the size of the particle-accelerating region." So even if AMS sees a cutoff, the observation will remain ambiguous, Tarlé says.

In fact, details of the AMS results themselves could make it harder to explain the excess in terms of dark matter, says John Ellis, a theorist at King's College London. The AMS data show that the positron excess extends to energies higher than previous measurements could probe. That implies that WIMPs must weigh at least 300 or 400 GeV, which strains theoretical models, Ellis says. "AMS is painting dark matter into a rather small corner," he says. "Whether there's enough room for it to stand up, I don't know."

Perhaps ironically, cosmic ray physicists argue that the positron excess can never be deciphered by staring at the sky. Instead, they seek insight from a different source: an atom smasher, such as CERN's Large Hadron Collider (LHC). According to some models, it ought to be possible to make WIMPs with the LHC. Spotting such production would be necessary to clinch a dark-matter explanation for AMS's observations, Coutu and Tarlé say.

How long will it take to settle this? Don't wait up. AMS may have to collect data for another few years to see if there is a cutoff in the positron fraction, Ting says. And the LHC has shut down until 2015 for repairs. "I'm 47," Coutu says. "I'd like the answer before I keel over, but who knows?"

The uncertainty aside, the results mark a triumph for Ting, who all but willed AMS into orbit. Proposed in 1994, the detector made a test flight on NASA's Space Shuttle in 1998. But it appeared permanently grounded after the shuttle Columbia disintegrated on reentry in 2003 and NASA rethought the shuttle program. Undaunted, in 2008 Ting

secured a congressional mandate that NASA launch AMS, to which the United States is one of 16 contributing nations. The AMS paper acknowledges nine current and former senators and representatives for their support.

—ADRIAN CHO

Online

sciencemag.org

Podcast interview with writer Adrian Cho (http://scim.ag/pod_6129).

From Cosmic Dawn To Milkomeda, And Beyond

The thoughts of Harvard theorist Avi Loeb traverse the universe, past and future—and he urges young researchers to be just as daring



CAMBRIDGE, MASSACHUSETTS—A file cabinet drawer in the office of Abraham (“Avi”) Loeb is simply labeled “IDEAS.” It holds a single hanging file with a few manila folders, each containing sheets of paper displaying equations in Loeb’s crisp penmanship. “I have ideas all the time; they just bubble up,” he says. “I keep adding a piece of paper here if I don’t have time to work on it.”

In Loeb’s 20 years at the Harvard-Smithsonian Center for Astrophysics, those minimalistic sheets have seeded a breadth of research rivaled by few theorists in astrophysics. His prodigious publication record spans three books (including an award-winning popular volume), 430 papers, and counting.

Loeb is best known to cosmologists for illuminating the messy physics of the “cosmic dawn,” when light from the first stars and galaxies seared holes into the hydrogen gas that suffused the new universe. He and his many colleagues have also described how to spot ancient gamma ray bursts, how giant black holes may have grown and merged, and how to take the first image of a black hole—key predictions that led to campaigns to observe such extreme physics. But his ruminations have also spawned papers on searching for imprints of life in exoplanet atmospheres, detecting light from nearby alien civilizations, and how astronomers of the far future might deduce the expansion history of the universe.

Loeb tries to foster this mix of serious data-driven theory and adventuresome projection among students and researchers at Harvard’s Institute for Theory and Computation (ITC), which he directs. “Following Avi’s work can be quite dizzying,” says Mordehai

Milgrom of the Weizmann Institute of Science in Rehovot, Israel, one of Loeb’s first tutors in astrophysics. Adds Frederic Rasio, an astrophysicist at Northwestern University in Evanston, Illinois: “There is hardly a question in astrophysics—any subject, really—that Avi has not touched at some point.”

Plucked from the farm

The 51-year-old Loeb traces his far-flung musings to his childhood on a village farm in Israel, about 20 kilometers from Tel Aviv. His father was head of Israel’s industry for pecans; the family also raised chickens and grew oranges and grapefruits. After collecting eggs and doing other chores with his two older sisters, Loeb would drive a tractor into the hills and spend hours reading books by existential philosophers. “I often considered returning,” he says. “It’s a more relaxing style of living.”

At age 18, Loeb was chosen with two dozen other young men for an elite Israeli military program called Talpit. He studied physics and mathematics at the Hebrew University of Jerusalem and underwent basic training in paratrooping, driving tanks, and other soldiering. During and after his graduate program he worked at the Soreq Nuclear Research Center, where he led a weapons project to propel masses using electric discharges to ignite material with lower atomic weight than gunpowder, such as polyethylene. He earned a Ph.D. in plasma physics at age 24 and completed his compulsory service 2 years later.

Loeb’s innovations at Soreq caught the attention of U.S. Air Force Gen. James Abrahamson, who came to Israel as the first director of President Ronald Reagan’s

Strategic Defense Initiative program. The general’s staff invited Loeb to visit the United States, where the era’s leading plasma physicist, Marshall Rosenbluth, steered him toward the Institute for Advanced Study (IAS) in Princeton, New Jersey. There, noted astrophysicist John Bahcall first invited Loeb for a 1-month stay, then stunned him with an offer of a 5-year appointment—but only if Loeb switched from plasma physics to astrophysics. Loeb marvels at the “wild risk” that Bahcall, who died in 2005, took in hiring him. “I owe him my career,” he says.

From IAS, Loeb took an assistant professor job at Harvard in 1993, despite warnings that promotion was improbable. “At the time, Harvard viewed junior faculty almost as a glorified postdoc,” says Harvard astrophysicist Jonathan Grindlay. “It was not a healthy environment.” But nearly 4 years later, when Loeb had tenure offers from Cornell University and the Weizmann Institute, Harvard made the rare decision to keep him. “He said we would be glad we hired him,” chuckles Robert Kirshner, the astronomy department chair at the time. “Avi has mellowed a bit, but this great self-confidence has remained in place.”

From darkness to light

Loeb’s promotion came at a time of profound personal change. He divorced his first wife, who lived separately in New York in a marriage that never had worked, and months later met Ofrit Liviatan in Israel—through a connection arranged by the pair’s mothers. Liviatan, a lawyer in Israel, joined Loeb in Cambridge a year later. She now lectures in Harvard’s Department of Government.

CRED: T. CLIVE GRAINGER

The couple lives in a quiet setting in Lexington, about 20 minutes outside Boston, with daughters Klil, age 11, and Lotem, age 7. Loeb works on their 110-year-old house and watches the sky from his back porch, amid a constant flow of ideas. "One day it may stop," he says. "But so far, it hasn't."

Many of those ideas concern the "epoch of reionization"—the long era when ultraviolet light from stars and galaxies split the universe's dark fog of neutral hydrogen into protons and electrons, starting about 100 million years after the big bang. In papers establishing a now-accepted paradigm, Loeb and his many students and postdocs built up the physics of how ionized hydrogen "bubbles" spread into ever-evolving patterns as stars and quasars lit up, like a cosmic sponge growing more porous with time.

The leftover neutral hydrogen emitted

pursuits that helped chart a course for observers. In a 1992 study at IAS, Loeb and Andrew Gould, who is now at Ohio State University, showed that planets circling other stars could reveal themselves by causing brief flares of light from background stars via gravitational "microlensing"—still the only method that exposes exoplanets in distant parts of the Milky Way. And about a decade ago, Loeb and colleagues calculated that gamma ray bursts—the most powerful explosions known—near the margins of the observable universe should remain visible to telescopes. NASA's Swift satellite soon confirmed the predictions.

The studies reflect an unshakable tenet of Loeb's work: contact with data. He avoids the mathematical conjectures of what he calls "theory bubbles," and he steers students away from them as well. "There is one real-

Aviv University, NASA's upcoming James Webb Space Telescope could spy that faint signal from planets orbiting white dwarfs, the dense Earth-size remnants of stars like our sun. In another E.T.-tinged study, Loeb and Princeton astrophysicist Edwin Turner proposed using future telescopes to look for "city lights" from other civilizations—and testing the method now by scanning the outskirts of our solar system.

Some colleagues compare him to visionary physicist Freeman Dyson of IAS, but Loeb knows that many others regard such speculative work with raised eyebrows or worse. "But frankly, I don't care," he says. Creativity and challenging convention spur the best research, he says. Federal funding agencies have lost sight of this, Loeb says, dooming pioneering missions like the Laser Interferometer Space Antenna to detect gravitational waves.



The Loeb files. At home in 1966 in Beit Hanan, Israel, with sister Shoshana; at the Hebrew University of Jerusalem in 1982 during Talpiot military training (Loeb at rear left); playing soccer in 2009 with Harvard University colleagues.

a hum of radiation at a wavelength of 21 centimeters. Loeb's calculations suggested that low-frequency radio antennae on Earth could tune into that hum, stretched out up to 3 meters long on its way here by the ongoing expansion of space. The more distant the hydrogen, the more its humming gets stretched. Loeb probed in detail how astronomers could harness that "redshift" to create a tomographic atlas of the hydrogen fog burning off during the cosmic dawn, a process that took up to a billion years.

Colleagues credit Loeb for the theoretical underpinnings supporting major radio-astronomy efforts in Australia, Europe, and South Africa to unveil those patterns. "Avi has done more than anybody to explain how important this period of time was and what facilities would be needed to unravel the physical detail of what happened," says astronomer Richard Ellis of the California Institute of Technology in Pasadena.

Loeb takes as much pride in two other

ity out there," he says. "It's dangerous to work on abstractions with no feedback from data. Some physicists do not understand this."

Astro-venture capital

Even Loeb's riskier papers—which gain far more public notice—are grounded in physics that extrapolates from today's data. For example, he and ITC postdoctoral fellow T. J. Cox, who is now at the Carnegie Observatories in Pasadena, simulated the crash of the Milky Way and our galactic neighbor, Andromeda, starting in about 2 billion years. Our solar system, they deduced, would probably be tossed near the outskirts of the gigagalaxy, which Loeb dubbed "Milkomeda." In the far future, he calculated, the relentless acceleration of the universe due to dark energy would render all other galaxies invisible. Still, he claimed in a recent paper, Milkomedan astronomers could retrace what had happened by studying light from closer stars ejected from the merged galaxy by its giant central black hole.

Lately, Loeb has been drawn to the prospects of detecting life elsewhere. One signpost would be spectral traces of oxygen in the atmosphere of a rocky world. According to Loeb and astrophysicist Dan Maoz of Tel

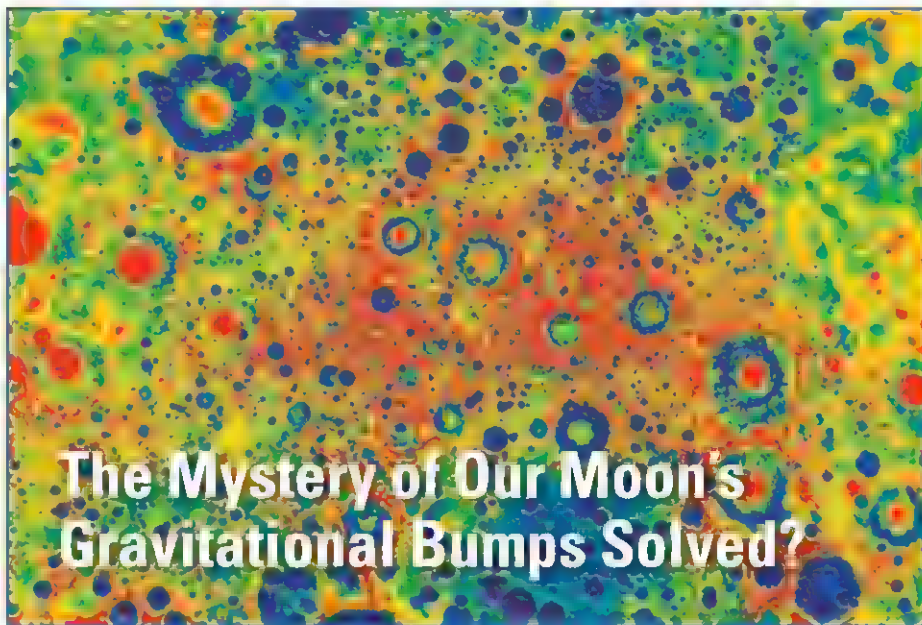
In a recent paper, Loeb made waves by urging young astrophysicists to devote 20% of their research to innovative "venture capital" projects outside the mainstream. "It requires a certain amount of bravery to come up with these things," Milgrom of the Weizmann Institute says. "People are afraid to do risky work, but words from Avi can be influential."

Loeb now has less time to publish papers at will. In addition to directing ITC, he is chair of the Harvard astronomy department. At ITC, his peers note, Loeb has built a team that is at once high-powered and collegial. Prize-winning postdoctoral fellows and graduate students like what they see. "They get all the best young people now," a colleague says privately. "No one can compete with them."

Despite the demands, notions keep coming to Loeb in his shower and on his porch. Now, edging ever closer to Earth, he and a co-author are honing a new theory of how the moon formed. "I still have a niche: ideas that other people do not think about," he says with a smile. "There is room for innovation"—and for another sheet in the file drawer.

—ROBERT IRION

Robert Irion directs the Science Communication Program at the University of California, Santa Cruz.



Mottled moon. In this GRAIL gravity map, mascon basins are red, circular, and blue-ringed.

The Mystery of Our Moon's Gravitational Bumps Solved?

Much to geophysicists' consternation, the first space probes to orbit the moon were misbehaving badly, showing up in the wrong places at the wrong times. Something about the gravitational pull of the moon was throwing off their orbits. But what? In 1968, two NASA scientists found the culprit, or rather culprits: The moon's great basins were exerting an unexpected extra pull on passing satellites.

That made no sense, of course. Those basins are low spots where huge impacts have gouged out megatons of rock, not added mass. Somehow, there is hidden extra mass under many lunar basins, making them basins with mass concentrations or mascon basins. How did the extra mass get there? At the meeting, a group of researchers reported how over millions of years the moon's subtle adjustment to an impact might eventually create a high spot

in the moon's bumpy gravitational field.

Two developments in planetary science have helped finally generate a solution to the mascon mystery. One was the advent of stunningly detailed lunar observations. NASA's twin-spacecraft Gravity Recovery and Interior Laboratory (GRAIL) mission mapped the subtle variations of gravitational pull with a resolution of 10 kilometers or so over the entire moon (*Science*, 7 December 2012, p. 1272). That painted a clear gravity picture of mascons: a bull's-eye pattern of higher-than-expected gravity across a basin hundreds of kilometers wide, ringed by a band of lower gravity and an outermost ring of higher gravity.

The other development came back on Earth. Computer modelers had managed to inject such realism into their models that they could hope to match their simulated mascon formation to the GRAIL gravity map. So at the meeting, physicist Brandon Johnson of Purdue University in West Lafayette, Indiana, and 10 colleagues showed how they simulated the impact of a 50-kilometer-diameter rock plunging vertically into the moon at 54,000 kilometers per hour. In the model, the collision left behind a broad, shallow basin, a ring of reduced gravity where

Pesky Perchlorates All Over Mars

Five years ago, the Phoenix lander found perchlorate salts in one spot in the martian arctic. Now, Curiosity rover has discovered perchlorates in equatorial Gale crater as well, implying that they carpet the martian surface. The discovery explains why the rover stumbled in its first search for organic traces of ancient martian life. Indeed, perchlorates, it seems, have been frustrating three generations of organic analyses on Mars.

Curiosity's discovery of perchlorate salts—compounds consisting of a chlorine atom, four oxygens, and an element like magnesium—came when it ran its first solid sample through its Sample Analysis at Mars (SAM) instrument package. The rover scooped windblown dust into SAM and gradually heated it up to 835°C. It continuously flushed the resulting gases—which researchers hoped might include volatile organic matter—through a mass spectrometer for identification.

At the meeting, Paul Archer of NASA's Johnson Space Center in Houston, Texas, and fellow Curiosity team members reported that as the sample temperature passed through about 400°C, SAM identified both molecular oxygen and a variety of chlorine-containing, single-carbon compounds. Together, those molecules made "a strong case for perchlorates" in the sample, Archer said.

That's because perchlorate salts in martian soil would have decomposed to chlorine and oxygen at that sort of temperature, and the chlorine would have combined with any nearby carbon to form the observed single-carbon compounds. Meanwhile, the oxygen would have burned any other carbon compounds present to carbon dioxide, which also came out then. The coincident release of oxygen and chlorinated compounds plus the previous detection of chlorine in every martian soil ever tested "lead to the conclusion that perchlorates are globally distributed on Mars," at least in the soil, the group said in its meeting abstract.

Pervasive perchlorates would explain a lot. Their presence on Mars wasn't so surprising once geo-

chemists thought about it: The ultraviolet of sunlight could produce them by zapping other compounds in the atmosphere or directly in the soil, where the aridity of Mars would preserve them, as the aridity of Earth's Atacama Desert does. Heating them together with any sort of carbon-containing compounds—once-living or not—in martian soil would yield Curiosity's result, which closely matches what the two Viking landers saw in their own heated-sample experiments in the late 1970s. The less sensitive Phoenix lander experiment detected only carbon dioxide in its heating experiments.

Bottom line: Experiments to date on Mars may or may not have detected martian organic matter. And because hot perchlorates react with any kind of carbon, it's unlikely that the question can be settled with heating experiments alone. But Curiosity isn't finished. In a first on Mars, SAM can isolate certain types of organic compounds at low temperatures before sending them on to the mass spectrometer. The catch is that SAM can run this "wet chemistry" analysis only seven times in the entire mission. Choose wisely, Curiosity. —R. A. K.

less dense ejecta had piled on the crust, and a central pool of melted mantle rock more than 100 kilometers deep.

In the next talk, planetary scientist Andrew Freed of Purdue, speaking for the same group, reported on their modeling of the next 100 million years of an impact basin's life: This is when all that hot rock slowly cools, a rigid lid of mostly mantle rock forms over top, and relatively dense or light chunks of rock can slowly sink or float in the still-viscous mantle. Both simulations had to get many steps right, Freed said. Most critically, the rigid lid must form and lock the temporarily elevated central basin in place before the ring of thickened crust—which is floating up—sucks mantle rock from beneath the central basin. Losing that mass would rob the central basin of the mass responsible for the mascon.

Freed reported that their two-step modeling produced the same bull's-eye gravity pattern seen in GRAIL data at two impact basins, even though the two sites had different preimpact crustal thicknesses. The same modeling approach even duplicated the mascon of the humongous 960-kilometer-diameter Orientale basin, the group reported at a poster the same day. The modeling includes physical “mechanisms we know are there,” Freed said. “If we model those mechanisms well, the mascons pop out. It's really hard to mess this calculation up.”

Planetary geophysicist William McKinnon of Washington University in St. Louis calls the results “very interesting and a nice step forward” but notes that the studies so far leave out some potentially important mechanisms, such as the flow of pulverized rock in an impact. He will be looking for another round of modeling.

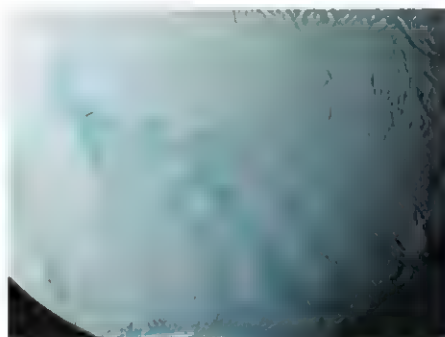
More Support for An Ocean in Enceladus

Now that the Cassini spacecraft has made its last close-up observations of Saturn's moon Enceladus, mission team members are pushing to prove once and for all that the 500-kilometer-diameter moon harbors a salty—and habitable—ocean far below its icy surface. They aren't there yet, but at the meeting, researchers argued that the latest Cassini observations make the most sense if liquid water is escaping from a deep ocean through cracks in Enceladus's outer ice shell to produce the plume spewing from the moon's south polar region.

Some planetary scientists had thought that they had figured out the mechanics of

Enceladus's plume. It appeared to them that Saturn's varying tidal pull on Enceladus was pushing on opposing sides of four great cracks running across the south pole region, moving them back and forth. The resulting frictional heat would melt some ice, sending plumes into the vacuum of space—no deep ocean required.

But at the meeting, Carolyn Porco of the Space Science Institute in Boulder, Colorado—Cassini's camera team leader—



Cracked up. The four bluish, parallel lines mark cracks on Enceladus from which a deep ocean may vent.

and colleagues suggested a scenario that better fits the observations. Saturn's tides are, in fact, working on the fractures, they found, but individual plume jets tend to occur where tidal stresses are calculated to be pulling cracks apart, rather than where they create frictional heat. And tidal opening of cracks tends to coincide with the times when the south polar plume is seen to intensify, suggesting that the opening cracks are letting something escape.

That something, Porco and colleagues conclude, is warm water from a deep ocean. If it were meltwater from any frictional heating in the cracks, their calculations show the surrounding ice would be noticeably heated for several kilometers along a crack. But researchers on Cassini's heat-sensing imager team reported last fall that hot spots on cracks are no bigger than a few tens of meters. So it looks as if tidal stresses are opening cracks through kilometers of ice and letting ocean water escape to space.

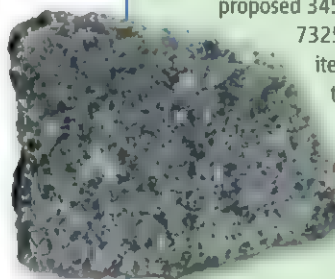
“That's definitely a possibility,” says planetary physicist David Stevenson of the California Institute of Technology in Pasadena. Frictional heating doesn't seem to be working out, he says, so “instead they are tapping heat from the ocean.” Next up, he adds, is showing how such a plumbing system could keep going for millennia. Still, Stevenson says, “progress is being made.”

—RICHARD A. KERR

Snapshots From the Meeting

Hot time on the ol' Mars? The Curiosity rover has come across hints of chemical reactions on Mars that could have produced the organic “building blocks of life,” but without any life. Jennifer Stern of NASA's Goddard Space Flight Center in Greenbelt, Maryland, and fellow Curiosity team members reported that when Curiosity gradually heated windblown dust, the process produced molecular fragments at about 800°C. These appear to be cyanide (a carbon-nitrogen compound) and hydrogen cyanide. Another Curiosity team member, Andrew Steele of the Carnegie Institution of Science's Geophysical Laboratory in Washington, D.C., reported the high-temperature release of the same molecules from another martian sample, a piece of the Tissint meteorite recently arrived from Mars. Using high-powered instruments in the lab, Steele could see that the nitrogen-containing compounds in Tissint likely formed when hot water interacted with martian rock. Another product of those reactions appears to have been organic matter. So if Curiosity turns up organic matter on Mars, the next chore will be telling whether it was ever alive.

A messenger from Mercury? Big impacts on the moon and Mars have blasted off bits of rock that have been picked up on Earth, so why not a meteorite from Mercury? At the meeting, meteoriticist Anthony Irving of the University of Washington, Seattle, and colleagues proposed 345-gram Northwest Africa 7325 as a Mercurial meteorite. “No one has a rock like this,” he says. It's a unique



Mercurian? Although its composition resembles Mercury's, this meteorite may be too old to be from there.

combination of elements, minerals, and isotopes that in many ways matches the properties of Mercury's surface as determined by the still-orbiting MESSENGER spacecraft. But “I was unimpressed,” says planetary scientist William Vaughan of Brown University. Some of the chemistry doesn't match at all, he notes. What's more, the meteorite is much older than the relatively youthful lavas that cover most of Mercury's surface, where it presumably would have to have originated. Most discouraging, perhaps: “I don't know how we'll get a conclusive result,” Irving says.

—R. A. K.



SCIENTIFIC CONFERENCES 2013-2014:

Presenting the most significant research on cancer etiology, prevention, diagnosis, and treatment

www.aacr.org/conferences

Frontiers in Basic Cancer Research

Chairperson: Scott W. Lowe

Co-Chairpersons: Joan S. Brugge, Hans Clevers, Carol L. Prives, and Davide Ruggero

September 18-22, 2013 • National Harbor, MD

Advances in Ovarian Cancer Research:

From Concept to Clinic

Co-Chairpersons: David G. Huntsman, Douglas A. Levine, and Sandra Orsulic

September 18-21, 2013 • Miami, FL

Advances in Breast Cancer Research

Co-Chairpersons: Carlos L. Arteaga, Jeffrey M. Rosen, Jane E. Visvader, and Douglas Yee

October 3-6, 2013 • San Diego, CA

AACR-NCI-EORTC International Conference on Molecular Targets and Cancer Therapeutics

Co-Chairpersons: Jeffrey A. Engelman, Lee J. Helman, and Sabine Tejpar

October 19-23, 2013 • Boston, MA

Twelfth Annual International Conference on Frontiers in Cancer Prevention Research

Chairperson: Paul J. Limburg

October 27-30, 2013 • National Harbor, MD

Pediatric Cancer at the Crossroads:

Translating Discovery into Improved Outcomes

Co-Chairpersons: John M. Maris, Stella M. Davies, James R. Downing, Lee J. Helman, and Michael B. Kastan

November 3-6, 2013 • San Diego, CA

The Translational Impact of Model Organisms in Cancer

Co-Chairpersons: Cory Abate-Shen, A. Thomas Look, and Terry A. Van Dyke
November 5-8, 2013 • San Diego, CA

CTRC-AACR San Antonio Breast Cancer Symposium

Co-Directors: Carlos L. Arteaga, C. Kent Osborne, and Peter M. Ravdin
December 10-14, 2013 • San Antonio, TX

Sixth AACR Conference on The Science of Cancer Health Disparities in Racial/Ethnic Minorities and the Medically Underserved

December 6-9, 2013 • Atlanta, GA

AACR-IASLC Conference on Molecular Origins of Lung Cancer

January 6-9, 2014 • San Diego, CA

AACR-Prostate Cancer Foundation Conference on Advances in Prostate Cancer Research

Co-Chairpersons: Arul M. Chinnaiyan, William G. Nelson, June M. Chan, and Jonathan W. Simons
January 18-21, 2014 • San Diego, CA

Cancer Susceptibility and Cancer Susceptibility Syndromes

Co-Chairpersons: Alan D. D'Andrea, Phillip A. Dennis and Pier Paolo Pandolfi
January 29-February 1, 2014 • San Diego, CA

AACR Annual Meeting 2014

April 5-9, 2014 • San Diego, CA

AACR EDUCATIONAL WORKSHOPS

Accelerating Anticancer Agent Development and Validation

Co-Chairpersons: H. Kim Lyerly and Richard Pazdur
May 8-10, 2013
Bethesda, MD

NEW! Integrative Molecular Epidemiology

Director: Thomas A. Sellers;
Co-Directors: Peter L. Kraft and Margaret R. Spitz
July 15-20, 2013
Boston, MA

Molecular Biology in Clinical Oncology

Co-Directors: William G. Kaelin Jr., Mark Geraci, and Suzanne Topalian
July 21-28, 2013
Snowmass, CO

ASCO/AACR Methods in Clinical Cancer Research

Co-Directors: Jamie H. von Roenn, Neal J. Meropol, and Mithat Gönen
July 27-August 2, 2013
Vail, CO

Translational Cancer Research for Basic Scientists

Co-Directors: Tom Curran, George D. Demetri, and Pasi A. Jänne
November 10-15, 2013
Boston, MA

LETTERS

edited by Jennifer Sills

Drawbacks to Natural Gas

E. KINTISCH RECENTLY REPORTED ON THE EVOLUTION OF THE climate stabilization wedge concept ("Climate study highlights wedge issue," *News & Analysis*, 11 January, p. 128), first conceptualized by Pacala and Socolow in 2004 (1). At the close of the *News* story, Socolow acknowledges the need for thoughtful assessment of the technological paths toward carbon neutrality, but not before he touts the recent expansion of natural gas as "a rare sign of progress."

Natural gas is increasingly held up as a clean-burning, domes-

tic "bridge fuel" paving the way toward energy independence. The problem with this assertion is that the recent proliferation of U.S. natural gas production is largely due to the expansion of hydraulic fracturing methodology to access shale gas (2). Once extracted, natural gas burns cleaner than coal or oil; however, the extraction-to-consumer carbon footprint of hydraulically fractured natural gas is greater than that of traditional energy sources (3). Moreover, hydraulic fracturing is increasingly linked with potentially irremediable freshwater contamination. In Pavillion, Wyoming, for instance, toxic or carcinogenic compounds added to fracking fluid have been found in drinking wells adjacent to drill pads (4). As we grapple with how to meet society's energy demands while obtaining carbon neutrality, we cannot pay for carbon offsets at the expense of other valuable natural resources, such as fresh water.

SARA SOUTHER

Department of Botany, University of Wisconsin, Madison, Madison, WI 53706, USA. E-mail: ssouther@wisc.edu

References

1. S. Pacala, R. Socolow, *Science* **305**, 968 (2004).
2. Energy Information Administration, "Annual energy outlook" (U.S. Department of Energy, Washington, DC, 2011).
3. R. W. Howarth, R. Santoro, A. Ingraffea, *Clim. Change* **106**, 679 (2011).
4. D. C. DiGiulio, R. T. Wilkin, C. Miller, G. Oberly, "Draft: Investigation of ground water contamination near Pavillion, Wyoming" (EPA, Office of Research and Development, Ada, OK, 2011); www.epa.gov/region8/superfund/wy/pavillion/EPA_ReportOnPavillion_Dec-8-2011.pdf.

Shale gas well site.



Biosecurity's Weakest Link

THE ONGOING DEBATE REGARDING THE biosecurity concerns arising from functional gain research on human pathogenic viruses has brought into clearer focus the major gap between academic and public perceptions of acceptable risk ("New U.S. rules increase oversight of H5N1 studies, other risky science," D. Malakoff and M. Enserink, *News*

& Analysis, 1 March, p. 1025). At the heart of the current controversy is anxiety over the safety of dual-use research and the risk that it will yield information or technologies with the potential to be misused to threaten public health or national security. These fears strongly shape the priorities of national biosecurity policies across the whole spectrum of the life sciences (1). Yet the most likely threat posed by dual-use research is not from a rogue individual or organization but simple human fallibility (2).

The increasing catalog of thefts, loss of samples, inadvertent infections, and unintentional releases of restricted pathogens demonstrates that the weakest link rests with those most directly involved with the research (3–5). Regardless of the effects that publishing sensitive research may have on our vulnerability to bioterrorism (6), it may increase the likelihood of unintentional biosafety

breaches by encouraging further, legitimate, functional gain studies.

Under new guidance ("A framework for decisions about research with HPAI H5N1 viruses" A. P. Patterson *et al.*, *Policy Forum*, 1 March, p. 1036), research support will be tied to sufficient mitigation and management of both biosafety and biosecurity risks. The unfortunate reality is that scientists exhibit considerable overconfidence in assessing the risks posed by their work and underestimate the probability of human error by several orders of magnitude (7). In addition, institutional oversight of dual-use research often fails to adhere to established guidelines (8). Despite good intentions, new guidelines are unlikely to make a major impact on the likelihood of human error. A more robust approach would be for scientists and funders to address the worst-case scenario and assess the adequacy of strategies in place to ensure an effective

Letters to the Editor

Letters (~300 words) discuss material published in *Science* in the past 3 months or matters of general interest. Letters are not acknowledged upon receipt. Whether published in full or in part, letters are subject to editing for clarity and space. Letters submitted, published, or posted elsewhere in print or online will be disqualified. To submit a letter, please email letters@science.sciencemag.org.



ZYMO RESEARCH

The Beauty of Science is to Make Things Simple

CATCH MORE.

with the most comprehensive
**Services for
Epigenetic Analysis**



Featuring...

Novel Platform Technologies for Genome-wide DNA Methylation Analysis

Exclusive services offered by Zymo Research.

- Methyl-MiniSeq: ~10% methylome coverage
- Methyl-MidiSeq: ~30% methylome coverage
- Methyl-MaxiSeq: Complete methylome coverage



Compare to the latest bead array technology,
with ~1.5% methylome coverage!

Targeted Sequencing for DNA Methylation Analysis

Any gene, any locus!

New RRHP for Genome-wide DNA Hydroxymethylation Analysis

To inquire, please e-mail
services@zymoresearch.com
or call us at 1-949-679-1190

www.zymoresearch.com

LETTERS

tive response to the various routes of potential biosecurity breaches. A sensible first step: Ensure that gain-of-function research on pathogenic viruses with high human impact is undertaken under the highest biosafety levels, in relatively few laboratories, and away from major population centers or transport nodes.

PHILIP E. HULME

The Bio-Protection Research Centre, Lincoln University,
Lincoln, 7647 Canterbury, New Zealand. E-mail: philip.hulme@lincoln.ac.nz

References

1. P. E. Hulme, *Science* **334**, 176 (2011).
2. B. Balmer, *Science* **326**, 1635 (2009).
3. D. Cressey, *Nature* **448**, 732 (2007).
4. J. Kaiser, *Science* **317**, 1852 (2007).
5. R. D. Henkel, T. Miller, R. S. Weyant, *Appl. Biosafety* **17**, 171 (2012).
6. P. Palese, *Nature* **481**, 115 (2012).
7. NRC, *Evaluation of the Updated Site-Specific Risk Assessment for the National Bio- and Agro-Defense Facility in Manhattan, Kansas* (National Academies Press, Washington, DC, 2012).
8. M. S. Race, E. Hammond, *Biosecurity Bioterrorism-Biodefense Strategy Practice Sci.* **6**, 19 (2008).

China's Nuclear Power Goals Surge Ahead

AFTER THE CHERNOBYL NUCLEAR ACCIDENT, many countries reduced their dependence on nuclear energy (1). The Fukushima disaster dealt a further blow to the industry, convincing nations such as Germany, Belgium, Italy, and Switzerland to phase out nuclear power (1). In contrast, China has undergone the fastest development of nuclear energy in the world since the opening of its first nuclear power station in 1991. In 2000, China's nuclear power capacity was 2.1 GW. China plans to have 40 GW in operation and 18 GW under construction by 2020 (2).

After putting its nuclear power expansion plans on hold after the Fukushima nuclear disaster, China's central government has once again begun to move forward by revising its energy and nuclear power plans last October (3). Under these new plans (3), the government will allow new nuclear plants in coastal areas only, issue more stringent construction permits for plants, and implement stricter nuclear safety measures, including the requirement that all new reactors comply with Generation III safety standards (4). China has recently approved new plants in Shidaowan with a total electricity-generating capacity of 6600 MW: a prototype high-temperature gas-cooled reactor (200 MW), pressurized water reactors (1400 MW), and four AP1000 reactors (each producing 1250 MW). China plans to build commercial Generation IV nuclear power stations (fast reactors) by 2030 (5).

Currently, 17 nuclear power units generating 12 GW of electricity (accounting for 1.8% of China's total production) are operating, and 29 units (with a total capacity of 30 GW) are under construction. The new and approved units will increase China's nuclear capacity to at least 70 GW by 2020. This increase in nuclear power generation would allow China to cut CO₂ emissions per unit of GDP in 2020 by 40 to 45% relative to the 2005 level (6). China's nuclear power capacity is expected to be 200 GW by 2030 and 400 GW by 2050, including many different manufactures and designs (7). A wide variety of nuclear power plant designs also poses many challenges associated with standardizing safety procedures to cope with seismic and tsunami events.

As China begins to address many of the safety and economic challenges posed by nuclear power, we urge caution against overdependence on this energy source.

X. JIN YANG,^{1*} DONGHUI ZHANG,² MI XU,²
JINYING LI³

¹State Key Laboratory of Organic-Inorganic Composites, Beijing University of Chemical Technology, Beijing 100029, China. ²China Institute of Atomic Energy, Xinzhen, Beijing, 102413, China. ³China Resources New Energy Group Co. Ltd., Beijing, 100033, China.

*Corresponding author. E-mail: yangxj@mail.buct.edu.cn

References

1. P. Bradford, *Nature* **483**, 151 (2012).
2. National Development and Reform Commission of P. R. China, China's Nuclear Power Mid- and Long-term Plan (2005–2020) (www.ndrc.gov.cn/gzdt/t20071102_170163.htm) [in Chinese].
3. The Central People's Government of the People's Republic of China, Energy Development Plan for the 12th Five-Year, Nuclear Power Safety Plan (2011–2020), Mid- and Long-Term Plan of China's Nuclear Power (2011–2020) (www.gov.cn/jdhd/2012-10/24/content_2250357.htm) [in Chinese].
4. World Nuclear Association, Advanced Nuclear Power Reactors (www.world-nuclear.org/info/Nuclear-Fuel-Cycle/Power-Reactors/Advanced-Nuclear-Power-Reactors/).
5. China National Nuclear Corporation (CNNC), Commercial Nuclear Fast Reactor Is Expected to Operate in 2030 (www.cnncc.com.cn/Tabid/283/InfoID/48764/rtid/446/Default.aspx) [in Chinese].
6. The State Council Information Office of the People's Republic of China, China's Energy Policy 2012 (www.scio.gov.cn/zxbd/wz/201210/1233785.htm) [in Chinese].
7. World Nuclear Association, Nuclear Power in China (www.world-nuclear.org/info/Country-Profiles/Countries-A-F/China—Nuclear-Power/#_UvItr9jeb9Ww).

CORRECTIONS AND CLARIFICATIONS

News & Analysis: "Siberian meteor spurs dash for data, calls for safeguards" by R. Stone (8 March, p. 1135). The sentence "The Chelyabinsk meteor's death throes emitted the most powerful infrasound waves ever recorded" should have specified "recorded by modern instruments."

Editors' Choice: "Sound judgment" by G. J. Chin (15 February, p. 739). The image showed Immanuel Kant. The HTML version online has been corrected.

News Focus: "Europe's €2 billion bet on the future" by K. Kupferschmidt (4 January, p. 28). The article says that the gold rush began 30 years after Lewis and Clark's expedition. The gold rush began 42 years later, in 1848. The HTML and PDF versions online have been corrected.

Editors' Choice: "Chick limb regeneration" by B. A. Purnell (7 December 2012, p. 1264). The image credit should be B. Özpolat *et al.*, *Dev. Biol.* **372**, 229 (2012). The HTML and PDF versions online have been corrected.

Perspectives: "Redder than red" by T. P. Sakmar (7 December 2012, p. 1299). The numbers to the right of the image on page 1299 were cut off. The correct numbers, clockwise, should be 570 and 577. The image has been corrected in the HTML and PDF versions online.

TECHNICAL COMMENT ABSTRACTS

Comment on "Apatite $^4\text{He}/^3\text{He}$ and (U-Th)/He Evidence for an Ancient Grand Canyon"

Ivo Lucchitta

Flowers and Farley (Reports, 21 December 2012, p. 1616; published online 29 November 2012) use thermochronometry to propose that the western paleo-Grand Canyon was nearly as deep 70 million years ago (Ma) as today. However, lithologies, facies relations, geomorphology, and paleotopography of Miocene interior-basin deposits near the mouth of the Grand Canyon show that no paleo-canyon existed in that area during filling of the basin, ~17 to ~5 Ma.

Full text at <http://dx.doi.org/10.1126/science.1234567>

Comment on "Apatite $^4\text{He}/^3\text{He}$ and (U-Th)/He Evidence for an Ancient Grand Canyon"

Karl E. Karlstrom, John Lee, Shari Kelley, Ryan Crow, Richard A. Young, Ivo Lucchitta, L. Sue Beard, Rebecca Dorsey, Jason W. Ricketts, William R. Dickinson, Laura Crossey

Flowers and Farley (Reports, 21 December 2012, p. 1616; published online 29 November 2012) propose that the Grand Canyon is 70 million years old. Starkly contrasting models for the age of the Grand Canyon—70 versus 6 million years—can be reconciled by a shallow paleocanyon that was carved in the eastern Grand Canyon 25 to 15 million years ago (Ma), negating the proposed 70 Ma and 55 Ma paleocanyons. Cooling models and geologic data are most consistent with a 5 to 6 Ma age for western Grand Canyon and Marble Canyon.

Full text at <http://dx.doi.org/10.1126/science.1233982>

Response to Comments on "Apatite $^4\text{He}/^3\text{He}$ and (U-Th)/He Evidence for an Ancient Grand Canyon"

R. M. Flowers and K. A. Farley

We reiterate that geological observations do not require Grand Canyon carving coeval with Colorado River integration. (U-Th)/He data from the western canyon, totaling 29 reproducible analyses from six samples and two labs, compellingly support an ancient canyon. Three dispersed analyses from one anomalous sample do not refute this conclusion, nor do the claimed shortcomings of our modeling have validity.

Full text at <http://dx.doi.org/10.1126/science.1234203>

CHEMBRIDGE

SCREENING LIBRARIES

Over 900,000 high quality, in-stock compounds

Diversity sets offering broad chemical space and pharmacophore coverage

Fragment compounds for fragment-based drug discovery

Targeted/biased sets for kinase, GPCR, ion channel and nuclear receptor targets

BUILDING BLOCKS



Over 14,000 unique reagents for medicinal chemistry and library synthesis

Available overnight from San Diego stock

Real time availability and pricing online at:
www.Hit2Lead.com

CHEMISTRY SERVICES



20th Anniversary

No Antibody.
No Problem.

Get immediate results with
HitScope® 700-444-4444
www.hit2lead.com



Be Amazed!





Sifting

Michael Pollastri, associate professor of chemistry and chemical biology,

Meet **Mike Pollastri**, whose unique approach to curing neglected diseases, like African sleeping sickness, is a breakthrough in drug development. He and his team sift through thousands of drugs, searching for those that can be repurposed to stop the parasite—a method that yields new therapeutics more quickly, and at a lower cost.

Learn how Pollastri and our other faculty researchers are making the world healthier. Northeastern University is making tomorrow happen.

northeastern.edu/tomorrow

Northeastern University

Making Tomorrow Happen



BIOGRAPHY

Nature's True Self

Jacobus J. Boomsma

About 50 years ago, William D. Hamilton completed the neo-Darwinian synthesis by extending Fisher's fundamental theorem of natural selection to include social interactions (1). He showed mathematically that to be truly general, Darwinian fitness had to be formulated in terms of gene copies rather than differential survival and progeny. Inclusive fitness (the number of gene copies in future generations passed on through both own offspring and the offspring of relatives) is what organisms are selected to maximize. In *Nature's Oracle*, Ullica Segerstrale offers an authoritative account that relates Hamilton's life and work.

Segerstrale (a sociologist at the Illinois Institute of Technology) takes us on a grand tour through the four decades of Hamilton's scholarship. We become familiar with his inductive reverse engineering of some of nature's most fundamental laws: a remarkable quest to unravel life's coherence and its challenges. Hamilton's insights were fueled by a profound interest in natural history very similar to Darwin's; he grew up just a few miles away from Down House, where Darwin had settled a century earlier. Hamilton endowed abstractions of genes with their own agendas, making it explicit that their interests would often conflict with one another and with the bodies carrying them. This gene's-eye perspective changed evolutionary biology by turning some of its branches into hypothesis-driven disciplines based on testable quantitative predictions of stable adaptive states.

In a single decade, Hamilton not only formulated inclusive fitness theory but also made lasting contributions to other evolutionary topics that were begging for quantitative understanding. Whereas his theories of senescence and extraordinary sex ratios were closely intertwined with the gene's-eye perspective, he also derived a universal geometry for group-living animals chased by predators, demonstrating that herds are ultimately driven by selfish interests. With others, he later developed deep insights into the evolutionary stability of dispersal, decision rules for cooperation among nonrelatives, and the

perpetual pressure of pathogens as drivers for maintaining sex and sexually selected ornaments. And he produced a selfish-herd theory for trees beleaguered by sap-sucking insects, which offered honest signaling of resistance as the ultimate explanation for autumn colors.

Segerstrale captures the essence of Hamilton's science and personality remarkably well. She skillfully unravels the intricate connections between his brilliant intellect, fearless engagement, skepticism toward established authority, fondness for Neotropical wasps, and uneasiness with social situations. I was somewhat disappointed by the rather sparse photographic material and in the choice of large *Morpho* butterflies for the dust jacket—rather than the giant blue carrion beetles with whom Hamilton had planned to team up for his ultimate graduation (2).

The book's title is intriguing. It seems to emphasize prophetic mission rather than scientific achievement, but the reason for choosing "oracle" emerges as we read along. In many chapters we find reminders that Hamilton combined a romantic interest in poetry and history with a rather bleak appreciation of human nature and the long-term perspectives of civilization. He increasingly felt the urge to share his inconvenient truth that our genomes would be no match for rapidly evolving diseases unless we continued to increase our dependence on the permanent surveillance of

a global health system—which he envisaged would be prone to episodes of disastrous failure and would erode our self-sustained individuality. These convictions were driven by what he considered the true self of nature that few are willing to face, possibly because we discount unimaginable futures even more readily than those we think we can predict.

Although his later derivation showed that inclusive fitness is fully equivalent with selection operating simultaneously at different levels (3), Hamilton continued to equate group selection logic in the human domain with totalitarian forces that would ultimately turn people into subdued citizens of a Huxleyan World State. With tribal nepotism and group-selected xenophobia as equally depressive

smaller-scale alternatives, he inferred that humanity's future would require careful management of our rare cooperative tendencies rather than trust in a primate heritage that seems hardly benign. Had he lived until now, I think he would have appreciated modern versions of the same idea, emphasizing that large-scale cooperation relies on institution-building rather than human nature (4).

Controversies abounded throughout Hamilton's career, most of them boiling down to being given a hard time by journal editors, reviewers of his manuscripts, and peers discrediting the novelty or general importance of his insights. Similar attitudes can still be found, but they receive little credit in the book. Few would argue that we can dismiss modern particle physics or big-bang theory because that would obviously reverse our state of civilization. Segerstrale makes a strong case for the Hamiltonian version of Darwinism being of the same caliber. Not because we neces-

Nature's Oracle
The Life and Work of
W. D. Hamilton
by Ullica Segerstrale
Oxford University Press,
Oxford, 2013. 459 pp. \$35, £25.
ISBN 9780198607274



The reviewer is at the Centre for Social Evolution, Department of Biology, Universitetsparken 15, University of Copenhagen, 2100 Copenhagen, Denmark. E-mail: jiboomsma@bio.ku.dk

sarily like it, but because it appears to be the only way to make rational sense of nature's true self. To ultimately weave nature's grand tapestry in humanistic colors, the gene had to be conceptually disconnected from the individual, and that is what Hamilton achieved.

References

1. A. Grafen, in *Narrow Roads of Gene Land*, vol. 3: *Last Words*, M. Ridley, Ed. (Oxford Univ. Press, Oxford, 2005), pp. 423–458.
2. W. D. Hamilton, *Ethol. Ecol. Evol.* **12**, 111 (2000).
3. O. Harman, *The Price of Altruism: George Price and the Search for the Origins of Kindness* (Bodley Head, London, 2010).
4. S. Pinker, *The Better Angels of Our Nature: Why Violence Has Declined* (Viking, New York, 2011).

10.1126/science.1236842

PHILOSOPHY OF SCIENCE

Pluralistic Paradigms

Erika Lorraine Milam

Irreconcilable differences have characterized the scientific study of human behavior for decades, even centuries. For some scientists and philosophers, like the late Thomas Kuhn, this inability to agree signaled the immaturity of the field. Preparadigm science, Kuhn held, “is regularly marked by frequent and deep debates over legitimate methods, problems, and standards of solution, though these serve rather to define schools than to produce agreement” (1). By way of contrast, Kuhn posited that mature science (characterized by normal, puzzle-solving activities) consisted of communities of scientists who worked unproblematically within a single research paradigm. Yet, as Helen E. Longino cogently argues in *Studying Human Behavior*, we would be foolish to assume such differences will vanish anytime soon. By rejecting Kuhnian expectations that one paradigm in the human behavioral sciences could ever come to dominate all research, Longino hopes to reconcile scientists, philosophers, and the popular press to the continued plurality of research programs in the study of human behavior as constituting a normal, and successful, scientific practice.

Longino (a philosopher of science at Stanford University) lucidly dissects five areas of active empirical research on the causes of human behavior: quantitative behavioral genetics, social-environmental approaches,

molecular behavioral genetics, neurobiological approaches, and more integrative approaches (for example, developmental systems theory and multifactorial path analysis). As a group, scientists in these areas concentrate on the proximate causes of behavior rather than evolutionary or functional explanations [as Ernst Mayr would have put it (2)]. And they seek to understand the biological structure constraining the expression of behavior rather than exploring the immediate physiological “triggers” of an instance of a behavior. Longino’s choice of research programs is doubly important: given these similarities, one could reasonably expect scientific agreement, and her researchers, from the outset, are invested in describing the genetic and developmental causes of behavior as it is expressed in the lifetime of individuals.

These differences in research questions correlate with similar disagreements over how to define or measure behavior. Take the two families of behavior on which Longino focuses. She notes that only some kinds of aggression are studied and that researchers vary widely in how they measure aggressive behavior, including through rates of “violent crime,” frequencies of “fighting” or “hitting a doll,” or even scores on psychological tests. When considering sexual orientation, behavioral researchers often follow Alfred Kinsey in defining homosexuality as a function of the frequency of sexual encounters with members of the same sex (3). But they vary in whether they consider homosexuals part of a sexual binary (as paired against heterosexuals) or existing on a sliding scale of sexual desire. Longino acknowledges that these definitions are set by social criteria. Scientists may only consider those aggressive acts that are reported to the police (surely a subset of the behavior, however defined). Kinsey’s sexuality scale emerged within a specific sociocultural context and may not be useful in defining homosexuality in other cultures (globally or temporally). In both instances, there is no unitary phenomenon under investigation. Thus, despite appearing to ask the same question, “what causes human behavior?” even the five ontological approaches Longino explores are irreconcilable because they operate in differentiated causal spaces.

Discussions of human behavior in the media tend to pit one of these “explanations” against another and ask which better accounts for our foibles and actions. Longino argues

that by relying too heavily on the nature-nurture debate and framing the conversation about human behavior in terms of competing research programs, the popular press has “fuel[ed] anticipation of intervention at the level of the individual”—providing (on aggression) superficial scientific support for the American incarceration culture and (on sexual orientation) contributing to a changing conversation about homosexuality as a civil rights issue. The political implications of research on human behavior are never clear-cut because they rely on a conflation of an individual’s behavior with her or his identity.

One possible escape from this dilemma, Longino posits, may be to think of behavior as social. After all, most aggressive or sexual acts involve more than one person and take place in a specific cultural context. This is the one place I feel her careful analysis falls short. After she meticulously examines how

scientists’ choice of ontological subjects affects their analyses, she is less attentive to the consequences of her own choices. If she had selected a wider swath of behavioral research from the outset (including, for example, ethological perspectives), Longino may have seen less of an individualist bias in

both the professional and popular literature (of course, such a choice would have made her project far less manageable). But this is a minor quibble with a fascinating book.

As a result of her commitment to methodological pluralism, Longino refuses to advocate for one research strategy over another. For human behavior, the obvious poles of the debate are defined by nature and nurture. But, she notes, all sides of the nature-nurture debate already agree that both genetic and environmental factors are important. So the far more interesting question is “how should scientific research on human behavior inform discussions of social policy?” In *Studying Human Behavior*, Longino has clearly articulated the methodological plurality of research on human behavior. She leaves to scientists and science writers the responsibility of shedding the last vestiges of their Kuhnian expectations.

References

1. T. Kuhn, *The Structure of Scientific Revolutions* (Univ. Chicago Press, Chicago, 1962).
2. E. Mayr, *Science* **134**, 1501 (1961).
3. A. Kinsey, W. Pomeroy, C. Martin, *Sexual Behavior in the Human Male* (Saunders, Philadelphia, 1948).

Studying Human Behavior
How Scientists Investigate
Aggression and Sexuality
by Helen E. Longino
University of Chicago Press
Chicago, 2013. 261 pp. \$75.
ISBN 9780226492872. Paper,
\$25, £16. ISBN 9780226492809.

The reviewer is at the Department of History, Princeton University, 136 Dickinson Hall, Princeton, NJ 08544, USA. E-mail: emilam@princeton.edu

10.1126/science.1236791

AGRICULTURE

Right-Sizing Stem-Rust Research

P. G. Pardey,^{1,2,3,4*} J. M. Beddow,^{1,2,3} D. J. Kriticos,^{1,3,5} T. M. Hurley,^{1,2,3} R. F. Park,⁶ E. Duveiller,⁷ R. W. Sutherst,⁸ J. J. Burdon,³ D. Hodson⁷

Stem rust caused by *Puccinia graminis* f. sp. *tritici* is a potentially devastating fungal disease that can kill wheat plants and small grain cereals but more typically reduces foliage, root growth, and grain yields [e.g., (1, 2)]. After years of success in keeping the disease at bay, new virulent races (collectively referred to as “Ug99”) have emerged, with the potential to infect much of the world’s wheat (3). Despite, or because of, the success of past research, these programs

saw an eventual rundown in support (4). We estimate global wheat losses over the past 50 years absent investments in research to limit impacts of stem rust and discuss how this can inform decisions about “right-sizing” research investments.

Potential annual stem-rust losses have been previously estimated by extrapolating reported losses from limited time periods and locations to broader spatial and temporal scales: \$1.4 billion for developing countries (5); up to \$3 billion for North Africa, the Middle East, and South Asia (6); and from \$7.6 to \$53.7 billion globally [derived from (7), see (8) and supplementary material (SM)]. However, global estimates derived from such “point-based” methods are misconceived and overstated, failing to account for the intrinsic variability of disease-induced crop losses over space and time.

From 1918 to 1960, U.S. wheat losses averaged 2.5% per year; losses dropped to less than an eighth of that rate (0.3% per year) thereafter (fig. S1). This reduction in U.S. wheat losses reflects the success of rust pathologists and wheat breeders in develop-

Is increased support needed for wheat disease research to avert crop losses from current and future strains?

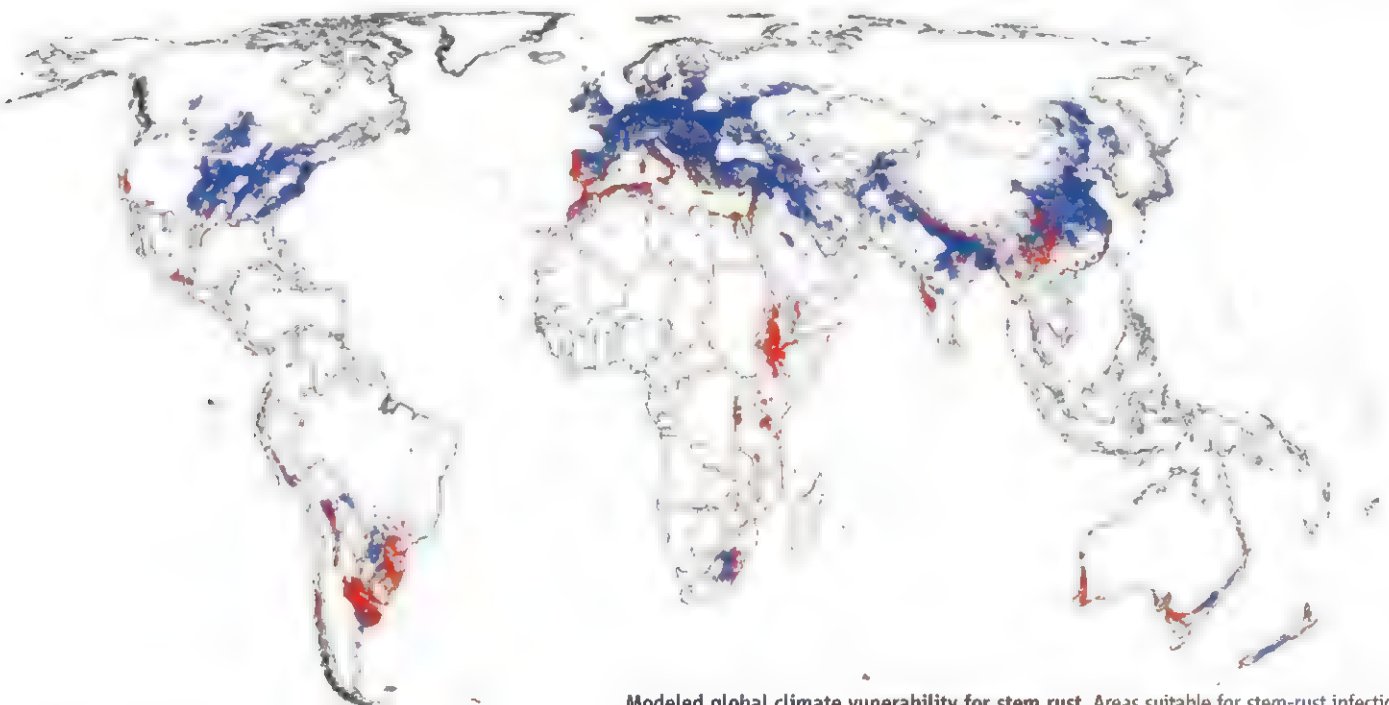
ing a series of stem rust-resistant wheat varieties (3). The more muted stem rust induced crop losses experienced in the United States during the past half-century were mirrored throughout most of the developed world. However, the more limited, and often slower, introduction of improved wheat varieties in many developing countries (9) likely exposed them to more frequent and larger wheat yield losses.

Probabilistic Stem Rust–Risk Assessment

We used stem-rust occurrence and long-term yield-loss data in conjunction with probabilistic methods to simulate global losses attributable to stem rust (8). The objective was to estimate global wheat losses in a counterfactual 1961–2009 world, where the probabilistic structure of losses was similar to that observed for the United States between 1918 and 1960, when U.S. farmers planted rust-susceptible wheat varieties. Extension of 1918–1960 characteristics to a 1961–2009 counterfactual period suggests what might have happened in the absence of research investments. These are indicative of what

¹International Science and Technology Practice and Policy Center, Department of Applied Economics, University of Minnesota, St. Paul, MN 55108, USA. ²Stakman-Borlaug Cereal Rust Center, University of Minnesota, St. Paul, MN 55108, USA. ³Commonwealth Scientific and Industrial Research Organization, Canberra, ACT 3190, Australia. ⁴Department of Agricultural Economics, Extension and Rural Development, University of Pretoria, Pretoria 0028 South Africa. ⁵E. H. Graham Center, Charles Sturt University Wagga Wagga, New South Wales 2678, Australia. ⁶Australian Cereal Rust Control Program, Plant Breeding Institute, University of Sydney, Eveleigh New South Wales 2015, Australia. ⁷International Maize and Wheat Improvement Center (CIMMYT), El Batán, CP 56130, México. ⁸Centre of Excellence for Environmental Decisions, University of Queensland, St. Lucia, Queensland 4072, Australia.

*Corresponding author. ppardey@umn.edu



Modeled global climate vulnerability for stem rust. Areas suitable for stem-rust infection are shown in blue, and the subset of those areas in which stem rust can establish and persist (that is, overwinter and oversummer) are shown in red. See (8) and SM for data and methods.

might occur should Ug99, or other virulent races, spread throughout the world and suggestive of the value of research investments (and crop management practices) in countering such threats.

We developed an ecological-niche model (10, 11) of stem rust and estimated that 66% (1.4 million km²) of the world's wheat area was climatically suitable for development of the disease (see the map). The present assessment considers differences in the probability distribution of yield losses under two scenarios: (i) one representing contemporary losses in largely resistant wheat (1961–2009 in the United States) and (ii) another characterizing the loss distribution that occurred historically with less resistant varieties deployed in the field (U.S. losses during 1918–1960). We identified 15 epidemiologically and statistically independent regions (2, 8) and used U.S. loss data (ii) to simulate a probabilistic pattern of proportional losses over each region. The pattern of climate suitability for stem rust across the epidemiological zones (8) suggests that we may be underestimating losses for areas outside the temperate wheat-growing regions of the northern hemisphere, where a small share of the world's wheat is grown.

The expected average total global losses in this 1961–2009 counterfactual world without durable stem-rust resistance is 306 million metric tons (MT) from a total production of 23 billion MT (i.e., a loss of U.S. \$54.7 billion when valued at 2010 average U.S. wheat prices) with a 90% chance (the 10th percentile) of losing at least 275 MT (or U.S. \$49.3 billion) (see the table). This expected 306 MT total loss equates to average annual losses for the counterfactual period of 6.2 MT (or U.S. \$1.12 billion per year) from annual average production of 470 MT. This annual loss is substantially less than the 104 MT calculated for a hypothetical single-year global pan-

demic but still sizable for the effects of just one disease on a staple food crop. Eliminating such an annual loss would save enough wheat to almost satisfy the entire annual calorie deficit of sub-Saharan Africa's undernourished population (8).

Spending on Stem-Rust Research

In 2008, the Bill and Melinda Gates Foundation (BMGF) launched the Durable Rust Resistance in Wheat global partnership, with a 3-year commitment totaling \$26.8 million. This was extended for 5 years in 2011 with an additional \$40 million from BMGF and the UK Department for International Development. These funds complement long-standing, but of late generally more limited, investments in stem-rust research conducted by public agencies the world over (12).

An economic approach to determining whether this is too much or too little investment is to compare the worldwide costs of research to develop rust-resistant varieties (plus the costs of other rust-mitigating efforts like fungicide use) against the global benefits of averting yield losses from stem rust by the development and deployment of resistant varieties or other means. This economic balance can best be struck by reference to the modified internal rate of return (MIRR): the rate that equates the expected present value of a stream of research benefits with the present value of the cost of the research given reinvestment and finance rates for benefits and costs (13).

Taking the estimated stream of counterfactual global losses attributed to stem rust since 1961 as an indication of potential benefits from successful wheat stem rust–resistance research over this period, we estimate that a sustained investment of \$51.1 million per year (2010 prices) in stem-rust research could be justified economically (8). With such a sustained investment, there is a 95% chance that the MIRR would exceed 10% per year, conditional on the success of the funded research. Looking forward, and assuming a nondecreasing total value of world wheat production, it seems prudent to invest at least this much annually (in inflation-adjusted terms) in stem-rust research. This amount is in addition to other investments that would be necessary to increase wheat yields generally, as well as to ameliorate the effects of other wheat pests and diseases. A \$51.1 million annual R&D expenditure is equivalent to investing \$0.23 per hectare of wheat pests and in 2009; by comparison, U.S. wheat farmers spent \$34.56 per hectare on seed in 2009 (14).

Our estimates of expected global losses attributable to stem rust are more modest

than those of other studies (5–7), but there is still a substantial funding shortfall. Averaging recent decades, global funding for research to maintain stem-rust resistance in wheat has been less than half the amount that appears necessary (15). We question the wisdom of cutting back on wheat-rust research as the U.S. Department of Agriculture has done recently, in line with similar trends over past decades in other countries (4, 16).

Maintaining yield growth rates necessary to meet anticipated future demands will require a sustained effort to develop wheat varieties that are resistant to contemporary races of rust. This requires an investment strategy that supports sustained research programs geared to identifying and addressing ever-evolving stem-rust threats. The need for sustained investment also applies to other crop and pest systems subject to coevolutionary pressure. Our methods can help right-size research investment streams needed to sustain or improve global food security.

References and Notes

- G. Agrios, *Plant Pathology* (Elsevier Academic Press, Boston, ed. 5, 2005).
- E. E. Saari, J. M. Prescott, in *The Cereal Rusts*, A. P. Roelfs, W. R. Bushnell, Eds. (Academic Press, Orlando, FL, 1985), vol. 2, chap. 9.
- R. P. Singh *et al.*, *Annu. Rev. Phytopathol.* **49**, 465 (2011).
- R. P. Singh *et al.*, *Adv. Agron.* **98**, 271 (2008).
- H. J. Dubin, J. P. Brennan, Combating stem and leaf rust of wheat: historical perspective, impacts, and lessons learned. (discussion paper 00910, International Food Policy Research Institute, Washington, DC, 2009).
- Durable rust resistance in wheat, Borlaug Global Rust Initiative (2012); wheatrust.cornell.edu/about/background-rationale.cfm.
- M. C. Fisher *et al.*, *Nature* **484**, 186 (2012).
- J. M. Beddow *et al.*, Measuring the worldwide spatial occurrence and probabilistic consequences of stem rust (HarvestChoice, Saint Paul, MN, 2012); <http://croppest.org/purl/20131>.
- R. E. Evenson, D. Gollin, *Science* **300**, 758 (2003).
- R. W. Sutherst *et al.*, *CLIMEX Version 3 User's Guide* (Hearne Scientific Software, Melbourne, 2007).
- J. M. Beddow *et al.*, Potential global crop pest distributions using CLIMEX: HarvestChoice applications (HarvestChoice, Saint Paul, MN, 2010).
- Key among these agencies are CIMMYT, ICARDA, the USDA's Cereal Disease Laboratory, the University of Minnesota's Stakman-Borlaug Cereal Rust Center, the University of Sydney's Plant Breeding Institute and CSIRO.
- X. Rao, T. M. Hurley, P. G. Pardey, Recalibrating the reported rates of return to food and agriculture R&D (University of Minnesota, Department of Applied Economics, Saint Paul, MN, 2012); <http://purl.umn.edu/135018>.
- Economic Research Service, USDA, Commodity costs and returns; www.ers.usda.gov.
- See SM for estimation details of comparative wheat pathology R&D spending.
- National Association of Wheat Growers, *Western Farm Press*, 20 March 2012; <http://westernfarmpress.com/government/agricultural-research-hrt-hard-usda-labs-close>.

Acknowledgments: The authors thank M. Carson, R. Singh, B. Steffenson, and Y. Chai.

Supplementary Materials

www.sciencemag.org/cgi/content/full/340/6129/147/DC1

10.1126/science.1229707

GLOBAL WHEAT LOSS ESTIMATES ATTRIBUTED TO STEM RUST, 1961–2009		
Probability of loss	Total period loss (1961–2009)	Implied average annual losses
Percentage	Million metric tons	
90	≥ 275	≥ 5.6
50	≥ 305	≥ 6.2
20	≥ 326	≥ 6.7
5	≥ 347	≥ 7.1

Single-year pandemic: 104

Distribution of wheat losses and corresponding average annual loss absent investment in stem-rust research. Single-year pandemic represents single-year loss if the historically highest 1935 U.S. loss is applied to all stem rust–susceptible production systems worldwide. See (8) and SM.

ENVIRONMENT

Latin America's Nitrogen Challenge

A. T. Austin,¹ M. M. C. Bustamante,² G. B. Nardoto,² S. K. Mitre,² T. Pérez,³ J. P. H. B. Ometto,⁴ N. L. Ascarrunz,⁵ M. C. Forti,⁴ K. Longo,⁴ M. E. Gavito,⁶ A. Enrich-Prast,⁷ L. A. Martinelli^{8*}

Latin America (LA) has many social indicators similar to those of highly developed economies but most frequently falls midway between least developed countries and industrialized regions. To move forward, LA must address uncontrolled urbanization, agricultural production, social inequity, and destruction of natural resources. We discuss these interrelated challenges in terms of human impact on the nitrogen (N) cycle. Human activity has caused unprecedented changes to the global N cycle; in the past century, total global fixation of reactive N (Nr) has at least doubled (1). Excess Nr leaked into the environment negatively affects soils, atmosphere, and water resources in temperate zones (1). In addition to N excess from human impact, mining of natural soil N creates N deficits in some regions (2, 3).

Agriculture resurged in LA with marked growth in soybean cultivation in the 1990s (3) and recent expansion of the biofuel market (4). Soybean cultivation in LA is 40% of global production, larger than any other world region (3). Because of the natural fertility of soil in Argentina's Pampa region, N fixation is not strongly stimulated; thus, N exported in soybeans is mostly from soil N, rather than fixation, causing a net loss of N (3, 5). In Brazil converting pristine ecosystems with high natural N fixation rates to fields can lead to negative N balance (6). In contrast, soybean crops that replace other cropping or grazing ecosystems, N in areas of low soil N and heavy application of phosphorus (P) fertilizer (7).

Biomass burning to clear land for agriculture has been estimated at >150,000 km² annually in LA (8). This transfers a large amount of Nr from the land to the atmosphere, which is then redistributed regionally (9). In addition to direct health effects of biomass burning (10), part of the Nr returns from the atmosphere to aquatic and terrestrial ecosystems via wet and dry deposition. Total N deposition in major

agricultural areas and urban zones in LA is on par with developed countries. By 2050, four of the eight LA biodiversity hotspots are projected to have potentially harmful levels of N deposition (11).

Because of lack of basic infrastructure, especially in low-income areas of megacities, most domestic sewage is released into water bodies without treatment, causing N and P enrichment (12), affecting trophic interactions (13), and increasing public health risks (14). Exacerbating the problem is rural-urban migration, a result of marginalization and extreme poverty faced by many small farmers.

Ecosystem and human health in LA depends on managing human impact on the N cycle. Antiquated political institutions inherited from European colonization concentrate political and economic power in a small fraction of the population. These must be replaced by inclusive political, economic, and academic institutions that enforce property rights, maintain a strong and independent judicial system, combat corruption, and encourage new technologies and skills (15).

Destruction of some of the world's largest intact areas of highly diverse tropical ecosystems must halt (16). It has been argued that sufficient land has been cleared for sustainable production of goods and services, but that most of the land is inefficiently used, especially in the livestock sector (17). Although deforestation in the Amazon basin has declined (16), recent environmental legislation may allow a resurgence of land-clearing (18). Increased efficiency of land already under cultivation should be a priority, without increasing inputs of N fertilization (19). Commitments from local governments and agriculture sectors, especially beef and soybean, are critical, acting in concert across LA. International mechanisms like REDD (Reducing Emissions from Deforestation and Forest Degradation) and financial support from developed nations would increase the likelihood of success (16).

Public agriculture policies must include small farmers and less-favored groups (20). Secure land rights are crucial (21), with potential to decrease land violence that constrains rural development (22). Agricultural practices must increase functional diversity, mimicking natural ecosystems. Techniques include no-

Human impacts on the N cycle require sustainable ecological solutions to preserve ecosystem and human health.

till agriculture, cover crops, crop rotation, and enhancement of natural N fixation (23). Intensification must only be encouraged under sustainable practices, where agroecosystems and neighboring landscapes provide key ecosystem services (24).

Basic science must address LA's ecological and social systems and their interactions. For example, long-term consequences of widespread practices of no-till agriculture and intense cultivation of a single species are not well understood (3, 5). We must improve our understanding of the terrestrial-aquatic interface, particularly in tropical zones, because models estimate that N discharge from untreated sewage will at least double in developing countries between 2000 and 2050 (25).

International policies related to N management and pollution across LA, similar to those in parts of Europe (e.g., the Nitrates Directive) and North America, could increase regional political consensus, a necessity considering the transboundary effects of N atmospheric deposition and water pollution.

References and Notes

1. J. N. Galloway *et al.*, *Science* **320**, 889 (2008).
2. L. A. Martinelli *et al.*, *Biogeochemistry* **79**, 3 (2006).
3. A. T. Austin *et al.*, *Biogeochemistry* **79**, 45 (2006).
4. R. Janssen, D. D. Rutz, *Energy Policy* **39**, 5717 (2011).
5. F. Salvagioti *et al.*, *Field Crops Res.* **108**, 1 (2008).
6. E. M. A. Smaling, R. Roscoe, J. Lesschen, A. Bouwman, E. Comunello, *Agric. Ecosyst. Environ.* **128**, 185 (2008).
7. S. Filoso *et al.*, *Biogeochemistry* **79**, 61 (2006).
8. E. Chuvpilo *et al.*, *Ecol. Appl.* **18**, 64 (2008).
9. I. Trebs *et al.*, *Atmos. Chem. Phys.* **6**, 447 (2006).
10. M. F. Alonso *et al.*, *Atmos. Environ.* **44**, 5072 (2010).
11. A. Bleeker *et al.*, *Environ. Pollut.* **159**, 2280 (2011).
12. M. H. B. Daniel *et al.*, *Water Air Soil Pollut.* **136**, 189 (2002).
13. J. P. H. B. Ometto *et al.*, *Freshw. Biol.* **44**, 327 (2000).
14. P. J. Hotez *et al.*, *PLoS Negl. Trop. Dis.* **2**, e1757 (2008).
15. D. Acemoglu, J. Robinson, *Why Nations Fail* (Crown, New York, 2012).
16. D. Nepstad *et al.*, *Science* **326**, 1350 (2009).
17. M. Herrero *et al.*, *Science* **327**, 822 (2010).
18. L. A. Martinelli, *Nature* **474**, 579 (2011).
19. X. P. Chen *et al.*, *Proc. Natl. Acad. Sci. U.S.A.* **108**, 6399 (2011).
20. L. A. Martinelli *et al.*, *Agric. Syst.* **104**, 419 (2011).
21. D. Acemoglu, G. Gancia, F. Zilibotti, *J. Econ. Theory* **147**, 570, 601.e3 (2012).
22. C. Kay, *Third World Q.* **22**, 741 (2001).
23. A. L. Cerdeira *et al.*, *J. Agric. Food Chem.* **59**, 5799 (2011).
24. J. Ferrera *et al.*, *J. Appl. Ecol.* **49**, 535 (2012).
25. L. F. van der Struijk, C. Kroeze, *Global Biogeochem. Cycles* **24**, n/a (2010).

Acknowledgments: The authors acknowledge support from C. Palm at the Inter-American Institute for Global Change Research and the New Phytologist Trust. R. Howarth, K. Cassman, and participants in the International Nitrogen Initiative, provided comments.

¹Universidad de Buenos Aires, IFEVA-CONICET, Buenos Aires, Argentina. ²Universidade de Brasília, Brasília, Brazil. ³Instituto Venezolano de Investigaciones Científicas, Caracas, Venezuela. ⁴Instituto Nacional de Pesquisas Espaciais, São José dos Campos, Brazil. ⁵Instituto Boliviano de Investigación Forestal, Santa Cruz, Bolivia. ⁶Universidad Nacional Autónoma de México, Distrito Federal, México. ⁷Universidade Federal do Rio de Janeiro, Rio de Janeiro, Brazil. ⁸CENA-Universidade de São Paulo, Piracicaba, Brazil

*Author for correspondence: martinelli@cena.usp.br

ECOLOGY

Self-Medication in Animals

Jacobus C. de Roode,^{1*} Thierry Lefèvre,² Mark D. Hunter³

The concept of antiparasite self-medication in animals typically evokes images of chimpanzees seeking out medicinal herbs to treat their diseases (1, 2). These images stem partly from the belief that animals can medicate themselves only when they have high cognitive abilities that allow them to observe, learn, and make conscious decisions (3). However, any concept of self-medication based solely on learning is inadequate. Many animals can use medication through innate rather than learned responses. The growing list of animal pharmacists includes moths (4), ants (5), and fruit flies (6). The fact that these animals self-medicate has profound implications for the ecology and evolution of animal hosts and their parasites.

Janzen (2) was the first to describe cases in which diseased vertebrates appeared to select secondary plant compounds with antiparasitic activity. Consequently, self-medication has often been defined as the antiparasitic use of secondary plant chemicals or other non-nutritive substances by herbivores (1). However, boundaries between nutrients, medicines, and toxins are permeable and are often defined only by the ingested dose of a chemical (7). Thus, whereas traditional examples of animal medication involve animals eating specific plants only when diseased (1), recent examples include animals increasing the ingestion of particular chemicals that are already in their diets (4).

Animals may use chemicals to relieve symptoms that are not caused by parasitic diseases, but we restrict our discussion to self-medication as a defense against parasites. Such defenses can come in two general forms (see the figure). In therapeutic medication, diseased individuals alter their behavior to medicate in response to parasite infection (4). In contrast, prophylaxis is used by infected and uninfected individuals alike to prevent parasite infection, often in response to high parasite risk (5).

Therapeutic and prophylactic medication can be further divided depending on the target of medication (see the figure). Much work has focused on cases in which animals medicate themselves, including baboons and woolly bear caterpillars (1, 4, 6), but animals may medicate their offspring or other genetic kin instead. Fruit flies have been shown to preferentially lay

Animal self-medication against parasites is more widespread than previously thought, with profound implications for host-parasite biology.



¹Department of Biology, Emory University, 1510 Clifton Road, Atlanta, GA 30322, USA. ²Maladies Infectieuses et Vecteurs: Écologie, Génétique, Évolution et Contrôle (UM1-UM2-CNRS 5290-IRD 224), Institut de Recherche pour le Développement, 911 Avenue Agropolis, BP 64501, Montpellier 34394, France. ³Department of Ecology and Evolutionary Biology, University of Michigan, 2053 Natural Sciences Building, 830 North University, Ann Arbor, MI 48109-1048, USA. E-mail: jderood@emory.edu

Types of animal medication.

els of parasite growth and virulence by laying their eggs on antiparasitic milkweed (9) (transgenerational therapeutic medication). These studies show that we should deemphasize the “self” in self-medication and base medication studies on an inclusive fitness framework.

There are many examples in which a behavior is strongly implicated as medication, but in which a fitness advantage for the actor remains to be demonstrated. Primates commonly ingest plant materials with antiparasitic properties but with little or no nutritional value. For example, they chew the bitter pith of *Vernonia amygdalina* and swallow rough plant leaves whole (1). Chewing bitter pith may release antiparasitic compounds, whereas swallowing rough leaves whole is apparently a means of physically expelling intestinal parasites (1). However, it remains to be shown whether parasite infection triggers the behavior and whether the behavior increases host fitness. Similarly, a recent study has suggested that house sparrows and finches add high-nicotine cigarette butts to their nests to reduce mite infestations (10), but it is unclear whether the birds gain higher fitness from the behavior.

To conclude definitively that a behavior is an adaptive form of therapeutic medication, several conditions must be met. First, the behavior involves the ingestion or external application of a third species or chemical compound. Second, the behavior must be initiated by parasite infection. This sounds easier to establish than it is. For example, it is hard to determine whether a behavior seen in a particular animal in a field study is a result of parasite infection or whether something else caused that individual both to be infected and to display the behavior. Manipulative experiments, in which some individuals are infected and others are left as uninfected controls, are the best way to evaluate this condition. Third, the behavior increases the fitness of the infected individual or its genetic kin. Fourth, the behavior is costly to uninfected individuals; if it were not, all individuals would display it (4). Fifth, the behavior is relevant in the natural environment of the host; showing the existence of medication with artificial diets alone does not demonstrate its relevance in nature.

The conditions are similar for prophylaxis, except that prophylaxis is displayed in response to parasite risk rather than infection. It may also be difficult to demonstrate costs if prophylaxis has evolved into a fixed phenotype over time.

We have omitted an oft-cited condition for self-medication: that the behavior must reduce parasite infection or fitness (10). The reason for our omission is that medication behavior may enhance host fitness by increasing tolerance of infection (allowing the host to maintain fitness despite being infected) without reducing parasite fitness (11).

Many published cases do not yet satisfy all these conditions, but animal medication is clearly much more widespread than originally thought. It is therefore important to understand how animal medication affects the ecology and evolution of host-parasite interactions. We argue that there are at least four major consequences of animal medication.

First, when animal medication reduces parasite fitness, we expect to observe effects on parasite transmission or virulence. Neither consequence has received much attention yet, but two studies indicate that medication can indeed influence the interactions between hosts and their parasites. For example, when gypsy moth caterpillars consume foliage high in phenolics, it reduces transmission of a polyhedrosis virus and facilitates moth outbreaks (12). There is also preliminary evidence that medication affects virulence evolution: increasing parasite virulence is predicted from models of medication behavior by monarch butterflies using toxic milkweed (13).

Second, animal medication should affect the evolution of animal immune systems. Immune responses are costly, suggesting that animals should not use or evolve immunity when they do not need it. Animal medication provides an alternative to cellular and humoral immune responses and may thus result in a reduction or loss of such immune responses. This hypothesis has not yet been tested formally, but there is suggestive evidence. Perhaps most strikingly, honeybees use a series of behavioral immune mechanisms, including the incorporation of antimicrobial resin into their nests (14). Analysis of their genome suggests that honeybees lack many of the cellular and humoral immune genes of other insects, raising the possibility that their use of medicine has been partly responsible—or has compensated—for a loss of other immune mechanisms (14).

Third, host-parasite interactions are often used to explore patterns of local adaptation, yet surprisingly few studies provide evidence for adaptation of parasites to their local hosts or vice versa (15). Most of these studies are based on experiments in which hosts and parasites from multiple populations are exposed to each other in sympatric

and allopatric combinations. By not allowing hosts to behave naturally, such studies preclude animals from medicating themselves or their kin. Thus, if animals have locally adapted to their parasites through medication behaviors, studies must be designed such that animals can display their naturally evolved behaviors. It is our expectation that when this is done, more studies will find that hosts have locally adapted their behavior to their parasites.

Finally, the study of animal medication will have direct relevance for human food production and health. Disease problems in agricultural organisms can worsen when humans interfere with the ability of animals to medicate. For example, increases in parasitism and disease in honeybees can be linked to selection by beekeepers for reduced resin deposition by their bees (14). A re-introduction of such behavior in managed bees would likely have great benefits for disease management. In addition, as self-medicating animals, humans still derive many of their medicines from natural products, and plants remain the most promising source of future drugs. Studies of animal medication may lead the way in discovering new drugs to relieve human suffering.

References and Notes

1. M. A. Huffman, *Proc. Nutr. Soc.* **62**, 371 (2003).
2. D. H. Janzen, in *The Ecology of Arboreal Folivores*, G. C. Montgomerie, Ed. (Smithsonian Institution Press, Washington, DC, 1978), pp. 73–84.
3. G. A. Lozano, in *Stress and Behavior*, A. P. Møller et al., Eds. (Academic Press, San Diego, CA, 1998), vol. 27, pp. 291–317.
4. M. S. Singer, K. C. Mace, E. A. Bernays, *PLoS ONE* **4**, e4796 (2009).
5. G. Castella, M. Chapuisat, P. Christe, *Anim. Behav.* **75**, 1591 (2008).
6. N. F. Milan, B. Z. Kacsoh, T. A. Schlenke, *Curr. Biol.* **22**, 488 (2012).
7. D. Raubenheimer, S. J. Simpson, *Integr. Comp. Biol.* **49**, 329 (2009).
8. B. Z. Kacsoh, Z. R. Lynch, N. T. Mortimer, T. A. Schlenke, *Science* **339**, 947 (2013).
9. T. Lefèvre, L. Oliver, M. D. Hunter, J. C. De Roode, *Ecol. Lett.* **13**, 1485 (2010).
10. M. Suárez-Rodríguez, I. López-Rull, C. M. García, *Biol. Lett.* **9**, 20120931 (2013).
11. L. Råberg, D. Sim, A. F. Read, *Science* **318**, 812 (2007).
12. M. A. Foster, J. C. Schultz, M. D. Hunter, *J. Anim. Ecol.* **61**, 509 (1992).
13. J. C. de Roode, C. Lopez Fernandez de Castillejo, T. Faits, S. Alizon, *J. Evol. Biol.* **24**, 712 (2011).
14. M. Simone-Finstrom, M. Spivak, *Apidologie (Celle)* **41**, 295 (2010).
15. M. A. Greischar, B. Koskella, *Ecol. Lett.* **10**, 418 (2007).

Acknowledgments: We thank M. Bushman, C. Gowier, Z. Lynch, K. Leon, M. Maudsley, and A. Pierce for discussion. J.C.d.R. and M.D.H. are funded by NSF grants DEB-1019746, DEB-1257160, and DEB-1256115, and T.L. is funded by Agence Nationale de la Recherche grant 11-PDOC-006-01.

CHEMISTRY

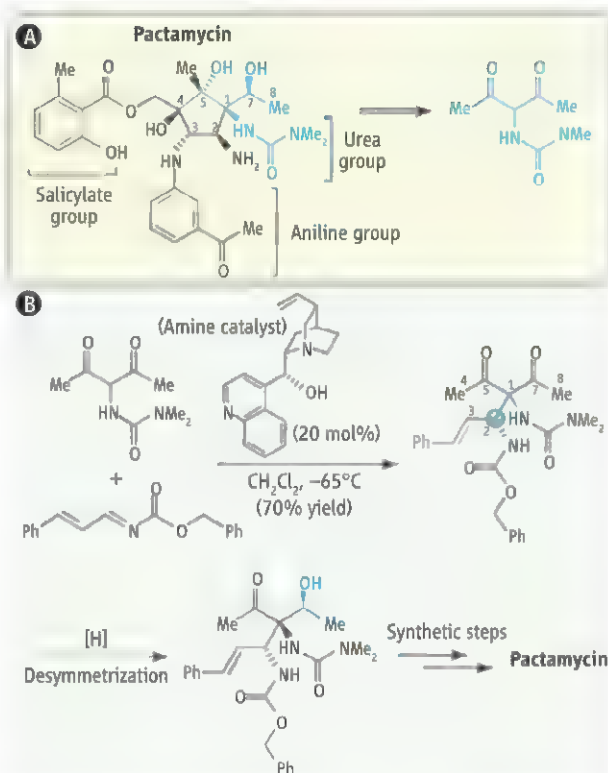
Pactamycin Made Easy

Julian A. Codelli and Sarah E. Reisman

Natural products—small molecules isolated from plants, fungi, bacteria, and other microorganisms—continue to serve as an important source of chemical tools for the study of biological systems and disease pathology, as well as new drugs. One example is the natural product pactamycin, which has been instrumental in the investigation of ribosome structure and function (1, 2). However, the structural complexity of this small molecule has historically rendered it—and by extension its unnatural analogs—synthetically inaccessible, hindering efforts at the development of pactamycin-derived therapeutics. On page 180 of this issue, Malinowski *et al.* (3) report a total chemical synthesis of pactamycin that elegantly addresses this challenge and opens a new chapter in the story of this natural product.

Isolated from *Streptomyces pactum* in 1961 (4), pactamycin has attracted the attention of both chemists and biologists for decades. Although originally categorized as an inhibitor of ribosomal initiation, recent structural and biochemical investigations have shown that it inhibits translocation, preventing the target ribosomal unit from continuing to move along the mRNA strand to which it is bound, and thus disrupting protein synthesis (1, 2). Unfortunately, pactamycin exhibits this activity against ribosomes across all phylogenetic domains: bacteria, archaea, and eukaryotes. Indeed, the toxicity of pactamycin in mammalian cells has largely precluded its use as a therapeutic agent in humans.

Recently, several independent studies have revealed that subtle changes to the pactamycin structure (see the figure, panel A) can greatly alter the molecule's biological activity (5–7). Culture extracts from a variety of *Streptomyces* species, including both



Pactamycin in 15 steps. (A) Malinowski *et al.* used a synthetic strategy to prepare pactamycin that relied on a hidden symmetry element in the natural product, depicted in blue (the open arrow denotes a planning step to identify possible reactants); Me, methyl. (B) In the key reaction sequence, a chiral catalyst assembles all of the carbons in the pactamycin framework. A desymmetrization step then sets the stereochemistry; Ph, phenyl.

wild-type and mutant strains, have given researchers access to a small collection of analogs possessing truncated or deoxygenated appendages of the seventh carbon atom (C7), some of which also lack the salicylate group. Some of these derivatives possess improved selectivity for killing protozoan cell lines (e.g., the parasites responsible for malaria and African sleeping sickness) versus both bacterial and human cell lines.

These findings have sparked a renewed interest in the development of a chemical synthesis of pactamycin, which could ultimately provide access to new synthetic analogs with therapeutically useful selectivity profiles. In 2011, Hanessian and co-workers reported the first total chemical synthesis of pactamycin, a breakthrough discovery that provides access to the molecule in 32 synthetic steps from commercial start-

A concise chemical synthesis of pactamycin, a natural product that targets the ribosome, may allow the development of less toxic derivatives.

ing materials (8, 9). Nonetheless, a systematic study of the correlation between molecular structure and biological function demands a more concise and modular synthesis.

In general terms, a practical chemical synthesis of a molecule should proceed in as few synthetic steps as possible, and when feasible, incorporate functional groups in their native form to minimize unnecessary oxidation, reduction, and protecting-group reactions. In the case of pactamycin, the five-membered ring at the core of the molecule, which is decorated at each carbon with a nitrogen or oxygen atom, poses a particular challenge to practicality. This compact system must be constructed not only with the correct connectivity, but also the correct stereochemistry (or three-dimensional orientation) between the atoms. The spatial relationships of the various appendages protruding from the ring are crucial to the molecular recognition events that constitute binding to a biological target.

One way to reduce the complexity of a synthetic problem is to exploit an element of symmetry in the target molecule. Although non-

obvious in a cursory inspection of pactamycin, Malinowski *et al.* identified a “hidden” symmetry element in the carbon chain extending from C4 to C8 that allowed them to design a synthetic plan that would begin with an inexpensive, symmetric starting material (see the figure, panel A). A variant of a Mannich reaction allowed the authors to use a chiral amine to catalyze carbon-carbon bond formation and also control the stereochemistry at the C2 atom. The stereochemical information at C2 is then relayed through the subsequent reductive desymmetrization of the methyl ketones at C5 and C7, such that the final product possesses the correct three-dimensional structure (see the figure, panel B). An important aspect of the synthesis is that the salicylate, aniline, and urea groups are all incorporated in their native form (without requiring pro-

Chemistry and Chemical Engineering, California Institute of Technology, 1200 East California Boulevard, Pasadena, CA 91125, USA. E-mail: jcodelli@caltech.edu; reisman@caltech.edu

tecting groups or other synthetic manipulations), which helps reduce the number of synthetic steps.

The synthesis developed by Malinowski *et al.* provides access to pactamycin in only 15 chemical steps (versus 32 steps previously) and 1.9% overall yield. Notably, several late-stage intermediates used in the synthesis represent suitable precursors for the preparation of analogs. Future investigations of the biological effects of such analogs could

lead to the development of therapeutic agents with attenuated toxicity in mammalian cells. Just as the synthesis reported by Malinowski *et al.* will likely prove to be an enabling development in the story of pactamycin, it also highlights the enabling power of symmetry as a design element in rendering complex molecules synthetically practical.

References

1. D. E. Brodersen *et al.*, *Cell* **103**, 1143 (2000).
2. G. Dinis *et al.*, *Mol. Cell* **13**, 113 (2004).
3. J. T. Malinowski *et al.*, *Science* **340**, 180 (2013).
4. A. D. Argoudelis, H. K. Jahnke, J. A. Fox, *Antimicrob. Agents Chemother.* **1962**, 191 (1962).
5. K. Otaguro *et al.*, *J. Antibiot. (Tokyo)* **63**, 381 (2010).
6. W. Lu, N. Roongsawang, T. Mahmud, *Chem. Biol.* **18**, 425 (2011).
7. M. Iwatsuki *et al.*, *J. Antibiot.* **65**, 169 (2012).
8. S. Hanessian *et al.*, *Angew. Chem. Int. Ed.* **50**, 3497 (2011).
9. S. Hanessian, R. R. Vakiti, S. Dorich, S. Banerjee, B. Deschênes-Simard, *J. Org. Chem.* **77**, 9458 (2012).

10.1126/science.1236882

PHYSICS

The Complete Quantum Hall Trio

Seongshik Oh

When an electric current I flows through a slab of conductor placed in an external magnetic field H perpendicular to the flow direction, the magnetic field deflects the current-carrying charge particles toward the edge of the conductor and a transverse voltage V_T develops across the sample. This effect, discovered by Edwin Hall in 1879 (1), is called the Hall effect. Because the transverse resistance (or Hall resistance) defined as V_T/I is proportional to H/n , where n is the sheet carrier density of the sample, the Hall effect has been widely used to quantify the carrier type (electron or hole), density, and mobilities of electronic materials. However, in the 1980s it was found that when the charge carriers are confined to a two-dimensional system (or sheet), the Hall resistance becomes exactly quantized at $h/(ve^2)$, where h is the Planck constant, e is the electron charge, and v is a positive integer, whenever H/n approaches specific values (2). This phenomenon, called the quantum Hall effect (QHE), always requires an external magnetic field. On page 167 this issue (3), Chang *et al.* have discovered that such exact quantization in the transverse resistance can occur even without an external magnetic field on a thin ferromagnetic topologi-

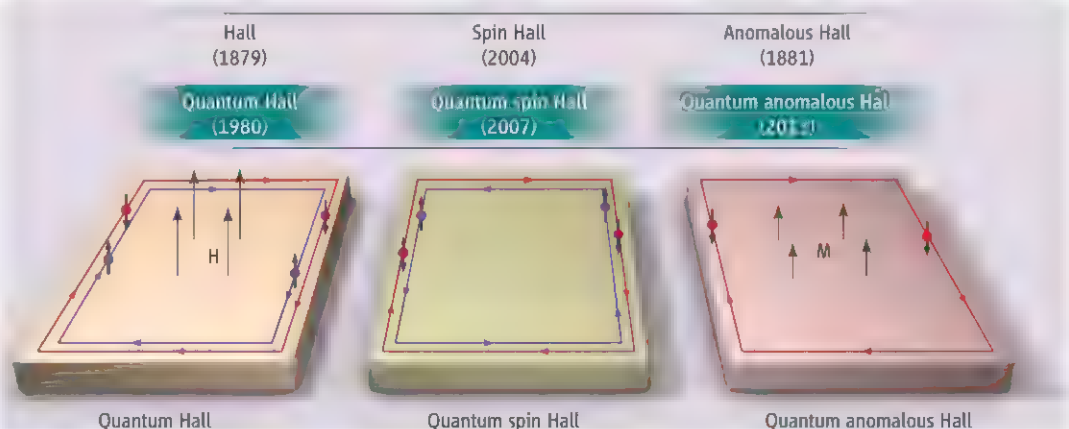
cal insulator; the result confirms the long-awaited quantum anomalous Hall effect (QAHE), the final member of the quantum Hall trio (see the figure).

Soon after the discovery of the QHE, it was realized that the quantization occurs when dissipationless (or lossless) one-dimensional channels form around the edges of the sheet while the rest of the sample remains insulating and that the number of these edge channels determines the integer value v . In such a case, electrons flowing on one side cannot be scattered backward because the backward channels exist only on the other side of the sample, which is separated by the insulating bulk in between, and whenever quantization occurs in the transverse resistance, the longitudi-

Observation of a quantized resistance state in the absence of an external magnetic field completes a trio of quantum Hall related effects.

nal resistance of the sample reduces to zero.

As understanding of the QHE matured, questions arose as to whether such lossless edge channels could exist even in the absence of an external magnetic field. In 1988, it was shown theoretically that such an edge channel can exist on a two-dimensional lattice (4). Then, almost 20 years later, experimental demonstration of the presence of lossless edge channels in a HgTe/CdTe quantum well in the absence of an external magnetic field was reported (5). However, due to the absence of a magnetic field forcing the current to flow one way or the other, there existed both clockwise and counter-clockwise edge channels, whose direction was determined by the spin orientation (either up or down) of the occupying electrons, forced



Quantum Hall trio. Numbers in parentheses indicate the years of each discovery. H is the external magnetic field, and M is the magnetization. For all three quantum Hall effects, electrons flow through the lossless edge channels, with the rest of the system insulating. When there is a net forward flow of electrons for Hall resistance measurement, (left) those extra electrons occupy only the left edge channels in the quantum Hall system regardless of their spins, (center) opposite-spin electrons occupy opposite sides in the quantum spin Hall system, and (right) only spin-down electrons flow through the left edge in the quantum anomalous Hall system. The locking schemes between spin and flow direction, and the number of edge channels depend on the material details, and only the simplest cases are illustrated here.

Department of Physics and Astronomy, and Institute for Advanced Materials, Devices and Nanotechnology, Rutgers, The State University of New Jersey, Piscataway, NJ 08854, USA. E-mail: ohsean@physics.rutgers.edu

by the strong spin-orbit coupling mechanism inherent in heavy elements. This is the quantum spin Hall effect (QSHE), a quantized version of the spin Hall effect (6).

If one of the spin channels in the QSH system is suppressed—for example, by ferromagnetism—it naturally leads to the QAHE. The Hall resistance in ferromagnetic conductors (7) is composed of the ordinary Hall effect proportional to the magnetic field and the anomalous Hall effect (AHE) proportional to the magnetization of the sample; the QAHE is the quantized version of this AHE. The discovery of the QSHE spurred active searches for the QAHE. It was proposed that the QAHE may be observable by suppressing one of the spin channels in the QSH state of the HgTe system with magnetic doping (8). Unfortunately, this system does not become ferromagnetic and thus failed to exhibit the QAHE. It was later predicted that when a topological insulator Bi₂Se₃ is made thin and magnetically doped, the system should exhibit the QAHE with a quantized Hall resistance of h/e^2 (9)—a proposal that Chang *et al.* have successfully implemented.

There were nontrivial material problems that Chang *et al.* had to overcome. The QAHE requires, among other things, bulk and surface conduction to be completely suppressed. However, the proposed Bi₂Se₃ system has highly electron-doped bulk and surface states due to unavoidable selenium vacancies (10). To get around this problem, they instead chose the (Bi_{1-x}Sb_x)₂Te₃ system (11), which, with the choice of *x*, allows tuning of its doping level toward the doping-neutral point, where ferromagnetism opens an energy gap. With optimization of the material parameters, they achieved the quantized Hall resistance of h/e^2 at around the doping-neutral point in the absence of an external magnetic field.

The observed properties of the QAHE are robust. First of all, unlike the QSHE, which required submicrometer feature sizes to avoid spin-flip scattering, the QAHE was observed over a macroscopic scale of hundreds of micrometers. It is also intriguing that the exact quantization is achieved even on a platform with a relatively low mobility and with nonzero bulk conduction. This implies that the QAHE is definitely more robust than the QSHE and could be comparable to or even more resilient than the QHE.

The exact quantization of the observed QAHE and the presence of a lossless edge channel could be used for a number of applications. For example, the edge channel could be used as a dissipationless spin-filtering path for spintronic devices, and the exactly quantized

Hall resistance without any magnetic field could be used as a simple resistance standard. The reported platform is yet far from such applications, considering the extremely low temperature requirement, currently enforced by the low ferromagnetic Curie temperature and other material imperfections. However, with further material breakthroughs, QAHE components might someday find their places in our mobile electronic devices.

References and Notes

1. E. H. Hall, *Am. J. Math.* **2**, 287 (1879).
2. K. v. Klitzing, G. Dorda, M. Pepper, *Phys. Rev. Lett.* **45**, 494 (1980).

3. C.-Z. Chang *et al.*, *Science* **340**, 167 (2013).
4. F. D. M. Haldane, *Phys. Rev. Lett.* **61**, 2015 (1988).
5. M. König *et al.*, *Science* **318**, 766 (2007).
6. Y. K. Kato, R. C. Myers, A. C. Gossard, D. D. Awschalom, *Science* **306**, 1910 (2004).
7. E. H. Hall, *Philos. Mag.* **12**, 157 (1881).
8. C.-X. Liu, X.-L. Qi, X. Dai, Z. Fang, S.-C. Zhang, *Phys. Rev. Lett.* **101**, 146802 (2008).
9. R. Yu *et al.*, *Science* **329**, 61 (2010).
10. N. Bansal, Y. S. Kim, M. Brahlek, E. Edrey, S. Oh, *Phys. Rev. Lett.* **109**, 116804 (2012).
11. J. Zhang *et al.*, *Nat. Comm.* **2**, 574 (2011).

Acknowledgments: I thank H. Zhang and D. Vanderbilt for discussions and M. Brahlek for help with the figure.

10.1126/science.1237215

CHEMISTRY

Lifting the Veil on an Old Mystery

Luc Vereecken

An elusive reaction intermediate of central importance to the atmosphere yields details on its nature, lifetime, and reactivity.

Criegee intermediates (CIs) (1) are the main intermediates in atmospheric reactions between ozone and organic molecules, resulting in the formation of free radicals, organic acids, carbonyl compounds, and organic aerosols. Such reactions contribute to local photochemical smog and global climate change. Advances in understanding the chemistry of CIs long remained elusive because these compounds could not be observed directly. On page 174 of this issue, Su *et al.* (2) report direct detection of a CI, and on page 177, Taatjes *et al.* (3) describe direct CI kinetics data that yield key information about their impact on the atmosphere.

In 2008, Taatjes *et al.* reported the direct gas-phase observation of the smallest CI, CH₂OO, with synchrotron photoionization mass spectrometry (4). Direct kinetics experiments followed in 2012, when Welz *et al.* (5) applied the same technique but used the reaction of iodoalkyl radicals with O₂ as a clean source of CIs. However, synchrotron ionization is not widely available. More accessible and inexpensive techniques are needed, especially for use in the field.

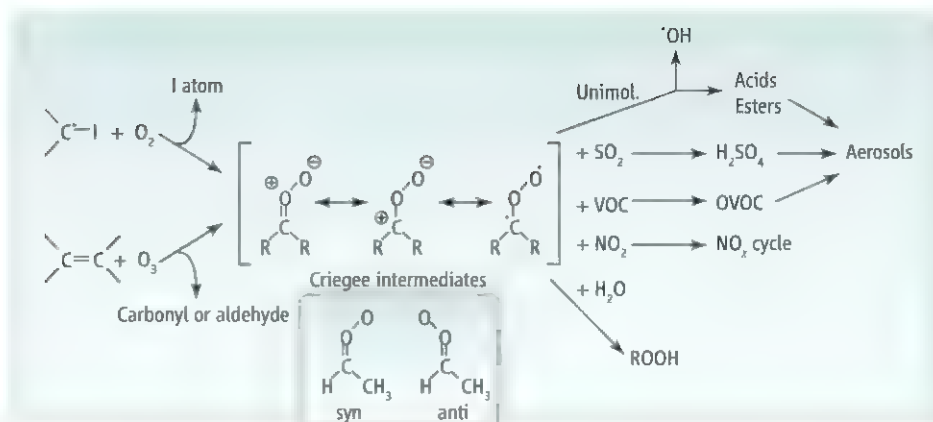
Su *et al.* now describe the gas-phase infrared absorption spectrum of CH₂OO, complementing earlier work by Beames *et al.* (6) and Lee *et al.* (7) on its ultraviolet electronic spectrum. Based on these spectra,

new spectroscopic detection methods using widely available apparatus can be devised. Other studies have characterized CI chemistry indirectly with equipment that can be used both in the field and in the lab. Berndt *et al.* (8) used a mass spectrometer to monitor CIs by SO₂ scavenging, whereas Novelli *et al.* (9) used an OH detector to trace CIs by their unimolecular OH production.

Until recently, CIs in the troposphere were thought to react almost exclusively with the ubiquitous water molecules. However, this assumption is based on indirect experimental data with uncertainties spanning several orders of magnitude and appears only partially correct. Furthermore, the experimental data frequently contradict theoretical predictions (10). The latter show a complex zwitterionic/biradical structure for CIs (see the figure). The chemistry of these compounds depends strongly on the CI structure; for example, even *syn* and *anti* forms differing only in the orientation of the outer oxygen (see the figure, inset) are predicted to react very differently.

Kinetic information for assessing the role of CIs in the atmosphere is now also becoming available. Welz *et al.* (5) provided direct kinetic measurements of CH₂OO with SO₂ and NO₂. Taatjes *et al.* (3) extend this approach to CH₃CHOO, even distinguishing between its *syn* and *anti* geometry. Both SO₂ and NO₂ display very fast reactions, with the rate depending on the CI structure by up to a factor of 3. Com-

Max Planck Institute for Chemistry, 55128 Mainz, Germany.
E-mail: luc.vereecken@mpic.de



Formation and reactions of CIs. Criegee intermediates (CIs) formed from ozonolysis or iodoalkyl radicals have been difficult to observe. Su *et al.* (2) report the infrared spectroscopic detection of the smallest CI, CH₂OO. Kinetic measurements by Taatjes *et al.* (3, 12) of their reaction with water, SO₂, NO₂, and volatile organic compounds (VOCs) suggest a specific role for CIs in the atmosphere. OVOC, oxygenated volatile organic compound. (Inset) *syn* and *anti* forms of CH₃CHOO.

pared to these rates, the H₂SO₄ formation rate from CI + SO₂ observed by Berndt *et al.* (8) is two orders of magnitude slower; Vereecken *et al.* (11) attributed this low yield to strong pressure dependence favoring other products.

The rate coefficient for the reaction of CH₃CHOO with water was found to be much slower, but—given the high water concentrations in the troposphere—still fast enough to make it the dominant atmospheric sink for *anti*-CH₃CHOO (3). Conversely, both *syn*-CH₃CHOO (3) and CH₂OO (5) react too slowly with water to measure, allowing other reactions to compete. These reactions include thermal decomposition of

CI to form radicals (5, 8, 10) and the reaction of CI with different carbonyl compounds, for which fast reaction rates spanning two orders of magnitude were recently measured (12). All these observations, and their strong dependence on CI structure, are in agreement with theoretical predictions (10, 11).

Inconsistencies remain, but the data discussed above suggest that CIs can play a role in the atmosphere well beyond their reaction with water. The reaction of CIs with SO₂ may be an important gas-phase source of low-volatility sulfuric acid, a key actor in the formation of atmospheric aerosols (13). The reaction of CIs with NO₂ may affect the

NO_x cycle, whereas their reaction with oxygenated hydrocarbons might be a source of aerosol precursors.

Theory-based analysis (11) of the impact of the CI structure on its atmospheric fate indicates that some smaller CIs will mainly react with water, but many others will partially react with other compounds or act as a source of free radicals. Additional experimental and theoretical studies are clearly needed on atmospherically relevant CIs. Atmospheric chemistry models will need to incorporate these new insights into CI chemistry.

References

1. R. Criegee, G. Wenner, *Justus Liebigs Ann. Chem.* **564**, 9 (1949).
2. Y.-T. Su, Y.-H. Huang, H. Witek, Y.-P. Lee, *Science* **340**, 174 (2013).
3. C. A. Taatjes *et al.*, *Science* **340**, 177 (2013).
4. C. A. Taatjes *et al.*, *J. Am. Chem. Soc.* **130**, 11883 (2008).
5. O. Welz *et al.*, *Science* **335**, 204 (2012).
6. J. M. Beames, F. Liu, L. Lu, M. I. Lester, *J. Am. Chem. Soc.* **134**, 20045 (2012).
7. E. P. F. Lee *et al.*, *Chemistry* **18**, 12411 (2012).
8. T. Berndt *et al.*, *J. Phys. Chem. Lett.* **3**, 2892 (2012).
9. A. Novelli *et al.*, paper presented at the Atmospheric Chemical Mechanisms Conference, Davis, CA, 10 to 13 December 2012; see <https://sites.google.com/site/atmoschemmech2012/>.
10. L. Vereecken, J. S. Francisco, *Chem. Soc. Rev.* **41**, 6259 (2012).
11. L. Vereecken, H. Harder, A. Novelli, *Phys. Chem. Chem. Phys.* **14**, 14682 (2012).
12. C. A. Taatjes *et al.*, *Phys. Chem. Chem. Phys.* **14**, 10391 (2012).
13. R. L. Mauldin III *et al.*, *Nature* **488**, 193 (2012).

10.1126/science.1236475

IMMUNOLOGY

An Interferon Paradox

Pamela M. Odorizzi and E. John Wherry

Type 1 interferons (IFN- α/β) are a major first line of host defense against viral infection. Because of this potent antiviral activity, IFN-based therapies have been developed for chronic infections with hepatitis B and C viruses, as well as for HIV. However, a poorly understood phenomenon has been the persistence of virus despite induction of antiviral immune responses by type 1 IFNs. On page 207 and 202 in this issue, Teijaro *et al.* (1) and Wilson *et al.* (2) address this long-standing question and find

that IFN- α/β can also suppress the immune system in ways that promote viral persistence. This paradoxical finding should spur a reassessment of the fundamental roles of IFN- α/β during chronic infections.

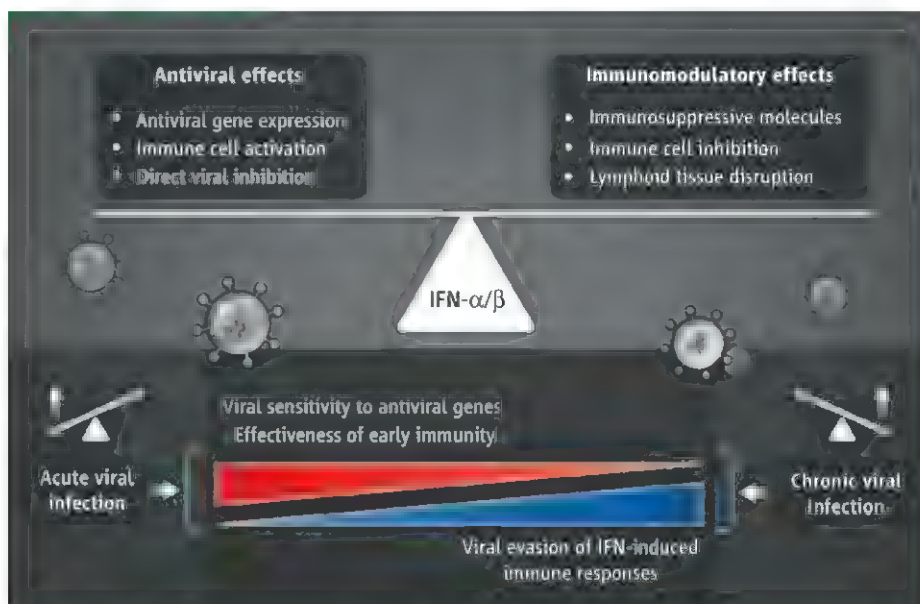
In the early stage of viral infection, recognition of pathogen-associated molecular patterns (PAMPs) through molecular sensors in the body, such as Toll-like receptors, leads to rapid production of type 1 IFNs by various cell types (3, 4). IFN- α/β acts in both an autocrine and paracrine manner to induce the expression of IFN-stimulated genes that limit viral replication and spread (4, 5). Importantly, loss of IFN- α/β signaling in animal models usually leads to uncontrolled

Interferons must balance antiviral actions against immunosuppressive effects during acute and chronic infections.

viral replication (6). Chronic viral infections can result in sustained IFN- α/β signaling, presumably due to ongoing recognition of viral PAMPs (7). It has been unclear, however, why this ongoing IFN- α/β signaling during chronic infections does not lead to viral control.

Teijaro *et al.* and Wilson *et al.* used a mouse model of chronic infection with either of two strains of lymphocytic choriomeningitis virus (LCMV)—the Armstrong strain, which is associated with T cell-mediated viral control, and the clone 13 strain, which induces broad immune dysfunction, including T cell exhaustion (gradual decrease in T cell function). Both strains trigger robust,

Institute for Immunology and Department of Microbiology, University of Pennsylvania Perelman School of Medicine, 421 Curie Boulevard, Philadelphia, PA 19104, USA. E-mail: wherry@mail.med.upenn.edu



Balancing dual roles. Type 1 interferons (IFN- α/β) may control viral replication and spread through two mechanisms. Antiviral responses include the expression of antiviral genes and the activation of specific immune cells. Immunomodulatory responses include the expression of immunosuppressive molecules, immune cell inhibition, and cell death. The balance of these responses may shift, with enhanced antiviral actions during acute infections and greater immunomodulatory effects during chronic infections.

but transient, IFN- α/β production; however, the expression of many IFN-stimulated genes persists during chronic infection. In these studies, the removal of IFN- α/β signaling in animals through genetic deletion of a subunit for the type 1 IFN receptor, or antibody-mediated blockade of the IFN receptor before infection, increased viral replication and acute LCMV infection was no longer controlled. Surprisingly, inhibiting IFN- α/β signaling also reduced the expression of immunosuppressive molecules, such as the regulatory cytokine interleukin-10 (IL-10) and the inhibitory receptor ligand programmed death ligand 1 (PD-L1). The IL-10 and PD-1 pathways promote viral persistence and T cell exhaustion during many chronic viral infections (8). Despite an initial increase in virus, blocking IFN- α/β during chronic LCMV infection led to a substantial reduction in viral titers by 2 months after infection. Therapeutic blockade of IFN- α/β signaling with an antibody against the IFN receptor after the establishment of chronic infection also enhanced viral control. Both studies observed improved virus-specific CD4⁺ T cell responses and preserved lymphoid tissue organization in the absence of IFN- α/β signaling.

The studies by Teijaro *et al.* and Wilson *et al.* highlight an unappreciated dual nature of IFN- α/β signaling during chronic viral infections (see the figure). Type 1 IFNs limit early viral replication through multiple direct

molecular mechanisms, including inhibition of viral transcription and translation, as well as degradation of viral nucleic acids (5). The production of IFN- α/β early upon infection also serves as an activation signal for immune cells by promoting lysis of infected cells by natural killer cells, enhancing antigen presentation—T cell priming by dendritic cells, and sustaining proliferation and activation of T cells (3–5). However, IFN- α/β also has regulatory effects that suppress immune responses. For example, IFN- α/β can trigger programmed cell death of activated T cells and increase production of immunosuppressive molecules, including IL-10, PD-L1, and indoleamine (2,3)-dioxygenase (4, 9). Thus, although early antiviral effects of IFN- α/β are critical, the potential immunoregulatory roles of IFNs later in chronic infection could explain paradoxical clinical observations using IFN-based treatments. For example, strong basal IFN- α/β signatures (increased expression of IFN-stimulated genes) correlate with poor responses to IFN- α therapy during chronic hepatitis C virus infection (10, 11). Such signatures are also associated with disease progression during chronic HIV and pathogenic SIV infections, as well as during active versus latent *Mycobacterium tuberculosis* infection (12–14).

Why might IFNs elicit direct antiviral effects while concurrently boosting immunoregulatory responses that prevent robust adaptive immune responses to infections?

One possibility is that the immunoregulatory functions of IFN- α/β may have evolved to limit immune-mediated pathology during infections where viral persistence is inevitable. In these settings, the IFN- α/β pathway may sense the level of ongoing viral replication and bolster immune suppression to avoid damaging immunopathology, such as a “cytokine storm” (uncontrolled cytokine production and immune cell activation), meningitis, or immune-mediated tissue destruction. An essential next step will be determining how this balance is influenced by pathogen virulence and the strength of the immune response. In addition, the ability of IFN- α/β to efficiently control early viral replication, and the capacity of different viruses to evade this response, may dictate the importance of these immunoregulatory effects.

How might these findings improve IFN-based treatment strategies? There are several issues to be addressed. Identifying the molecular basis for the antiviral versus immunomodulatory effects of IFN- α/β will be necessary to selectively manipulate these opposing activities. It will also be critical to determine how the balance between antiviral and immunoregulatory effects varies from virus to virus or during a single viral infection over time. The studies of Teijaro *et al.* and Wilson *et al.* suggest that patients currently on IFN therapy could be monitored for the induction of antiviral versus immunoregulatory effects, allowing physicians to modify treatment strategies accordingly. It also may be possible to further improve the antiviral therapeutic potential of IFNs and perhaps exploit the immunoregulatory properties of this pathway for nonviral diseases.

References

1. J. R. Teijaro *et al.*, *Science* **340**, 207 (2013).
2. E. B. Wilson *et al.*, *Science* **340**, 202 (2013).
3. A. Iwasaki, R. Medzhitov, *Science* **327**, 291 (2010).
4. J. M. González-Navajas, J. Lee, M. David, E. Raz, *Nat. Rev. Immunol.* **12**, 125 (2012).
5. A. G. Bowie, L. Unterholzner, *Nat. Rev. Immunol.* **8**, 911 (2008).
6. U. Müller *et al.*, *Science* **264**, 1918 (1994).
7. L. N. Lee, S. Burke, M. Montoya, P. Borrow, *J. Immunol.* **182**, 7178 (2009).
8. E. J. Wherry, *Nat. Immunol.* **13**, 492 (2011).
9. A. Boasso, A. W. Hardy, S. A. Anderson, M. J. Doan, G. M. Shearer, *PLoS ONE* **3**, e2961 (2008).
10. P. M. George, R. Badtger, W. Alazawi, G. R. Foster, J. A. Mitchell, *Pharmacol. Ther.* **135**, 44 (2012).
11. M. Sarasin-Filipowicz *et al.*, *Proc. Natl. Acad. Sci. U.S.A.* **105**, 7034 (2008).
12. J. -P. Herbeval *et al.*, *Proc. Natl. Acad. Sci. U.S.A.* **103**, 7000 (2006).
13. B. Jacquelin *et al.*, *J. Clin. Invest.* **119**, 3544 (2009).
14. M. Berry *et al.*, *Nature* **466**, 973 (2010).

Deep Homology of Arthropod Central Complex and Vertebrate Basal Ganglia

Nicholas J. Strausfeld^{1*} and Frank Hirth^{2*}

The arthropod central complex and vertebrate basal ganglia derive from embryonic basal forebrain lineages that are specified by an evolutionarily conserved genetic program leading to interconnected neuropils and nuclei that populate the midline of the forebrain-midbrain boundary region. In the substructures of both the central complex and basal ganglia, network connectivity and neuronal activity mediate control mechanisms in which inhibitory (GABAergic) and modulatory (dopaminergic) circuits facilitate the regulation and release of adaptive behaviors. Both basal ganglia and central complex dysfunction result in behavioral defects including motor abnormalities, impaired memory formation, attention deficits, affective disorders, and sleep disturbances. The observed multitude of similarities suggests deep homology of arthropod central complex and vertebrate basal ganglia circuitries underlying the selection and maintenance of behavioral actions.

Vertebrate basal ganglia are evolutionarily conserved interconnected nuclei traceable to stem group taxa (1). Their ground pattern comprises four principal volumes: the striatum, the internal and external domains of the

globus pallidus, the subthalamic nucleus, and the substantia nigra. Basal ganglia play a key role in selecting and maintaining adaptive behavior by conveying sensorimotor, limbic, and associative information corresponding to action selection among behavioral modules that are competing for the control of a limited set of motor programs (2). Focal lesions and dysfunction of the basal ganglia are associated with movement disorders, such as parkinsonism, dystonia, and abulia, as well as neuropsychiatric disorders (3), essentially affecting goal-directed behavior and habitual control (4).

Similar behavioral manifestations have been attributed to the arthropod central complex (5, 6), which in insects and crustaceans comprises three interconnected midline centers: the protocerebral bridge, fan-shaped body, and ellipsoid body leading to the paired lateral accessory lobes (fig. S1). Central complexes can be traced to related arthropods, including Onychophora, and to Lophotrochozoa represented by polychaete annelids (5). Here, we review multiple lines of evidence suggesting deep homology of the vertebrate basal ganglia and the arthropod central complex in the selection and maintenance of adaptive behavior.

Basal Forebrain Origin and Developmental Genetics

Nuclei of the basal ganglia derive from precursor cells of the ventral telencephalon, with neural stem cells from the ganglionic eminences giving rise to striatum and pallidum to become located at the segmental border between the prosencephalon and mesencephalon, where they populate the midline of the basal forebrain (7). In insects, specific embryonic and larval neural stem cells in the basal forebrain give rise to components of the central complex that populate the midline of the posterior protocerebrum (6). Thus, the vertebrate basal ganglia and arthropod central complex share comparable embryological derivation and topography.

In mice, forebrain patterning, prosencephalic and mesencephalic boundary formation, and genesis and specification of the ventral telencephalon (especially the ganglionic eminences) are under

¹Department of Neuroscience, School of Mind, Brain and Behavior, University of Arizona, Tucson, AZ 85721, USA. ²MRC Centre for Neurodegeneration Research, Department of Neuroscience, Institute of Psychiatry, King's College London, London SE5 8AF, UK.

*Corresponding author. E-mail: flybrain@neurobio.arizona.edu (N.J.S.); frank.hirth@kcl.ac.uk (F.H.)

Table 1. Genetic programs underlying the formation of vertebrate basal ganglia and insect central complex. Abbreviations: FB, fan-shaped body; EB, ellipsoid body; DA, dopaminergic.

Vertebrate basal ganglia	Gene homologs	Insect central complex
Patterning of forebrain/midbrain and ventral telencephalon (9, 62, 63)	<i>Otx2/otd</i> <i>FGF8/pyramus, thisbe</i> <i>SHH/hh</i> <i>BMP/dpp</i>	Patterning of forebrain and basal protocerebrum (71)
Patterning of ventral telencephalon and formation of striatum and pallidum (7, 8)	<i>Six3/Tc-Six3</i> <i>SHH/hh</i>	Patterning of anterior neuroectoderm and formation of FB+EB (13)
Formation and specification of striatum and pallidum (7, 64, 65)	<i>Dlx1,2/Dll</i> <i>Tlx/tll</i> <i>Nkx2.1/vnd</i>	Formation and specification of basal protocerebrum (13, 71)
Specification of striatum and pallidum (9, 65–67)	<i>Otx2/otd</i> <i>Pax6/eyeless</i> <i>Emx2/ems</i> <i>Gsh1,2/ind</i> <i>Lhx6,7/–</i>	Specification of protocerebral bridge, FB, and EB (13, 14, 16)
Specification and maintenance of DA neurons (substantia nigra) (10, 68)	<i>Otx2/otd</i> <i>En1,2/en</i> <i>FGF8/pyramus, thisbe</i> <i>SHH/hh</i> <i>LRRK2/lrrk2</i>	Specification and maintenance of DA neurons (PPM3, PPL1) (15)
Formation of subthalamic nucleus (69, 70)	<i>Pitx2/Pitx1</i>	?
Nigropallidal projections (10), EtOH-induced reward/addiction (52)	<i>AUTS2/tay-bridge</i>	PPL1-FB projections, EtOH-induced reward/addiction (40, 43, 52, 72)

the control of signals including fibroblast growth factor 8 (FGF8), sonic-hedgehog (SHH), and members of the bone morphogenetic protein (BMP) family; FGF8 and SHH play essential roles in the neurogenesis of dopaminergic cells of the substantia nigra (7). The *Six3* gene interacts and is required with SHH for early ventral telencephalon formation (8), and *Otx2* is required for early forebrain and midbrain development (9). Later in development, *Otx2* is involved in the genesis of substantia nigra dopaminergic neurons and the formation of the dopaminergic nigrostriatal pathway (10). *Dlx1/2*, *Tlx*, *Nkx2.1*, *Pax6*, *Emx2*, *Gsh1/2*, and *Lhx6/7* play essential roles in the development and specification of the striatum and pallidum; *Engrailed1/2* (*En1/2*) genes are required for substantia nigra formation; and *Pitx2* is required for the formation of the subthalamic nucleus (Table 1).

In *Drosophila* and the beetle *Tribolium*, homologs of FGF8, SHH, BMP, *Otx2*, *Dlx1/2*, *Tlx*, *Nkx2.1*, *Pax6*, *Emx2*, *Gsh1/2*, *En1/2*, and *Pitx2* have all been identified. The region-specific gene expression patterns in the developing brain correspond to those in vertebrates (11–13). For example, the *Drosophila* *Otx2* homolog *otd* is required for embryonic forebrain development and, later during development, for the formation of the protocerebral bridge (14) and the specification of central dopaminergic neuron clusters (15). The *Tribolium* homolog of the vertebrate *Six3* gene is required for formation of the fan-shaped body and ellipsoid body; knockdown of *Tc-Six3* leads to early patterning defects in the anterior neuroectoderm and the complete absence of central body lineages (13). The *Drosophila* *Pax6* homolog *eyeless* is required for fan-shaped body and ellipsoid body specification (16). Thus, the genesis and specification of the basal ganglia and central complex share underlying developmental genetic programs that extend from homologous gene structure to patterned expression and function (Table 1).

Neural Architectures of Striatum/Fan-Shaped Body and Pallidum/Ellipsoid Body

The adult striatum and fan-shaped body are distinguished by their three-dimensional architectures. A cardinal feature of the striatum, best resolved in mammals, is its differentiation into modular islets, the striosomes, embedded in the surrounding neural matrix, and a system of domains adjacent to striosomes, termed matrisomes (17) (Fig. 1, A to C). Matrisomes relate to body parts and their representations in sensory cortices (17), whereas striosomes receive relays via the prefrontal cortex from the amygdala, hippocampus, and limbic system (17–19). Combinatorial interactions among modules provide substrates for associations among the representations of body parts and of their spatial coordinates, with striosomal afferents relating to stored associations and functions that are loosely referred to as motivational levels, reafference, and autonomic functions (20).

In the insect central complex, the fan-shaped body comprises an arrangement of successive

synaptic layers intersected by a repeated arrangement of modules (Fig. 1, D to F). Each arrangement reflects the clonal organization of uniquely identifiable columnar, tangential, and fan-shaped arborizations of efferent, intrinsic, and afferent neurons (21–24). Sensory representations at the level of the protocerebral bridge are exemplified by maps of the e-vector of polarized light, which are combinatorially intermingled by a system of chiasmatal projections to modules spanning the underlying fan-shaped body (25). Haptic information, also encoding sensory space and provided by mechanosensory appendages, is represented across the protocerebral bridge and fan-shaped body (26, 27). Insects with evolved blindness demonstrate the robustness of such modularity and its independence from a single sensory modality (28). Stratifications of the fan-shaped body are further denoted by systems of modulatory peptidergic neurons (23) and inputs to it from the protocerebrum carrying information of higher-order visual primitives and learned discrimination of visual cues (29–31). Thus, distinctive modules representing sensory attributes, and modules provided by afferents from association and modulatory centers, can be identified in both phyla (Fig. 1).

The vertebrate pallidum and the arthropod ellipsoid body share comparable organizational features. In vertebrates, the internal and external globus pallidus (GPi and GPe) are dominated by GABAergic neurons that connect to the subthalamic nucleus and the thalamus, with reciprocal glutamatergic connections from the subthalamic nucleus back to the GPe. Inhibitory outputs from the globus pallidus serve to select specific motor actions by suppressing inhibition of their activating circuits (2). In insects, inhibitory GABAergic neurons, which provide dense networks in the fan-shaped body, ellipsoid body, and two satellite centers (noduli), extend their axons laterally from the central complex to the flanking lateral accessory lobe neuropils (30, 32). The identification of metabotropic glutamate receptors at discrete branching processes suggests reciprocal glutamatergic pathways to the ellipsoid and fan-shaped bodies (33). Fibrous distributions of monoamines and peptides, as well as their corresponding metabotropic receptors in neural processes, point to the presence of complex modulatory circuits within and between ellipsoid and fan-shaped body neuropils (34).

Dopaminergic Neuron and Receptor Distribution

In vertebrates, the substantia nigra provides the primary source of dopaminergic neurons that ascend to the striatum, leading to a dense innervation via the nigrostriatal pathway (35). All known G protein-coupled dopamine receptors are expressed in the striatum, with D1 and D2 receptors the most abundant. D1 receptors, together with substance P, are expressed by GABAergic spiny projection neurons (SPNs) constituting 90% of the striatal neurons that project to the GPi and substantia nigra reticulata, thereby defining the

direct pathway (36). Projections to the GPe, defining the indirect pathway, express D2 dopamine receptor together with enkephalin (36).

As evidenced in *Drosophila*, clusters of dopamine-containing neurons identified at the level of single nerve cells have stereotypic anatomical and location-specific projection patterns. Whereas several such clusters are associated with the mushroom bodies (37), two clusters termed PPM3 and PPL1, revealed at the single-cell level, provide dense dendritic arborizations within the central complex (37–41). Thus, individual dopaminergic neurons of the PPM3 cluster target fan-shaped body, ellipsoid body, and lateral accessory lobes (37–39), and single neurons of the PPL1 cluster target the fan-shaped body, with both PPM3 and PPL1 targeting the mushroom bodies as well (40, 41) (Fig. 2). D1-like dopamine receptor expression and immunoreactivity have been demonstrated for the fan-shaped body, ellipsoid body, and lateral accessory lobes (42, 43). Substance P immunolabeling has been described in the central complex of insects (locusts), chelicerates (*Limulus*), and decapod crustaceans (*Homarus*) (44–46). In the locust, columnar substance P immunoreactive fibers project to the protocerebral bridge, from which they extend to the lower division of the central body (the locust term for the ellipsoid body); substance P immunoreactive terminals extend out to the central complex's lateral triangle and the lateral accessory lobes (46). However, comparative analysis reveals limited evidence for enkephalin and D2 receptor expression. These data suggest the presence of a direct pathway in the arthropod central complex, with substance P and D1 receptor expression linking ellipsoid and fan-shaped bodies (42–46) and direct GABAergic output to the lateral accessory lobes (30, 32).

Selection and Maintenance of Behavioral Actions

In insects, the central complex is critical in the selection of motor actions and the control of multijoint movement (47). Genetic deletion of parts of the central complex, developmental errors that disrupt central complex circuitry, or the misexpression of neuropeptides can all give rise to ataxia, tripping, hesitancy, and other parkinsonism-like defects. In addition, targeted synaptic inactivation of central complex substructures impairs visual orientation and place memory, diminishes startle- or ethanol-induced arousal, and results in attention deficits and sleep disorders (table S1).

The behavioral outcomes of neuronal activity of the central complex are reminiscent of action selection and maintenance mediated by the vertebrate basal ganglia, which includes a raft of functions (table S1). Dysfunction of the basal ganglia caused by injury, viral or bacterial infection, or age-related degeneration of neuronal subpopulations, along with other pathological deficiencies, results in a spectrum of motor system disorders ranging from hypokinesia to hyperkinesia (including ataxias, parkinsonism, Tourette syndrome, chorea, and dystonia) as well as neu-

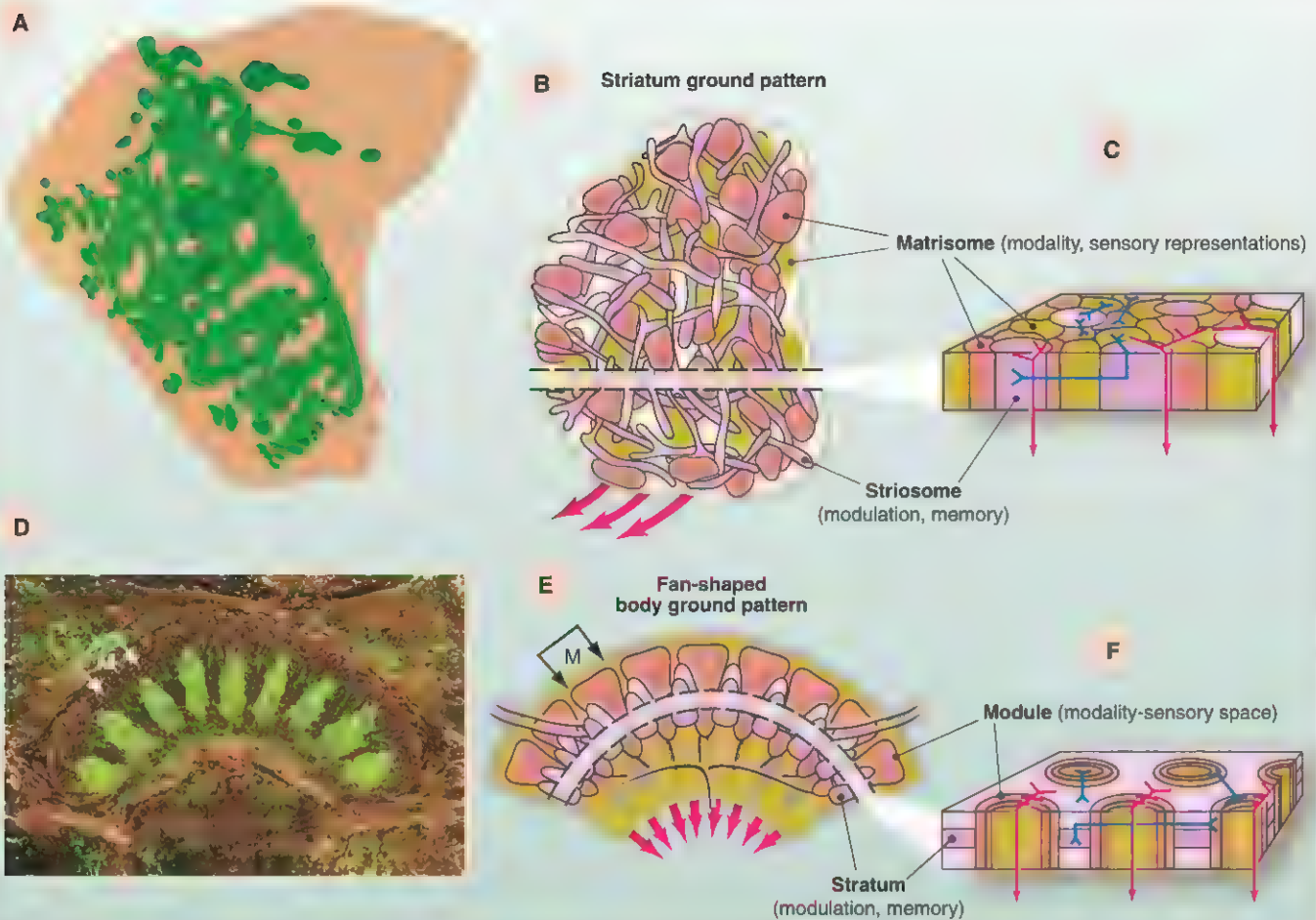


Fig. 1. Ground pattern and modular arrangement of the mammalian striatum and the insect fan-shaped body. (A to C) The mammalian striatum [(A), modified from (73)] consists of two principal subunits. Striosomes [green in (A)] within the matrix of the striatum [schematized in mauve, purple in (B) and (C)] are associated with discrete volumes of the striatal matrix, called matrisomes [brown, yellow in (B) and (C)]. In mammals, striosomes receive inputs from the hippocampus and amygdala via the frontal cortex, among other brain regions, carrying information about internal physiological states (modulations, memories) (17, 20). Matrisomes are supplied by cortical representations of sensory space and sensory modalities (17). (C) Interactions and associations among matrisomes, and between matrisomes and striosomes, are mediated by local interneurons (blue) that integrate and provide information to striatal afferents supplying direct and indirect GABAergic pathways (red arrows) to the globus pallidus and subthalamic nucleus [see (3, 36)]. (D to F) The insect fan-shaped body [(D),

from *Mantis religiosa*, labeled with antisera against allatostatin (green) and β -tubulin (ochre)] consists of two principal subunits: tangential stratifications (schematized in mauve, purple) that intersect columnar modules (yellow, brown), one indicated by bracketed arrows M in (D) and (E) [see (22, 24, 32)]. Columnar modules are supplied by afferents carrying information about sensory modalities and the organization of sensory space (5, 25, 26). (E) Tangential elements comprise relays mainly from the protocerebrum. These can carry information about higher-order sensory cues, learned sensory associations, and physiological states [modulations, memories (5, 25–27, 29, 30)]. (F) Cross section of a stratum of the fan-shaped body, showing routes of interactions and associations among columnar elements, and between columnar elements and planar tangentials, that are mediated by local interneurons (blue) at several levels through the fan-shaped body (5, 21). These are assumed to provide integrated information to outgoing GABAergic pathways (red arrows).

ropsychiatric disorders (including impaired memory formation, attention deficits, affective disorders, and sleep disturbances) (3). Thus, both central complex substructures and nuclei of the vertebrate basal ganglia mediate sensorimotor integration, motivational and affective behavior, and cognition related to comparable behavioral manifestations (table S1).

Dopaminergic Modulation of Action Selection and Maintenance

In vertebrates, dopamine innervation of the striatum via the nigrostriatal pathway is critical for

normal function of the striatum and basal ganglia. Substantia nigra neurons are autonomous pacemakers that provide a tonic release of dopamine onto GABAergic SPNs in the striatum, thereby modulating the tonic inhibitory output of GABAergic SPNs and allowing movements to occur. Depletion of dopamine or its receptors, or dysfunction of the nigrostriatal pathway, can result in a range of pathologies, most of which refer to dysfunction of inhibitory or activation control of motor behaviors (36). Progressive loss of dopaminergic neurons in the substantia nigra causes loss of the nigrostriatal pathway, which in

turn results in Parkinson's disease characterized by a progressive increase in the brain's inability to suppress motor actions, leading to rigidity, bradykinesia, and nonmotor symptoms including sleep and mood disorders (3). The activity of nigrostriatal dopaminergic neurons also modulates motivated behaviors related to aversion and reward. Aversive events transiently decrease the activity of nigrostriatal dopaminergic neurons, whereas reward transiently increases it, thereby providing bidirectional signaling to the striatum. Addiction disorders such as alcohol abuse have been linked to an imbalance or dysfunction of

this system, especially of the striatal nucleus accumbens (48). Recent optogenetic and genetic work confirms the modulation of both the direct and indirect pathways by dopamine or dopamine receptor activity; these mediate action selection and reward- or aversion-driven maintenance of behavioral actions (36).

Insects show similar dopamine-dependent behaviors and deficits. Dopaminergic neurons and D1 receptor activation in the central complex play crucial roles in behavioral action selection and maintenance. Central nervous system (CNS)-specific depletion of dopamine in *Drosophila* results in reduced activity and locomotor deficits, extended sleep time, and defects in aversive olfactory memory formation, suggesting that arousal and choice require normal dopamine levels (49). Age-related degeneration of dopaminergic neuron clusters leads to parkinsonism in *Drosophila* characterized by severely impaired motor behavior (50, 51). Specifically, dopaminergic PPM3 neurons projecting to the central complex (see above) regulate locomotor activity and promote ethanol-induced hyperactivity (6, 43). Expression of the D1-like receptor DopR in the ellipsoid body is required for locomotor activity elicited by ethanol exposure (43) and for the regulation of repetitive startle-induced arousal (table S1). Optogenetic and genetic manipulation of PPL1 dopaminergic neurons that project to both mushroom bodies and the fan-shaped body reveal that these cells are essential for motivated behaviors, including reward- and aversion-driven maintenance of behavioral actions that relate to memory retrieval and reinforcement (table S1).

Thus, in both the central complex and basal ganglia, comparable systems of dopaminergic neurons, their projections, and dopaminergic receptor activities are involved in the modulation and maintenance of normal behavioral actions (table S1). Perturbation of dopaminergic pathway activity or of its modulatory output interferes with the selection and maintenance of behavioral actions. This is further exemplified by nigrostriatal pathway and PPL1/fan-shaped body projections: Both are involved in the modulation of reward behavior that is distorted by abusive alcohol consumption leading to addiction modulated by *tay-bridge* in *Drosophila* and its *AUTS2* homolog in mammals, including humans (52); in both cases, parts of the underlying, deregulated neural circuitry have been identified, including dopaminergic innervation of the ellipsoid body (37–39, 43) and dopaminergic innervation of the pallidum via nigropallidal projection neurons (48).

Deep Homology of Neural Circuitry for Action Selection and Maintenance

The multiplicity of similarities described here identifies a highly conserved structural and functional organization of the arthropod central complex and vertebrate basal ganglia (Fig. 2). Differences, beyond shape and size, suggest that an indirect pathway including a subthalamic nucleus-like structure is either absent or remains to be iden-

tified in the arthropod central brain. In mammals, bipartite activity of direct and indirect pathways results in action selection by disinhibition of a selected motor program and the simultaneous inhibition of other competing actions (2, 3). Although there is ample evidence for a direct pathway in the arthropod central complex, it remains to be shown whether a comparable interplay between disinhibitory activity and enhanced inhibition mediates action selection and behavioral output in arthropods. Moreover, the evolved loss of central complex components, as in Branchiopoda

(5), or loss of a centralized nervous system entirely (11) are likewise phylum-specific departures from a corresponding ground pattern.

Similarities of brain structure, function, and behavior have been ascribed to convergent evolution (53). However, microRNA and ribosomal RNA data (54, 55) support a common origin of arthropods and vertebrates—a conjecture further corroborated by recent morphological and molecular evidence suggesting that Cnidaria represent a true outgroup to Bilateria (56). Monophyly of Bilateria, together with the presence of a midline

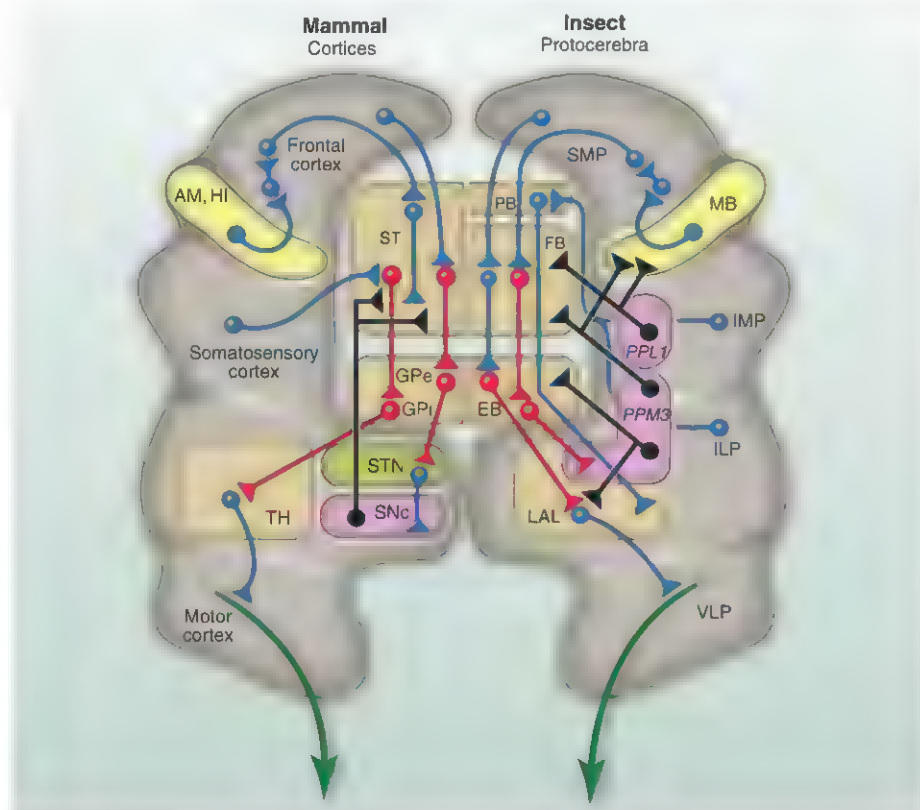


Fig. 2. Proposed correspondences of neural organization of the mammalian basal ganglia and insect central complex. Corresponding regions of the basal ganglia (left) and insect central complex (right) and their associated regions are aligned, as are their relevant connections. Inhibitory pathways are shown in red, dopaminergic pathways in black, and other pathways (excitatory or modulatory) in blue. The striatum (ST = caudate nucleus + putamen) corresponds to the fan-shaped body and protocerebral bridge (FB+PB); the external and internal globus pallidus (GPe, GPi) correspond to the ellipsoid body (EB). There is no center in the insect corresponding to the vertebrate subthalamic nucleus (STN) as an intermediate station between the GP and the dopaminergic substantia nigra pars compacta (SNc). Inputs to the striatum derive from sensory and association cortices (gray), from the hippocampus and amygdala (HI, AM; yellow), and from the limbic system (not shown) via the frontal cortex (17, 20). In insects, inputs to the FB and PB derive from sensory intermediate and inferior lateral protocerebra (IMP, ILP) (21, 22, 25–27, 30) and associative superior medial protocerebrum (SMP), which receives learned visual cues and outputs from the mushroom bodies (MB) (29, 74), the latter center corresponding to the mammalian hippocampus (5, 59). The PB, FB, and EB are connected by through-going presumably excitatory columnar neurons, many of which also extend to the lateral accessory lobes (LAL) (21, 24, 25). GABAergic outputs from the insect EB supply the LAL and its associated neuropils (30, 32). The LAL is here equated to the vertebrate thalamus (TH) supplied from the globus pallidus (2). Both the TH and LAL supply motor centers [mammal: motor cortices (2); insect: inferior and ventrolateral protocerebra (ILP, VLP) (75)]. In insects, dopamine pathways extending from PPM3 and PPL1 domains to the FB and EB (37–43) correspond to dopamine innervation of the striatum from the SNc (35, 76). Descending pathways [vertebrate: from motor cortices to spinal cord; insect: from the ILP, VLP to the ventral cord and ganglia (77)] are shown in green.

neuropil in both annelids and arthropods, suggests that a central complex-like midline structure already existed in the common bilaterian ancestor before the split to Protostomia and Deuterostomia, which likely possessed a complex, tripartite brain (11, 57). It follows that genealogical correspondence due to common evolutionary origin (58) is the most parsimonious explanation for the observed multitude of similarities between basal ganglia and the central complex, which suggests that homologous circuits mediate comparable behavioral functions across phyla.

There is no a priori reason for rejecting the notion that the selection of an appropriate motor program by a brain is a plesiomorphic trait and that this trait, which is common across phyla, is provided by homologous circuits. Adaptive behaviors, selected by the CNS as responses to one or another environmental challenge, are universal phenotypes of organisms equipped with rostral brains that integrate bilateral sensory input for coordinated behavioral output. The likelihood that such a relationship was present in the ancestor of protostomes and deuterostomes is suggested by trace fossils from the end-Vendian and early Cambrian, which show that organisms accomplished bouts of elaborate searching strategies (59, 60)—that is, complex actions that were switched on and off.

The multitude of commonalities reviewed here suggests deep homology of the arthropod central complex and vertebrate basal ganglia. They indicate that the ancestral bilaterian brain already possessed clusters of midline-associated, interconnected basal forebrain neurons mediating the selection and maintenance of behavioral actions. Together with recent evidence for a common origin of higher brain centers involved in allocentric memory in worms and mice (61), these data suggest that the ground pattern of circuits essential for behavioral choice originated very early and have been maintained across phyla throughout evolutionary time.

References and Notes

1. M. Stephenson-Jones, E. Samuelsson, J. Ericsson, B. Robertson, S. Grillner, *Curr. Biol.* **21**, 1081 (2011).
2. S. Grillner, J. Hellgren, A. Ménard, K. Saitoh, M. A. Wikström, *Trends Neurosci.* **28**, 364 (2005).
3. A. M. Graybiel, *Curr. Biol.* **10**, R509 (2000).
4. P. Redgrave et al., *Nat. Rev. Neurosci.* **11**, 760 (2010).
5. N. J. Strausfeld, *Arthropod Brains: Evolution, Functional Elegance, and Historical Significance* (Harvard Univ. Press, Cambridge, MA, 2012).
6. K. Furukubo-Tokunaga, Z. N. Ludlow, F. Hirth, in *Memory Mechanisms in Health and Disease*, K. P. Giese, Ed. (World Scientific, Singapore, 2012), pp. 269–306.
7. S. W. Wilson, J. L. Rubenstein, *Neuron* **28**, 641 (2000).
8. D. Carlin et al., *Development* **139**, 2614 (2012).
9. A. Simeone, E. Puelles, D. Acampora, *Curr. Opin. Genet. Dev.* **12**, 409 (2002).
10. M. P. Smidt, J. P. Burbach, *Nat. Rev. Neurosci.* **8**, 21 (2007).
11. F. Hirth, *Brain Behav. Evol.* **76**, 3 (2010).
12. R. Urbach, G. M. Technau, *Adv. Exp. Med. Biol.* **628**, 42 (2008).
13. N. Posnien, N. D. Koniszewski, H. J. Hein, G. Bucher, *PLoS Genet.* **7**, e1002416 (2011).
14. F. Hirth et al., *Neuron* **15**, 769 (1995).
15. J. Blanco, R. Pandey, M. Wasser, G. Udolph, *Neural Dev.* **6**, 34 (2011).
16. P. Caljaerts et al., *J. Neurobiol.* **46**, 73 (2001).
17. A. W. Faherty, A. M. Graybiel, *J. Neurosci.* **14**, 599 (1994).
18. F. Eblen, A. M. Graybiel, *J. Neurosci.* **15**, 5999 (1995).
19. A. M. Graybiel, T. Aosaki, A. W. Flaherty, M. Kimura, *Science* **265**, 1826 (1994).
20. K.-I. Amemori, L. G. Gibb, A. M. Graybiel, *Front. Hum. Neurosci.* **5**, 47 (2011).
21. U. Hanesch, K.-F. Fischbach, M. Heisenberg, *Cell Tissue Res.* **257**, 343 (1989).
22. K. Ito, T. Awasaki, *Adv. Exp. Med. Biol.* **628**, 137 (2008).
23. Z. Herbert et al., *J. Morphol.* **271**, 1509 (2010).
24. G. Boyan, L. Williams, *Arthropod Struct. Dev.* **40**, 334 (2011).
25. U. Homberg, S. Heinze, K. Pfeiffer, M. Kinoshita, B. el Jundi, *Philos. Trans. R. Soc. London Ser. B* **366**, 680 (2011).
26. R. E. Ritzmann, A. L. Ridgel, A. J. Pollack, *J. Comp. Physiol. A* **194**, 341 (2008).
27. P. Guo, R. E. Ritzmann, *J. Exp. Biol.* **216**, 992 (2013).
28. H. Ghaffar, J. Larsen, G. Booth, R. Perkes, *Int. J. Insect Morphol. Embryol.* **13**, 357 (1984).
29. G. Liu et al., *Nature* **439**, 551 (2006).
30. J. Phillips-Portillo, *J. Comp. Neurol.* **520**, 3088 (2012).
31. S. Kuntz, B. Poock, M. B. Sokolowski, R. Strauss, *Learn. Mem.* **19**, 337 (2012).
32. U. Homberg, H. Vitzthum, M. Müller, U. Binkle, *J. Comp. Neurol.* **409**, 495 (1999).
33. L. Kahsai, M. A. Carlsson, A. M. Winther, D. R. Nässel, *Neuroscience* **208**, 11 (2012).
34. L. Kahsai, A. M. Winther, *J. Comp. Neurol.* **519**, 290 (2011).
35. J. P. Bolam, J. J. Hanley, P. A. Booth, M. D. Bevan, *J. Anat.* **196**, 527 (2000).
36. C. R. Gerfen, D. J. Surmeier, *Annu. Rev. Neurosci.* **34**, 441 (2011).
37. Z. Mao, R. L. Davis, *Front. Neural Circuits* **3**, 5 (2009).
38. K. E. White, D. M. Humphrey, F. Hirth, *Front. Neurosci.* **4**, 205 (2010).
39. T. Ueno et al., *Nat. Neurosci.* **15**, 1516 (2012).
40. M. J. Krashes et al., *Cell* **139**, 416 (2009).
41. Q. Liu, S. Liu, L. Kodama, M. R. Driscoll, M. N. Wu, *Curr. Biol.* **22**, 2114 (2012).
42. Y. C. Kim, H. G. Lee, C. S. Seong, K. A. Han, *Gene Expr. Patterns* **3**, 237 (2003).
43. E. C. Kong et al., *PLoS ONE* **5**, e9954 (2010).
44. T. J. Lewandowski, H. K. Lehman, S. C. Chamberlain, *J. Comp. Neurol.* **288**, 136 (1989).
45. K. Langworthy, S. Helluy, J. Benton, B. Beltz, *Cell Tissue Res.* **288**, 191 (1997).
46. H. Vitzthum, U. Homberg, *J. Comp. Neurol.* **390**, 455 (1998).
47. R. Strauss, *Curr. Opin. Neurobiol.* **12**, 633 (2002).
48. E. Tupala, J. Tiihonen, *Prog. Neuropsychopharmacol. Biol. Psychiatry* **28**, 1221 (2004).
49. T. Riemsperger et al., *Proc. Natl. Acad. Sci. U.S.A.* **108**, 834 (2011).
50. F. Hirth, *CNS Neurol. Disord. Drug Targets* **9**, 504 (2010).
51. D. M. Humphrey et al., *Hum. Mol. Genet.* **21**, 2698 (2012).
52. G. Schumann et al., *Proc. Natl. Acad. Sci. U.S.A.* **108**, 7119 (2011).
53. R. G. Northcutt, *Proc. Natl. Acad. Sci. U.S.A.* **109** (suppl. 1), 10626 (2012).
54. F. Christodoulou et al., *Nature* **463**, 1084 (2010).
55. J. Mallatt, C. W. Craig, M. J. Yoder, *Mol. Phylogenet. Evol.* **64**, 603 (2012).
56. P. R. Steinmetz et al., *Nature* **487**, 231 (2012).
57. X. Ma, X. Hou, G. D. Edgecombe, N. J. Strausfeld, *Nature* **490**, 258 (2012).
58. B. K. Hall, *Biol. Rev. Camb. Philos. Soc.* **78**, 409 (2003).
59. D. M. Raup, A. Seilacher, *Science* **166**, 994 (1969).
60. L. A. Buatois, M. G. Mangano, *J. Paleontol.* **86**, 7 (2012).
61. R. Tomer, A. S. Denes, K. Tessmar-Raible, D. Arendt, *Cell* **142**, 800 (2010).
62. J. L. Rubenstein, K. Shimamura, S. Martinez, L. Puelles, *Annu. Rev. Neurosci.* **21**, 445 (1998).
63. W. Ye, K. Shimamura, J. L. Rubenstein, M. A. Hynes, A. Rosenthal, *Cell* **93**, 755 (1998).
64. L. Sussel, O. Marin, S. Kimura, J. L. Rubenstein, *Development* **126**, 3359 (1999).
65. T. Mueller, M. F. Wullmann, S. Guo, *J. Comp. Neurol.* **507**, 1245 (2008).
66. H. Toresson, K. A. Campbell, *Development* **128**, 4769 (2001).
67. L. Muzio et al., *Nat. Neurosci.* **5**, 737 (2002).
68. A. Abetovitch, R. Hammond, *Dev. Biol.* **304**, 447 (2007).
69. S. T. Phillips, R. L. Albin, D. M. Martin, *Exp. Neurol.* **192**, 320 (2005).
70. D. M. Martin et al., *Dev. Biol.* **267**, 93 (2004).
71. F. Hirth, H. Reichert, in *Evolution of Nervous Systems, Vol. 1*, T. H. Bullock et al., Eds. (Elsevier, London, 2005), pp. 55–72.
72. B. Poock, T. Triphan, K. Neuser, R. Strauss, *Dev. Neurobiol.* **68**, 1046 (2008).
73. M. Desban, C. Gauchy, M. L. Kemel, M. J. Besson, J. Glowinski, *Neuroscience* **29**, 551 (1989).
74. K. Ito et al., *Learn. Mem.* **5**, 52 (1998).
75. M. Iwano et al., *J. Comp. Neurol.* **518**, 366 (2010).
76. M. W. Shiflett, B. W. Balleine, *Prog. Neurobiol.* **95**, 1 (2011).
77. W. Gronenberg, N. J. Strausfeld, *J. Comp. Neurol.* **316**, 87 (1992).

Acknowledgments: Supported by grants from the UK Medical Research Council (G070149), Royal Society (Hirth2007/R2), Parkinson's UK (G-0714), Motor Neurone Disease Association (Hirth/Mar12/6085, Hirth/Oct07/6233), Alzheimer Research UK (Hirth/ARUK/2012), and Fondation Thierry Latran (DrosALS) (to F.H.); the Air Force Research Laboratories (NJS/AFRL FA86511010001) (to N.J.S.); and the Center for Insect Science, University of Arizona, Tucson (to N.J.S.). We thank G. Wolf for the image in Fig. 1D.

Supplementary Materials

www.sciencemag.org/cgi/content/full/340/6129/157/DC1
Table S1

Fig S1

References (78–88)

10.1126/science.1231828



Last Call for Symposium Proposals

The deadline for submission is **23 April 2013, 11:59 p.m. PT**. To submit a proposal, visit www.aaas.org/meetings.

Meeting Global Challenges: Discovery and Innovation

Scientific discovery and innovation are helping to drive solutions to current and future global challenges. Economic progress in every community worldwide has meanwhile become increasingly interdependent with advances in science and technology. Challenges related to ensuring sufficient food for a growing population, quality healthcare, renewable fuels, and a sustainable and enriching environment demand innovation and international dialogue. Addressing these challenges depends upon discoveries emerging from the convergence of physical, life, engineering, and social sciences in innovative ways that are most useful to society.

In a weakened global economy, many countries have begun to limit their investments in the future. Yet, investments in innovations – including funding for education as well as basic and applied research – represent our best prospect for a sustainable environment and increased economic growth. Economists estimate, after all, that innovation in science and technology are the source of more than half of the economic growth in many countries. By increasing innovation in sustainable products and processes, world economies can continue to enhance human welfare across society.

Innovation springs from the translation, production, and distribution of discovery and invention to society. In the contemporary world, this is not a linear process, but rather, a matrix of interactions. Societies, with support from public and private sectors and institutions, struggle to integrate the necessary disciplines and interests into this matrix. Within the scientific and engineering community, we need to better integrate different disciplines and voices into a consensus supporting innovation. Developed and developing countries that accomplish this will become the economies of the future.

At the same time, it is imperative that we work in ways that are transparent and open to a diversity of contributors and ideas. Assessing risk versus benefit in adopting an innovation is complex and depends upon an open dialogue. Only then will we realize the promise of furthering scientific discovery and innovation to meet pressing global challenges and improve quality of life.

Call for Poster Submissions

Online entries will be accepted at www.aaas.org/meetings beginning **14 May 2013**.

The Mosaic Nature of *Australopithecus sediba*

THE SITE OF MALAPA, SOUTH AFRICA, HAS YIELDED PERHAPS THE RICHEST assemblage of early hominin fossils on the continent of Africa. The fossil remains of *Au. sediba* were discovered in August of 2008, and the species was named in 2010 (1)* and given a provisional age of ~1.78 to 1.95 Ma (2). In 2011, detailed studies of four critical areas of anatomy of these remains were published (3–6), and a refined date of ~1.977 to 1.98 Ma was proposed (7). The six articles presented in full in the online edition of *Science* (www.sciencemag.org/site/extra/sediba), with abstracts in print (pp. 164–165), complete the initial examination of the prepared material attributed to three individuals: the holotype and paratype skeletons, commonly referred to as MH1 and MH2, and the adult isolated tibia referred to as MH4. They, along with the cumulative research published over the past 3 years, provide us with a comprehensive examination of the anatomy of a single species of early hominin.

Irish *et al.* examine highly heritable nonmetric dental traits in *Au. sediba*. The species appears phylogenetically distinct from East African australopiths but close to *Au. africanus*, forming a southern African australopith clade. The latter shares some derived states with a clade comprising four fossil samples of the genus *Homo*. This result has implications for our present understanding of hominin phylogeny through the terminal Pliocene and suggests a possibility that *Au. sediba*, and perhaps *Au. africanus*, did not descend from the *Au. afarensis* lineage. De Ruiter *et al.* examine mandibular material attributable to MH2, including the previously unknown mandibular incisors and premolars of *Au. sediba*. As seen elsewhere in the cranium and skeleton, these mandibular remains share similarities with those of other australopiths but differ from *Au. africanus* in both size and shape, as well as in their ontogenetic growth trajectory. These results further support the claim that *Au. sediba* is taxonomically distinct from *Au. africanus*. Where the *Au. sediba* mandibles differ from those of *Au. africanus*, they appear most similar to those of representatives of early *Homo*.

Churchill *et al.* explore the upper limb elements of *Au. sediba*, describing the most complete and undistorted humerus, radius, ulna, scapula, clavicle, and manubrium yet described from the early hominin record, all associated with one individual. With the exception of the hand skeleton (3), the upper limbs of the Malapa hominins are largely primitive in their morphology. *Au. sediba* thus shares with other australopiths an upper limb that was well suited for arboreal climbing and possibly suspension, although perhaps more so than has previously been suggested for this genus.

Remains of the rib cage of *Au. sediba* are described by Schmid *et al.* and reveal a mediolaterally narrow upper thorax like that of the large-bodied apes and unlike the broad cylindrical chest seen in humans. In conjunction with the largely complete remains of the shoulder girdle, the morphological picture that emerges is one of a conical thorax with a high shoulder joint (producing an ape-like “shrugged” shoulder appearance) and thus a configuration that is perhaps uniquely australopith and would not have been conducive to human-like swinging of the arms during bipedal striding and running. The less well-preserved

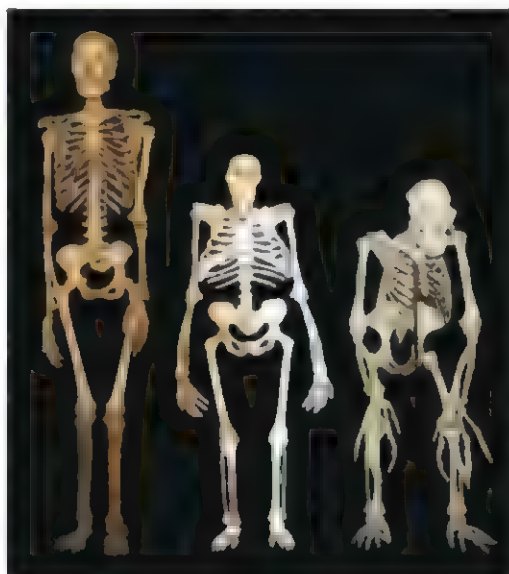
elements of the lower rib cage suggest a degree of human-like mediolateral narrowing to the lower thorax, indicating a rather unsuspected mosaic anatomy in the chest that is not like that observed in *Homo erectus* or *H. sapiens*.

Williams *et al.* analyze elements of the cervical, thoracic, lumbar, and sacral regions of the vertebral column, showing that *Au. sediba* had the same number of lumbar vertebrae as modern humans but possessed a functionally longer and more flexible lower back. Morphological indicators of strong lumbar curvature suggest that *Au. sediba* was derived in this regard relative to *Au. africanus* and was more similar to the Nariokotome *H. erectus* skeleton.

Finally, DeSilva *et al.* describe the lower limb anatomy of *Au. sediba* and propose a specific biomechanical hypothesis for how this species walked. In isolation, the anatomies of the heel, midfoot, knee, hip, and back are unique and curious, but in combination they are internally consistent for a biped walking with a hyperpronating gait. The implications are that multiple forms of bipedalism were once practiced by our early hominin ancestors.

This examination of a large number of associated, often complete and undistorted elements gives us a glimpse of a hominin species that appears to be mosaic in its anatomy and that presents a suite of functional complexes that are different from both those predicted for other australopiths and those of early *Homo*. Such clear insight into the anatomy of an early hominin species will clearly have implications for interpreting the evolutionary processes that affected the mode and tempo of hominin evolution and the interpretation of the anatomy of less well-preserved species.

— LEE R. BERGER



Composite reconstruction of *Au. sediba* based on recovered material from MH1, MH2, and MH4 and based on the research presented in the accompanying manuscripts. Because all individuals recovered to date are approximately the same size, size correction was not necessary. Femoral length was established by digitally measuring a complete femur of MH1 still encased in rock. For comparison, a small-bodied female modern *H. sapiens* is shown on the left and a male *Pan troglodytes* on the right.

Evolutionary Studies Institute, University of the Witwatersrand, Private Bag 3, Wits 2050, South Africa. E-mail: profteeberger@yahoo.com

*References may be found on page 165 after the abstracts.

ABSTRACTS

Dental Morphology and the Phylogenetic "Place" of *Australopithecus sediba*

Joel D. Irish,^{1*} Debbie Guatelli-Steinberg,² Scott S. Legge,³ Darryl J. de Ruiter,^{4,5} Lee R. Berger⁵

*Corresponding author. E-mail: j.d.irish@ljamu.ac.uk

To characterize further the *Australopithecus sediba* hypodigm, we describe 22 dental traits in specimens MH1 and MH2. Like other skeletal elements, the teeth present a mosaic of primitive and derived features. The new non-metric data are then qualitatively and phenetically compared with those in eight other African hominin samples, before cladistic analyses using a gorilla outgroup. There is some distinction, largely driven by contrasting molar traits, from East African australopiths. However, *Au. sediba* links with *Au. africanus* to form a South African australopith clade. These species present five apomorphies, including shared expressions of Carabelli's upper first molar (UM1) and protostylid lower first molar (LM1). Five synapomorphies are also evident between them and monophyletic *Homo habilis/rudolfensis* + *H. erectus*. Finally, a South African australopith + *Homo* clade is supported by four shared derived states, including identical LM1 cusp 7 expression.

>> Read the full article at <http://dx.doi.org/10.1126/science.1233062>

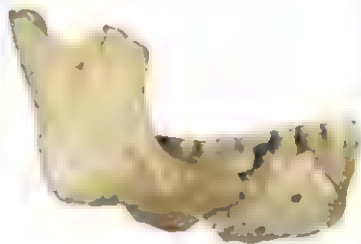
Mandibular Remains Support Taxonomic Validity of *Australopithecus sediba*

Darryl J. de Ruiter,^{4,5*} Thomas J. DeWitt,⁶ Keely B. Carlson,⁴ Juliet K. Brophy,^{4,5,7} Lauren Schroeder,⁸ Rebecca R. Ackermann,⁸ Steven E. Churchill,^{5,9} Lee R. Berger⁵

*Corresponding author. E-mail: deruiter@tamu.edu

Since the announcement of the discovery of *Australopithecus sediba*, questions have been raised over whether the Malapa fossils represent a valid taxon or whether inadequate allowance was made for intraspecific variation, in particular with reference to the temporally and geographically proximate species *Au. africanus*. The morphology of mandibular remains of *Au. sediba*, including newly recovered material discussed here, shows that it is not merely a late-surviving morph of *Au. africanus*. Rather—as is seen elsewhere in the cranium, dentition, and postcranial skeleton—these mandibular remains share similarities with other australopiths but can be differentiated from the hypodigm of *Au. africanus* in both size and shape, as well as in their ontogenetic growth trajectory.

>> Read the full article at <http://dx.doi.org/10.1126/science.1232997>



The Upper Limb of *Australopithecus sediba*

Steven E. Churchill,^{5,9*} Trenton W. Holliday,^{10,5} Kristian J. Carlson,^{5,11} Tea Jashashvili,^{5,12} Marisa E. Macias,⁹ Sandra Mathews,⁶ Tawnee L. Sparling,⁹ Peter Schmid,^{13,5} Darryl J. de Ruiter,^{4,5} Lee R. Berger⁵

*Corresponding author. E-mail: churchy@duke.edu

The evolution of the human upper limb involved a change in function from its use for both locomotion and prehension (as in apes) to a predominantly prehensile and manipulative role. Well-preserved forelimb remains of 1.98-million-year-old *Australopithecus sediba* from Malapa, South Africa, contribute to our understanding of this evolutionary transition. Whereas other aspects of their postcranial anatomy evince mosaic combinations of primitive (australopith-like) and derived (*Homo*-like) features, the upper limbs (excluding the hand and wrist) of the Malapa hominins are predominantly primitive and suggest the retention of substantial climbing and suspensory ability. The use of the forelimb primarily for prehension and manipulation appears to arise later, likely with the emergence of *Homo erectus*.

>> Read the full article at <http://dx.doi.org/10.1126/science.1233477>



Mosaic Morphology in the Thorax of *Australopithecus sediba*

Peter Schmid,^{13,5*} Steven E. Churchill,^{5,9} Shahed Nalla,^{4,5} Eveline Weissen,¹³ Kristian J. Carlson,^{5,11} Darryl J. de Ruiter,^{4,5} Lee R. Berger⁵

*Corresponding author. E-mail: smidi@aim.uzh.ch

The shape of the thorax of early hominins has been a point of contention for more than 30 years. Owing to the generally fragmentary nature of fossil hominin ribs, few specimens have been recovered that have rib remains complete enough to allow accurate reassembly of thoracic shape, thus leaving open the question of when the cylindrical-shaped chest of humans and their immediate ancestors evolved. The ribs of



Australopithecus sediba exhibit a mediolaterally narrow, ape-like upper thoracic shape, which is unlike the broad upper thorax of *Homo* that has been related to the locomotor pattern of endurance walking and running. The lower thorax, however, appears less laterally flared than that of apes and more closely approximates the morphology found in humans.

>> Read the full article at <http://dx.doi.org/10.1126/science.1234598>

The Vertebral Column of *Australopithecus sediba*

Scott A. Williams,^{15,16*} Kelly R. Ostrofsky,⁹ Nakita Frater,¹³ Steven E. Churchill,^{5,9} Peter Schmid,^{13,5} Lee R. Berger⁵

*Corresponding author. E-mail: sawilliams@nyu.edu

Two partial vertebral columns of *Australopithecus sediba* grant insight into aspects of early hominin spinal mobility, lumbar curvature, vertebral formula, and transitional vertebra position. *Au. sediba* likely possessed five non-rib-bearing lumbar vertebrae and five sacral elements, the same configuration that occurs modally in modern humans. This finding contrasts with other interpretations of early hominin regional vertebral numbers. Importantly, the transitional vertebra is distinct from and above the last rib-bearing vertebra in *Au. sediba*, resulting in a functionally longer lower back. This configuration, along with a strongly wedged last lumbar vertebra and other indicators of lordotic posture, would have contributed to a highly flexible spine that is derived compared with earlier members of the genus *Australopithecus* and similar to that of the Nariokotome *Homo erectus* skeleton.

>> Read the full article at <http://dx.doi.org/10.1126/science.1232996>



See all of *Science's* *Australopithecus sediba* coverage, including News, Research, and Multimedia, at www.sciencemag.org/site/extra/sediba

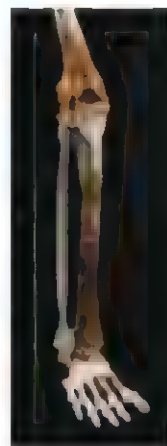


The Lower Limb and Mechanics of Walking in *Australopithecus sediba*

Jeremy M. DeSilva,^{17,5*} Kenneth G. Holt,¹⁸ Steven E. Churchill,^{5,9} Kristian J. Carlson,^{5,11} Christopher S. Walker,⁹ Bernhard Zipfel,^{5,19} Lee R. Berger⁵

*Corresponding author. E-mail: jdesilva@bu.edu

The discovery of a relatively complete *Australopithecus sediba* adult female skeleton permits a detailed locomotor analysis in which joint systems can be integrated to form a comprehensive picture of gait kinematics in this late australopithecine. Here, we describe the lower limb anatomy of *Au. sediba* and hypothesize that this species walked with a fully extended leg and with an inverted foot during the swing phase of bipedal walking. Initial contact of the lateral foot with the ground resulted in a large pronatory torque around the joints of the foot that caused extreme medial weight transfer (hyperpronation) into the toe-off phase of the gait cycle (late pronation). These bipedal mechanics are different from those often reconstructed for other australopithecines and suggest that there may have been several forms of bipedalism during the Plio-Pleistocene.



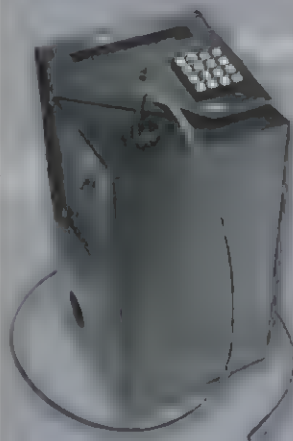
>> Read the full article at <http://dx.doi.org/10.1126/science.1232999>

References

1. L. R. Berger et al., *Australopithecus sediba*: a new species of *Homo*-like australopithecine from South Africa. *Science* **328**, 195 (2010).
2. P. H. G. M. Dirks et al., Geological setting and age of *Australopithecus sediba* from southern Africa. *Science* **328**, 205 (2010).
3. T. L. Kivell, J. M. Kibin, S. E. Churchill, P. Schmid, L. R. Berger, *Australopithecus sediba* hand demonstrates mosaic evolution of locomotor and manipulative abilities. *Science* **333**, 1411 (2011).
4. J. M. Kibin et al., A partial pelvis of *Australopithecus sediba*. *Science* **333**, 1407 (2011).
5. K. J. Carlson et al., The endocast of MH1, *Australopithecus sediba*. *Science* **333**, 1402 (2011).
6. B. Zipfel et al., The foot and ankle of *Australopithecus sediba*. *Science* **333**, 1417 (2011).
7. R. Pickering et al., *Australopithecus sediba* at 1.977 Ma and implications for the origins of the genus *Homo*. *Science* **333**, 1421 (2011).

¹Research Centre in Evolutionary Anthropology and Palaeoecology, School of Natural Sciences and Psychology, Liverpool John Moores University, Liverpool L3 3AF, UK. ²Department of Anthropology and Department of Evolution, Ecology, and Organismal Biology, Ohio State University, Columbus, OH 43210, USA. ³Department of Anthropology, Macalester College, St. Paul, MN 55105, USA. ⁴Department of Anthropology, Texas A&M University, College Station, TX 77843, USA. ⁵Evolutionary Studies Institute, University of the Witwatersrand, Private Bag 3, Wits 2050, South Africa. ⁶Department of Wildlife and Fisheries Sciences, Texas A&M University, College Station, TX 77843, USA. ⁷Department of Anthropology, Loyola University, Chicago, IL 60660, USA. ⁸Department of Archaeology, University of Cape Town, Rondebosch 7701, South Africa. ⁹Department of Evolutionary Anthropology, Box 90383, Duke University, Durham, NC 27708, USA. ¹⁰Department of Anthropology, Tulane University, New Orleans, LA 70118, USA. ¹¹Department of Anthropology, Indiana University, Bloomington, IN 47405, USA. ¹²Georgian National Museum, 0105 Tbilisi, Georgia. ¹³Anthropological Institute and Museum, University of Zürich, Winterthurerstrasse 190, CH-8057 Zürich, Switzerland. ¹⁴Department of Human Anatomy and Physiology, Faculty of Health Sciences, University of Johannesburg, Johannesburg, South Africa. ¹⁵Center for the Study of Human Origins, Department of Anthropology, New York University, 25 Waverly Place, New York, NY 10003, USA. ¹⁶New York Consortium in Evolutionary Primatology, New York, NY 10024, USA. ¹⁷Department of Anthropology, Boston University, 232 Bay State Road, Boston, MA 02215, USA. ¹⁸Department of Physical Therapy and Athletic Training, Sargent College, 635 Commonwealth Avenue, Boston University, Boston, MA 02215, USA. ¹⁹Bernard Price Institute for Palaeontological Research, School of Geosciences, University of the Witwatersrand, Private Bag 3, Wits 2050, South Africa.

High Speed Wavelength Switcher



FEATURES

SUTTER INSTRUMENT

Produced by the Science/AAAS Custom Publishing Office

Life Science Technologies
Fluorescence Multiplexing

In This Issue

Think of any multiplexed biological technique: RT-PCR, DNA sequencing, Flow cytometry, Microscopy. All work on different principles. Yet all have one common factor: fluorescence. The ever-expanding variety of fluorescent molecules, nanoparticles, and proteins has expanded the palette, so to speak, of biological experimentation. The pages of research journals may be filled mostly with reds and greens, but today's researchers have literally dozens of hues available from which to choose. Such variety has expanded the spectrum of applications and instrumentation available to the research community. The future of fluorescence multiplexing has never seemed so...ahem, bright.

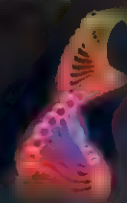
See full story on page 220.

Upcoming Features

The Microbiome—May 10

Proteomics: MALDI Imaging—May 31

Data Management: Cloud-Based—June 14



SICILY

October 10-22, 2013



Explore the cultural heritage and landscapes of this fascinating land of myth and legend with an intoxicating blend of archaeology, history, and nature... the envy of the Mediterranean. See ancient temples, theatres, discover a Roman palace, and marvel at the rich heritage of this land of volcanic Mt. Etna! \$3,995 + air

**For a detailed brochure,
please call (800) 252-4910**

All prices are per person twin share + air



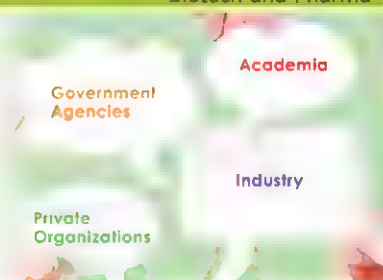
BETCHART EXPEDITIONS INC.

17050 Montebello Rd, Cupertino, CA 95014
Email: AAASInfo@betchartexpeditions.com
www.betchartexpeditions.com

Produced by the Science/AAAS Custom Publishing Office

Focus on Careers
Biotech and Pharma

Opening Industry-Academic Partnerships



In This Issue

Research and development today is about networking, sharing, and partnering. Collaborations between industry and academia are promoted by open innovation programs, which have become a near-universal model for R&D. Pharmaceutical and biotechnology companies offer university researchers access to resources and funding. Academic scientists bring in-depth expertise and basic research data to the table. Open innovation has exploded into megapartnerships of academia, industry, government agencies, and private organizations. These consortia have the potential to solve major medical and public health issues, if they can set terms and goals that reward all parties.

See the full story on page 225.

Upcoming Features

Regional Focus: Wales—April 26

Diversity (online only)—June 7

Postdoc—August 23

Dental Morphology and the Phylogenetic "Place" of *Australopithecus sediba*

Joel D. Irish,^{1*} Debbie Guatelli-Steinberg,² Scott S. Legge,³ Darryl J. de Ruiter,^{4,5} Lee R. Berger⁵

To characterize further the *Australopithecus sediba* hypodigm, we describe 22 dental traits in specimens MH1 and MH2. Like other skeletal elements, the teeth present a mosaic of primitive and derived features. The new nonmetric data are then qualitatively and phenetically compared with those in eight other African hominin samples, before cladistic analyses using a gorilla outgroup. There is some distinction, largely driven by contrasting molar traits, from East African australopithecids. However, *Au. sediba* links with *Au. africanus* to form a South African australopithecine clade. These species present five apomorphies, including shared expressions of Carabelli's upper first molar (UM1) and protostylid lower first molar (LM1). Five synapomorphies are also evident between them and monophyletic *Homo habilis/rudolfensis* + *H. erectus*. Finally, a South African australopithecine + *Homo* clade is supported by four shared derived states, including identical LM1 cusp 7 expression.

Given their propensity to outlast other hard tissues, teeth provide sizable, although restricted, data sets to define and characterize fossils. Thus, when alternative remains are available, as with *Australopithecus sediba* (1), the focus shifts readily to elements that give insight into hominin abilities such as cognition (2), manipulation (3, 4), parturition (5), and locomotion (5–9). Still, teeth have three key attributes that permit a singular perspective on hominins and their origins. First, crowns come into actual contact with the environment, so that direct inferences can be made about diet and certain behaviors (10). Second, because teeth preserve their record of incremental growth, a fine-grained understanding about the pace of hominin life histories is possible (11). Third, their high genetic component, among other features in expression (12), facilitates phylogenetic interpretations. Focusing on the latter attribute, we describe 22 nonmetric crown and root traits. These descriptions are then contrasted with those of six fossil and two recent hominin samples. Finally, after coding characters across these samples and an outgroup for cladistic analysis, we present additional phylogenetic information concerning this 1.977 million-year-old (13) South African australopithecine.

Some dental data in *Au. sediba* have been presented (1, 14). However, many of those characters are unique to Plio-Pleistocene hominins

(15–17). The traits used here are from the Arizona State University Dental Anthropology System (ASUDAS) (18), most of which are expressed in modern and fossil hominins, plus various other primates. Traits in the ASUDAS are highly heritable and minimally affected by sexual dimorphism, among other attributes (12). Further, as "minor" variants they should be little affected by selection, and pairwise correlations are negligible (18, 19). A lack of selection would reduce potential homoplasy (12). Low or no correlations address character redundancy that would bias cladistic analyses; this issue is crucial for molar traits,

given the identified linkage, albeit minor, between accessory cusp formation and intercuspal spacing and crown size (20). Only low intertrait correlations were detected for the present traits (12).

We inspected >340 fossil and 4571 recent hominin specimens retaining teeth, along with 44 gorilla dentitions; recording of the requisite traits (12) yielded the samples presented herein. The *Au. sediba* dental remains derive from MH1, a juvenile male, and MH2, an adult female (1). Data from the fossil comparative samples were collected in original specimens and 11 high-resolution casts (table S1) (21, 22). The east African australopithecine sample consists of *Au. anamensis* and *Au. afarensis*. Shared ASUDAS expression in these two time-successive species permitted pooling [see (21)] so as to most comprehensively characterize the *Australopithecus* genus in this region. *Homo habilis/rudolfensis* includes specimens assigned by some to different, albeit contemporaneous, species that also share ASUDAS expression. Similarly, *H. erectus* (also known as *ergaster*) includes specimens from what some maintain are different species (23). The remaining samples comprise *Au. africanus*, *Paranthropus robustus*, and *P. boisei*. The rationale to assign specimens to species is presented elsewhere (21, 22). In brief, sample composition is based on a majority consensus of researchers, while maximizing characterization for comparative purposes.

The recent hominin samples consist of post-Pleistocene *H. sapiens* from sub-Saharan ($n = 2309$) and North Africa ($n = 2262$) (24–26). Crown data in *Gorilla gorilla* were recorded in a collection from Cameroon; root descriptions are extrapolated from published sources (27, 28). The

Table 1. ASUDAS traits, grades, and descriptions in *Australopithecus sediba* specimens.

	MH1	MH2
Labial curvature U1	2: Weak convexity	
Shovel U1	1: Faint lingual ridges	
Double shovel U1	0: No labial ridges	
Bushman canine UC	0: Mesial and distal ridges same size	
Distal accessory ridge UC	0: Absent	
Root no. UP1	2: Two roots	
Carabelli's cusp UM1	4: Large depression (possible cusp)*	
Cusp 5 UM1	1: Faint cuspule	
Enamel extension UM1	0: Enamel border straight	
Hypocone UM2	4: Large cusp	
UM3 agenesis	0: Absent (tooth present)	
Tome's root LP1	5: Two free roots	5: Two free roots
Lingual cusp no. LP2		5: Two, distal larger than mesial
Anterior fovea LM1	2: Weak expression	
Cusp no. LM1	5: Hypoconulid present	5: Hypoconulid present
Protostylid LM1	4: Pronounced secondary groove	>1: Likely present, but expression uncertain
Cusp 7 LM1	2: Small*	>1: Likely present, but expression uncertain
Root no. LM1	2: Two	2: Two
Groove pattern LM2	Y: Cusps 2 and 3 touch	Y: Cusps 2 and 3 touch
Cusp no. LM2	5: Hypoconulid present	5: Hypoconulid present
Root no. LM2	2: Two	2: Two
Torsomolar angle LM3	0: No crown rotation	0: No crown rotation

¹Research Centre in Evolutionary Anthropology and Palaeoecology, School of Natural Sciences and Psychology, Liverpool John Moores University, Liverpool L3 3AF, UK. ²Department of Anthropology, and Department of Evolution, Ecology, and Organismal Biology, Ohio State University, Columbus, OH 43210, USA. ³Department of Anthropology, Macalester College, St. Paul, MN 55105, USA. ⁴Department of Anthropology, Texas A&M University, College Station, TX 77843, USA. ⁵Evolutionary Studies Institute, University of the Witwatersrand, Private Bag 3, Wits 2050, South Africa.

*Corresponding author. E-mail: j.d.irish@ljmu.ac.uk

*Estimated from worn or damaged tooth and/or interpolated from alternate member of same tooth class.

Table 2. ASUDAS traits and grades and the distribution of their states across the gorilla outgroup and hominin samples.

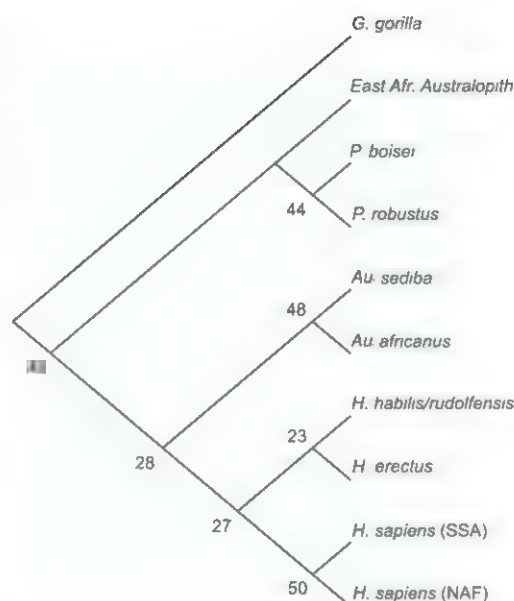
Trait	<i>G. gorilla</i>	East African australopith	<i>Au. sediba</i>	<i>Au. africanus</i>	<i>H. habilis/ rudolfensis</i>	<i>H. erectus</i>	<i>P. robustus</i>	<i>P. boisei</i>	<i>H. sapiens</i> (S. Africa)	<i>H. sapiens</i> (N. Africa)
Labial curvature UI1	Pronounced 4	Weak 2	Weak 2	Weak 2	Weak 2	Weak 2	Moderate 3	Weak 2	Weak 2	Trace 1
Shovel UI1	Absent 0	Faint 1	Faint 1	Faint 1	Faint 1	Trace 2	Trace 2	Faint 1	Faint 1	Faint 1
Double shovel UI1	Absent 0	Absent 0	Absent 0	Absent 0	Absent 0	Absent 0	Absent 0	Absent 0	Absent 0	Faint 1
Bushman canine UC	Absent 0	Absent 0	Absent 0	Absent 0	Absent 0	Absent 0	Absent 0	Absent 0	Present, moderate TD attachment†	Present, weak TD attachment†
Distal acc. ridge UC	Absent 0	Absent 0	Absent 0	Faint 1	Faint 1	Faint 1	Absent 0	?	Weak 2	Faint 1
Root no. UP3	Two 2	Two 2	Two 2	>Two 3	>Two 3	>Two 3	Two 2	?	Two 2	Two 2
Carabelli's cusp UM1*	Lingual cingulum†	Groove—small cusp 2	Large depression—cusp 5	Large depression—large cusp 5	Pit—small cusp 3	Pit—small cusp 3	Large depression—large cusp 5	Absent 1	Pit—small cusp 3	Large depression—large cusp 5
Cusp 5 UM1	Faint cuspule 1	Trace cuspule 2	Faint cuspule 1	Trace cuspule 2	Faint cuspule 1	Trace cuspule 2	Small cuspule 3	Small cuspule 3	Trace cuspule 2	Faint cuspule 1
Enamel extension UM1	Absent 0	Absent 0	Absent 0	Absent 0	Absent 0	Absent 0	Absent 0	Faint 1	Absent 0	Faint 1
Hypocone UM2	Very large cusp 5	Large cusp 4	Large cusp 4	Very large cusp 5	Large cusp 4	Large cusp 4	Very large cusp 5	Large cusp 4	Large cusp 4	Small cusp 3
UM3 agenesis	Absent 0	Absent 0	Absent 0	Absent 0	Absent 0	Absent 0	Absent 0	Absent 0	Absent 0	Minimal 1
Tome's root LP3	Two roots 5	Two roots 5	Two roots 5	Two roots 5	One root, deep groove 3	Two roots 5	Two roots 5	?	One root, moderate groove 2	One root, shallow groove 1
Lingual cusp no. LP4	Two, cusps equal size 4	Two, mesial cusp larger 3	Two, distal cusp larger 5	Two, mesial cusp larger 3	Two, cusps equal size 4	Two, mesial cusp much larger 2	Two, mesial cusp larger 3	Two, mesial cusp larger 3	Two, mesial cusp much larger 2	Two, mesial cusp larger 3
Anterior fovea LM1	Weak 2	Weak 2	Weak 2	Moderate 3	Moderate 3	Moderate 3	Moderate 3	Large 4	Weak 2	Faint 1
Cusp no. LM1	Five 5	Six 6	Five 5	Five 5	Five 5	Five 5	Six 6	Six 6	Five 5	Five 5
Protostylid LM1	Curved buccal groove 2	Absent-pit 1	Trace cusp 4	Small cusp 5	Curved buccal groove 2	Absent-pit 1	Absent-pit 1	Curved mesial and distal grooves 3	Absent 0	Absent-Pit 1
Cusp 7 LM1	Faint 1	Absent 0	Small 2	Small 2	Small 2	Small 2	Faint 1	Absent 0	Small 2	Absent 0
Root no. LM1	Two 2	Two 2	Two 2	Two 2	Two 2	Two 2	Two 2	Two 2	Two 2	Two 2
Groove pattern LM2	Y 0	Some X 1	Y 0	Y 0	Y 0	Y 0	Y 0	Y 0	Y 0	X 2
Cusp no. LM2	Five 5	Six 6	Five 5	Five 5	Five 5	Five 5	Six 6	≥Six 7	Five 5	Four 4
Root no. LM2	Two 2	Two 2	Two 2	Two 2	Two 2	Two 2	Two 2	?	Two 2	≤Two 1
Torsomolar angle LM3	Absent 0	Absent 0	Absent 0	Absent 0	Absent 0	Absent 0	Minimal 1	Minimal 1	Minimal 1	Minimal 1

*Numeric character states do not correspond to ASUDAS grades as presented in Table 1.

†This state is not present in the hominin samples and is considered, like all others in the outgroup, to be plesiomorphic.

‡TD, tuberculum dentale.

Fig. 1. Maximum parsimony cladogram of gorilla outgroup and nine hominin samples based on ASUDAS characters. Numbers are from a separate, although analogous 50% majority consensus tree of 10,000 bootstrapped replicate data sets; they represent the proportion of included trees that support the given node. SSA, sub-Saharan Africans; NAF, North Africans. See text for all methods employed and sample compositions.



latter species is used as an outgroup for cladistic analysis, which is appropriate given that it and *Pan* are the closest extant relatives of hominins (15).

Twenty-two traits that could be recorded in the two *Au. sediba* specimens, their ASUDAS grades, and expressions in the species are listed in Table 1. Comprehensive trait and grade definitions are available elsewhere (18, 19). Similar descriptions and character states for the cladistic analysis are listed in Table 2 for all samples. In this table, state values replicate ASUDAS grades, with one exception. The ASUDAS grade range of 0 to 7 for Carabelli's upper first molar (UM1) was increased to 0 to 8, with definitions (19) shifted up for each value to account for the gorilla cingulum variant (now given a value of 0); grade 0 is treated here as the primitive state, although not all researchers may concur. This modification accounts for the change in *Au. sediba* Carabelli's values (from 4 to 5) between tables.

Fourteen of 22 character states are identical between *Au. sediba* and east African australopithecus. The count between *Au. sediba* and *Au. africanus* is 15, and both are similar for a 16th state (protostylid lower first molar, LM1). All *Australopithecus* hypodigmata are somewhat similar, but the South African taxa are notably alike for lower molar cusp number, size, and pattern expression. *Australopithecus sediba* has 15 states in common with *H. habilis/rudolfensis*, and 13 of 21 with *H. erectus*; it is less akin to recent *H. sapiens* and is distinct from *Paranthropus*—owing to the latter's mass-additive molar morphology. Shared states among other species are also instructive; for example, *Au. africanus* shares additional ASUDAS traits with early *Homo*. The most expeditious way to present these links is with a dendrogram (fig. S1), where an *Au. sediba/Au. africanus* group is adjacent to an early/late *Homo* cluster, and east African australopithecus and *Paranthropus* are more distant. Of course, character states of these traits

were not determined for this phenetic comparison; some are symplesiomorphic, so results should be interpreted with caution.

Both primitive and derived dental features are present in *Au. sediba*. The former, like many hominins including *Au. africanus*, includes two-rooted upper third premolar (UP3), hypocone UM2, UM3 presence, Tome's root lower third premolar (LP3), two-rooted LM1, two-rooted LM2, five-cusped LM1, five-cusped LM2, and LM2 Y-groove. The last three traits in east African australopithecus often include six cusps for LM1 and LM2, and some occurrence of an X-groove pattern (below). Derived traits in *Au. sediba* include a decrease in labial curvature upper first incisor (UI1), slight UI1 shoveling, and increases in Carabelli's UM1, LM1 protostylid, and LM1 cusp 7 expression (fig. S2). Other derived dental features, including overall size reduction and a specific decrease in size and complexity of the canine and posterior teeth, are detailed elsewhere (1, 14).

Numeric states in *Gorilla*, *Au. sediba*, and the comparative samples were next submitted for cladistic analysis with PAUP 4.0b10 (29). Coding of binary and multistate characters emulates a standard approach in the above (1, 15–17) and other systematic studies. Polarity was determined via rooting of the outgroup, and all characters were treated as ordered and of equal weight. Wagner parsimony and the branch and bound method were used to identify optimal cladograms. Of the 22 characters, root number LM1 is constant, and three were deemed parsimony-uninformative (double shovel UI1, UM3 agenesis, and root number LM2); the expression of all four represents the primitive condition. The remaining 18 traits yielded one cladogram (Fig. 1) with a tree length of 76, consistency index of 0.62, retention index of 0.48, and rescaled consistency index of 0.3 [interpretation in (12)].

In parallel with the phenetic findings, *Au. sediba* is depicted as a sister species of *Au. africanus* to form a South African australopithecus clade. These species share five apomorphies: (i) weak labial curvature UI1; (ii) faint shovel UI1 (both are parallel with the east African australopithecus, *Paranthropus*, and *Homo* clades); (iii) large depression-to-cusp Carabelli's UM1 (parallel with *P. robustus* and North African *H. sapiens*); (iv) trace-small cusp protostylid LM1; and (v) small cusp 7 LM1 (parallel with *H. habilis/rudolfensis* + *H. erectus* clade and sub-Saharan African *H. sapiens*). Synapomorphies between the South African gracile australopithecus and monophyletic *H. habilis/rudolfensis* + *H. erectus* include (i) weak labial curvature UI1; (ii) faint shovel UI1 (both parallel with the east African australopithecus, *Paranthropus*, and *H. sapiens*); (iii) faint distal accessory ridge UC (parallel with *H. sapiens*); (iv) >2 root number UP3; and (v) small cusp 7 LM1 (parallel with sub-Saharan African *H. sapiens*). A South African australopithecus + *Homo* clade is supported by four shared derived states: (i) weak labial curvature UI1, (ii) faint shovel UI1 (both parallel with east African australopithecus and *Paranthropus*), (iii) faint distal accessory ridge UC, and (iv) small cusp 7 LM1.

Although the focus is on *Au. sediba*, the remaining clades are defined by characters of interest as well, and warrant brief mention, i.e., *H. habilis/rudolfensis* + *H. erectus* (e.g., Carabelli's cusp UM1), *Homo sapiens* (e.g., Bushman canine), and east African australopithecus + *Paranthropus*. The latter grouping is seemingly nonintuitive but not unique; comparable classifications were identified using a wide range of characters (30, 31). Here, *Paranthropus* and, as noted, the east African australopithecus—especially *Au. afarensis*, are characterized by some unique molar states such as trace-small cusplike for cusp 5 UM1, six-cusped LM1, absent-pit protostylid LM1, absent cusp 7, and six-cusped LM2. These shared expressions were reported elsewhere (12, 22) and were suggested to be symplesiomorphies and/or homoplasies.

A 50% majority-rule consensus tree of 10,000 bootstrapped replicate data sets was used to assess the stability of all clades; it is analogous to the maximum parsimony cladogram, so percentages of included trees supporting each clade were simply added to Fig. 1. Overall, the location of *Au. sediba* + *Au. africanus* at the stem of the *Homo* clade corresponds well with prior phylogenetic findings using >60 craniodental characters (1), which suggested that *Au. sediba* was derived from *Au. africanus*. This proposal is sustained here. Berger *et al.* (1) also stated that *Au. sediba* is more derived toward *Homo* than are east African australopithecus and *Au. africanus*; as such, *A. sediba* may represent (i) a sister group to a later ancestor that was an initial contemporary of early *Homo*, or (ii) a candidate ancestor to the latter genus (1). Both scenarios are supported, although, at least for these new data, *Au. africanus* does share additional ASUDAS traits

with early *Homo*; as such, Fig. 1 and the study's (1) 60-character cladogram differ in that the latter depicts *Au. africanus* as more distant than *Au. sediba* from the *Homo* clade.

The conclusions from the dental data presented here concur with those derived from the virtual brain endocast, and hand, spine, pelvis, foot, and ankle elements of *Au. sediba* (2–7); each area presents a mosaic of primitive and derived characters that, assuming they are homologies, is not unexpected in a transitional species or one that, minimally, reflects a close phyletic relationship with *Homo* (5). Moreover, with regard to east African australopithecids, it is possible that disparity in expression of molar states with their southern counterparts is also paralleled by other elements; differences in the foot, for example, prompted Zipfel *et al.* (6) to remark that an ancestor-descendant relationship between *Au. afarensis* and *Au. sediba* is unlikely or, if it existed, would have required several evolutionary reversals.

Although the phylogenetic place of *Au. sediba* has not been settled, the dental data serve to further define its position relative to other genera. It is distinct from *Au. afarensis*, close to *Au. africanus* and, along with the latter, shares a number of apomorphies with *Homo*. The relationship to *H. habilis/rudolfensis* had been suggested to reflect an adaptive evolution some two million years ago toward a definitive *Homo* grade (13); that is, *Au. sediba* could just as likely be the candidate ancestor of *H. erectus* as that of the majority consensus *H. habilis* and/or *H. rudolfensis* (13). However, determination of which taxon (or taxa) led to *Homo erectus* is, at present, not explicitly demonstrable. The difficulty is, to paraphrase Pickering *et al.* (13), under an assumption of substantial homoplasy, to discern phylogenetic affinities in such closely related species based on so few remains. Only recovery of additional *Au. sediba* and other Plio-Pleistocene remains can fill in the missing pieces of this evolutionary puzzle.

References and Notes

1. L. R. Berger *et al.*, *Australopithecus sediba*: A new species of *Homo*-like australopithecine from South Africa. *Science* **328**, 195 (2010). doi: 10.1126/science.1184944; pmid: 20378811
2. K. J. Carlson *et al.*, The endocast of MH1, *Australopithecus sediba*. *Science* **333**, 1402 (2011). doi: 10.1126/science.1203922; pmid: 21903804
3. T. L. Kivell, J. M. Kibii, S. E. Churchill, P. Schmid, L. R. Berger, *Australopithecus sediba* hand demonstrates mosaic evolution of locomotor and manipulative abilities. *Science* **333**, 1411 (2011). doi: 10.1126/science.1202625; pmid: 21903806
4. S. E. Churchill *et al.*, The upper limb of *Australopithecus sediba*. *Science* **340**, 1233477 (2013). doi: 10.1126/science.1233477
5. J. M. Kibii *et al.*, A partial pelvis of *Australopithecus sediba*. *Science* **333**, 1407 (2011). doi: 10.1126/science.1202521; pmid: 21903805
6. B. Zipfel *et al.*, The foot and ankle of *Australopithecus sediba*. *Science* **333**, 1417 (2011). doi: 10.1126/science.1202703; pmid: 21903807
7. S. A. Williams *et al.*, The vertebral column of *Australopithecus sediba*. *Science* **340**, 1232996 (2013). doi: 10.1126/science.1232996
8. P. Schmid *et al.*, Mosaic morphology in the thorax of *Australopithecus sediba*. *Science* **340**, 1234598 (2013). doi: 10.1126/science.1234598
9. J. M. DeSilva *et al.*, The lower limb and mechanics of walking in *Australopithecus sediba*. *Science* **340**, 1232999 (2013). doi: 10.1126/science.1232999
10. P. S. Ungar, Dental evidence for the diets of Plio-Pleistocene hominins. *Yearb. Phys. Anthropol.* **54**, 47 (2011). doi: 10.1002/ajpa.21610; pmid: 22101687
11. C. Dean *et al.*, Growth processes in teeth distinguish modern humans from *Homo erectus* and earlier hominins. *Nature* **414**, 628 (2001). doi: 10.1038/414628a; pmid: 11740557
12. Methods and background are available as supplementary materials on Science OnLine.
13. R. Pickering *et al.*, *Australopithecus sediba* at 1.977 Ma and implications for the origins of the genus *Homo*. *Science* **333**, 1421 (2011). doi: 10.1126/science.1203697; pmid: 21903808
14. D. J. de Ruiter *et al.*, Mandibular remains support taxonomic validity of *Australopithecus sediba*. *Science* **340**, 1232997 (2013). doi: 10.1126/science.1232997
15. D. S. Strait, F. E. Grine, M. A. Moniz, A reappraisal of early hominid phylogeny. *J. Hum. Evol.* **32**, 17 (1997). doi: 10.1006/jhev.1996.0097; pmid: 9034954
16. D. S. Strait, F. E. Grine, Inferring hominoid and early hominid phylogeny using craniodental characters: The role of fossil taxa. *J. Hum. Evol.* **47**, 399 (2004). doi: 10.1016/j.jhev.2004.08.008; pmid: 15566946
17. H. F. Smith, F. E. Grine, Cladistic analysis of early *Homo* crania from Swartkrans and Sterkfontein, South Africa. *J. Hum. Evol.* **54**, 684 (2008). doi: 10.1016/j.jhev.2007.10.012; pmid: 18289640
18. G. R. Scott, C. G. Turner II, *The Anthropology of Modern Human Teeth: Dental Morphology and its Variation in Recent Human Populations* (Cambridge Univ. Press, Cambridge, 1997).
19. C. G. Turner, C. R. Nichol, G. R. Scott, in *Advances in Dental Anthropology*, M. A. Kelley and C. S. Larsen, Eds. (Wiley, New York, 1991), pp. 13–32.
20. J. P. Hunter, D. Guatelli-Steinberg, T. C. Weston, R. Durner, T. K. Betsinger, Model of tooth morphogenesis predicts carabelli cusp expression, size, and symmetry in humans. *PLoS ONE* **5**, e11844 (2010). doi: 10.1371/journal.pone.0011844; pmid: 20689576
21. J. D. Irish, D. Guatelli-Steinberg, Ancient teeth and modern human origins: An expanded comparison of African Plio-Pleistocene and recent world dental samples. *J. Hum. Evol.* **45**, 113 (2003). doi: 10.1016/S0047-2484(03)00090-3; pmid: 14529648
22. D. Guatelli-Steinberg, J. D. Irish, Brief communication: Early hominid variability in first molar dental trait frequencies. *Am. J. Phys. Anthropol.* **128**, 477 (2005). doi: 10.1002/ajpa.20194; pmid: 16028225
23. F. E. Grine *et al.*, in *The First Humans—Origin and Early Evolution of the Genus Homo: Contributions from the Third Stony Brook Human Evolution Symposium and Workshop*, 3 to 7 October 2006, F. E. Grine, J. G. Fleagle, R. E. Leakey, Eds. (Springer Science + Business Media B.V., Amsterdam, 2009), pp. 49–64.
24. J. D. Irish, thesis, Arizona State University (1993).
25. J. D. Irish, Ancestral dental traits in recent Sub-Saharan Africans and the origins of modern humans. *J. Hum. Evol.* **34**, 81 (1998). doi: 10.1006/jhev.1997.0191; pmid: 9467783
26. J. D. Irish, Population continuity vs. discontinuity revisited: Dental affinities among late Pleistocene through Christian-era Nubians. *Am. J. Phys. Anthropol.* **128**, 520 (2005). doi: 10.1002/ajpa.20109; pmid: 15895433
27. S. A. Abbott, thesis, University of London (1984).
28. K. Kupczik, thesis, University of London (2003).
29. D. L. Swofford, *Phylogenetic Analysis using Parsimony (PAUP)*, Ver. 4.0. (Illinois Natural History Survey, Champaign, IL, 2002).
30. T. R. Olson, in *Ancestors. The Hard Evidence*, E. Delson, Ed. (Liss, New York, 1985), pp. 102–119.
31. D. Falk, in *Evolutionary History of the “Robust” Australopithecines*, F. E. Grine, Ed. (de Gruyter, New York, 1988), pp. 85–96.

Acknowledgments: Collection of the recent African comparative data was funded by monies to J.D.I. from the National Science Foundation (BCS-0840674, BNS-0104731, BNS-9013942), National Geographic Society, Wenner-Gren Foundation, Institute for Bioarchaeology, University of Alaska, and the Combined Prehistoric and Hierarchy Expeditions. The innumerable individuals at >25 institutions from which the data were collected cannot be listed in this restricted space, but their help is greatly appreciated. These and the *Au. sediba* ASUDAS raw data are in the possession of J.D.I. Collection of the early hominid comparative data was funded by grants to D.G. S. from the Leakey Foundation and Ohio State University. The authors thank D. Johanson and W. Kimbel for allowing D.G.-S. to study the Hadar fossils, M. Yima of the National Museum of Ethiopia, C. Kiane of the National Museums of Kenya, P. Msemwa and E. Maro of the National Museum of Tanzania, the Ethiopian government, and the governments of Kenya and Tanzania. H. Fourie and F. Thackeray provided access to fossils at the Transvaal Museum in Pretoria; P. Tobias, B. Kramer, and K. Kuykendall provided access to the fossils at the University of the Witwatersrand. I. Tattersall, J. Schwartz, J. Lukacs, H. McHenry, I. Pike, J. McKee, and T. Harrison advised D.G.-S. regarding the logistics of her research in east and South Africa. The ASUDAS hominid data are in the possession of D.G.-S. The assistance of A. Gill and M. Harman at the Powell-Cotton Museum, Birmington, UK, from which the gorilla crown data (in the possession of S.S.L.) were recorded, is greatly appreciated. Funding for S.S.L. was provided by the Wallace Travel Fund, Macalester College, and the Paul Anderson Interdisciplinary Summer Research Fund; funding for D.J.D. was provided by the Ray A. Rothrock Fellowship, Texas A&M University.

For the entire project, we also thank the South African Heritage Resource agency for the permits to work at the Malapa site; the Nash family for granting access to the Malapa site and continued support of research on their reserve; the South African Department of Science and Technology, the African Origins Platform (AOP), the Gauteng Provincial Government, the South African National Research Foundation, the Institute for Human Evolution, University of the Witwatersrand, the University of the Witwatersrand's Vice Chancellor's Discretionary Fund, the National Geographic Society, the Palaeontological Scientific Trust, the Andrew W. Mellon Foundation, the Ford Foundation, the U.S. Diplomatic Mission to South Africa, the French Embassy of South Africa, the A. H. Schultz Foundation, Duke University, Ray A. Rothrock '77 Fellowship and International Research Travel Assistance Grant of Texas A&M University, and the Oppenheimer and Ackerman families and Sir Richard Branson for funding; the University of the Witwatersrand's Schools of Geosciences and Anatomical Sciences and the Bernard Price Institute for Palaeontology for support and facilities; the Gauteng Department of Agriculture, Conservation and Environment and the Cradle of Humankind Management Authority; and our respective universities for ongoing support. For access to other comparative specimens, E. Mbua, P. Kiura, V. Imirigli, and the National Museums of Kenya; B. Billings, B. Zipfel, and the School of Anatomical Sciences at the University of the Witwatersrand; and S. Potze, L. C. Kgasi, and the Ditsong Museum. For technical and material support, Duke University, the University of Zurich 2009 and 2010 Field Schools, A. B. Taylor, C. E. Terhune, and C. E. Wall. Numerous individuals have been involved in the ongoing preparation and excavation of these fossils, including C. Dube, C. Kemp, M. Kgasi, M. Languza, J. Malaza, G. Mokoma, P. Mkarrela, T. Nermhundi, M. Ngcamphalala, S. Jirah, S. Tshabalala, and C. Yates. Other individuals who have given significant support to this project include B. de Klerk, W. Lawrence, C. Steininger, B. Kuhn, L. Pollarolo, B. Zipfel, J. Kretzen, D. Conforti, J. McCaffery, C. Damini, H. Visser, R. McCrae-Samuel, B. Nkosi, B. Louw, L. Backwell, F. Thackeray, and M. Peltier. J. Smily facilitated computed tomography scanning of the specimens. The *Au. sediba* specimens are archived at the Institute of Human Evolution at the University of the Witwatersrand.

Supplementary Materials

www.sciencemag.org/content/340/6129/1233062/suppl/DC1
Materials and Methods
Supplementary Text
Figs. S1 and S2
Table S1
References (32–65)

21 November 2012; accepted 12 March 2013
10.1126/science.1233062

Mandibular Remains Support Taxonomic Validity of *Australopithecus sediba*

Darryl J. de Ruiter,^{1,2*} Thomas J. DeWitt,³ Keely B. Carlson,¹ Juliet K. Brophy,^{1,2,4} Lauren Schroeder,⁵ Rebecca R. Ackermann,⁵ Steven E. Churchill,^{2,6} Lee R. Berger²

Since the announcement of the species *Australopithecus sediba*, questions have been raised over whether the Malapa fossils represent a valid taxon or whether inadequate allowance was made for intraspecific variation, in particular with reference to the temporally and geographically proximate species *Au. africanus*. The morphology of mandibular remains of *Au. sediba*, including newly recovered material discussed here, shows that it is not merely a late-surviving morph of *Au. africanus*. Rather—as is seen elsewhere in the cranium, dentition, and postcranial skeleton—these mandibular remains share similarities with other australopiths but can be differentiated from the hypodigm of *Au. africanus* in both size and shape as well as in their ontogenetic growth trajectory.

Mandibular remains are well represented in the hominin fossil record and have been included among the holotypes of numerous early hominin taxa, including *Australopithecus sediba* from Malapa (1, 2). The suggestion (3–5) that insufficient consideration was given to intraspecific variation when *Au. sediba* was diagnosed as a discrete taxon can be further investigated by using recently recovered mandibular remains. Most notable among these are two conjoined fragments, UW88-128 and UW88-129, that can be refit to the previously published mandibular specimen UW88-54 (7) to form a near complete right hemi-mandible with complete dentition of an adult individual, Malapa Hominin 2 (MH2) (Fig. 1). These new portions allow us to examine the premolar and M₁ regions of the mandibular corpus of an adult probable female of *Au. sediba* and provide a first look at the mandibular incisors and premolars of this taxon. In addition, we can now directly compare the mandibular canines of probable male and female individuals of *Au. sediba*.

As is seen in the cranium and postcranial skeleton of *Au. sediba* (1, 6–14), the reassembled mandible of MH2 exhibits a mosaic of morphological characters that align it with specimens attributed to both *Australopithecus* and early *Homo*. For instance, the mandible of MH2 shares with *Au. africanus* such features as a moderately developed lateral prominence, moderately developed lateral superior and marginal tori, weakly delineated anterior and posterior marginal tubercles,

a well-developed ectocondyloid buttress, and a well-developed lateral eminence of the ramus. However, it differs from *Au. africanus* and resembles specimens of early *Homo* by evincing relief between the alveolar prominence and the subalveolar fossa; possessing a small, steeply inclined postincisive planum; and revealing weakly developed endocoronoid and endocondyloid buttresses, which result in a triangular planum that is ill-defined along its inferior extent (15). However, gross morphology in hominin mandibles tends to be variable, as is seen in a direct comparison of MH1 and MH2; thus, we turn to size and shape analyses of mandibular corpora to assess the taxonomic validity of *Au. sediba*.

Linear dimensions of mandibular corpora have been shown to be taxonomically informative within fossil representatives of the genus *Homo* (2). In absolute measures, the mandibular corpus of MH2 is slightly taller and narrower than that of MH1 (Fig. 2 and table S1). There is considerable overlap in mandibular corpus height between *Au. afarensis*, *Au. africanus*, *Au. sediba*, *H. habilis*, *H. erectus*, and even *H. sapiens*. The corpus of MH1 is narrower than *Au. africanus* at the level of the P₄; it overlaps with the lower end of the range of *Au. africanus* at the level of the M₁, although only a single specimen of *Au. africanus*, the otherwise large-toothed Stw 498, is narrower. MH1 overlaps with *H. habilis* and *H. erectus* in width at the level of the P₄ and M₁, although again plotting near the lower end of the range of both taxa. The newly reassembled mandible of MH2 is narrower still than MH1 at the level of the P₄ and M₁, plotting below the range for *Au. africanus*, *H. habilis*, and *H. erectus*; it appears among the narrowest in the African hominin fossil record. Calculating corpus cross-sectional area by using the formula for an ellipse, MH1 and MH2 have similar values at the level of both the P₄ and M₁. The cross-sectional areas of the mandibular corpora of *Au. sediba* are small at the level of the P₄ and

M₁, plotting at or below the lowest end of the range of values for *Au. africanus* and within the ranges of *H. habilis* and *H. erectus*. In linear dimensions, mandibular corpus width—and to a lesser extent cross-sectional area—thus appear useful for discriminating *Au. sediba* from *Au. africanus* and for aligning the former taxon with specimens attributed to early *Homo*. This is particularly the case with the adult specimen MH2.

To better understand the nature of differentiation between early hominin taxa in both size and shape of mandibular corpora, we replicated the approach of Lague and colleagues (2) using specimens attributed to species of *Australopithecus* and early *Homo* in Africa and Georgia (15). Seven of the eight measures originally used (2) could be replicated in the reassembled mandible of MH2 and form the basis of our analyses. Randomization of “distinctness values” (RDV) (2, 16) reveals that within-group variance is less than between-group variance; thus, it appears that the mandibles of *Australopithecus* and *Homo* that we examined do indeed reflect a taxonomic signal. We therefore investigated the size and shape of the mandibular corpus of *Au. sediba* in relation to other hominins. We performed a multivariate analysis of variance (MANOVA) (15), the overall results of which can be visualized as a plot of between-group differences, scaled to within group variances (Fig. 3A). The major result illustrated in this plot is that *H. sapiens* are clearly distinct from early hominins, especially the robust australopiths, whereas *Au. sediba* clusters with the nonrobust australopiths and early *Homo*. This major axis indicates that human mandibles are small overall, have relatively narrow corpora, and relatively mesiodistally (MD) elongated (though small overall) canine alveoli (table S2).

Among the early hominins, *Au. sediba* most closely matches this pattern. A planned contrast within the MANOVA results explicitly comparing *Au. sediba* and *Au. africanus* revealed a significant difference between them ($F_{8,23} = 2.55$, $P = 0.037$). The difference between these two taxa primarily involved the smaller overall size of the mandible, the relatively deeper mandibular corpus, and the relatively MD elongated premolar row in *Au. sediba* when compared with that of *Au. africanus* (table S3). In other words, the mandibles of *Au. sediba* are not only scaled differently than those of *Au. africanus*, they are also shaped differently. Removal of humans from the ordination resulted in a primary axis that principally defined differences between the robust australopiths and the remaining early hominins (Fig. 3B). However, the secondary axis—approximately one-third the magnitude of the first—separated *Au. sediba* clearly from all other early hominins (planned contrast, $P = 0.034$). This effect was due to *Au. sediba* having a relatively MD elongated canine alveolus (table S3). Excluding size as a variable results in ordinations similar to those in Fig. 3, demonstrating that size is not unduly influencing the analysis (fig. S1).

¹Department of Anthropology, Texas A&M University, College Station, TX 77843, USA. ²Evolutionary Studies Institute, University of the Witwatersrand, Private Bag 3, Wits 2050, South Africa.

³Department of Wildlife and Fisheries Sciences, Texas A&M University, College Station, TX 77843, USA. ⁴Department of Anthropology, Loyola University, Chicago, IL 60660, USA. ⁵Department of Archaeology, University of Cape Town, Rondebosch 7701, South Africa. ⁶Department of Evolutionary Anthropology, Box 90383, Duke University, Durham, NC 27708, USA.

*Corresponding author. E-mail: deruiter@tamu.edu

Australopithecus sediba

The mandibular molars of *Au. sediba* were recorded as being small, similar to specimens attributed to early *Homo* (1), and we now have data on the remaining mandibular dentition from MH2 (figs. S2 and S3). Although the incisors of MH2 are too worn to reliably reconstruct their mesiodistal (MD) lengths, the buccolingual (BL) breadth of the I₁ plots at the lowest end of the range of *Au. africanus* and *H. erectus* but within the range of *Au. robustus* and *H. sapiens*. The BL breadth of the I₂ plots at the lowest end of the range of *Au. africanus*, but within the range of *Au. robustus*, *Au. boisei*, *H. erectus*, and *H. sapiens*. The only specimen of *Au. africanus* that overlaps with MH2 in the BL breadth of both incisors is Stw 151, a specimen described as more derived toward *Homo* than are the remainder of the Sterkfontein Member 4 sample (17). As in MH1 (1), the MD length of the canine of MH2 is small, plotting below the range for *Au. africanus* and *H. habilis*, and within the range of *H. erectus* and *H. sapiens*. In BL breadth, the canine of MH1 plots near the lowest end of the range for *Au. africanus* and close to the mean for *H. habilis* and *H. erectus*, whereas the canine of MH2 falls below the range of these early *Homo* taxa as well as *Au. africanus*. Indeed, the canine of MH2, and to a lesser extent of MH1, is among the smallest in the hominin fossil record. Likewise, the premolars of MH2 are small and generally plot at or below the lower end of the ranges seen in *Au. africanus* and *H. habilis*, appearing especially MD shortened; where the P₄ of *Au. sediba* overlaps with *Au. africanus*, only a single specimen attributed to *Au. africanus*, Stw 112, appears smaller than MH2. Conversely, the premolars of *Au. sediba* plot within the ranges of *H. erectus* and *H. sapiens* dentitions.

The shape of the premolars is also diagnostic; occlusal outline analysis of both the P₃ and the P₄ by using elliptical function Fourier analysis (EFFA) positions them as outliers relative to both *Au. africanus* and *Au. robustus*, demonstrating that these teeth differ in both size and shape from other South African australopiths (fig. S4) (15). Although the complete dentition of MH2 appears small in size similar to that of *Homo*, it shares with *Australopithecus* a pattern of increasing tooth size along the molar row (fig. S5).

Using mandibular molars, it was originally estimated that the dentition of MH1 was between 8.1 and 10.7% larger than that of MH2 (1). We can now extend this to include canines: The canine of MH1 is ~9.6% larger than the canine of MH2 in MD length and ~20.0% larger in BL breadth. Converting this to a square root of the basal crown area, the canine of MH1 is ~15% larger than that of MH2. This can be compared with canine dimorphism levels derived for other hominins by using the “mean” method of estimation (15, 18). With a value of 1.15, *Au. sediba* is intermediate between taxa such as *Au. afarensis* (1.21) and *Au. boisei* (1.21) on the one hand and taxa such as *Au. africanus* (1.11), *Au. robustus* (1.11), *H. erectus* (1.13), and *H. sapiens* (1.07)

on the other. Although the “mean” method tends to overestimate dimorphism in fossil species for which sex is generally unknown (18), with probable male and female individuals *Au. sediba* provides a known sample. Sample sizes are small for the hominin taxa, although these data nonetheless serve to highlight the dimorphism evident in the otherwise small canines of *Au. sediba*. Although the canines of *Au. sediba* are small and lack the diagnostic lingual relief seen in *Au. africanus*, a pattern shared with early *Homo*, they reveal a degree of canine dimorphism that approaches levels seen in several other australopith taxa and that is also close to that of *H. erectus*.

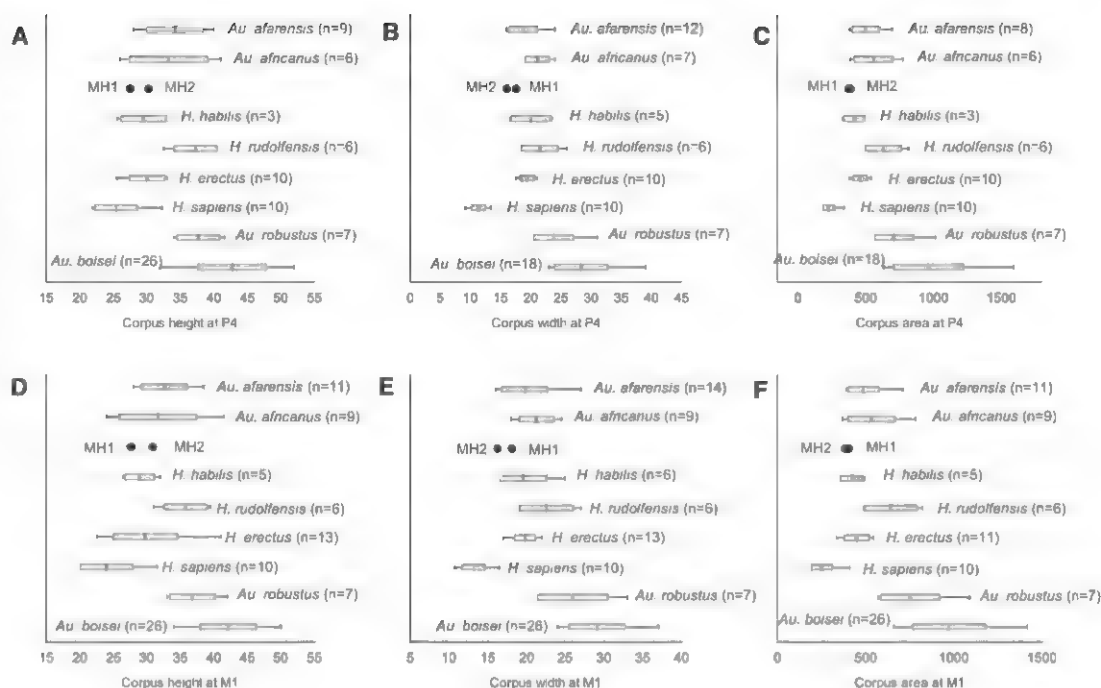
Last, we tested whether *Au. sediba* shares a common pattern of development with *Au. africanus* using Euclidean distance matrix analysis (EDMA) (15). We examine the ontogeny of mandibular shape in the fossil species *Au. sediba*, *Au. africanus*, and *H. erectus* and in the extant species *H. sapiens* and *Pan troglodytes*. Juvenile samples are roughly the same developmental age as MH1 (pre-M₃ eruption), and therefore by necessity this comparison captures only one stage of development. EDMA was performed on mean forms of extant samples and on individual fossil juvenile and adult specimens as representatives of their respective species (table S4) (19–22). In addition, simulated hypothetical juvenile *Au.*



Fig. 1. Right hemi-mandible of adult probable female individual MH2 from Malapa. Conjoined fragments UW88-128 and UW88-129 refit to UW88-54 in (A) occlusal view, (B) medial view, and (C) lateral view. The coronoid process is truncated because of damage. Scale bar, 5 cm.

Fig. 2. Mandibular corpus measures of *Au. sediba* compared with other early hominin taxa.

(A) Corpus height at P₄. (B) Corpus width at P₄. (C) Corpus area at P₄ computed by using the formula for an ellipse [$\pi(\text{height}/2) * (\text{width}/2)$]. (D) Corpus height at M₁. (E) Corpus width at M₁. (F) Corpus area at M₁ computed by using the formula for an ellipse [$\pi(\text{height}/2) * (\text{width}/2)$]. Measures for *Au. afarensis*, *Au. boisei*, *H. habilis*, *H. rudolfensis*, and *H. erectus* specimens are from (23–25); measures of *Au. africanus*, *Au. sediba*, *Au. robustus*, and *H. sapiens* specimens were taken by D.J.d.R. on original materials.



sediba forms were created by using species-specific growth patterns derived from *Au. africanus* and *H. erectus* in order to explore the effect of these respective growth patterns when applied to *Au. sediba* (15). The overall EDMA results can be visualized in a principal coordinates plot (PCOORD) (Fig. 4) and show that *Au. sediba* displays a pattern of growth that differs from *Au. africanus*, *P. troglodytes*, and *H. sapiens* [further discussion is available in (15)]. Rather, the growth pattern of *Au. sediba* is most similar to *H. erectus*. *Au. sediba* also differs in magnitude of growth from *Au. africanus* and *H. erectus* as well as both of the extant taxa (Fig. 4). Because these data are scaled to facilitate cross-species comparisons, the magnitude of change should be interpreted as the magnitude of shape change during growth rather than absolute size. Additionally, the simulated hypothetical juvenile forms and their associated growth trajectories further support a distinction between mandibular growth in *Au. sediba* versus both fossil hominin species [further discussion is available in (15)], with neither a *H. erectus*-like nor an *Au. africanus*-like pattern or magnitude of growth resulting in simulated final juvenile forms similar to the actual MH1 juvenile, which further suggests that ontogenetic change in the mandible of *Au. sediba* is unique.

The small size of the newly recovered mandibular corpus of *Au. sediba*—combined with its reduced dentition, in particular of the canines and premolars—separate it from its otherwise close morphological affinity, *Au. africanus*. The distinction between *Au. sediba* and *Au. africanus* extends to more than just a size difference; the two taxa differ in shape as well, with *Au. sediba* possessing a relatively smaller and deeper corpus, and a relatively elongated premolar row when compared

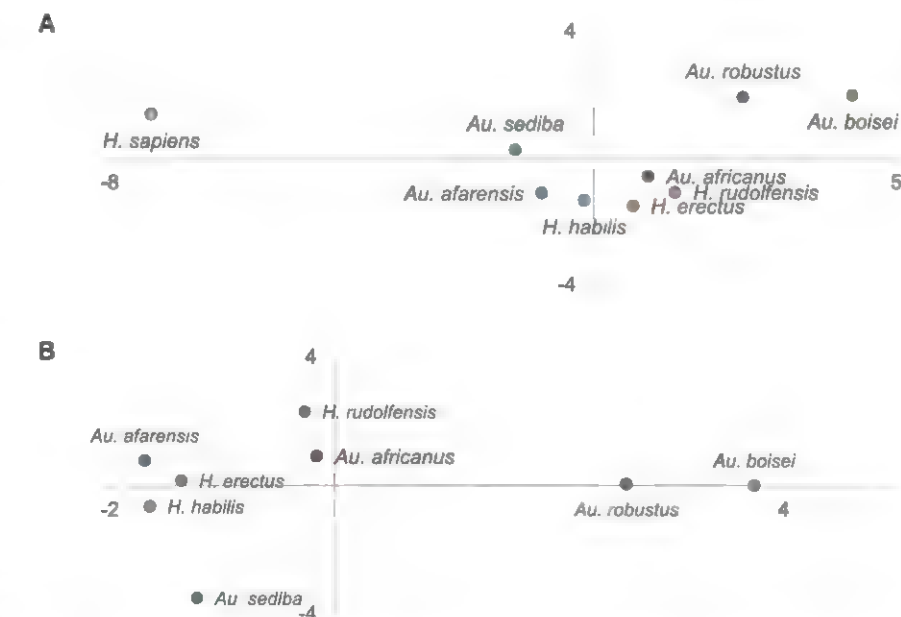


Fig. 3. Visualization of the first two canonical axes from the MANOVA on form. (A) Including humans. (B) Excluding humans. Details of canonical plot interpretation are available in the text, and computation is available in supplementary text S1. Measures for *Au. afarensis*, *Au. boisei*, *H. habilis*, *H. rudolfensis*, and *H. erectus* specimens are from (23–25); measures of *Au. africanus*, *Au. sediba*, *Au. robustus* and *H. sapiens* specimens were taken by D.J.d.R. on original materials. Plot aspect ratio indicates the relative magnitude (eigenvalues) of the respective canonical axes.

with those of *Au. africanus*. Likewise, the premolars of *Au. sediba* differ in occlusal outline shape from those of *Au. africanus* and *Au. robustus*, plotting as distinct outliers relative to the South African australopiths. The divergent growth trajectory of *Au. sediba* compared with those of both extant and fossil taxa further highlights the singular nature of the mandible of *Au. sediba*.

We interpret these substantial size and shape differences as upholding the taxonomic distinction initially proposed for *Au. sediba* (1), in particular as compared with specimens of *Au. africanus*. And where the *Au. sediba* mandibles differ from those of *Au. africanus*, they appear most similar to representatives of early *Homo* in both size and shape.

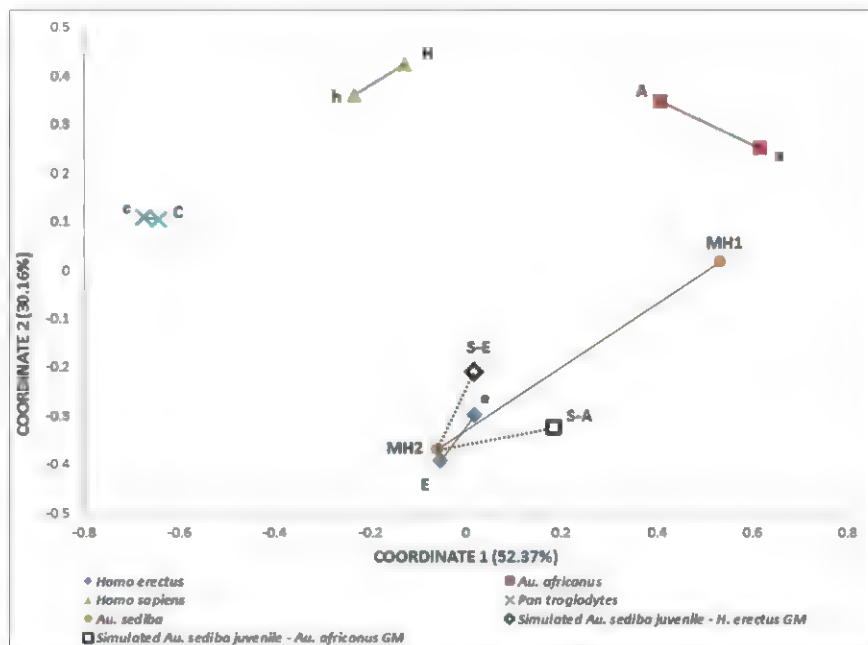


Fig. 4. Ontogenetic trajectories of mandibular shape variability for *Au. sediba* (MH1, MH2), *Au. africanus* (A,a), *H. erectus* (E,e), *H. sapiens* (H,h), *P. troglodytes* (C,c), and two simulated trajectories for *Au. sediba* (S-A, S-E). Upper- and lowercase labels indicate adults and juveniles, respectively, and are connected by a line that indicates a “growth trajectory” in shape space. Black dotted lines denote simulated growth trajectories connecting MH2 with “hypothetical” juvenile forms. Details of interpretation are available in the text. Details of the samples and analysis can be found in (15). Linear measurements for all specimens are derived from laser surface scans taken by L.S. and K.B.C. on original material.

References and Notes

1. L. R. Berger *et al.*, *Australopithecus sediba*: A new species of *Homo*-like australopithecine from South Africa. *Science* **328**, 195 (2010). doi: 10.1126/science.1184944; pmid: 20378811
2. M. R. Lague, N. J. Collard, B. G. Richmond, B. A. Wood, Hominid mandibular corpus shape variation and its utility for recognizing species diversity within fossil *Homo*. *J. Anat.* **213**, 670 (2008). doi: 10.1111/j.1469-7580.2008.00989.x; pmid: 19094183
3. M. Bitter, Paleanthropology. Candidate human ancestor from South Africa sparks praise and debate. *Science* **328**, 154 (2010). doi: 10.1126/science.328.5975.154; pmid: 20378782
4. M. Cherry, Claim over ‘human ancestor’ sparks furore. *Nature*, published online 08 April 2010 (10.1038/news.2010.171). doi: 10.1038/news.2010.171
5. B. A. Wood, T. Harrison, The evolutionary context of the first hominins. *Nature* **470**, 347 (2011). doi: 10.1038/nature09709; pmid: 21331035
6. K. J. Carlson *et al.*, The endocast of MH1, *Australopithecus sediba*. *Science* **333**, 1402 (2011). doi: 10.1126/science.1203922; pmid: 21903804
7. J. D. Irish, D. Guatelli-Steinberg, S. S. Legge, L. R. Berger, D. J. de Ruiter, Dental morphology and the phylogenetic ‘place’ of *Australopithecus sediba*. *Science* **340**, 1233062 (2013).
8. J. M. Kibbi *et al.*, A partial pelvis of *Australopithecus sediba*. *Science* **333**, 1407 (2011). doi: 10.1126/science.1202521; pmid: 21903805
9. T. L. Kivell, J. M. Kibbi, S. E. Churchill, P. Schmid, L. R. Berger, *Australopithecus sediba* hand demonstrates mosaic evolution of locomotor and manipulative abilities. *Science* **333**, 1411 (2011). doi: 10.1126/science.1202625; pmid: 21903806
10. B. Zipfel *et al.*, The foot and ankle of *Australopithecus sediba*. *Science* **333**, 1417 (2011). doi: 10.1126/science.1202703; pmid: 21903807
11. S. E. Churchill *et al.*, The upper limb of *Australopithecus sediba*. *Science* **340**, 1233477 (2013). doi: 10.1126/science.1233477
12. P. Schmid *et al.*, Mosaic morphology in the thorax of *Australopithecus sediba*. *Science* **340**, 1234598 (2013). doi: 10.1126/science.1234598
13. S. A. Williams *et al.*, The vertebral column of *Australopithecus sediba*. *Science* **340**, 1232996 (2013). doi: 10.1126/science.1232996
14. J. M. DeSilva *et al.*, The lower limb and mechanics of walking in *Australopithecus sediba*. *Science* **340**, 1232999 (2013). doi: 10.1126/science.1232999
15. Methods and results are available as supplementary materials on Science Online.
16. R. R. Sokal, F. J. Rohlf, *Biometry* (W. H. Freeman, New York, ed. 3, 1995).
17. J. Moggi-Cecchi, P. V. Tobias, A. D. Beynon, The mixed dentition and associated skull fragments of a juvenile fossil hominid from Sterkfontein, South Africa. *Am. J. Phys. Anthropol.* **106**, 425 (1998). doi: 10.1002/(SICI)1096-8644(199808)106:4<425::AID-AJPA2>3.0.CO;2-I; pmid: 9712475
18. J. M. Plavcan, C. P. van Schaik, Interpreting hominid behavior on the basis of sexual dimorphism. *J. Hum. Evol.* **32**, 345 (1997). doi: 10.1006/jhev.1996.0096; pmid: 9085186
19. J. T. Richtsmeier, S. R. Lele, A coordinate-free approach to the analysis of growth patterns: Models and theoretical considerations. *Biol. Rev. Camb. Philos. Soc.* **68**, 381 (1993). doi: 10.1111/j.1469-185X.1993.tb00737.x; pmid: 8347767
20. S. R. Lele, J. T. Richtsmeier, Euclidean distance matrix analysis: Confidence intervals for form and growth differences. *Am. J. Phys. Anthropol.* **98**, 73 (1995). doi: 10.1002/ajpa.1330980107; pmid: 8579192
21. J. T. Richtsmeier, T. M. Cole 3rd, G. Krovitz, C. J. Valen, S. Lele, Preoperative morphology and development in sagittal synostosis. *J. Craniofac. Genet. Dev. Biol.* **18**, 64 (1998). pmid: 9672839
22. R. R. Ackermann, G. E. Krovitz, Common patterns of facial ontogeny in the hominid lineage. *Anat. Rec.* **269**, 142 (2002). doi: 10.1002/ar.10119; pmid: 12124900
23. W. H. Kimbel, Y. Rak, D. C. Johanson, *The Skull of Australopithecus afarensis* (Oxford Univ. Press, Oxford, 2004).
24. B. A. Wood, *Koobi Fora Research Project: Volume 4, Hominid Cranial Remains* (Clarendon Press, Oxford, 1991).
25. L. Gabunia, A. Vekua, A Plio-Pleistocene hominid from Dmanisi, East Georgia, Caucasus. *Nature* **373**, 509 (1995). doi: 10.1038/373509a0; pmid: 7845461

Acknowledgments: We thank the South African Heritage Resource agency for the permits to work on the Malapa site and the Nash family for granting access to the Malapa site and continued support of research on their reserve. The South African Department of Science and Technology, and the African Origins Platform (AOP), the South African National Research Foundation, the Institute for Human Evolution (IHE), the Palaeontological Scientific Trust (PAST), the Andrew W. Mellon Foundation, the L.S.B. Leakey Foundation Baldwin Fellowship, the United States Diplomatic Mission to South Africa, the French Embassy in South Africa, the National Geographic Society, the A. H. Schultz Foundation, the Oppenheimer and Ackerman families, Sir Richard Branson, and the Program to Enhance Scholarly and Creative Activities and the International Research Travel Award Grant of Texas A&M University all provided funding for this research. D.J.d.R. holds a Ray A. Rothrock ‘77 Fellowship at Texas A&M University, which provided additional funding. The University of the Witwatersrand’s Schools of Geosciences and Anatomical Sciences and the Bernard Price Institute for Palaeontology provided support and facilities. The authors declare that they have no real or apparent conflicts of interest. We thank E. Mbua, P. Kiura, V. Iminjili, and the National Museums of Kenya; P. Msemwa and the National Museum and House of Culture of Tanzania; S. Potze of the Ditsong Museum; B. Billings of the School of Anatomical Sciences of the University of the Witwatersrand; W. Seconna of the Iziko South African Museum; and L. M. Jellema of the Ede and Museum of Natural History for access to comparative fossil and extant primate and human materials in their care. Numerous individuals have been involved in the ongoing preparation and excavation of these fossils, including C. Dube, B. Eloff, C. Kemp, M. Kgasi, M. Languza, J. Malaza, G. Mokoma, P. Mukanela, T. Nemvundi, M. Ngcamphalala, S. Jirah, S. Tshabalala, and C. Yates. Other individuals who have given substantial support to this project include B. de Klerk, C. Steininger, B. Kuhn, L. Pollaro, B. Zipfel, J. Kretzen, D. Conforti, J. McCaffery, C. Dlamini, H. Visser, R. McCrae-Samuel, B. Nkosi, B. Louw, L. Backwell, F. Thackeray, M. Peltier, J. Cheverud, and D. Roach. The *Au. sediba* specimens are archived at the Evolutionary Studies Institute at the University of the Witwatersrand. All data used in this study are available upon request, including access to the original specimens, by bona fide scientists.

Supplementary Materials

www.sciencemag.org/content/340/6129/1232997/suppl/DC1
Methods and Results
Supplementary Text
Figs. S1 to S5
Tables S1 to S5
References (26–33)

20 November 2012; accepted 13 March 2013
10.1126/science.1232997

The Upper Limb of *Australopithecus sediba*

Steven E. Churchill,^{1,2*} Trenton W. Holliday,^{3,2} Kristian J. Carlson,^{2,4} Tea Jashashvili,^{2,5} Marisa E. Macias,¹ Sandra Mathews,⁶ Tawnee L. Sparling,¹ Peter Schmid,^{6,2} Darryl J. de Ruiter,^{7,2} Lee R. Berger²

The evolution of the human upper limb involved a change in function from its use for both locomotion and prehension (as in apes) to a predominantly prehensile and manipulative role. Well-preserved forelimb remains of 1.98-million-year-old *Australopithecus sediba* from Malapa, South Africa, contribute to our understanding of this evolutionary transition. Whereas other aspects of their postcranial anatomy evince mosaic combinations of primitive (australopith-like) and derived (*Homo*-like) features, the upper limbs (excluding the hand and wrist) of the Malapa hominins are predominantly primitive and suggest the retention of substantial climbing and suspensory ability. The use of the forelimb primarily for prehension and manipulation appears to arise later, likely with the emergence of *Homo erectus*.

Paleoanthropological fieldwork in Africa and western Asia continues to enhance the fossil representation of Plio-Pleistocene hominin upper limb remains (1–7). Improvement in this record has fostered a new appreciation for variability in hominin forelimb morphology and limb proportions but has at the same time raised new issues about the locomotor and manipulative behavior of various species of *Australopithecus* and early *Homo*. One area of current uncertainty involves the functional and phylogenetic importance of variation within the genus *Australopithecus*. Compared with the earlier species *Au. anamensis* and *Au. afarensis*, limb and joint pro-

portions in *Au. africanus* reflect a more ape-like morphology and possibly a greater degree of arboreality (8, 9). The same may be true of postcranial material attributed to *H. habilis* (10, 11), although the fragmentary condition of the representative specimens prevents definitive conclusions (12–14), as does the possibility that these two partial skeletons do not represent *H. habilis* (7). In addition, a 2.5-million-year-old partial skeleton that may represent *Au. garhi* is said to evince derived, *Homo*-like interlimb proportions (i.e., relative elongation of the lower limb) coupled with ape-like brachial (forearm to arm) proportions that are more primitive than seen in earlier *Au.*

afarensis (15). There thus appears to have been considerable evolvability in hominin limb proportions (16), likely involving substantial parallelism as well as evolutionary reversals, making it difficult to identify the immediate morphological precursors to the human-like proportions seen in early *H. erectus* (4, 17, 18).

A second open question concerns the functional meaning of morphological variation within *Au. afarensis*. Two relatively complete scapulae of this species have recently been discovered in Ethiopia, one representing a 3.3-million-year-old juvenile from Dikika (DIK-1-1) (3, 19), the other a 3.6-million-year-old adult from Woranso-Mille (KSD-VP-1/1 g) (6, 20). Multivariate analysis of linear and angular measurements of DIK-1-1 highlights its similarities to gorilla and orangutan scapulae in the orientations of both its spine and glenoid fossa and in the proportions of its supraspinous and infraspinous fossae, suggesting a high degree of arboreality in *Au. afarensis* (3, 19). Conversely, in a multivariate analysis of angular measurements, the adult Woranso-Mille scapula clusters with modern humans and not African apes, suggesting a loss of arboreal function in

¹Department of Evolutionary Anthropology, Box 90383, Duke University, Durham, NC 27708, USA. ²Evolutionary Studies Institute, University of the Witwatersrand, Private Bag 3, Wits 2050, South Africa. ³Department of Anthropology, Tulane University, New Orleans, LA 70118, USA. ⁴Department of Anthropology, Indiana University, Bloomington, IN 47405, USA. ⁵Georgian National Museum, 0105 Tbilisi, Georgia. ⁶Anthropological Institute and Museum, University of Zürich, Winterthurerstrasse 190, CH-8057 Zürich, Switzerland. ⁷Department of Anthropology, Texas A&M University, College Station, TX 77843, USA.

*Corresponding author. E-mail: churchy@duke.edu

Fig. 1. Malapa upper limb elements in anterior view (unless otherwise noted). MH1: UW88-1 right clavicle (superoanterior view); UW88-34, 42, and 88 right humerus; UW88-36 left humerus; UW88-3 right ulna; and UW88-12 right radial epiphysis (distal view). MH2: UW88-172 manubrium, UW88-38 right clavicle (superoanterior view), UW88-94 left clavicle (superoanterior view), UW88-56 right scapula, UW88-103 left scapular acromion, UW88-104 left scapular glenoid fossa (lateral view), UW88-197 left scapular body fragment, UW88-57 right humerus, UW88-101 left humerus, UW88-62 right ulna, and UW88-85 right radius.



Australopithecus sediba

Au. afarensis (6). It is not clear whether this disparity in results is the consequence of differences in the developmental ages of the two specimens [but see (19)] or is the result of using different variable sets and comparative samples in the analyses of the two specimens [see (6)].

Upper limb remains of *Au. sediba* (7), from the 1.98-million-year-old site of Malapa, South Africa (21, 22), enhance our understanding of variation in australopith morphology. The forelimb is particularly well represented in the Malapa hominins (Fig. 1). The subadult male, Malapa Hominin 1 (MH1), preserves the lateral half of the right clavicle, a right humerus that is complete save for the proximal epiphysis and apophysis of the medial epicondyle, a proximal shaft fragment of the left humerus, the proximal half of the right ulna (lacking the olecranon apophysis), and the distal epiphysis of the right radius. The adult female (MH2) preserves a complete clavicle, humerus, radius, and ulna and a relatively complete scapula from the right side, as well as portions of the left clavicle, scapula, and humerus. Both specimens also preserve manual remains, which have been treated elsewhere (23).

The Pectoral Girdle

The overall morphology of the upper limbs of *Au. sediba* broadly resembles that of other australopiths. The right clavicle of MH2 is absolutely and relatively short and is relatively gracile compared with the Woranso-Mille (*Au. afarensis*) specimen KSD-VP-1/1f (6) and early and modern *Homo* (table S1), all of which are larger bodied. When the acromial ends of the clavicles of both MH1 and MH2 are held horizontally, their shafts inflect inferomedially (Fig. 2), indicating a shoulder position higher than that of living humans (24). The morphology of the sternoclavicular joint surfaces of the clavicle and manubrium of MH2 also suggest an oblique orientation to the clavicle (Fig. 2) and imply a high scapular position. Like other australopiths and *Homo*, the deltoid scar is on the anterior surface of the lateral curve of the shaft, not on the superoanterior surface as in chimpanzees, indicating a human-like lack of clavicular rotation (24). However, unlike humans, MH2 and, to a lesser extent, MH1, have prominent conoid tubercles that form distinct posterior flanges (although not as prominent as those seen in chimpanzees) (Fig. 2). Both specimens have a pronounced angular margin continuous with the tubercle medially and separating the inferior from the posterior surfaces, as also seen in *Au. afarensis* specimens A.L. 288-1 (25), A.L. 333x-6/9 (26), A.L. 438-1 (27), and StW 606 (28). Similar but perhaps less-developed angular margins are present in the *Au. africanus* specimens StW 431 and StW 582.

The scapula (Fig. 3) possesses a cranially oriented glenoid fossa (as indicated by its high glenoid-medial angle), a markedly cranially directed spine (reflected in its low spinal-medial angle), and a large attachment area for supraspinatus (relative to the size of the glenoid fossa

and the infraspinous fossa) (tables S3 and S4). Supraspinous to infraspinous fossae proportions are very similar to those of the juvenile *Au. afarensis* specimen DIK-1-1 (3) and are intermediate between those of *Homo* and the African apes (table S4). The glenoid fossa of MH2 is narrow relative to its height, with proportions most similar to orangutans and gorillas (table S4). The vertebral border is convex, the acromion process is long

and curved (as in apes), and the inferior axillary border has a prominent flange at the origin of teres major, indicating hypertrophy of this adductor and medial rotator of the humerus (Fig. 3).

Based on multivariate analyses of size-standardized shape variables, the MH2 scapula is morphologically most similar to scapulae of *Pongo* (29). In one analysis, MH2 also was not significantly different from *Gorilla*, but in no



Fig. 2. Clavicular morphology in *Au. sediba*, *Pan troglodytes*, and *Homo sapiens*. (A) Specimens in anterior view, from top: MH1 right side, MH2 left side, MH2 right side, chimpanzee, and human (comparative specimens from the A. H. Schultz collection). All specimens are oriented such that the acromial ends are in the horizontal plane, showing the inferomedial inclination of the clavicular shafts in *Au. sediba* and *Pan*. Note the enlarged conoid tubercle in MH2 (arrow). The enlarged conoid tubercle of MH1 extends more dorsally than inferiorly. (B) The MH2 clavicle in inferior perspective. The inferomedial aspect of the sternoclavicular joint surface (white arrow) forms a 124° angle with the medial surface of the joint, such that when the clavicle is articulated with the manubrium, the shaft is oriented at an angle of ~120° to the vertical. An elevated margin (black arrow) bounds the articular surface, such that when the clavicular shaft is lowered beyond 115°, contact between the clavicular and sternal articular surfaces is no longer possible. All specimens to same scale.

cases did it cluster with *Homo*, *Pan*, or *Hylobates*. MH2 is most similar to *Pongo* in measures of glenoid and spinal angle (table S3), including measures of glenoid fossa or spine orientation relative to the superoinferior long axis of the scapular body (the glenoid-medial and spinal-medial angles, respectively). The long axis of the scapula is defined by the superior and inferior angles of the body (30) and lies parallel to the vertebral column in humans, providing an indication of the anatomical orientation of the bone (31). Thus, angles based on this axis are likely to be better indicators of glenoid fossa and spinal orientation than are angles based on the more commonly used axillary border. In its axillary-vertebral angle, the MH2 scapula falls closest to

the mean value observed in the *Gorilla* sample (table S3), denoting a scapula that is mediolaterally long relative to its superoinferior breadth, but not quite to the extent seen in humans. MH2 is also similar to *Pongo* and *Gorilla* in having a glenoid fossa that is dorsoventrally narrow relative to its superoinferior height (as reflected by its low glenoid fossa index) (table S4). The shape of the body of the MH2 scapula, as measured by the scapular index, is most similar to that seen in *Homo* and *Pan* (table S4). The relative size of the supraspinous fossa (relative to the size of both the infraspinous fossa and the glenoid fossa) is greater than the mean values seen in *Pongo* and *Homo* but smaller than the means of the African apes and gibbons (table S4).

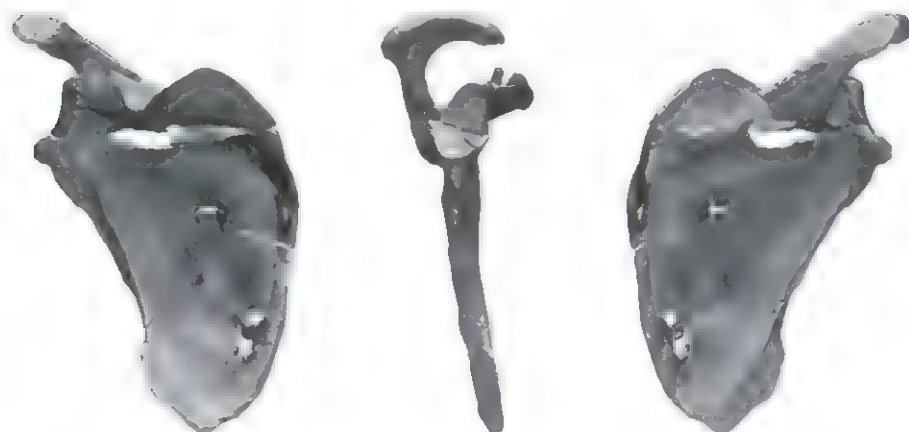
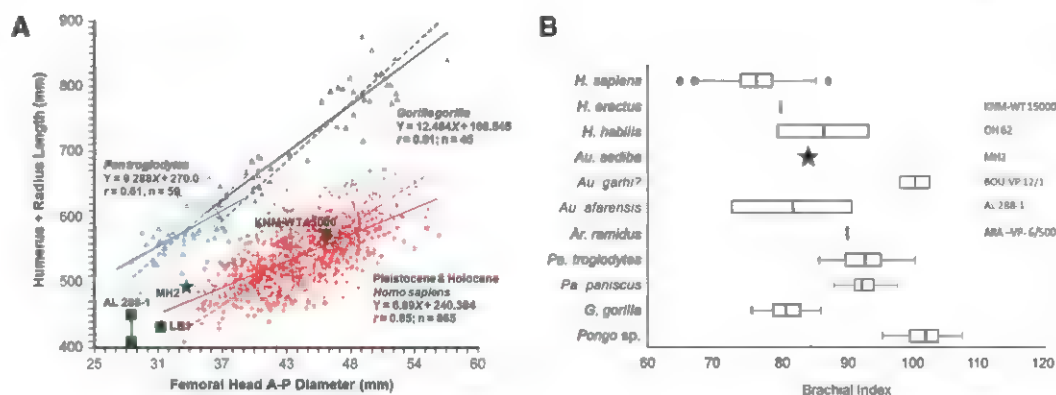


Fig. 3. Three-dimensional rendering of the reconstructed MH2 right scapula in ventral (left), lateral (middle), and dorsal (right) views. In silico reconstruction involved rejoining the superior fragment (preserving much of the supraspinous fossa, the lateral root of the acromion, and the superior half of the glenoid fossa) with the body inferiorly. When possible, aligning separate fragments was performed at the level of individual trabecular struts. The right scapula lacks the acromion process; thus, the left side acromion process was mirrored and aligned to obtain the best fit with overlapping preserved portions of the lateral spine.

Fig. 4. Limb proportions in *Au. sediba*, fossil hominins, and extant hominoids.

(A) Scatter plot of upper limb length (humerus maximum length + radius maximum length) regressed on femoral anteroposterior (A-P) head diameter for Pleistocene/Holocene *Homo*, recent *Pan* and *Gorilla*, and fossil hominins. *Homo sapiens* is indicated by red crosses, *Pan troglodytes* by blue triangles, and *Gorilla gorilla* by black triangles. Fossil hominins are indicated in green, with MH2 represented by a star. Potential range of upper limb length values for A.L. 288-1 are indicated by a solid line between its minimum and maximum values. The point for KNM-WT 15000 is based on the specimen's superoinferior femoral head diameter. The ordinary least squares regression lines for the comparative samples are represented by solid lines, and the reduced major axis (RMA) regression lines for the comparative samples are the dashed lines. *H. sapiens* RMA formula: $Y = 10.643X + 76.078$, $r = 0.65$, $n = 865$; *P. troglodytes* RMA formula: $Y = 15.235X + 71.368$, $r = 0.61$, $n = 59$; *G. gorilla* RMA formula: $Y = 15.353X + 35.459$, $r =$



0.81, $n = 45$. (B) Brachial indices in *Au. sediba* (MH2), extant hominoids, and fossil hominins. Box-and-whiskers plots show the median (vertical line), upper and lower quartiles (box), range (whiskers), and outliers (circles) for each group. For individual specimens, boxes represent the range of estimated values [see (12)]. Redrawn from (12) using data from that study, except for *H. sapiens* ($n = 1093$ samples), *P. troglodytes* ($n = 59$ samples), and *G. gorilla* ($n = 46$ samples) [see (29)] and ARA-VP-6/500 [data from (42)].

the only large-bodied ape to retain a predominantly arboreal lifestyle, and they engage in the greatest amount of forelimb suspension during locomotion of any of the great apes (33). However, orangutans also display the greatest degree of variability in locomotor and positional behaviors of any of the apes, including vertical climbing, quadrumanous climbing and suspension, quadrupedalism, and a small amount of pronograde (33). *Pongo*-like scapular morphology, related to highly variable arboreal positional and locomotor behaviors, has been argued to represent the primitive condition for hominids, with the scapulae of *Pan* and *Gorilla* reflecting derived specializations for greater suspension and quadrupedalism (20). By this model, the *Pongo*-like morphology of australopith scapulae reflects their descent from a generalized arboreal ancestor that was not specialized for arboreal suspension (20, 34). The *Pongo*-like morphology of MH2 is consistent with this hypothesis. However, it is important to note that *Pongo* engages in substantially more forelimb suspensory locomotion than do African hominids (33, 35), making it difficult to argue that the African apes are somehow more specialized for suspensory behavior. In most aspects of scapular shape (tables S3 and S4) MH2 is intermediate between *Pan* and *Homo*, and thus also consistent with the hypothesis that the chimpanzee-human last common ancestor was largely chimpanzee-like in its postcranial morphology (36). By this model, the morphological and possibly behavioral intermediacy of the australopiths between a *Pan*-like arboreal ancestor and fully terrestrial modern humans resulted in scapular morphology homoplasitically similar to that of *Pongo*. Regardless of which of these models is correct, the comparative evidence shows that MH2 possessed a scapula that would have been well suited to the arm positions associated with the kinds of antipronograde postures and forelimb suspensory behaviors commonly employed by highly arboreal orangutans.

The Arm and Forearm

Humeral torsion angles in the Malapa hominins (29) (table S8 and fig. S12) suggest a more posteriorly directed humeral head than that seen in the only other australopith (A.L. 288-1) for which this morphology can be determined [although estimated torsion in partial proximal humeri attributed to australopiths suggest even more medially directed heads than A.L. 288-1 (37)]. MH1 and MH2 thus support the conclusion that the high torsion angles seen in humans and African apes evolved in parallel (37, 38). The low degree of torsion in the Malapa humeri suggests that the scapula occupied a more lateral position on the mediolaterally narrow, ape-like upper thorax (39) [otherwise the elbow would have a lateral set, which among extant apes is seen only in gibbons as an adaptation to brachiation (38)]. The inference of a laterally positioned scapula is also supported by the absolutely and relatively short clavicle of MH2 (table S1) (40). Other aspects

of humeral size and shape fall within the range of variation of other australopiths (tables S9 and S10). Both MH1 and MH2 have humeri with elevated and rugose (MH1) to moderately rugose (MH2) deltopectoral crests [as seen in other australopiths and humans (34)].

The morphology of *Au. sediba*'s elbow also falls comfortably within the range of variation of *Au. afarensis* and *Au. africanus* in most aspects of size and shape (tables S9 to S12). The Malapa hominins share with other australopiths and African apes a strongly projecting humeral medial epicondyle and a pronounced humeral lateral epicondyle with an elongated and distinct brachioradialis crest. They also share with other australopiths a relatively large insertion for biceps brachii on the radius (table S11), enhanced leverage for triceps brachii on the ulna, and an anteriorly oriented ulnar trochlear notch (table S12). Although these and other features (7) indicate retention of the primitive condition of enhanced brachial and antebrachial musculature, the forelimb of MH2 exhibits relatively poor mechanical advantage for the elbow flexors biceps brachii and brachialis compared with other australopiths (tables S11 and S12). The trochlear surfaces of both the MH1 and MH2 ulnae exhibit keeling greater than that seen in humans. The ulnar shaft of MH2 is straight (like a human) in lateral view, whereas her radius is mildly curved in anterior perspective. The distal radii of both MH1 and MH2 are like those of other australopiths in having larger lunate than scaphoid articular surfaces and in possessing weakly developed but distinct dorsal ridges on the radiocarpal articular margin (41).

Limb Proportions

MH2 is the only australopith with complete preservation of the long bones of the upper limb. Early hominin specimens preserving even relatively complete long bones are rare; thus, forelimb proportions tend to involve considerable estimation for most taxa, and their ranges of variation and sample central tendencies are incompletely known. Still, some tentative conclusions can be reached. Humeral length relative to femoral head diameter in *Au. sediba* (7.86 to 8.15) is intermediate between that of *Au. afarensis* (9.20) and early *H. erectus* (6.93 to 7.38) (7). When humeral plus radial length is plotted against femoral head diameter (Fig. 4A), MH2 can be seen to have an arm that is long for her body size (as measured by femoral head diameter) relative to most humans but still within the 95% confidence limits of the human sample. MH2's brachial index ($100 \times \text{radial/humeral length}$) of 84 falls within the estimates for A.L. 288-1 (*Au. afarensis*) and OH 62 [attributed to *H. habilis*, but see (7)] and above that of the Nariokotome *H. erectus* specimen (Fig. 4B). In a regression of radial on humeral length, MH2 falls above the 95% confidence limits about the human sample but within that of the chimpanzee sample (29) (fig. S13). Although it is important to note that

some modern humans have brachial indices as or more extreme than that observed in MH2, one would have less than a 1% chance of drawing such an individual at random from a sample of modern humans. The high brachial index observed in the *Ardipithecus ramidus* specimen ARA-VP-6/500 has been argued to represent the primitive condition for hominins (42), and the high estimated value for Lucy [a value of 92 being the preferred estimate of (42)] has been interpreted as a retention of primitive arm proportions in *Au. afarensis*. If this is the case, the lower value seen in MH2 would then represent another derived, *Homo*-like feature in *Au. sediba* and, importantly, one not observed in OH 62. Nevertheless, given the great uncertainty involved in the estimation of the brachial index in other australopiths and OH 62, there is at present little basis for inferring in *Au. sediba* a reduction in relative forearm length from the primitive condition. The taxonomically unassigned [but possibly *Au. garhi* (15)] BOU-VP-12/1 specimen has an estimated brachial index of 97.9 to 102.2 (15), and in bivariate space it straddles the upper 95% confidence limits about the *Pan* sample (fig. S13). Given the positions of the other fossil hominins in bivariate space, this extreme result (relative elongation of the forearm greater than that of most chimpanzees) is highly improbable. It is therefore likely that the humeral length of this specimen has been underestimated—and, thus, the inference of human-like humeral/femoral proportions in this 2.5-million-year-old fossil (15) is unsupported.

Forelimb Function and Locomotion

Au. sediba shares with other australopiths forelimb features that have been interpreted as indicative of an arboreal habitus (43, 44). Both relatively high shoulders and pronounced clavicular conoid tubercles have been suggested to be adaptations for enhanced elevation of the clavicle and arm in climbing and suspension (24). Likewise, an upturned scapular glenoid fossa is thought to reflect habitual use of the arms in elevated positions (43). The high spinal angle seen in *Au. sediba* increases the mechanical advantage of the serratus anterior in upward rotation of the scapula, as well as increasing the horizontal component of the force vector of the upper part of the trapezius (the component that contributes to the rotary force couple with the serratus anterior) (45), allowing for more forceful rotation of the scapula when moving the trunk on a fixed arm during suspensory behaviors. The arm is moderately long relative to body size, and the brachial index of *Au. sediba* is high, reminiscent of the condition in apes for whom arboreal forelimb suspension remains a substantial portion of their behavioral repertoire. Muscle attachment surface areas and entheses rugosity from the shoulder to the hand in the Malapa hominins indicate moderate hypertrophy (that is, greater than usually seen in humans but less than commonly seen in the large-bodied apes)

of the brachial and antebrachial musculature, including supraspinatus, teres major, brachioradialis, flexor carpi ulnaris, and the other extrinsic wrist and digital flexors (7, 23). Two features that have been argued to be developmentally plastic traits associated with climbing and suspension in the apes (46, 47) can be observed in *Au. sediba*: The ulnar trochlear surface is moderately keeled, and the manual phalanges are moderately curved (23). Although it could be argued that many of these features reflect functionally irrelevant retentions of primitive traits from a more arboreal ancestor, the presence of developmentally plastic features indicative of climbing and suspension during ontogeny supports the inference of the retention of some degree of arboreal behavior in the locomotor repertoire of *Au. sediba*. In the aggregate, the upper limb of the Malapa hominins was well adapted for arboreal locomotion.

The growing fossil record of australopithecids and early *Homo* shoulder and forelimb remains (3, 4, 6, 27, 48, 49) shows that the emergence of the *Homo* body plan entailed a reorganization of the pectoral girdle, involving relocation of the scapula from high and dorsal to lower and more lateral on the thorax, with a concomitant shift from an obliquely to horizontally oriented clavicle (37). This change was accompanied by a downward rotation of the scapular glenoid fossa (less cranial to more lateral) and changes in the angular relationships between the scapular spine, glenoid fossa, and body from a *Pongo*-like to a human-like morphology (3, 6, 37). This reorganization of the shoulder, first evident in *H. erectus*, was accomplished in the context of relative stasis in clavicular length (proportional to body size) and a moderate decrease in humeral torsion angle (37). If the Malapa hominins represent a stem species of the *Homo* clade (7, 22), they show that relocation of the scapula to the lateral thorax preceded its downward shift and the concomitant reorganization of scapular architecture. Given the evidence for the retention of some climbing abilities in *Au. sediba*, this suggests that downward relocation of the hominin scapula only occurred later with a full-time commitment to terrestrial environments. The establishment of a shoulder configuration intermediate between that of australopithecids and modern humans, as seen in early *H. erectus* (4, 37), likely signals the initial transition to upper limb function away from locomotion and predominantly toward manipulation and prehension.

References and Notes

- R. J. Clarke, First ever discovery of a well-preserved skull and associated skeleton of *Australopithecus*. *S. Afr. J. Sci.* **94**, 460 (1998).
- M. Toussaint, G. A. Macho, P. V. Tobias, T. C. Partridge, A. R. Hughes, The third partial skeleton of a late Pliocene hominin (StW 431) from Sterkfontein, South Africa. *S. Afr. J. Sci.* **99**, 215 (2003).
- Z. Alemseged et al., A juvenile early hominin skeleton from Dikika, Ethiopia. *Nature* **443**, 296 (2006). doi: 10.1038/nature05047; pmid: 16988704
- D. Lordkipanidze et al., Postcranial evidence from early *Homo* from Dmanisi, Georgia. *Nature* **449**, 305 (2007). doi: 10.1038/nature06134; pmid: 17882214
- B. Richmond et al., in *Paleoanthropology Society Meetings* (PaleoAnthropology, Chicago, 2009), vol. 2009, abstract A31.
- Y. Haile-Selassie et al., An early *Australopithecus afarensis* postcranium from Woranso-Mille, Ethiopia. *Proc. Natl. Acad. Sci. U.S.A.* **107**, 12121 (2010). doi: 10.1073/pnas.1004527107; pmid: 20566837
- L. R. Berger et al., *Australopithecus sediba*. A new species of *Homo*-like australopithecine from South Africa. *Science* **328**, 195 (2010). doi: 10.1126/science.1184944; pmid: 20378811
- H. M. McHenry, L. R. Berger, Body proportions of *Australopithecus afarensis* and *A. africanus* and the origin of the genus *Homo*. *J. Hum. Evol.* **35**, 1 (1998). doi: 10.1006/jhev.1997.0197; pmid: 9680464
- D. J. Green, A. D. Gordon, B. G. Richmond, Limb-size proportions in *Australopithecus afarensis* and *Australopithecus africanus*. *J. Hum. Evol.* **52**, 187 (2007). doi: 10.1016/j.jhev.2006.09.001; pmid: 17049965
- D. C. Johanson et al., New partial skeleton of *Homo habilis* from Olduvai Gorge, Tanzania. *Nature* **327**, 205 (1987). doi: 10.1038/327205a0; pmid: 3106831
- R. E. Leakey, A. Walker, C. V. Ward, H. M. Gausz, A partial skeleton of a gracile hominid from the Upper Burgi Member of the Koobi Fora formation, East Lake Turkana, Kenya, in *Hominidae: Proceedings of the 2nd International Congress of Human Paleontology*, G. Giacobini, Ed. (Jaca Book, Turin, 1989), pp. 167–173.
- B. G. Richmond, L. C. Aiello, B. A. Wood, Early hominid limb proportions. *J. Hum. Evol.* **43**, 529 (2002). pmid: 12393007
- P. L. Reno et al., Plio-Pleistocene hominid limb proportions. *Curr. Anthropol.* **46**, 575 (2005). doi: 10.1086/431528
- M. Haeussler, H. M. McHenry, Body proportions of *Homo habilis* reviewed. *J. Hum. Evol.* **46**, 433 (2004). doi: 10.1016/j.jhev.2004.01.004; pmid: 15066379
- B. Asfaw et al., *Australopithecus garhi*: A new species of early hominid from Ethiopia. *Science* **284**, 629 (1999). doi: 10.1126/science.284.5414.629; pmid: 10213683
- N. M. Young, G. P. Wagner, B. Hailgrüßson, Development and the evolvability of human limbs. *Proc. Natl. Acad. Sci. U.S.A.* **107**, 3400 (2010). doi: 10.1073/pnas.0911856107; pmid: 20133636
- C. Ruff, A. C. Walker, Body size and shape, in *The Nariokotome Skeleton*, A. C. Walker, R. E. Leakey, Eds. (Harvard Univ. Press, Cambridge, MA, 1993), pp. 234–265.
- H. Pontzer et al., Locomotor anatomy and biomechanics of the Dmanisi hominins. *J. Hum. Evol.* **58**, 492 (2010). doi: 10.1016/j.jhev.2010.03.006; pmid: 20447679
- D. J. Green, Z. Alemseged, *Australopithecus afarensis* scapular ontogeny, function, and the role of climbing in human evolution. *Science* **338**, 514 (2012). doi: 10.1126/science.1227123; pmid: 23112331
- S. M. Melillo, thesis, Stanford University, Stanford, CA (2011).
- P. H. G. M. Dirks et al., Geological setting and age of *Australopithecus sediba* from southern Africa. *Science* **328**, 205 (2010). doi: 10.1126/science.1184950; pmid: 20378812
- R. Pickering et al., *Australopithecus sediba* at 1.977 Ma and implications for the origins of the genus *Homo*. *Science* **333**, 1421 (2011). doi: 10.1126/science.1203697; pmid: 21903808
- T. L. Kivell, J. M. Kibii, S. E. Churchill, P. Schmid, L. R. Berger, *Australopithecus sediba* hand demonstrates mosaic evolution of locomotor and manipulative abilities. *Science* **333**, 1411 (2011). doi: 10.1126/science.1202625; pmid: 21903806
- J. C. Ohman, The first rib of hominoids. *Am. J. Phys. Anthropol.* **70**, 209 (1986). doi: 10.1002/ajpa.1330700208; pmid: 3090892
- D. C. Johanson et al., Morphology of the Pliocene partial hominid skeleton (A.L. 288-1) from the Hadar Formation, Ethiopia. *Am. J. Phys. Anthropol.* **57**, 403 (1982). doi: 10.1002/ajpa.1330570403
- C. O. Lovejoy, D. C. Johanson, Y. Coppens, Hominid upper limb bones recovered from the Hadar Formation: 1974–1977 collections. *Am. J. Phys. Anthropol.* **57**, 637 (1982). doi: 10.1002/ajpa.1330570409
- M. S. M. Drapeau, C. V. Ward, W. H. Kimbel, D. C. Johanson, Y. Rak, Associated cranial and forelimb remains attributed to *Australopithecus afarensis* from Hadar, Ethiopia. *J. Hum. Evol.* **48**, 593 (2005). doi: 10.1016/j.jhev.2005.02.005; pmid: 15927662
- T. C. Partridge, D. E. Granger, M. W. Caffee, R. J. Clarke, Lower Pliocene hominid remains from Sterkfontein. *Science* **300**, 607 (2003). doi: 10.1126/science.1081651; pmid: 12714736
- Methods and background are available as supplementary materials on Science Online
- W. W. G. Graves, The types of scapulae: A comparative study of some correlated characters in human scapulae. *Am. J. Phys. Anthropol.* **4**, 111 (1921). doi: 10.1002/ajpa.1330040202
- Haile-Selassie et al. (6), citing Graves (30), argue that the scapular axis is too variable in *Homo* to be of use in evaluating scapular architectural differences between taxa. The study by Graves (30), however, concerned variation in the form of the vertebral border and says nothing about variation in the position of the superior and inferior angles (that is, the scapular axis). Radiographic analysis of scapular position in humans at rest shows that the two landmarks that define the axis lie equidistant to the spinous processes of their adjacent vertebrae (50). Furthermore, in our samples, although it is the case that the glenoid-medial angle tends to be more variable than other angles, the spinal-medial angle is not (table S3). This suggests that variance in the glenoid-medial angle is reflecting variation in the orientation of the glenoid fossa more so than variation in the anatomical reference axis. These observations suggest that the long axis of the scapula can be used as a reliable indicator of the orientation of the bone with the arm at rest.
- N. M. Young, A comparison of the ontogeny of shape variation in the anthropoid scapula: Functional and phylogenetic signal. *Am. J. Phys. Anthropol.* **136**, 247 (2008). doi: 10.1002/ajpa.20799; pmid: 18324623
- S. K. S. Thorpe, R. H. Crompton, Orangutan positional behavior and the nature of arboreal locomotion in Hominoidea. *Am. J. Phys. Anthropol.* **131**, 384 (2006). doi: 10.1002/ajpa.20422; pmid: 16617429
- C. O. Lovejoy, S. W. Simpson, T. D. White, B. Asfaw, G. Suwa, Careful climbing in the Miocene: The forelimbs of *Ardipithecus ramidus* and humans are primitive. *Science* **326**, 70e1 (2009). doi: 10.1126/science.1175827; pmid: 19810196
- K. D. Hunt, Mechanical implications of chimpanzee positional behavior. *Am. J. Phys. Anthropol.* **86**, 521 (1991). doi: 10.1002/ajpa.1330860408; pmid: 1776659
- B. Wood, T. Harrison, The evolutionary context of the first hominins. *Nature* **470**, 347 (2011). doi: 10.1038/nature09709; pmid: 21331035
- S. G. Larson, Evolutionary transformation of the hominid shoulder. *Evol. Anthropol.* **16**, 172 (2007). doi: 10.1002/evan.20149
- S. G. Larson, Estimating humeral torsion on incomplete fossil anthropoid humeri. *J. Hum. Evol.* **31**, 239 (1996). doi: 10.1006/jhev.1996.0059
- P. Schmid et al., Mosaic morphology in the thorax of *Australopithecus sediba*. *Science* **340**, 1234598 (2013). doi: 10.1126/science.1234598
- J. L. Voisin, L'architecture de l'épaule au sein de genre *Homo*: Nouvelles interprétations. *Anthropologie* **114**, 354 (2010). doi: 10.1016/j.anthro.2010.05.005
- W. H. Kimbel, L. K. Delezenne, "Lucy" redux. A review of research on *Australopithecus afarensis*. *Am. J. Phys. Anthropol.* **140**, (suppl. 49), 2 (2009). doi: 10.1002/ajpa.21183; pmid: 19890859
- C. O. Lovejoy, G. Suwa, S. W. Simpson, J. H. Matternes, T. D. White, The great divides: *Ardipithecus ramidus* reveals the postcrania of our last common ancestors with African apes. *Science* **326**, 100 (2009). doi: 10.1126/science.1175833; pmid: 19810199
- J. T. J. Stern Jr., R. L. Susman, The locomotor anatomy of *Australopithecus afarensis*. *Am. J. Phys. Anthropol.* **60**, 279 (1983). doi: 10.1002/ajpa.1330600302; pmid: 6405621

44. J. T. Stern, Climbing to the top: A personal memoir of *Australopithecus afarensis*. *Evol. Anthropol.* **9**, 113 (2000). doi: 10.1002/1520-6505(2000)9:3<113::AID-EVAN2>3.0.CO;2 W
45. E. H. Ashton, C. E. Oxnard, Functional adaptations in the primate shoulder girdle. *J. Zool.* **142**, 49 (1964).
46. M. S. M. Drapeau, Articular morphology of the proximal ulna in extant and fossil hominoids and hominins. *J. Hum. Evol.* **55**, 86 (2008). doi: 10.1016/j.jhevol.2008.01.005; pmid: 18472143
47. B. G. Richmond, Biomechanics of phalangeal curvature. *J. Hum. Evol.* **53**, 678 (2007). doi: 10.1016/j.jhevol.2007.05.011; pmid: 17761213
48. A. C. Walker, R. E. Leakey, The postcranial bones, in *The Nankotome Skeleton*, A. C. Walker, R. E. Leakey, Eds. (Harvard Univ. Press, Cambridge, MA, 1993), pp. 95–160.
49. J. M. Carretero, C. Lorenzo, J. L. Arsuaga, Axial and appendicular skeleton of *Homo antecessor*. *J. Hum. Evol.* **37**, 459 (1999). doi: 10.1006/jhevol.1999.0342; pmid: 10496997
50. D. C. Sobush *et al.*, The lennie test for measuring scapular position in healthy young adult females: A reliability and validity study. *J. Orthop. Sports Phys. Ther.* **23**, 39 (1996). pmid: 8749749

Acknowledgments: We thank the South African Heritage Resource agency for the permits to work at the Malapa site; the Nash family for granting access to the Malapa site and continued support of research on their reserve; the Gauteng Provincial Government, the South African Department of

Science and Technology, the African Origins Platform (AOP), the South African National Research Foundation (NRF), the Evolutionary Studies Institute (University of the Witwatersrand), the University of the Witwatersrand's Vice Chancellor's Discretionary Fund, the National Geographic Society, the Palaeontological Scientific Trust, the Andrew W. Mellon Foundation, the Ford Foundation, the U.S. Diplomatic Mission to South Africa, the French Embassy of South Africa, the Claude Leon Foundation, the Strategic Planning and Resource Allocation Committee of the University of the Witwatersrand, the A.H. Schultz Foundation, Duke University, the Ray A. Rothrock '77 Fellowship and International Research Travel Assistance Grant of Texas A&M University, and the Oppenheimer and Ackerman families and Sir Richard Branson for funding; the University of the Witwatersrand's Schools of Geosciences and Anatomical Sciences and the Bernard Price Institute for Palaeontology for support and facilities; Gauteng Department of Agriculture, Conservation and Environment and the Cradle of Humankind Management Authority; and our respective universities for ongoing support. We thank the Virtual Image Processing Laboratory and the Microfocus X-ray Computed Tomography Facility of the Palaeosciences Centre at the University of the Witwatersrand; for funding these facilities, we thank the University of the Witwatersrand Office of Research and the NRF SRIG (Strategic Research Infrastructure Grant) and AOP funding programs. For access to comparative specimens, we thank E. Mbua, P. Kiura, V. Iminjili, and the National Museums of Kenya; B. Billings, B. Zipfel, and the School of Anatomical Sciences at the University of the Witwatersrand; S. Potze and L.C. Kgasi at the Ditsong Museum;

E. Westwig at the American Museum of Natural History; L. Gordon at the National Museum of Natural History; and M. Ponce de León and C. Zollikofer at the Anthropological Institute and Museum. For technical and material support we thank, Duke University, the University of Zurich 2009 and 2010 Field Schools, A.B. Taylor, C.E. Terhune, and C.E. Wall. Numerous individuals have been involved in the ongoing preparation and excavation of these fossils, including C. Dube, C. Kemp, M. Kgasi, M. Languza, J. Malaza, G. Mokoma, P. Mukanela, T. Nemvundi, M. Ngcamphalala, S. Jirah, S. Tshabalala, and C. Yates. Other individuals who have given major support to this project include B. de Klerk, W. Lawrence, C. Steininger, B. Kuhn, L. Pollaro, B. Zipfel, J. Kretzen, D. Conforti, J. McCaffery, C. Dlamini, H. Visser, R. McCrae-Samuel, B. Nkosi, B. Louw, L. Backwell, F. Thackeray, and M. Peltier. J. Smilg facilitated computed tomography scanning of the specimens. The *Au. sediba* specimens are archived at the Evolutionary Studies Institute at the University of the Witwatersrand. All data used in this study are available upon request, including access to the original specimens, by bona fide scientists.

Supplementary Materials

www.sciencemag.org/content/340/6129/1233477/suppl/DC1

Methods and Results
Figs S1 to S13
Tables S1 to S12
References (51–67)

20 November 2012; accepted 12 March 2013
10.1126/science.1233477

Mosaic Morphology in the Thorax of *Australopithecus sediba*

Peter Schmid,^{1,2*} Steven E. Churchill,^{3,2} Shahed Nalla,^{4,2} Eveline Weissen,¹ Kristian J. Carlson,^{2,5} Darryl J. de Ruiter,^{6,2} Lee R. Berger²

The shape of the thorax of early hominins has been a point of contention for more than 30 years. Owing to the generally fragmentary nature of fossil hominin ribs, few specimens have been recovered that have rib remains complete enough to allow accurate reassembly of thoracic shape, thus leaving open the question of when the cylindrical-shaped chest of humans and their immediate ancestors evolved. The ribs of *Australopithecus sediba* exhibit a mediolaterally narrow, ape-like upper thoracic shape, which is unlike the broad upper thorax of *Homo* that has been related to the locomotor pattern of endurance walking and running. The lower thorax, however, appears less laterally flared than that of apes and more closely approximates the morphology found in humans.

Since the early 1980s, the question of the shape of the thorax of early hominins has been debated (1–6). In apes, the morphology of the thorax is integral to the function of the upper limb in arboreal locomotion and positional behaviors (7, 8), and thus reconstruction of thoracic shape in early hominins is central to resolving questions about the degree of arboreality in members of the human lineage before the genus *Homo* (9). The study of the evolution of human thoracic form and function has, however, been impeded by the incompleteness of the fossil rib record. It has been difficult to reconstruct the overall shape of this anatomical region owing to the large number of fragile bones of which it is composed and the complex interactions of rib size, curvature, torsion, and declination that combine to determine the shape of the rib cage (thus limiting the utility of rib fragments). The fragility of costal elements has led to a dearth of both isolated thoracic remains and the more informative remains associated with partial skeletons of known species. Even the most complete preserved early hominin rib cages, such as those of the two *Australopithecus afarensis* partial skeletons A.L. 288 (Lucy) (10) and KSD-VP-1/1 (Woranso-Mille) (6) or the *Au. africanus* partial skeleton Sts 14 (11), preserve only fragmentary elements. Nonetheless these, along with the few fragmentary remains associated with other partial skeletons, have stimulated debate over thoracic

shape and the evolution of human-like bipedalism and respiratory physiology (1–6).

Both apes and humans have rib cages that are transversely broad and dorsoventrally flattened relative to other catarrhine primates (12). The great apes also have a rib cage that is conically shaped in anterior view, forming a mediolaterally narrow cupola superiorly and progressively flaring laterally from superior to inferior, such that at the

level of the 11th and 12th ribs, the mediolateral width of the rib cage matches that of the transversely broad iliac blades (12, 13). This configuration has been linked to arboreal locomotion, in that it effectively positions the ribs so as to best resist large bending moments generated either by the forceful contraction of thoracoscapular and thoracohumeral muscles during support and acceleration of body mass with the upper limbs during climbing and suspension (14) or by gravity operating on body mass during suspension (15). Human thoraces are more barrel-shaped: The upper rib cage is mediolaterally broad, such that relatively little additional lateral flaring occurs moving inferiorly. Furthermore, the lower ribs in the series have greater curvatures than the homologous ribs in apes (16), resulting in a rib cage overall that is more cylindrical (barrel-shaped), rather than the funnel shape characteristic of apes.

If one assumes that the primitive condition for hominins was an ape-like, conical thorax [but see (4, 5)], the change to the derived, *Homo*-like condition should serve as a potential critical marker of the transition from a locomotor repertoire involving both terrestrial bipedalism and arboreal climbing/suspension (1, 3, 15) to one emphasizing endurance bipedal walking or running (in which wider shoulders increase the effectiveness of arm-swinging as a means of countering



Fig. 1. Rib remains of MH1 and MH2 in cranial view (see tables S1 and S2). Not pictured: UW88-193 (shaft fragment). UW88-192 derives from a different individual (MH2) than UW88-74/165 (MH1) and is only illustrated with those fragments to show its relative anatomical position.

¹Anthropological Institute and Museum, University of Zurich, Winterthurerstrasse 190, CH-8057 Zurich, Switzerland. ²Evolutionary Studies Institute, University of the Witwatersrand, Private Bag 3, Wits 2050, South Africa. ³Department of Evolutionary Anthropology, Box 90383, Duke University, Durham, NC 27708, USA. ⁴Department of Human Anatomy and Physiology, Faculty of Health Sciences, University of Johannesburg, Johannesburg, South Africa. ⁵Department of Anthropology, Indiana University, Bloomington, IN 47405, USA. ⁶Department of Anthropology, Texas A&M University, College Station, TX 77843, USA.

*Corresponding author. E-mail: smidi@aim.uzh.ch

rotational moments in the trunk (14, 17). Thus, as the probable precursors of the genus *Homo*, great importance has been attached to the thoracic remains of the australopiths, about which two interpretations have emerged. One view is that australopith remains are largely human in form (2, 5, 6), and thus indicative of essentially human-like bipedalism, reflecting an ability to both run and walk long distances (18). An alternative view is that their thoracic shape was essentially

ape-like, and thus they were not only still habitual arborealists, but were incapable of human-like running and long-distance walking (3).

More recently, the thorax of the proposed stem species of all hominins, *Ardipithecus ramidus*, has been argued to have been largely derived toward the human condition (5). This argument is predicated on inferences about the locomotor behavior of this species and the supposition that a conically shaped thorax is convergently de-

rived in the extant large-bodied apes (4). This would imply that the shape of the thorax in stem hominins was broadly like that of humans, suggesting a shift to a fundamentally human-shaped thorax with the earliest establishment of terrestrial bipedalism in our lineage. However, in *Ar. Ramidus*, the remains of the trunk skeleton are limited to a partial first rib, several associated crushed ribs, the neural arches of two thoracic vertebrae, and a fragmentary and distorted pelvis without a sacrum (5). The poor representation of the thorax in *Ar. ramidus* highlights the paucity of thoracic remains that plague early hominin research and urges caution in uncritically accepting conclusions about thoracic form in this species.

Since mid-2008, the Malapa site in South Africa has yielded a large number of hominin fossil remains, most of which are associated with two partial skeletons, namely a juvenile probable male (Malapa Hominin 1: MH1) and an adult probable female (MH2). Both specimens have been ascribed to a new species of early hominin, *Au. sediba* (19). Postcranial remains of both individuals are well preserved, and aspects of their skeletons have been recently described (20–22). Both individuals preserve a number of thoracic remains that were found in near articulation and that elucidate the form of the thorax in *Au. sediba*. The preserved costal elements (Fig. 1: listed in tables S1 and S2) range in completeness from undamaged or largely complete ribs of both individuals to unidentifiable fragments of the shafts of lower ribs. In both skeletons, the upper thoracic region is better preserved than its lower parts. MH1 and MH2 preserve complete first ribs, and MH2 retains proximal portions of the second, third, and fifth ribs, along with a nearly complete fourth rib (23). MH1 preserves four partial ribs from the lower part of the vertebrostermal series, including the proximal portions of what likely represent the right and left 6th and left 7th ribs (23), and shaft fragments that likely derive from the left 7th, 8th, or 9th rib. The constellation of relatively intact and partial ribs provides information about the upper and middle portions of the thorax: The preservation of a shaft fragment from a 9th (or possibly 10th) rib in MH2, along with the well-preserved iliac regions of both individuals (21), enables us to reconstruct at least the general shape of the lower thoracic region.

The Upper Thorax

The overall shape of the upper thorax of *Au. sediba* is clearly more ape-like, being mediolaterally narrow in the region of the first six ribs to form a typical ape-like apex to the cranial portion of the thorax. An ape-like, less acute posterior bending of the upper ribs (producing ribs that flare less laterally, and thus a mediolaterally narrower rib cage) and possibly a less ventrally positioned vertebral column [i.e., less invagination; see (24)] in *Au. sediba* is indicated by its low posterior angle index (Fig. 2A) (23). This conclusion is also supported by the shape index of the second

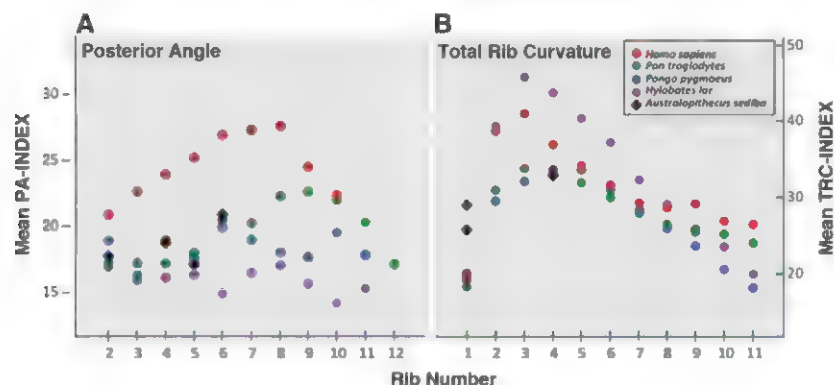


Fig. 2. Rib curvature in *Au. sediba* and fossil and extant hominoids. *H. sapiens* ($26 \leq n \leq 30$), *Pa. troglodytes* ($13 \leq n \leq 16$), *Po. pygmaeus/abelii* ($11 \leq n \leq 12$), *Hy. lar* ($n = 20$), *Au. sediba* ($n = 2$). (A) Posterior angle (PA) index versus rib number. Larger values of this index reflect ribs that are more curved at the posterior angle [see (23)]. (B) Total rib curvature (TRC) index versus rib number. Larger values of this index reflect ribs with shafts that are more curved from the tubercle proximally to the sternal end distally (see 23).

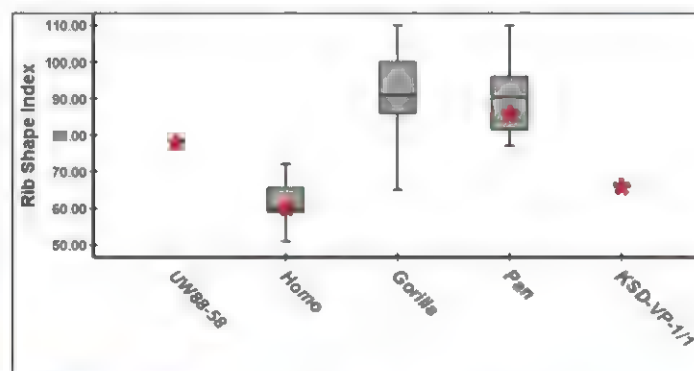


Fig. 3. Rib shape indices [taken following (6)] in the second ribs of *Au. sediba* (UW88-58), *Au. afarensis* (KSD-VP-1/1), and extant hominoids. Box-and-whisker plots show the median, upper and lower quartiles, and ranges of the *Homo sapiens*, *Gorilla gorilla*, and *Pan troglodytes* samples. Red asterisks denote the index values of the exemplars illustrated below the plots, which have all been aligned by their "costal neck axes" (6). Lower left: the *Au. sediba*, *Au. afarensis*, and *Pan* and *Homo* second ribs have been overlain in costal neck axis alignment. The parity in curvature is apparent between UW88-58 (top) and the chimpanzee 2nd rib, and KSD-VP-1/1 with the human 2nd rib.

rib [the curvature index of (6)], which in MH2 is estimated to be 78. This value is higher than and outside of the range of observed values in humans, and within that of gorillas and chimpanzees (Fig. 3). This value is also 12 index units above that of the KSD-VP-1/1n *Au. afarensis* second rib (6).

Between-group differences in thoracic shape are also reflected in indices of rib total curvature (Fig. 2B) (23). In large-bodied apes (*Pan* and *Pongo*), rib curvature reaches its zenith in the upper vertebrosteral ribs, with the costae becoming progressively straighter moving inferiorly to the asternal ribs. However, because of a reduction in the angle between the transverse processes of the thoracic vertebrae and the sagittal plane [angle Σ of (16)] from superior to inferior, these straighter asternal ribs project more laterally, forming a mediolaterally broad lower thorax. The derived thoracic morphology of *H. sapiens* can be seen to result from substantially greater curvature of ribs 2 to 4 (shared homoplastically with the barrel-chested *Hylobates*), which produces a mediolaterally broad upper thorax, combined with greater curvature of the lower ribs 9 to 11 (not shared with *Hylobates*), which redirects the lower ribs anteriorly and produces a relatively mediolaterally narrow lower rib cage (16) (and thus a cylindrically shaped thorax overall as seen in anterior view). As with the posterior angle index, *Au. sediba* has a rib total curvature index at the fourth rib that is below the mean value of *Homo* and most similar to those of *Pan* and *Pongo* (Fig. 2B and fig. S9).

The ape-like, conical thoracic shape of *Au. sediba* is also apparent when the trunk skeleton is rearticulated (Fig. 4). To create a three-dimensional reconstruction, we articulated ribs R1-5 of MH2

and R6-7 of MH1, using MH2's thoracic vertebrae T3-7 and interpolating the morphology of the T1 and T2 from the preserved vertebrae plus that of the T2 of MH1 (25). The shape of the thoracic inlet was obtained by articulating the right first rib and the manubrium (fig. S2) in MH2, allowing an appropriate gap for the costal cartilage. This hemithorax was then mirror-imaged to obtain the upper portion of the complete rib cage. The thoracic inlet shape, as seen from above, appears typically hominoid, being broadly kidney-shaped with the vertebral column positioned ventrally (invaginated) within the thorax, but less so than in modern humans.

The Lower Thorax

In both apes (7, 26) and humans (16), there is correspondence between the shapes of the inferior rib cage and the false pelvis (formed by the iliac blades). Thus, the derived, human-like vertical reorientation and greater curvature of the iliac blades of *Au. sediba* (21) lead us to suggest that its lower thoracic shape could not be like that of an ape. This inference is supported by a fragment of a 9th rib (or possibly 10th), found in association with the MH2 skeleton. This rib is slenderer than the more cranial fragments, a condition very different from that of the inferior ribs of apes (which are the largest and longest in the series). In addition, it appears to show distinct torsion along its body, which is characteristic of the reduced last ribs of humans (but not apes) (Fig. 5).

Thoracic Morphology, Respiration, and Locomotion

The thoracic shape of *Au. sediba* thus appears to be an unusual combination of the primitive con-

dition of an ape-like upper thoracic shape, with a more derived, human-like shape to the lower thorax. Thoracic shape in *Au. sediba* thus may contrast with that of KSD-VP-1/1, which has been attributed to *Au. afarensis* (6), but may not contrast with another specimen of that species, A.L. 288-1 (1, 3). The morphology of the upper thorax and elements of the pectoral girdle (27) suggest that *Au. sediba* had habitually elevated, "shrugged" shoulders like that of a chimpanzee. The shape of the thorax and the positioning of the scapulae are critical in bipedal gait, as they affect the pendular mechanics of the upper limbs in their role as counterbalances to trunk rotation (14, 17). In combination with features found in the foot (22) and lower limb (28), the thoracic shape of *Au. sediba* implies a gait unlike that predicted for any other early hominin species. If interpretations of a derived, *Homo*-like thorax in *Au. afarensis* are correct (2, 6, 10), it calls into question the possibility that *Au. sediba* derives from this species, even via an intermediate taxon such as *Au. africanus*, as it would require a large number of reversals in two forms already practicing a form of terrestrial bipedalism. More critically, if the thoracic region of *Ar. ramidus* is indeed as derived as recently claimed (5), then by implication, *Ardipithecus* makes a poor ancestor for at least the lineage leading to *Au. sediba*.

The morphology seen in the rib cage of *Au. sediba* also contrasts with that of *H. erectus*, based on the KNM-WT 15000 juvenile skeleton (16, 29). Medirolateral expansion of the upper thorax in *H. erectus* (and *H. sapiens*) has been argued to be the necessary consequence of narrowing of the pelvis and lower rib cage relative to body size (16) in early *Homo*. Reduced bi-iliac breadth (relative to body size) in early *Homo* may have been a response to reduction in gut size following from improvement in dietary quality (30), or maintenance of body volume-to-surface area relationships important to thermoregulation in a lineage increasing in stature (31), or was perhaps related to altered energetic or biomechanical demands (17, 32–34) of long-distance bipedalism in the context of expanded ranging behavior (35, 36). Reductions in the size of the lower rib cage may necessitate expansion of the upper thorax to maintain a proper lung volume-to-body mass relationship (37), and if so, the emergence of cylindrical thoraces in early *Homo* may have more to do with relative reduction in pelvic breadth (16) than with upper limb pendular mechanics related to striding bipedalism or long-distance running (14, 17). However, the mosaic morphology seen in the trunk of *Au. sediba*, combining a narrow upper thorax with a relatively narrow pelvis (21) and (presumably) narrow lower thorax, suggests a degree of uncoupling of upper and lower trunk shape in hominin evolution. This argues against a physiological (lung volume) explanation for the *Homo* thoracic bauplan (especially since *Au. sediba* appears to compensate for reduced lower rib cage volume through an

Fig. 4. Two-dimensional reconstruction of the thorax of MH2. Colored areas represent parts preserved in MH2 [scapula represented by a virtual rendering of the original specimen; see (27)]. Gray-scale-illustrated bones are associated with MH1 or are mirror-imaged elements from MH2. Light gray areas represent hypothesized outlines.





Fig. 5. Ninth rib morphology in *Au. sediba*, *Homo*, and *Pan*. Ribs are shown in superior view on the left, inferior view on the right. UW88-60, the right 9th rib of MH2, is toward the center and is illustrated twice in each perspective. Torsion to the superior and inferior margins of the rib (dotted lines) is similar to that seen in the curved and twisted 9th rib of humans (middle in each perspective) and unlike that of a chimpanzee (lateral in each perspective).

anteroposterior, rather than mediolateral, expansion of the upper thorax) (23). In *Au. Sediba*, we see an incipient development of a narrow, *Homo*-like waist (with a relatively functionally long and mobile lumbar vertebral column) (25) with repositioned abdominal oblique muscles that can better resist trunk rotation during walking and running (32). *Au. sediba* also appears to exhibit incipient widening of the iliocostalis (fig. S3), which would improve the mechanical advantage of the muscle for counteracting lateral trunk flexion during bipedal walking (38). However, the narrow upper thorax of *Au. sediba*, combined with a high scapular position (27) and thus probably incomplete decoupling of the head and pectoral girdle, would be expected to constrain arm-swinging during walking or running (17, 32). Furthermore, this morphology in the upper thorax and pectoral girdle would have restricted elevation of the upper part of the rib cage during inspiration, limiting the ability of *Au. sediba* to engage in heavy breathing during fast walking or running (32). A commitment to a fully terrestrial life-style in *H. erectus* may have relaxed the functional constraints operating on early hominin shoulder and upper thoracic morphology, allowing for a reorganization of the thorax and shoulder more conducive to the kinematic and respiratory demands of full striding bipedalism and endurance running. This reorganization established the basic *Homo* thoracic

bauplan (16) seen in all later species of Pleistocene *Homo* (39–41).

References and Notes

- P. Schmid, Eine Rekonstruktion des Skelettes von A.L. 288-1 (Hadar) und deren Konsequenzen [A reconstruction of the skeleton of A.L. 288-1 (Hadar) and its consequences]. *Folia Primatol. (Basel)* **40**, 283 (1983). doi: 10.1159/000156111; pmid: 6414917
- J. C. Ohman, The first rib of hominoids. *Am. J. Phys. Anthropol.* **70**, 209 (1986). doi: 10.1002/ajpa.1330700208; pmid: 3090892
- P. Schmid, The trunk of the australopithecines, in *Origine(s) de la Bipedie chez les Hominides. Cahier de Paleanthropologie*, Y. Coppens, B. Senut, Eds. (Editions du CNRS, Paris, 1991), pp. 225–234.
- C. O. Lovejoy, G. Suwa, S. W. Simpson, J. H. Matternes, T. D. White, The great divides: *Ardipithecus ramidus* reveals the postcrania of our last common ancestors with African apes. *Science* **326**, 100 (2009). doi: 10.1126/science.1175833; pmid: 19810199
- C. O. Lovejoy, G. Suwa, L. Spurlack, B. Asfaw, T. D. White, The pelvis and femur of *Ardipithecus ramidus*: The emergence of upright walking. *Science* **326**, 71 (2009). doi: 10.1126/science.1175831
- Y. Haile-Selassie et al., An early *Australopithecus afarensis* postcranium from Woranso-Mille, Ethiopia. *Proc. Natl. Acad. Sci. U.S.A.* **107**, 12121 (2010). doi: 10.1073/pnas.1004527107; pmid: 20566837
- C. V. Ward, Torso morphology and locomotion in *Proconsul nyanzae*. *Am. J. Phys. Anthropol.* **92**, 291 (1993). doi: 10.1002/ajpa.1330920306; pmid: 8291620
- L. K. Chan, Scapular position in primates. *Folia Primatol. (Basel)* **78**, 19 (2007). doi: 10.1159/000095683; pmid: 17170554
- C. V. Ward, Interpreting the posture and locomotion of *Australopithecus afarensis*: Where do we stand? *Am. J. Phys. Anthropol.* **119** (suppl. 35), 185 (2002). doi: 10.1002/ajpa.10185; pmid: 12653313
- D. C. Johanson et al., Morphology of the Pliocene partial hominid skeleton (A.L. 288-1) from the Hadar Formation, Ethiopia. *Am. J. Phys. Anthropol.* **57**, 403 (1982). doi: 10.1002/ajpa.1330570403
- J. T. Robinson, *Early Hominid Posture and Locomotion* (Univ. of Chicago Press, Chicago, 1972).
- A. H. Schultz, Vertebral column and thorax, in *Primate Biology*, H. Hofer, A. H. Schultz, D. Starck, Eds. (S. Karger, Basel, 1961), vol. 4, pp. 1–66.
- M. Kagaya, N. Ogihara, M. Nakatsukasa, Morphological study of the anthropoid thoracic cage. Scaling of thoracic width and an analysis of rib curvature. *Primates* **49**, 89 (2008). doi: 10.1007/s10329-007-0064-z; pmid: 17902025
- H. Preuschoft, Mechanisms for the acquisition of habitual bipedality: Are there biomechanical reasons for the acquisition of upright bipedal posture? *J. Anat.* **204**, 363 (2004). doi: 10.1111/j.0021-8782.2004.00303.x; pmid: 15198701
- K. D. Hunt, Mechanical implications of chimpanzee positional behavior. *Am. J. Phys. Anthropol.* **86**, 521 (1991). doi: 10.1002/ajpa.1330860408; pmid: 1776659
- L. M. Jellema, B. Latimer, A. Walker, The rib cage, in *The Nariokotome Homo erectus Skeleton*, A. Walker, R. Leakey, Eds. (Harvard Univ. Press, Cambridge, MA, 1993), pp. 294–325.
- D. M. Bramble, D. E. Lieberman, Endurance running and the evolution of *Homo*. *Nature* **432**, 345 (2004). doi: 10.1038/nature03052; pmid: 15549097
- C. O. Lovejoy, Evolution of human walking. *Sci. Am.* **118** (November 1988).
- L. R. Berger et al., *Australopithecus sediba*: A new species of *Homo*-like australopithecine from South Africa. *Science* **328**, 195 (2010). doi: 10.1126/science.1184944; pmid: 20378811
- T. L. Kivell, J. M. Kibii, S. E. Churchill, P. Schmid, L. R. Berger, *Australopithecus sediba* hand demonstrates mosaic evolution of locomotor and manipulative abilities. *Science* **333**, 1411 (2011). doi: 10.1126/science.1202625; pmid: 21903806
- J. M. Kibii et al., A partial pelvis of *Australopithecus sediba*. *Science* **333**, 1407 (2011). doi: 10.1126/science.1202521; pmid: 21903805
- B. Zipfel et al., The foot and ankle of *Australopithecus sediba*. *Science* **333**, 1417 (2011). doi: 10.1126/science.1202703; pmid: 21903807
- Methods and background are available as supplementary materials on Science Online.
- C. O. Lovejoy, The natural history of human gait and posture. Part 1. Spine and pelvis. *Gait Posture* **21**, 95 (2005). pmid: 15536039
- S. A. Williams et al., The vertebral column of *Australopithecus sediba*. *Science* **340**, 1232996 (2013). doi: 10.1126/science.1232996
- W. C. O. Hill, Observations on a giant Sumatran orang. *Am. J. Phys. Anthropol.* **24**, 449 (1939). doi: 10.1002/ajpa.1330240324
- S. E. Churchill et al., The upper limb of *Australopithecus sediba*. *Science* **340**, 1233477 (2013). doi: 10.1126/science.1233477
- J. M. DeSilva et al., The lower limb and mechanics of walking in *Australopithecus sediba*. *Science* **340**, 1232999 (2013). doi: 10.1126/science.1232999
- M. Haessler, R. Schiess, T. Boeni, New vertebral and rib material point to modern bauplan of the Nariokotome *Homo erectus* skeleton. *J. Hum. Evol.* **61**, 575 (2011). doi: 10.1016/j.jhevol.2011.07.004; pmid: 21868059
- L. C. Aiello, P. Wheeler, The expensive-tissue hypothesis. *Curr. Anthropol.* **36**, 199 (1995). doi: 10.1086/204350
- C. Ruff, A. C. Walker, Body size and shape, in *The Nariokotome Skeleton*, A. C. Walker, R. E. Leakey, Eds. (Harvard Univ. Press, Cambridge, MA, 1993), pp. 234–265.
- P. Schmid, Functional interpretation of the Laetoli footprints, in *From Biped to Strider: The Emergence of Modern Human Walking, Running, and Resource*

- Transport., D. J. Meldrum, C. E. Hilton, Eds. (Kluwer Academic/Plenum, New York, 2004), pp. 49–62.
- 33 P. A. Kramer, A. D. Sylvester, Bipedal form and locomotor function: Understanding the effects of size and shape on velocity and energetics. *PaleoAnthropology* **2009**, 238 (2009). doi: 10.4207/PA.2009.ART32
 - 34 C. N. Shaw, J. T. Stock, The influence of body proportions on femoral and tibial midshaft shape in hunter-gatherers. *Am. J. Phys. Anthropol.* **144**, 22 (2011). doi: 10.1002/ajpa.21363; pmid: 20623683
 - 35 S. Cachel, J. W. K. Harris, The paleobiology of *Homo erectus*: Implications for understanding the adaptive zone of this species, in *Aspects of African Archaeology*, G. Pwiti, R. Soper, Eds. (Univ. of Zimbabwe Publications, Harare, 1996), pp. 3–9.
 - 36 H. Pontzer *et al.*, Locomotor anatomy and biomechanics of the Dmanisi hominins. *J. Hum. Evol.* **58**, 492 (2010) doi: 10.1016/j.jhevol.2010.03.006; pmid: 20447679
 - 37 P. Gehr *et al.*, Design of the mammalian respiratory system. V. Scaling morphometric pulmonary diffusing capacity to body mass: Wild and domestic mammals *Respir. Physiol.* **44**, 61 (1981). doi: 10.1016/0034-5687(81)90077-3; pmid: 7232887
 - 38 L. J. Shapiro, W. L. Jungers, Back muscle function during bipedal walking in chimpanzee and gibbon: Implications for the evolution of human locomotion. *Am. J. Phys. Anthropol.* **77**, 201 (1988). doi: 10.1002/ajpa.1330770208; pmid: 3207169
 - 39 A. Gómez-Olivencia *et al.*, The costal skeleton of *Homo antecessor*: Preliminary results. *J. Hum. Evol.* **59**, 620 (2010). doi: 10.1016/j.jhevol.2010.07.023; pmid: 20965547
 - 40 A. Gómez-Olivencia, K. L. Eaves-Johnson, R. G. Franciscus, J. M. Carretero, J. L. Arsuaga, Kebara 2: New insights regarding the most complete Neandertal thorax. *J. Hum. Evol.* **57**, 75 (2009). doi: 10.1016/j.jhevol.2009.02.009; pmid: 19540563
 - 41 R. G. Franciscus, S. E. Churchill, The costal skeleton of Shanidar 3 and a reappraisal of Neandertal thoracic morphology. *J. Hum. Evol.* **42**, 303 (2002). doi: 10.1006/jhev.2001.0528; pmid: 11846533

Acknowledgments: We thank the South African Heritage Resource agency for permits to work at the Malapa site; the Nash family for granting access to the Malapa site and continued support of research on their reserve; the South African Department of Science and Technology and the African Origins Platform (AOP), the South African National Research Foundation, the Institute for Human Evolution, University of the Witwatersrand, the University of the Witwatersrand's Vice Chancellor's Discretionary Fund, the National Geographic Society, the Palaeontological Scientific Trust, the Andrew W. Mellon Foundation, the Ford Foundation, the U.S. Diplomatic Mission to South Africa, the French Embassy of South Africa, the A. H. Schuttz Foundation, Duke University, Ray A. Rothrock '77 Fellowship and IRTAG of Texas A&M University, and the Oppenheimer and Ackerman families and Sir Richard Branson for funding; the University of the Witwatersrand's Schools of Geosciences and Anatomical Sciences and the Bernard Price Institute for Palaeontology for support and facilities; the Gauteng Government, Gauteng Department of Agriculture, Conservation and Environment and the Cradle of Humankind Management Authority; and our respective universities for ongoing support. We thank the Virtual Image Processing Lab and the Microfocus X-ray CT facility of the Palaeosciences Centre at Wits, and for funding these facilities, we thank the University of the Witwatersrand Office of Research and the NRF Strategic

Research Infrastructure Grant and AOP funding programs. For access to comparative specimens, we thank E. Mbua, P. Kiura, V. Iminjili, and the National Museums of Kenya; B. Billings, B. Zipfel, and the School of Anatomical Sciences at the University of the Witwatersrand; S. Potze and L. C. Kgasi at the Ditsong Museum; and M. Ponce de León and C. Zollikofer at the Anthropological Institute and Museum. For technical and material support, we thank Duke University and the University of Zurich 2009 and 2010 Field Schools. Numerous individuals have been involved in the ongoing preparation and excavation of these fossils, including C. Dube, C. Kemp, M. Kgasi, M. Languza, J. Malaza, G. Mokoma, P. Mukanela, T. Nemvuhundi, M. Ngcamphalala, S. Jirah, S. Tshabalala, and C. Yates. Other individuals who have given notable support to this project include B. de Klerk, W. Lawrence, C. Steininger, B. Kuhn, L. Pollarolo, B. Zipfel, J. Kretzen, D. Conforti, J. McCaffery, C. Dlamini, H. Visser, R. McCrae-Samuel, B. Nkosi, B. Louw, L. Backwell, F. Thackeray, and M. Peltier. J. Smilg facilitated computed tomography scanning of the specimens. The *Au. sediba* specimens are archived at the Evolutionary Studies Institute at the University of the Witwatersrand. All data used in this study are available upon request, including access to the original specimens, by bona fide scientists.

Supplementary Materials

www.sciencemag.org/content/340/6129/1234598/suppl/DC1

Methods and Results

Tables S1 to S8

Figs. S1 to S11

References (42–45)

27 December 2012; accepted 12 March 2013
10.1126/science.1234598



AAAS is here – bringing scientific expertise to policy making.

Good science policy is the result of politicians understanding science and scientists understanding policy. Toward this end, AAAS manages the Science & Technology Policy Fellowships program, which embeds scientists and engineers in the federal government for up to two years. From Congress to the State Department, each class of Fellows contributes to the policy-making process while getting hands-on experience at the intersection of science and policy. As a AAAS member your dues support these efforts. If you're not yet a AAAS member, join us. Together we can make a difference.

To learn more, visit aaas.org/plusyou/fellows



The Vertebral Column of *Australopithecus sediba*

Scott A. Williams,^{1,2*} Kelly R. Ostrofsky,³ Nakita Frater,⁴ Steven E. Churchill,^{3,5} Peter Schmid,^{4,5} Lee R. Berger⁵

Two partial vertebral columns of *Australopithecus sediba* grant insight into aspects of early hominin spinal mobility, lumbar curvature, vertebral formula, and transitional vertebra position. *Au. sediba* likely possessed five non-rib-bearing lumbar vertebrae and five sacral elements, the same configuration that occurs modally in modern humans. This finding contrasts with other interpretations of early hominin regional vertebral numbers. Importantly, the transitional vertebra is distinct from and above the last rib-bearing vertebra in *Au. sediba*, resulting in a functionally longer lower back. This configuration, along with a strongly wedged last lumbar vertebra and other indicators of lordotic posture, would have contributed to a highly flexible spine that is derived compared with earlier members of the genus *Australopithecus* and similar to that of the Nariokotome *Homo erectus* skeleton.

The vertebral column plays a central role in posture, locomotion, and overall trunk stability and mobility in vertebrate animals. The hominin vertebral column is distinct in its role in force transmission and weight-bearing in an upright torso balanced over two legs. Owing to these biomechanical demands, the hominin spine has several specialized traits not seen in other mammals, including sigmoid curvature; a pyramidal configuration of articular facets with descent through the lower lumbar column; and a wide, curved sacrum (1–6). Whereas these adaptations are present in modern humans and currently known extinct hominins, other aspects of the modern human vertebral column—for instance, large relative lumbosacral body size—are not present in early hominins such as *Australopithecus afarensis* and *Au. africanus* (2, 3, 7), suggesting that the vertebral column evolved in a mosaic fashion. Therefore, an understanding of which adaptations characterized various fossil species and when the full complement of modern humanlike features evolved is integral to reconstructing postural and locomotor evolution in the hominin lineage.

Recently, two key components of the hominin vertebral column—its numerical composition and degree of lumbar lordosis—have been at the forefront of discussion (4, 6, 8–17). However, adequately preserved vertebral columns that lend themselves to reconstructions of regional vertebral numbers are rare in the hominin fossil record, particularly before 50 thousand years ago, and are best represented by partial skeletons assigned

to *Au. africanus* (Sts 14 and Stw 431) and *Homo erectus* (KNM-WT 15000). Thoracic and lumbar vertebrae have been defined in two ways in the recent literature: (i) based on the presence and absence of ribs (i.e., the last thoracic vertebra is identified as the last rib-bearing vertebra) (8, 15, 16), and (ii) based on the orientation of the articular facets (i.e., the last thoracic vertebra is identified as the transitional vertebra, one that bears thoracic-like, coronally oriented superior articular facets and lumbar-like, curved and laterally directed inferior articular facets) (6, 17, 18). In modern humans and other extant hominoids, the last rib-bearing vertebra and the transitional vertebra generally occur at the same vertebral level (i.e., are the same vertebral element) and, therefore, yield identical numbers of thoracic and lumbar vertebrae under either definition [(15, 18, 19), but see (20)].

In contrast, recent evidence indicates that early fossil hominins may not follow this pattern (9, 15). Newly identified vertebral and rib fragments associated with KNM-WT 15000 show that the transitional vertebra is cranially adjacent to the last rib-bearing vertebra in this specimen (9). This configuration yields contrasting numbers of lumbar vertebrae when different operational definitions are employed: five nonribbed lumbar vertebrae and six vertebrae with sagittally oriented upper articular facets (posttransitional vertebrae). Sts 14 also seems to demonstrate this pattern (8, 15), although the last rib-bearing vertebra in this specimen is somewhat anomalous in that it bears a lumbar-like structure on one side, giving it an intermediate (half-thoracic-, half-lumbar) appearance (8, 10, 15, 21, 22). Dissociated vertebral bodies and neural arches at the thoraco-lumbar border in Stw 431 have led to contrasting reconstructions of this specimen (8, 23), precluding a definitive assessment of the relationship between last rib-bearing and transitional vertebrae. Clearly, additional specimens that preserve this region of the vertebral column are needed. The 1.977 Ma partial skeletons of *Au. sediba* from Malapa,

Gauteng, South Africa (24, 25) preserve 23 presacral vertebrae and a partial, five-element sacrum (Fig. 1). Here, we describe vertebrae assigned to the juvenile male holotype [Malapa Hominin 1 (MH1)] and the adult female paratype (MH2), in addition to the previously published sacrum of MH2 (26).

The MH1 partial vertebral column consists of four cervical, six thoracic, and two lumbar vertebrae; that of MH2 is composed of two cervical, seven thoracic, and two lumbar vertebrae, as well as a sacrum. Specimen numbers and identifications are provided in table S1. Vertebrae belonging to MH1 are readily distinguished from those of MH2 by their lack of apophyseal rings. As with modern human juveniles and the Nariokotome juvenile skeleton (KNM-WT 15000) (1), MH1 possesses short vertebral centra relative to superior-inferior interfacet distance, consistent with its juvenile status (27). In contrast, MH2's centra demonstrate ratios similar to those of adult modern humans.

Cervical Vertebrae

A small cervical body fragment of unknown serial position, two fragmentary mid-cervical vertebrae, and a nearly intact last cervical (C7) vertebra (fig. S1) are associated with MH1. Two mid-level cervical vertebrae are attributed to MH2: a nearly complete C3 or C4 (fig. S2) and a partially complete C5 or C6. These vertebrae do not articulate and, thus, likely represent either C3 and C5 or C4 and C6.

Rib-Bearing Vertebrae

Six rib-bearing vertebrae are attributed to MH1: two upper thoracic, one mid-thoracic, and three lower thoracic vertebrae. An upper thoracic vertebra (fig. S3) demonstrates superior articular facet shape and orientation and relationships among the body, transverse process, and superior articular facets diagnostic of a second thoracic vertebra (T2). The middle thoracic vertebra, which likely represents T7, is complete but pathological: The dorsal surface of the right lamina exhibits a rounded triangular lytic lesion extending ventrally into the lamina (fig. S4). Poor preservation precludes certainty of articulation between the three lower thoracic vertebrae, although spinous and transverse process morphologies and orientations and costal facet configurations suggest the association and possible affiliation of two of these vertebrae as T9 and T10.

There are seven rib-bearing vertebrae associated with MH2 (table S1), including a block of four consecutive upper-to-mid-thoracic vertebrae and a block of three articulating lower rib-bearing vertebrae. The upper block contains variably complete fragments of what likely represent either a T3–T6 or T4–T7 series. The lower block is of particular interest because it preserves in articulation the penultimate and ultimate rib-bearing vertebrae (Fig. 2). The antepenultimate rib-bearing vertebra is also preserved but is displaced slightly

¹Center for the Study of Human Origins, Department of Anthropology, New York University, 25 Waverly Place, New York, NY 10003, USA. ²New York Consortium in Evolutionary Primatology, New York, NY 10024, USA. ³Department of Evolutionary Anthropology, Box 90383, Duke University, Durham, NC 27708, USA. ⁴Anthropological Institute and Museum, University of Zurich, Winterthurerstrasse 190, CH-8057 Zurich, Switzerland. ⁵Evolutionary Studies Institute, University of the Witwatersrand, Private Bag 3, Wits 2050, South Africa.

*Corresponding author. E-mail: sawilliams@nyu.edu

from articulation with the penultimate vertebra. The penultimate vertebra bears a full costal facet at the body-pedicle border and lacks an inferior facet or demi-facet. The zygapophyses bear flat, dorsally (and slightly laterally) directed superior articular facets and curved, laterally directed inferior articular facets; that is, the penultimate rib-bearing vertebra is the transitional vertebra. The ultimate thoracic vertebra bears a full costal facet on the superior aspect of the posterior vertebral body that extends onto the pedicle. Its superior and inferior articular facets are curved and dorso-medially directed; therefore, it is both rib-bearing and posttransitional.

Lumbar Vertebrae

There are two non-rib-bearing lumbar vertebrae associated with MH1, both lacking apophyseal rings. One is a nearly complete first lumbar (L1) vertebra that bears asymmetrical lumbar transverse processes (fig. S5). Another lumbar vertebra is also nearly complete, with a broken left transverse process (fig. S6). Body-proportion differences that can be observed between the two vertebrae suggest that they were separated by an additional element, rendering this likely the third lumbar vertebra (L3). In both vertebrae, but particularly marked on L3, "imbrication pockets" (4) are present on the dorsal neural arch inferior to the superior articular facets in a region known as the pars interarticularis (1, 5). These laminar fossae are nonarticular and thought to be mechanically induced (5). They allow room for the inferior zygapophyses of the cranially adjacent vertebra during extension of the articular facet joints and are indicative of a lordotic spine (1, 4, 5). Body dimensions and vertebral wedging are reported in table S2. These measurements and wedging estimates should be treated with caution due to both the lack of apophyses and the associated juvenile developmental status of MH1. The first lumbar vertebra is ventrally wedged (4.1°), whereas L3 is wedged dorsally (−1.6°).

The penultimate and ultimate lumbar vertebrae belonging to MH2 directly articulate with each other and, in turn, with the sacrum (Fig. 3). The lumbar bodies and neural arches are separated, broken at the pedicle bases. The neural arches were discovered in articulation with each other and with the articular facets of the sacrum; the vertebral bodies were found in articulation with each other (with a fragment of the sacral S1 body) and refit cleanly with their respective neural arches. The MH2 lumbar vertebrae were reconstructed digitally (fig. S7), combining the broken neural arches with the vertebral bodies. The cranial portion of the neural arch of the penultimate lumbar vertebra is missing and preserves only a partial spinous process and inferior zygapophyses; that of the ultimate lumbar is intact, except for the left transverse process and pedicle, the latter of which is broken along with part of the superior zygapophysis. The ultimate lumbar vertebra bears strong imbrication pockets on the pars, again consistent with extension of

the articular facet joints onto the laminae and habitual lordotic posture (fig. S7). Both the penultimate and ultimate lumbar vertebra are wedged dorsally (1.5° and 10.9°, respectively) (Fig. 4, fig. S8, and table S2).

Sacrum

The MH2 sacrum is cranio-caudally complete along the anterior midline (except for the detached portion of the S1 body) from the cra-

nial body of S1 through the caudal body of S5; five distinct sacral bodies are recognizable. The sacrum is incomplete medio-laterally, with the alae broken at its lateral aspects on both sides. The left ala and sacral foramina are missing entirely, whereas the right side retains four large and complete sacral foramina and part of the auricular surface. The preserved right zygapophysis is curved and postero-medially oriented at an angle of ~45°. The posterior surface of the sacrum



Fig. 1. Vertebral specimens for MH1 (left) and MH2 (right). See corresponding specimen identifications in table S1. MH1 cervical vertebrae UW88-71 and UW88-73 are encased in matrix and, thus, not shown here.

is mostly complete on the right side and along the midline, with the maintenance of largely separate S1, S2, S3, and S4 spinous processes. Overall sacral curvature is greater and more humanlike in MH2 than in A.L. 288-1 (fig. S9).

Thoraco-Lumbar Transition and Inferred Numerical Composition

Ever since the description and interpretation of a partial *Au. africanus* skeleton (Sts 14) from Sterkfontein, Gauteng, South Africa more than 40 years ago (21), researchers have grappled with the number of lumbar vertebrae in early hominins (1–3, 8–13, 16, 17, 21–23, 28–32).

Although a full complement of lumbar vertebrae is not associated with either MH1 or MH2, both the thoraco-lumbar transition and the sacrum of MH2 provide indirect evidence that *Au. sediba* possessed five non-rib-bearing lumbar vertebrae. Hypotheses for six lumbar vertebrae in early hominins due to an interspecific homeotic shift at the lumbo-sacral border have been proposed on the basis of recent interpretations of four-element sacra in A.L. 288-1 and KNM-WT 15000 (10, 13, 33). However, both fossil specimens are damaged and preclude certainty in this assessment (22). The presence of five sacral elements in MH2 challenges the hypothesis of a six-four

configuration (6L:4S) due to homeotic change and, rather, suggests a five-five configuration (5L:5S), which is consistent with the majority of modern humans. Although this does not entirely rule out the possibility of six lumbar vertebrae in combination with a five-element sacrum (6L:5S), this configuration occurs at a very low frequency in modern humans (10, 34).

Additionally, the dissociation between the transitional and last rib-bearing vertebrae in MH2 provides further support for the presence of five non-rib-bearing lumbar vertebrae in this specimen. In other early hominins, the thoraco-lumbar transition is either anomalous in appearance (Sts 14, which includes what superficially resembles a half-thoracic, half-lumbar vertebra) (8, 15, 21, 22) or damaged (Stw 431 and KNM-WT 15000); reconstructions of the latter differ and result in divergent numbers of lumbar vertebrae (1, 3, 8, 9, 23, 28, 29). In MH2, if six instead of five non-rib-bearing lumbar vertebrae were present, seven vertebrae with curved, sagittally oriented articular facets would follow the transitional vertebra, a configuration that is not observed in other fossil hominins or modern humans [(9, 15, 19), but see (20)]. Rather, cranial placement of the transitional vertebra relative to the last rib-bearing vertebra suggests that the MH2 vertebral column consisted of five non-rib-bearing lumbar vertebrae and six posttransitional vertebrae. In fact, recent evidence and interpretations suggest that other early hominins demonstrate this configuration as well, including KNM-WT 15000 (9), Sts 14 (8, 15), and possibly Stw 431, depending on the association between its broken neural arches and vertebral bodies (8, 23, 29). Unlike the case with other partial hominin vertebral columns, the penultimate and ultimate thoracic vertebrae of MH2 are articulated and were found as such in situ, rendering discrepancies

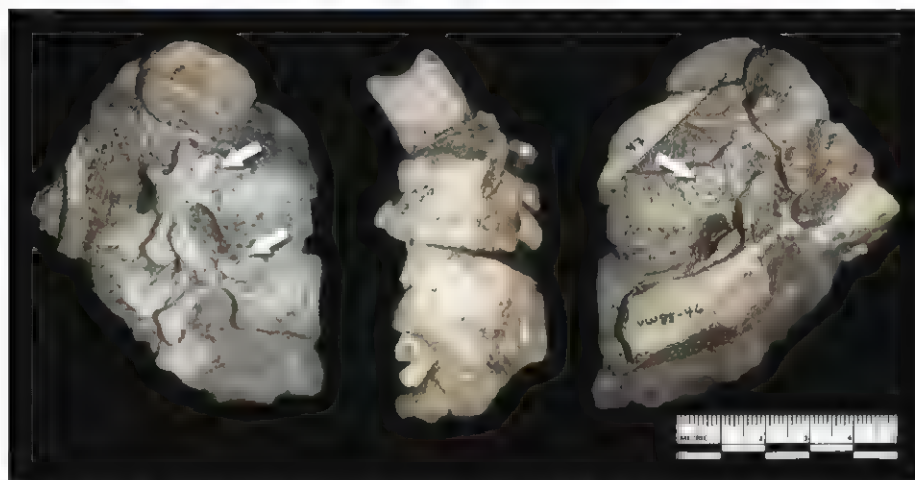


Fig. 2. Lower thoracic block of MH2. Right lateral (left), anterior (middle), and left lateral (right) views of the antepenultimate (top, off-set vertebra), penultimate (middle), and ultimate (bottom) rib-bearing vertebrae. Arrows identify costal facets (note that the ultimate vertebra is obscured by an unassociated rib on its left side; however, computed tomography (CT) slices confirm the presence of costal facets on both sides). Notice that the penultimate rib-bearing vertebra bears flat, posteriorly oriented superior articular facets and curved, sagittally oriented inferior articular facets—it is the transitional vertebra; thus, the ultimate rib-bearing vertebra is posttransitional.

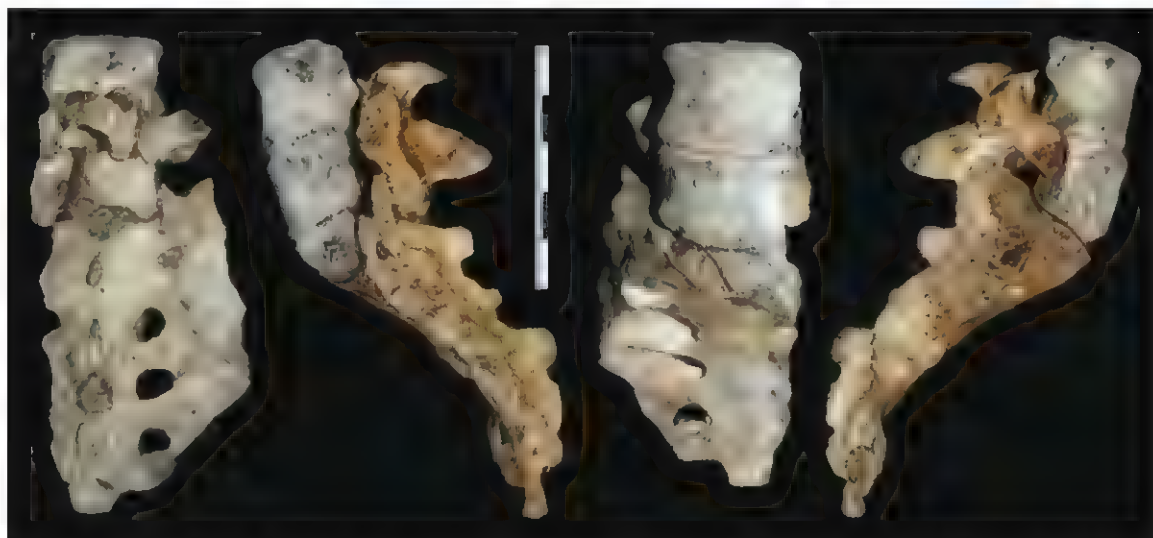


Fig. 3. Penultimate (L4) and ultimate (L5) lumbar vertebrae and sacrum of MH2. The articulated lumbar bodies are united with their respective neural arches, which are, in turn, cemented in articulation to the sacrum. Note the high degree of dorsal wedging of L5 and the presence of four large and complete sacral foramina on the right side of the sacrum.

in reconstructions that plague other specimens a nonissue.

Function, Posture, and Locomotion

The presence of lumbar dorsal wedging and other morphological features (for instance, imbrication pockets on lumbar laminae) in the MH1 and MH2 partial vertebral columns demonstrates an intrinsic lumbar lordosis and adaptation to upright posture and bipedal locomotion in *Au. sediba*. MH2 also shows a cranial position of the transitional vertebra relative to the last rib-bearing vertebra, resulting in six vertebrae with curved, sagittally oriented articular facets on the zygapophyses that allow flexion and extension of the torso and constrain its rotation (35, 36). A numerically longer posttransitional region would, therefore, facilitate postural lordosis over a longer range of the lower back than the modal condition in modern humans [(1, 2, 4, 15, 17), but see (9)]. In addition, the L5 vertebra of MH2 is extremely dorsally wedged (-10.9°), greatly surpassing lordotic wedging observed at the last lumbar vertebrae in other *Australopithecus* specimens and, although within the range of modern human variation, outside the lower limit of their 95% prediction intervals. In this regard, the MH2 L5 vertebra is very similar to that of KNM-WT 15000 (Fig. 4). When lordotic wedging is estimated from both L4 and L5, KNM-WT 15000 possesses a greater degree of summed dorsal wedging (-16.0°) than MH2 (-12.4°), both surpassing values calculated for *Au. africanus* specimens (Stw 431 at -5.7° , Sts 14 at -8.9°) (fig. S8 and table S2). Although a complete lumbar column is required to measure the overall lumbar angle (14), this trend toward strong lordotic wedging of the lower lumbar bodies may represent an evolutionary trend in

Au. sediba and *H. erectus* relative to earlier species; together with a more anterior position of the shoulder joint (37), this high degree of lordosis helps to position the center of gravity of the trunk more posteriorly. However, as other partial skeletons belonging to early members of the genus *Homo* do not preserve lower lumbar vertebrae (38–41), this hypothesis awaits future discoveries.

The likely presence of six posttransitional vertebrae (probably shared with other early hominins), in combination with dorsal wedging of the lower lumbar vertebrae (MH1 L3, as well as MH2 L4 and L5), including extreme dorsal wedging at L5, reveals a highly mobile lower back in *Au. sediba* (Fig. 4 and fig. S8). Functional analyses of lower limb remains suggest that MH2 employed a bipedal gait characterized by hyperpronation of the feet during stance phase (42, 43). Based on biomechanical principles and clinical assumptions, a kinematic chain involving foot pronation, anterior pelvic tilt, and increased lumbar lordosis has been proposed and tested in modern humans, with mixed results (44–47). Previous studies have assessed these relationships only during quiet stance on two feet, and data on the kinematics of bipedal locomotion are needed; nevertheless, the relatively strong lordotic morphology observed in the lower back of MH2 is consistent with such a kinematic hypothesis (43). Additionally, this finding suggests that MH2 may have been characterized by a pelvis tilted more anteriorly than that of modern humans (fig. S10), which has also been proposed for other members of the genus *Australopithecus* (48, 49). Whether or not these morphologies characterized *Au. sediba* as a species is unknown and will require the recovery and biomechanical analysis of additional skeletal materials. The relationship be-

tween the orientation of the pelvis and vertebral column (48–50) and integration within (51, 52) and between morphologies in these complex anatomical systems are understudied areas (49, 50) that will undoubtedly contribute to our understanding of posture and gait in *Au. sediba* and other early hominins.

References and Notes

1. B. Latimer, C. V. Ward, in *The Nariokotome Homo erectus Skeleton*, A. Walker, Ed. (Harvard Univ. Press, Cambridge, MA, 1993), pp. 266–293.
2. W. J. Sanders, thesis, New York University (1995).
3. W. J. Sanders, Comparative morphometric study of the australopithecine vertebral series Stw-H8/H41. *J. Hum. Evol.* **34**, 249 (1998). doi: 10.1006/jhev.1997.0193; pmid: 9547457
4. C. O. Lovejoy, The natural history of human gait and posture. Part 1. Spine and pelvis. *Gait Posture* **21**, 95 (2005). pmid: 15536039
5. C. V. Ward, B. Latimer, Human evolution and the development of spondylolysis. *Spine* **30**, 1808 (2005). doi: 10.1097/01.brs.0000174273.85164.67; pmid: 16103848
6. K. K. Whitcome, L. J. Shapiro, D. E. Lieberman, Fetal load and the evolution of lumbar lordosis in bipedal hominins. *Nature* **450**, 1075 (2007). doi: 10.1038/nature06342; pmid: 18075592
7. L. Shapiro, Evaluation of “unique” aspects of human vertebral bodies and pedicles with a consideration of *Australopithecus africanus*. *J. Hum. Evol.* **25**, 433 (1993). doi: 10.1006/jhev.1993.1061
8. M. Haeusler, S. A. Martelli, T. Boeni, Vertebrae numbers of the early hominid lumbar spine. *J. Hum. Evol.* **43**, 621 (2002). doi: 10.1006/jhev.2002.0595; pmid: 12457852
9. M. Haeusler, R. Schiess, T. Boeni, New vertebral and rib material point to modern bauplan of the Nariokotome *Homo erectus* skeleton. *J. Hum. Evol.* **61**, 575 (2011). doi: 10.1016/j.jhev.2011.07.004; pmid: 21868059
10. D. Pilbeam, The anthropoid postcranial axial skeleton: comments on development, variation, and evolution. *J. Exp. Zool. B Mol. Dev. Evol.* **302**, 241 (2004). pmid: 15211685
11. B. A. Rosenman, thesis, Kent State University (2008).
12. C. O. Lovejoy, G. Suwa, S. W. Simpson, J. H. Matternes, T. D. White, The great divides: *Ardipithecus ramidus* reveals the postcrania of our last common ancestors with African apes. *Science* **326**, 100 (2009). doi: 10.1126/science.1175833; pmid: 19810199
13. M. A. McCollum, B. A. Rosenman, G. Suwa, R. S. Meindl, C. O. Lovejoy, The vertebral formula of the last common ancestor of African apes and humans. *J. Exp. Zool. B Mol. Dev. Evol.* **314**, 123 (2010). pmid: 19688850
14. E. Been, A. Gómez-Olivencia, P. A. Kramer, Lumbar lordosis of extinct hominins. *Am. J. Phys. Anthropol.* **147**, 64 (2012). doi: 10.1002/ajpa.21633; pmid: 22052243
15. S. A. Williams, Placement of the diaphragmatic vertebra in catarrhines: Implications for the evolution of dorsoventral stability in hominoids and bipedalism in hominins. *Am. J. Phys. Anthropol.* **148**, 111 (2012). doi: 10.1002/ajpa.22049; pmid: 22419482
16. S. A. Williams, Variation in anthropoid vertebral formulae: Implications for homology and homoplasy in hominoid evolution. *J. Exp. Zool. B Mol. Dev. Evol.* **318**, 134 (2012). doi: 10.1002/jevb.21451; pmid: 22532475
17. K. K. Whitcome, Functional implications of variation in lumbar vertebral count among hominins. *J. Hum. Evol.* **62**, 486 (2012). doi: 10.1016/j.jhev.2012.01.008; pmid: 22425070
18. L. Shapiro, in *Postcranial Adaptation in Nonhuman Primates*, D. L. Gebo, Ed. (North Illinois Univ. Press, De Kalb, IL, 1993), pp. 121–149
19. S. A. Williams, Modern or distinct axial bauplan in early hominins? Comments on Haeusler et al. (2011). *J. Hum. Evol.* **63**, 552 (2012). doi: 10.1016/j.jhev.2012.01.007; pmid: 22414447
20. M. Haeusler, S. Regula, B. Thomas, Modern or distinct axial bauplan in early hominins? A reply

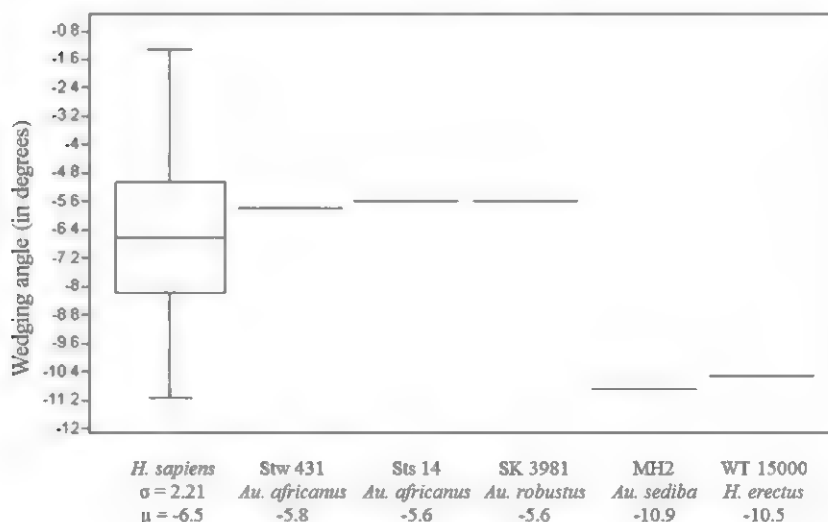


Fig. 4. Wedging angle of the last lumbar vertebra in MH2 compared with other fossil hominins and modern humans. Modern human ($n = 88$ specimens) sex differences are not significant [female ($n = 45$): $\mu = -6.4^\circ$, male ($n = 43$): $\mu = -6.6^\circ$; $P = 0.576$]. Notice that MH2 is at the extreme end of modern human variation and lies outside the range of 95% prediction intervals ($\mu \pm 1.96\sigma$) (-2.2° , -10.8°) for *H. sapiens*. Whiskers represent the minimum and maximum values of the modern human data set. See table S1 for raw data used to calculate wedging angles.

- to Williams (2012). *J. Hum. Evol.* **63**, 557 (2012). doi: 10.1016/j.jhevol.2012.05.011
21. J. T. Robinson, *Early Hominid Posture and Locomotion* (Univ. of Chicago Press, Chicago, 1972).
 22. Supplementary materials are available on Science Online.
 23. M. Toussaint, G. A. Macho, P. V. Tobias, T. C. Partridge, A. R. Hughes, The third partial skeleton of a late Pliocene hominin (Stw 431) from Sterkfontein, South Africa. *S. Afr. J. Sci.* **99**, 215 (2003).
 24. L. R. Berger *et al.*, *Australopithecus sediba*: A new species of Homo-like australopithecine from South Africa. *Science* **328**, 195 (2010). doi: 10.1126/science.1184944; pmid: 20378811
 25. R. Pickering *et al.*, *Australopithecus sediba* at 1.977 Ma and implications for the origins of the genus *Homo*. *Science* **333**, 1421 (2011). doi: 10.1126/science.1203697; pmid: 21903808
 26. J. M. Kibii *et al.*, A partial pelvis of *Australopithecus sediba*. *Science* **333**, 1407 (2011). doi: 10.1126/science.1205221; pmid: 21903805
 27. Vertebral centrum growth occurs in a similar way as long bone growth. Substantial longitudinal growth of the centrum occurs until at ~10 years of age, after which a small amount of growth takes place until the obliteration of the growth plates occurs at ~25 years of age (53).
 28. A. Walker, R. Leakey, in *The Nariokotome Homo erectus skeleton*, A. Walker, Ed. (Harvard Univ. Press, Cambridge, MA, 1993), pp. 95–160.
 29. M. M. Benade, thesis, University of Witwatersand (1990).
 30. P. V. Tobias, New researches at Sterkfontein and Taung with a note on Piltdown and its relevance to the history of palaeo-anthropology. *Trans. R. Soc. S. Afr.* **48**, 1 (1992). doi: 10.1080/00359199209520253
 31. P. V. Tobias, Ape-like *Australopithecus* after seventy years. Was it a hominid? *J. R. Anthropol. Inst.* **4**, 283 (1998). doi: 10.2307/3034503
 32. H. M. McHenry, in *Integrative Paths to the Past: Paleanthropological Advances in Honor of F. Clark Howell*, R. S. Corruccini, R. L. Ciochon, Eds. (Prentice-Hall, Englewood Cliffs, NH, 1994), pp. 251–268.
 33. C. O. Lovejoy, M. A. McCollum, Spinopelvic pathways to bipedality: Why no hominids ever relied on a bent-hip-bent-knee gait. *Philos. Trans. R. Soc. London Ser. B* **365**, 3289 (2010). doi: 10.1098/rstb.2010.0112; pmid: 20855303
 34. S. A. Williams, thesis, University of Illinois, Urbana-Champaign, IL (2011).
 35. H. Rockwell, F. G. Evans, H. C. Pheasant, The comparative morphology of the vertebrate spinal column. Its form as related to function. *J. Morphol.* **63**, 87 (1938). doi: 10.1002/jmor.1050630105
 36. G. A. Russo, Prezygapophyseal articular facet shape in the catarrhine thoracolumbar vertebral column. *Am. J. Phys. Anthropol.* **142**, 600 (2010). doi: 10.1002/ajpa.21283; pmid: 20310062
 37. S. E. Churchill *et al.*, The upper limb of *Australopithecus sediba*. *Science* **340**, 1233477 (2013). doi: 10.1126/science.1233477
 38. M. R. Meyer, thesis, University of Pennsylvania (2005).
 39. D. Lordkipadze *et al.*, Postcranial evidence from early *Homo* from Dmanisi, Georgia. *Nature* **449**, 305 (2007). doi: 10.1038/nature06134; pmid: 17882214
 40. A. Walker, M. R. Zimmerman, R. E. Leakey, A possible case of hypervitaminosis A in *Homo erectus*. *Nature* **296**, 248 (1982). doi: 10.1038/296248a0; pmid: 7038513
 41. D. C. Johanson *et al.*, New partial skeleton of *Homo habilis* from Olduvai Gorge, Tanzania. *Nature* **327**, 205 (1987). doi: 10.1038/327205a0; pmid: 3106831
 42. B. Zipfel *et al.*, The foot and ankle of *Australopithecus sediba*. *Science* **333**, 1417 (2011). doi: 10.1126/science.1207203; pmid: 21903807
 43. J. M. DeSilva *et al.*, The lower limb and mechanics of walking in *Australopithecus sediba*. *Science* **340**, 1232999 (2013). doi: 10.1126/science.1232999
 44. D. Levine, M. W. Whittle, The effects of pelvic movement on lumbar lordosis in the standing position. *J. Orthop. Sports Phys. Ther.* **24**, 130 (1996). pmid: 8866271
 45. S. Khamis, Z. Yizhar, Effect of feet hyperpronation on pelvic alignment in a standing position. *Gait Posture* **25**, 127 (2007). doi: 10.1016/j.gaitpost.2006.02.005; pmid: 16621569
 46. K. Duval, T. Lam, D. Sanderson, The mechanical relationship between the rearfoot, pelvis and low-back. *Gait Posture* **32**, 637 (2010). doi: 10.1016/j.gaitpost.2010.09.007; pmid: 20889344
 47. M. Betsch *et al.*, Influence of foot positions on the spine and pelvis. *Arthritis Care Res.* **63**, 1758 (2011). doi: 10.1002/acr.20601; pmid: 22127967
 48. M. M. Abitbol, Evolution of the lumbosacral angle. *Am. J. Phys. Anthropol.* **72**, 361 (1987). doi: 10.1002/ajpa.1330720309; pmid: 3107397
 49. C. Berge, D. Goullaras, A new reconstruction of Sts 14 pelvis (*Australopithecus africanus*) from computed tomography and three-dimensional modeling techniques. *J. Hum. Evol.* **58**, 262 (2010). doi: 10.1016/j.jhevol.2009.11.006; pmid: 20138331
 50. M. M. Abitbol, Lateral view of *Australopithecus afarensis*: Primitive aspects of bipedal positional behavior in the earliest hominids. *J. Hum. Evol.* **28**, 211 (1995). doi: 10.1006/jhevol.1995.1017
 51. M. W. Grabowski, J. D. Polk, C. C. Roseman, Divergent patterns of integration and reduced constraint in the human hip and the origins of bipedalism. *Evolution* **65**, 1336 (2011). doi: 10.1111/j.1558-5646.2011.01226.x; pmid: 21521191
 52. K. L. Lewton, Evolvability of the primate pelvic girdle. *Evol. Biol.* **39**, 126 (2012). doi: 10.1007/s11692-011-9143-6
 53. R. A. Dickson, P. Deacon, Spinal growth. *J. Bone Joint Surg. Br.* **69**, 690 (1987). pmid: 3680325

Acknowledgments: We thank the South African Heritage Resource agency for the permits to work at the Malapa site; the Nash family for granting access to the Malapa site and continued support of research on their reserve; the South African Department of Science and Technology, the Gauteng Provincial Government, the South African National Research

Foundation and the African Origins Platform, the Institute for Human Origins, University of the Witwatersrand, the University of the Witwatersrand's Vice Chancellor's Discretionary Fund, the National Geographic Society, the Palaeontological Scientific Trust, the Andrew W. Mellon Foundation, the Ford Foundation, the U.S. Diplomatic Mission to South Africa, the French Embassy of South Africa, the A.H. Schultz Foundation, Duke University, the Ray A. Rothrock '77 Fellowship and International Research Travel Assistance Grant of Texas A&M University, and the Oppenheimer and Ackerman families and R. Branson for funding; the University of the Witwatersrand's Schools of Geosciences and Anatomical Sciences and the Bernard Price Institute for Palaeontology for support and facilities; the Gauteng Government, and the Gauteng Department of Agriculture, Conservation and Environment and the Cradle of Humankind Management Authority; and our respective universities for ongoing support. We thank E. Mbua, P. Kiura, V. Iminjili, the National Museums of Kenya, B. Billings, B. Zipfel, the School of Anatomical Sciences at the University of the Witwatersrand, S. Potze, L. C. Kgasi, and the Ditsong Museum for access to comparative specimens; the Virtual Image Processing lab of the Palaeosciences Centre and the Microfocus X-ray CT facility of the Palaeosciences Centre at Wits for funding these facilities; the University of the Witwatersrand Office of Research and the National Research Fund Strategic Research Infrastructure Grant and African Origins Platform funding programs; and Duke University and the University of Zurich 2009 and 2010 Field Schools for technical and material support. Numerous individuals have been involved in the ongoing preparation and excavation of these fossils, including C. Dube, C. Kemp, M. Kgasi, M. Languza, J. Malaza, G. Mokoma, P. Mukanela, T. Nemvuhundi, M. Ngcamphaala, S. Jirah, S. Tshabalala, and C. Yates. Other individuals who have given substantial support to this project include B. de Klerk, W. Lawrence, C. Steininger, B. Kuhn, L. Pollaroio, B. Zipfel, J. Kretzen, D. Conforti, J. McCaffery, C. Dlamini, H. Visser, R. McCrae-Samuel, B. Nkosi, B. Louw, L. Backwell, F. Thackeray, and M. Peltier. J. Smilg facilitated computed tomography scanning of the specimens, A. Val provided information of CT slices, W. Sanders and K. Whitcome made data on fossil specimens and casts available, M. Grabowski provided helpful comments on the manuscript, and M. Shattuck provided valuable comments and assisted substantially with the revision of this manuscript. The *Au. sediba* specimens are archived at the Evolutionary Studies Institute at the University of the Witwatersrand. All data used in this study are available upon request, including access to the original specimens. Data reported in this study are available in the supplementary materials.

Supplementary Materials

www.sciencemag.org/content/340/6129/1232996/suppl/DC1
Supplementary Text
Figs. S1 to S11
Tables S1 and S2
References (54–58)

20 November 2012; accepted 12 March 2013
10.1126/science.1232996

Stem Cell Lawsuit Finally Over. Russian Team Retrieves First Sample from Lake Vostok. Surprise Choices Mark New Leadership on U.S. House Science Panel. India Unveils Ambitious Science Policy.



Now, more than ever, developments in the lab are directly connected to decisions made in the halls of government.

*Science*Insider, the policy blog from the journal *Science*, is your source for news from the intersection of science and policy. From budget debates in the United States Congress, to climate change agreements at the United Nations, *Science*Insider covers the issues that have an impact on your work, your field, and your world.

Keep up to date and keep informed. Go inside the issues at www.ScienceInsider.org



ScienceInsider

Breaking news and analysis from the world of science policy



The Lower Limb and Mechanics of Walking in *Australopithecus sediba*

Jeremy M. DeSilva,^{1,2*} Kenneth G. Holt,³ Steven E. Churchill,^{4,2} Kristian J. Carlson,^{2,5} Christopher S. Walker,⁴ Bernhard Zipfel,^{2,6} Lee R. Berger²

The discovery of a relatively complete *Australopithecus sediba* adult female skeleton permits a detailed locomotor analysis in which joint systems can be integrated to form a comprehensive picture of gait kinematics in this late australopith. Here we describe the lower limb anatomy of *Au. sediba* and hypothesize that this species walked with a fully extended leg and with an inverted foot during the swing phase of bipedal walking. Initial contact of the lateral foot with the ground resulted in a large pronatory torque around the joints of the foot that caused extreme medial weight transfer (hyperpronation) into the toe-off phase of the gait cycle (late pronation). These bipedal mechanics are different from those often reconstructed for other australopiths and suggest that there may have been several forms of bipedalism during the Plio-Pleistocene.

The locality of Malapa, South Africa, has yielded two relatively complete skeletons of *Australopithecus sediba*, dated at 1.977 million years ago (1, 2). This species has a combination of primitive and derived features in the hand (3), upper limb (4), thorax (5), spine (6), and foot (7) in a hominin with a relatively small brain (8), a human-like pelvis (9), and a mosaic of *Homo*- and *Australopithecus*-like craniodental anatomy (1, 10, 11). The foot in particular possesses an anatomical mosaic not present in either *Au. afarensis* or *Au. africanus* (7), supporting the contention that there were multiple forms of bipedal locomotion in the Plio-Pleistocene (12). The recent discovery of an *Ardipithecus*-like foot from 3.4-million-year-old deposits at Burtule, Ethiopia, further shows that at least two different kinematic solutions to bipedalism coexisted in the Pliocene (13). Here we describe the lower limb of *Au. sediba* [specimen numbers and attributions are provided in table S1 (14)] and propose a hypothesis for how this late australopith walked.

Lower Limb of MH1

The holotype of *Au. sediba* is Malapa Hominin 1 (MH1), a juvenile male partial skeleton whose lower limb consists of a right proximal femur (fig. S1), small shaft fragments from the tibia and fibula, and foot bones already described (7) (table S1). The proximal femur is australopith-like, with a long, anteroposteriorly compressed

femoral neck (fig. S2) and low neck-shaft angle (110° to 115°) (table S2). Posterolaterally, there is a third trochanter, inferior to which is a well-developed hypotrochanteric fossa, a human feature reflecting a large insertion area for the gluteus maximus (15).

Lower Limb of MH2

The lower limb of MH2, an adult female, consists of a right femoral head and neck, part of the proximal femoral shaft, the left proximal fibula, and the right knee joint (including the patella). Additionally, as already described (7), MH2 preserves an articulated distal tibia, talus, and calcaneus and a partial fifth metatarsal. The proximal femur preserves much of the head and neck (fig. S1). As in MH1, the neck is anteroposteriorly compressed (table S2). Viewed superiorly, the head appears to be prolonged anteriorly, as is the case in most humans (16).

The right knee of MH2 is represented by an 86.7-mm-long fragment of the distal femur (fig. S3), two fragments that conjoin to form most of the tibial plateau (fig. S4), and a relatively complete patella composed of two conjoining frag-

ments, one of which remains partially embedded in calcified sediment. This part of the patella has been digitally extracted from micro-computed tomography (μ CT) scans, and a nearly complete knee cap has been reconstructed (fig. S5). The posteromedial part of the distal femur has been sheared away, but the lateral condyle, patellar articular surface, distal shaft, and most of the medial condyle are well preserved. The bicondylar angle is estimated to be ~9°, which is within the range of modern humans but is low for an australopith (table S3). There is a sutured hollow just superior to the patellar surface, evidence of contact with the patella in a fully extended position (17) (fig. S6). There is a strong medial condylar boss, an anatomy unique to hominins, and evidence for a “tibial dominant” knee capable of full extension (18) (fig. S7). Most notable is the high lateral patellar lip. The lateral trochlear groove angle (19) is 31.3°, 3 SD above the modern human mean (20) and far greater than any ape trochlear angle, because apes tend to have flat trochlear grooves (Fig. 1). A high lateral patellar lip serves as a bony mechanism for patellar retention during bipedal gait (21, 22). The extension of the lateral lip in *Au. sediba* is not a function of overall anterior expansion of the patellar surface, as is found in *Homo* (18), and is restricted just to the lateral side (fig. S8). Laterally, there is a deep groove for the popliteus, an internal rotator of the tibia and stabilizer of the knee. This muscle may have been important in resisting internal rotation of the femur during stance phase. The relatively narrow tibial spines on the MH2 tibial plateau suggest enhanced knee mobility (23), although this anatomy may also be related to the small size of *Au. sediba* (24).

On the proximal tibia, the medial condyle is flat and the lateral condyle is slightly convex anteroposteriorly, similar to the condition found in other small australopiths (specimens A.L. 129-1 and StW 514), although the functional importance of this convexity is unclear (25). There appears to be a small notch on the lateral plateau, perhaps indicating the presence of a double meniscus attachment and thus possibly greater osteoligamentous

Fig. 1. The lateral patellar lip. The lateral trochlear groove angle (19) is similar in *Australopithecus* (TM 1513, Sts 34, A.L. 129-1, A.L. 333-4, and A.L. 333w-56), early *Homo* (KNM-ER 1472, KNM-ER 1481, and KNM-WT 15000), and modern humans (20). This measurement in MH2 (U.W. 88-63) is over 3 SD higher than in modern humans. Apes have flat trochlear grooves (18) (fig. S7) and thus lateral trochlear groove angles near zero. Bottom images, from left to right, are as follows: TM 1513, KNM-ER 1472, modern human, and MH2, all scaled to the same size. They have been positioned so that the medial patellar surface is horizontal, which corresponds closely to the orientation recommended in (18). Note the extreme lateral patellar lip in MH2.



¹Department of Anthropology, Boston University, 232 Bay State Road, Boston, MA 02215, USA. ²Evolutionary Studies Institute, University of the Witwatersrand, Private Bag 3, Wits 2050, South Africa. ³Department of Physical Therapy and Athletic Training, Sargent College, 635 Commonwealth Avenue, Boston University, Boston, MA 02215, USA. ⁴Department of Evolutionary Anthropology, Box 90383, Duke University, Durham, NC 27708, USA. ⁵Department of Anthropology, Indiana University, Bloomington, IN 47405, USA. ⁶Bernard Price Institute for Palaeontological Research, School of Geosciences, University of the Witwatersrand, Private Bag 3, Wits 2050, South Africa.

*Corresponding author. E-mail: jdesilva@bu.edu

control over rotation at the knee as in *Homo* proximal tibiae (26). However, the absence of this notch in other australopithecids does not necessarily imply the absence of a double insertion (27).

The patella is small, measuring 27.1 mm wide mediolaterally and 13.1 mm thick anteroposteriorly. It is 24.7 mm tall superoinferiorly, which is probably just short of the actual height, because there is some damage to the distolateral aspect of the apex. The posterior part of the patella is human-like in being strongly convex mediolaterally (fig. S9), with a high central keel separating the condylar facets medially and laterally.

The most proximal 97.1 mm of the left fibula of MH2 is preserved as four conjoining fragments (fig. S10). The fibula is more gracile than modern

ape fibulae and in this respect resembles specimen OH 35 (fig. S11). The MH2 fibula has an osteophytic growth at the biceps femoris insertion.

Lower Limb of MH4

MH4, an adult or near-adult individual of unknown sex, is represented by two conjoining pieces of a tibia described previously (7). Here we provide an estimated total length, possible because the proximal tibia, though not recovered, has left a natural cast of its anterior surface in the calcified sediment (fig. S12). We estimate total tibial length at approximately 271 mm, with a possible range of 267 to 275 mm, depending on the degree of proximal tibial retroversion and the proximal projection of the tibial spines.

Fig. 2. Hyperpronation. (A) The pedal bones of *Au. sediba* are superimposed on a human foot in dorsal view.

These bones are not all from the same individual (see table S1 for details). We hypothesize that MH2 would have contacted the ground along the lateral edge of an inverted foot. This would generate a ground reaction resultant (blue arrows) that would be positioned lateral to the joints of the foot, creating a large pronatory torque (red arrows). Although apes often land along the lateral edge of an inverted foot (30, 31), they swing their body mass laterally over the stance foot during bipedal gait, effectively producing a counteracting supinatory torque. *Au. sediba* had a pelvis with sagittally oriented ilia (9), suggesting a human-like abductor mechanism

and in turn suggesting a medially positioned center of mass relative to the stance leg (illustrated by the large blue arrow at bottom left). This position of the center of mass would exacerbate the pronatory torque at the subtalar, midtarsal, and tarsometatarsal joints. (B) Excessive pronation on a weight-bearing foot (curved red arrow) causes a chain of rotatory movements proximal to the foot. The tibia internally rotates (green arrow) as the talus plantarflexes and adducts. The femur also internally rotates (42, 43; curved blue arrow), increasing the lateral deviation of the patella (small blue arrow). Pronation at the foot causes an anterior pitch of the center of mass (34, 43; black arrow), counteracted by hyperlordosis of the lumbar region (6). *Au. sediba* possesses anatomies that are adaptive to, or consequences of, these motions.

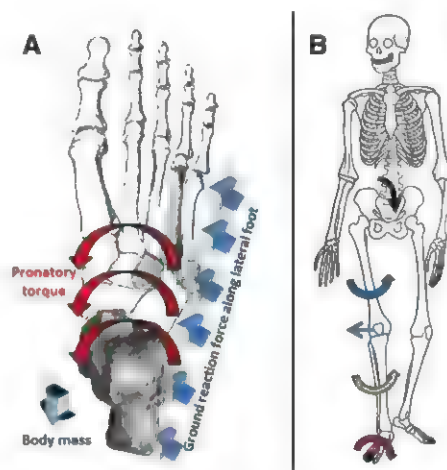
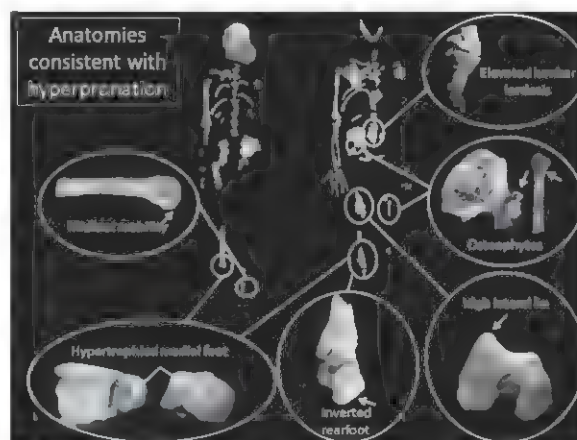


Fig. 3. Skeletons of *Au. sediba*:

left, MH1 (pictured with MH4 tibia); right, MH2. Several anatomies of these skeletons are consistent with a hyperpronating gait. The base of the fourth metatarsal is convex, indicating that the midfoot was hypermobile. The medial malleolus and talar head are hypertrophied, reflecting loading of an inverted foot and mobility at the talonavicular joint, respectively. The rearfoot is in an inverted position, a risk factor for hyperpronation in modern humans. Hyperpronators internally rotate the femur and tibia and are at a greater risk for patellar dislocation. The high lateral patellar lip reduces the risk of patellar subluxation. Osteophytes on the origin of the rectus femoris/iliofemoral ligament proximal attachment and insertion of the biceps femoris indicate soft tissue strain: possible consequences of a hyperpronating gait. MH2 has elevated lumbar lordosis (6), perhaps to compensate for the excessive anterior pitch of the center of mass common in hyperpronators.



The Kinematics of Walking in *Au. sediba*

The anatomy of the foot (7), spine (6), pelvis (9), and knee (this paper) indicate that *Au. sediba* was an obligate biped. Based primarily on the lower limb, pelvic, and vertebral morphology of MH2, and to a lesser extent on the pedal morphology of MH1, we propose that *Au. sediba* was a hyperpronator (28) with exaggerated medial weight transfer during the stance phase of terrestrial bipedalism (Fig. 2). Modern human hyperpronators serve as a kinematic reference model for this gait and its musculoskeletal consequences. We suggest that MH2 expressed this kinematic variation, and *Au. sediba* did with regular frequency, although the hypothesis that the entire species walked in this manner will require further testing with additional fossil material (14).

At heel strike of bipedal locomotion, humans commonly have a slightly supinated rearfoot and forefoot, which are passively driven by the ground reaction force into pronation of the subtalar and more distal joints during the subsequent mid-stance phase of walking. Video and plantar pressure data reveal that apes contact the ground with the heel (29) and often the lateral midfoot simultaneously in what has been termed "inverted heel-strike plantigrady" (30, 31). The abducted hallux serves a stabilizing role during quadrupedal walking in apes, contributing little to propulsion (31). The divergent hallux is suggested to have served a similar stabilizing role during bipedal walking in *Ardipithecus ramidus* (32).

In a small percentage of modern humans, the foot is excessively inverted (termed forefoot and/or rearfoot varus) during the swing phase of walking, resulting in heel strike with the foot in a highly supinated posture, with ground contact established along the lateral border of the heel and forefoot (33). Contact between the ground and the lateral side of the foot introduces a large pronatory torque around the subtalar and more distal joints, which drives the foot into pronation (33, 34). As the foot is driven into pronation, there are high medially directed torques that can not only cause excess loading on the bones of the medial column of the foot (35) but also stress the soft tissues, such as the ligaments supporting the medial longitudinal arch and the muscles whose tendons insert plantomedially, particularly the tibialis anterior and tibialis posterior. Plantar fasciitis, medial tibial stress syndrome (shin splints), and tibial stress fractures are therefore common injuries experienced by late and hyperpronating modern humans (34). Although hyperpronation can have pathological consequences in modern humans, we are proposing here that the skeleton of *Au. sediba* reveals a suite of anatomies that are adaptive for, or consequences of, this kind of walking (Fig. 3).

Reconstruction of the conjoined elements of the rearfoot of MH2 demonstrates that the calcaneus had an inverted set (fig. S13), which is a contributing factor to hyperpronation in modern humans (36). However, the inverted heel itself

would not necessarily produce a pronatory torque, because there is considerable variation in the position of the subtalar joint axis relative to the ground reaction force location (37). MH2 also had a gracile calcaneal tuber (7), with a superiorly positioned lateral plantar process, which reduced the surface area of the plantar aspect of the heel in *Au. sediba* and would have reduced the effectiveness of the subcalcaneal heel pad (based on size information rather than material properties), which has been shown to dissipate peak stress during heel strike (38). To compensate, we hypothesize that *Au. sediba* landed simultaneously on the heel and along the lateral foot at touch down, in much the same way that African apes walk (inverted heel-strike plantigrady) (31). This is achievable in a bipedal hominin that has full knee extension by slightly increasing normal plantarflexion angle during foot contact. Because of the wider midfoot and forefoot, landing along the lateral side of an inverted foot would provide a large moment arm around the midtarsal and tarsometatarsal joints that would also transfer to the subtalar joint. Thus, a large

pronatory torque would drive the foot into pronation (Fig. 2). There is suggestive evidence for excessive pronation in the *Au. sediba* tarsals. An elevated degree of pronation is possible in *Au. sediba*, because the subtalar joint has a high radius of curvature and is therefore quite mobile and capable of an extreme range of motion (7). The relatively large talar head of MH2 (7) may signal elevated talonavicular mobility, especially because this joint is central to midfoot pronation in humans (39).

Landing on an inverted foot would also load the medial portion of the tibiotalar joint and introduce a shear force across the medial malleolus. This may explain the form of the medial malleoli of both MH2 and MH4, which are mediolaterally thicker than those of other fossil hominins or modern humans (7). However, pronation does not occur at the tibiotalar joint but at the subtalar joint and joints of the midfoot. As the foot is driven into pronation by a high pronatory torque, the more distal parts of the medial foot would be excessively loaded (35). A foot adapted for this kind of locomotion may therefore be expected to

exhibit increased mechanical reinforcement of bones in the medial portion of the foot. We predict that, if additional foot elements are recovered, we will see greater joint and diaphyseal robusticity in medial relative to lateral tarsals, metatarsals, and phalanges (Table 1).

During midstance, the foot is more mobile and better able to conform to its substrate. In hyperpronators, the talus adducts and plantarflexes excessively, dropping the longitudinal arch and contributing to hypermobility of the midfoot. Although we hypothesize that *Au. sediba* possessed an arched foot (7) (fig. S14), there is also evidence for midfoot mobility. A right fourth metatarsal, possibly from MH1, has a highly convex base dorsoplantarily, suggesting the presence of midfoot flexion or a "midtarsal break" (40). Other hominin fourth metatarsal bases from *Au. afarensis*, *Au. africanus*, and the OH 8 foot are human-like and do not exhibit evidence for a midtarsal break (Fig. 4) (40, 41). The convexity of the Malapa fourth metatarsal is thus unexpected and implies more mobility at the lateral tarsometatarsal joint in this hominin than in any other. We suggest that the seemingly contradictory anatomies in the foot of *Au. sediba* (possession of an arched foot and long plantar ligament together with midfoot mobility) can only be explained in the context of a bipedal foot that hyperpronates when weight-bearing (14).

In modern humans, excessive pronation may have damaging effects in lower limb joints proximal to the foot. In hyperpronators, the tibia and femur both internally rotate excessively (42, 43) under a patella that is relatively fixed by the rectus femoris attachment to the anterior inferior iliac spine (AIIS) as the quadriceps femoris contracts to extend the leg during toe-off (34). Because this occurs late in the gait cycle, during knee extension, the patella is pulled laterally, and thus hyperpronators are at risk for both patellofemoral pain (44) and patellar subluxation (45, 46). A hominin bony adaptation that helps prevent patellar subluxation is a raised lateral lip of the distal femur (21, 22). The extreme lateral patellar lip of MH2 (Fig. 1) (figs. S7 and S8) may be an adaptation to resist injurious lateral translation of the patella during hyperpronation of the foot and resulting internal rotation of the tibia and femur during late stance phase. This skeletal adaptation in *Au. sediba* may also implicate a reduced or absent vastus medialis obliquus in counteracting lateral translation of the patella. The fact that a lateral lip is present at birth (17, 18) can be extrapolated to indicate that the species *Au. sediba* (and not just MH2) was adapted for this kind of locomotion (14). Furthermore, the large popliteal groove present on the MH2 femur may indicate strong muscular involvement in counteracting the internal rotation of the femur on a fixed tibia, because the popliteus acts as an external rotator of the femur during stance phase.

Hyperpronation drives the entire leg medially during stance phase and may strain any muscle

Table 1. Evidence for hyperpronation in *Au. sediba*.

Hyperpronating biomechanics	Anatomical predictions	Morphology in <i>Au. sediba</i>
Initial ground contact on an inverted foot, resulting in high medially directed forces on tibiotalar joint	Inverted calcaneus and thick medial malleolus	Calcaneus in inverted set and predicted forefoot in varus set; thickest medial malleoli of any known hominin.
Excessive pronation at subtalar joint	Increased mobility at subtalar joint	High radius of curvature of talar facet on calcaneus.
Excessive pronation at midtarsal joints and tarsometatarsal joints	Mobile midfoot in coronal plane	Greatly enlarged talar head, suggestive of talonavicular mobility.
Increased strain on soft tissue of medial foot	Components of medial arch, plantar aponeurosis (if present), and tibialis posterior tendon under stress	Currently unknown. Predicted robust navicular tuberosity; reduced metatarsophalangeal joint extension if plantar aponeurosis taut.
Increased strain on foot bones distally and medially	Increased robusticity of medial tarsals, metatarsals, and phalanges	Currently unknown. Predicted to be relatively robust medially; if partially divergent, hallux could also help counter pronatory torque.
Lowered arch and increased midfoot mobility	Increased sagittal plane dorsiflexion evident in bones of midfoot	Convex surface to base of fourth metatarsal indicative of midtarsal break; predicted concavity of metatarsal facets on cuboid.
Increased knee mobility	Greater rotatory capacity and greater role for knee stabilizers, such as popliteus and biceps femoris	Tibial spines close together and enlarged popliteal groove on distal femur.
Increased internal rotation of femur	Increased strain on muscles crossing both hip and knee joints	Osteophytic growths on both origin for rectus femoris and insertion of biceps femoris. Predicted to have enlarged origin on the anterior superior iliac spine for sartorius.
Increased risk of patellar subluxation	Bony adaptations for patellar retention	Highest lateral patellar lip of any known hominin.
Anterior tilt of the pelvis	Increased lumbar lordosis	Last lumbar vertebra has very high wedging angle.

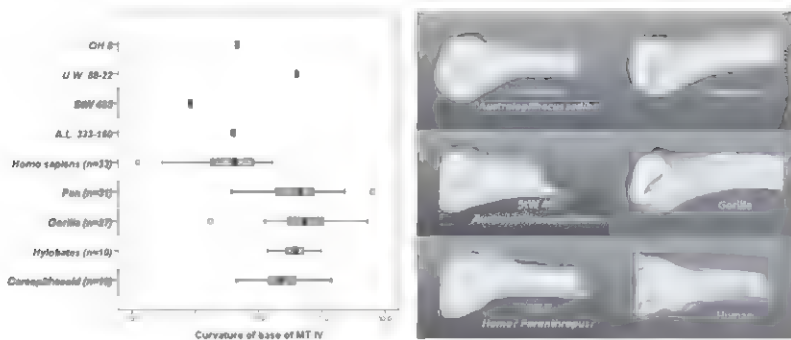


Fig. 4. The fourth metatarsal. (Left) Curvature of the base of the fourth metatarsal in fossil hominins, humans, apes, and monkeys (40). Humans and most fossil hominins, including *Au. afarensis* (41), have flat bases, consistent with a stiff and immobile midfoot. The *Au. sediba* fourth metatarsal has a convex base. [The box-and-whiskers plot shows the median (vertical line), upper and lower quartiles (box), range (whiskers), and outliers (circles) for each group.] (Right) Digital renderings of the fourth metatarsal in medial view, illustrating the dorsoplantarly curved base morphology in apes and *Au. sediba* and the flat base in other hominins and in modern humans.

crossing both the knee and the hip joints (e.g., the rectus femoris), particularly those inserting laterally in the leg (e.g., the long head of the biceps femoris). As previously mentioned, the insertion for the biceps femoris on the proximal fibula is osteophytic, indicative of elevated strain on this insertion area (fig. S10). The MH2 ilium has an unusually large and projecting AIFS (fig. S15), suggesting that the rectus femoris (and/or iliofemoral ligament) was under considerable strain during gait. As the femur internally rotates and adducts, the AIFS will be stressed by excessive stretching of the rectus femoris tendinous origin. Finally, hyperpronators experience an anterior pitch of the center of mass relative to the hip joint (43), requiring compensatory hyperlordosis to shift the center of mass posteriorly back over the hip joints, often resulting in lower back pain (34). The last lumbar vertebra of *Au. sediba* has very high dorsal wedging, suggesting elevated lordosis (6), which may have adapted this species to the challenges of being a hyperpronating biped.

Although we find the evidence compelling that *Au. sediba*, or at least MH2, was a hyperpronating biped (Fig. 3 and Table 1), the selective advantage of this form of bipedality is unclear. There is little evidence that other known australopithecids were hyperpronators, because the peculiar anatomies of the *Au. sediba* foot, knee, and hip are not found in earlier australopithecids. Recent work on the Laetoli footprints (47, 48) suggests that although the makers of the prints (presumably *Au. afarensis*) walked with a human-like gait, they had slightly less medial weight transfer. The hallux of *Au. afarensis* is domed and robust (49), indicating that weight transfer was more human-like than ape-like, but there probably were at least subtle differences in how *Au. afarensis* walked as compared to most modern humans. We hypothesize that terrestrial bipedalism in *Au. sediba* also differed subtly from that in most humans today, with *Au. sediba* engaging in more weight transfer on to the medial foot (hyper-

pronation) rather than less, as may have been the case with *Au. afarensis*.

Our interpretation of Malapa skeletal morphology extends the variation in *Australopithecus* locomotion. As suggested by others (7, 12, 13), there were different kinematic solutions for being a bipedal hominin in the Plio-Pleistocene. The MH2 skeleton provides insight into one of those potential solutions: hyperpronation. This mode of locomotion may be a compromise between an animal that is adapted for extended knee bipedalism and one that either still had an arboreal component or had re-evolved a more arboreal lifestyle from a more terrestrial ancestor. There is some postcranial evidence that the South African species *Au. africanus* may have been more arboreal than the east African *Au. afarensis* (50, 51), and a hypothesized close relationship between *Au. africanus* and *Au. sediba* (1, 11), along with features in the upper limbs of the latter thought to reflect adaptations to climbing and suspension (3, 4), is consistent with a retained arboreal component in the locomotor repertoire of *Au. sediba*. Pronation is an important foot motion that shifts weight onto the medial side of the foot in climbing apes (52, 53) and serves a role in weight transfer, shock absorption, and negotiation of uneven substrates during human bipedal gaits. An animal that was adapted to do both reasonably well may have had to support an increasingly mobile foot by evolving a large mobile medial column and important stabilizing anatomies at the knee and hip, in order to survive in these dual worlds.

References and Notes

1. L. R. Berger et al., *Australopithecus sediba*: A new species of *Homo*-like australopithec from South Africa. *Science* **328**, 195 (2010). doi: 10.1126/science.1184944; pmid: 20378811
2. R. Pickering et al., *Australopithecus sediba* at 1.977 Ma and implications for the origins of the genus *Homo*. *Science* **333**, 1421 (2011). doi: 10.1126/science.1203697; pmid: 21903808
3. T. L. Kivell, J. M. Kibbi, S. E. Churchill, P. Schmid, L. R. Berger, *Australopithecus sediba* hand demonstrates mosaic evolution of locomotor and manipulative abilities.

- Science* **333**, 1411 (2011). doi: 10.1126/science.1202625; pmid: 21903806
4. S. E. Churchill et al., The upper limb of *Australopithecus sediba*. *Science* **340**, 1233477 (2013). doi: 10.1126/science.1233477
5. P. Schmid et al., Mosaic morphology in the thorax of *Australopithecus sediba*. *Science* **340**, 1234598 (2013). doi: 10.1126/science.1234598
6. S. Williams et al., The vertebral column of *Australopithecus sediba*. *Science* **340**, 1232996 (2013). doi: 10.1126/science.1232996
7. B. Zipfel et al., The foot and ankle of *Australopithecus sediba*. *Science* **333**, 1417 (2011). doi: 10.1126/science.1202703; pmid: 21903807
8. K. J. Carlson et al., The endocast of MH1, *Australopithecus sediba*. *Science* **333**, 1402 (2011). doi: 10.1126/science.1203922; pmid: 21903804
9. J. M. Kibbi et al., A partial pelvis of *Australopithecus sediba*. *Science* **333**, 1407 (2011). doi: 10.1126/science.1202521; pmid: 21903805
10. D. J. de Ruiter et al., Mandibular remains support taxonomic validity of *Australopithecus sediba*. *Science* **340**, 1232997 (2013). doi: 10.1126/science.1232997
11. J. D. Irish, D. Guatelli-Steinberg, S. S. Legge, L. R. Berger, D. J. de Ruiter, Dental morphology and the phylogenetic "place" of *Australopithecus sediba*. *Science* **340**, 1233062 (2013). doi: 10.1126/science.1233062
12. W. E. H. Harcourt-Smith, L. C. Aiello, Fossils, feet and the evolution of human bipedal locomotion. *J. Anat.* **204**, 403 (2004). doi: 10.1111/j.0021-8782.2004.00296.x; pmid: 15198703
13. Y. Haile-Selassie et al., A new hominin foot from Ethiopia shows multiple Pliocene bipedal adaptations. *Nature* **483**, 565 (2012). doi: 10.1038/nature10922; pmid: 22460901
14. Methods and background are available as supplementary materials on Science Online.
15. C. O. Lovejoy, R. S. Meindl, J. C. Ohman, K. G. Heiple, T. D. White, The Maka femur and its bearing on the antiquity of human walking: Applying contemporary concepts of morphogenesis to the human fossil record. *Am. J. Phys. Anthropol.* **119**, 97 (2002). doi: 10.1002/ajpa.10111; pmid: 12237933
16. B. Asfaw, Proximal femur articulation in Pliocene hominids. *Am. J. Phys. Anthropol.* **68**, 535 (1985). doi: 10.1002/ajpa.1330680409; pmid: 3936365
17. C. Tardieu, Development of the human hind limb and its importance for the evolution of bipedalism. *Evol. Anthropol.* **19**, 174 (2010). doi: 10.1002/evan.20276
18. C. O. Lovejoy, The natural history of human gait and posture. Part 3. The knee. *Gait Posture* **25**, 325 (2007). doi: 10.1016/j.gaitpost.2006.05.001; pmid: 16766186
19. C. Tardieu et al., Relationship between formation of the femoral bicondylar angle and trochlear shape: Independence of diaphyseal and epiphyseal growth. *Am. J. Phys. Anthropol.* **130**, 491 (2006). doi: 10.1002/ajpa.20373; pmid: 16425192
20. J. A. Wanner, Variations in the anterior patellar groove of the human femur. *Am. J. Phys. Anthropol.* **47**, 99 (1977). doi: 10.1002/ajpa.1330470117; pmid: 888940
21. W. E. Clark, Observations on the anatomy of the fossil *Australopithecinae*. *J. Anat.* **81**, 300 (1947). pmid: 17105037
22. K. G. Heiple, C. O. Lovejoy, The distal femoral anatomy of *Australopithecus*. *Am. J. Phys. Anthropol.* **35**, 75 (1971). doi: 10.1002/ajpa.1330350109; pmid: 5003051
23. C. Tardieu, Morpho-functional analysis of the articular surfaces of the knee-joint in primates, in *Primate Evolutionary Biology*, A. B. Chiarelli, R. S. Corruccini, Eds. (Springer-Verlag, New York, 1981), pp. 68–80.
24. L. C. Aiello, M. C. Dean, *An Introduction to Human Evolutionary Anatomy* (Academic Press, London, 1990).
25. J. M. Organ, C. V. Ward, Contours of the hominoid lateral tibial condyle with implications for *Australopithecus*. *J. Hum. Evol.* **51**, 113 (2006). doi: 10.1016/j.jhevol.2006.01.007; pmid: 16563467
26. B. Senut, C. Tardieu, Functional aspects of Plio-Pleistocene hominid limb bones: Implications for taxonomy and phylogeny, in *Ancestors: The Hard Evidence*, E. Delson, Ed. (Alan R. Liss, New York, 1985), pp. 193–201.

27. J. Dugan, T. W. Holliday, Utility of the lateral meniscal notch in distinguishing hominin taxa. *J. Hum. Evol.* **57**, 773 (2009). doi: 10.1016/j.jhevol.2009.07.006; pmid: 19878967
28. Pronation of the foot is a triplanar motion (eversion, abduction, and dorsiflexion occurring simultaneously) and is a normal function of bipedal foot mechanics in order to absorb ground reaction forces and accommodate uneven substrates. It converts the foot from a rigid structure at heel strike to a more mobile one at midstance. Hyperpronation is poorly defined in a clinical sense, because there is no distinct cutoff between those that excessively pronate and those that do not. However, here we define it as continued pronation into the part of stance phase when the foot should be resupinating (usually at the later part of midstance and during the entire propulsive phase). Extended (timing-wise) pronation is caused both by the magnitude of pronation (in degrees) that occurs as a result of the large pronatory torque generated by contacting the ground on a varus heel and forefoot, and the timing of foot motion. Because of the excessive motion occurring at the subtalar, midtarsal, and tarsometatarsal joints, the foot fails to resupinate at late stance and pushoff
29. D. L. Gebo, Plantigrady and foot adaptation in African apes: Implications for hominid origins. *Am. J. Phys. Anthropol.* **89**, 29 (1992). doi: 10.1002/ajpa.1330890105; pmid: 1530061
30. H. Eftman, J. Manter, Chimpanzee and human feet in bipedal walking. *Am. J. Phys. Anthropol.* **20**, 69 (1935). doi: 10.1002/ajpa.1330200109
31. E. Vereecke, K. D'Août, D. De Clercq, L. Van Elsacker, P. Aerts, Dynamic plantar pressure distribution during terrestrial locomotion of bonobos (*Pan paniscus*). *Am. J. Phys. Anthropol.* **120**, 373 (2003). doi: 10.1002/ajpa.10163; pmid: 12627532
32. C. O. Lovejoy, B. Latimer, G. Suwa, B. Asfaw, T. D. White, Combining prehension and propulsion: The foot of *Ardipithecus ramidus*. *Science* **326**, 72e1-e8 (2009).
33. K. D. Gross *et al.*, Varus foot alignment and hip conditions in older adults. *Arthritis Rheum.* **56**, 2993 (2007). doi: 10.1002/art.22850; pmid: 17763430
34. K. G. Holt, J. Hamill, Running injuries and treatment: A dynamic approach, in *Rehabilitation of the Foot and Ankle*, G. J. Sammarco, Ed. (Mosby, St. Louis, MO, 1995), pp. 241–258.
35. L. Wong, A. Hunt, J. Burns, J. Crosbie, Effect of foot morphology on center-of-pressure excursion during barefoot walking. *J. Am. Podiatr. Med. Assoc.* **98**, 112 (2008). pmid: 18347119
36. T. C. Michaud, The foot: Hyperpronation and hypopronation, in *Functional Soft-Tissue Examination and Treatment by Manual Methods*, W. I. Hammer, Ed. (Jones and Bartlett, Sudbury, MA, 2005), pp. 399–426.
37. K. A. Kirby, Subtalar joint axis location and rotational equilibrium theory of foot function. *J. Am. Podiatr. Med. Assoc.* **91**, 465 (2001). pmid: 11679628
38. M. B. Bennett, R. F. Ker, The mechanical properties of the human subcalcaneal fat pad in compression. *J. Anat.* **171**, 131 (1990). pmid: 2081699
39. T. J. Ozounian, M. J. Shereff, In vitro determination of midfoot motion. *Foot Ankle* **10**, 140 (1989). doi: 10.1177/107110078901000305; pmid: 2613125
40. J. M. DeSilva, Revisiting the “midtarsal break.” *Am. J. Phys. Anthropol.* **141**, 245 (2010). pmid: 19672845
41. C. V. Ward, W. H. Kimbel, D. C. Johanson, Complete fourth metatarsal and arches in the foot of *Australopithecus afarensis*. *Science* **331**, 750 (2011). doi: 10.1126/science.1201463; pmid: 21311018
42. D. Tiberio, The effect of excessive subtalar joint pronation on patellofemoral mechanics: A theoretical model. *J. Orthop. Sports Phys. Ther.* **9**, 160 (1987). pmid: 18797010
43. S. Khamis, Z. Yizhar, Effect of feet hyperpronation on pelvic alignment in a standing position. *Gait Posture* **25**, 127 (2007). doi: 10.1016/j.gaitpost.2006.02.005; pmid: 16621569
44. C. M. Powers, R. Maffucci, S. Hampton, Rearfoot posture in subjects with patellofemoral pain. *J. Orthop. Sports Phys. Ther.* **22**, 155 (1995). pmid: 8535473
45. B. A. Rothbart, L. Estabrook, Excessive pronation: A major biomechanical determinant in the development of chondromalacia and pelvic lists. *J. Manipulative Physiol. Ther.* **11**, 373 (1988). pmid: 2976805
46. J. J. Eng, M. R. Pierrynowski, Evaluation of soft foot orthotics in the treatment of patellofemoral pain syndrome. *Phys. Ther.* **73**, 62, discussion 68 (1993). pmid: 8421719
47. M. R. Bennett *et al.*, Early hominin foot morphology based on 1.5-million-year-old footprints from Ileret, Kenya. *Science* **323**, 1197 (2009). doi: 10.1126/science.1168132; pmid: 19251625
48. R. H. Crompton *et al.*, Human-like external function of the foot, and fully upright gait, confirmed in the 3.66 million year old Laetoli hominin footprints by topographic statistics, experimental footprint-formation and computer simulation. *J. R. Soc. Interface* **9**, 707 (2012). doi: 10.1098/rsif.2011.0258; pmid: 21775326
49. B. Latimer, C. O. Lovejoy, Hallucal tarsometatarsal joint in *Australopithecus afarensis*. *Am. J. Phys. Anthropol.* **82**, 125 (1990). doi: 10.1002/ajpa.1330820202; pmid: 2360609
50. H. M. McHenry, L. R. Berger, Body proportions of *Australopithecus afarensis* and *A. africanus* and the origin of the genus *Homo*. *J. Hum. Evol.* **35**, 1 (1998). doi: 10.1006/jhevol.1997.0197; pmid: 9680464
51. D. J. Green, A. D. Gordon, B. G. Richmond, Limb-size proportions in *Australopithecus afarensis* and *Australopithecus africanus*. *J. Hum. Evol.* **52**, 187 (2007). doi: 10.1016/j.jhevol.2006.09.001; pmid: 17049965
52. J. T. Stern Jr., R. L. Susman, The locomotor anatomy of *Australopithecus afarensis*. *Am. J. Phys. Anthropol.* **60**, 279 (1983). doi: 10.1002/ajpa.1330600302; pmid: 6405621
53. R. Wunderlich, thesis, State University of New York at Stony Brook, Stony Brook, NY (1999).

Acknowledgments: We thank the South African Heritage Resource agency for the permits to work at the Malapa site; the Nash family for granting access to the Malapa site and continued support of research on their reserve; the South African Department of Science and Technology and the African Origins Platform (AOP), the South African National Research Foundation, the Evolutionary Studies Institute, the University

of the Witwatersrand, the University of the Witwatersrand's Vice Chancellor's Discretionary Fund, the National Geographic Society, the Leakey Foundation, the Palaeontologica Scientifica Trust, the Andrew W. Mellon Foundation, the Ford Foundation, the U.S. Diplomatic Mission to South Africa, the French Embassy of South Africa, the A.H. Schultz Foundation, Boston University, Duke University, a Ray A. Rothrock '77 Fellowship and International Research Travel Assistance Grant of Texas A&M University, and the Oppenheimer and Ackerman families and Sir Richard Branson for funding; the University of the Witwatersrand's Schools of Geosciences and Anatomical Sciences and the Bernard Price Institute for Palaeontology for support and facilities; the Gauteng Government, Gauteng Department of Agriculture, Conservation and Environment and the Cradle of Humankind Management Authority; and our respective universities for ongoing support. We thank the VIP lab of the Palaeosciences Centre and the Microfocus X-ray CT facility of the Palaeosciences Centre at Wits; and for funding these facilities, we thank the University of the Witwatersrand Office of Research and the National Research Foundation Strategic Research Infrastructure Grant and AOP funding programs. For access to comparative specimens, we thank E. Mbua, P. Kiura, V. Iminjili, and the National Museums of Kenya; A. Kwekason, P. Mserewa, and the Tanzania Commission for Science and Technology; B. Billings, Fossil Primate Access Advisory and the School of Anatomical Sciences at the University of the Witwatersrand; S. Potze, L. C. Kgsi, and the Ditsong Museum; Y. Haile-Selassie, L. Jellema, and the Cleveland Museum of Natural History; J. Chupasko and the Harvard Museum of Comparative Zoology; D. Pilbeam, M. Morgan, O. Herschensohn, J. Rousseau, and the Harvard Museum of Archeology and Ethnology; E. Westwig and the American Museum of Natural History; M. Wopoff and the Department of Anthropology at the University of Michigan; and O. Lovejoy (Kent State University). For technical and material support, we thank Duke University and the University of Zurich 2009 and 2010 Field Schools. Numerous individuals have been involved in the ongoing preparation and excavation of these fossils, including C. Dube, C. Kemp, M. Kgsi, M. Lunguza, J. Malaza, G. Mokoma, P. Mukanela, T. Nemyhundi, M. Ngcamphalala, S. Jirah, S. Tshabalala, and C. Yates. Other individuals who have given significant support to this project include B. de Klerk, W. Lawrence, C. Steininger, B. Kuhn, L. Pollarolo, J. Kretzen, D. Conforti, J. McCaffery, C. Dlamini, H. Visser, R. McCrae-Samuel, B. Nkosi, B. Louw, L. Backwell, F. Thackeray, and M. Peltier. J. Smilg facilitated medical CT scanning of the specimens. The *Au. sediba* specimens are archived at the Evolutionary Studies Institute at the University of the Witwatersrand. All data used in this study are available upon request, including access to the original specimens, by bona fide scientists.

Supplementary Materials

www.sciencemag.org/content/340/6129/1232999/suppl/DC1
Materials and Methods

Supplementary Text

Figs. S1 to S15

Tables S1 to S3

References (54–78)

20 November 2012; accepted 13 March 2013

10.1126/science.1232999

Support the sciences. **Get rewarded.**

Show your AAAS pride and reward yourself with the new AAAS Platinum Advantage Rewards Card from NASA Federal Credit Union.

Apply now and get
10,000 bonus points!

Go to nasafcu.com/AAASpromo



Get **10,000 bonus points** if you sign up for a card and spend \$3,000 within 90 days of account opening.

Learn more at
nasafcu.com/AAASpromo.

Subject to credit approval.
Membership in AAAS and NASA FCU is required.
NASA FCU is federally insured by NCUA.



Experimental Observation of the Quantum Anomalous Hall Effect in a Magnetic Topological Insulator

Cui-Zu Chang,^{1,2*} Jinsong Zhang,^{1*} Xiao Feng,^{1,2*} Jie Shen,^{2*} Zuocheng Zhang,¹ Minghua Guo,¹ Kang Li,² Yunbo Ou,² Pang Wei,² Li-Li Wang,² Zhong-Qing Ji,² Yang Feng,¹ Shuaihua Ji,¹ Xi Chen,¹ Jinfeng Jia,¹ Xi Dai,² Zhong Fang,² Shou-Cheng Zhang,³ Ke He,^{2†} Yayu Wang,^{1†} Li Lu,² Xu-Cun Ma,² Qi-Kun Xue^{1†}

The quantized version of the anomalous Hall effect has been predicted to occur in magnetic topological insulators, but the experimental realization has been challenging. Here, we report the observation of the quantum anomalous Hall (QAH) effect in thin films of chromium-doped (Bi,Sb)₂Te₃, a magnetic topological insulator. At zero magnetic field, the gate-tuned anomalous Hall resistance reaches the predicted quantized value of h/e^2 , accompanied by a considerable drop in the longitudinal resistance. Under a strong magnetic field, the longitudinal resistance vanishes, whereas the Hall resistance remains at the quantized value. The realization of the QAH effect may lead to the development of low-power-consumption electronics.

The quantum Hall effect (QHE), a quantized version of the Hall effect (1), was observed in two-dimensional (2D) electron systems more than 30 years ago (2, 3). In QHE, the Hall resistance, which is the voltage

across the transverse direction of a conductor divided by the longitudinal current, is quantized into plateaus of height h/ve^2 , with h being Planck's constant, e the electron's charge, and v an integer (2) or a certain fraction (3). In these systems, the

QHE is a consequence of the formation of well-defined Landau levels and thus only possible in high-mobility samples and strong external magnetic fields. However, there have been numerous proposals to realize the QHE without applying any magnetic field (4–11). Among these proposals, using the thin film of a magnetic topological insulator (TI) (6–9, 11), a new class of quantum matter discovered recently (12, 13), is one of the most promising routes.

Magnetic field-induced Landau quantization drives a 2D electron system into an insulating phase that is topologically different from the vacuum (14, 15); as a consequence, dissipationless states appear at sample edges. The topologically nontrivial electronic structure can also occur in certain 2D insulators with time reversal symmetry (TRS) broken by current loops (4) or by magnetic ordering (6), requiring neither Landau

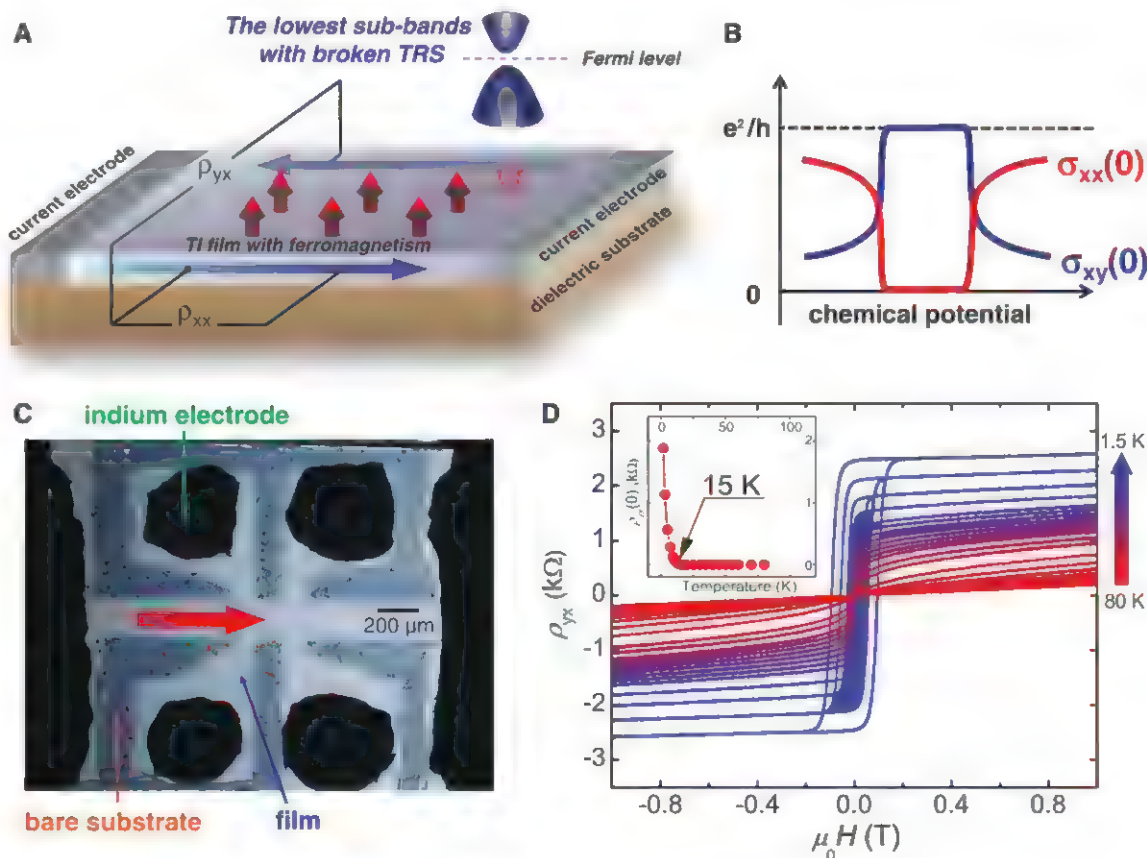
¹State Key Laboratory of Low-Dimensional Quantum Physics, Department of Physics, Tsinghua University, Beijing 100084, China. ²Beijing National Laboratory for Condensed Matter Physics, Institute of Physics, The Chinese Academy of Sciences, Beijing 100190, China. ³Department of Physics, Stanford University, Stanford, CA 94305–4045, USA.

*These authors contributed equally to this work.

†Corresponding author. E-mail: qkxue@mails.tsinghua.edu.cn (Q.-K.X.); kehe@iphy.ac.cn (K.H.); yayuwang@tsinghua.edu.cn (Y.W.)

Fig. 1. Sample structure and properties. (A)

A schematic drawing depicting the principle of the QAH effect in a TI thin film with ferromagnetism. The magnetization direction (M) is indicated by red arrows. The chemical potential of the film can be controlled by a gate voltage applied on the back side of the dielectric substrate. (B) A schematic drawing of the expected chemical potential dependence of zero field σ_{xx} [$\sigma_{xx}(0)$, in red] and σ_{xy} [$\sigma_{xy}(0)$, in blue] in the QAH effect. (C) An optical image of a Hall bar device made from a $\text{Cr}_{0.15}(\text{Bi}_{0.1}\text{Sb}_{0.9})_{1.85}\text{Te}_3$ film. The red arrow indicates the current flow direction during the measurements. The light gray areas are the remained film, and the dark gray areas are bare substrate with the film removed. The black areas are the attached indium electrodes. (D) Magnetic field dependence of ρ_{yx} curves of the $\text{Cr}_{0.15}(\text{Bi}_{0.1}\text{Sb}_{0.9})_{1.85}\text{Te}_3$ film measured at different temperatures (from 80 K to 1.5 K). The inset shows the temperature dependence of zero field ρ_{yx} , which indicates a Curie temperature of ~ 15 K.



levels nor an external magnetic field. This type of QHE induced by spontaneous magnetization is considered the quantized version of the conventional (nonquantized) anomalous Hall effect (AHE) discovered in 1881 (16). The quantized Hall conductance is directly given by a topological characteristic of the band structure called the first Chern number. Such insulators are called Chern insulators.

One way to realize a Chern insulator is to start from a time-reversal-invariant TI. These materials, whose topological properties are induced by spin-orbit coupling, were experimentally realized soon after the theoretical predictions in both 2D and 3D systems (12, 13). Breaking the TRS of a suitable TI (17) by introducing ferromagnetism can naturally lead to the quantum anomalous Hall (QAH) effect (6–9, 11). By tuning the Fermi level of the sample around the magnetically induced energy gap in the density of states, one is expected to observe a plateau of Hall conductance (σ_{xy}) of e^2/h and a vanishing longitudinal conductance (σ_{xx}) even at zero magnetic field [figure 14 of (7) and Fig. 1, A and B].

The QAH effect has been predicted to occur by Mn doping of the 2D TI realized in HgTe quantum wells (8); however, an external magnetic field was still required to align the Mn moments in order to realize the QAH effect (18). As proposed in (9), due to the van Vleck mechanism doping the Bi_2Te_3 family TIs with isovalent 3d magnetic ions can lead to a ferromagnetic insulator ground state and, for thin film systems, this will further induce the QAH effect if the magnetic exchange field is perpendicular to the plane and overcomes the semiconductor gap. Here, we investigate thin films of $\text{Cr}_{0.15}(\text{Bi}_{0.1}\text{Sb}_{0.9})_{1.85}\text{Te}_3$ (19, 20) with a thickness of 5 quintuple layers (QL), which are grown on dielectric SrTiO_3 (111) substrates by molecular beam epitaxy (MBE) (20, 21) (fig. S1). With this composition, the film is nearly charge neutral so that the chemical potential can be fine-tuned to the electron- or hole-conductive regime by a positive or negative gate voltage, respectively, applied on the backside of the SrTiO_3 substrate (20). The films are manually cut into a Hall bar configuration (Fig. 1C) for transport measurements. Varying the width (from 50 μm to 200 μm) and the aspect ratio (from 1:1 to 2:1) of the Hall bar does not influence the result. Figure 1D displays a series of measurements, taken at different temperatures, of the Hall resistance (ρ_{yx}) of the sample in Fig. 1C, as a function of the magnetic field ($\mu_0 H$). At high temperatures, ρ_{yx} exhibits linear magnetic field dependence due to the ordinary Hall effect (OHE). The film mobility is $\sim 760 \text{ cm}^2/\text{Vs}$, as estimated from the measured longitudinal sheet resistance (ρ_{xx}) and the carrier density determined from the OHE. The value is much enhanced compared with the samples in our previous study (20, 21), but still much lower than that necessary for QHE (2, 3). With decreasing temperature, ρ_{yx} develops a hysteresis loop characteristic of the AHE, induced by the ferro-

magnetic order in the film (22). The square-shaped loop with large coercivity ($H_c = 970$ Oersted at 1.5 K) indicates a long-range ferromagnetic order with out-of-plane magnetic anisotropy. The Curie temperature is estimated to be ~ 15 K (Fig. 1D, inset) from the temperature dependence of the zero field ρ_{yx} that reflects spontaneous magnetization of the film.

Figure 2, A and C, shows the magnetic field dependence of ρ_{yx} and ρ_{xx} , respectively, measured at $T = 30$ mK at different bottom-gate voltages (V_g s). The shape and coercivity of the ρ_{yx} hysteresis loops (Fig. 2A) vary little with V_g , thanks to the robust ferromagnetism probably

mediated by the van Vleck mechanism (9, 20). In the magnetized states, ρ_{yx} is nearly independent of the magnetic field, suggesting perfect ferromagnetic ordering and charge neutrality of the sample. On the other hand, the AH resistance (height of the loops) changes dramatically with V_g , with a maximum value of h/e^2 around $V_g^0 = -1.5$ V. The magnetoresistance (MR) curves (Fig. 2C) exhibit the typical shape for a ferromagnetic material: two sharp symmetric peaks at the coercive fields.

The V_g dependences of ρ_{yx} and ρ_{xx} at zero field [labeled $\rho_{yx}(0)$ and $\rho_{xx}(0)$, respectively] are plotted in Fig. 2B. The most important obser-

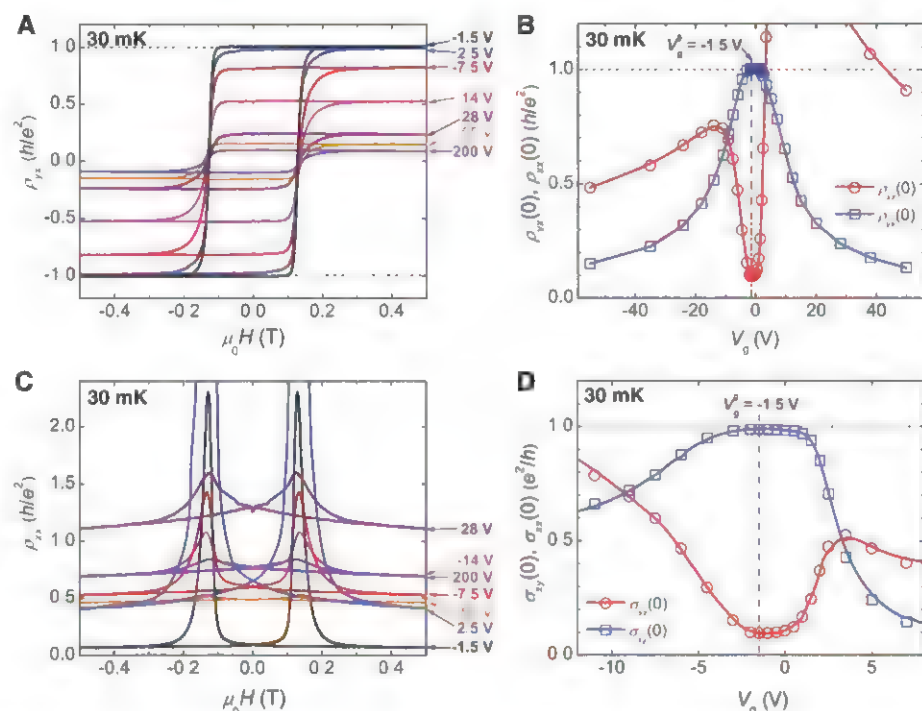


Fig. 2. The QAH effect measured at 30 mK. (A) Magnetic field dependence of ρ_{yx} at different V_g s. (B) Dependence of $\rho_{yx}(0)$ (empty blue squares) and $\rho_{xx}(0)$ (empty red circles) on V_g . (C) Magnetic field dependence of ρ_{xx} at different V_g s. (D) Dependence of $\sigma_{xy}(0)$ (empty blue squares) and $\sigma_{xx}(0)$ (empty red circles) on V_g . The vertical purple dashed-dotted lines in (B) and (D) indicate the V_g for V_g^0 . A complete set of the data is shown in fig. S3.

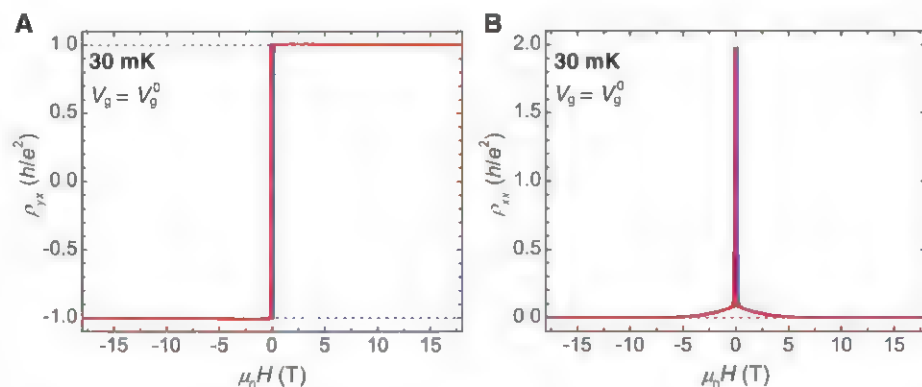


Fig. 3. The QAH effect under strong magnetic field measured at 30 mK. (A) Magnetic field dependence of ρ_{yx} at V_g^0 . (B) Magnetic field dependence of ρ_{xx} at V_g^0 . The blue and red lines in (A) and (B) indicate the data taken with increasing and decreasing fields, respectively.

vation here is that the zero field Hall resistance exhibits a distinct plateau with the quantized value h/e^2 , which is centered around the gate voltage $V_g = 1.5$ V. This observation constitutes the discovery of the QAH effect. According to the OHE measurements, the maximum of ρ_{yx} is always located at the charge neutral point (V_g^0) (20, 21). Accompanying the quantization in ρ_{yx} , the longitudinal resistance $\rho_{xx}(0)$ exhibits a sharp dip down to $0.098 h/e^2$. The $\rho_{yx}(0)/\rho_{xx}(0)$ ratio corresponds to a Hall angle of 84.4° . For comparison with theory, we transform $\rho_{yx}(0)$ and $\rho_{xx}(0)$ into sheet conductance through the relations $\sigma_{xy} = \rho_{yx}/(\rho_{yx}^2 + \rho_{xx}^2)$ and $\sigma_{xx} = \rho_{xx}/(\rho_{yx}^2 + \rho_{xx}^2)$ and plot them in Fig. 2D. Around V_g^0 , $\sigma_{xy}(0)$ has a notable plateau at $0.987 e^2/h$, whereas $\sigma_{xx}(0)$ has a dip down to $0.096 e^2/h$, similar to the behavior of the corresponding resistances.

In addition to the observation of the QAH effect, the MR ratio $\{[\rho_{xx}(H_c) - \rho_{xx}(0)]/\rho_{xx}(0)\}$ is dramatically enhanced at V_g^0 to a surprisingly large value of 2251% (Fig. 2C and fig. S3). The huge MR can also be understood in terms of the QAH phenomenology. In the magnetized QAH state, the existence of dissipationless edge state leads to a nearly vanishing ρ_{xx} (21). At the coer-

cive field, the magnetization reversal of a QAH system leads to a quantum phase transition between two QH states (7) via a highly dissipative phase with a large ρ_{xx} , although the exact mechanism may be complex (23). The huge MR thus reflects the distinct difference in transport properties between an ordinary insulator and a QAH insulator.

For a QH system (2, 3), when the Fermi level lies in the gap between Landau levels, σ_{xy} reaches a plateau at ve^2/h and σ_{xx} drops to zero. If the system contains nonlocalized dissipative conduction channels, σ_{xx} has a nonzero value, whereas σ_{xy} deviates slightly from the quantized plateau (24). For a QAH system, only one σ_{xy} plateau of e^2/h appears at zero field when the Fermi level falls in the mobility edges around the magnetically induced gap (Fig. 1B). The observations of $\sigma_{xy}(0) = e^2/h$ plateau and the dip in $\sigma_{xx}(0)$ near the charge neutral point in Fig. 2D thus agree with the theoretical prediction for a QAH system with residual dissipative channels. The channels are expected to vanish completely at zero temperature (11, 24).

To confirm the QAH effect observed in Fig. 2, we apply a magnetic field, aiming to localize all

possible dissipative states in the sample. Figure 3, A and B, displays the magnetic field dependence of ρ_{yx} and ρ_{xx} of the same sample as in Fig. 2, respectively. Except for the large MR at H_c , increasing the field further suppresses ρ_{xx} toward zero. Above 10 T, ρ_{xx} vanishes completely, corresponding to a perfect QH state. It is noteworthy that the increase in ρ_{xx} from zero (above 10 T) to $0.098 h/e^2$ (at zero field) is very smooth and ρ_{yx} remains at the quantized value h/e^2 , which indicates that no quantum phase transition occurs, and the sample stays in the same QH phase as the field sweeps from 10 T to zero field. Therefore, the complete quantization above 10 T can only be attributed to the same QAH state at zero field.

The observation of the QAH effect is further supported by the behavior with varying temperatures. In Fig. 4A, we show V_g dependences of $\rho_{yx}(0)$ and $\rho_{xx}(0)$ measured at different temperatures in another sample with the same growth conditions. The $\rho_{yx}(0)$ always exhibits a single maximum, with the peak value considerably suppressed by increasing temperatures, accompanied by the disappearance of the dip in $\rho_{xx}(0)$. The $\sigma_{xx}(0)$ extracted from these measurements (in logarithmical scale) (Fig. 4B) exhibits a temperature dependence similar to that in integer QH systems: The drop of σ_{xx} is at first rapid, resulting from the freezing of the thermal activation mechanism, and then becomes much slower when the temperature is below 1 K. It can be attributed to variable range hopping (VRH) (24), but its exact mechanism remains unknown. Similar to the QHE, zero field σ_{xx} is expected to decrease to zero at sufficiently low temperature. In Fig. 4C, we plot the relation between $\sigma_{xx}(0)$ and $\delta\sigma_{xy}(0)$ ($\delta\sigma_{xy} = e^2/h - \sigma_{xy}$, which reflects the contribution of dissipative channels). A power law relation $\delta\sigma_{xy} \propto \sigma_{xx}^\alpha$ with $\alpha \sim 1.55$ is obtained. For a ferromagnetic insulator in the VRH regime, the AH conductivity is related to the longitudinal conductivity through $\sigma_{AH} = A\sigma_{xx}^\alpha$ [the power α is ~ 1.6 ; the prefactor A can be positive or negative depending on materials (22)]. The above result can thus be qualitatively understood within the VRH framework.

Our results demonstrate the realization of the QAH effect in magnetic TIs. Compared with QHE systems, all the samples studied in this work have a rather low mobility ($<1000 \text{ cm}^2/\text{Vs}$). Such robust QAH states not only reflect the topological character of TIs but also make the QAH systems readily achievable in experiments. Because the realization of the QAH effect and dissipationless edge states does not require any magnetic field, the present work paves a path for developing low-power-consumption, topological quantum electronic and spintronic devices.

References and Notes

1. E. H. Hall, *Am. J. Math.* **2**, 287 (1879)
2. K. Klitzing, G. Dorda, M. Pepper, *Phys. Rev. Lett.* **45**, 494 (1980).
3. D. C. Tsui, H. L. Stormer, A. C. Gossard, *Phys. Rev. Lett.* **48**, 1559 (1982).

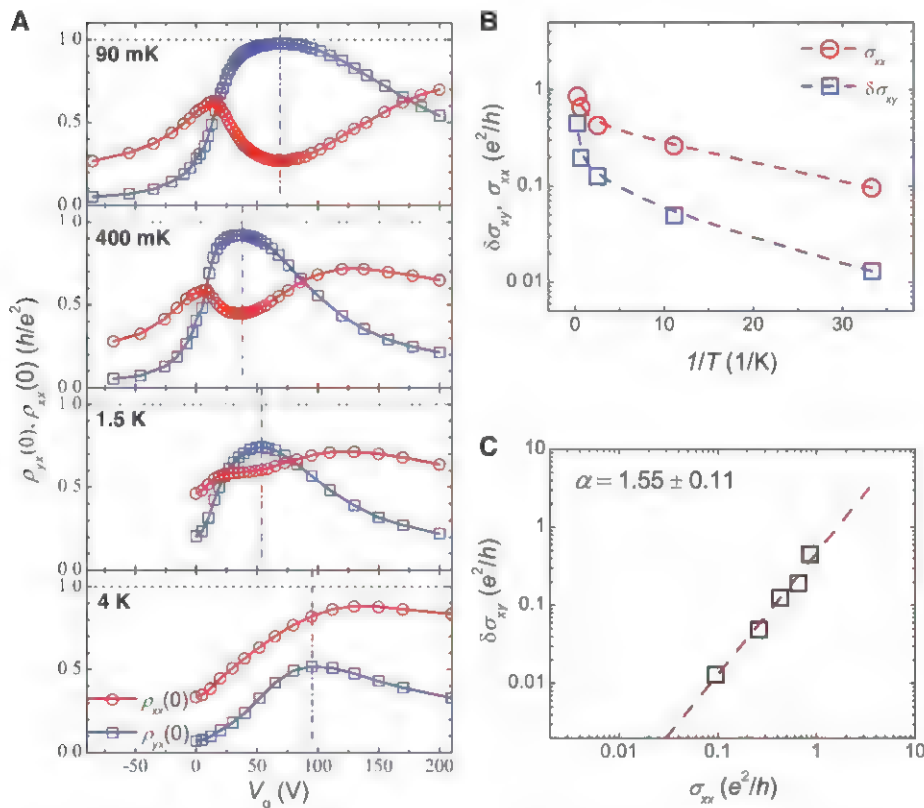


Fig. 4. Temperature dependence of the QAH effect on a different sample. (A) V_g -dependent $\rho_{yx}(0)$ and $\rho_{xx}(0)$ measured at 90 mK, 400 mK, 1.5 K, and 4 K, respectively. The vertical purple dashed-dotted line indicates the V_g for V_g^0 . The variation in the position and width of the $\rho_{yx}(0)$ peak at different temperatures results from the change in substrate dielectric properties induced by temperature and charging cycles. (B) Dependences of logarithmically scaled $\sigma_{xx}(0)$ (empty red circles) and $\delta\sigma_{xy}(0)$ (empty blue squares) at V_g^0 on inverse temperature. The dashed lines are a guide to the eye. (C) The relation between $\delta\sigma_{xy}(0)$ and $\sigma_{xx}(0)$ at V_g^0 in double logarithmic scale. The red dashed line indicates the fit with a power law $\delta\sigma_{xy} \propto \sigma_{xx}^\alpha$ with $\alpha \sim 1.55$.

4. F. D. M. Haldane, *Phys. Rev. Lett.* **61**, 2015 (1988).
5. M. Onoda, N. Nagaosa, *Phys. Rev. Lett.* **90**, 206601 (2003).
6. X. L. Qi, Y. S. Wu, S. C. Zhang, *Phys. Rev. B* **74**, 085308 (2006).
7. X. L. Qi, T. L. Hughes, S. C. Zhang, *Phys. Rev. B* **78**, 195424 (2008).
8. C. X. Liu, X. L. Qi, X. Dai, Z. Fang, S. C. Zhang, *Phys. Rev. Lett.* **101**, 146802 (2008).
9. R. Yu *et al.*, *Science* **329**, 61 (2010).
10. Z. Qiao *et al.*, *Phys. Rev. B* **82**, 161414 (2010).
11. K. Nomura, N. Nagaosa, *Phys. Rev. Lett.* **106**, 166802 (2011).
12. M. Z. Hasan, C. L. Kane, *Rev. Mod. Phys.* **82**, 3045 (2010).
13. X. L. Qi, S. C. Zhang, *Rev. Mod. Phys.* **83**, 1057 (2011).
14. R. B. Laughlin, *Phys. Rev. B* **23**, 5632 (1981).
15. D. J. Thouless, M. Kohmoto, M. P. Nightingale, M. Nijs, *Phys. Rev. Lett.* **49**, 405 (1982).
16. E. H. Hall, *Philos. Mag.* **12**, 157 (1881).
17. H. Zhang *et al.*, *Nat. Phys.* **5**, 438 (2009).
18. H. Buhmann, *Bulletin of the American Physical Society* **57**(1), P27.1 (2012), <http://meetings.aps.org/bnk/BAPS.2012.MAR.P27.1>.
19. J. Zhang *et al.*, *Nat. Commun.* **2**, 574 (2011).
20. C.-Z. Chang *et al.*, *Adv. Mater.* **25**, 1065 (2013).
21. See supplementary materials.
22. N. Nagaosa, J. Sinova, S. Onoda, A. H. MacDonald, N. P. Ong, *Rev. Mod. Phys.* **82**, 1539 (2010).
23. J. G. Checkelsky, J. Ye, Y. Onose, Y. Iwasa, Y. Tokura, *Nat. Phys.* **8**, 729 (2012).
24. B. Jeckelmann, B. Jeanneret, *Rep. Prog. Phys.* **64**, 1603 (2001).

Acknowledgments: The authors thank X. Xie, C. Yang, and X.-L. Qi for stimulating discussions and X.-C. Hong and S.-Y. Li for help with experiments. We are grateful to the National Science Foundation and Ministry of Science and Technology of China and the Chinese Academy of Sciences for financial support.

Supplementary Materials

www.sciencemag.org/cgi/content/full/science.1234414/DC1

Materials and Methods
Supplementary Text
Figs. S1 to S5

References (25, 26)

21 December 2012; accepted 1 March 2013

Published online 14 March 2013;

10.1126/science.1234414

Evidence for Two Distinct Populations of Type Ia Supernovae

Xiaofeng Wang,^{1,2*} Lifan Wang,^{2,3} Alexei V. Filippenko,⁴ Tianmeng Zhang,⁵ Xulin Zhao¹

Type Ia supernovae (SNe Ia) have been used as excellent standardizable candles for measuring cosmic expansion, but their progenitors are still elusive. Here, we report that the spectral diversity of SNe Ia is tied to their birthplace environments. We found that those with high-velocity ejecta are substantially more concentrated in the inner and brighter regions of their host galaxies than are normal-velocity SNe Ia. Furthermore, the former tend to inhabit larger and more luminous hosts. These results suggest that high-velocity SNe Ia likely originate from relatively younger and more metal-rich progenitors than do normal-velocity SNe Ia and are restricted to galaxies with substantial chemical evolution.

Type Ia supernovae (SNe Ia) are among the most energetic and relatively uniform stellar explosions in the universe and were used to discover its accelerating expansion (1, 2). They are thought to originate from a thermonuclear explosion of an accreting carbon-oxygen (C-O) white dwarf (WD) near the Chandrasekhar mass limit [$M_{\text{Ch}} \approx 1.4$ solar mass (M_{\odot})] in a close binary system (3, 4). Two competing scenarios have been proposed for the progenitor systems: single-degenerate (SD) (5, 6) and double-degenerate (DD) models (4, 7). In the former, the mass-donating star could be a main-sequence (MS)/subgiant star (8), a red-giant star (RG) (9), or even a helium star (10, 11), whereas it is another WD in the latter scenario (4, 7). Recent results suggest that both scenarios are possible (12–18).

There is increasing evidence for spectral diversity among SNe Ia. Of particular interest are those showing higher expansion velocities as inferred from the blueshifted Si II 615-nm feature in optical spectra (19). These fast-expanding SNe Ia also generally exhibit a steep Si II temporal

velocity gradient (20). This spectral difference in velocity or velocity evolution of the ejecta has been proposed to be a geometric effect of an asymmetric explosion (21, 22). Given a common origin for SNe Ia having different ejecta velocities, they should be found in similar stellar environments. This can be tested by examining SN positions in their hosts, the surface brightness at these locations, and the properties of their hosts.

We conducted such an analysis with a well-defined SN sample having 188 SNe Ia (supplementary text S1) from the Lick Observatory Supernova Search (LOSS) (23). The SN Ia sample consists of 123 “Branch-normal” (spectroscopically normal) objects (24), 30 peculiar ones of the SN 1991bg variety (25), 13 peculiar ones such as SN 1991T (26, 27), and 7 peculiar ones such as SN 2002cx (28), with respective fractions of 65.4, 16.0, 6.9, and 3.7% (table S1). There are 15 SNe Ia (8.0% of all) that cannot be subclassified because of an absence of early-time spectra. We concentrated on the Branch-normal SNe Ia, which are thought to be relatively uniform. We obtained the main parameters of the host galaxies from two large online astronomical databases: the NASA/Infrared Processing and Analysis Center (IPAC) Extragalactic Database (NED) (29) and HyperLeda (30).

The location of a SN in its host galaxy can be estimated by the radial distance of the SN from the nucleus (R_{SN}). Assuming that the galaxies are circular disks and only appear to have different major and minor axes because of their inclina-

tion, R_{SN} can be calculated if we know the position angle and the axial ratio of each galaxy. The radius of the galaxy (R_{gal}) is simply the semi-major axis at the 25.0 B -mag arc sec⁻² isophote. The ratio $R_{\text{SN}}/R_{\text{gal}}$ is then the fractional radial distance of the SN. For SNe Ia in elliptical galaxies, no tilt correction is applied because these galaxies can be regarded as spheroids. The typical host galaxy of our sample (fig. S1) has a major axis of about 1.3' to 1.4' and can be measured with a precision of $\sim 0.1'$. This results in a typical uncertainty of ~ 0.05 in the determination of $R_{\text{SN}}/R_{\text{gal}}$.

We measured the velocity of the Si II 615-nm line for 165 SNe Ia (out of 188) by using the published spectral data sets (31–33). We normalized this velocity to the maximum-light value with a series of templates of Si II velocity evolution established from well-observed SNe Ia, with a typical uncertainty of 300 to 400 km s⁻¹ (supplementary text S1 and fig. S2).

It is clear that Branch-normal SNe Ia with $v_{\text{Si II}} < 12,000$ km s⁻¹ [the normal-velocity group (NV)] span a wide radial distribution, occurring at places from the innermost region to about two to three times the optical radius of the entire galaxy. In contrast, those with $v_{\text{Si II}} \geq 12,000$ km s⁻¹ [the high-velocity group (HV)] are rarely found at large galactic radii (Fig. 1B). For example, only 3 out of the 40 HV SNe Ia are detected in regions with $R_{\text{SN}}/R_{\text{gal}} > 0.7$ (two of which are in elliptical galaxies), whereas 14 ± 2 would have been expected at the detection rates of the NV SNe Ia (which are about $34 \pm 5\%$ at $R_{\text{SN}}/R_{\text{gal}} > 0.7$). Such a difference has a statistical significance of about 5σ , highlighting the paucity of HV SNe Ia in outskirts of galaxies. Binning the data in velocity space with an interval of about 2000 km s⁻¹ further shows a correlation between the ejecta velocity of SNe Ia and the locations in their host galaxies (Fig. 1A, gray quadrangles).

To better understand such a birthplace versus ejecta-velocity relation for SNe Ia, it is important to know how the Si II velocity itself is distributed. Most of the sample of Branch-normal SNe Ia clusters at velocities between 10,000 and 12,000 km s⁻¹ (Fig. 1C), with a tail extending up to $\sim 16,000$ km s⁻¹. Such a velocity distribution can be fit by a double-Gaussian model. One com-

¹Department of Physics, Tsinghua University, Beijing 100084, China.

²Mitchell Institute for Fundamental Physics and Astronomy, Texas A&M University, College Station, TX 77843, USA.

³Purple Mountain Observatory, Nanjing, 201008 Jiangsu, China.

⁴Department of Astronomy, University of California, Berkeley, CA 94720–3411, USA. ⁵National Astronomical Observatory of China, Chinese Academy of Sciences, Beijing 100012, China.

*Corresponding author. E-mail: wang_xf@mails.tsinghua.edu.cn

ponent, with a stronger and narrower peak at $10,800 \text{ km s}^{-1}$, is responsible for the NV group, whereas the other component, with a weaker and broader peak at $13,000 \text{ km s}^{-1}$, accounts for the HV group. Adopting a velocity cut of $v_{\text{Si II}} = 12,000 \text{ km s}^{-1}$ to divide these two groups puts 40 SNe Ia in the HV group and 83 in the NV group. Accordingly, we estimate the fraction of the HV population to be 1/3 of the Branch-normal sample and 1/5 to 1/4 of the entire SN Ia sample. The Si II velocity distinction is not sharp between these two groups, so blending could occur to some extent. Nevertheless, this blending is small at larger velocities and will not affect the result that the SNe Ia with higher velocities tend to occur nearer the galaxy centers.

HV SNe Ia show the highest central concentration among the samples, with 90% occurring in regions within $R_{\text{SN}}/R_{\text{gal}} \leq 0.7$; this fraction is 66, 77, and 89% for NV SNe Ia, SNe II, and SNe Ibc, respectively (Fig. 2). The contrast is even more apparent when examining the distribution

toward the galaxy center. We caution, however, that a higher fraction of CC SNe may be missing in the central regions of galaxies during LOSS because of their lower luminosity relative to SNe Ia.

A Kolmogoroff-Smirnoff (K-S) test finds a probability of 0.5% that HV and NV SN Ia groups have a similar radial distribution in galaxies. This probability further decreases to 0.1% if one increases the velocity cut dividing these two groups from 12,000 to $13,000 \text{ km s}^{-1}$. Possible selection effects in the radial distribution have been explored, and none can account for such a significant discrepancy between HV and NV SN Ia groups (supplementary text S2 and fig. S3). Thus, HV SNe Ia have higher metallicities, and their progenitors are therefore less likely to be from the halo population that consists of old, metal-poor stars located far away from the galactic center (34).

Because the radial distances give only a rough estimate of the properties of SN progenitors, more sophisticated methods are necessary to provide

additional constraints. A simple statistic of the “fractional flux” allows a measurement of how SNe are distributed within their hosts (35). This can be achieved by measuring in the host-galaxy images the fraction of total galaxy light contained in pixels fainter than or equal to the light in the pixel at the location of the SN. The “fractional flux” was obtained with the Sloan Digital Sky Survey (SDSS) $u'g'r'$ -band images (36) for 64 “Branch-normal” SNe Ia (39 NV + 25 HV), 102 SNe II, and 39 SNe Ibc of the entire SN sample (supplementary text S3).

The surface brightness of SN II locations has an approximately linear distribution, roughly tracing the distribution of the light in their hosts (Fig. 3). SNe Ibc seem to be more concentrated in brighter regions of the host galaxies, which is consistent with the knowledge that they arise in larger star-forming regions that produce more-massive stars. Of the SN Ia sample, the locations of the HV group and the NV group track their hosts' light differently, with a very low

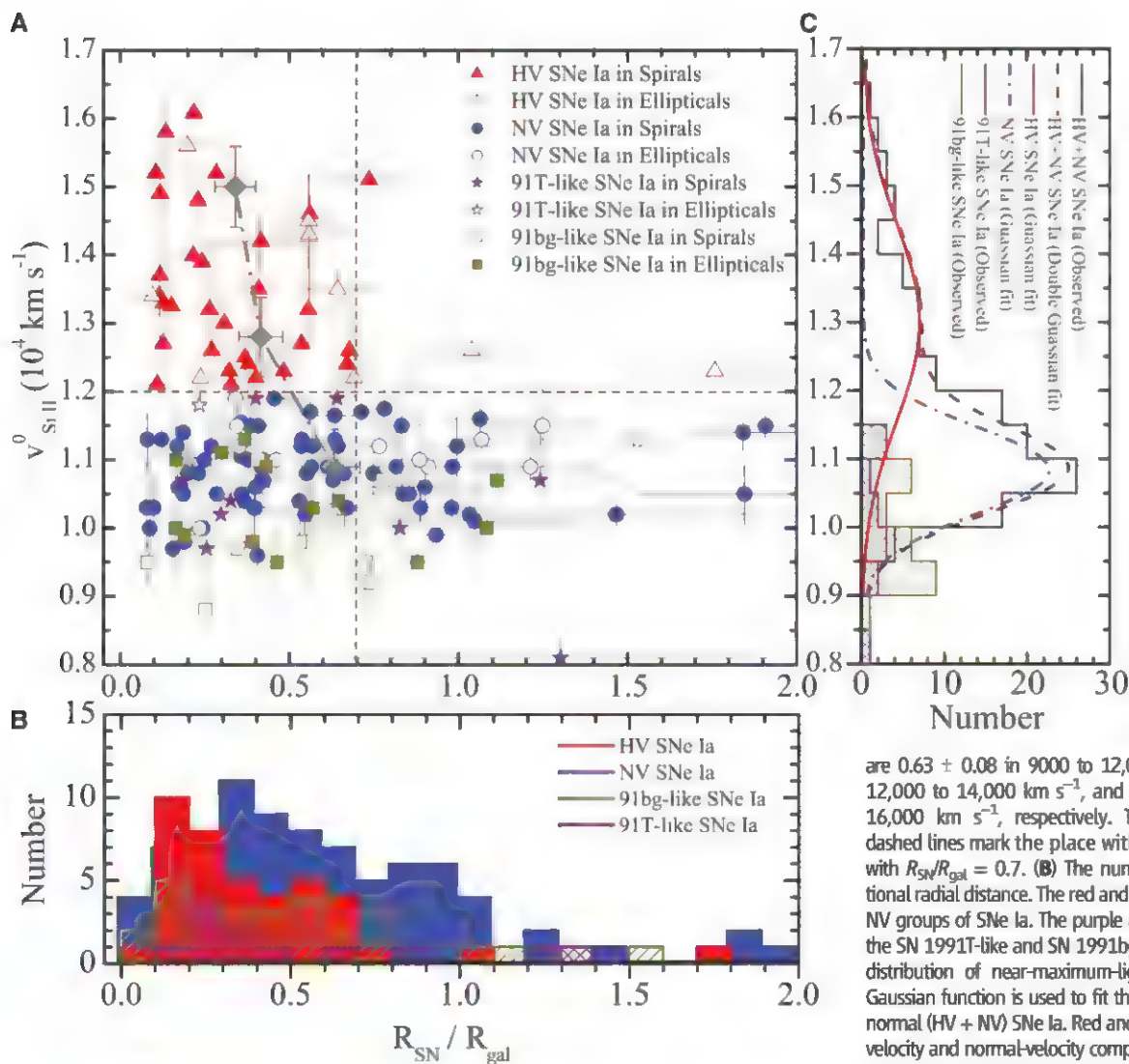


Fig. 1. Relations between the Si II velocity of SNe Ia and the birth location in their host galaxies. (A) The Si II velocity obtained around B-band maximum light ($v_{\text{Si II}}^0$, ordinate) as compared with the fractional radial distance in the host galaxy ($R_{\text{SN}}/R_{\text{gal}}$, abscissa) for 165 SNe Ia. The Branch-normal SNe Ia with $v_{\text{Si II}}^0 \geq 12,000 \text{ km s}^{-1}$ (HV group), those with $v_{\text{Si II}}^0 < 12,000 \text{ km s}^{-1}$ (NV group), SN 1991T-like SNe, and SN 1991bg-like SNe are shown by red triangles, blue circles, purple stars, and dark yellow squares, respectively. The SNe Ia in spiral and elliptical/lenticular galaxies are represented with solid and open symbols, respectively. The gray diamonds show the radial distances averaged in binned velocity space, which

are 0.63 ± 0.08 in 9000 to $12,000 \text{ km s}^{-1}$, 0.42 ± 0.06 in $12,000$ to $14,000 \text{ km s}^{-1}$, and 0.34 ± 0.06 in $\sim 14,000$ to $16,000 \text{ km s}^{-1}$, respectively. The horizontal and vertical dashed lines mark the place with $v_{\text{Si II}} = 12,000 \text{ km s}^{-1}$ and with $R_{\text{SN}}/R_{\text{gal}} = 0.7$. (B) The number distribution of the fractional radial distance. The red and blue areas are for the HV and NV groups of SNe Ia. The purple and dark yellow areas are for the SN 1991T-like and SN 1991bg-like SNe Ia. (C) The number distribution of near-maximum-light Si II velocity. A double Gaussian function is used to fit the distribution of 123 Branch-normal (HV + NV) SNe Ia. Red and blue curves are for the high-velocity and normal-velocity components, with respective peaks centered at $13,000$ and $10,800 \text{ km s}^{-1}$. The black curve represents the combined result of these two components.

probability ($P = 0.04$ in u' , 0.07 in g' , and 0.08 in r') that they come from the same stellar populations. The NV SN Ia locations are apparently fainter than those of CC SNe (Fig. 3); the HV SN Ia distribution, on the other hand, is similar to the CC SN distribution.

The light radii and luminosities of galaxies in the HV sample and the NV sample also differ significantly (Fig. 4). A two-dimensional K-S test gives a probability of 0.5% that they come from the same population. The mean-light radius of the hosts estimated for these two groups is 20.67 ± 0.83 kpc for HV and 16.61 ± 0.67 kpc for NV. The mean absolute K -band magnitudes are -24.53 ± 0.13 mag (HV) and -24.17 ± 0.10 mag (NV), with the HV hosts being, on average, brighter by about 40%. In general, the HV SNe Ia tend to occur in larger and more luminous hosts, and the fraction found in galaxies with $R_{\text{gal}} < 15$ kpc is very low, 15% (versus 46% for the NV counterparts). This difference is not due to an observational bias because the host galaxies of these two groups do not show significantly different distributions in either morphologies or redshifts (supplementary text S4 and figs. S4 and S5).

Our analysis thus reveals substantial differences in the progenitor environments of SNe Ia having different Si II velocities. The HV SNe Ia are much more concentrated in regions close to the galaxy center and in bright regions of their host galaxies and also tend to reside in larger and more luminous hosts relative to the NV group. It is generally accepted that all galaxies (on average) have metallicities that systematically decrease outward from their galactic centers and that their global metallicities increase with galaxy size (39). Higher metallicity is therefore expected for the HV SN Ia progenitor population. Meanwhile, the fact that the surface brightness at HV SN Ia locations roughly traces the light of their host galaxies, as with CC SNe, suggests that the progenitor populations are relatively young. Thus, the HV SN Ia population may have a younger and more metal-rich progenitor system than that of the NV SN Ia population, and a larger initial MS mass of the exploding WD may be expected for the former because of the shorter evolutionary time needed before explosion.

Calculations of stellar evolution show that both stellar mass and metallicity have substantial effects on the nature of C-O WDs that may become progenitors of SNe Ia. The maximum MS mass to form C-O WDs is found to increase dramatically toward higher metallicity (40); stars with MS masses up to 8 to 9 M_{\odot} produce massive WDs ($\sim 1.1 M_{\odot}$) that can reach 1.4 M_{\odot} in a shorter time via mass transfer from a companion star. Thus, the HV SN Ia group might represent the young-population SNe Ia, corresponding to the “prompt” component with short delay times (41, 42), whereas the NV group may belong to the “older” component with long delay times. Five out of the 40 (12.5%) SNe Ia in the HV sample are in elliptical galaxies that are luminous

Fig. 2. A plot of the cumulative fraction of our SN samples (HV SNe Ia, NV SNe Ia, SNe II, and SNe Ibc). The gray solid line represents the distribution of SNe Ia with $v_{\text{Si II}} > 13,000 \text{ km s}^{-1}$.

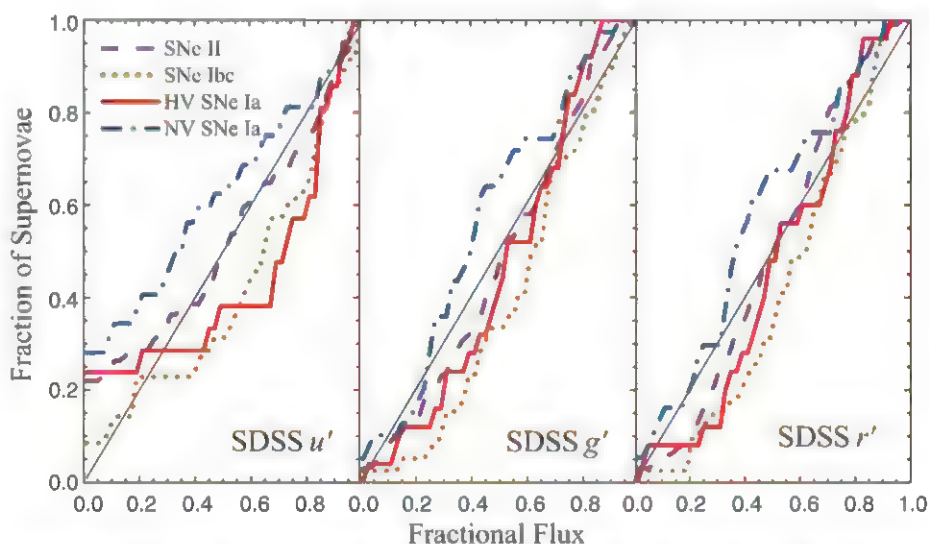
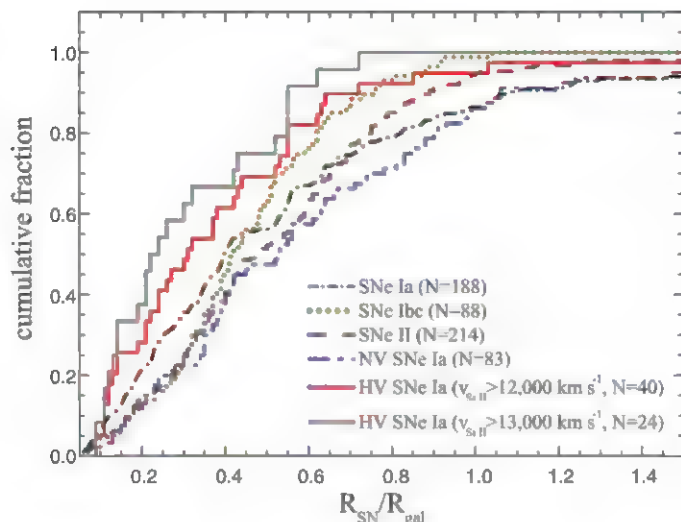


Fig. 3. Histogram distribution of the fractional flux of the host-galaxy light at the location of SN explosions in the u' (left), g' (middle), and r' (right) bands. The diagonal black lines represent the case that the SN progenitors follow exactly the distribution of galaxy light.

(table S1 and fig. S4) and massive. However, among these, some (such as SN 2002dj and SN 2000B) show dust structure and molecular gas (43, 44), which is suggestive of recent or ongoing star formation in them; they do not contradict the conclusion that HV SNe Ia likely arise from young stellar populations.

Having young and metal-rich progenitors may explain the numerous recent detections of circumstellar medium (CSM) signatures among HV SNe Ia. Time-variable absorption features of the Na I doublet (D1 589.6 nm and D2 589.0 nm), which is likely suggestive of changes in CSM ionization due to a variable SN radiation field, have been reported for a few SNe Ia such as SNe 2006X, 2007le, and 1999cl (12, 45, 46). A common feature of these SNe Ia is that they belong to the HV subclass (table S1). Additionally, the velocity structure of the line-of-sight Na I lines provides another possible diagnostic of CSM

around SNe. A trend of blueshifts was found among SNe Ia according to a study of Na I absorption lines of a larger SN sample (13). It was noticed, however, that the SNe Ia with a blueshifted absorption feature generally have higher Si II velocities (47). This evidence is consistent with their systematically redder color around maximum light (perhaps because of additional CSM absorption) relative to the NV population (19) and can be understood in terms of an empirical metallicity dependence of mass outflow (48). At higher metallicity, stars lose more mass and produce stronger outflows than those of their lower-metallicity counterparts. Thus, detection of abundant outflows in the vicinity of the HV SNe Ia is not unexpected.

The higher Si II velocity seen in HV SNe Ia may be related in part to an increase in stellar metallicity. As the metallicity increases in the C+O layer of the exploding WDs, the line-forming

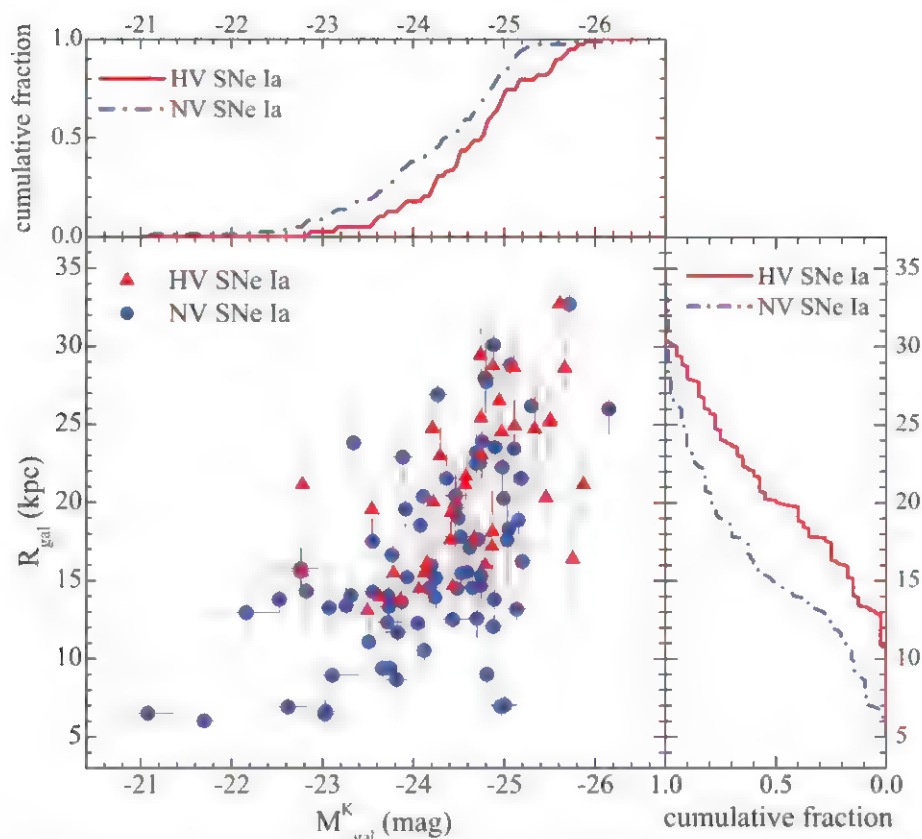


Fig. 4. A comparison of the physical sizes (B -band light radius at 25 mag arcsec $^{-2}$ isophote) and absolute K -band magnitude distributions of the SN hosts. These two parameters have been derived by adopting the mass density (Ω_m) = 0.27, the cosmological constant (Ω_Λ) = 0.73, and the Hubble constant (H_0) = 73 km s $^{-1}$ Mpc $^{-1}$ (37). Foreground galactic absorption corrections (38) have been applied to the absolute magnitudes. In the center, the high-velocity SN Ia hosts are represented as red triangles, and the normal-velocity SN Ia hosts are represented as blue dots. The absolute magnitudes of the hosts are shown on the abscissa, and the lengths of the semimajor axes of the hosts are shown on the ordinate. The plot is then projected to the top and the right, where a histogram is displayed for each host population in each of the dimensions, absolute magnitude, and semimajor axis.

region moves toward shallower parts of the atmosphere because of an increased line opacity, leading to larger line velocities (49). In addition, the high-velocity Si II layers are perhaps formed because of the density increase caused by interaction between the SN ejecta and the material around the exploding WD, which could be an accretion disk or a filled Roche lobe (50). The angular variations in observing such an interacting system may explain the variation of the polarization across the Si II line (51) and its correlation with the ejecta velocity for HV SNe Ia (22). This is consistent with the result that the observed differences in some SNe Ia might be due to a projection effect (21). However, these data and analyses are insensitive to a separate population of NV SNe Ia that is intrinsically different from HV SNe Ia.

The dependence of SN Ia ejecta velocity on progenitor environment could be relevant when using SNe Ia as cosmological yardsticks because the HV and NV populations have different colors around maximum light (19), and their ratio may change with redshift. The observed relative frac-

tion of the HV and NV population might become smaller at great distances because of a decrease in the HV SN Ia rate in low-metallicity environments and the increased difficulty of spectroscopically classifying SNe in the central regions of distant galaxies.

References and Notes

1. A. G. Riess et al., *Astron. J.* **116**, 1009 (1998).
2. S. Perlmutter et al., *Astrophys. J.* **517**, 565 (1999).
3. K. Nomoto, *Astrophys. J.* **253**, 798 (1982).
4. I. Iben Jr., A. V. Tutukov, *Astrophys. J. Suppl. Ser.* **54**, 335 (1984).
5. K. Nomoto, K. Iwamoto, N. Kishimoto, *Science* **276**, 1378 (1997).
6. P. Podsiadlowski, P. Mazzali, P. Lesaffre, Z. Han, F. Förster, *New Astron. Rev.* **52**, 381 (2008).
7. R. F. Webbink, *Astrophys. J.* **277**, 355 (1984).
8. E. P. J. van den Heuvel, D. Bhattacharya, K. Nomoto, S. A. Rappaport, *Astron. Astrophys.* **262**, 97 (1992).
9. U. Munari, A. Renzini, *Astrophys. J.* **397**, L87 (1992).
10. B. Wang, Z. W. Han, *Astron. Astrophys.* **515**, A88 (2010).
11. S.-C. Yoon, N. Langer, *Astron. Astrophys.* **412**, L53 (2003).
12. F. Patat et al., *Science* **317**, 924 (2007).
13. A. Sternberg et al., *Science* **333**, 856 (2011).
14. P. E. Nugent et al., *Nature* **480**, 344 (2011).
15. W. Li et al., *Nature* **480**, 348 (2011).
16. J. Bloom et al., *Astrophys. J.* **744**, L17 (2012).
17. P. Brown et al., *Astrophys. J.* **753**, 22 (2012).
18. B. E. Schaefer, A. Pagnotta, *Nature* **481**, 164 (2012).
19. X. Wang et al., *Astrophys. J.* **699**, L139 (2009).
20. S. Benetti et al., *Astrophys. J.* **623**, 1011 (2005).
21. K. Maeda et al., *Nature* **466**, 82 (2010).
22. J. R. Maund et al., *Astrophys. J.* **725**, L167 (2011).
23. J. Leaman, W. Li, R. Chornock, A. V. Filippenko, *Mon. Not. R. Astron. Soc.* **412**, 1419 (2011).
24. D. Branch, A. Fisher, P. Nugent, *Astron. J.* **106**, 2383 (1993).
25. A. V. Filippenko et al., *Astron. J.* **104**, 1543 (1992).
26. A. V. Filippenko et al., *Astrophys. J.* **384**, L15 (1992).
27. M. M. Phillips et al., *Astron. J.* **103**, 1632 (1992).
28. W. Li et al., *Publ. Astron. Soc. Pac.* **115**, 453 (2003).
29. <http://ned.ipac.caltech.edu>
30. <http://leda.univ-lyon1.fr>
31. S. Blondin et al., *Astron. J.* **143**, 126 (2012).
32. J. M. Silverman et al., *Mon. Not. R. Astron. Soc.* **425**, 1789 (2012).
33. T. Matheson et al., *Astrophys. J.* **135**, 1598 (2008).
34. K. M. Gilbert et al., *Astrophys. J.* **652**, 1188 (2006).
35. A. S. Fruchter et al., *Nature* **441**, 463 (2006).
36. D. G. York et al., *Astron. J.* **120**, 1579 (2000).
37. D. N. Spergel et al., *Astrophys. J. Suppl. Ser.* **170**, 377 (2007).
38. D. J. Schlegel, D. P. Finkbeiner, M. Davis, *Astrophys. J.* **500**, 525 (1998).
39. R. B. C. Henry, G. Worthey, *Publ. Astron. Soc. Pac.* **111**, 919 (1999).
40. H. Umeda, K. Nomoto, H. Yamaoka, S. Wanajo, *Astrophys. J.* **513**, 861 (1999).
41. E. Scannapieco, L. Bildsten, *Astrophys. J.* **629**, L85 (2005).
42. F. Mannucci, M. Della Valle, N. Panagia, *Mon. Not. R. Astron. Soc.* **370**, 773 (2006).
43. P. Goudfroi et al., *Astron. Astrophys. Suppl. Ser.* **105**, 341 (1994).
44. L. M. Young et al., *Mon. Not. R. Astron. Soc.* **414**, 940 (2011).
45. J. D. Simon et al., *Astrophys. J.* **702**, 1157 (2009).
46. S. Blondin et al., *Astrophys. J.* **693**, 207 (2009).
47. R. J. Foley et al., *Astrophys. J.* **752**, 101 (2012).
48. P. R. Wood, *ASP Conf. Ser.* **404**, 255 (2009).
49. E. J. Lentz, E. Baron, D. Branch, P. H. Hauschildt, P. E. Nugent, *Astrophys. J.* **530**, 966 (2000).
50. C. Gerardy et al., *Astrophys. J.* **607**, 391 (2004).
51. L. Wang, D. Baade, F. Patat, *Science* **315**, 212 (2007).

Acknowledgments: We thank I. Dominguez for helpful discussions and C. Wu for assistance with the SDSS images. This work is supported by the National Natural Science Foundation of China (NSFC grants 11073013 and 11178003), the Major State Basic Research Development Program (2009CB824800 and 2013CB834903), and the Foundation of Tsinghua University (2011202170). The work of L.W. is supported by NSF grant AST-0708873. A.V.F. is grateful for financial assistance from NSF grant AST-1211916, the TABASGO Foundation, and the Christopher R. Redlich Fund. We dedicate this paper to the memory of our dear friend and colleague, Weidong Li, whose unfailing devotion to the Lick Observatory Supernova Search made this work possible; his premature, tragic passing has deeply saddened us.

Supplementary Materials

www.sciencemag.org/cgi/content/full/science.1231502/DC1
Supplementary Text
Figs. S1 to S5
Table S1
References (52–58)

15 October 2012; accepted 7 February 2013
Published online 7 March 2013,
10.1126/science.1231502

Infrared Absorption Spectrum of the Simplest Criegee Intermediate CH_2OO

Yu-Te Su,¹ Yu-Hsuan Huang,¹ Henryk A. Witek,^{1*} Yuan-Pern Lee^{1,2*}

The Criegee intermediates are carbonyl oxides postulated to play key roles in the reactions of ozone with unsaturated hydrocarbons; these reactions constitute an important mechanism for the removal of unsaturated hydrocarbons and for the production of OH in the atmosphere. Here, we report the transient infrared (IR) absorption spectrum of the simplest Criegee intermediate CH_2OO , produced from $\text{CH}_2\text{I} + \text{O}_2$ in a flow reactor, using a step-scan Fourier-transform spectrometer. The five observed bands provide definitive identification of this intermediate. The observed vibrational frequencies are more consistent with a zwitterion rather than a diradical structure of CH_2OO . The direct IR detection of CH_2OO should prove useful for kinetic and mechanistic investigations of the Criegee mechanism.

The gaseous reactions of ozone (O_3) with unsaturated hydrocarbons have been extensively investigated, given their roles in atmospheric depletion of these molecules and associated build-up of OH free-radical and particulate material in the troposphere (1–3). In summer, the dominant OH-production channel in the atmosphere includes photolysis of ozone to produce $\text{O}(^1\text{D})$, which subsequently reacts with H_2O to produce OH. During the winter season, the efficiency of ozone photolysis drops by 50% or more, and the atmospheric production of OH via ozonolysis of alkenes was proposed to account for the difference in the photolytic production of OH between summer and winter (4).

Decades of research suggest the initiation of the ozonolysis reactions involves the cycloaddition of ozone to the $\text{C}=\text{C}$ double bond to form a cyclic trioxolane intermediate (ozonide) with a $\text{C}-\text{C}$ single bond. The large exothermicity of this reaction leads to a rapid cleavage of this $\text{C}-\text{C}$ bond and one $\text{O}-\text{O}$ bond of the ozonide to form a carbonyl molecule and a carbonyl oxide that is commonly referred to as the Criegee intermediate, which was first postulated by Criegee in 1949 (5). The simplest ozone-alkene reaction involves ethene (C_2H_4); the products from fragmentation of ethene ozonide ($\text{C}_2\text{H}_4\text{O}_3$) are formaldehyde (H_2CO) and formaldehyde oxide (or peroxymethylene, CH_2OO), which is hence the simplest Criegee intermediate. The structure and reactions of gaseous Criegee intermediates have been extensively investigated and debated (6–9). Four isomers of CH_2O_2 include formaldehyde oxide, dioxirane, methylenebis(oxy), and formic acid, as shown in Fig. 1. The large exothermicity of the reaction of $\text{O}_3 + \text{C}_2\text{H}_4$ might lead to isomerization among these isomers and the decomposition of these species to produce H, OH, CH_3 , CO, CO_2 , and other products (1–3).

The highly reactive Criegee intermediates have until recently eluded detection in the gaseous phase. Taatjes and co-workers produced CH_2OO from the

reactions of $\text{CH}_3\text{SOCH}_2 + \text{O}_2$ (10) and $\text{CH}_2\text{I} + \text{O}_2$ (11) in a flow cell and detected its cation with vacuum ultraviolet photoionization. They confirmed that the Criegee intermediate, rather than other isomers, was observed because the observed photoionization threshold near 10 eV conforms to theoretical predictions of 9.98 eV (12), which is much smaller than the values of 10.82 eV predicted for dioxirane (12) and 11.3 eV determined for formic acid (13). Beames *et al.* used the $\text{CH}_2\text{I} + \text{O}_2$ reaction to prepare CH_2OO in a supersonic jet and reported that a broad ultraviolet (UV) spectrum of CH_2OO peaked near 335 nm; the spectrum was obtained through UV-induced depletion of the ion signal of CH_2OO produced upon photoionization (14). The infrared (IR) absorption spectrum of gaseous CH_2OO would supply more detailed structural information as well as an alternative means for performing kinetic measurements.

Theoretical investigations of the structure and reactivity of CH_2OO have been extensive (12, 15–18), but predictions of the enthalpy of formation, electronic structure, and vibrational wave numbers vary considerably. The reported enthalpy of formation of CH_2OO at 298 K, ΔH_f° , varies from 26 to 48 kcal mol^{−1} but settles toward the smaller value when more sophisticated methods are used. Earlier theoretical calculations indicated CH_2OO to have a planar, singlet biradical structure, with nearly equally long O–O and C–O bonds of about 1.34 Å (19), whereas coupled-cluster theory CCSD(T) and multiconfigurational complete active space self-consistent field (CASSCF) calculations predicted that CH_2OO is better described as a zwitterion with a shorter C–O bond (~1.28 Å) and a longer O–O bond (~1.35 Å) (Fig. 1A) (12, 16, 17). The vibrational frequencies predicted for CH_2OO also vary considerably. For example, predictions of the wave number of the O–O stretching mode ranged from 849 to 1077 cm^{−1}, and of the C–O stretching mode from 1269 to 1407 cm^{−1}.

Because CH_2OO is unstable, its detection with a conventional Fourier-transform IR (FTIR) spectrometer is difficult. We have demonstrated that coupling a step-scan FTIR spectrometer with a multipass absorption cell enables the recording of temporally resolved IR absorption spectra of gaseous reaction intermediates such as ClCO (20)

and CH_3OO (21); distinct absorption bands of various isomers of CH_3SO_2 (22), CH_3SOO (23), and CH_3OSO (24) were recorded to provide definitive structural identification. Here, we report a further application of this technique to characterize the IR absorption spectra of gaseous CH_2OO species.

A step-scan FTIR [Vertex 80v (Bruker Optik, Ettlingen, Germany)] spectrometer coupled with a multireflection White cell was used to record the IR spectra of transient species. The laser beam, of wavelength 248 nm, passed through the White cell and was reflected six times with two external mirrors so as to photodissociate a flowing mixture of CH_2I_2 in N_2/O_2 and thereby produced CH_2I that subsequently reacted with O_2 to form CH_2OO . The derivation of conventional time-resolved difference absorption spectra from the temporal profiles recorded at each scan step has been established (20, 25).

The partial IR absorption spectrum (800 to 1500 cm^{−1}) of the flowing mixture of $\text{CH}_2\text{I}_2/\text{N}_2/\text{O}_2$ (1/20/760, 94 torr) at 340 K (Fig. 2A) exhibits absorption lines of CH_2I_2 near 1229, 1188, and 1113 cm^{−1}. Upon irradiation with light at 248 nm, the absorption of CH_2I_2 decreased owing to photolysis, whereas new bands near 1435, 1286, 908, and 848 cm^{−1} appeared, as shown in the difference spectrum recorded at 0- to 12.5-μs delays (Fig. 2B); a band with a weak Q-branch near 1241 cm^{−1} (indicated by an arrow) might belong to the same group but is interfered with by absorption of parent or other products. The intensities of these new lines decreased rapidly with time and diminished after ~100 μs; a spectrum recorded 50 to 62.5 μs after photo-irradiation is shown in Fig. 2C. The decay of CH_2OO resulted in increased absorption of H_2CO .

Because photolysis of CH_2I_2 produces mainly the CH_2I radical (26) and because this radical reacts readily with excess O_2 in the system (27, 28), the possible carriers of the observed new bands include CH_2IOO and isomers of CH_2O_2 . Most pre-

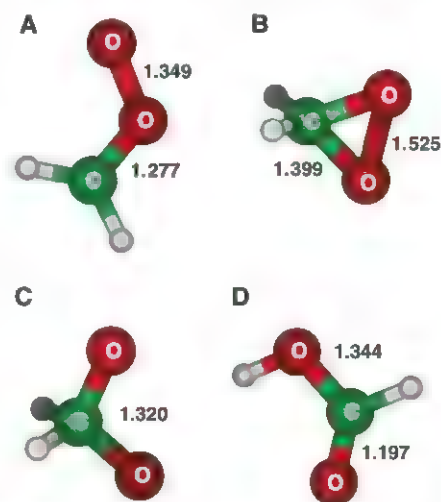


Fig. 1. Geometries of possible isomers of CH_2O_2 . (A) Formaldehyde oxide CH_2OO , (B) dioxirane, (C) methylenebis(oxy), and (D) formic acid predicted with the NEVPT2/aVTZ method [(A) to (C)] and the B3LYP/aVTZ method (D). The O–O and C–O bond distances are given in angstroms.

¹Department of Applied Chemistry and Institute of Molecular Science, National Chiao Tung University, 1001, Ta-Hsueh Road, Hsinchu 30010, Taiwan. ²Institute of Atomic and Molecular Sciences, Academia Sinica, Taipei 10617, Taiwan.

*Corresponding author. E-mail: yplee@mail.nctu.edu.tw (Y.-P.L.); hwitek@mail.nctu.edu.tw (H.W.)

vious experimental attempts to generate and detect CH_2OO used either the reaction of $\text{CH}_2 + \text{O}_2$ or $\text{C}_2\text{H}_4 + \text{O}_3$, but the large exothermicity of these reactions makes the stabilization of CH_2OO difficult. In contrast, in the reaction of $\text{CH}_2\text{I} + \text{O}_2 \rightarrow \text{CH}_2\text{OO} + \text{I}$ chosen here, the stabilization of CH_2OO is possible because of the small exothermicity of $\sim 13 \text{ kJ mol}^{-1}$.

The observed vibrational wave numbers and relative intensities are compared with theoretical predictions for CH_2OO in Table 1. Previous in-

vestigations (12, 18) reported only harmonic vibrational frequencies, so we performed new calculations in order to derive the anharmonic frequencies. The potentially zwitterionic character of the CH_2OO molecule requires appropriate multireference treatment. The harmonic and anharmonic vibrational frequencies have been computed by using a quadratic force field obtained with the n -electron valence state perturbation theory (NEVPT2) method (29) implemented in the Molpro quantum chemistry package (30) by using

the CASSCF(8,8) reference wave function. No symmetry has been used in these calculations so as to avoid numerical problems. The anharmonic frequencies (31) have only approximate character because the effects of three- and four-mode couplings have been neglected owing to high computational complexity. Nevertheless, the computed NEVPT2/aVDZ anharmonic frequencies correspond well to the observed experimental bands.

The IR spectra of CH_2OO , dioxirane, methylenebis(oxy), and *cis*- CH_2IOO simulated according to the geometries and anharmonic vibrational frequencies that were predicted with quantum-chemical calculations are shown in Fig. 2, D to G, respectively. A compilation of anharmonic vibrational levels and IR intensities for the isomers of CH_2OO and other possible intermediate structures used in the simulations is given in tables S1 and S2. The rotational constants used in the simulation are compiled in table S3. For CH_2IOO and CH_2OO , the characteristic OO-stretching modes have wave numbers near 900 cm^{-1} . For dioxirane, two intense features near 1238 and 911 cm^{-1} are characteristic of symmetric and antisymmetric CO-stretching modes (17). For methylenebis(oxy), only an anharmonic NEVPT2 (2,2) stick spectrum is shown because the B3LYP (Becke, three-parameter, Lee-Yang-Parr) rotational constants for each fundamental mode could not be assessed (supplementary text). A comparison of the observed new spectral features with these simulated spectra indicates that the best agreement in terms of relative intensities and positions is obtained for the predicted spectrum of CH_2OO . The Criegee intermediate is predicted to have intense lines at 1435 (52), 1302 (100), 1220 (33), 892 (100), and 853 (31) cm^{-1} ; the relative IR intensities are listed in parentheses. The observed features are at 1435 (33), 1286 (42), 1241 (39), 908 (100), and 848 (24) cm^{-1} , with typical deviations of 5 to 23 cm^{-1} from predicted anharmonic vibrational wave numbers. The predicted spectra of other candidate species disagree with the observed spectrum. For example, although dioxirane is predicted to have two intense lines near 1238 and 911 cm^{-1} , near the observed features at 1286 and 848 cm^{-1} the relative intensities and the rotational contours do not match. The widths of the rotational contours of bands of CH_2IOO are predicted to be much smaller than the observed widths because the massive I atom induces small rotational parameters; the possibility that the observed new features are due to CH_2IOO is positively eliminated. In contrast, the predicted rotational contours of each vibrational band of CH_2OO agree well with observations, except for a weak Q-branch near 1241 cm^{-1} that might experience interference from absorption of the precursor or other product. A comparison of observed and simulated rotational contours for the ν_6 and ν_8 modes is shown in Fig. 3; those for the ν_3 and ν_4/ν_5 modes are shown in figs. S1 and S2, respectively. Most bands of CH_2OO have a mixed *a/b*-type contour with P-, Q-, and R-branches, whereas the out-of-plane CH_2 -wagging (ν_8) mode near 848 cm^{-1}

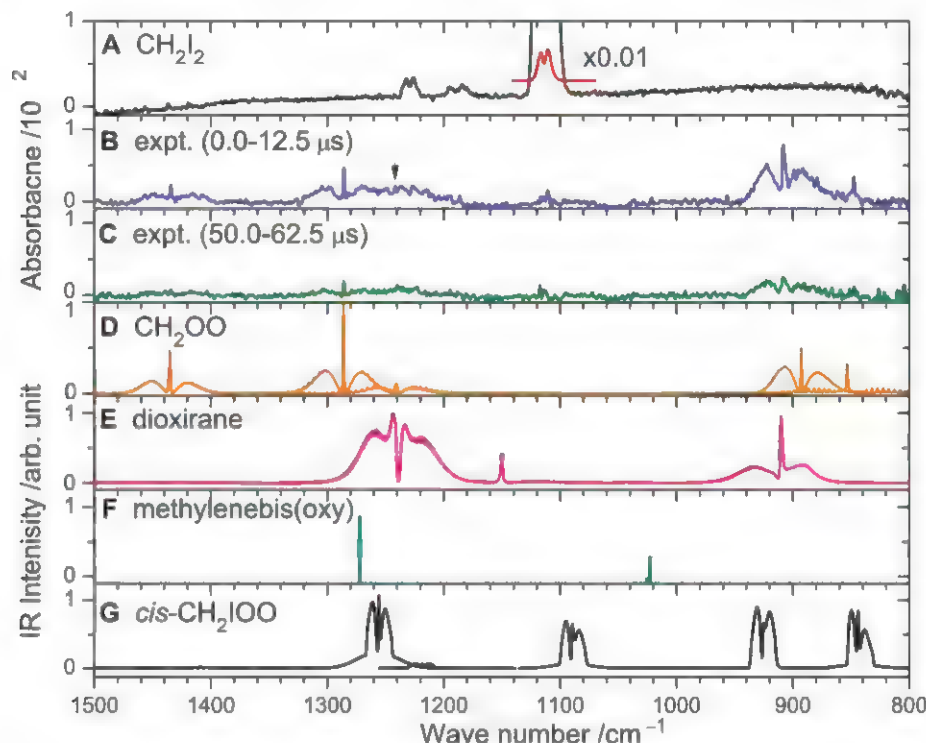


Fig. 2. Comparison of observed spectra with simulated spectra of possible species. (A) IR absorption spectrum of a flowing mixture of $\text{CH}_2\text{I}_2/\text{N}_2/\text{O}_2$ (1/20/760, 94 torr) before photolysis. (B) Difference spectra recorded 0 to 12.5 μs and (C) 50 to 62.5 μs after irradiation of the sample at 248 nm; the spectrum at 300 to 312.5 μs was subtracted for background correction. IR spectra of (D) CH_2OO , (E) dioxirane, (F) methylenebis(oxy), and (G) *cis*- CH_2IOO were simulated by using the predicted rotational constants, vibrational frequencies, and IR intensities listed in tables S1 and S3.

Table 1. Comparison of experimentally observed wave numbers (per centimeter) and intensities with the vibrational wave numbers (per centimeter) and IR intensities of CH_2OO predicted with various methods. Sym., symmetry.

Mode	Sym.	Experiment	NEVPT2/aVDZ		CAS(14,12)	CCSD(T)	Description†
			Harmonic	Anharmonic	/VDZ*	/aVTZ*	
ν_1	A'		3370	3149 (5)‡	3215	3290	<i>a</i> -CH str.
ν_2	A'		3197	3030 (1)	3065	3137	<i>s</i> -CH str.
ν_3	A'	1435 (33)§	1500	1458 (52)	1465	1483	CH_2 scissor/CO str.
ν_4	A'	1286 (42)	1338	1302 (100)	1269	1306	CO str./ CH_2 scissor
ν_5	A'	1241 (39)	1235	1220 (33)	1233	1231	CH_2 rock
ν_6	A'	908 (100)	916	892 (100)	849	935	OO str.
ν_7	A'		536	530 (1)	537	529	COO deform
ν_8	A''	848 (24)	856	853 (31)	793	862	CH_2 wag
ν_9	A''		620	606 (2)	618	632	CH_2 twist
Reference		This work	This work	This work	(18)	(12)	

*Harmonic wave numbers. †Approximate mode description. *a*, asymmetric; *s*, symmetric; str., stretch. ‡Relative IR intensities are normalized to the most intense line (ν_4) with intensity 124 km mol^{-1} . §Integrated IR intensities relative to ν_6 are listed in parentheses.

has a characteristic *c*-type structure with a prominent Q-branch because the dipole moment oscillates mainly along the *c* axis (perpendicular to the molecular plane) upon vibrational excitation. This unique *c*-type feature of a planar molecule near 848 cm^{-1} further supports the assignment of the observed features to CH_2OO .

The observed wave number of the OO-stretching mode of CH_2OO near 908 cm^{-1} is much smaller than that of the corresponding modes of CH_3OO at 1117 cm^{-1} (27), $\text{CH}_3\text{C(O)OO}$ (32) at 1102 cm^{-1} , and $\text{C}_6\text{H}_5\text{C(O)OO}$ at 1108 cm^{-1} (33) determined with a similar technique. The observed wave number of the CO-stretching mode near 1286 cm^{-1} is much larger than that of the corresponding mode of CH_3OO at 902 cm^{-1} (34) observed in a matrix, indicating some double-bond character. These trends strongly support a zwitterionic, rather than singlet biradical, structural description of CH_2OO because of a strengthened C–O bond and a weakened O–O bond.

The $\sim 50\text{-}\mu\text{s}$ lifetime of CH_2OO observed in our experiment is much shorter than that (~ 2 ms) reported by Welz *et al.* (11), who used $[\text{CH}_2\text{I}]_0 \cong 9 \times 10^{11}$ molecules cm^{-3} in their experiments. Because the sensitivity of IR absorption is not as good as that of mass detection, a higher concentration of $[\text{CH}_2\text{I}]_0 \cong 4 \times 10^{13}$ molecules cm^{-3} is needed in our experiments in order to record a satisfactory spectrum of CH_2OO . In some preliminary low-resolution experiments, we varied $[\text{CH}_2\text{I}]_0$ from 1.0×10^{13} to 2.8×10^{14} molecules cm^{-3} and found that the lifetime of CH_2OO decreased from ~ 150 to 15 μs , indicating that the bimolecular reaction—either $\text{CH}_2\text{OO} + \text{I}$ or $\text{CH}_2\text{OO} + \text{CH}_2\text{OO}$ —might be responsible for this rapid decay. More detailed kinetic measurements are in progress.

With our detection method, we can probe CH_2OO directly in a reaction. The advantage is demonstrated in the investigation of the yield of CH_2OO from the reaction $\text{CH}_2\text{I} + \text{O}_2$. Solar photolysis of CH_2I_2 , one major source of iodine in the marine boundary layer, generates CH_2I and I. The reaction of $\text{CH}_2\text{I} + \text{O}_2$ is important in the atmosphere partly because this reaction releases the second I atom to form IO, which can affect O_3 , HO_x , and NO_x levels and also lead to the formation of particulates in the atmosphere (35). Huang *et al.* detected I atom as a product of the reaction of CH_2I with O_2 by probing the IR absorption of I atom at 7603.138 cm^{-1} . These authors reported that O_2 stabilizes CH_2IOO with remarkable efficiency (13 times that of N_2), hence decreasing the yield of I atoms (28). The yield of CH_2OO from $\text{CH}_2\text{I} + \text{O}_2$ was estimated to be 0.04 in air at 760 torr because CH_2IOO is expected to be readily stabilized. However, because these authors probed only I atoms, their measurements could not distinguish between the stabilization of CH_2IOO and other secondary reactions. With our new detection method, we can probe CH_2OO directly to provide direct measurements of the yield of CH_2OO . Contrary to their predictions, in our experiment with O_2 at 90 torr we observed no CH_2IOO , and the yield of CH_2OO was estimated to be at least 35% of CH_2I with the assumption that the predicted IR intensities of CH_2OO are correct. Whether this discrepancy is due to the difference in photolysis wavelengths [355 nm in experiments of Huang *et al.* (28) and 248 nm in this work]—in which the total available energy of $\text{CH}_2\text{I} + \text{I}$ (118 and 263 kJ mol^{-1} , respectively) might affect the efficiency of stabilization of CH_2IOO and CH_2OO produced from $\text{CH}_2\text{I} + \text{O}_2$ —requires further investigation.

References and Notes

1. D. Johnson, G. Marston, *Chem. Soc. Rev.* **37**, 699 (2008).
2. J. G. Calvert *et al.*, *The Mechanisms of Atmospheric Oxidation of the Alkenes* (Oxford University Press, Oxford, UK, 2000), pp. 172–335.
3. O. Horie, G. Moortgat, *Acc. Chem. Res.* **31**, 387 (1998).
4. R. M. Harrison *et al.*, *Sci. Total Environ.* **360**, 5 (2006).
5. R. Criegee, G. Wenner, *Chem. Ber.* **9**, 564 (1949).
6. W. Sander, *Angew. Chem. Int. Ed. Engl.* **29**, 344 (1990).
7. W. H. Bunelle, *Chem. Rev.* **91**, 335 (1991).
8. S. Hatakeyama, H. Akimoto, *Res. Chem. Intermed.* **20**, 503 (1994).
9. G. Marston, *Science* **335**, 178 (2012).
10. C. A. Taatjes *et al.*, *J. Am. Chem. Soc.* **130**, 11883 (2008).
11. O. Welz *et al.*, *Science* **335**, 204 (2012).
12. M. T. Nguyen, T. L. Nguyen, V. T. Ngan, H. M. T. Nguyen, *Chem. Phys. Lett.* **448**, 183 (2007) and references therein.
13. T. A. Cool, J. Wang, K. Nakajima, C. A. Taatjes, A. McIlroy, *Int. J. Mass Spectrom.* **247**, 18 (2005).
14. J. M. Beames, F. Liu, L. Lu, M. I. Lester, *J. Am. Chem. Soc.* **134**, 20045 (2012).
15. J. M. Anglada, J. González, M. Torrent-Sucarrat, *Phys. Chem. Chem. Phys.* **13**, 13034 (2011).
16. L. Vereecken, J. S. Francisco, *Chem. Soc. Rev.* **41**, 6259 (2012).
17. D. Cremer, J. Gauss, E. Kraka, J. F. Stanton, R. J. Bartlett, *Chem. Phys. Lett.* **209**, 547 (1993).
18. D.-C. Fang, X.-Y. Fu, *J. Phys. Chem. A* **106**, 2988 (2002) and references therein.
19. L. B. Harding, W. A. Goddard, *J. Am. Chem. Soc.* **100**, 7180 (1978).
20. S.-H. Chen, L.-K. Chu, Y.-J. Chen, I.-C. Chen, Y.-P. Lee, *Chem. Phys. Lett.* **333**, 365 (2001).
21. D.-R. Huang, L.-K. Chu, Y.-P. Lee, *J. Chem. Phys.* **127**, 234318 (2007).
22. L.-K. Chu, Y.-P. Lee, *J. Chem. Phys.* **124**, 244301 (2006).
23. L.-K. Chu, Y.-P. Lee, *J. Chem. Phys.* **133**, 184303 (2010).
24. J.-D. Chen, Y.-P. Lee, *J. Chem. Phys.* **134**, 094304 (2011).
25. Materials and methods are available as supplementary materials on Science Online.
26. S. L. Baughcum, S. R. Leone, *J. Chem. Phys.* **72**, 6531 (1980).
27. T. J. Gravestock, M. A. Blitz, W. J. Bloss, D. E. Heard, *ChemPhysChem* **11**, 3928 (2010).
28. H. Huang, A. J. Eskola, C. A. Taatjes, *J. Phys. Chem. Lett.* **3**, 3399 (2012).
29. C. Angeli, R. Cimmaraglia, S. Evangelisti, T. Leiminger, J. P. Matrieu, *J. Chem. Phys.* **114**, 10252 (2001).
30. H.-J. Werner, P. J. Knowles, G. Knizia, F. R. Manby, M. Schütz, *WIREs Comput. Mol. Sci.* **2**, 242 (2012).
31. M. Neff, G. Rauhut, *J. Chem. Phys.* **131**, 124129 (2009).
32. S.-Y. Chen, Y.-P. Lee, *J. Chem. Phys.* **132**, 114303 (2010).
33. B. Golec, J.-D. Chen, Y.-P. Lee, *J. Chem. Phys.* **135**, 224302 (2011).
34. S. Nandi *et al.*, *J. Phys. Chem. A* **106**, 7547 (2002).
35. G. McFiggans *et al.*, *Atmos. Chem. Phys.* **4**, 701 (2004).

Acknowledgments: Calculation details and a compilation of anharmonic vibrational levels and IR intensities for possible intermediate structures with additional simulation plots are presented in the supplementary materials. National Science Council of Taiwan (grants NSC102-2745-M009 001 ASP and NSC99-2113-M-009-011-MY3) and the Ministry of Education, Taiwan ("Aim for the Top University Plan" of National Chiao Tung University) supported this work. The National Center for High-Performance Computing provided computer time. We thank G. Rauhut for his assistance in the calculations of anharmonic vibrational frequencies.

Supplementary Materials

www.sciencemag.org/cgi/content/full/340/6129/174/DC1

Materials and Methods

Supplementary Text

Figs. S1 and S2

Tables S1 to S3

References (36–44)

20 December 2012; accepted 1 March 2013

10.1126/science.1234369

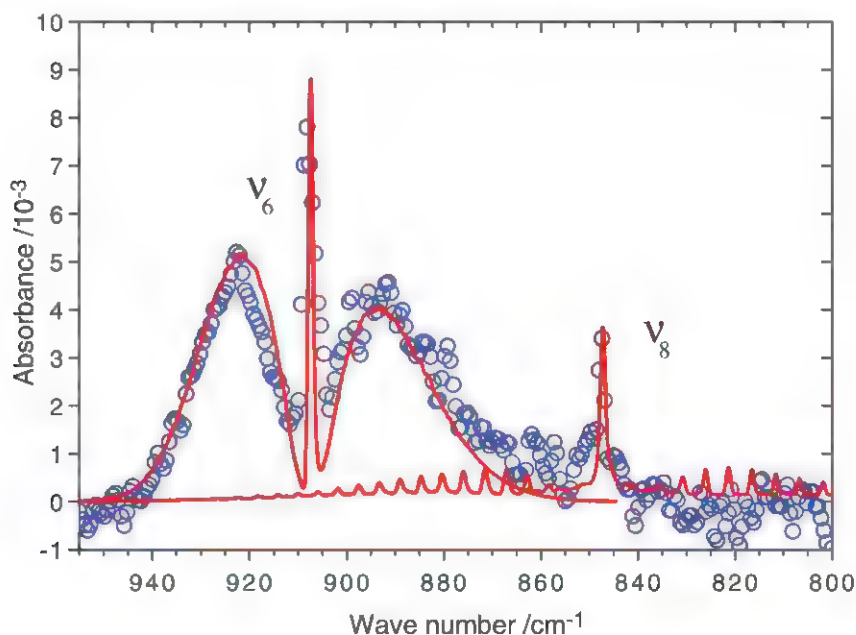


Fig. 3. Comparison of observed and simulated spectra of CH_2OO in the region of 800 to 955 cm^{-1} at resolution 1.0 cm^{-1} . Simulated absorption bands for the ν_6 ($\nu_6 = 908 \text{ cm}^{-1}$ and *a*-*b*-type = 8.2/1) and ν_8 ($\nu_8 = 848 \text{ cm}^{-1}$ and *c*-type) modes are shown with red lines, and the observed spectrum is shown with open circles. Spectral width = 1 cm^{-1} , $J_{\text{max}} = 150$, and $T = 340 \text{ K}$.

Direct Measurements of Conformer-Dependent Reactivity of the Criegee Intermediate CH_3CHOO

Craig A. Taatjes,^{1*} Oliver Welz,¹ Arkke J. Eskola,¹ John D. Savee,¹ Adam M. Scheer,¹ Dudley E. Shallcross,² Brandon Rotavera,¹ Edmond P. F. Lee,^{3,4} John M. Dyke,³ Daniel K. W. Mok,⁴ David L. Osborn,¹ Carl J. Percival^{5*}

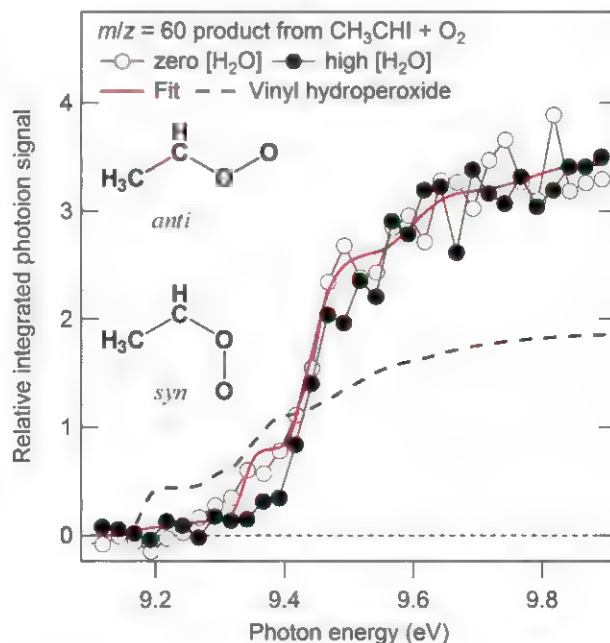
Although carbonyl oxides, "Criegee intermediates," have long been implicated in tropospheric oxidation, there have been few direct measurements of their kinetics, and only for the simplest compound in the class, CH_2OO . Here, we report production and reaction kinetics of the next larger Criegee intermediate, CH_3CHOO . Moreover, we independently probed the two distinct CH_3CHOO conformers, *syn*- and *anti*-, both of which react readily with SO_2 and with NO_2 . We demonstrate that *anti*- CH_3CHOO is substantially more reactive toward water and SO_2 than is *syn*- CH_3CHOO . Reaction with water may dominate tropospheric removal of Criegee intermediates and determine their atmospheric concentration. An upper limit is obtained for the reaction of *syn*- CH_3CHOO with water, and the rate constant for reaction of *anti*- CH_3CHOO with water is measured as $1.0 \times 10^{-14} \pm 0.4 \times 10^{-14}$ centimeter³ second⁻¹.

Ozonolysis of alkenes is generally understood to proceed via a 1,3-cycloaddition of ozone across the olefinic bond to produce a primary ozonide, the decomposition of which forms a carbonyl moiety and a Criegee intermediate (CI) (1). The fate of the CI determines the end products of the ozonolysis reaction and can have a substantial impact on the atmosphere (1–4). Recently, the simplest CI, CH_2OO , has been directly produced in the gas phase with low internal energies from reaction of O_2 with CH_3SOCH_2 (5, 6) or CH_2I (4, 7, 8) and unambiguously detected by tunable synchrotron or laser photoionization mass spectrometry. These techniques allowed direct measurements of the reaction kinetics of CH_2OO with several important tropospheric species, including SO_2 and NO_2 , both of which react much faster with CH_2OO than models had assumed (4). Since those direct measurements appeared, new high-level calculations (9), field measurements (10), and ozonolysis experiments (10–12) continue to suggest that CI reactions are important in tropospheric sulfate chemistry. However, substantial uncertainty remains, partly because of the absence of direct kinetic measurements of any larger CI and partly because of uncertainty in the products of CI reactions. Moreover, the reactivity of larger CIs is predicted to be affected by the nature and location of the substituents (13), with a particularly large effect for the crucial reaction of CI with water (13, 14). Because of the large amount of water in Earth's atmosphere, the rate of CI removal by

water is a key determinant of the tropospheric impact of all CI reactions. Determining the conformer dependence of CI reactions is therefore not only a vital aspect of understanding their fundamental reactivity, it is also a key component for improving atmospheric chemistry models.

We have successfully extended our earlier technique of reacting α -iodoalkyl radicals with O_2 to prepare CIs (4, 7, 15), and here we show that the reaction of the 1-iodoethyl radical (CH_3CHI) with O_2 forms both conformers of the CI acetaldehyde oxide (CH_3CHOO) at 298 K and 4 torr. The conformers of acetaldehyde oxide, *syn*- CH_3CHOO and *anti*- CH_3CHOO , differ in the orientation of the C–O–O group (depicted in Fig. 1). By taking advantage of the difference in ionization energy of the two conformers, we demonstrate a dramatic conformer dependence of CH_3CHOO reactivity toward SO_2 and H_2O .

Fig. 1. The photoionization spectrum for the $m/z = 60$ product from photolysis of CH_3CHI in the presence of O_2 . The best fit of the zero-water trace to the calculated photoionization spectra for *syn*- and *anti*- CH_3CHOO is also shown. The fit allows the energies for the excited (A') cationic state of each conformer to vary within a range of ~ 50 meV about their calculated values. The black dashed line shows the calculated photoionization spectrum of vinyl hydroperoxide. Addition of water preferentially removes the *anti* conformer, as seen in the decreased signal between 9.3 and 9.4 eV for the high- H_2O trace.



Kinetic measurements were carried out in the Multiplexed Chemical Kinetics Reactor, which has been described in detail elsewhere (4, 16, 17). Reactions are initiated by pulsed laser photolysis in a slow-flow reactor. The contents are continuously sampled through a small orifice in the reactor and probed by photoionization time-of-flight mass spectrometry. Ionizing with tunable photon energy, from the Chemical Dynamics Beamline (9.0.2) of the Advanced Light Source, allows isomers to be distinguished on the basis of their photoionization spectra (17–19). The reaction of CH_3CHI with O_2 shows similar behavior to the reaction of CH_2I with O_2 , with the most prominent products being the stabilized CI (CH_3CHOO), an I atom, and secondary products IO and HOI. (A time-resolved mass spectrum of the reaction initiated by photolysis of CH_3CHI_2 in the presence of oxygen is displayed in fig. S2.)

The mass/charge (m/z) = 60 signal is identified as the CI, acetaldehyde oxide, on the basis of its exact mass and a comparison of its photoionization spectrum with a predicted spectrum derived from *ab initio* calculations (19) of both the adiabatic ionization energy (AIE) and Franck-Condon factors for photoionization of both conformers of CH_3CHOO , as shown in Fig. 1. Detailed results of these calculations are given in the supplementary text.

Calculations place the *syn* conformer ~ 15 kJ mol^{-1} lower in energy than *anti*- CH_3CHOO (14). Reflecting the zwitterionic character of the C–O bond, the barrier to interconversion of these conformers is substantial (14), ~ 160 kJ mol^{-1} . Therefore, *syn*- and *anti*- CH_3CHOO act as distinct chemical species at atmospheric temperatures. The *syn* and *anti* conformers of CH_3CHOO also have different photoionization spectra. In the threshold region, each conformer has ionization transitions to both A'' and A' cationic states, and the

¹Combustion Research Facility, Mail Stop 9055, Sandia National Laboratories, Livermore, CA 94551–0969, USA. ²School of Chemistry, University of Bristol, Bristol BS8 1TS, UK. ³School of Chemistry, University of Southampton, Highfield, Southampton SO17 1BJ, UK. ⁴Department of Applied Biology and Chemical Technology, The Hong Kong Polytechnic University, Hung Hom, Hong Kong. ⁵School of Earth, Atmospheric and Environmental Sciences, The University of Manchester, Williamson Building, Oxford Road, Manchester M13 9PL, UK.

*Corresponding author. E-mail: cataatj@sandia.gov (C.A.T.); Carl.Percival@manchester.ac.uk (C.J.P.)

calculated four photoionization bands overlap (fig. S4). Allowing a small adjustment to the computed ionization energies for each conformer gives a very close fit to the observed spectrum (Fig. 1). The low-energy edge of the spectrum is dominated by the anti conformer, which can be detected below the ionization energy of the syn conformer. Assuming that the electronic transition moments for the two conformers are similar, the fit parameters suggest a far larger overall production (90%) of the more stable syn conformer. The signals observed at higher ionizing photon energies will be dominated by photoionization of *syn*-CH₃CHO (supplementary text). The two conformers are independently detected, but their ratio is not varied in these experiments.

Acetaldehyde oxide has several other isomers (scheme S1), most of which have ionization energies well above the threshold observed for the *m/z* = 60 product of the reaction of CH₃CHI with O₂, including acetic acid, the AIE of which is 10.70 eV, and methyl formate, with an AIE of 10.85 eV (20). Only vinyl hydroperoxide has a low enough calculated AIE, 9.18 eV, to be considered as a carrier for the *m/z* = 60 product spectrum. However, the predicted ionization onset and Franck-Condon envelope of vinyl hydroperoxide (Fig. 1) is not consistent with the observed spectrum.

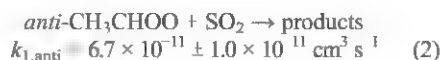
Vinyl hydroperoxide is calculated to be the dominant product of isomerization from *syn*-CH₃CHO, with a calculated barrier to isomerization of >80 kJ mol⁻¹ (21). [Isomerization of *anti*-CH₃CHO is more likely to lead to methyl dioxirane (21), with a calculated AIE of 10.36 eV.] The O-O bond in vinyl hydroperoxide is weak (22), and fission of that bond is a pathway to formation of OH in ozonolysis reactions (23). In fact, recent multireference calculations predict extremely rapid dissociation of vinyl hydroperoxide after isomerization from CH₃CHO (24).

The first-order decay rate of CH₃CHO in the absence of additional reactants is the sum of unimolecular and heterogeneous loss reactions. The decay depends on the coating of the reactor, suggesting that heterogeneous reaction contributes substantially. The slowest decay observed in this context, ~250 s⁻¹, is an upper limit to the thermal (298 K) rate coefficient for decomposition of CH₃CHO, consistent with the determination of 76 s⁻¹ by Fenske *et al.* (25). Upon adding SO₂ or NO₂ as reagent, the decay of the CH₃CHO signal becomes more rapid (shown in Fig. 2 for SO₂ reaction with CH₃CHO). A linear fit of the decay constant versus reactant concentration measured at photon energies where photoionization of the syn conformer dominates (Fig. 3 and fig. S5) returns as its slope *k*_{1,syn}, the second-order rate coefficient for the reaction of *syn*-CH₃CHO with SO₂ (uncertainty limits are 95%):



A similar plot measured with 9.37-eV photons, where photoionization of the *anti*-CH₃CHO

conformer dominates (open symbols in Fig. 3), yields a rate coefficient more than twice as large,



Similar measurements on the overall reaction of *syn*- and *anti*-CH₃CHO with NO₂ (described in supplementary text) suffer from reduced signal-to-noise ratio but show a rate coefficient of $2 \times 10^{-12} \pm 1 \times 10^{-12} \text{ cm}^3 \text{ s}^{-1}$, with a slight (statistically significant at 1σ confidence interval) conformer dependence. This rate coefficient is substantially smaller than that for CH₂OO reacting with NO₂, $k(\text{CH}_2\text{OO} + \text{NO}_2) = 7 \times 10^{-12} \text{ cm}^3 \text{ s}^{-1}$ (4).

The rapid reaction of CH₃CHO with SO₂ supports predictions of barrierless addition of SO₂

to CI (9, 26, 27) and indicates that the reactions of CI with SO₂ should be generally facile. The substantial difference in reactivity between *syn*- and *anti*-CH₃CHO may partly reflect increased steric hindrance for formation of the CI-SO₂ secondary ozonide in the *syn* conformation or conformer-selective electron donating effects from the methyl group, as theoretically described, for example, in the CH₃CHO + H₂O reaction (13). The rate coefficient for *syn*-CH₃CHO reaction with SO₂ is slightly smaller than that measured earlier for CH₂OO reacting with SO₂ [$k(\text{CH}_2\text{OO} + \text{SO}_2) = 3.9 \times 10^{-11} \pm 0.7 \times 10^{-11} \text{ cm}^3 \text{ s}^{-1}$] (4), but that for *anti*-CH₃CHO is larger. Both are orders of magnitude larger than estimates typically used in tropospheric models (28).

Measurements have also been carried out at higher ionizing photon energies (13 eV), where

Fig. 2. Representative time-dependent CH₃CHO signals.

The time behavior of the *m/z* = 60 signal (mainly from ionization of *syn*-CH₃CHO) from photolysis of CH₃CHI in the presence of SO₂ and [O₂] = $1.2 \times 10^{16} \text{ cm}^{-3}$, measured with Lyman-α radiation at 10.2 eV.

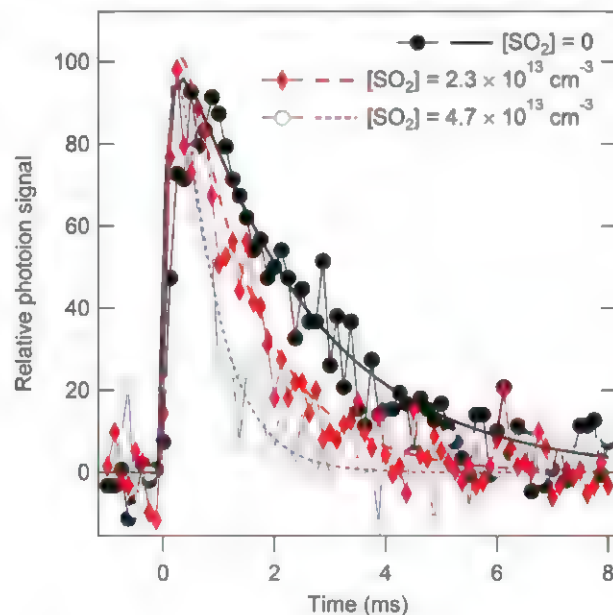
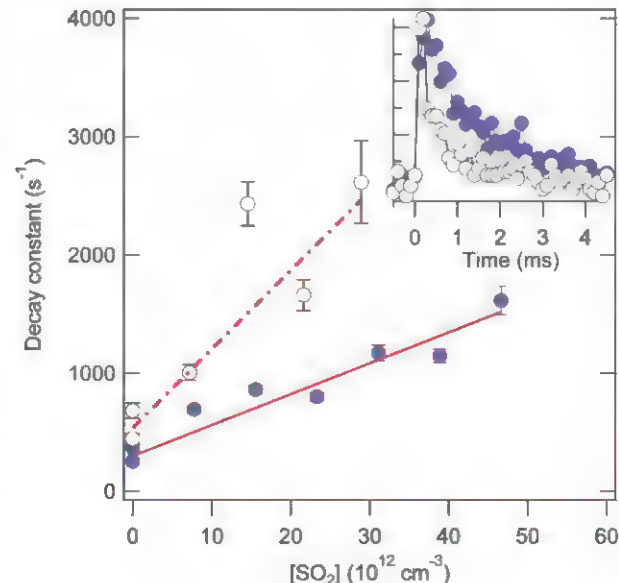


Fig. 3. Rate coefficients for reaction of CH₃CHO conformers with SO₂. Fitted pseudo-first-order decay constants of *syn*-CH₃CHO (solid circles) and *anti*-CH₃CHO (open circles) are shown as a function of SO₂ concentration. The lines are linear fits to the data, weighted by the statistical uncertainty in the exponential fit to the individual decay traces ($\pm 1\sigma$ error bars shown in the figure). Each fit included >20 points across the relevant decay. (Inset) The decay of CH₃CHO measured with 10.50 eV (solid circles, predominantly *syn*) and 9.37 eV (open circles, predominantly *anti*) in the presence of [SO₂] = $7.2 \times 10^{12} \text{ cm}^{-3}$.



the SO₃ co-product [AIE of 12.81 eV (29)] can be directly observed. To within the experimental uncertainty, SO₃ is formed with a rise time that correlates with the decay time of the CI (figs. S6 to S9), showing that SO₃ is a direct product of the reactions of both CH₂OO and CH₃CHOO with SO₂. Vereecken *et al.* (9), improving on earlier calculations (26, 27), predicted that formation of SO₃ and a carbonyl compound will be the principal product channel for small CIs and at low pressure but that stabilization of a CI-SO₂ secondary ozonide becomes dominant for larger CIs under atmospheric conditions. Under the conditions of the present experiments, no stabilized CI-SO₂ product is observed for either CH₂OO or CH₃CHOO reaction with SO₂. The eventual fate of the CI-SO₂ secondary ozonide may determine the relevance of CI reactions with SO₂ to tropospheric sulfate chemistry and particulate formation, and will affect the interpretation and intercomparison of laboratory ozonolysis experiments that are sensitive to either CI consumption or H₂SO₄ formation (10–12).

Because reaction with water dominates tropospheric CI removal (9), its rate constant is critical to modeling the CI concentration. The reaction of CH₂OO with water is too slow to measure in the present apparatus (4), and only an upper limit could be obtained, $4 \times 10^{-15} \text{ cm}^3 \text{ s}^{-1}$. However, the reaction of water with CH₃CHOO is predicted to favor the anti conformer by five orders of magnitude (13), and indeed (Fig. 1) the addition of H₂O preferentially depletes the photoionization spectrum at the low-energy edge, where *anti*-CH₃CHOO dominates. Measurements of CH₃CHOO with 10.5-eV photons in the presence of H₂O concentrations of $2.4 \times 10^{16} \text{ cm}^{-3}$ showed an identical decay to those with no added water, suggesting similar upper limits for the reaction of water with *syn*-CH₃CHOO and with CH₂OO: $4 \times 10^{-15} \text{ cm}^3 \text{ s}^{-1}$ (4). However, a sig-

nificant and systematic increase in the decay rate with water addition was observed for measurements with 9.37-eV photons (Fig. 4), permitting direct measurement of the rate coefficient (uncertainty limits are 95%),

$$\text{anti-CH}_3\text{CHOO} + \text{H}_2\text{O} \rightarrow \text{products} \\ k_{3,\text{anti}} = 1.0 \times 10^{-14} \pm 0.4 \times 10^{-14} \text{ cm}^3 \text{ s}^{-1} \quad (3)$$

This result is more than a factor of 10 below the high-pressure limiting rate coefficient from the transition state theory predictions of Anglada *et al.* (13), $k_{3,\text{anti}} = 1.68 \times 10^{-13} \text{ cm}^3 \text{ s}^{-1}$ but is a factor of 35 above the prediction of Kuwata *et al.* (14), $k_{3,\text{anti}} = 2.87 \times 10^{-16} \text{ cm}^3 \text{ s}^{-1}$. In any case, the rate coefficient is substantially larger than that calculated for other CI reactions with water and tends to validate the theoretical prediction of a dramatic lowering of the activation energy for the anti conformer (13, 14). Because the reaction is predicted to proceed by stabilization (supplementary text), it is possible that the rate coefficient is pressure dependent. Master-equation calculations, including accurate treatment of the association kinetics, could give the most rigorous comparison for the present experiments.

We emphasize that the low-pressure rate coefficients measured here for reactions of the CIs with SO₂, NO₂, and water are lower limits for the total removal of CI by these species at the higher pressures of the troposphere or laboratory ozonolysis experiments. Furthermore, even in cases where the CI removal is independent of pressure, the products may change substantially with pressure (9). Interpretation of indirect measurement of CI reactions often depends on product detection and on derived yields of stabilized CI in ozonolysis that are in turn based on inferences about CI scavenger reactions. Apparent discrepancies among indirect determinations, for example, for reactions of CI with SO₂ (10–12), may

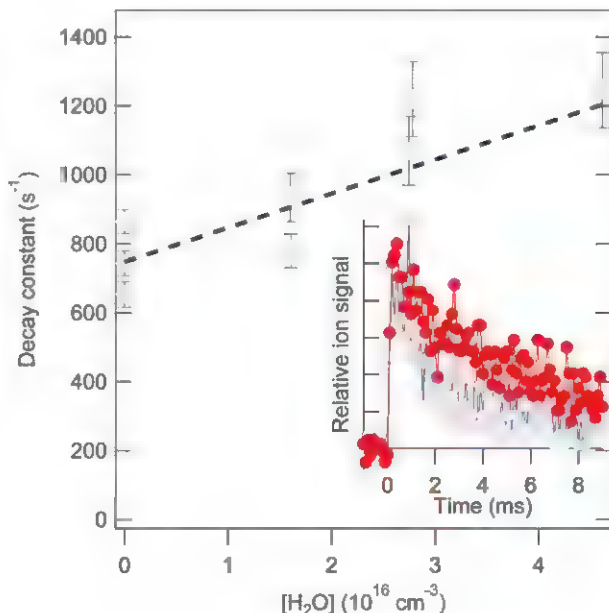
be related to that web of inference. The present measurements break the connection to ozonolysis, directly producing stabilized CIs in a nearly thermoneutral reaction, characterizing the Criegee reactant by its photoionization spectrum, and determining absolute rate constants by pseudo-first-order kinetics methods. Comparing indirect measurements to the present direct kinetics determinations may therefore provide a means to refine the detailed modeling of ozonolysis.

Moreover, computed rate coefficients for substituted CI calculated by state-of-the-art quantum chemistry and advanced theoretical kinetics (9, 30) will be of increasing importance in the development of chemical models for complex systems such as atmospheric chemistry. The present results are a benchmark for such calculations and will enable a more rigorous understanding of CI chemistry and a more accurate description of the role of CI in the troposphere.

References and Notes

- D. Johnson, G. Marston, *Chem. Soc. Rev.* **37**, 699 (2008).
- R. M. Harrison *et al.*, *Sci. Total Environ.* **360**, 5 (2006).
- S. Gäß, E. Hellpointner, W. V. Turner, F. Korte, *Nature* **316**, 535 (1985).
- O. Welz *et al.*, *Science* **335**, 204 (2012).
- R. Asatryan, J. W. Bozzelli, *Phys. Chem. Chem. Phys.* **10**, 1769 (2008).
- C. A. Taatjes *et al.*, *J. Am. Chem. Soc.* **130**, 11883 (2008).
- C. A. Taatjes *et al.*, *Phys. Chem. Chem. Phys.* **14**, 10391 (2012).
- J. M. Beames, F. Liu, L. Lu, M. I. Lester, *J. Am. Chem. Soc.* **134**, 20045 (2012).
- L. Vereecken, H. Harder, A. Novelli, *Phys. Chem. Chem. Phys.* **14**, 14682 (2012).
- R. L. Mauldin 3rd *et al.*, *Nature* **488**, 193 (2012).
- P. T. M. Carlsson, C. Keunecke, B. C. Krüger, M.-C. Maaß, T. Zeuch, *Phys. Chem. Chem. Phys.* **14**, 15637 (2012).
- T. Berndt *et al.*, *J. Phys. Chem. Lett.* **3**, 2892 (2012).
- J. M. Anglada, J. González, M. Torrent-Sucarrat, *Phys. Chem. Chem. Phys.* **13**, 13034 (2011).
- K. T. Kuwata, M. R. Hermes, M. J. Carlson, C. K. Zogg, *J. Phys. Chem. A* **114**, 9192 (2010).
- H. Huang, A. J. Eskola, C. A. Taatjes, *J. Phys. Chem. Lett.* **3**, 3399 (2012).
- D. L. Osborn *et al.*, *Rev. Sci. Instrum.* **79**, 104103 (2008).
- C. A. Taatjes *et al.*, *Phys. Chem. Chem. Phys.* **10**, 20 (2008).
- C. A. Taatjes *et al.*, *Science* **308**, 1887 (2005); 10.1126/science.1112532.
- Materials and methods are available as supporting materials on Science Online.
- D. A. Sweigart, D. W. Turner, *J. Am. Chem. Soc.* **94**, 5592 (1972).
- J. M. Anglada, J. M. Bofill, S. Olivella, A. Solé, *J. Am. Chem. Soc.* **118**, 4636 (1996).
- N. Sebban, H. Bockhorn, J. W. Bozzelli, *Phys. Chem. Chem. Phys.* **5**, 300 (2003).
- N. M. Donahue, G. T. Drozd, S. A. Epstein, A. A. Presto, J. H. Kroll, *Phys. Chem. Chem. Phys.* **13**, 10848 (2011).
- T. Kurtén, N. M. Donahue, *J. Phys. Chem. A* **116**, 6823 (2012).
- J. D. Fenske, A. S. Hasson, A. W. Ho, S. E. Paulson, *J. Phys. Chem. A* **104**, 9921 (2000).
- L. Jiang, Y. S. Xu, A. Z. Ding, *J. Phys. Chem. A* **114**, 12452 (2010).
- T. Kurtén, J. R. Lane, S. Jørgensen, H. G. Kjaergaard, *J. Phys. Chem. A* **115**, 8669 (2011).
- M. E. Jenkin, S. M. Saunders, M. J. Pilling, *Atmos. Environ.* **31**, 81 (1997).
- D. S. Alderdice, R. N. Dixon, *J. Chem. Soc., Faraday Trans. II* **72**, 372 (1976).
- L. Vereecken, J. S. Francisco, *Chem. Soc. Rev.* **41**, 6259 (2012).

Fig. 4. Rate coefficient for reaction of *anti*-CH₃CHOO with H₂O. Fitted pseudo-first-order decay constants of *anti*-CH₃CHOO are shown as a function of H₂O concentration. The dashed line is a fit to the data, weighted by the statistical uncertainty in the exponential fits to the individual decay traces ($\pm 1\sigma$ error bars shown in the figure). Each fit included >20 points across the relevant decay. (Inset) The decay of CH₃CHOO measured with 10.50 eV (solid circles, predominantly *syn*) and 9.37 eV (open circles, predominantly *anti*) in the presence of [H₂O] = $2.7 \times 10^{16} \text{ cm}^{-3}$.



Acknowledgments: Additional pseudo-first-order rate constants, details of the experiments and calculations, and spectroscopic data underpinning this work are presented in the supplementary materials. The participation of O.W., A.J.E., J.D.S., D.L.O., and C.A.T. and the development of the experimental kinetics apparatus were funded by the Division of Chemical Sciences, Geosciences, and Biosciences, the Office of Basic Energy Sciences, the U.S. Department of Energy. D.E.S., J.M.D., and C.J.P. thank the Natural Environment Research Council for funding, and J.M.D. thanks the Leverhulme Trust for a senior fellowship. The Advanced Light Source is supported by the Director, Office of Science, Office of Basic Energy Sciences, of the U.S. Department of Energy under contract DE-AC02-05CH11231

at Lawrence Berkeley National Laboratory. Sandia is a multiprogram laboratory operated by Sandia Corporation, a Lockheed Martin Company, for the National Nuclear Security Administration under contract DE-AC04-94-AL85000. D.K.W.M., J.M.D., C.J.P., and E.P.F.L. acknowledge support from the Research Grant Council of the Hong Kong Special Administrative Region (grant no. PolyU 5019/11P) and the National Service for Computational Chemistry Software (UK) for computational resources. The experiments were conceived by C.A.T., C.J.P., and D.E.S.; designed by C.A.T., D.L.O., C.J.P., O.W., and A.J.E.; and carried out by O.W., J.D.S., A.J.E., A.M.S., B.R., C.J.P., C.A.T., and D.L.O. E.P.F.L., D.K.W.M., and J.M.D. were responsible for the quantum chemistry and Franck-Condon calculations. All authors

participated in the data analysis and interpretation and contributed to the manuscript.

Supplementary Materials

www.sciencemag.org/cgi/content/full/340/6129/17//DC1
Materials and Methods
Supplementary Text
Figs. S1 to S19
Schemes S1 and S2
Tables S1 to S8
References (31–49)

2 January 2013; accepted 15 February 2013
10.1126/science.1234689

Enantioselective Synthesis of Pactamycin, a Complex Antitumor Antibiotic

Justin T. Malinowski,* Robert J. Sharpe,* Jeffrey S. Johnson†

Medicinal application of many complex natural products is precluded by the impracticality of their chemical synthesis. Pactamycin, the most structurally intricate aminocyclopentitol antibiotic, displays potent antiproliferative properties across multiple phylogenetic domains, but it is highly cytotoxic. A limited number of analogs produced by genetic engineering technologies show reduced cytotoxicity against mammalian cells, renewing promise for therapeutic applications. For decades, an efficient synthesis of pactamycin amenable to analog derivatizations has eluded researchers. Here, we present a short asymmetric total synthesis of pactamycin. An enantioselective Mannich reaction and symmetry-breaking reduction sequence was designed to enable assembly of the entire carbon core skeleton in under five steps and control critical three-dimensional (stereochemical) functional group relationships. This modular route totals 15 steps and is immediately amenable for structural analog synthesis.

Complex organic molecules produced by bacteria have been used to treat numerous disease types for nearly a century (1–4). However, many naturally derived compounds that exhibit interesting bioactivities are practically inaccessible via synthetic organic chemistry. A natural product's structural complexity can create an insurmountable impediment to the preparation of analogs that might exhibit improved characteristics. An ongoing challenge in the field of synthetic chemistry is the development of methods that close the gap between the efficiency of biosynthetic machinery and laboratory synthesis. Because of the inherent flexibility of the latter, success in this endeavor could provide access to useful structural variants that might otherwise be inaccessible.

Pactamycin (**1**; Fig. 1) was isolated from *Streptomyces pactum* var. *pactum* in 1961 by Argoudelis *et al.* (5). The bioactivity profile of this natural product is especially notable, as it displays antitumor, antimicrobial, antiviral, and anti-protozoal properties by acting as a universal inhibitor of translocation (6–9). Within the ribosomal subunit in which it interacts, pactamycin mimics an RNA dinucleotide through interactions of its aniline and salicylate moieties with stem loops in the 16S RNA (10). Unfortunately, pactamycin's therapeutic benefits have yet to be realized, due

to high cytotoxicity (median inhibitory concentration of 95 nM against human diploid embryonic cell line MRC-5) (11). Pactamycin is a prototypical example of a promising bioactive natural product whose complexity hampers the investigation of structure-activity relationships (SARs) that might lead to a serviceable therapeutic application and/or a better understanding of intrinsic bioactivity.

Genetic engineering studies have reignited promise for medicinal application, as 7-deoxy- and 8'-hydroxy-derivatives were isolated and displayed diminished cytotoxicity (11–14). In the context of the work described herein, it is worth noting that Lu *et al.* contend that the structural complexity of **1** renders these and related structural modifications "inaccessible by synthetic organic chemistry" (12). Conversely, we have proceeded from the hypothesis that the genetic engineering approach to pactamycin analogs might be inherently limited by the biosynthetic machinery (15, 16). Though pactamycin is commercially available, a chemical approach to its synthesis could, in principle, provide far greater opportunity and flexibility for discovering and advancing useful compounds. However, this tactic will only be feasible in the presence of an efficient synthesis platform that rapidly develops the appropriate level of structural complexity. In fact, synthetic interest in pactamycin has recently flourished, culminating in the landmark 32-step total synthesis from Hanessian and co-workers (17, 18), as well as numerous partial synthetic studies (19–23). Despite these creative, state-of-the-art approaches,

a compelling case can be made that a more practical synthesis solution is needed.

In this Report, we disclose a 15-step total synthesis of pactamycin, which has, in the initial pass, produced the natural product on a milligram scale and a key branch-point intermediate on a gram scale. We emphasized both modular construction and introduction of functionality in the final desired form of pactamycin, enabling an approach amenable to derivatization for analog synthesis. Late-stage introduction of the aniline- and salicylate-binding elements provides an opportunity for future SAR studies.

The recognition of a hidden symmetry in the northeast quadrant of pactamycin (**1**) was critical to our synthetic plan. Depicted in Fig. 2A, the carbon chain connecting C-4 and C-8 can be extracted to a symmetrical α -ureido-2,4-pentanedione **2**. We envisaged simplified formation of the fully substituted C-1 center via a Mannich reaction. Due to the symmetrical methyl ketone substituents at C-1, diastereoselectivity considerations are obviated, allowing for a focus on the enantioselective C-2-amino incorporation during the C-1–C-2 bond construction. The nascent C-2 stereocenter would then need to direct a site- and diastereoselective diketone monoreduction, setting the C-2/C-1/C-7 stereotriad (red dashed arrows in Fig. 2B). This sequence would provide the entire pactamycin carbon-core skeleton from which modular delivery of various functionality (Fig. 2C) could provide **1** and/or its congeners in rapid fashion.

The first challenge we faced was implementation of the Mannich reaction with an appropriately configured imine electrophile. We were encouraged by results reported by Schaus and co-workers,

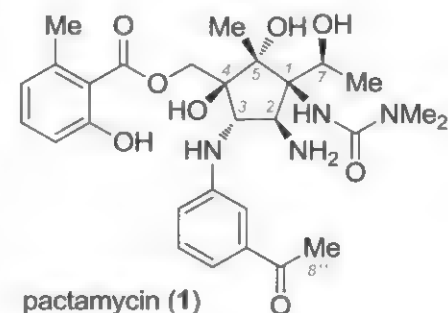


Fig. 1. Structure of pactamycin (1). Me, methyl.

Department of Chemistry, University of North Carolina at Chapel Hill, Chapel Hill, NC 27599, USA.

*These authors contributed equally to this work.

†Corresponding author. E-mail: jsj@unc.edu

wherein *Cinchona* alkaloids were effective in catalyzing the enantioselective addition of simple 1,3-dicarbonyls to acyl imines (24, 25). However, the required asymmetric Mannich addition of α -amino-substituted dicarbonyls was heretofore unknown. Additionally, with our goal of modular construction in mind, we planned to install the unusual 1,1-dimethylurea in its native form early in our route, a tactic that was expected to obviate the protection, deprotection, and acylation steps that characterize all other pactamycin synthetic studies.

Pronucleophile **2** was synthesized in two steps (26) from commodity chemical acetylacetone (2.5 kg ~\$75) and subjected to adapted Mannich conditions with cinnamaldehyde-derived imine **3** (Fig. 3). An evaluation of Lewis bases led to se-

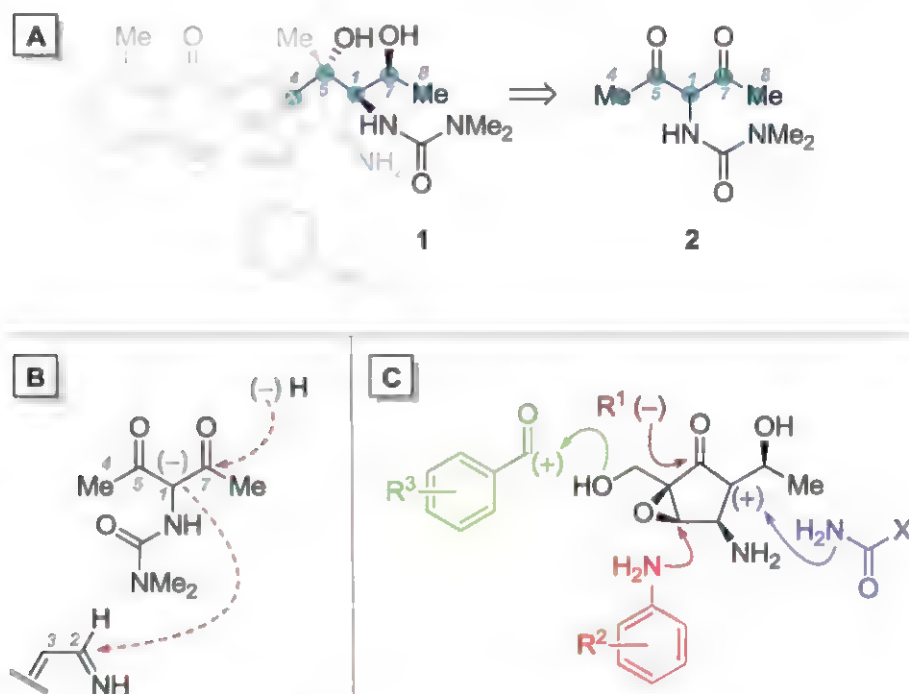
lection of cinchonidine (**7**) as the catalyst of choice, providing Mannich product **4** in 70% isolated yield and 98:2 enantiomeric ratio (er) (94% yield, 84:16 er before removal of the racemate by trituration). An x-ray diffraction study of a derivative (26) revealed the formation of the illustrated (*R*) configuration at C-2. Note that this nominally corresponds to the incorrect configuration at C-2, but the advancement of this stereochemical mistake was, in fact, critical to orchestrate downstream stereochemical outcomes and efficiently complete the synthesis (see below). The strategic selection of cinnamyl imine **3** as the Mannich electrophile translated to the installation all five carbons of the pactamycin core, with appropriate functional handles, in this initial C-C bond construction. This

reaction constitutes a useful advance in the synthesis of differentiated, highly functionalized 1,2-diamines by adaptation of the Schaus conditions to a new nucleophile-electrophile pair; extension to other urea-carbamate combinations can be envisaged.

The proposed desymmetrization of the Mannich adduct (**4** \rightarrow **5**) is complicated by the fact that four diastereomeric monoreduction products are possible. Lithium tri(*tert*-butoxy)aluminum hydride (LTBA) emerged as a superior reducing agent for the desymmetrization, affording hydroxyketone **5** with high diastereoselectivity [$>10:1$ ratio of **5**: Σ (other diastereomers)] in 72% yield. This reduction delivered the illustrated (1*R*,2*R*,7*S*)-product; therefore, the incorrect C-2 isomer was parlayed into the correct C-1/C-7 configurations. Subsequent silyl protection of the C-7 hydroxyl gave methyl ketone **6**.

Our attention then shifted to installation of the C-4 side chain and cyclization to complete the cyclopentenone core (Fig. 4). We treated the lithium enolate of ketone **6** with formaldehyde gas (generated *in situ* by the pyrolysis of paraformaldehyde), which resulted in the single-aldol addition product **8** (27, 28). Alkene ozonolysis furnished aldehyde **9** poised for intramolecular aldol condensation. Cyclization of the β -hydroxy ketone (29) was effected upon treatment with sodium methoxide to provide the five-membered pactamycin core structure (**10**) in 50% yield over two steps. Under the basic reaction conditions, the configurationally labile C-2 stereocenter was inverted, and only the correct C-2 isomer was observed in the product enone **10**. This serendipitous event corrected our initial stereochemical error, simplifying subsequent core manipulation.

With cyclopentenone **10** in hand, three challenges remained: (i) C-5 methide addition, (ii) C-4 hydroxylation, and (iii) C-3 aniline installation. Inspired by a related approach by Hanessian and co-workers (17, 18), we pursued an epoxidation-nucleophilic aniline ring-opening sequence for access to the *trans*-anilinoalcohol. We anticipated that subsequent nucleophilic methylation of the C-5 ketone would complete the core functionalization. As we explored this proposed route, we discovered the importance of both the order of



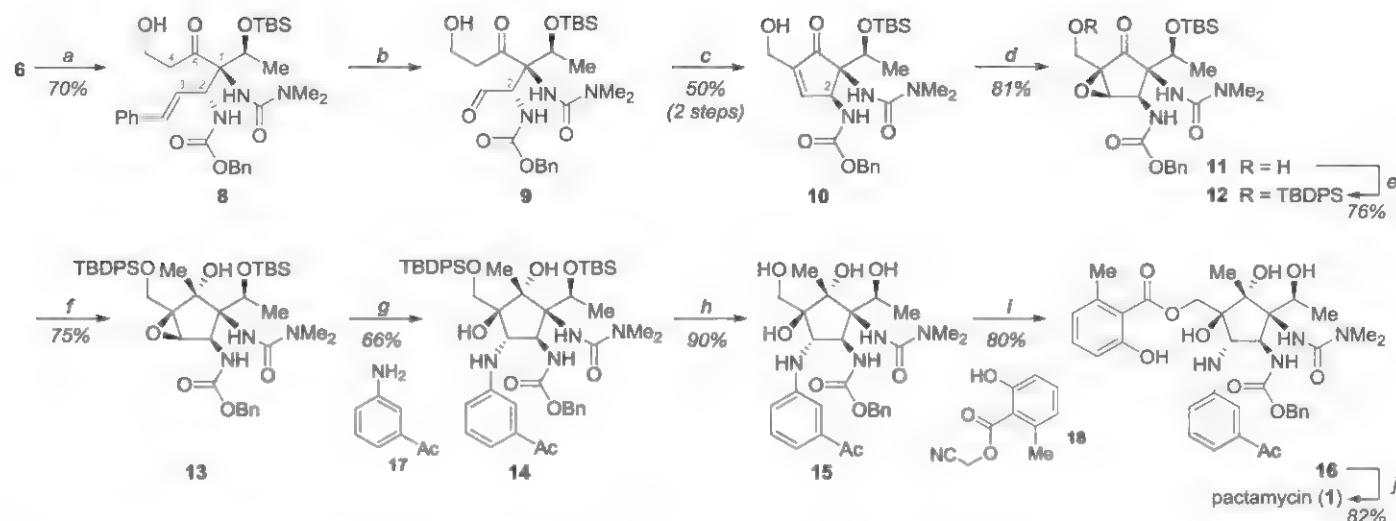


Fig. 4. Elaboration of 6 to pactamycin (1) via modular incorporation of unprotected functionality. Reagents and conditions are as follows: (a) lithium diisopropylamide, formaldehyde [$\text{CH}_2\text{O}_{(g)}$], THF, -78° to -45°C ; (b) ozone (O_3), CH_2Cl_2 , -78°C , then dimethylsulfide (Me_2S), -78°C to room temperature (rt); (c) sodium methoxide (NaOMe), THF, 0°C ; (d) hydrogen peroxide (H_2O_2), sodium hydroxide (NaOH), 7:1 CH_2Cl_2 :methanol (MeOH), 0°C ; (e)

chloro(*tert*-butyl)diphenylsilane (TBDPSCl), triethylamine (NEt_3), dimethylaminopyridine (10 mol %), CH_2Cl_2 , 0°C to rt; (f) methylmagnesium bromide (MeMgBr), THF, 0°C ; (g) 3-acetylaniline (**17**), scandium(III) trifluoromethanesulfonate [$\text{Sc}(\text{OTf})_3$], toluene, 60°C ; (h) TBAF, THF, 0°C ; (i) potassium carbonate (K_2CO_3), **18**, dimethylacetamide; (j) palladium hydroxide on carbon [$\text{Pd}(\text{OH})_2/\text{C}$], H_2 (1 atm), MeOH .

these steps and the protecting group identity at the C-4 hydroxymethylene.

Nucleophilic epoxidation of enone **10** with basic hydrogen peroxide provided epoxy alcohol **11** with high diastereoselectivity. The sterically demanding *tert*-butyldiphenylsilyl (TBDPS) protecting group was imperative to ensure diastereoselective addition in the subsequent C-5 methylation and to withstand the aniline epoxide-opening conditions. Installation of the silyl group provided ketone **12**, which was then treated with a methyl Grignard reagent to provide carbinol **13**, from the required concave facial trajectory. Nucleophile approach from the convex surface of analogous oxabicyclo[3.1.0]hexane systems is well documented (**17**, **18**, **30**) and would have provided the wrong stereochemical outcome. In the present case, we surmise that this innate preference is overridden, at least in part, via direction by the urea functionality, lending additional support to the strategic decision to incorporate this functionality in its native form from the outset. Epoxide **12** is the crucial branch point for analog synthesis and has been reached in gram quantity on a single pass. The epoxide was subjected to a $\text{Sc}(\text{OTf})_3$ -promoted (OTf , trifluoromethanesulfonate) nucleophilic ring opening with 3-acetylaniline (**17**), proceeding in 66% yield with 18% recovery of the starting material to install the C-3 aniline derivative. The addition of this anilino functionality in its desired, unprotected form completed functionalization of the pactamycin core (**14**).

Deprotection of both silyl ethers was accomplished upon treatment with tetrabutylammonium fluoride (TBAF) to provide tractable tetraol **15** in 90% yield, leaving a highly reactive primary alcohol for selective acylation. A ketene-mediated acylation protocol developed by Serrano *et al.* (**31**)

and exploited by Hanessian *et al.* (**17**, **18**) proved effective in completing the sterically encumbered acylation and providing penultimate intermediate **16**. Carboxybenzyl deprotection occurred rapidly under hydrogenolysis conditions with the use of Pearlman's catalyst (**32**) in 82% yield. This deprotection completed the synthesis of pactamycin in 15 steps and 1.9% overall yield. The route is flexible and should be amenable to the preparation of congeners since the introduction of highly functionalized side chains in unprotected form (urea, salicylate, *meta*-acetyl aniline) has been demonstrated.

References and Notes

- Y.-W. Chin, M. J. Balunas, H. B. Chai, A. D. Kinghorn, *AAPS J.* **8**, E239 (2006).
- F. von Nussbaum, M. Brands, B. Hinz, S. Weigand, D. Habich, *Angew. Chem. Int. Ed.* **45**, 5072 (2006).
- C. Drahl, B. F. Cravatt, E. J. Sorensen, *Angew. Chem. Int. Ed.* **44**, 5788 (2005).
- K. Nakanishi, in *Comprehensive Natural Products Chemistry*, D. Barton *et al.*, Eds. (Elsevier, New York, 1999), vol. 1, p. 23.
- A. D. Argoudelis, H. K. Jahnke, J. A. Fox, *Antimicrob. Agents Chemother.* **1962**, 191 (1962).
- G. Dinos *et al.*, *Mol. Cell* **13**, 113 (2004).
- D. D. Weller, A. Haber, K. L. Rinehart Jr., P. F. Wiley, *J. Antibiot.* **31**, 997 (1978).
- P. F. Wiley, H. K. Jahnke, F. MacKellar, R. B. Kelly, A. D. Argoudelis, *J. Org. Chem.* **35**, 1420 (1970).
- D. J. Duchamp, abstract no. 23 presented at the American Crystallographic Association Winter Meeting, Albuquerque, NM, 3 to 7 April 1972.
- D. E. Brodersen *et al.*, *Cell* **103**, 1143 (2000).
- M. Iwatsuki *et al.*, *J. Antibiot.* **65**, 169 (2012).
- W. Lu, N. Roongsawang, T. Mahmud, *Chem. Biol.* **18**, 425 (2011).
- K. Otaguro *et al.*, *J. Antibiot.* **63**, 381 (2010).
- K. Dobashi *et al.*, *J. Antibiot.* **39**, 1779 (1986).
- For an instructive debate on this point, please see (**16**).
- J. D. Keasling, A. Mendoza, P. S. Baran, *Nature* **492**, 188 (2012).

- S. Hanessian *et al.*, *Angew. Chem. Int. Ed.* **50**, 3497 (2011).
- S. Hanessian, R. R. Vakiti, S. Dorich, S. Banerjee, B. Deschênes-Simard, *J. Org. Chem.* **77**, 9458 (2012).
- T. Tsujimoto, T. Nishikawa, D. Urabe, M. Isobe, *Synlett* **2005**, 433 (2005).
- S. Knapp, Y. Yu, *Org. Lett.* **9**, 1359 (2007).
- J. T. Malinowski, S. J. McCarver, J. S. Johnson, *Org. Lett.* **14**, 2878 (2012).
- T. J. Haussener, R. E. Looper, *Org. Lett.* **14**, 3632 (2012).
- N. Matsumoto, T. Tsujimoto, A. Nakazaki, M. Isobe, T. Nishikawa, *RSC Adv.* **2**, 9448 (2012).
- S. Lou, B. M. Taoka, A. Ting, S. E. Schaus, *J. Am. Chem. Soc.* **127**, 11256 (2005).
- A. Ting, S. Lou, S. E. Schaus, *Org. Lett.* **8**, 2003 (2006).
- For details, please refer to the supplementary materials on Science Online.
- Y. Li, J.-P. Feng, W.-H. Wang, J. Chen, X.-P. Cao, *J. Org. Chem.* **72**, 2344 (2007).
- B. M. Trost, C. D. Haffner, D. J. Jebaratnam, M. J. Krische, A. P. Thomas, *J. Am. Chem. Soc.* **121**, 6183 (1999).
- J. M. J. Verlaak, A. J. H. Klunder, B. Zwanenburg, *Tetrahedron Lett.* **23**, 5463 (1982).
- L. Shi, K. Meyer, M. F. Greaney, *Angew. Chem. Int. Ed.* **49**, 9250 (2010).
- P. Serrano, A. Llebaria, A. Delgado, *J. Org. Chem.* **67**, 7165 (2002).
- W. M. Pearlman, *Tetrahedron Lett.* **8**, 1663 (1967).

Acknowledgments: The project described was supported by award no. R01 GM084927 from the National Institute of General Medical Sciences. J.T.M. acknowledges an American Chemical Society Division of Organic Chemistry graduate fellowship. R.J.S. acknowledges an NSF graduate research fellowship. X-ray crystallography was performed by P. White (University of North Carolina). The Cambridge Crystallographic Data Centre (CCDC) contains the supplementary crystallographic data for this paper, under deposition no. 914582. These data can be obtained free of charge from via www.ccdc.cam.ac.uk/data_request/cif. A patent application on the route and compounds presented in this paper has been filed through the University of North Carolina.

Supplementary Materials

www.sciencemag.org/cgi/content/full/340/6129/180/DC1
Materials and Methods
References (33, 34)

3 January 2013; accepted 11 February 2013
10.1126/science.1234756

Speleothems Reveal 500,000-Year History of Siberian Permafrost

A. Vaks,^{1*} O. S. Gutareva,² S. F. M. Breitenbach,³ E. Avirmed,⁴ A. J. Mason,¹ A. L. Thomas,¹ A. V. Osinzev,⁵ A. M. Kononov,² G. M. Henderson¹

Soils in permafrost regions contain twice as much carbon as the atmosphere, and permafrost has an important influence on the natural and built environment at high northern latitudes. The response of permafrost to warming climate is uncertain and occurs on time scales longer than those assessed by direct observation. We dated periods of speleothem growth in a north-south transect of caves in Siberia to reconstruct the history of permafrost in past climate states. Speleothem growth is restricted to full interglacial conditions in all studied caves. In the northernmost cave (at 60°N), no growth has occurred since Marine Isotopic Stage (MIS) 11. Growth at that time indicates that global climates only slightly warmer than today are sufficient to thaw extensive regions of permafrost.

Permafrost regions (in which the ground is frozen throughout the year) cover 24% of the Northern Hemisphere land surface and hold ~1700 Gt of organic carbon. When it thaws, permafrost releases CO₂ and CH₄, turning a long-term carbon sink into a source and enhancing the greenhouse effect (1, 2). Permafrost degradation also intensifies thermo-karst development, coastline erosion, and liquefaction of ground previously cemented by ice. The latter endangers infrastructure, including major Siberian oil and gas facilities (3). An ability to predict the extent of future permafrost degradation is desirable.

Assessing the response of permafrost to changing climate can be difficult. Instrumental records during the past 20 years indicate substantial warming and thawing of local permafrost conditions (4), but permafrost at regional scales is slow to respond to warming, and instrumental records are insufficient to capture the long-term behavior. To understand the long-term response of permafrost to climate change requires knowledge of past permafrost conditions. Dating of organic material (5) or ground ice (6) can indicate the age of existing permafrost but cannot reveal the longer-term history of permafrost.

Here, we used cave carbonates (speleothems) as a tool to date past permafrost and its relationship to global climate. Vadose speleothems (stalactites, stalagmites, and flowstones) form when meteoric waters (i.e., originating from atmospheric precipitation) seep through the vadose zone into caves. Cave temperatures usually approximate the local mean annual air temperature (MAAT) because of buffering by the surrounding rock (7). When cave temperatures drop below 0°C, waters freeze and speleothem growth ceases. Speleothems found in modern permafrost regions are therefore relicts from warmer periods before permafrost

formed (8–10). Absence of water also prevents speleothem growth in arid settings, so speleothem growth episodes in modern deserts are proxies for past wet periods (11). Because speleothems can be robustly and precisely dated with U-Th techniques, they provide a detailed history of pe-

riods when liquid water was available and when both permafrost and desert conditions were absent.

We reconstructed the history of Siberian permafrost (and the aridity of the Gobi Desert) during the past ~500,000 years, by means of U-Th dating of speleothems in six caves along a north-south transect in northern Asia from Eastern Siberia at 60.2°N to the Gobi Desert at 42.5°N (Fig. 1). The northernmost cave, Lenskaya Ledyanaya, sits today on the boundary of continuous permafrost with MAAT substantially below 0°C (12). The permafrost type changes toward the southwest to discontinuous, sporadic, and then permafrost-free conditions (13) (Fig. 1). Annual precipitation in this Siberian region is 400 to 600 mm/year, falling mainly during summer. To the south, in the Gobi, MAAT ranges from +2°C to +8°C and little precipitation falls (80 to 200 mm/year) (14).

Speleothem thickness provides an indication of long-term liquid water availability along the transect. Only 8 cm of growth is seen in the northernmost cave, increasing to ~70 cm in the

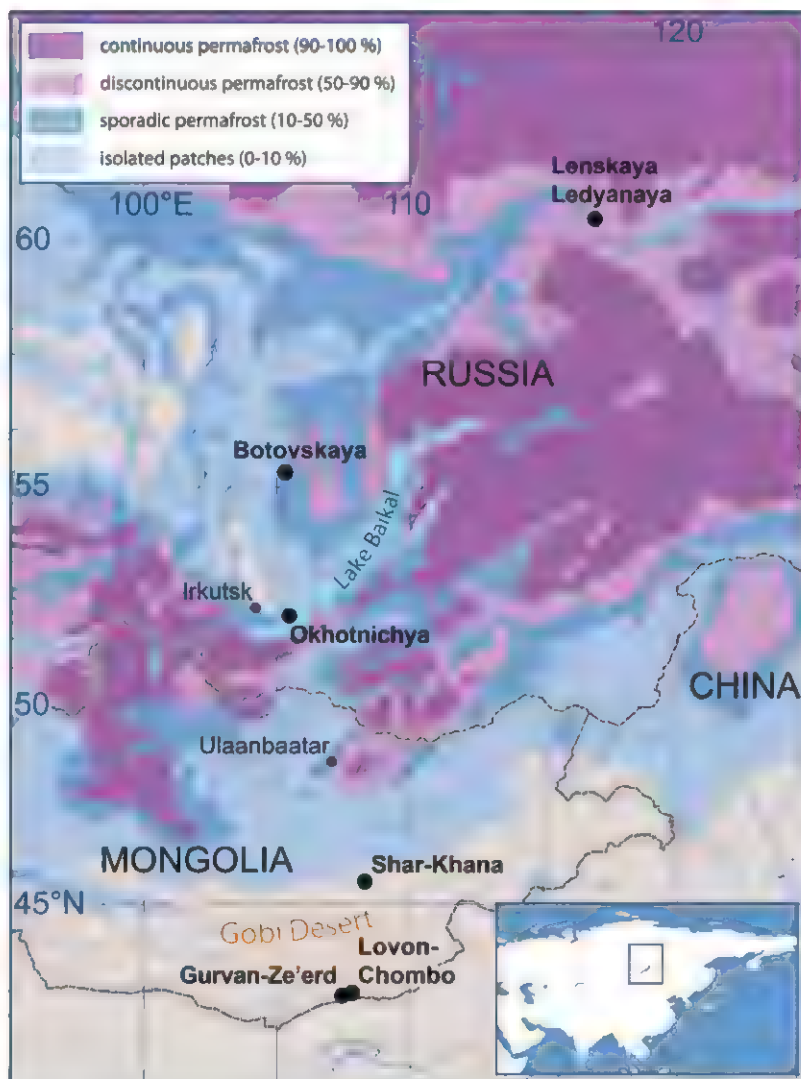


Fig. 1. Map showing the extent of permafrost types in eastern Siberia, the Gobi Desert, and locations of studied caves. Caves are indicated as black circles. [Permafrost data are from (30)].

¹Department of Earth Sciences, University of Oxford, Oxford OX1 3AN, UK. ²Institute of Earth's Crust, Russian Academy of Sciences, Siberian Branch, 128 Lermontova Street, Irkutsk 664033, Russia. ³Swiss Federal Institute of Technology Zürich (ETH Zürich), CH-8092 Zürich, Switzerland. ⁴Institute of Geography, Mongolian Academy of Sciences, 210620 Ulaanbaatar, Mongolia. ⁵Arabica Speleological Club, Mamin-Sibirskiy Street, Box 350, Irkutsk 554082, Russia.

*Corresponding author. E-mail: anton.vaks@earth.ox.ac.uk

caves of southern Siberia and decreasing again to less than 30 cm in the Gobi. As expected, southern Siberia is more suitable for speleothem growth than the cold north or the dry south. All recovered speleothems show a texture of calcium carbonate layers alternating with growth hiatuses (see supplementary materials).

Thirty-six speleothems were collected from the caves, and 111 U-Th ages were determined (Fig. 2A). In each speleothem, at least one sample was taken from the outermost layer and from each section of growth (i.e., between hiatuses) inward, until the limits of the U-Th chronology were reached (age ~500,000 years) to assess all periods of growth. A full description of the samples and their subsampling and dating is given in the supplementary materials.

The youngest speleothem growth in the region of modern continuous permafrost (i.e., at 60°N) occurred during interglacial Marine Isotopic Stage 11 (MIS-11), contrasting with the center of the transect where speleothems grew during all interglacials (Fig. 2, A and B). Age ranges in southern Siberia also demonstrate that the duration of speleothem deposition in MIS-11 was longer than during subsequent interglacials. These observations indicate that permafrost thawing during MIS-11 was more extensive than at any other point during the last 450,000 years and extended northward of 60°N, significantly further north than the present limit of continuous permafrost. Some similar thawing may also have occurred at MIS-13 in this most northerly cave. The absence of any observed speleothem growth since MIS-11 in the northerly Lenskaya Ledianaya cave, despite dating the outer edges of eight speleothems, suggests the permanent presence of permafrost at this latitude since the end of MIS-11. Speleothem growth in this cave occurred during early MIS-11, ruling out the possibility that the unusual length of MIS-11 caused the permafrost thawing.

MIS-11 was also characterized by wetter conditions in the Mongolian Gobi Desert, as shown by two ages from Shar-Khana Cave speleothems (Fig. 2A), which contrast with the absence of growth during subsequent interglacials. The existence of a humid event in the Gobi during early MIS-11 is supported by mollusk assemblages from the Chinese Loess Plateau (15) and by the dominance of input into Lake Baikal via the Selenga River during MIS-11 (16).

The degradation of permafrost at 60°N during MIS-11 allows an assessment of the warming required globally to cause such extensive change in the permafrost boundary. There is compelling evidence that MIS-11 was the warmest of recent interglacials, including the presence of boreal forest on South Greenland at that time (17), the absence of ice-rafted debris in the North Atlantic (18), increased sea levels (19), and higher sea surface temperatures (SSTs) in the tropical Pacific (20–22). Mg/Ca reconstructions (21, 22) indicate that the SST of the Pacific Warm Pool (PWP) reached >30°C in early MIS-11, compared to 29.5°C in MIS-5.5 and ~28.5°C during

the pre-industrial Late Holocene (Fig. 2D). This tropical heat was transported poleward (23), and there is evidence of unusual warmth in Siberia during MIS-11, evidenced by the high fraction of

biogenic silica in the sediments of Lake Baikal (24) (Fig. 2C) and high spruce pollen content in Lake El'gygytyn, suggesting local temperatures 4° to 5°C above the present (25). When PWP

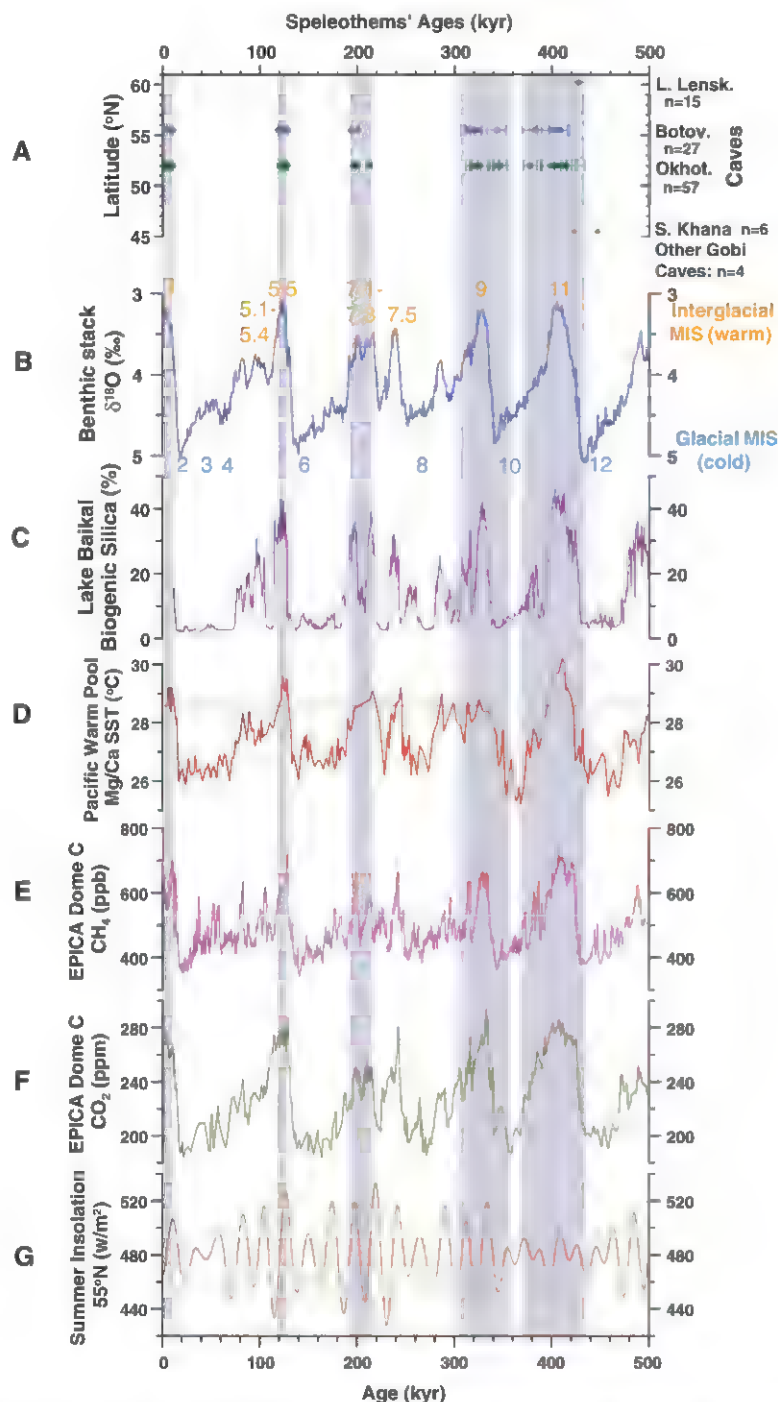


Fig. 2. Comparison of speleothems' growth periods in Siberia and Mongolia with other paleoclimate records of the past 500,000 years. Gray vertical bars indicate periods of growth in Okhotnichya and Botovskaya caves. (A) Distribution of speleothem U-Th ages [in thousands of years (kyr); $\pm 2\sigma$] in time and space; n = total number of U-Th age determinations per cave, including those beyond the U-Th range. (B) Benthic $\delta^{18}\text{O}$ stack (31) with MIS numbers. (C) Concentration of biogenic silica in Lake Baikal sediments (24). (D) Pacific Warm Pool Mg/Ca SST, with the pre-industrial Late Holocene SST shown by red horizontal fragmented line (21, 22). (E and F) CH_4 and CO_2 records, respectively, of EPICA Dome C (26, 27). (G) Summer insolation at 55°N (29). Speleothems with ages exceeding 500,000 years (within $\pm 2\sigma$ range) are not shown in (A) but are accounted for in n . Two samples, SLL9-2-A+B and SOP-32-B, are not included because they reflect a mixture of material from different layers; see table S1.

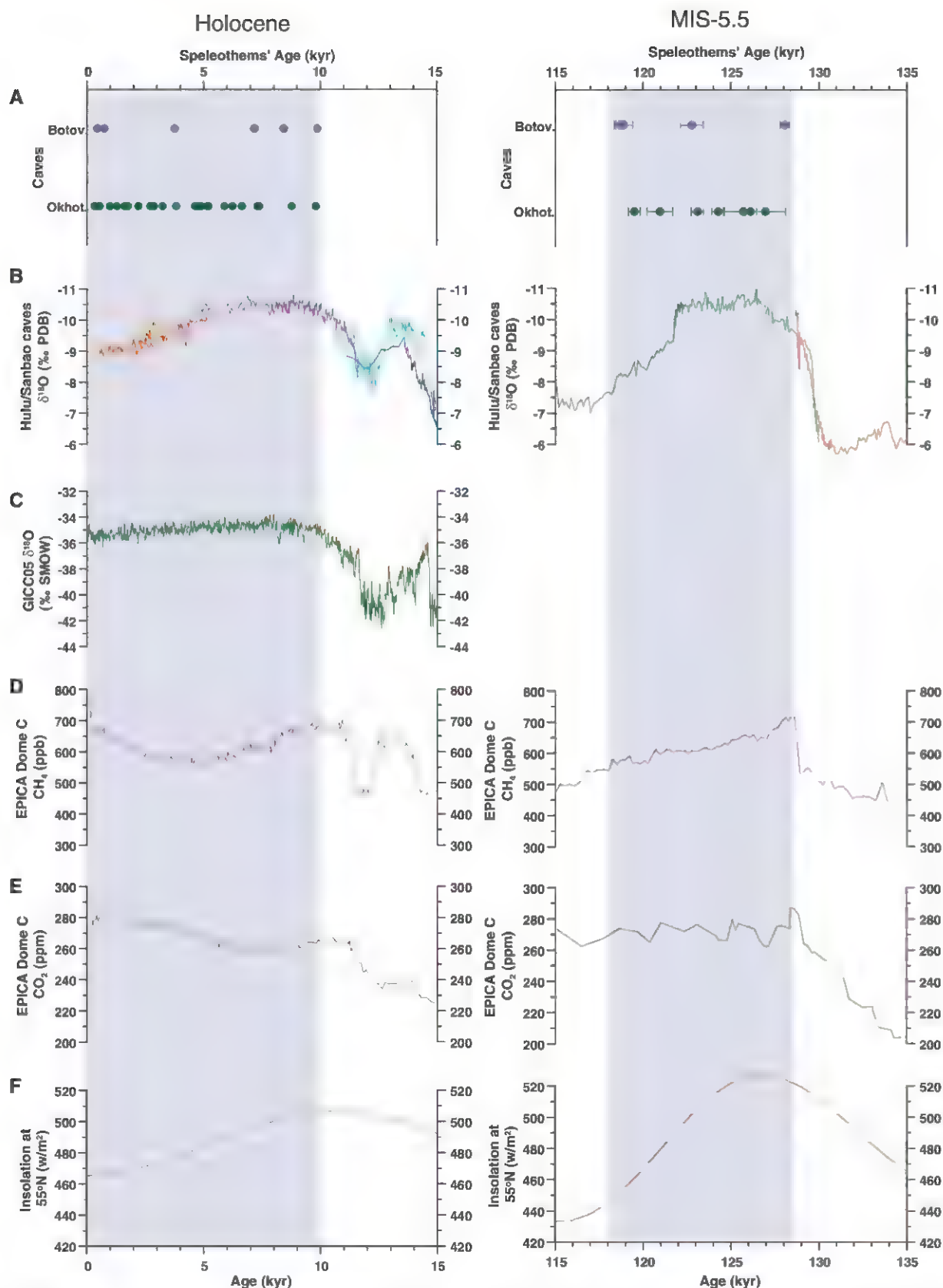


Fig. 3. Comparison of MIS-5.5 and Holocene speleothems' growth periods with other paleoclimate records. Gray vertical bars indicate periods of growth. (A) Siberian speleothem growth periods during the Holocene and

MIS-5.5. (B) East Asian monsoon records from Hulu and Sanbao caves (32). (C) GICC05 $\delta^{18}\text{O}$ (33, 34). (D and E) CH_4 and CO_2 records, respectively, of EPICA Dome C (26, 27). (F) Summer insolation at 55°N (29).

temperatures reached 30°C, this appears to have caused more pronounced warming of northern continents and to have led to substantial northward migration of the permafrost boundary.

Periods of Siberian speleothem growth since MIS-11 suggest a close link between greenhouse warming (hence global temperatures) and permafrost extent. After a brief hiatus in growth after MIS-11 (from 370,000 to 355,000 years ago), coinciding with a minimum in atmospheric CO₂ and in PWP SST during MIS-10 (Fig. 2, D and F), large thicknesses of speleothem grew in Southern Siberia during MIS-9 as greenhouse gases returned to higher values. Speleothems also grew actively during MIS-5.5 and the Holocene (>5 cm) when CO₂ levels were high. In contrast, growth during MIS-7, a period of lower CO₂ and cooler global conditions, is minimal (maximum 1.5 cm in any studied cave), and no growth is observed during MIS-5.4 to 5.1. Conditions during MIS-7 were at the very limit for growth in southern Siberia: Speleothems grew during MIS-7.3 and 7.1 in Okhotnichya Cave (52°N) but only during MIS-7.1 just to the north at Botovskaya Cave (55°N). No growth occurred during MIS-7.5 at either cave despite higher concentrations of CO₂ and CH₄ than later in MIS-7 (26, 27) and high PWP SST (Fig. 2, D to F) (21, 22). Lake Baikal biogenic silica (24) and the percentage of arboreal pollen in Lake El'gygytyn sediments (28) are also lower during MIS-7.5 than during MIS-7.3 and 7.1. Lower local summer insolation during MIS-7.5 (Fig. 2G) (29) suggests a role for local insolation in overprinting a Siberian climate dominantly controlled by global greenhouse gas levels.

U-Th dating of Siberian speleothem growth during recent interglacials allows detailed comparison of permafrost history with other aspects of the global climate system (Fig. 3). During MIS-5.5, speleothems started growing between 128,700 and 127,300 years ago, and this growth ended between 119,200 and 118,100 years ago (as determined from Bayesian analysis of U-Th data using OxCal-4.1; see supplementary materials). The permafrost thawing initiated when insolation was close to its maximum and greenhouse gases had just reached maximum values. Holocene permafrost degradation at our sites lags maximum insolation and greenhouse gas concentrations slightly, and starts between 10,000 and 9800 years ago. This lag may be due to the time required for permafrost to thaw at the slightly lower insolation and CO₂ levels of the Holocene (relative to MIS-5.5).

Overall, dated periods of speleothem growth allow an assessment of the relationship between global temperature and permafrost extent. PWP SST was 0.5° to 1.0°C higher during MIS-5.5 and ~1.5°C higher during early MIS-11 relative to the pre-industrial Late Holocene (Fig. 2D) (21, 22). Using PWP SST as a surrogate for global temperature (21) suggests that an increase in global temperatures by 0.5° to 1.0°C will degrade only noncontinuous permafrost in southern Siberia, with the Gobi Desert remaining arid. Warming of

~1.5°C (i.e., as in MIS-11) may cause a substantial thaw of continuous permafrost as far north as 60°N and may create wetter conditions in the Gobi Desert. Such warming is therefore expected to markedly change the environment of continental Asia and can potentially lead to substantial release of carbon trapped in the permafrost into the atmosphere.

References and Notes

- G. Grosse et al., *EOS* **92**, 73 (2011).
- E. A. G. Schuur et al., *Bioscience* **58**, 701 (2008).
- O. Anisimov, S. Reneva, *AMBIO* **35**, 169 (2006).
- V. E. Romanovsky, S. L. Smith, H. H. Christiansen, *Permafrost. Periglac. Proc.* **21**, 106 (2010).
- Y. K. Vasil'chuk, J.-C. Kim, A. C. Vasil'chuk, *Nucl. Instrum. Methods Phys. Res. B* **223–224**, 650 (2004).
- D. A. Gilichinsky et al., *Quat. Sci. Rev.* **26**, 1547 (2007).
- H. P. Schwarcz, in *Handbook of Environmental Isotope Geochemistry*, P. Fritz, J. C. Fontes, Eds. (Elsevier, Amsterdam, 1986), vol. 2, pp. 271–300.
- R. A. Ciff, C. Spötl, A. Mangini, *Quat. Geochronol.* **5**, 452 (2010).
- B. Lauriol, D. C. Ford, J. Cinq-Mars, W. A. Morris, *Can. J. Earth Sci.* **34**, 902 (1997).
- S. E. Lauritzen, *Quat. Res.* **43**, 133 (1995).
- A. Vaks, M. Bar-Matthews, A. Matthews, A. Ayaon, A. Frumkin, *Quat. Sci. Rev.* **29**, 2647 (2010).
- Philip's Modern School Atlas, 95th Edition* (Philip's/Octopus, London, 2007).
- A. Jones et al., Eds., *Soil Atlas of the Northern Circumpolar Region* (Publication Office of the European Union, Luxembourg, 2010).
- D. Dorjotov, N. Orshikh, T. Oyunchimeg, *Geographic Atlas of Mongolian Republic* (Mongolian Institute of Geodesy and Cartography, Ulaanbaatar, 2004). [in Mongolian]
- N. Wu et al., *Quat. Sci. Rev.* **26**, 1884 (2007).
- A. W. Mackay et al., *J. Quat. Sci.* **23**, 365 (2008).
- A. de Vernal, C. Hillaire-Marcel, *Science* **320**, 1622 (2008).
- J. F. McManus, D. W. Oppo, J. L. Cullen, *Science* **283**, 971 (1999).
- M. E. Raymo, J. X. Mitrovica, *Nature* **483**, 453 (2012).
- L. Ortlieb, A. Diaz, N. Guzman, *Quat. Sci. Rev.* **15**, 857 (1996).
- J. Hansen et al., *Proc. Natl. Acad. Sci. U.S.A.* **103**, 14288 (2006).
- M. Medina-Elizalde, D. W. Lea, *Science* **310**, 1009 (2005).
- A. J. Dickson et al., *Nat. Geosci.* **2**, 428 (2009).
- A. A. Prokopenko et al., *Quat. Res.* **55**, 123 (2001).
- M. Melles et al., *Science* **337**, 315 (2012).
- L. Loulergue et al., *Nature* **453**, 383 (2008).
- D. Lüthi et al., *Nature* **453**, 379 (2008).
- N. R. Nowaczyk et al., *Geophys. J. Int.* **150**, 109 (2002).
- J. Laskar et al., *Astron. Astrophys.* **428**, 261 (2004).
- J. Brown, O. J. Ferrians Jr., J. A. Heginbottom, E. S. Melnikov, *Circum-Arctic Map of Permafrost and Ground Ice Conditions* (National Snow and Ice Data Center/World Data Center for Glaciology, Boulder, CO, 2001).
- L. E. Lisiecki, M. E. Raymo, *Paleoceanography* **20**, PA1003 (2005).
- Y. Wang et al., *Nature* **451**, 1090 (2008).
- S. O. Rasmussen et al., *J. Geophys. Res.* **111**, D06102 (2006).
- See references 16 to 19 in the supplementary materials.

Acknowledgments: This article is dedicated to the memory of Prof. Y. Trzchinski, who during the last months of his life made a big effort to establish the cooperation between the University of Oxford and Institute of Earth's Crust (IEC) in Irkutsk. We thank D. Sokolnikov and other "Arabica" members, E. Kozireva (IEC), V. Alexio, and V. Balaev from Lensk for their help during the fieldwork in Siberia; the Mongolian Speleological Society for their help with the fieldwork in Mongolia; J. Fritz and L. Zehnder (ETH Zürich) for preparing Fig. 1 and for assistance with XRD analyses, respectively; and C. Day, V. Ersek, L. Zanna, P. Holdship, O. Green, S. Wyatt, Y. Nakajima, P. Pousada Solino, J. Cox, S. Usher, M. Chung, and others from University of Oxford for the help with the laboratory work, administration and computing issues, obtainment of funding, and fruitful discussions. Supported by NERC Fellowship NE/G013829/1, Royal Society grant JP080831, and Russian Foundation for Basic Research joint grant 09-05-92605 KO_a.

Supplementary Materials

www.sciencemag.org/cgi/content/full/science.1228729/DC1
Materials and Methods
Supplementary Text
Figs. S1 to S16
Tables S1 to S3
References

13 August 2012; accepted 6 February 2013
Published online 21 February 2013;
10.1126/science.1228729

A Long-Lived Relativistic Electron Storage Ring Embedded in Earth's Outer Van Allen Belt

D. N. Baker,^{1*} S. G. Kanekal,² V. C. Hoxie,¹ M. G. Henderson,³ X. Li,¹ H. E. Spence,⁴ S. R. Elkington,¹ R. H. W. Friedel,³ J. Goldstein,⁵ M. K. Hudson,⁶ G. D. Reeves,³ R. M. Thorne,⁷ C. A. Kletzing,⁸ S. G. Claudepierre⁹

Since their discovery more than 50 years ago, Earth's Van Allen radiation belts have been considered to consist of two distinct zones of trapped, highly energetic charged particles. The outer zone is composed predominantly of megaelectron volt (MeV) electrons that wax and wane in intensity on time scales ranging from hours to days, depending primarily on external forcing by the solar wind. The spatially separated inner zone is composed of commingled high-energy electrons and very energetic positive ions (mostly protons), the latter being stable in intensity levels over years to decades. In situ energy-specific and temporally resolved spacecraft observations reveal an isolated third ring, or torus, of high-energy (>2 MeV) electrons that formed on 2 September 2012 and persisted largely unchanged in the geocentric radial range of 3.0 to ~3.5 Earth radii for more than 4 weeks before being disrupted (and virtually annihilated) by a powerful interplanetary shock wave passage.

The magnetically confined radiation zones surrounding Earth were the first major discovery of the Space Age in 1958 (1–4).

Long-term observations of these energetic particle populations have subsequently shown dramatic, highly dynamic changes of the outer Van

Allen belt. Previous, rather sparse measurements of the radiation environment suggested that powerful acceleration events for relativistic electrons occur on time scales ranging from minutes (5, 6) to many hours (7, 8). Thus, there has been direct, as well as circumstantial evidence that an immensely powerful and efficient accelerator operates within the terrestrial magnetosphere just a few thousand kilometers above Earth's surface.

On 30 August 2012, twin NASA spacecraft, the Radiation Belt Storm Probes (RBSPs), were launched into highly elliptical, low-inclination orbits around Earth. The RBSP satellites are fully instrumented with identical energetic particle, plasma, magnetic field, and plasma wave sensors to measure and thoroughly characterize the radiation belt regions (9). The scientific payloads on board the RBSP spacecraft (renamed the "Van Allen Probes mission" by NASA at a formal ceremony on 9 November 2012) have unprecedented detection sensitivity, energy resolution, and temporal sampling capability. In particular, the Relativistic Electron-Proton Telescope (REPT) experiment (10) measures the key ~1- to ~20-MeV electron population throughout the RBSP orbit, which extends from geocentric distances of radius $r = 1.2R_E$ to $5.8R_E$ (R_E : Earth radius = 6372 km). The REPT sensors were among the first instruments turned on and have been return-

ing nearly continuous data from both Van Allen Probes spacecraft since 1 September 2012.

Prior key measurements of Earth's radiation environment have been made (11–13), but some of the longest and most comprehensive radiation belt observations have previously come from sensors on board the Solar, Anomalous, and Magnetospheric Particle Explorer (SAMPEX) mission (14). This spacecraft made low-Earth orbit observations of inner- and outer-zone particles from its launch in July 1992 until its recent atmospheric reentry and demise on 13 November 2012 (15, 16). SAMPEX measured energy $E > 1$ MeV electrons at the near-Earth foot of magnetic field lines but was never able to look into the "throat" of the radiation belt accelerator in the magnetospheric equatorial plane. This contrasts dramatically with the REPT-A and REPT-B instrument data collected by the Van Allen Probes from 1 September 2012 through early October 2012 (Fig. 1). These data show that a powerful electron acceleration event was already in progress when the instruments were first turned on. The entire outer radiation belt was enhanced in electron flux from $E \sim 3.0$ MeV (Fig. 1A) up to energies well above the $5.0 \leq E \leq 6.2$ MeV channel (Fig. 1C). At this time, the radiation belt populations clearly had the expected double-belt structure with an inner zone, an outer zone, and a "slot" region of greatly diminished intensity separating the two.

What is most notable (and unexpected) is the clear emergence of a separate, previously unseen belt, or "storage ring," of high-energy electrons that stands out clearly after 2 September 2012. This belt is evident in the $E = 4.0$ to 5.0 MeV range (Fig. 1B) and is the dominant flux feature in the $E = 5.0$ to 6.2 MeV energy range (Fig. 1C). This distinctive ring of highly relativistic electrons persists, changing only gradually, until its abrupt and almost complete disappearance late on 1 October 2012. Though the inner zone, the

slot region, and the relativistic storage ring ($3.0 < L^* < \sim 3.5$, where L^* is the distance in Earth radii at which a magnetic field line crosses the magnetic equatorial plane) change relatively little over this 4-week period, the more distant part of the outer Van Allen belt shows huge dynamical changes with new electron populations appearing at $L^* > 4.0$, beginning on ~7 September and intensifying greatly over a period of 2 weeks. Subsequently, the outermost parts of the outer Van Allen zone grew and diminished further with little effect on the storage-ring feature until the abrupt demise of virtually the entire outer-zone electron population at the end of 1 October. Other electron sensor systems on board the Van Allen Probes spacecraft, overlapping partially in energy coverage with the REPT sensors, also detected the storage-ring feature (17).

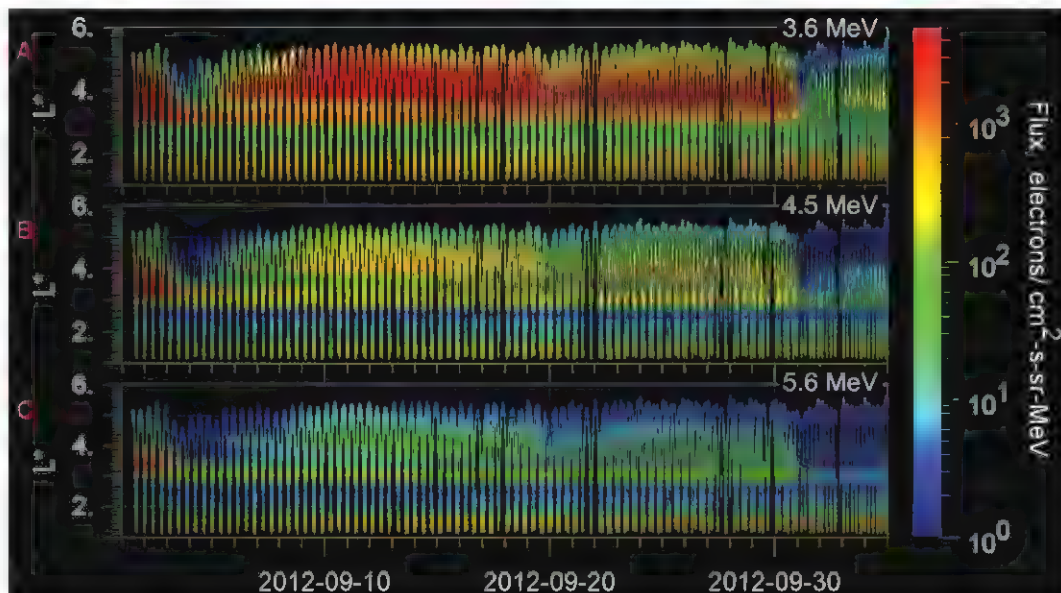
The distinct storage-ring feature is more clearly evident in the meridional plane projection of 4.0- to 5.0-MeV electrons from the combined REPT-A and REPT-B instrument records (Fig. 2). In the earliest observational phase (1 to 3 September 2012), the expected two-belt structure of the Van Allen zones is clear (Fig. 2A). In the next phase from 3 to 6 September, the relativistic storage ring was formed (Fig. 2B), probably largely by erosion and loss of the more distant parts of the outer zone. The storage ring persisted in a notably stable fashion (Fig. 2, C and D) throughout the remainder of September until its almost complete annihilation in early October 2012.

Instruments on board the Combined Release and Radiation Effects Satellite (CRRES) spacecraft (13) observed a powerful "injection" of high-energy electrons and protons deep into the inner part of Earth's magnetosphere on 24 March 1991 (5, 18, 19). This was a highly impulsive event caused by an exceptionally strong interplanetary shock wave (5, 6). This event is a stark example of the sudden appearance of a newly energized

¹Laboratory for Atmospheric and Space Physics, University of Colorado, Boulder, CO, USA. ²Goddard Space Flight Center, Greenbelt, MD, USA. ³Los Alamos National Laboratory, Los Alamos, NM, USA. ⁴Institute for the Study of Earth, Oceans, and Space, University of New Hampshire, Durham, NH, USA. ⁵Space Science and Engineering Division, Southwest Research Institute, San Antonio, TX, USA. ⁶Department of Physics and Astronomy, Dartmouth College, Hanover, NH, USA. ⁷Department of Atmospheric and Oceanic Sciences, University of California–Los Angeles, Los Angeles, CA, USA. ⁸Department of Physics and Astronomy, University of Iowa, Iowa City, IA, USA. ⁹The Aerospace Corporation, Los Angeles, CA, USA.

*Corresponding author. E-mail: daniel.baker@lasp.colorado.edu

Fig. 1. Relativistic Electron Probe Telescope data. Energetic electron data from the RBSP satellites in eccentric orbits around Earth showing several discrete energy channels of the REPT instruments on board the spatially separated RBSP-A and RBSP-B spacecraft. Each panel's left y axis shows the L^* parameter; the x axis shows time from 1 September to 4 October 2012. Electron differential flux values (in units of electrons per square centimeter · second · steradian · megaelectron volt) are in a color-coded logarithmic scale as shown to the right of the figure. (A) Electrons in the energy range $3.2 \leq E \leq 4.0$ MeV. (B) Electrons with $4.0 \leq E \leq 5.0$ MeV. (C) Electrons with $5.0 \leq E \leq 6.2$ MeV.



population of both protons and electrons in a localized portion of the slot region of the radiation belts that is normally almost devoid of very energetic particles (19, 20). Moreover, this prior event contrasts with the storage-ring feature observed by the Van Allen Probes sensors: The storage ring clearly resulted largely from loss of the more distant portion of the outer-zone electron population rather than fresh, localized injection of the March 1991 type. The original acceleration of the electron population (before the turn-on of REPT on 1 September 2012) that eventually formed the storage ring may have resulted from local wave heating (21, 22), enhanced radial diffusion (23, 24), or both.

Based on prior radiation belt research [e.g., (7, 15)], the outer Van Allen zone electron populations would be expected to respond rather directly to changes in the solar wind, interplanetary magnetic field (IMF), and geomagnetic activity. The development of the storage-ring feature itself (Fig. 3) was closely associated with the loss of outer-belt electrons after passage of an interplanetary shock wave on 3 September 2012, seen as a sharp increase in solar wind speed (Fig. 3B) and abrupt change in the IMF (Fig. 3C). Subsequently, a new population of highly relativistic electrons emerged at a region around $L^* \sim 4.0$ and grew in intensity and spatial extent (Fig. 3A) after a high-speed solar wind episode (Fig. 3B) on 5 September. Another such period of high-energy electron flux diminution, reappearance, and intensification was seen from ~21 September to 1 October 2012 (Fig. 3A), with this sequence again occurring in the wake of a powerful high-speed solar wind stream on 20 to 21 September (Fig. 3B). As noted above, one of the most abrupt and notable features of the entire data set was the nearly complete disappearance of the entire outer-zone electron population late on 1 October associated with another interplanetary shock wave (Fig. 3, B and C) and relatively strong geomagnetic storm [seen in disturbance storm time (Dst), which measures global magnetic field disturbance (Fig. 3D)].

Figure 3A shows that for the period of 1 to 4 September 2012, the average plasmapause boundary was relatively close to Earth ($L^* \sim 3$), and a powerful outer-zone electron acceleration event was occurring in the low-plasma-density region outside the plasmasphere. However, from ~4 September until ~6 October, the plasmapause was much farther outward, around $L^* > 4$. Thus, the storage-ring feature, as well as most of the outer Van Allen zone $E > 4.5$ MeV electron population, was inside the high-density plasmasphere. However, in the traditional picture, the outer-zone electron belt would be largely outside the plasmasphere, and the slot region would be inside the plasmasphere outer boundary (21–23, 25).

The radiation belt particle populations are determined by a complex superposition of acceleration, transport, and loss processes modulated by their interactions with plasma waves (24). We are now seeing unexpected radiation

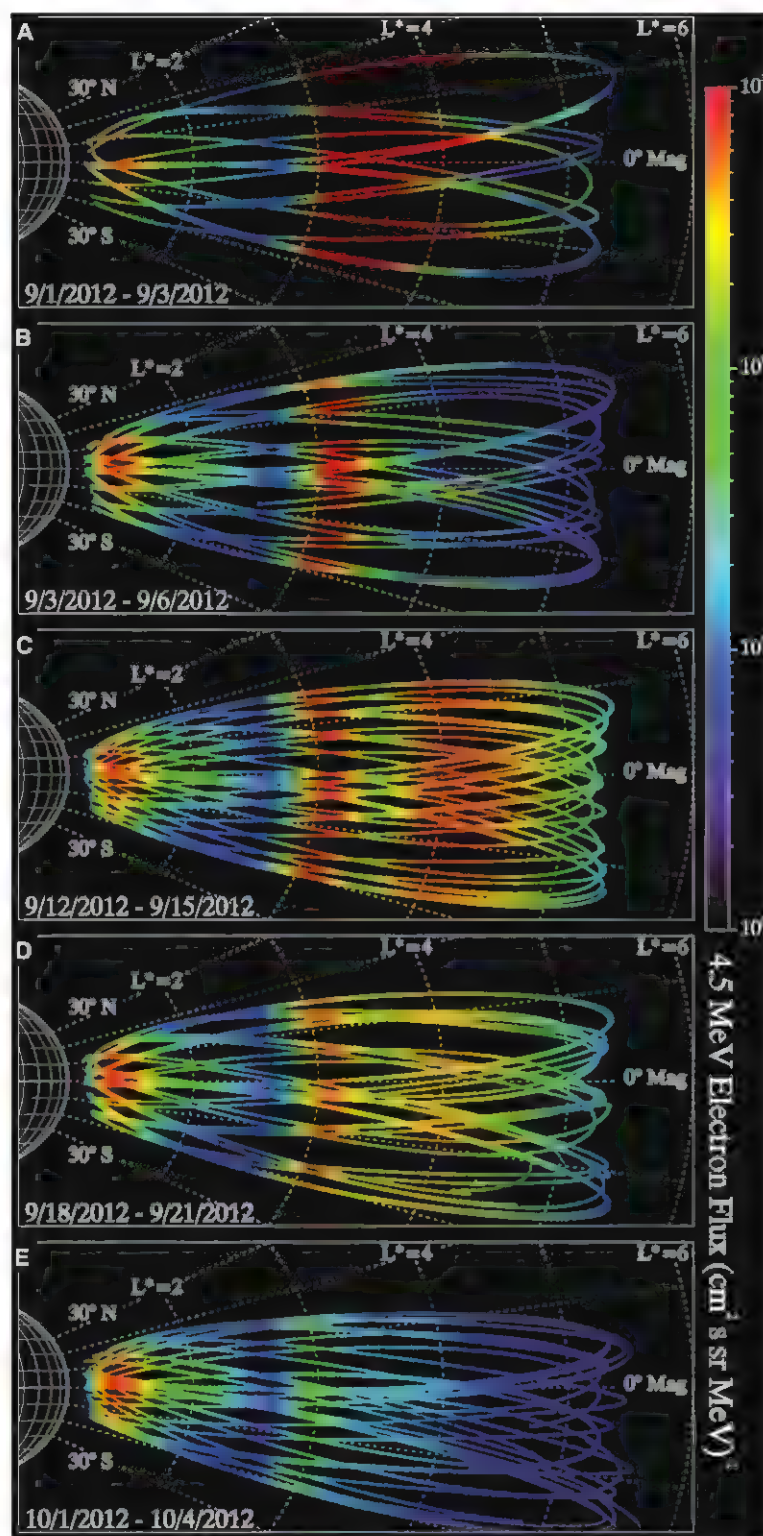


Fig. 2. Meridional plane projections. Projections of the REPT-A and REPT-B electron flux (4.0 to 5.0 MeV) values, as shown according to the logarithmic color scale to the right of the figure. Each panel shows a limited interval of time in a magnetic latitude L^* coordinate system. (A) For 1 to 3 September 2012, the expected two-belt Van Allen zone structure consists of an inner-zone electron population ($L^* < 2.5$), a relatively empty slot region ($2.5 < L^* < 3.0$), and an outer-zone population ($L^* > 3.0$). (B) From 3 to 6 September, only an intense belt of electrons remains in the range $3.0 < L^* < 3.5$; the inner zone and traditional slot region have not changed. (C) The storage-ring belt, or torus, feature persists at $3.0 < L^* < 3.5$, whereas a new slot region is seen at $3.5 < L^* < 3.8$, and a completely new outer-zone population has formed at $L^* > 3.8$. (D) The storage-ring feature remains, whereas the outer zone at $L^* > 3.8$ decays away. (E) The entire outer zone ($L^* > \sim 3.0$) has virtually disappeared at these energies.

Fig. 3. Development of the storage ring. (A)

Image similar to Fig. 1B, but also including the plasmapause, the outer boundary of the plasmasphere (26) for the period 1 September to 7 October 2012. The white curve overplotted on the color-coded electron particle flux data in Fig. 3A shows the modeled, 3-day averaged plasmapause radial location that is in agreement with concurrent plasma wave data (17, 27, 28). (B) Concurrently measured solar wind speed upstream of Earth's magnetosphere. (C) Interplanetary magnetic field for the interval under study. $|B|$, the magnitude of the interplanetary magnetic field components parallel to the ecliptic in nanotesla (nT); B_z , the values of the components perpendicular. (D) Geomagnetic activity index (Dst) for the period under study.

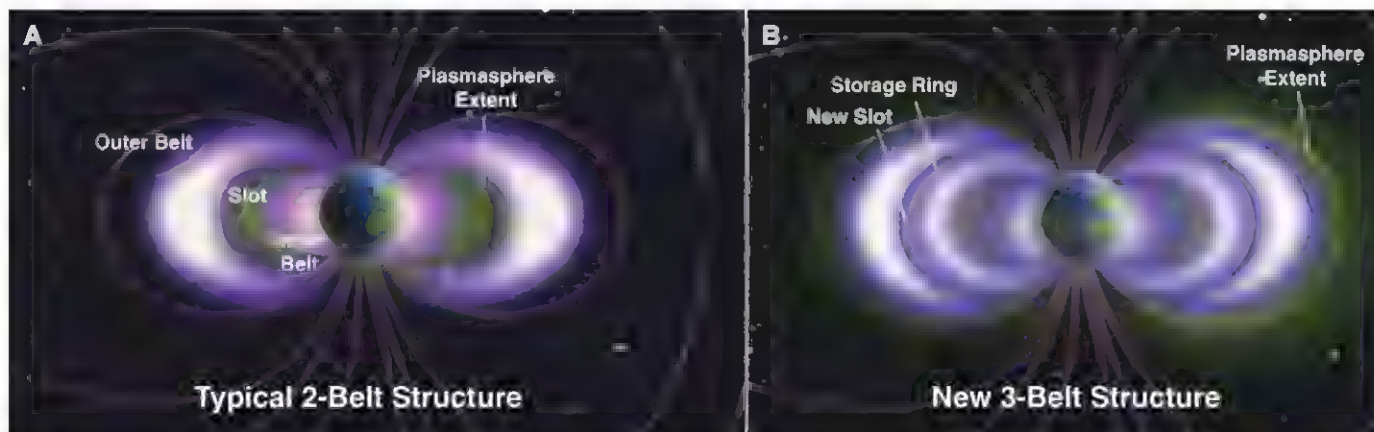
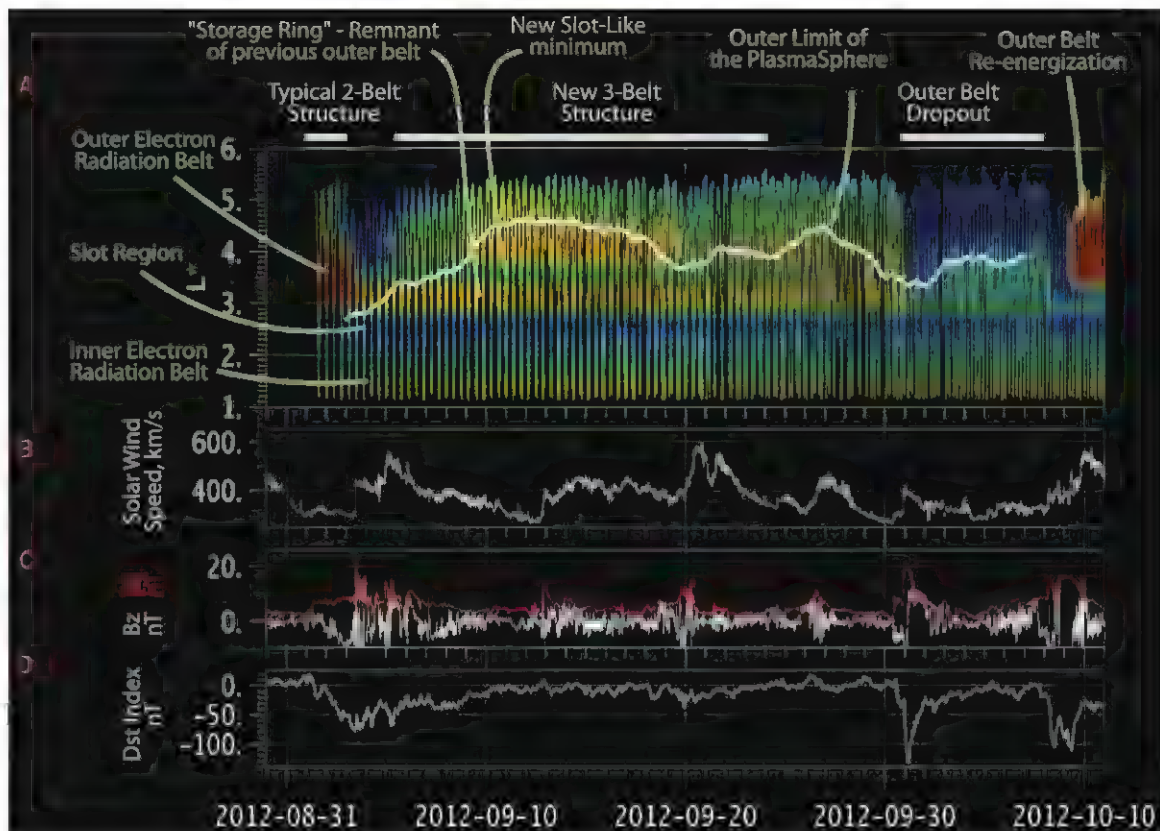


Fig. 4. Radiation belt structures. Diagrams providing a cross-sectional view of Earth's radiation belt structure and relation to the plasmasphere. (A) Schematic diagram showing Earth, the outer and inner radiation belts, and the normal plasmaspheric location. (B) Similar to (A), but showing a more highly distended plasmasphere and unexpected triple radiation belt

properties during the September 2012 period. The radiation belts are really "doughnut-" or torus-shaped entities in three dimensions. Earth is portrayed at the center. White denotes the highest electron fluxes; blue indicates the lowest fluxes. The translucent green overlay denotes the plasmasphere.

belt structures (Fig. 4), but have yet to fully understand them in the context of present radiation belt theory.

References and Notes

1. J. A. Van Allen *et al.*, *Jet Propuls.* **28**, 588 (1958).
2. J. A. Van Allen, *J. Geophys. Res.* **64**, 1683 (1959).
3. J. A. Van Allen, L. A. Frank, *Nature* **183**, 430 (1959).
4. S. C. Freden, R. S. White, *Phys. Rev. Lett.* **3**, 9 (1959).
5. J. B. Baker, W. A. Kolasinski, R. W. Fillius, E. G. Mullen, *Geophys. Res. Lett.* **19**, 821 (1992).
6. X. Li *et al.*, *Geophys. Res. Lett.* **20**, 2423 (1993).
7. D. N. Baker *et al.*, *Geophys. Res. Lett.* **21**, 409 (1994).
8. R. B. Horne *et al.*, *J. Geophys. Res.* **110**, A03225 (2005).
9. B. H. Mauk *et al.*, *Space Sci. Rev.* 10.1007/s11214-012-9908-y (2012).
10. D. N. Baker *et al.*, *Space Sci. Rev.* 10.1007/s11214-012-9950-9 (2012).
11. Since the initial Van Allen belt discovery, there have been many missions that have measured key aspects of the radiation properties around Earth. Some of these have been from operational satellite systems such as the National Oceanic and Atmospheric Administration weather satellites in geostationary Earth orbit (GEO) (www.oso.noaa.gov/goesstatus) or polar low-Earth

(www.oso.noaa.gov/poesstatus) orbits. Other measurements have been made using sensors on board operational GEO spacecraft or the Global Positioning Satellite timing and navigation constellation of spacecraft, as well as the Polar and Cluster scientific satellites (12). These prior satellites have provided key long-term monitoring of radiation belt changes, but have generally not made measurements directly in the heart of the radiation belt regions. Only the CRRES mission (13) operated briefly (1990 to 1991) in the heart of the radiation belts, but this mission lacked the background rejection and the temporal, energy, and spatial resolution now provided by the dual Van Allen Probes.

12. R. H. W. Friedel, G. D. Reeves, T. Obara, *J. Atmos. Sol. Terr. Phys.* **64**, 265 (2002).
13. M. H. Johnson, J. Kierein, *J. Spacecr. Rockets* **29**, 556 (1992).
14. D. N. Baker *et al.*, *IEEE Trans. Geosci. Rem. Sens.* **31**, 531 (1993).
15. X. Li, M. Temerin, D. N. Baker, G. D. Reeves, *J. Geophys. Res.* **116**, A11207 (2011).
16. D. N. Baker, J. F. Mazur, G. M. Mason, *Space Weather* **10**, S05006 (2012).
17. See data and methods in the accompanying supplementary materials on Science Online.
18. A. L. Vampola, A. Korth, *Geophys. Res. Lett.* **19**, 625 (1992).
19. E. G. Mullen, M. S. Gussenhoven, K. Ray, M. Violet, *IEEE Trans. Nucl. Sci.* **38**, 1713 (1991).
20. D. H. Brautigam, *JASTP* **64**, 1709 (2002).
21. R. B. Horne *et al.*, *Nature* **437**, 227 (2005).
22. Y. Y. Shprits *et al.*, *Geophys. Res. Lett.* **33**, L05104 (2006).
23. X. Li, D. N. Baker, T. P. O'Brien, L. Xie, Q. G. Zong, *Geophys. Res. Lett.* **33**, L14107 (2006).
24. R. M. Thorne, *Geophys. Res. Lett.* **37**, L22107 (2010).
25. L. R. Lyons, R. M. Thorne, *J. Geophys. Res.* **78**, 2142 (1973).
26. J. Goldstein, *Space Sci. Rev.* **124**, 203 (2006).
27. J. Goldstein, B. R. Sandel, W. T. Forrester, M. F. Thomsen, M. R. Hairston, *J. Geophys. Res.* **110**, A12218 (2005).
28. R. E. Denton *et al.*, *J. Geophys. Res.* **117**, A03221 (2012).

Acknowledgments: This work was supported by RBSP-Energetic Particle Composition and Thermal Plasma Suite funding provided by the Johns Hopkins

University Applied Physics Laboratory (JHU/APL) contract no. 967399, Electric and Magnetic Field Instrument Suite and Integrated Science (EMFISIS) work was supported on JHU/APL contract no. 921649, and both were funded under NASA's Prime contract no. NA55-01072. All Van Allen Probes observations used in this study, along with display and analysis software, are publicly available at the Web site www.rbsp-ect.lanl.gov.

Supplementary Materials

www.sciencemag.org/cgi/content/full/science.1233518/DC1
Supplementary Text
Figs. S1 and S2
References

3 December 2012; accepted 5 February 2013
Published online 28 February 2013,
10.1126/science.1233518

A Guanosine-Centric Mechanism for RNA Chaperone Function

Jacob K. Grohman,^{1,2} Robert J. Gorelick,⁵ Colin R. Lickwar,³ Jason D. Lieb,³ Brian D. Bower,⁴ Brent M. Znosko,⁶ Kevin M. Weeks^{1*}

RNA chaperones are ubiquitous, heterogeneous proteins essential for RNA structural biogenesis and function. We investigated the mechanism of chaperone-mediated RNA folding by following the time-resolved dimerization of the packaging domain of a retroviral RNA at nucleotide resolution. In the absence of the nucleocapsid (NC) chaperone, dimerization proceeded through multiple, slow-folding intermediates. In the presence of NC, dimerization occurred rapidly through a single structural intermediate. The RNA binding domain of heterogeneous nuclear ribonucleoprotein A1 protein, a structurally unrelated chaperone, also accelerated dimerization. Both chaperones interacted primarily with guanosine residues. Replacing guanosine with more weakly pairing inosine yielded an RNA that folded rapidly without a facilitating chaperone. These results show that RNA chaperones can simplify RNA folding landscapes by weakening intramolecular interactions involving guanosine and explain many RNA chaperone activities.

Outside the cellular environment or in the absence of chaperone proteins, most RNAs fold via complex pathways involving multiple, long-lived intermediates. RNA chaperone proteins with non- or semispecific RNA binding activities accelerate adoption of the thermodynamically most stable RNA structure by lowering the energetic barriers between RNA states and by facilitating rearrangement of misfolded states (1–4). Retroviruses package two RNA genomes in each virus particle (5). These genomes dimerize near their 5' ends, and dimerization is catalyzed by an RNA chaperone, nucleocapsid (NC), which is derived from the retroviral Gag protein that coassembles with the viral RNA to generate replication-competent virus (2, 6, 7). By

following the dimerization of a region of the Moloney murine leukemia virus (MuLV) genomic RNA at single-nucleotide resolution, we uncovered a simple mechanism for how a retroviral nucleocapsid chaperone protein functions.

We studied an RNA construct spanning the 170-nucleotide (nt) MuLV dimerization region (8–10) and including 5' and 3' flanking sequences of 46 and 115 nucleotides, respectively. This RNA dimerizes under physiological-like conditions in vitro and has a structure similar to that of genomic RNA isolated from virions (11, 12). Point mutations in this region of the MuLV genome eliminate its selective packaging into virions (10). We followed dimerization at single-nucleotide resolution using time-resolved, selective 2'-hydroxyl acylation analyzed by primer extension (SHAPE) (13, 14). A fast-acting reagent, benzoyl cyanide (BzCN), that either reacts to form a 2'-O-adduct at conformationally flexible nucleotides or undergoes rapid self-inactivation by hydrolysis (with a 0.25-s half-life), was used (14). Each time point, obtained over reactions spanning tens of minutes, thus yields a structural snapshot of ~1 s duration.

SHAPE profiles for the initial monomer and final dimer forms agree well with accepted structures for the MuLV dimerization domain (fig. S1

and text S1). Five key regions underwent large-scale structural changes during dimerization (Fig. 1). The loops of hairpins SL1 and SL2 (positions 329 to 332 and 363 to 366, respectively) were reactive in the monomer and became unreactive during dimerization (within 7 s), consistent with formation of a stable intermolecular loop-loop kissing interaction (15). Two palindromic sequences, PAL1 (positions 210 to 219) and PAL2 (positions 283 to 298), were initially reactive but became unreactive because of intermolecular duplex formation in the dimer. Conversely, two regions that form the "anchoring helix" (positions 231 to 251 and 290 to 315) in the monomer became more reactive upon dimer formation (Fig. 1 and fig. S1).

We obtained SHAPE data for every nucleotide within the 170-nt MuLV domain in 16 1-s snapshots yielding more than 2700 structural data points. We grouped nucleotides with similar kinetic behaviors by *k*-means clustering (16). In the presence of 5 mM Mg²⁺ and without a protein chaperone, there were seven distinct kinetic behaviors involving four net rates (Fig. 2A). Rates were identical, within error, over a three-fold change in RNA concentration (fig. S2), indicating that most conformational changes reflect pseudo-unimolecular transitions between two interacting RNAs. The fastest rate of $\geq 5 \text{ min}^{-1}$ (Fig. 2A; cluster 1a, in orange on structures at bottom) occurred at nucleotides at the apexes of SL1 and SL2, suggesting formation of a complex between two RNAs before the first time point. PAL1 nucleotides became less reactive at a net rate of $1.6 \pm 0.4 \text{ min}^{-1}$ (Fig. 2A, cluster 1b, green on structures). The anchoring helix and PAL2 nucleotides demonstrated opposing kinetic behaviors (rates of $0.30 \pm 0.03 \text{ min}^{-1}$) (Fig. 2A, clusters 2 and 3, in red), suggestive of a single process involving both structures. Positions in a large, flexible domain (positions 251 to 282) showed slower kinetic behavior with a net rate of $0.11 \pm 0.02 \text{ min}^{-1}$ (Fig. 2A, cluster 4, in black on structures). Finally, nucleotides in clusters 5 and 6 showed biphasic kinetic behavior in which the SHAPE reactivity first increased and then decreased over time, or vice versa, with rates of 1.6 and 0.1 min^{-1} . Time-resolved SHAPE anal-

¹Department of Chemistry, University of North Carolina, Chapel Hill, NC 27599–3290, USA. ²Department of Biochemistry and Biophysics, University of North Carolina, Chapel Hill, NC 27599, USA. ³Department of Biology and Carolina Center for Genome Sciences, University of North Carolina, Chapel Hill, NC 27599, USA. ⁴Department of Genetics, University of North Carolina, Chapel Hill, NC 27599, USA. ⁵AIDS and Cancer Virus Program, SAIC-Frederick, Inc., Frederick National Laboratory for Cancer Research, Frederick, MD 21702–1201, USA. ⁶Department of Chemistry, Saint Louis University, Saint Louis, MO 63103, USA.

*Corresponding author. E-mail: weeks@unc.edu

ysis of the MuLV domain thus reveals that dimerization is complex, slow, and characterized by multiple structurally distinct transitions and intermediates.

We next performed an analogous set of experiments initiating dimerization by simultaneous

addition of magnesium ion and the MuLV NC protein. With the addition of chaperone, clustering of the SHAPE data revealed that the NC protein collapsed dimerization into a single kinetic process that occurred at a net rate of $1.6 \pm 0.4 \text{ min}^{-1}$ (Fig. 2B). There was no evidence of

the slow and multistate processes that characterized the RNA-only reaction.

Initial binding interactions between the NC chaperone and RNA monomer were readily detected in a difference analysis in which the SHAPE profile, immediately after NC binding, was subtracted from that of the reactivity profile of the free RNA (Fig. 3A). Of the 29 nucleotides with the largest changes in SHAPE reactivity, 19 (or 66%) are guanosine residues (Fig. 3, A and B, and text S2), consistent with studies showing that NC contains a cleft that binds guanosine (17). Sites of protection (positive peaks) likely correspond to sites of stable binding by NC during the 1-s window of the time-resolved SHAPE experiment; the smaller number of guanosine residues with higher reactivity in the presence of NC (negative peaks) likely reflect either a rapid binding and release or NC-induced conformational changes.

The preference of NC to interact at guanosine residues prompted us to consider whether NC exerts its RNA chaperone activity by destabilizing interactions between guanosine and other nucleotides. We explored the dimerization reaction using an RNA in which all guanosine residues were replaced by inosine, in essence removing a single amine group from each guanosine position. Inosine-cytosine pairs are iso-structural with guanosine-cytosine pairs, but are $\sim 1 \text{ kcal/mol}$ less stable (Fig. 4A); inosine also pairs more weakly with uridine than guanosine (18). The guanosine-to-inosine substitution will thus reduce both the strength and the promiscuity of alternative base pairs during the RNA folding reaction.

The inosine-substituted RNA formed essentially the same final dimer structure as the guanosine-containing MuLV domain as indicated by SHAPE-directed modeling (19) (fig. S3A), and individual nucleotide SHAPE reactivities for the inosine and native MuLV domain dimers are strongly correlated ($R^2 = 0.88$) (Fig. 4B). Although the overall secondary structures for inosine and native RNAs in the monomer states are similar (fig. S3, B and C), SHAPE reactivities correlate poorly ($R^2 = 0.26$) (Fig. 4C). However, adding NC to the guanosine-containing monomer converts this RNA to a structure that has a SHAPE profile highly similar to that of the inosine RNA monomer ($R^2 = 0.87$) (Fig. 4D). The inosine-substituted RNA is thus a good model both for the NC-destabilized native RNA in the monomer state and for the final dimer.

Time-resolved SHAPE analysis of dimerization of the inosine-substituted RNA in the absence of NC revealed a single, fast kinetic step involving similar nucleotides as NC-mediated dimerization of the native sequence RNA (compare Fig. 2B and 2C). The dimerization rate of the inosine RNA was accelerated by a factor of 7 relative to that of the free native RNA. The NC protein does not affect the structure of the inosine-substituted RNA (Fig. 3C). A non-denaturing gel-based analysis confirmed that addition

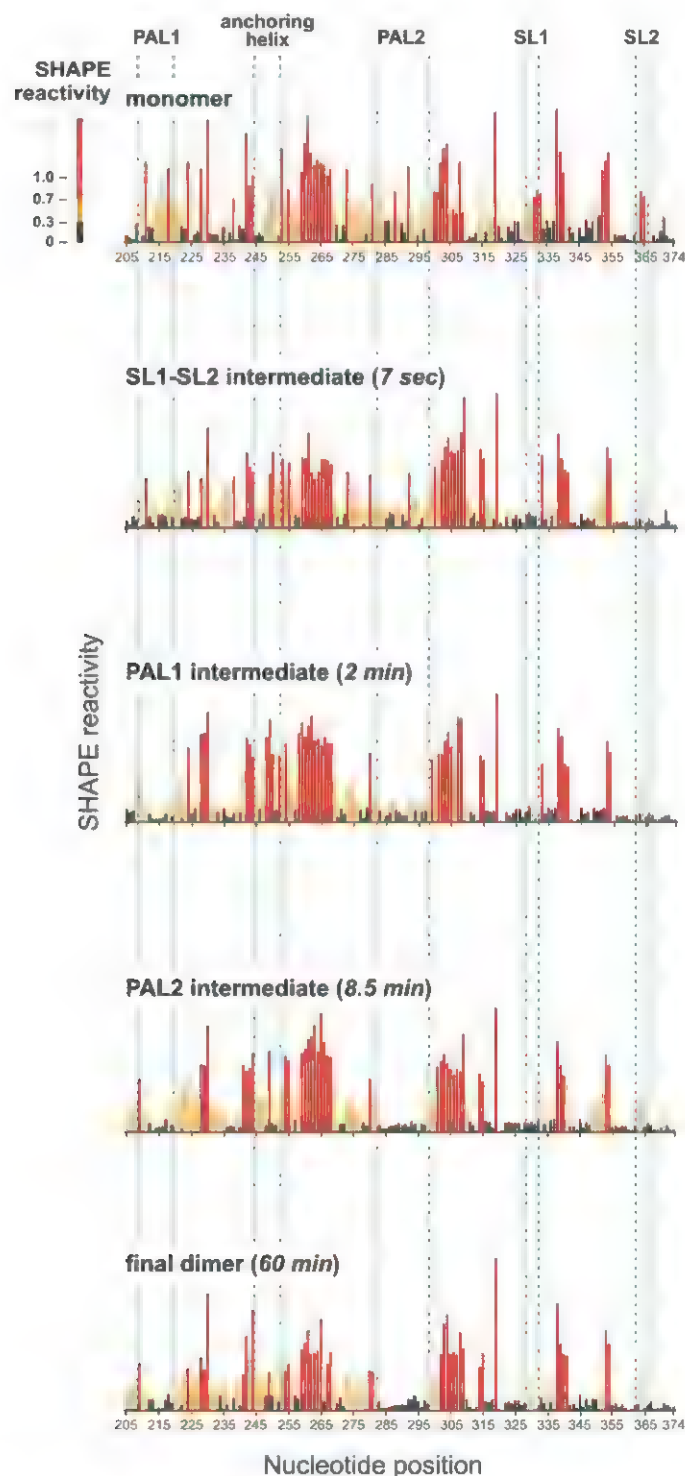


Fig. 1. Time-resolved SHAPE analysis of MuLV RNA dimerization. SHAPE reactivities are shown for monomer (no magnesium), dimer (60 min), and representative time points in which specific structural intermediates predominate. Key structural interactions that change during dimerization are highlighted within sets of dashed blue lines.

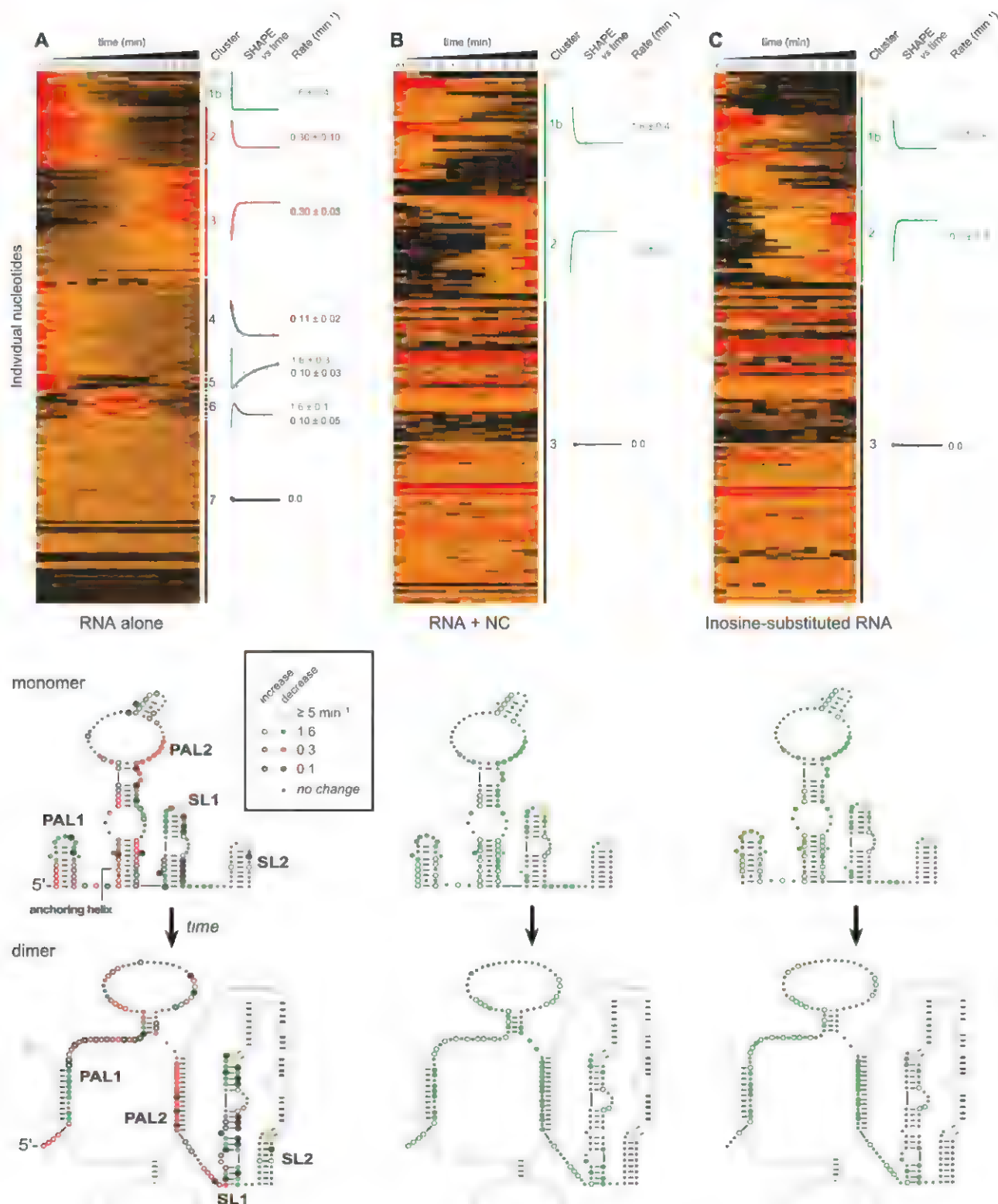


Fig. 2. Model-free clustering of nucleotide-resolution kinetic profiles for dimerization. SHAPE reactivities at 600 nM MuLV RNA (A) in the absence of and (B) in the presence of 8 μM NC, and (C) for an RNA containing inosine in place of guanosine. Each data point is shown on a scale (black to red) corresponding to its SHAPE reactivity (see Fig. 1). The y axis shows every nucleotide (170 positions) in the MuLV dimerization domain RNA in an order determined by

k-means clustering rather than linear sequence. Major kinetic clusters are labeled, and representative kinetic profiles and observed net rates are shown for each cluster. Rates are reported as the mean for all nucleotides in each cluster \pm the standard deviation. Positions of nucleotides in each cluster are shown in structural cartoons below each kinetic profile, colored by rate: orange > green > red > black. For clarity, only one strand of the dimer is colored.

of NC protein had no effect on the rate of formation of the final dimer state for the inosine-substituted RNA (fig. S4). Replacement of guanosine with inosine thus both abrogates most of the need for the RNA chaperone activity of the NC protein and converts the RNA into a form that folds via a simple and direct pathway (compare Fig. 2A and 2C).

The unwinding domain of the heterogeneous nuclear ribonucleoprotein (hnRNP) A1 protein (UP1) contains an arginine-rich RNA recognition motif and has potent RNA chaperone activity (1, 20). UP1 has no structural similarity with NC except that both proteins contain clefts

that bind guanosine (Fig. 4, E and F). As in the presence of NC, UP1-mediated dimerization of the MuLV domain proceeded in a single, fast kinetic step (fig. S5) accelerated by a factor of ~ 20 ($k_{\text{obs}} > 2 \text{ min}^{-1}$) relative to the RNA alone. Of the initial interaction sites (at $\sim 7 \text{ s}$) for UP1 on the native monomer RNA, 52% were guanosine residues (Fig. 3D and text S2). The set of guanosines contacted most strongly by UP1 included some but not all of the guanosines contacted by NC (compare Fig. 3B and 3E). UP1 had no effect on the dimerization rate of the inosine-substituted RNA (Fig. 3F and fig. S4). UP1 is not known to play a role in structure re-

arrangements for the MuLV RNA genome, yet is a potent facilitator of RNA dimerization of the MuLV domain and does so by a mechanism similar to the cognate NC chaperone.

Our data support a model of MuLV genomic dimerization in which two MuLV monomers initially associate rapidly via loop-loop interactions; subsequent steps for RNA-only folding are complex, involve multiple intermediates, and proceed slowly (Fig. 4G). In the presence of the chaperone, RNA dimerization was accelerated by a factor of more than 10 and appeared to occur in a single kinetic step, indicating that the chaperone function accelerated multiple classes

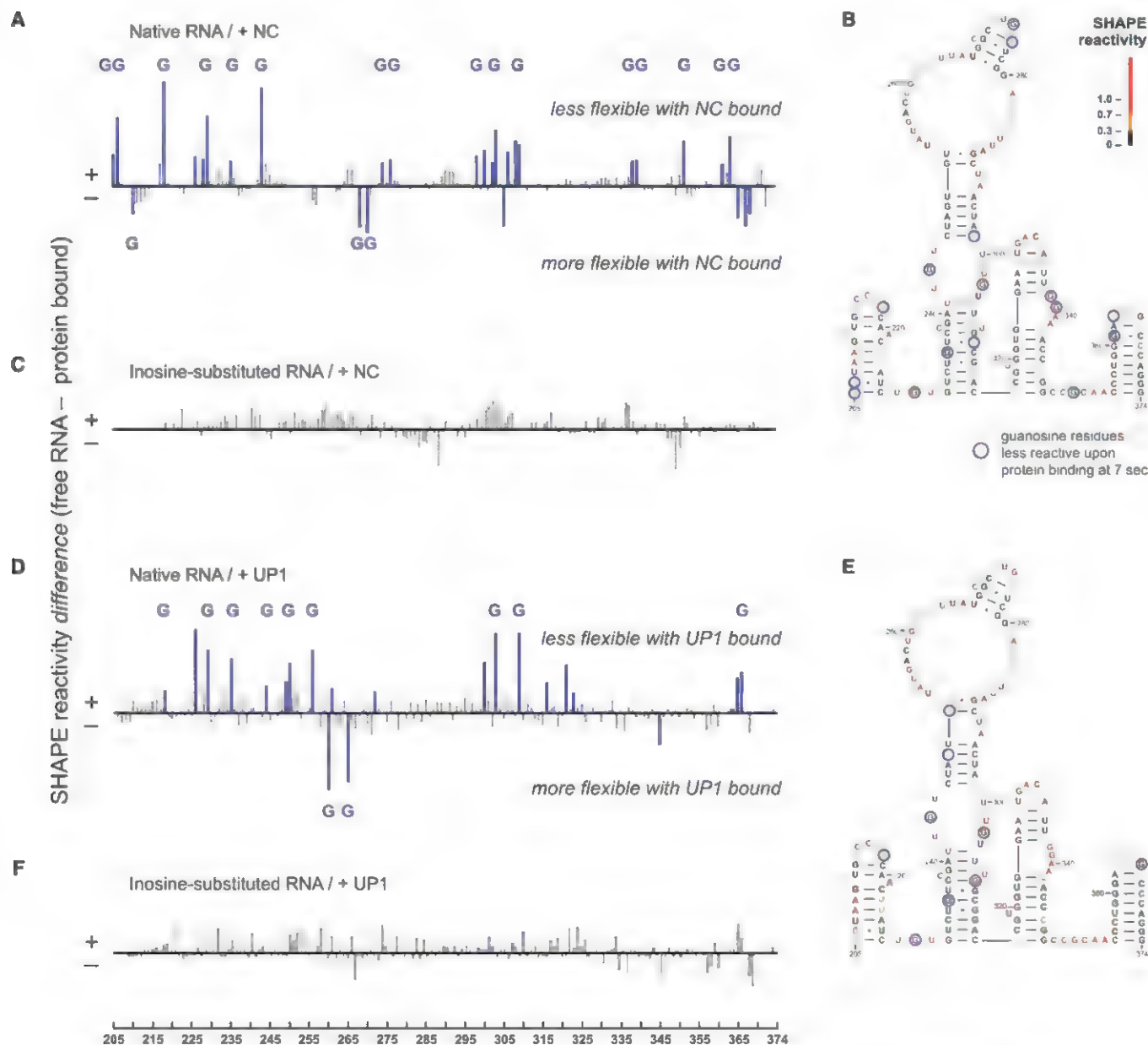


Fig. 3. Initial interactions between NC and UP1 with the MuLV monomer. (A and D) SHAPE difference plots illustrating the effect of (A) NC or (D) UP1 binding to the native dimerization domain 7 s after protein addition. Sites of strongest interaction, corresponding to SHAPE differences greater than 20%, are highlighted in blue; those that occur at guanosine residues are labeled

with a G. (B and E) Superposition of strongest initial interaction sites for (B) NC and (E) UP1 on a MuLV dimerization domain secondary structure model. Structures are colored by SHAPE reactivity before protein binding. (C and F) SHAPE difference plots illustrating the lack of an effect of (C) NC or (F) UP1 binding to the inosine-substituted RNA.

of slow RNA conformational changes (Fig. 4G). Our data indicate that RNA chaperones NC and UP1 both act by binding to exposed guanosine residues in RNA, thereby destabilizing stron-

ger base pairings and creating a simplified folding pathway (text S3). The two proteins contact distinct, partially overlapping sets of guanosine residues in their initial interactions with RNA;

thus, many possible guanosine-binding activities may support RNA chaperone function. The NC and UP1 chaperones also bind to the final native sequence dimer in patterns that are distinct

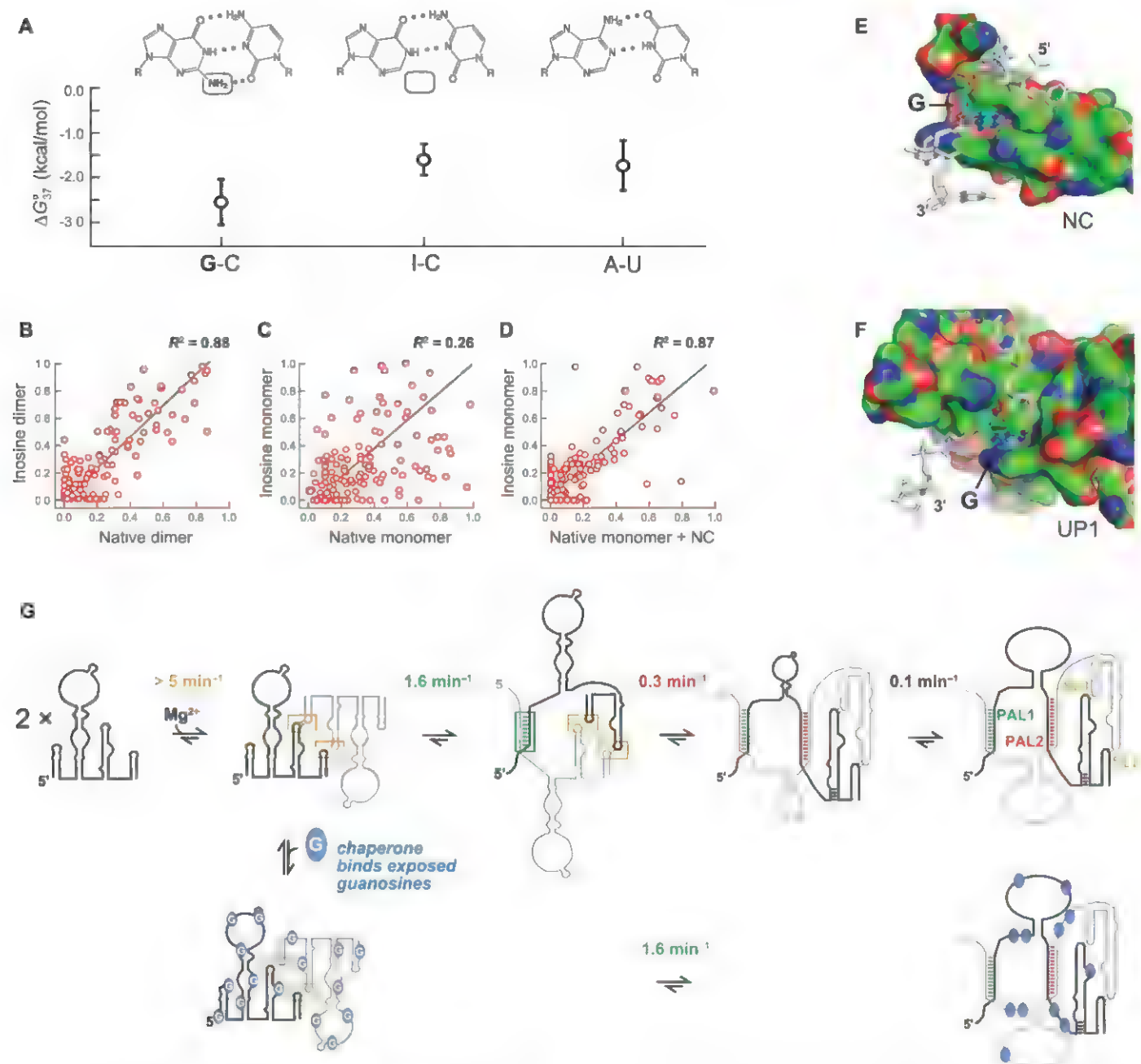


Fig. 4. Role of guanosine in RNA structure and mechanism of chaperone-mediated RNA folding. (A) Average stabilities (ΔG_{37}°) of nearest neighbor base pair combinations involving one G-C, I-C, or A-U pair and one Watson-Crick pair in 1 M NaCl (18, 22), with representative structures. Standard deviations for the nearest-neighbors combinations are shown with lines. (B to D) Correlations between SHAPE reactivity profiles of (B) native and inosine-substituted dimers (obtained at 30 min dimerization time points), (C) native and inosine-substituted monomers (obtained just before addition of Mg^{2+}), and (D) the native RNA after a 7-s interaction with NC versus the protein-free inosine-substituted monomer (both in the presence of Mg^{2+}). The inosine dimer and native dimer in the presence of NC (not shown) also show a strong correlation ($R^2 = 0.89$) reflecting that NC binds at relatively few sites in the native dimer (fig. S6). (E and F)

Structures of (E) NC (17) and (F) UP1 (23) chaperones, emphasizing that both have a guanosine-binding pocket and that flanking nucleotides interact in an extended conformation. NC and UP1 bind guanosine in distinct ways involving anti and syn nucleotide conformations, respectively. (G) RNA-only (top) and chaperone-catalyzed (bottom) MuLV genome assembly mechanisms. Net rates are reported for each step. The overall reaction proceeds sequentially as indicated by (i) the change in reaction order (from second to first, yielding a large increase in effective RNA concentration) upon formation of the initial SL1-SL2 kissing interaction in the first step and (ii) the observation of biphasic profiles (Fig. 2) that include both the 1.6 and 0.1 min^{-1} processes. Evidence for a specific order of the 0.3 min^{-1} process is less strong, and this step may occur in parallel with the 0.1 min^{-1} conformational change.

from their initial interactions with the monomer state (fig. S6). These data suggest that chaperone binding does not discriminate between folded and misfolded RNA states per se but that guanosine nucleotides are ultimately arranged in the final structure in such a way that chaperone binding (or inosine substitution) does not overly destabilize the final RNA structure. In this way, a guanosine-centric mechanism for RNA chaperone function is analogous to the mechanism of some chaperones that facilitate protein folding that destabilizes interactions involving hydrophobic amino acid residues (21). In these cases, both RNA and protein chaperones simply interact with residues especially prone to forming stable intermediate and non-native states.

References and Notes

1. D. Herschlag, *J. Biol. Chem.* **270**, 20871 (1995).
2. A. Rein, L. E. Henderson, J. G. Levin, *Trends Biochem. Sci.* **23**, 297 (1998).
3. L. Rajkowsky et al., *RNA Biol.* **4**, 118 (2007).
4. S. A. Woodson, *RNA Biol.* **7**, 677 (2010).
5. J. M. Coffin, S. H. Hughes, H. E. Varmus, *Retroviruses* (Cold Spring Harbor Press, Plainview, NY, 1997).
6. A. Rein, *RNA Biol.* **7**, 700 (2010).
7. J. A. Thomas, R. J. Gorelick, *Virus Res.* **134**, 39 (2008).
8. M. A. Adam, A. D. Miller, *J. Virol.* **62**, 3802 (1988).
9. C. S. Hibbert, J. Mirro, A. Rein, *J. Virol.* **78**, 10927 (2004).
10. C. Gherghe et al., *Proc. Natl. Acad. Sci. U.S.A.* **107**, 19248 (2010).
11. C. S. Badorrek, K. M. Weeks, *Biochemistry* **45**, 12664 (2006).
12. C. Gherghe, C. W. Leonard, R. J. Gorelick, K. M. Weeks, *J. Virol.* **84**, 898 (2010).
13. S. A. Mortimer, K. M. Weeks, *J. Am. Chem. Soc.* **130**, 16178 (2008).
14. S. A. Mortimer, K. M. Weeks, *Nat. Protoc.* **4**, 1413 (2009).
15. P. T. Li, C. Bustamante, I. Tinoco Jr., *Proc. Natl. Acad. Sci. U.S.A.* **103**, 15847 (2006).
16. M. B. Eisen, P. T. Spellman, P. O. Brown, D. Botstein, *Proc. Natl. Acad. Sci. U.S.A.* **95**, 14863 (1998).
17. A. Dey, D. York, A. Smalis-Mantey, M. F. Summers, *Biochemistry* **44**, 3735 (2005).
18. D. J. Wright, J. L. Rice, D. M. Yanker, B. M. Znosko, *Biochemistry* **46**, 4625 (2007).
19. K. E. Deigan, T. W. Li, D. H. Mathews, K. M. Weeks, *Proc. Natl. Acad. Sci. U.S.A.* **106**, 97 (2009).
20. D. S. Portman, G. Dreyfuss, *EMBO J.* **13**, 213 (1994).
21. F. U. Hartl, M. Hayer-Hartl, *Nat. Struct. Mol. Biol.* **16**, 574 (2009).
22. T. Xia et al., *Biochemistry* **37**, 14719 (1998).
23. J. Ding et al., *Genes Dev.* **13**, 1102 (1999).

Acknowledgments: We are indebted to D. Grawoig for a critical review of the manuscript and to D. Johnson and C. Hixson for assistance in preparing MuLV NC protein. This work was supported by the U.S. National Institutes of Health (GM064803 to K.M.W., GM072518 to J.D.L., and GM031819 to Jack Griffith and B.D.B.) and by the National Cancer Institute (under contract HH5N261200800001E with SAIC-Fredrick, Inc. to R.J.G.). Data sets of representative clustered kinetic data are provided in the supplementary materials.

Supplementary Materials

www.sciencemag.org/cgi/content/full/science.1230715/DC1
Materials and Methods
Supplementary Text
Figs. S1 to S6
References (24–32)

25 September 2012; accepted 14 February 2013
Published online 7 March 2013;
10.1126/science.1230715

A Histone Acetylation Switch Regulates H2A.Z Deposition by the SWR-C Remodeling Enzyme

Shinya Watanabe,¹ Marta Radman-Livaja,² Oliver J. Rando,² Craig L. Peterson^{1*}

The histone variant H2A.Z plays key roles in gene expression, DNA repair, and centromere function. H2A.Z deposition is controlled by SWR-C chromatin remodeling enzymes that catalyze the nucleosomal exchange of canonical H2A with H2A.Z. Here we report that acetylation of histone H3 on lysine 56 (H3-K56Ac) alters the substrate specificity of SWR-C, leading to promiscuous dimer exchange in which either H2A.Z or H2A can be exchanged from nucleosomes. This result was confirmed in vivo, where genome-wide analysis demonstrated widespread decreases in H2A.Z levels in yeast mutants with hyperacetylated H3K56. Our work also suggests that a conserved SWR-C subunit may function as a “lock” that prevents removal of H2A.Z from nucleosomes. Our study identifies a histone modification that regulates a chromatin remodeling reaction and provides insights into how histone variants and nucleosome turnover can be controlled by chromatin regulators.

The H2A.Z histone variant is typically found within nucleosomes that flank promoters of genes transcribed by RNA polymerase II, as well as nucleosomes that flank chromatin boundary elements, centromeres, and replication origins (1–3). These nucleosomes also exhibit rapid, replication-independent turnover, which is thought to function in erasing histone marks, preventing the spread of chromatin states, and ensuring general plasticity of the epigenome (4, 5). H2A.Z appears to enhance rapid turnover of pro-

motor proximal nucleosomes in yeast (4), and nucleosomes subject to rapid turnover kinetics are also enriched for histone H3 acetylated at lysine 56 (H3-K56Ac) (6). H3-K56Ac is also required for enhanced turnover of promoter nucleosomes (6, 7). Recent work indicates that vertebrate gene promoters are also enriched in nucleosomes harboring both H2A.Z and H3-K56Ac, suggesting a conserved regulatory relationship (2, 8, 9). How they cooperate in this process, though, is not clear.

To test whether nucleosomes that harbor both H2A.Z and H3-K56Ac are inherently unstable, recombinant yeast mononucleosomes were immobilized on streptavidin beads, and nucleosome stability was monitored after exposure to increasing salt concentration (fig. S1). Nucleosomes were reconstituted with either H2A/H2B

or H2A.Z/H2B dimers, and with histone H3 that contained either a lysine at position 56 or a glutamine residue to mimic acetylation (H3-K56Q). H3-K56Q had no detectable effect on the stability of the H2A/H2B dimer–H3/H4 tetramer interaction (fig. S1, top panels) (10, 11). By contrast, incorporation of H2A.Z led to a decreased salt stability of both H3 and H3-K56Q mononucleosomes (fig. S1, bottom left panel) (12). However, the combination of H2A.Z and H3-K56Q did not further decrease stability (fig. S1, bottom right panel), indicating that this H3 modification does not itself contribute to marked instability of nucleosomes.

The conserved SWR-C chromatin remodeling enzyme controls H2A.Z deposition in yeast (13, 14), and so we next tested whether H3-K56Ac might regulate its histone exchange activity. Recombinant yeast H2A mononucleosomes that harbored either H3-K56 or H3-K56Q were incubated with purified SWR-C, recombinant H2A.Z/H2B dimers, and adenosine 5′-triphosphate (ATP), and then histone exchange was quantified by a Western blot assay, probing for different epitope-tagged, H2A histones. The integrity of the mononucleosome was analyzed by both Western blotting for H3 and by visualizing DNA (Fig. 1). SWR-C catalyzed robust deposition of H2A.Z when incubated with the wild-type H2A nucleosomes (14). By contrast, nearly 80% less H2A.Z was deposited by SWR-C when incubated with the H3-K56Q substrate (Fig. 1A and fig. S2).

SWR-C-catalyzed dimer exchange involves at least two coupled steps—ATP-dependent eviction of the H2A/H2B dimer from the nucleosome, followed by deposition of H2A.Z/H2B (15). We predicted that H3-K56Ac might facilitate both the forward and reverse reactions and might display altered substrate specificity more like that of the related INO80 enzyme (16). We

¹Program in Molecular Medicine, 373 Plantation Street, University of Massachusetts Medical School, Worcester, MA 01605, USA. ²Department of Biochemistry and Molecular Pharmacology, 364 Plantation Street, University of Massachusetts Medical School, Worcester, MA 01605, USA.

*Corresponding author. E-mail: craig.peterson@umassmed.edu

incubated SWR-C with H2A.Z nucleosomes, ATP, and H2A/H2B dimers and found that SWR-C had no effect on the histone composition of the wild-type H2A.Z nucleosome, as expected (Fig. 1B) (14, 16). By contrast, SWR-C showed robust eviction of nucleosomal H2A.Z when the nucleosome harbored H3-K56Q (Fig. 1B and fig. S3). Furthermore, SWR-C catalyzed the ATP-dependent incorporation of H2A when incubated with the H2A.Z/H3-K56Q mononucleosome (Fig. 1B). H2A.Z exchange was efficient, with nearly 30% H2A replacement (Fig. 1C). H3-K56Q also stimulated a low level of H2A.Z exchange in the absence of SWR-C, indicating that this modification may poise the H2A.Z nucleosome for exchange events (Fig. 1B), perhaps due to enhanced breathing of nucleosomal DNA (11). Robust H2A.Z exchange reaction was dependent on the concentration of SWR-C (fig. S3), ATP, and the time of incubation (fig. S4). H3-K56Q also enhanced the H2A.Z replacement activity of the related INO80 enzyme (Fig. 1B and fig. S5). These effects of H3-K56Q were not due to alterations in the nucleosome binding affinity of the SWR-C or INO80 enzymes (fig. S6). We fur-

ther examined whether the alterations in SWR-C could also be observed with bona fide H3-K56Ac mononucleosomes (fig. S7) that were incubated with SWR-C in the presence of H2A/H2B dimers (Fig. 1D and fig. S8). SWR-C catalyzed the ATP-dependent incorporation of H2A, similar to our results with an H2A.Z nucleosome harboring H3-K56Q.

The substrate specificity of the SWR-C dimer-exchange reaction is reflected by the adenosine triphosphatase (ATPase) properties of SWR-C, as an H2A nucleosome, but not an H2A.Z nucleosome, stimulates the ATPase activity of SWR-C (15). Because ATP-dependent remodeling enzymes are DNA-stimulated ATPases, these results suggest that SWR-C productively interacts only with the nucleosomal DNA of an H2A nucleosome, consistent with the dimer exchange specificity of SWR-C. To determine if H3-K56Q alters the ATPase properties of SWR-C, ATPase assays were performed with wild-type and H3-K56Q nucleosomes. The ATPase activity of SWR-C was stimulated by an H2A nucleosome, but no stimulation was observed with the H2A.Z nucleosome (Fig. 2A). The addition of free H2A.Z/H2B

dimers led to a further stimulation (15). By contrast, nucleosomal incorporation of H3-K56Q led to equal ATPase stimulation by both the H2A and H2A.Z nucleosomes, and addition of free dimers had no effect (Fig. 2B).

The Swc2p subunit of SWR-C binds to H2A.Z, and Swc2p is required for deposition of H2A.Z in vitro (17) and in vivo (13), suggesting that Swc2p functions during the H2A.Z deposition step of the dimer-exchange reaction, presumably by binding and delivering H2A.Z (17). We hypothesized that Swc2p might also function at the end of the reaction cycle, functioning as a molecular "lock" that binds to H2A.Z and prevents SWR-C from removing the newly incorporated H2A.Z.

SWR-C was purified from a *swc2Δ* strain, yielding a SWR-C that lacks the Swc2p and Swc3p subunits and was depleted for Arp6 and Swc6 (fig. S9). The Swc2Δ subcomplex was unable to deposit H2A.Z into an H2A nucleosome (fig. S10) (17), but it catalyzed the ATP-dependent eviction of H2A.Z and promoted H2A incorporation (Fig. 2C). Thus, the activity of the Swc2Δ subcomplex shows similarity to that of SWR-C

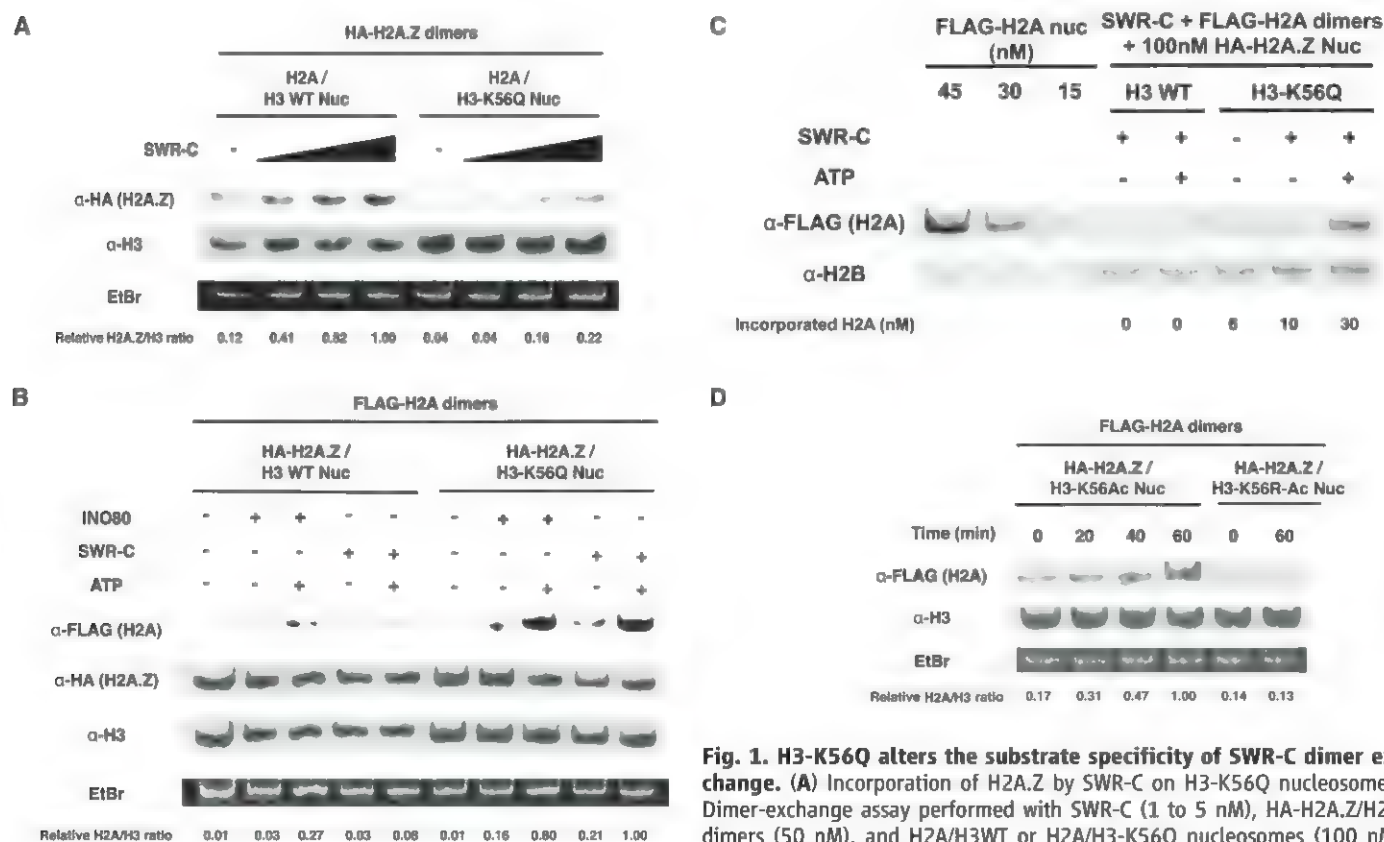


Fig. 1. H3-K56Q alters the substrate specificity of SWR-C dimer exchange. (A) Incorporation of H2A.Z by SWR-C on H3-K56Q nucleosomes. Dimer-exchange assay performed with SWR-C (1 to 5 nM), HA-H2A.Z/H2B dimers (50 nM), and H2A/H3WT or H2A/H3-K56Q nucleosomes (100 nM) with 1 mM ATP. H2A.Z/H3 ratios were normalized to lane 4. (B) SWR-C incor-

porates H2A into H2A.Z/H3-K56Q nucleosomes and H3-K56Q stimulates dimer-exchange activity of INO80. Dimer-exchange assay performed with 5 nM SWR-C or 1 nM INO80, FLAG-H2A/H2B dimers (50 nM), and HA-H2A.Z/H3WT or HA-H2A.Z/H3-K56Q nucleosomes (100 nM) with (+) or without (-) 1 mM ATP. Each H2A/H3 ratio was normalized to lane 10. (C) SWR-C-mediated deposition of H2A quantified by quantitative western blotting (LI-COR). Dimer-exchange assays performed with 10 nM SWR-C, FLAG-H2A/H2B dimer and NAP1 (200 nM), and HA-H2A.Z/H3WT or HA-H2A.Z/H3-K56Q nucleosomes (100 nM) with or without 1 mM ATP. (D) H3K56Ac stimulates H2A deposition by SWR-C. Dimer-exchange assay performed with SWR-C (5 nM), ATP (1 mM), FLAG-H2A/H2B dimers (50 nM), and HA-H2A.Z/H3-K56Ac or HA-H2A.Z/H3-K56R-Ac nucleosomes (100 nM) generated by in vitro acetylation with Rtt109/Vps75 acetyltransferase. EtBr, ethidium bromide.

with an H3-K56Q nucleosome. The ATPase activity of the Swc2A subcomplex was stimulated by an H2A.Z nucleosome, but not an H2A nucleosome, the opposite substrates compared to intact SWR-C (Fig. 2D). Thus, the Swc2/3 module appears to play a key role in substrate specificity, promoting activity on an H2A nucleosome and preventing the remodeling of an H2A.Z nucleosome. Swc2p binds to the C-terminal domain of H2A.Z that is near H3-K56 within the nucleosome; thus, we propose that H3-K56Ac might disrupt Swc2p function, allowing SWR-C to act on an H2A.Z nucleosome. Consistent with this view, the activity of the Swc2A subcomplex was not influenced by H3-K56Q (fig. S11).

Our model predicts that constitutive acetylation of H3-K56 in vivo should promote H2A.Z exchange, leading to decreased steady-state levels. To test this model, we carried out genome-wide mapping of H2A.Z in yeast with globally increased levels of H3K56Ac. For these analyses, yeast strains were used that either express H3K56Q, or lack the Hst3p and Hst4p deacetylases that target H3-K56Ac (18, 19). In our wild-type control, we recapitulated the previously reported localization of H2A.Z (1, 3), with maximal enrichment at genic +1 nucleosomes and more modest enrichment at the -1 nucleosome. Notably, in both strains carrying globally increased

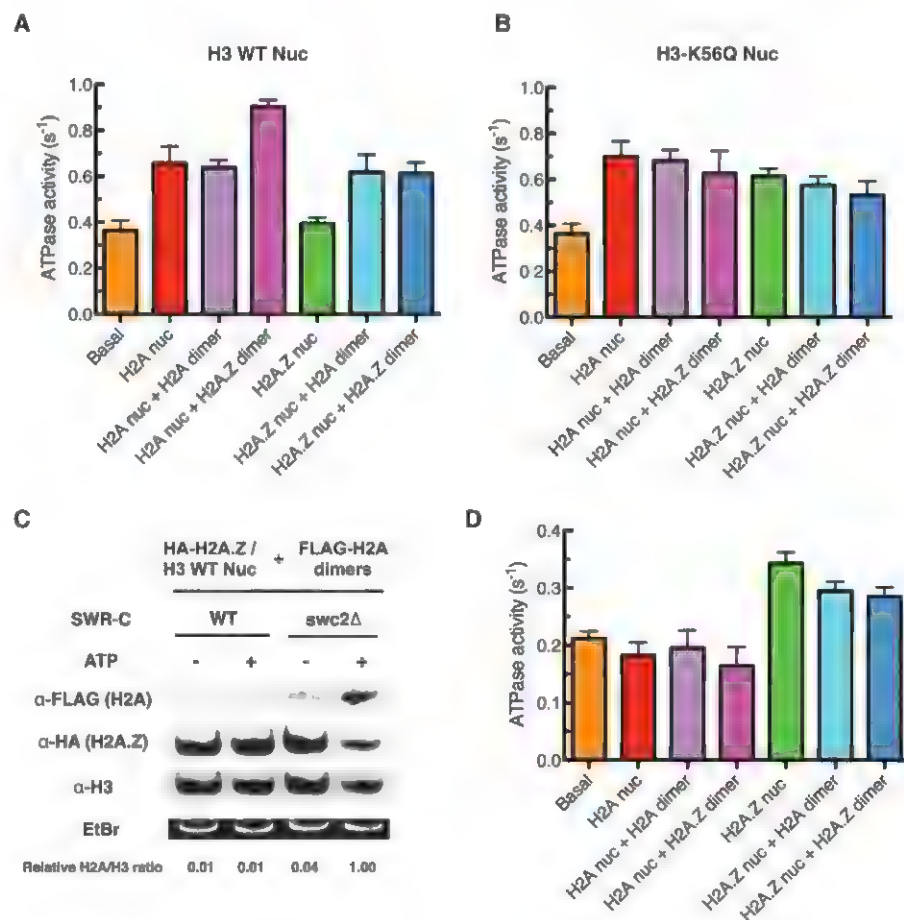
H3-K56ac, H2A.Z levels were on average diminished at promoters (Fig. 3A). *HTZ1* (H2A.Z) mRNA levels were unchanged in H3-K56Q and *hst3Δ/hst4Δ* strains (fig. S12). Because Fig. 3A shows an averaged view over all genes, we also sought to understand whether this loss of H2A.Z was universal or specific to a small subset of genes. As shown in Fig. 3, B and C, H2A.Z was generally lost from +1 nucleosomes—nucleosomes normally exhibiting modest or minimal enrichment of H2A.Z (H2A.Z levels in wild type from 0 to 3) were little affected by global hyperacetylation, whereas nucleosomes carrying higher amounts of H2A.Z almost universally lost H2A.Z in strains harboring constitutive H3-K56Ac (see also fig. S13). Consistent with the idea that H3K56Ac leads to SWR-C-dependent H2A.Z replacement, H2A.Z was lost in hyperacetylation mutants primarily at genes associated with SWR-C, whereas genes lacking SWR-C in prior mapping studies (20) were largely unaffected in these mutants (Fig. 3D and fig. S13C).

H2A.Z incorporation was also monitored in wild-type and H3-K56Q strains during the re-establishment of transcriptional repression at the *PHO5* gene. In both the wild-type and H3-K56Q strains, H3 levels were restored to similar extents when *PHO5* was repressed; however, H2A.Z was at least 50% less in the H3-K56Q

strain (fig. S14). Finally, we tested whether the gene expression profiles of an H3-K56Q strain are similar to that of a strain that lacks H2A.Z. We observed a significant overlap in gene expression defects and a positive correlation between changes in mRNA levels between *htz1Δ* and H3K56Q strains (Fig. 4). These data are consistent with H3K56Ac modulating SWR-C dimer-exchange activity in vivo.

A functional connection between histone modifications and ATP-dependent remodeling enzymes has long been recognized (21). Here we find that H3-K56Ac (or H3-K56Q) functions as a switch that changes the remodeling specificity of the SWR-C dimer-exchange reaction, leading to removal of H2A.Z from the nucleosomal product. Our data indicate that Swc2p functions to prevent activation of the Swr1 ATPase by an H2A.Z nucleosome, and that it may function at the end of the reaction cycle to “lock” H2A.Z and prevent its eviction. Swc2p is conserved from yeast to human (17), and YL-1, the metazoan counterpart of Swc2p, is found in the *Drosophila* and human counterparts of SWR-C, the dTip60 and SRCAP complexes, respectively (22, 23). Thus, it is likely that both the proposed “lock” function of Swc2 and the role of H3-K56Ac are conserved in higher eukaryotes. Our work suggests a model whereby an H3-K56Ac

Fig. 2. Roles for H3-K56Q and Swc2p in modulating the ATPase cofactor requirements of SWR-C. (A) Substrate specificity of SWR-C ATPase activity on H3WT nucleosomes. SWR-C (1 nM) and 0.1 mM ATP was incubated with (+) or without (−) nucleosomes (15 nM) or free dimers (15 nM). ATPase assays measured fluorescent change of 7-diethylamino-3-((2-maleimidyl)-ethyl)amino)carbonyl)coumarin-labeled phosphate-binding protein (MDCC-PBP) upon phosphate binding. Data represent the results from three independent experiments and error bars reflect standard deviations. (B) Substrate specificity of ATPase activity of SWR-C on H3-K56Q nucleosomes. As in (A), but nucleosomes harbored H3-K56Q. (C) The Swc2A subcomplex exchanges H2A.Z with H2A. The dimer-exchange assay performed with 5 nM SWR-C WT or Swc2A subcomplex, FLAG-H2A/H2B dimers (50 nM), and HA-H2A.Z/H3WT nucleosomes (100 nM) with or without 1 mM ATP. Each H2A/H3 ratio was normalized to lane 4. EtBr, ethidium bromide. (D) Substrate specificity of the Swc2A subcomplex.



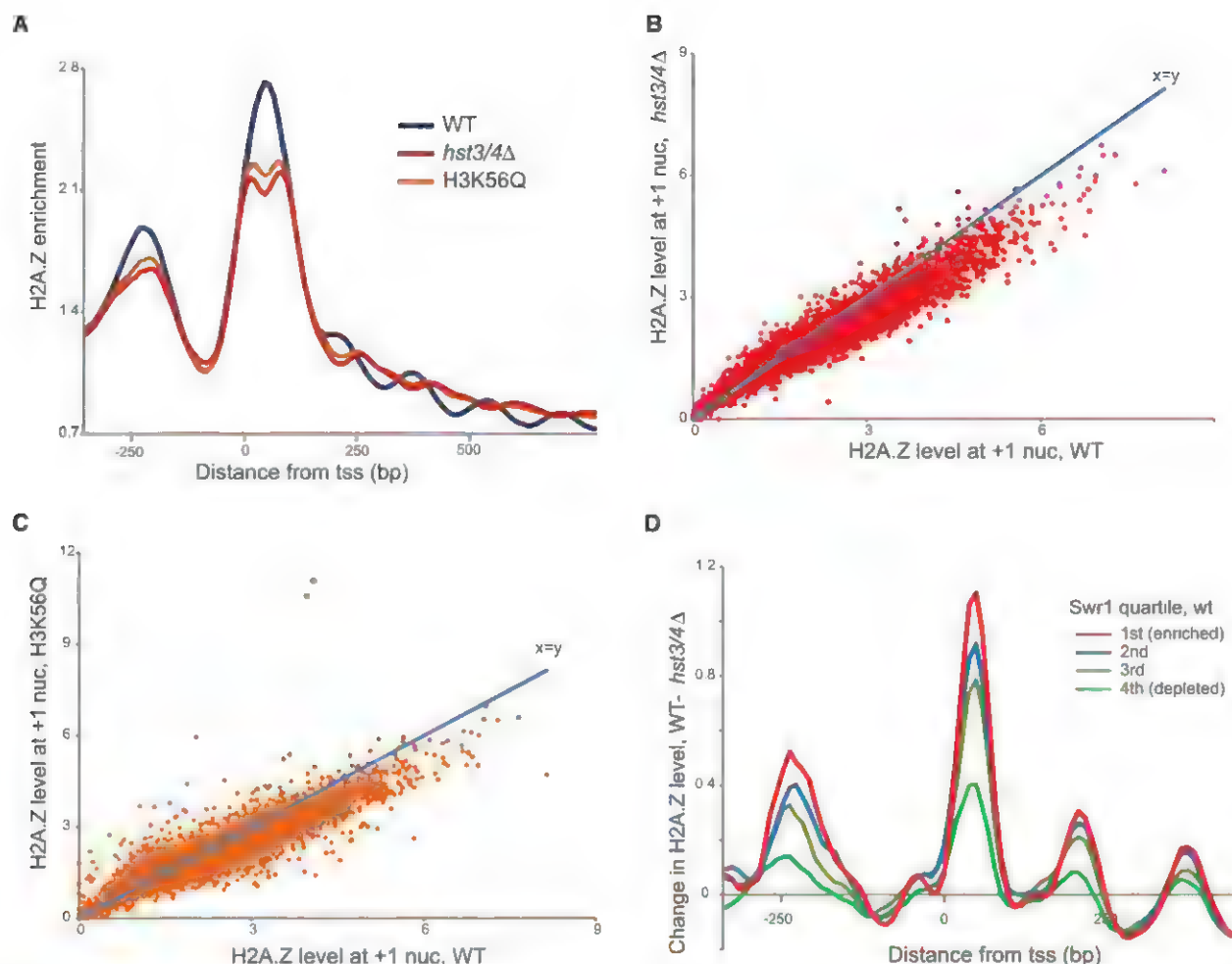


Fig. 3. Constitutive H3-K56Ac decreases steady-state levels of promoter-proximal H2A.Z in vivo. (A) H2A.Z enrichments at promoter regions in wild-type (WT) and H3-K56Q strains. Chromatin immunoprecipitation sequencing (ChIP-Seq) using antibody against H2A.Z in WT, *hst3Δ hst4Δ*, and H3K56Q strains. After alignment to the genome, normalized read counts were averaged for all genes aligned on the basis of their transcriptional start sites (TSS). (B and C) Scatterplot of H2A.Z levels at genic +1 nucleosomes for WT (x axis) versus either *hst3Δ hst4Δ* (B) or H3K56Q (C) mutants. Blue lines

show $x = y$ line. The vast majority of genes exhibit a decrease in H2A.Z levels in either of the H3K56 hyperacetylated mutants. (D) H2A.Z loss preferentially occurs at genes associated with the SWR-C complex. Swr1 levels [from (20)] were calculated for all genes, and genes are grouped into four quartiles according to Swr1 abundance. Change in H2A.Z levels at the +1 nucleosome in WT and *hst3Δ hst4Δ* strains is shown at promoters, showing that genes with the lowest Swr1 levels exhibited lower changes in H2A.Z levels than remaining genes with moderate to high Swr1 levels.

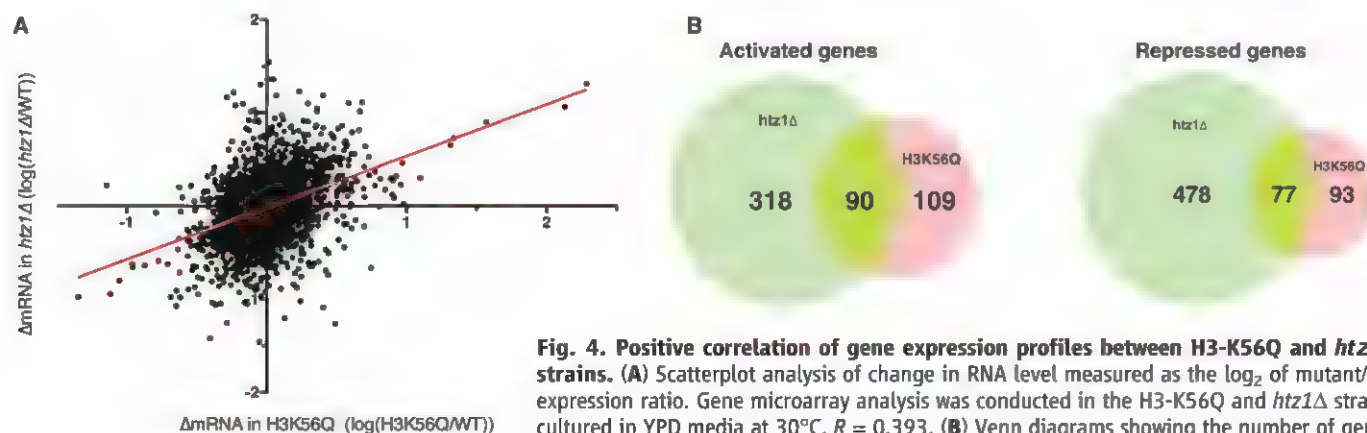


Fig. 4. Positive correlation of gene expression profiles between H3-K56Q and *htz1Δ* strains. (A) Scatterplot analysis of change in RNA level measured as the \log_2 of mutant/WT expression ratio. Gene microarray analysis was conducted in the H3-K56Q and *htz1Δ* strains cultured in YPD media at 30°C. $R = 0.393$. (B) Venn diagrams showing the number of genes for which RNA levels changed by 1.25-fold in mutants relative to the WT strain. P values were 8×10^{-54} (45% overlap in activated genes) and 9×10^{-36} (45% overlap in repressed genes).

nucleosome may be subject to multiple rounds of SWR-C-catalyzed dimer exchange and such promiscuous dimer exchange may promote subsequent histone H3/H4 turnover (fig. S15). This model provides a mechanistic explanation for how H3-K56Ac and H2A.Z might coordinately control nucleosome turnover at regulatory regions (3) by regulating the activity and substrate specificity of chromatin remodeling enzymes.

References and Notes

1. R. M. Raisner *et al.*, *Cell* **123**, 233 (2005).
2. A. Barski *et al.*, *Cell* **129**, 823 (2007).
3. I. Albert *et al.*, *Nature* **446**, 572 (2007).
4. M. F. Dion *et al.*, *Science* **315**, 1405 (2007).
5. R. B. Deal, J. G. Henikoff, S. Henikoff, *Science* **328**, 1161 (2010).
6. A. Rufange, P. E. Jacques, W. Bhat, F. Robert, A. Nourani, *Mol. Cell* **27**, 393 (2007).
7. T. Kaplan *et al.*, *PLoS Genet.* **4**, e1000270 (2008).
8. W. Xie *et al.*, *Mol. Cell* **33**, 417 (2009).
9. K. A. Lo *et al.*, *PLoS ONE* **6**, e19778 (2011).
10. S. Watanabe *et al.*, *Biochim. Biophys. Acta* **1799**, 480 (2010).
11. H. Neumann *et al.*, *Mol. Cell* **36**, 153 (2009).
12. H. Zhang, D. N. Roberts, B. R. Cairns, *Cell* **123**, 219 (2005).
13. N. J. Krogan *et al.*, *Mol. Cell* **12**, 1565 (2003).
14. G. Mizuguchi *et al.*, *Science* **303**, 343 (2004).
15. E. Luk *et al.*, *Cell* **143**, 725 (2010).
16. M. Papamichos-Chronakis, S. Watanabe, O. J. Rando, C. L. Peterson, *Cell* **144**, 200 (2011).
17. W. H. Wu *et al.*, *Nat. Struct. Mol. Biol.* **12**, 1064 (2005).
18. I. Celic *et al.*, *Curr. Biol.* **16**, 1280 (2006).
19. N. L. Maas, K. M. Miller, L. G. DeFazio, D. P. Toczyski, *Mol. Cell* **23**, 109 (2006).
20. R. T. Koerber, H. S. Rhee, C. Jiang, B. F. Pugh, *Mol. Cell* **35**, 889 (2009).
21. K. J. Pollard, C. L. Peterson, *Bioessays* **20**, 771 (1998).
22. T. Kusch *et al.*, *Science* **306**, 2084 (2004).
23. Y. Cai *et al.*, *J. Biol. Chem.* **280**, 13665 (2005).

Acknowledgments: We thank P. D. Kaufman (University of Massachusetts Medical School) for the gift of purified Rtt109/Vps75. We apologize to colleagues whose work we could not cite due to space constraints. This work was supported by grants from the NIH to C.L.P. (R01 GM49650) and to O.J.R. (R01 GM079205). Chip-Seq data sets have been assigned the Gene Expression Omnibus accession no. GSE43935.

Supplementary Materials

www.sciencemag.org/cgi/content/full/340/6129/195/DC1
Materials and Methods
Figs. S1 to S15
References (24–31)

5 September 2012, accepted 20 February 2013
10.1126/science.1229758

Latency-Associated Degradation of the MRP1 Drug Transporter During Latent Human Cytomegalovirus Infection

Michael P. Weekes,^{1*} Shireen Y. L. Tan,^{1*} Emma Poole,^{2*} Suzanne Talbot,^{1*} Robin Antrobus,¹ Duncan L. Smith,³ Christina Montag,⁴ Steven P. Gygi,⁵ John H. Sinclair,² Paul J. Lehner^{1†}

The reactivation of latent human cytomegalovirus (HCMV) infection after transplantation is associated with high morbidity and mortality. In vivo, myeloid cells and their progenitors are an important site of HCMV latency, whose establishment and/or maintenance require expression of the viral transcript UL138. Using stable isotope labeling by amino acids in cell culture–based mass spectrometry, we found a dramatic UL138-mediated loss of cell surface multidrug resistance–associated protein-1 (MRP1) and the reduction of substrate export by this transporter. Latency-associated loss of MRP1 and accumulation of the cytotoxic drug vincristine, an MRP1 substrate, depleted virus from naturally latent CD14⁺ and CD34⁺ progenitors, all of which are in vivo sites of latency. The UL138-mediated loss of MRP1 provides a marker for detecting latent HCMV infection and a therapeutic target for eliminating latently infected cells before transplantation.

Human cytomegalovirus (HCMV) is a ubiquitous beta-herpesvirus that infects 60 to 90% of individuals (1). After primary infection, HCMV establishes a latent infection under the control of a healthy immune system. Reactivation from viral latency to productive infection causes serious disease in immunocompromised individuals, such as transplant recipients and AIDS patients (1, 2).

Cells of the myeloid lineage, such as CD34⁺ bone marrow progenitors and CD14⁺ monocytes, are sites of latent HCMV infection (3–5). The viral genome persists in these cells with little gene expression and no detectable virus production (6, 7). Reactivation from latency occurs upon myeloid differentiation, resulting in chromatin-mediated activation of the lytic gene expression cascade, viral DNA replication, and the production of infectious virions (8). Latent viral infection is thus required for viral persistence. Establishing how latency is maintained and how latently infected cells avoid immune recognition is crucial to understanding how HCMV persists in vivo. Furthermore, the elimination of latently infected cells is a key target in preventing recurrent HCMV infection in immunocompromised individuals.

A limited number of viral transcripts have been identified during natural latency in myeloid cells (6, 7) and include UL138 (9, 10), which en-

codes a 21-kD transmembrane Golgi-associated protein (10). UL138 is expressed with early-late kinetics during productive HCMV infection (10) but is also required for efficient latent carriage in vitro (9, 10). The expression of UL138 during lytic infection results in increased tumor necrosis factor receptor 1 (TNFR1) cell surface expression (11, 12), but little is known about UL138 during latency.

To address how UL138 affects host cell surface receptor expression during latent HCMV infection, we used plasma membrane profiling (PMP) (13), a proteomic technique that employs stable isotope labeling by amino acids in cell culture–based differential analysis to compare the expression of plasma membrane (PM) proteins in the presence and absence of UL138 in undifferentiated myeloid cells. Of the 592 PM proteins isolated from the monocytic cell line (THP-1), only 3 were reproducibly affected more than twofold (Fig. 1A and tables S1 and S2). Most notable was multidrug resistance–associated protein-1 (MRP1) (down-regulated 6.7- to 10.3-fold in three independent experiments), whereas Notch-ligand Delta-like protein 1 (DLL1) was down-regulated 2.1- to 2.6-fold. As expected, cell surface expression of TNFR1 increased (2.4- to 2.8-fold) (11, 12).

These cell surface changes were confirmed by cell surface flow cytometry (DLL-1, TNFR1, and CD36) or intracellular flow cytometry (MRP1), whereas expression of the control protein (CCR7) was unaffected (Fig. 1B). UL138 down-regulated MRP1 in all four cell lines tested, including fibroblasts (Fig. 1C), HL60-ADR cells, a promyelocytic leukemia cell line that overexpresses MRP1 (14), and HeLa cells (fig. S1).

We focused on MRP1, the most dramatically down-regulated protein. In the presence of UL138, not only did MRP1 cell surface expression decrease but the protein was undetectable (Fig. 1, C and D). UL138 expression is not restricted to latent HCMV infection, is detected 6 hours after lytic infection, and accumulates over 48 hours (10). We analyzed the temporal

¹Cambridge Institute for Medical Research, University of Cambridge, Hills Road, Cambridge CB2 0XY, UK. ²Department of Medicine, University of Cambridge Clinical School, Addenbrookes Hospital, Hills Road, Cambridge CB2 2QQ, UK. ³Paterson Institute for Cancer Research, University of Manchester, Wilmslow Road, Withington, Manchester M20 4BX, UK. ⁴Laboratory for Molecular Biology, Children's Hospital, Charité Universitätsmedizin Berlin, Ziegelstrasse 5-9, D-10117 Berlin, Germany. ⁵Department of Cell Biology, Harvard Medical School, 240 Longwood Avenue, Boston, MA 02115, USA

*These authors contributed equally to this work.

†Corresponding author. E-mail: pjl30@cam.ac.uk

relationship between UL138 expression and MRP1 degradation during lytic infection in human fibroblasts (HFFs) with the TB40 isolate of HCMV. The observed loss of MRP1 at 48 hours coincided with high levels of UL138 expression (Fig. 2A). UL138 is encoded at the 3' end of a polycistronic transcript that also encodes UL133, UL135, and UL136 (10, 15). Consequently, we used Toledo UL133-UL138 and UL138 open reading frame deletion mutants of HCMV (12) to determine whether this region is necessary for MRP1 down-regulation. As expected, these viruses replicated similarly to wild-type viruses (12) (Fig. 2B). Forty-eight hours after HFF infection with the deletion viruses, no UL138 expression was detected by reverse transcription polymerase chain reaction (RT-PCR), and MRP1 expression was restored (Fig. 2B). Thus, UL138 is necessary for MRP1 down-regulation and degradation, although other HCMV genes might also target MRP1. Human monocyte-derived macrophages infected with wild-type TB40 but not TB40 Δ UL138 (an additional UL138 deletion mutant) (11) also showed decreased cell surface expression of MRP1 (Fig. 2C).

To determine the functional consequence of UL138-mediated MRP1 down-regulation,

we examined export of the fluorescent reporter 5-carboxysemicarbazorhodamine (SNARF-1), an MRP1-specific substrate (16), and leukotriene C₄ (LTC₄), an endogenous MRP1 substrate (17). The loss of SNARF-1 from cells loaded with the SNARF-1 ester is a robust measure of MRP1 activity (fig. S2A). Preincubation with the MRP1-specific inhibitor MK571 allowed the accumulation of SNARF-1 and slowed export (Fig. S2B). In THP-UL138 cells, SNARF-1 was exported more slowly than THP-1 controls (Fig. 3A and fig. S2C); by 8 hours, 97% of control cells, compared with 35% of THP-UL138 cells, had unloaded dye. SNARF-1 was also exported significantly more slowly from HCMV than mock-infected fibroblasts (Fig. 3B), and the export of LTC₄ was inhibited in THP-UL138 cells (Fig. 3C).

Because hemagglutinin (HA) peptide-tagged UL138 did not alter MRP1 mRNA levels, despite the loss of MRP1 protein (Fig. 3D), MRP1 down-regulation by UL138 was likely to be post-transcriptional. In the presence of UL138, [³⁵S]-methionine radiolabeled 170-kD MRP1 matured normally through the secretory pathway before rapidly degrading (Fig. 3E), with a reduction in half-life from 16 to 20 hours (18) to less than

3 hours, suggesting that MRP1 targets UL138 for degradation in the late secretory pathway. Consistent with this, the loss of MRP1 was inhibited by the vacuolar adenosine triphosphatase inhibitor concanamycin A (CcmA) but was insensitive to proteasome inhibition (Fig. 3, E and F). Furthermore, UL138-HA interacted with MRP1 in cells preincubated with CcmA, due to the increased MRP1 expression (Fig. 3G). Thus, UL138 associates with MRP1 and induces its lysosomal degradation.

CD34⁺ bone marrow progenitors and CD14⁺ monocytes are key sites of latent HCMV infection in vivo (3–5, 19). Experimental models of latent infection in both cell types are routinely used to analyze HCMV latency in vitro (4, 19–23). To address how UL138 expression affects latent HCMV infection, we latently infected primary CD34⁺ progenitor cells with a green fluorescent protein (GFP)-labeled recombinant HCMV (TB40 gfp) and found that latently infected cells (GFP-positive) also showed specific loss of cell surface MRP1 (Fig. 4A).

MRP1 exports a number of cytotoxic agents, including vincristine, a Vinca alkaloid mitotic inhibitor which is relatively MRP1-specific (24). We initially tested the ability of vincristine to

Fig. 1. HCMV UL138 down-regulates cell surface MRP1 and other targets. (A) Scatter plot of proteins identified in PMP and quantified by more than 2 unique peptides. The summed ion intensity (y axis) is shown as log₁₀. Significance A was used to estimate *P* values (28). (B) Cytofluorometric analysis of the indicated proteins in THP-1 cells stably expressing HCMV-encoded UL138 (THP-UL138) and control THP-1 cells. (C and D) Immunoblot for MRP1/UL138 in control or UL138-transduced fibroblasts (C) or in control or UL138-transduced THP-1 cells (D).

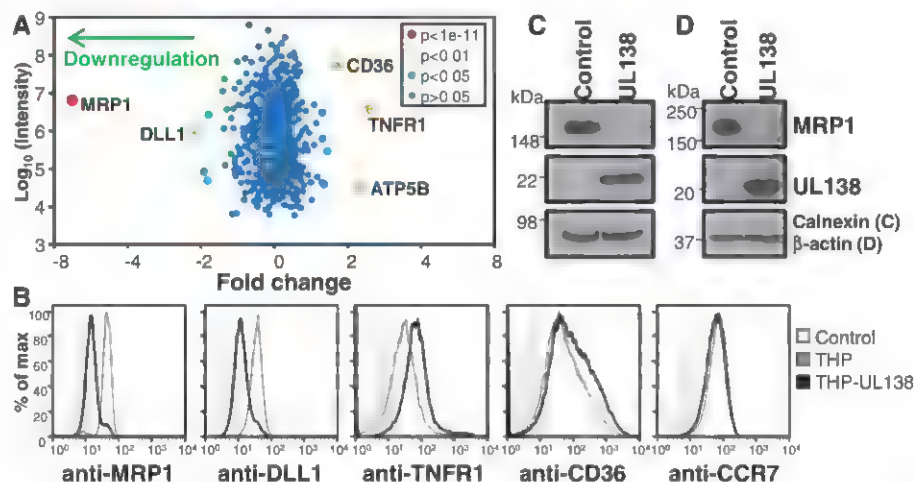
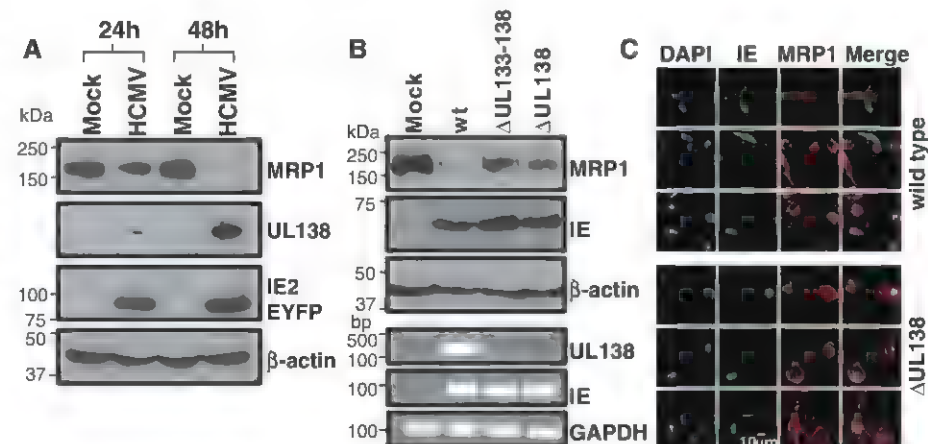


Fig. 2. UL138 down-regulates MRP1 during productive HCMV infection. (A) Mock- or TB40 IE2-eYFP-infected HFFs [multiplicity of infection (moi) 5] were analyzed by immunoblot 24 and 48 hours after infection. (B) Mock, Toledo wild type (wt), Toledo Δ UL133-138, or Toledo Δ UL138 virus-infected HFFs were analyzed by immunoblot 48 hours after infection (top three panels). UL138 and IE mRNA was analyzed by RT-PCR with GAPDH as an internal mRNA control (bottom three panels). (C) Differentiated primary monocytes were infected with wtTB40 or TB40 Δ UL138. Seventy-two hours after infection, cells were stained for MRP1, IE, and DAPI before being examined by confocal microscopy.



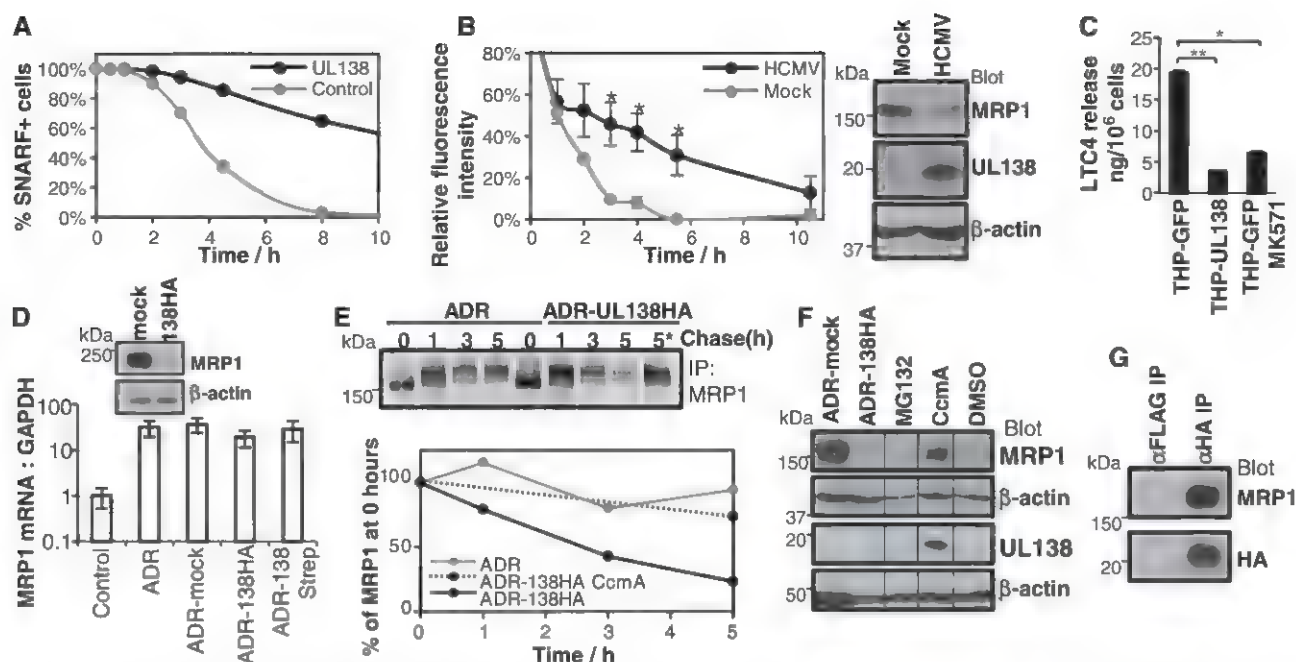


Fig. 3. UL138 targets mature MRP1 for lysosomal degradation and inhibits export of MRP1-specific substrates. (A) THP-1 or THP-UL138 cells were loaded with SNARF-1 ester, and intracellular SNARF-1 was measured by cytofluorometry. The proportion of cells retaining SNARF-1 was plotted. (B) Fifteen hours after infection, HCMV-infected HFFs (moi 5) were analyzed for intracellular SNARF-1 (left panel) and immunoblot (right panel). Three independent replicates were used per time point. Plotted are mean \pm SEM, relative to the post-load HCMV-infected sample. Two-tailed P values ($^{*}P < 0.05$). (C) LTC4 export assayed in A23187-stimulated cells

(fig. S3) (28), with three independent replicates per condition. Plotted: mean \pm SEM and two-tailed P values ($^{*}P < 1 \times 10^{-6}$, $^{**}P < 0.0005$). (D) Quantitative RT-PCR (RT-qPCR) analysis of MRP1 and GAPDH (28). (E) MRP1 immunoprecipitations (with QCRL3 antibody) from cells radiolabeled and chased as indicated, with CcmA included at the 5-hour time point (5*). Total MRP1 is quantified as percentage of MRP1 at time 0. (F) Cells incubated with MG132, CcmA, or DMSO (28) and immunoblotted as indicated. (G) HA immunoprecipitation from ADR-UL138HA cells preincubated with CcmA for 24 hours to increase MRP1 expression. Anti-FLAG beads were used as a control.

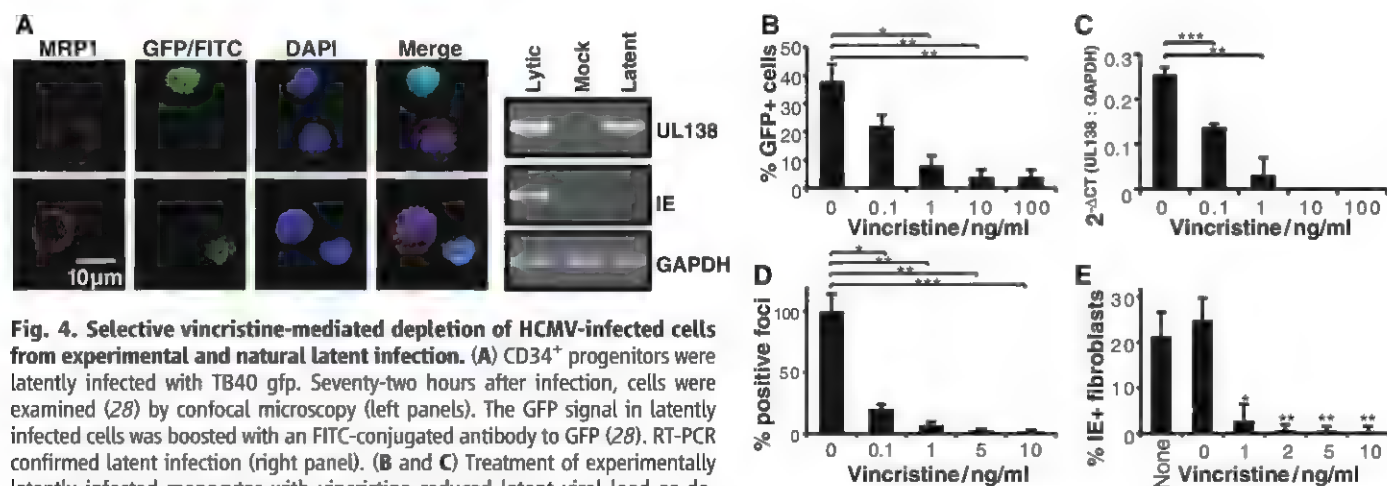


Fig. 4. Selective vincristine-mediated depletion of HCMV-infected cells from experimental and natural latent infection. (A) CD34⁺ progenitors were latently infected with TB40 gfp. Seventy-two hours after infection, cells were examined (28) by confocal microscopy (left panels). The GFP signal in latently infected cells was boosted with an FITC-conjugated antibody to GFP (28). RT-PCR confirmed latent infection (right panel). (B and C) Treatment of experimentally latently infected monocytes with vincristine reduced latent viral load as determined by detection of latently expressed UL138 mRNA by RT-qPCR, and the relative number of latently infected cells. Primary CD14⁺ monocytes were latently infected with TB40 gfp. After 3 days, vincristine was added at the indicated concentration (28). Four days later, the GFP⁺ cells were counted in five independent replicates. Three further independent replicates were analyzed by RT-qPCR for UL138, IE, and GAPDH (C). IE RT-qPCR was always below the limit of detection. Plotted are mean \pm SEM and two-tailed P values ($^{*}P < 0.005$, $^{**}P < 0.001$, $^{***}P < 0.05$). (D) Primary CD14⁺ monocytes from HCMV-seropositive donor D were treated for 4 days with vincristine (28). Endogenous HCMV was reactivated by differentiation and maturation to mature DCs (22), cocultured with fibroblasts for 2 weeks (four replicates per condition), which were examined for viral IE protein, and foci were counted. Plotted are mean \pm SEM % of IE+ foci as compared to 0 ng of vincristine per milliliter (0 ng/ml) and two-tailed P values ($^{*}P < 0.005$, $^{**}P < 0.001$, $^{***}P < 0.0005$). (E) Primary CD34⁺ progenitors were treated for 4 days with vincristine (28). Endogenous HCMV was reactivated by differentiation and maturation to mature DCs (22), then cocultured with fibroblasts for 2 weeks. Cell supernatants were transferred onto fresh fibroblasts (eight replicates per condition), and 100 cells per replicate were examined after 4 days for viral IE protein with DNA counterstaining. Plotted are mean \pm SEM and two-tailed P values (each treatment versus 0 ng/ml vincristine): $^{*}P < 5 \times 10^{-8}$, $^{**}P < 5 \times 10^{-9}$.

reduce the latent load of HCMV by killing experimentally latent CD14⁺ monocytes in vitro. Monocytes latently infected with TB40 gfp and then treated with vincristine for 4 days showed a reduced number of latently infected (GFP-positive) cells (Fig. 4B and fig. S4) as well as a concomitant reduction in detectable latently expressed UL138 RNA (Fig. 4C), which is consistent with vincristine-mediated killing of latently infected cells and a reduction in latency-associated viral load.

Experimentally latent CD14⁺ monocytes or CD34⁺ progenitors can be induced to reactivate latent virus by differentiation to dendritic cells (DCs) and subsequent maturation (8). If vincristine was reducing latent viral load by killing latently infected cells, this should also be reflected in a reduction in reactivating virus. Indeed, treatment of experimentally latently infected cells with vincristine reduced reactivation of latent HCMV from CD14⁺ monocytes after their differentiation to DCs (fig. S5). CD14⁺ monocytes and CD34⁺ progenitors isolated from latently infected donors routinely reactivate infectious HCMV after differentiation and maturation to mature DCs, detected by coculture with indicator fibroblasts (Fig. 4, D and E, and fig. S6) (5). Vincristine treatment of CD14⁺ monocytes, from 7 out of 7 healthy HCMV-seropositive donors, as well as CD34⁺ cells, showed reduced reactivation of infectious virus after differentiation and maturation (Fig. 4D-E). Thus, MRP1 is a potential therapeutic target for eliminating latent HCMV-infected cells from bone marrow before transplantation.

The study of HCMV latency has been hampered by the inability to identify low-frequency latently infected cells ex vivo. The down-regulation of MRP1 by UL138 provides a novel marker of latent infection, but why is MRP1 targeted? DCs from MRP1-deficient mice fail to respond to chemotactic stimuli or migrate into afferent lymphatics (25), because the endogenous MRP1 substrate LTC4 (17) sensitizes the CCR7 chemokine receptor to CCL19 (25). UL138-mediated down-regulation of MRP1 reduced cellular LTC4 export, suggesting that UL138 could inhibit the migration of infected DCs to draining lymph nodes and impair the generation of an HCMV-specific immune response. Decreased MRP1 expression could also help maintain latent infection by inhibiting premature terminal differentiation of DC progenitors until conditions for reactivation are established, as reported for other HCMV latency proteins (UL111.5A) (26), and the terminal differentiation of DC progenitors is dependent on functional MRP1 (27).

UL138-mediated down-regulation of MRP1 was functionally significant, leading to a dramatic reduction in the export of MRP1-specific substrates and predicted that MRP1-transported cytotoxic drugs would accumulate and kill UL138-expressing cells. Indeed, vincristine treatment of experimentally latent myeloid cells and naturally latent CD14⁺ cells and their CD34⁺ progenitors decreased the latent CMV viral load. Vincristine

treatment dramatically reduced levels of reactivated virus after myeloid cell differentiation and maturation to mature DCs, a well-established signal for virus reactivation (5).

Our results open up the possibility of developing strategies using MRP1-specific reagents to clear bone marrow or hematopoietic stem cells of latently infected cells before transplantation, either based on the selection of HCMV-negative cell subpopulations or the targeted killing of latently infected cells, using cytotoxic agents normally exported by MRP1.

References and Notes

1. E. S. Mocarski, T. Shenk, R. F. Pass, Eds., *Cytomegaloviruses* (Lippincott Williams and Wilkins, Philadelphia, PA, ed. 5, 2007), pp. 2701–2773.
2. W. G. Nichols, L. Corey, T. Gooley, C. Davis, M. Boeckh, *J. Infect. Dis.* **185**, 273 (2002).
3. J. Taylor-Wiedeman, J. G. Sissons, L. K. Borysiewicz, J. H. Sinclair, *J. Gen. Virol.* **72**, 2059 (1991).
4. G. Hahn, R. Jores, E. S. Mocarski, *Proc. Natl. Acad. Sci. U.S.A.* **95**, 3937 (1998).
5. M. B. Reeves, P. A. MacAry, P. J. Lehner, J. G. Sissons, J. H. Sinclair, *Proc. Natl. Acad. Sci. U.S.A.* **102**, 4140 (2005).
6. B. Slobedman et al., *Future Microbiol.* **5**, 883 (2010).
7. J. Sinclair, *J. Clin. Virol.* **41**, 180 (2008).
8. J. Sinclair, *Biochim. Biophys. Acta* **1799**, 286 (2010).
9. F. Goodrum, M. Reeves, J. Sinclair, K. High, T. Shenk, *Blood* **110**, 937 (2007).
10. A. Petrucci, M. Rak, L. Grainger, F. Goodrum, *J. Virol.* **83**, 5615 (2009).
11. V. T. Le, M. Trilling, H. Hengel, *J. Virol.* **85**, 13260 (2011).
12. C. Montag et al., *J. Virol.* **85**, 11409 (2011).
13. M. P. Weekes et al., *J. Proteome Res.* **11**, 1475 (2012).
14. D. Marquardt, S. McCrone, M. S. Center, *Cancer Res.* **50**, 1426 (1990).
15. L. Grainger et al., *J. Virol.* **84**, 9472 (2010).
16. J. Jin, A. T. Jones, *Int. J. Cancer* **124**, 233 (2009).
17. A. H. Schinkel, J. W. Jonker, *Adv. Drug Deliv. Rev.* **55**, 3 (2003).

18. K. C. Almquist et al., *Cancer Res.* **55**, 102 (1995).
19. D. Hargrett, T. E. Shenk, *Proc. Natl. Acad. Sci. U.S.A.* **107**, 20039 (2010).
20. K. Kondo, H. Kaneshima, E. S. Mocarski, *Proc. Natl. Acad. Sci. U.S.A.* **91**, 11879 (1994).
21. F. D. Goodrum, C. T. Jordan, K. High, T. Shenk, *Proc. Natl. Acad. Sci. U.S.A.* **99**, 16255 (2002).
22. M. B. Reeves, P. J. Lehner, J. G. Sissons, J. H. Sinclair, *J. Gen. Virol.* **86**, 2949 (2005).
23. M. M. Huang, V. G. Kew, K. Jestic, M. R. Wills, M. B. Reeves, *J. Virol.* **86**, 8507 (2012).
24. A. Rajagopal, A. C. Pant, S. M. Simon, Y. Chen, *Cancer Res.* **62**, 391 (2002).
25. D. F. Robbani et al., *Cell* **103**, 757 (2000).
26. S. Avdic, J. Z. Cao, A. K. Cheung, A. Abendroth, B. Slobedman, *J. Virol.* **85**, 7465 (2011).
27. R. van de Ven et al., *J. Immunol.* **176**, 5191 (2006).
28. Information on materials and methods is available as supplementary material on Science Online.

Acknowledgments: We are grateful to M. Reeves for discussions and cells. All data are tabulated in the main paper and the supplementary materials. This work was supported by a Next Generation Fellowship from the Cambridge Institute for Medical Research and a Wellcome Trust Fellowship (093966/Z/10/Z) to M.P.W.; a grant from the Agency for Science, Technology and Research, Singapore to S.Y.L.T.; an MRC Programme grant (G0701279) to J.H.S.; and a Wellcome Trust Senior Fellowship (084957/Z/08/Z) to P.J.L. This work was also supported by the NIHR Cambridge Biomedical Research Centre, and the Cambridge Institute for Medical Research is in receipt of a Wellcome Trust Strategic Award. P.J.L., J.H.S., M.P.W., and R.A. are authors on patent application PCT/GB2012/051094 filed by Cambridge Enterprise, entitled "Detection and depletion of HCMV infected cells."

Supplementary Materials

www.sciencemag.org/cgi/content/full/340/6129/199/DC1
Materials and Methods
Figs. S1 to S6
Tables S1 and S2
References (29–43)

11 January 2013; accepted 14 February 2013
10.1126/science.1235047

Blockade of Chronic Type I Interferon Signaling to Control Persistent LCMV Infection

Elizabeth B. Wilson,¹ Douglas H. Yamada,¹ Heidi Elsaesser,¹ Jonathan Herskovitz,¹ Jane Deng,² Genhong Cheng,¹ Bruce J. Aronow,³ Christopher L. Karp,^{4*} David G. Brooks^{1†}

Type I interferons (IFN-I) are critical for antiviral immunity; however, chronic IFN-I signaling is associated with hyperimmune activation and disease progression in persistent infections. We demonstrated in mice that blockade of IFN-I signaling diminished chronic immune activation and immune suppression, restored lymphoid tissue architecture, and increased immune parameters associated with control of virus replication, ultimately facilitating clearance of the persistent infection. The accelerated control of persistent infection induced by blocking IFN-I signaling required CD4 T cells and was associated with enhanced IFN- γ production. Thus, we demonstrated that interfering with chronic IFN-I signaling during persistent infection redirects the immune environment to enable control of infection.

Despite initially robust antiviral immune activity, some viruses, including HIV and hepatitis C virus (HCV) in humans and

lymphocytic choriomeningitis virus (LCMV) in mice, outpace the immune response and establish persistent infections (1, 2). Besides virus-

mediated evasion tactics, the host initiates an immunosuppressive program that actively suppresses antiviral T cell responses and facilitates persistent infection (3, 8). The expression of

suppressive factors is tightly linked to viral burden (3, 4, 8), suggesting the presence of an immunologic sensory system that continually measures the magnitude and duration of viral replication and then dynamically modulates the balance between antiviral immunity and immune exhaustion.

In order to identify the mechanisms orchestrating the immunosuppressive program during virus infection, we performed RNA microarray-based splenic network analysis. We compared mice infected with one of two LCMV strains: the Armstrong (Arm) strain, which induces a robust T cell response that resolves infection within 8 to 10 days, or the clone 13 (Cl13) strain, which generates a persistent infection because of the sustained expression of an immunosuppressive program, including production of interleukin (IL)-10 and expression of the inhibitory molecule PD-L1 (programmed cell death 1 ligand 1) (4, 5, 9–13). PD-L1 and IL-10 are sim-

ilarly expressed at the onset of both acute and persistent infection; however, expression of these molecules wanes with resolution of acute infection, whereas they are maintained or elevated in persistent infection (3, 4, 8). Similarly, antigen-presenting cell (APC) populations expressing multiple suppressive factors with the ability to inhibit T cell responses are present early in acute infection but are elevated in the context of persistent infection (8). We focused our microarray analysis to identify factors exhibiting a similar kinetic that might be used to sense virus replication dynamics and control immunosuppressive programs. Tissue-wide cytokine expression patterns were similar in acute and persistent infections (fig. S1A). However, analogous to virus clearance kinetics, type I interferon (IFN-I) receptor (IFNR)-stimulated genes, signal transducer and activator of transcription (STAT) genes, and IFN-I regulatory factors were initially similarly expressed in LCMV-Arm and

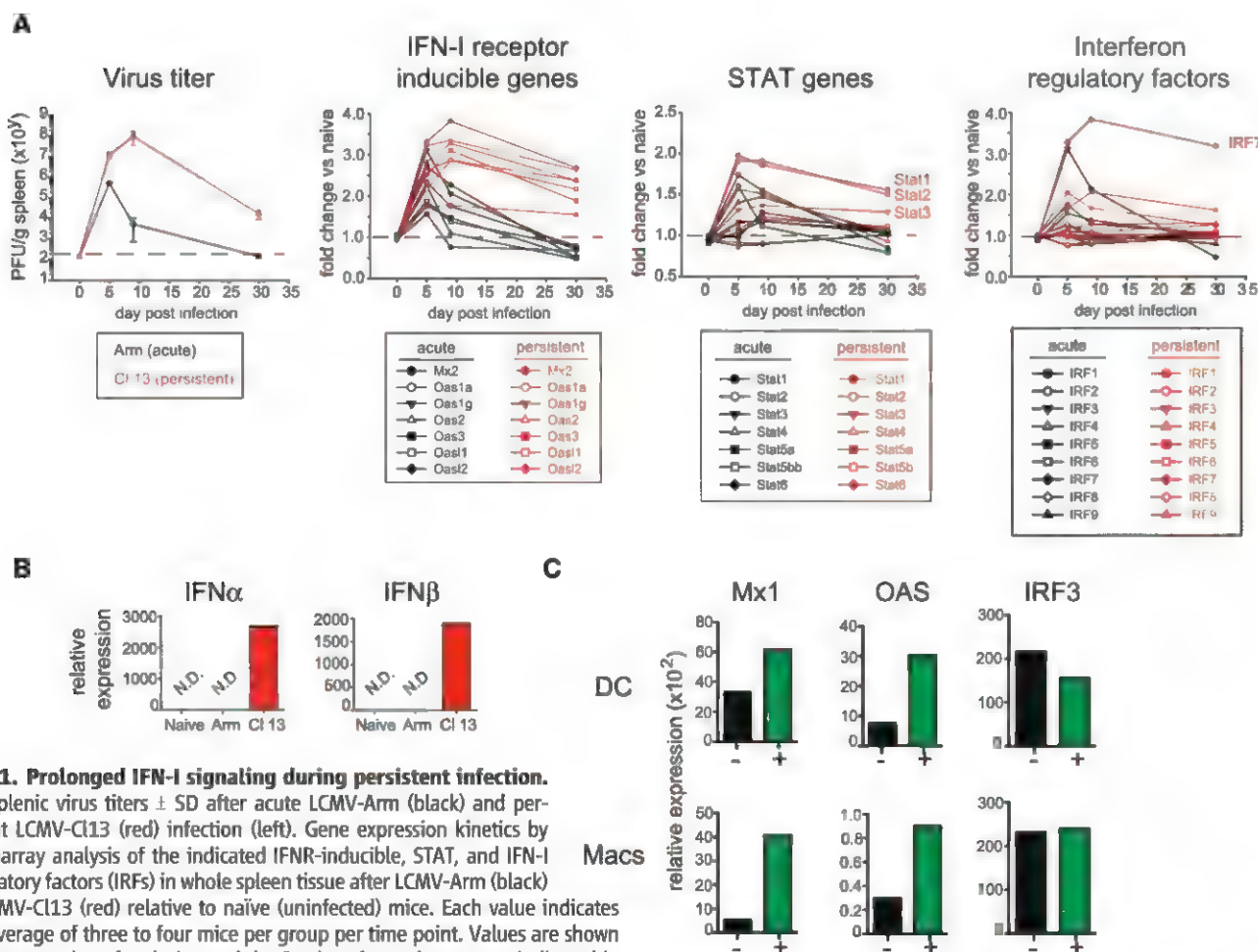


Fig. 1. Prolonged IFN-I signaling during persistent infection.

(A) Splenic virus titers \pm SD after acute LCMV-Arm (black) and persistent LCMV-Cl13 (red) infection (left). Gene expression kinetics by microarray analysis of the indicated IFNR-inducible, STAT, and IFN-I regulatory factors (IRFs) in whole spleen tissue after LCMV-Arm (black) or LCMV-Cl13 (red) relative to naive (uninfected) mice. Each value indicates the average of three to four mice per group per time point. Values are shown without error bars for clarity, and the *P* values for each gene are indicated in table S1. PFU, plaque-forming units. (B) IFN α (left) and IFN β (right) mRNA expression relative to a control gene, *HPRT*, in splenic DCs from naive or LCMV-Arm- or LCMV-Cl13-infected mice (day 9). N.D. indicates that IFN α or IFN β transcripts were not detected after 40 cycles of amplification. *HPRT* mRNA expression was measurable in all samples. (C) *Mx1*, *OAS*, and *IRF3*

mRNA expression relative to *HPRT* in the indicated IL-10+ (GFP+, green) or IL-10- (GFP-, black) splenic DCs (top) or macrophages (bottom) 9 days after LCMV-Cl13 infection of Vert-X IL-10 reporter mice. For (B) and (C), each group is a pool of cells from six to eight mice and is representative of two independent experiments.

LCMV-Cl13 infections but then rapidly dissipated as acute LCMV-Arm infection resolved, whereas they remained elevated in LCMV-Cl13 infection (Fig. 1A and table S1). In total spleen, the expression of IFN- α and IFN- β was not elevated above uninfected mice (fig. S1B); however, at day 9 postinfection IFN- α and IFN- β transcripts were still present in dendritic cells (DCs) from LCMV-Cl13-infected mice (Fig. 1B). Analysis of IL-10–green fluorescent protein (GFP) (Vert-X) reporter mice (8, 14) revealed that *OAS* and *Mx1* (genes directly stimulated by IFNR signaling) expression levels were specifically enriched in the immunoregulatory APCs that co-express the highest levels of PD-L1 and IL-10 and can suppress antiviral T cell responses (8) (Fig. 1C), suggesting a link between prolonged IFN-I signaling and immunosuppression. Expression of *IRF3*, a gene involved in the IFN-I

response but whose expression is not directly regulated by IFNR signaling (15), was not differentially increased in immunoregulatory APCs (Fig. 1C).

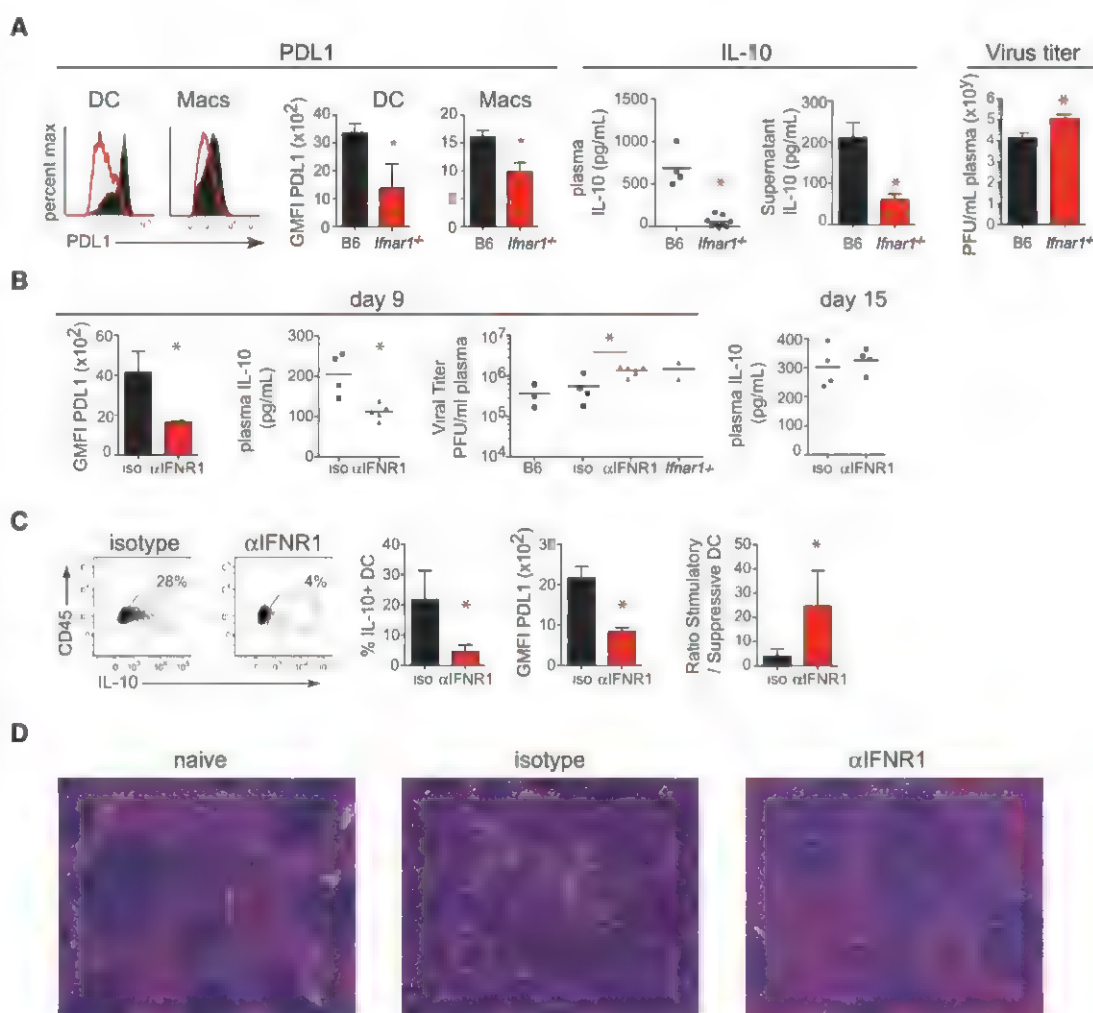
We next determined the impact of IFN-I signaling on the immunosuppressive program in vivo. Although levels of virus replication usually correlate with expression of suppressive factors (1), *Ifnar1*^{−/−} mice exhibited decreased expression of PD-L1 and IL-10 compared with wild-type mice at day 9 after LCMV-Cl13 infection (Fig. 2A and fig. S2A) despite elevated levels of viral replication and viral antigen (fig. S2, A and B). Furthermore, treatment of splenocytes with IFN β stimulated increased PD-L1 and IL-10 expression (fig. S2C). Taken together, these data suggest that IFN-I signaling drives the immunosuppressive program in vivo. *Ifnar1*^{−/−} mice failed to clear LCMV-Arm by day 9 after infection (fig. S2D),

consistent with the antiviral and immune stimulatory effect of IFN-I during viral infection (16).

To resolve the role of IFN-I in induction of the immunosuppressive program separate from potential abnormalities of life-long genetic deficiency in *Ifnar1*^{−/−} mice (17), we treated wild-type mice with an IFNR1-blocking antibody beginning 1 day before LCMV-Cl13 infection. IFNR1 blockade diminished *Mx1*, *OAS*, and *IRF7* expression in multiple tissues and cell types (fig. S3A), indicating the ability to inhibit IFN-I signaling in vivo. Analogous to persistently infected *Ifnar1*^{−/−} mice, IFNR1 antibody blockade led to decreased PD-L1 and IL-10 expression and elevated virus titers compared with isotype antibody-treated LCMV-Cl13-infected mice on day 9 after infection (Fig. 2B). IL-10 levels rebounded when IFNR1 blocking antibody treatment was withdrawn (day 15; Fig. 2B), indicating sensitive

Fig. 2. The immunosuppressive program during persistent infection is dependent on IFN-I signaling. (A) Representative histograms and summarized quantification of geometric mean fluorescence intensity (GMFI) show PD-L1 on splenic DCs and macrophages 9 days after LCMV-Cl13 infection in wild-type (WT, black) and *Ifnar1*^{−/−} (red) mice.

Scatter plots show plasma IL-10 levels on day 9 after LCMV-Cl13 infection. Bar graphs measure IL-10 production by cultured splenocytes (in the absence of exogenous stimulation) isolated 9 days after LCMV-Cl13 infection from WT or *Ifnar1*^{−/−} mice. Plasma viral titers in WT or *Ifnar1*^{−/−} mice on day 9 after LCMV-Cl13 infection are shown to the far right. Dashed lines indicate the level of detection of the plaque assay (200 PFU). (B to D) WT mice were treated with isotype or IFNR1 blocking antibody beginning 1 day before LCMV-Cl13 infection. (B) Graphs indicate GMFI of PD-L1 on splenic CD45+ cells (left), plasma levels of IL-10 (middle), and plasma viral titers (right) of untreated mice (B6), isotype-treated mice, IFNR1 blocking antibody (α IFNR1)-treated mice, and untreated *Ifnar1*^{−/−} mice. Plasma IL-10 levels on day 15 after LCMV-Cl13 infection are shown on the far right. (C) Flow cytometry plots of IL-10 reporter expression (GFP) in splenic DCs from Vert-X mice treated with isotype or IFNR1 blocking antibody. Bar graphs show the frequency of IL-10 expression and the GMFI of PD-L1 expression by splenic DCs. The ratio of IL-10–nonproducing to IL-10–producing DCs is shown on the far right. (D) Hematoxylin and eosin staining of spleens



from naïve mice (left) or on day 9 after LCMV-Cl13 infection of mice treated with isotype (middle) or IFNR1 blocking antibody (right). Symbols represent individual mice with bars indicating the mean of the group. In bar graphs, the data represent the average \pm SD of three to six mice per group. All data are representative of two or more independent experiments. * $P < 0.05$.

surveillance and rapid modulation of the immunosuppressive state through IFN-I signaling. Heightened IFN-I signaling can inhibit inflammasome activity in some situations (18). However, despite higher levels of virus replication and LCMV antigen in splenic APCs from persistently infected mice treated with IFNR1 blocking antibody (Fig. 2B and fig. S2B), reduced amounts of IL-1, IL-18, and inflammasome activation were observed (fig. S3B), indicating that blockade of IFN-I signaling decreases chronic inflammation during persistent infection. The reduced levels of inhibitory factors and chronic activation after IFNR1 blockade were not indicative of global down-regulation of pro-inflammatory cytokines, and in fact expression of IFN- γ , a factor critical for control and therapeutic resolution of persistent LCMV infection (16, 19, 20), was elevated after IFNR1 blockade (fig. S3B). Thus, IFNR blockade during persistent infection diminishes immunosuppressive

signals and chronic inflammation during persistent infection.

IFNR1 antibody blockade before infection also decreased the level of IL-10- and PD-L1-expressing immunoregulatory DCs (Fig. 2C), leading to an enhanced ratio of stimulatory to immunoregulatory DCs. Moreover, IFNR1 antibody blockade prevented the splenic disorganization associated with impaired immune cell interactions and the inability to control persistent infection (21–23) (Fig. 2D and fig. S3C). Thus, immune cells are likely better positioned to interact with one another, and, because of the decrease in immunoregulatory DC frequency, those interactions are more likely to be stimulatory.

We next determined how blockade of IFN-I signaling before infection contributed to control of persistent infection. Although virus titers were initially increased in mice treated with IFNR1 blocking antibody, by 30 days postinfection viremia was reduced compared with isotype treat-

ment, and many of the mice had already controlled infection (Fig. 3A). Furthermore, virus titers were decreased in multiple compartments, including the kidney (a life-long reservoir of LCMV-Cl13) (Fig. 3B). Mirroring findings in *Ifnar1*^{−/−} mice (16), IFNR1 blockade in wild-type mice led to persistent infection with LCMV-Arm (fig. S2D), demonstrating the antiviral activity of IFN-I and its requirement to control acute viral infection.

We next sought to understand the immune mechanisms through which IFNR1 blockade enables control of persistent viral infection. IFNR1 blockade before infection induced a numerical increase in many immune subsets 9 days after infection including the total number of functional virus-specific CD4 T cells (Fig. 3C and fig. S4A). However, despite an overall increase in B cells and CD4 T cells, LCMV-specific antibody titers were not elevated in IFNR1 blocking antibody-treated mice at day 9 or 30 after infection (fig. S4B). Unlike virus-specific CD4 T

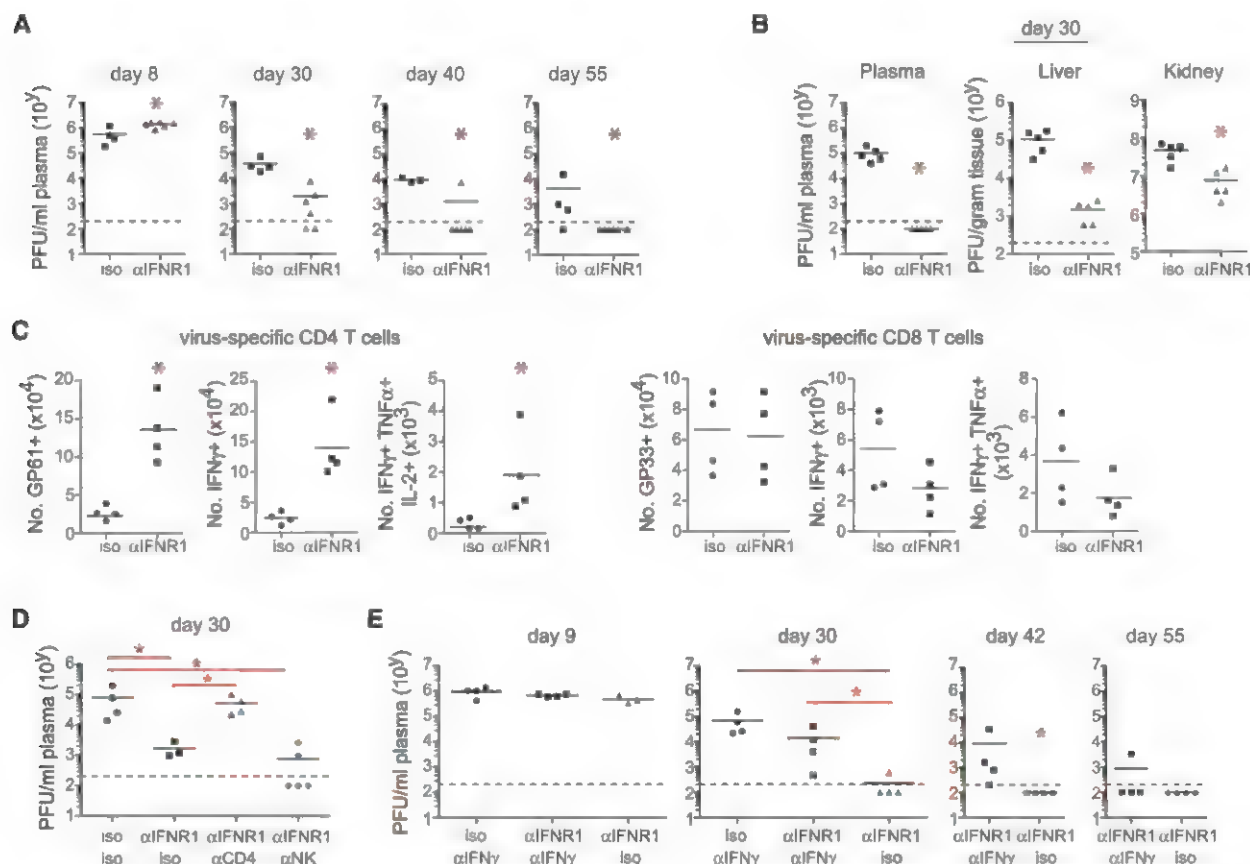


Fig. 3. IFNR1 blockade enhances control of persistent infection. WT mice were treated with isotype or IFNR1 blocking antibody beginning 1 day before LCMV-Cl13 infection. (A) Plasma virus titers at the indicated time points after infection. (B) Viral titers in plasma, liver, and kidney 30 days after infection. (C) Graphs indicate total numbers of IFN- γ -expressing and of multicytokine-producing (polyfunctional) LCMV-GP₆₁₋₈₀-specific CD4 T cells and LCMV-GP₃₃₋₄₁-specific CD8 T cells. (D) Plasma viral titers at day 30 after LCMV-Cl13 infection in mice that were either undepleted of cells and treated with isotype (iso/iso) or IFNR1 (α IFNR1/iso) blocking antibody or depleted of

CD4 T cells (α CD4) or NK cells (α NK) before infection and IFNR1 blocking antibody treatment. (E) Plasma virus titers at the indicated time point after LCMV-Cl13 infection in mice that were either treated with isotype or IFNR1 blocking antibody with or without anti-IFN- γ (α IFN- γ). x axis labels indicate (top) IFNR1 or isotype and (bottom) cell or IFN- γ depleting antibody treatments. Each symbol in the scatter plots represents an individual mouse with bars indicating the mean of the group. Dashed lines indicate the level of detection of the plaque assay (200 PFU). Data are representative of two or more independent experiments. * P < 0.05.

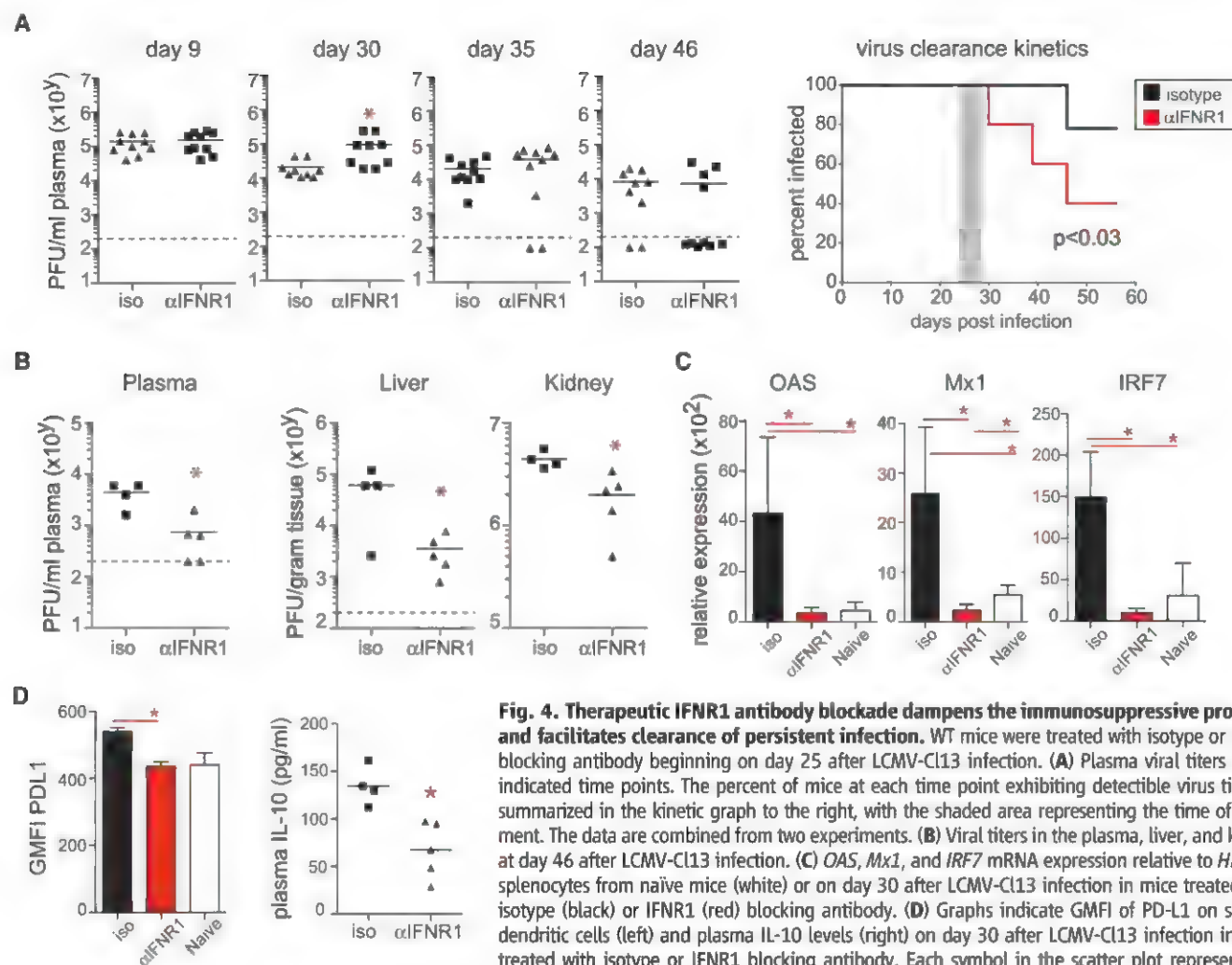


Fig. 4. Therapeutic IFN1 antibody blockade dampens the immunosuppressive program and facilitates clearance of persistent infection. WT mice were treated with isotype or IFN1 blocking antibody beginning on day 25 after LCMV-Cl13 infection. **(A)** Plasma viral titers at the indicated time points. The percent of mice at each time point exhibiting detectable virus titers is summarized in the kinetic graph to the right, with the shaded area representing the time of treatment. The data are combined from two experiments. **(B)** Viral titers in the plasma, liver, and kidney at day 46 after LCMV-Cl13 infection. **(C)** *OAS*, *Mx1*, and *IRF7* mRNA expression relative to *HPRT* in splenocytes from naïve mice (white) or on day 30 after LCMV-Cl13 infection in mice treated with isotype (black) or IFN1 (red) blocking antibody. **(D)** Graphs indicate GMFI of PD-L1 on splenic dendritic cells (left) and plasma IL-10 levels (right) on day 30 after LCMV-Cl13 infection in mice treated with isotype or IFN1 blocking antibody. Each symbol in the scatter plot represents an individual mouse, and bar graphs indicate the average value \pm SD. All data are representative of two to five independent experiments. * $P < 0.05$.

cells, virus-specific CD8 T cell numbers and cytokine production were similar or slightly reduced when IFN-I signaling was blocked (Fig. 3C and fig. S4C). On the basis of the increase in natural killer (NK) cells, virus-specific CD4 T cells, and systemic IFN- γ levels (Fig. 3C and figs. S3B and S4A), we sought to examine the role of each of these factors in accelerating virus clearance after IFN1 blockade. CD4 depletion before infection abrogated the accelerated virus control engendered by IFN1 blockade, whereas NK cell depletion did not affect IFN1 blockade-mediated clearance (Fig. 3D). To assess the role of increased IFN- γ in IFN1 blockade-induced virus clearance, we treated mice with IFN1 blocking antibody with or without IFN- γ blocking antibodies at the time of LCMV-Cl13 infection. The accelerated clearance of persistent infection after IFN1 blockade was abrogated in mice cotreated with IFN- γ blocking antibody (anti-IFN- γ) (Fig. 3E). Although occurring later than in IFN- γ knockout mice (24), mice treated with anti-IFN- γ alone died ~35 days after infection, whereas mice receiving IFN1 block-

ing antibody plus anti-IFN- γ survived and cleared infection similar to untreated mice. Together, these results indicate that IFN1 antibody stimulates accelerated clearance of persistent virus infection through CD4 T cell and IFN- γ -dependent mechanisms.

We next determined whether therapeutic blockade of IFN-I signaling affected an established LCMV-Cl13 infection. Blockade of IFN1 beginning 25 days after infection accelerated control of persistent infection in multiple compartments compared with isotype treatment (Fig. 4, A and B). The enhanced control of infection occurred despite the initial increase in virus titers immediately after IFN1 blocking antibody therapy (Fig. 4A). Blockade of IFN1 beginning 25 days after infection reduced the IFN-I gene expression signature and decreased IL-10 and PD-L1 levels (Fig. 4, C and D), demonstrating that IFN-I continues to be a key component of an immunologic surveillance system and stimulator of the immunosuppressive program throughout persistent infection. Thus, therapeutically ablating chronic IFN-I immune acti-

vation in vivo enhances control of persistent LCMV infection.

Our results demonstrate that chronic IFN-I signaling during persistent infection drives the immunosuppressive program and that interfering with IFN-I signaling restores multiple parameters of productive immunity, allowing for viral clearance. IFN-I treatment in combination with the antiviral drug ribavirin is often effective at eradicating HCV infection. However, some patients fail to have a sustained virologic response. A characteristic of patients that fail IFN-I/ribavirin therapy is a heightened IFN-I signature before treatment that fails to substantially increase with therapy (25, 26). Thus, the initially high IFN-I signature may lead to enhanced immune dysfunction, and consequently adding more IFN-I is ineffective. These results highlight the duality of IFN-I during viral infection: Acute IFN-I signals possess antiviral and immune stimulatory potential required for clearance of infection, but when virus cannot be controlled, acutely sustained IFN-I signaling induces immunosuppression that facilitates persistent virus infection. Considering that

HIV and HCV infections are also associated with immune activation driven by chronic IFN-I signaling (23, 27–29), a similar blockade of IFN-I may improve control of these infections. In total, our data support IFN-I as a central rheostat and regulator of the immunosuppressive program and the possibility that it may be feasible to redirect entire immunologic programs by modulating activity of a single pathway: IFN-I.

References and Notes

1. E. B. Wilson, D. G. Brooks, *Immunol. Res.* **48**, 3 (2010).
2. Q. Li et al., *Science* **323**, 1726 (2009).
3. D. L. Barber et al., *Nature* **439**, 682 (2006).
4. D. G. Brooks et al., *Nat. Med.* **12**, 1301 (2006).
5. M. Ejrnaes et al., *J. Exp. Med.* **203**, 2461 (2006).
6. C. L. Day et al., *Nature* **443**, 350 (2006).
7. M. A. Brockman et al., *Blood* **114**, 346 (2009).
8. E. B. Wilson et al., *Cell Host Microbe* **11**, 481 (2012).
9. M. Clerici et al., *J. Clin. Invest.* **93**, 768 (1994).
10. A. L. Landay et al., *J. Infect. Dis.* **173**, 1085 (1996).
11. E. I. Rigopoulou, W. G. Abbott, P. Haigh, N. V. Naoumov, *Clin. Immunol.* **117**, 57 (2005).
12. M. A. Brockman et al., *Blood* **114**, 346 (2009).
13. J. K. Flynn et al., ATAHC Study Group, *J. Viral Hepat.* **18**, 549 (2011).
14. R. Madan et al., *J. Immunol.* **183**, 2312 (2009).
15. W. C. Au, P. A. Moore, W. Lowther, Y. T. Juang, P. M. Pitha, *Proc. Natl. Acad. Sci. U.S.A.* **92**, 11657 (1995).
16. U. Müller et al., *Science* **264**, 1918 (1994).
17. D. J. Gough, N. L. Messina, C. J. Clarke, R. W. Johnstone, D. E. Levy, *Immunity* **36**, 166 (2012).
18. G. Guarda et al., *Immunity* **34**, 213 (2011).
19. A. Tishon, H. Lewicki, G. Rail, M. Von Herrath, M. B. Oldstone, *Virology* **212**, 244 (1995).
20. M. G. Von Herrath, B. Coon, M. B. Oldstone, *Virology* **229**, 349 (1997).
21. A. Tishon, P. Borrow, C. Evans, M. B. Oldstone, *Virology* **195**, 397 (1993).
22. S. Müller et al., *J. Virol.* **76**, 2375 (2002).
23. S. Moir, T. W. Chun, A. S. Fauci, *Annu. Rev. Pathol.* **6**, 223 (2011).
24. R. Ou, S. Zhou, L. Huang, D. Moskopidis, *J. Virol.* **75**, 8407 (2001).
25. L. Chen et al., *Gastroenterology* **128**, 1437 (2005).
26. M. Sarasin-Filipowicz et al., *Proc. Natl. Acad. Sci. U.S.A.* **105**, 7034 (2008).
27. S. E. Bosinger et al., *J. Clin. Invest.* **119**, 3556 (2009).
28. B. Jacquelin et al., *J. Clin. Invest.* **119**, 3544 (2009).
29. C. R. Bolen et al., *J. Interferon Cytokine Res.* **33**, 15 (2013).

Acknowledgments: We thank S. Bensinger for insightful discussion and critical review of the manuscript, all the members of the Brooks laboratory for discussions and technical assistance, and the UCLA Translational Pathology Core Facility for expert histological tissue processing and analysis. The data presented in the manuscript are tabulated in the main paper and in the supplementary materials. D.G.B. and E.B.W. are named inventors on a provisional patent assigned to The Regents of the University of California relating in part to methods of treating chronic viral infections by administering agents that inhibit IFN. The microarray data set from this study is available at www.ncbi.nlm.nih.gov/geo/ (accession no. GSE44322). Our work was supported by the NIH (grants AI085043 and AI082975 to D.G.B., AI060567 to E.B.W., and HL108949 to J.D.), an Institutional Clinical and Translational Science Award (NIH/NCATS 8UL1TR000077-04 to B.J.A.), and the UCLA Center for AIDS Research (P30 AI028697).

Supplementary Materials

www.sciencemag.org/cgi/content/full/340/6129/202/DC1
Materials and Methods
Figs. S1 to S4
Table S1
Reference (30)

15 January 2013; accepted 20 February 2013
10.1126/science.1235208

Persistent LCMV Infection Is Controlled by Blockade of Type I Interferon Signaling

John R. Teijaro,^{1*} Cherie Ng,^{1*} Andrew M. Lee,^{1†} Brian M. Sullivan,¹ Kathleen C. F. Sheehan,² Megan Welch,¹ Robert D. Schreiber,² Juan Carlos de la Torre,¹ Michael B. A. Oldstone^{1‡}

During persistent viral infections, chronic immune activation, negative immune regulator expression, an elevated interferon signature, and lymphoid tissue destruction correlate with disease progression. We demonstrated that blockade of type I interferon (IFN-I) signaling using an IFN-I receptor neutralizing antibody reduced immune system activation, decreased expression of negative immune regulatory molecules, and restored lymphoid architecture in mice persistently infected with lymphocytic choriomeningitis virus. IFN-I blockade before and after establishment of persistent virus infection resulted in enhanced virus clearance and was CD4 T cell-dependent. Hence, we demonstrate a direct causal link between IFN-I signaling, immune activation, negative immune regulator expression, lymphoid tissue disorganization, and virus persistence. Our results suggest that therapies targeting IFN-I may help control persistent virus infections.

Persistent viral infections such as HIV, hepatitis B virus, and hepatitis C virus (HCV) represent important global health problems. Persistent viruses take advantage of negative immune regulatory molecules to suppress antiviral CD4 and CD8 T cell responses (1, 2),

resulting in T cell exhaustion (3, 4) and facilitating virus persistence. Hyperimmune activation is also observed after persistent virus infection and is characterized by prolonged activation of T cells, B cells, and natural killer (NK) cells; elevated pro-inflammatory mediators; and a sustained interferon signature (5–7). Type I interferon (IFN-I) signaling is upstream of hundreds of inflammatory genes, suggesting that IFN-I may be responsible for generating the hyperactivated immune environment during virus persistence. We investigated the role of IFN-I in regulating immune activation, immune suppression, and virus control after persistent virus infection in mice.

To elucidate the role of IFN-I in virus persistence, we used lymphocytic choriomeningitis virus (LCMV). In adult mice, the Armstrong (Arm) strain causes an acute infection that is cleared 8 days postinfection (dpi) because of robust antiviral CD8 T cell responses. In contrast to the Arm strain, the clone 13 (Cl13) strain causes a systemic viral infection lasting over 90 days (8–13). Cl13-infected mice had significantly elevated IFN-I in the serum compared with Arm-infected counterparts at 18 and 24 hours postinfection (hpi) (Fig. 1, A and B). By using IFN- β -yellow fluorescent protein (YFP) reporter mice (14), we detected YFP expression in plasmacytoid dendritic cells (pDCs) at 18 hours post-Cl13 infection, with minimal YFP expression in pDCs during Arm infection (fig. S1A). IFN- β -YFP expression was not observed in other splenocytes (fig. S1B), suggesting that Cl13 infection induces IFN- β production in pDCs. pDCs are reported to be an early target of Cl13 infection (13, 15). To address whether Cl13 preferentially infected pDCs, we used nonreplicating Arm or Cl13 viruses, in which their glycoproteins (GPs) were replaced with a green fluorescent protein (GFP) marker (denoted Δ GP-Cl13 or Δ GP-Arm). As expected, pDCs exhibited a 2- to 2.5-fold increase in GFP expression upon infection with Δ GP-Cl13 compared with Δ GP-Arm (Fig. 1C). Consistent with IFN-I signaling being upstream of inflammatory gene expression, we observed elevated expression of multiple pro-inflammatory cytokines and chemokines 18 hours post-Cl13 infection versus Arm infection (fig. S1C). To determine whether elevated pro-inflammatory cytokines and chemokines in Cl13 infection were due to IFN-I signaling, we treated mice with an antibody against interferon alpha-beta

¹Department of Immunology and Microbial Science, The Scripps Research Institute, La Jolla, CA 92037, USA. ²Department of Pathology and Immunology, Washington University School of Medicine, St. Louis, MO 63110, USA.

*These authors contributed equally to this work.

†Present address: Center for Genetics of Host Defense, Immunology, University of Texas Southwestern, Dallas, TX 75390–8505, USA

‡Corresponding author. E-mail: mbaobo@scripps.edu

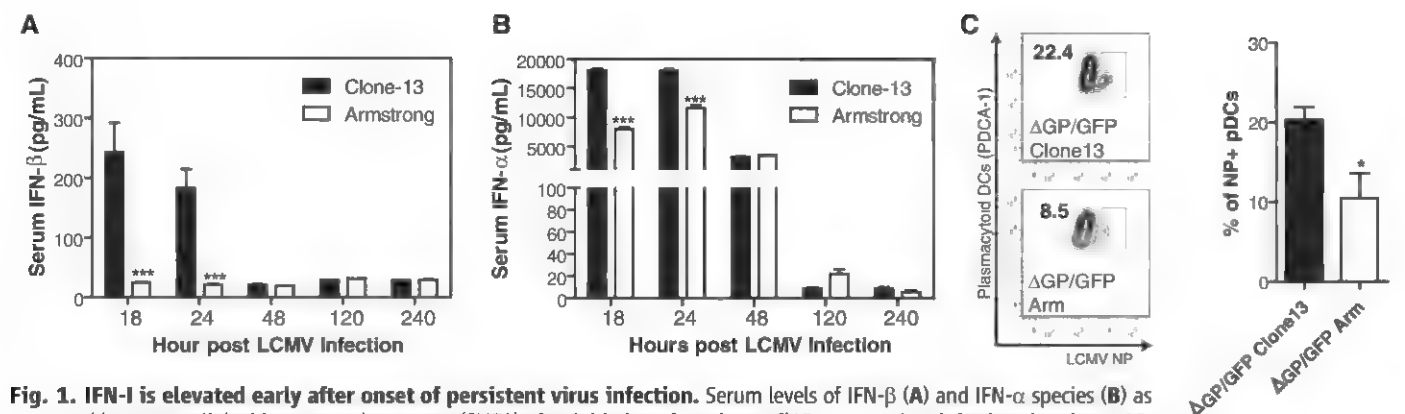


Fig. 1. IFN-I is elevated early after onset of persistent virus infection. Serum levels of IFN-β (A) and IFN-α species (B) as measured by enzyme-linked immunosorbent assay (ELISA) after initiation of persistent Cl13 or acute Arm infections in mice at 18, 24, 48, 120, and 240 hpi in C57BL/6 mice. (C) pDCs are preferentially infected early after Cl13 infection. Percent of GFP-positive pDCs infected with ΔGP-Cl13 or ΔGP-ARM viruses 24 hpi. * $P < 0.05$; *** $P < 0.005$. Results are representative of two to three independent experiments and represent the SEM from three to five mice per group.

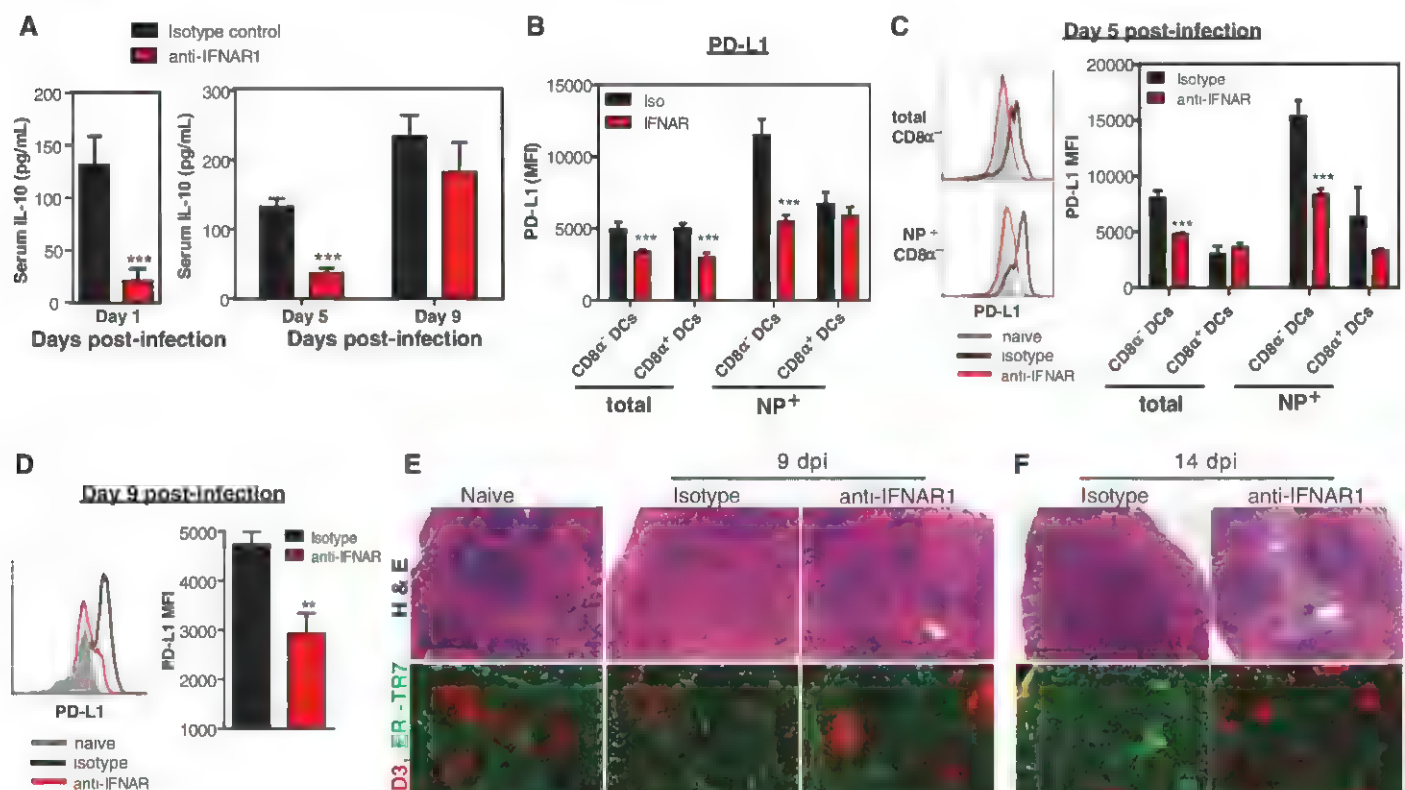


Fig. 2. IFN-I signaling is essential for the expression of the negative immune regulators IL-10 and PD-L1 and lymphoid tissue disorganization after persistent virus infection. Mice were treated with anti-IFNAR1 1 day before infection. (A) Serum levels of IL-10 as measured by ELISA on days 1, 5, and 9 after Cl13 infection in C57BL/6 mice treated with either isotype control antibodies or anti-IFNAR1. (B) Mean fluorescent intensity (MFI) of PD-L1 expression as determined by flow cytometry on either LCMV viral antigen positive (VL-4⁺) or viral antigen negative (VL-4⁻) splenic DCs 1 day after Cl13 infection. (C) Representative histograms of PD-L1 expression as determined by flow cytometry on either infected or uninfected (shaded histograms) CD8α-negative DCs (left) or compiled PD-L1 expression (right) at day 5 after Cl13 infection. (D) Histogram of PD-L1 expression (left) and mean fluorescent intensity (right) as determined by flow cytometry on splenic CD8α-

negative dendritic cells at day 9 after Cl13 infection. Histopathological and immunofluorescent analysis of spleens on days 9 (E) and 14 (F) after Cl13 infection from naive mice or mice infected with Cl13 and treated with isotype antibodies or anti-IFNAR1 as above. (Top) Hematoxylin and eosin (H&E) histopathological analysis. (Middle) Staining for a stromal cell marker (ER-TR7, a marker for fibroblastic reticular cells) and T cells (CD3). (Bottom) B cell staining (B220). Images were taken with a 5× objective. Scale bars indicate 500 μm. ** $P < 0.01$; *** $P < 0.005$. Results are representative of two independent experiments and represent the SEM from five mice per group.

receptor 1 (anti-IFNAR1) before infection and measured cytokine and chemokine levels in the serum 18, 24, and 48 hpi (16). Blockade of IFN-I signaling significantly blunted production of multiple pro-inflammatory cytokines and chemokines after C113 infection at 18, 24, and 48 hpi (fig. S1, C to E).

We asked whether IFN-I signaling contributes to the C113-induced immunosuppressive state. The IFN-I signaling blockade resulted in significant suppression of interleukin-10 (IL-10) production 1 and 5 dpi (Fig. 2A). We also detected significant suppression of programmed cell death 1 ligand 1 (PD-L1) on both CD8 α^+ and CD8 α^- DCs 1 dpi (Fig. 2B), which was retained 5 and 9 dpi in CD8 α^+ but not CD8 α^- DCs (Fig. 2, C and D). Together, these results demonstrate that IFN-I signaling inhibits negative regulatory molecule expression. Because DCs are primary targets of C113 infection and DC infection is crucial for virus persistence (8, 17, 18), we asked whether blockade of IFN-I signaling altered the DC compartment. IFN-I blockade increased virus nucleoprotein (NP) expression in DCs and macrophages 5 dpi (fig. S2C). Blockade of IFN-I signaling significantly increased both the frequency and number of CD8 α^+ and CD8 α^- DCs and macrophages (fig. S2A). Moreover, we observed a significant increase in DCs with an immune-stimulatory phenotype after blockade of IFN-I signaling (fig. S2B).

The regulation of IL-10 and PD-L1 expression by IFN-I led us to investigate how IFN-I affects the immune environment during persistent virus infection. IFN-I blockade before C113 infection resulted in increased splenocyte numbers in anti-IFNAR1 compared with control treated mice 9 dpi (fig. S3A). This correlated with significant increases in B cells, CD4 and CD8 T cells, NK cells, DCs, and macrophages (fig. S3, B and C). Although IFN-I blockade resulted in early inhibition of multiple pro-inflammatory cytokines and chemokines and negative immune regulatory molecules after C113 infection (Fig. 2 and fig. S1,

C to E), we detected increases in IFN- γ production 24 hpi (fig. S2D) and similar levels of pro-inflammatory cytokines and chemokines 5 dpi (fig. S3D).

Lymphoid architecture is integral to induction and maintenance of immune responses (19–23). C113 infection resulted in severe lymphoid disorganization (23) with indistinguishable marginal zones and follicular structures and scattered B and T cell zones 9 dpi (Fig. 2E), which was more apparent at 14 dpi (Fig. 2F). IFN-I blockade preserved splenic architecture, so that white pulp, follicle margins, and T and B cell zones appeared similar to naïve spleens (Fig. 2E, middle and bottom). Fibroblastic reticular cell staining (ER-TR7; Fig. 2E, middle row) highlighted preservation of splenic organization and architecture after IFN-I blockade. These data demonstrate that IFN-I signaling contributes to splenic architecture disorganization during C113 infection.

We next asked whether blockade of IFN-I signaling altered control of C113. IFN-I blockade resulted in increased percentages of lymphocytes expressing LCMV viral antigen 24 hpi (fig. S2, C and D) and significantly higher C113 titers in the serum 10 dpi (Fig. 3A), suggesting that anti-IFNAR1 antibody treatment blocked early antiviral effects of IFN-I. By 30 dpi, we observed significant reductions in C113 titers after IFN-I blockade (>1.5 logs) compared with isotype control treated mice (Fig. 3A). By 40 dpi, IFN-I blockade resulted in significant reductions of viral titers in both serum and tissues (Fig. 3B). By 50 dpi, virus was undetectable in the serum after IFN-I blockade, whereas control mice retained >3 logs of virus (fig. S4A), demonstrating that IFN-I blockade hastens clearance of C113 infection.

IFN-I transcripts are detectable in DCs several weeks after C113 infection (24). We postulated that blocking IFN-I signaling during an established C113 infection would result in faster viral clearance. After an initial spike in viral titers

20 dpi, we observed >1-log reduction in serum viral titers in anti-IFNAR1 compared with isotype-treated mice by 40 dpi (fig. S4B). By 50 dpi, 75% of the anti-IFNAR1 treated mice had undetectable levels of virus, whereas 75% of control animals maintained >3 logs of virus (Fig. 3D). Analysis of virus in liver and lung 50 dpi revealed reductions in viral titers in both tissues after IFN-I blockade (Fig. 3D). These results demonstrate the therapeutic potential of IFN-I signaling blockade.

We asked whether enhanced virus clearance after IFN-I blockade could be duplicated after Arm infection. IFN-I blockade during Arm infection resulted in significantly elevated viral titers in the serum compared to control mice (fig. S5A). Anti-IFNAR1 treated animals maintained >3 logs of virus in serum 20 dpi (fig. S5B). Moreover, after IFN-I blockade, viral titers were detectable in lungs, kidneys, and brains 30 dpi, a time when virus was undetectable in tissues of control mice (fig. S5C). The inability to clear Arm correlated with reduced expansion, functional potential, and cytolytic capacity of LCMV-specific CD8 T cells (fig. S5, D to G) with minimal effects on LCMV-specific CD4 T cells (fig. S5H). Clearance of Arm infection relies solely on antiviral CD8 T cells; thus, inhibition of IFN-I antiviral effects coupled to abrogation of CD8 T-cell responses likely contributed to defective control of Arm infection.

To measure localization of naïve T cells to T cell zones in the spleen, we adoptively transferred carboxyfluorescein diacetate succinimidyl ester (CFSE)-labeled naïve T cells into C113-infected mice treated with isotype antibodies or anti-IFNAR1. Naïve T cells migrated to T cell zones in anti-IFNAR1 treated mice similar to naïve controls 5 dpi. Although T cell zones were intact in isotype-treated mice, naïve T cells did not remain in these areas (Fig. 4, A and B) despite similar numbers of naïve CFSE-labeled T cells in the spleen. At 14 dpi, differences in naïve T cell localization between anti-IFNAR1 and isotype

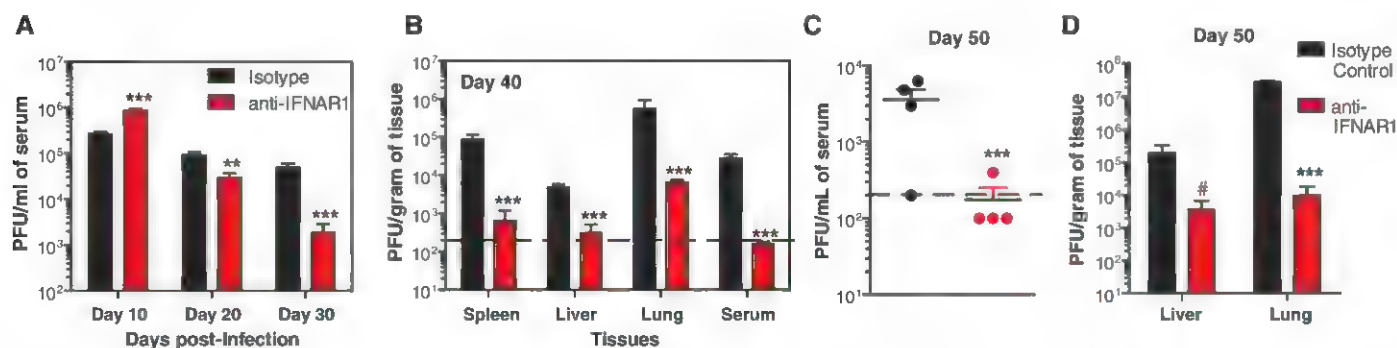


Fig. 3. IFN-I signaling blockade controls persistent virus infection. C57BL/6 mice were treated with either isotype control antibody or anti-IFNAR1 1 day before infection with C113 (A and B) or 10 days after C113 infection (C and D). (A) Serum viral titers determined by plaque assay at the indicated times postinfection. (B) Viral titers in serum or indicated tissues at day 40 after infection. (C and D) Mice were infected with C113

and, 10 dpi, treated with three doses of anti-IFNAR1 (500 μ g on days 10 and 12 and 250 μ g on day 14). The graphs illustrate serum titers of mice 50 dpi in the serum (C) and lung and liver (D). ** P < 0.01; *** P < 0.005; # P = 0.07. Results are representative of more than five independent experiments and represent the SEM from five mice per group. PFU, plaque-forming units.

control treated mice were maintained (Fig. 4B). Analysis of virus-specific T cell function revealed that the numbers of GP₃₃₋₄₁-specific IFN- γ ⁺ or IFN- γ ⁺ tumor necrosis factor α (TNF- α) IL-2⁺ multifunctional cytokine-producing cells (Fig. 4C) along with cytolytic potential (fig. S6A) after anti-IFNAR1 treatment were comparable to those in isotype control treated mice, whereas there was a significant decrease in IFN- γ ⁺ TNF- α ⁺ GP33-specific CD8 T cells (Fig. 4C). In contrast, GP61-specific IFN- γ ⁺ and multifunctional CD4 T cells 9 dpi were elevated in anti-IFNAR1 compared with control treated mice (Fig. 4D). De-

spite elevated numbers and enhanced functional potential of virus-specific CD4 T cells, we observed similar levels of LCMV-specific immunoglobulin G (IgG) in the serum (fig. S6B), demonstrating that IFN-I blockade enhances virus-specific CD4 T cell responses while maintaining antiviral CD8 T cell and antibody levels.

Because blockade of IFN-I signaling resulted in significantly elevated virus-specific CD4 T cell responses, we asked whether CD4 T cells were required for virus control after IFN-I blockade. Antibody depletion of CD4 T cells had little effect on anti-IFNAR1 mediated reduction of viral

titers on day 21 postinfection (Fig. 4E); however, by 40 and 50 dpi, CD4 depletion completely abrogated the anti-IFNAR1 mediated reduction in viral titers compared with CD4-sufficient, IFNAR1-treated mice (Fig. 4, E and F). Anti-IFNAR1 treatment after CD4 depletion had no effect on controlling C113 replication in lungs, kidneys, and brains 75 dpi (Fig. 4G). These data demonstrate CD4 T cells are required for enhanced control of persistent virus infection after IFN-I blockade.

We identify IFN-I signaling as essential for immune activation, up-regulation of negative

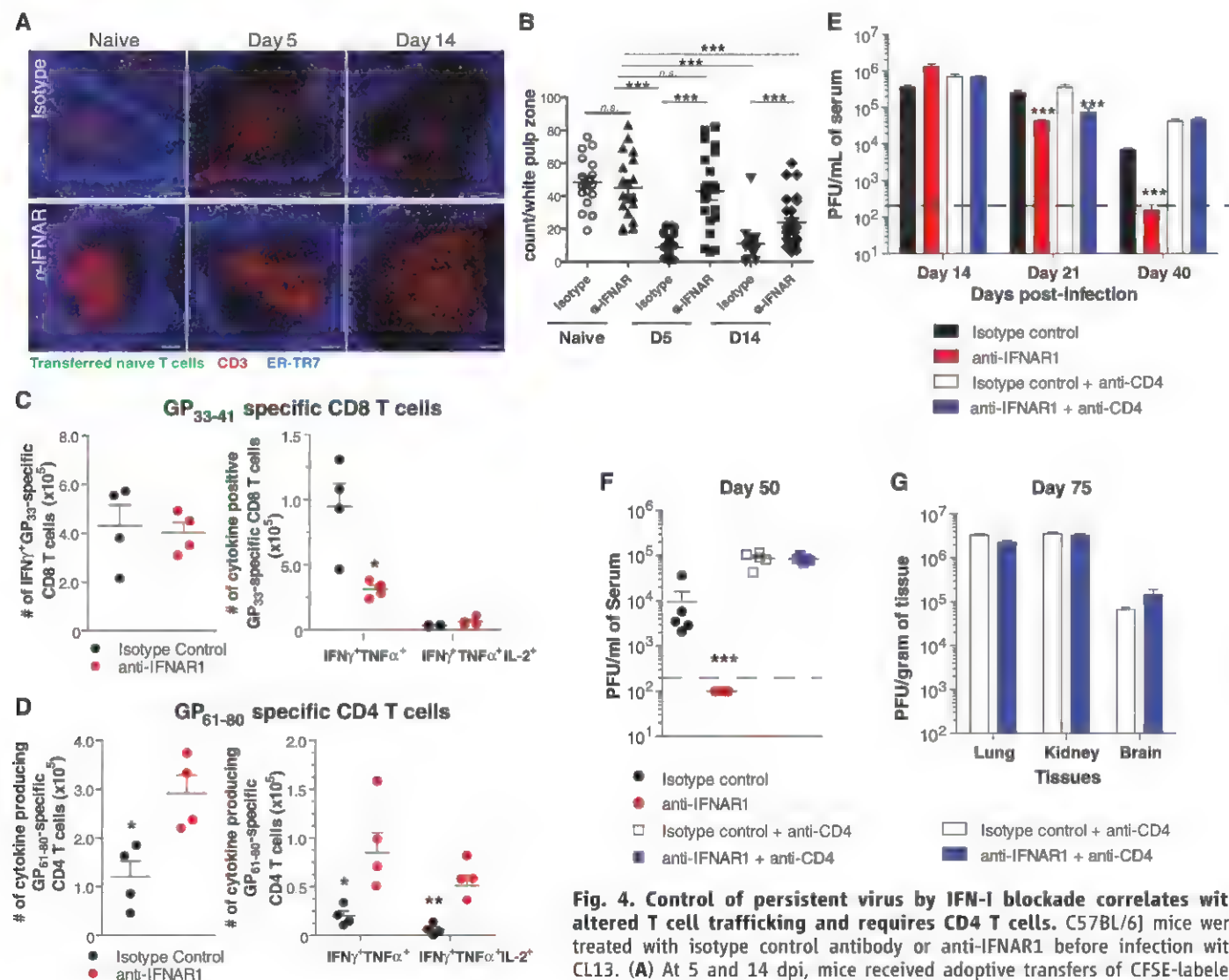


Fig. 4. Control of persistent virus by IFN-I blockade correlates with altered T cell trafficking and requires CD4 T cells. C57BL/6J mice were treated with isotype control antibody or anti-IFNAR1 before infection with CL13. (A) At 5 and 14 dpi, mice received adoptive transfers of CFSE-labeled naive T cells. Two hours after transfer, spleens were harvested to analyze homing and localization of naive T cells (green) to T cell zones [CD3, red; fibroblastic reticular cells (ER-TR7), blue]. Images were taken with a 20 \times objective. Scale bars, 100 μ m. (B) Quantitation of naive T cell localization. The number of transferred CFSE-labeled naive T cells was counted in 10 random white pulp regions per spleen. (C) Total number of cytokine-producing GP₃₃₋₄₁ LCMV-specific CD8 T cells in the spleen on day 9 postinfection. (D) Total number of cytokine-producing GP₆₁₋₈₀ LCMV-specific CD4 T cells in the spleen on day 9 postinfection. (E to G) Mice treated with anti-CD4 and/or anti-IFNAR1 or control antibodies were infected with 2×10^6 PFU of CL13, and viral titers were measured in the serum and tissues at the indicated times postinfection. Viral titers in the serum were quantified by plaque assay on days 14, 21, and 40 (E) and 50 (F) in the serum. (G) Viral titers in the lung, kidney, and brain in CD4-depleted mice treated with isotype or anti-IFNAR1 on day 75 postinfection. n.s., not significant; * $P < 0.05$; ** $P < 0.01$; *** $P < 0.005$. Results are representative of two independent experiments and represent SEM from four or five mice per group.

immune regulators, lymphoid disorganization, and virus persistence. IFN-I has pleiotropic effects on multiple cellular processes. Aside from antiviral effects (25), IFN-I signaling influences cell differentiation, proliferation, and apoptosis (26). Further, multiple pro-inflammatory mediators are downstream of IFN-I signaling; thus, IFN-I can regulate multiple physiological processes. Despite discovery of IFN-I over 50 years ago (27), its mechanisms of action with respect to immune modulation (25) or antiviral activity (28, 29) remain unsettled.

Chronic immune activation after HIV infection is documented, and suppression of this hyperactivated state may alleviate pathologies associated with HIV infection (7). Disease after experimental simian immunodeficiency virus (SIV) infection in rhesus macaques correlates with elevated IFN-I and inflammatory signatures (30, 31). In contrast, SIV infection in sooty mangabeys and African green monkeys, which develop modest pathology despite similar viral loads as macaques, correlates with reduced IFN-I and inflammatory signatures (32). Similar correlations with respect to reduced immune activation exist in HIV-infected elite controllers, although whether reduced immune activation follows better control of virus infection is debatable (33, 34). Moreover, an elevated interferon signature is observed in HCV-infected patients despite limited control of virus replication and development of liver pathology (35, 36). Thus, the IFN-I signaling pathway may be a viable target to control persistent viral infections.

References and Notes

1. D. G. Brooks *et al.*, *Nat. Med.* **12**, 1301 (2006).
2. D. L. Barber *et al.*, *Nature* **439**, 682 (2006).
3. J. S. Yi, M. A. Cox, A. J. Zajac, *Immunology* **129**, 474 (2010).
4. A. J. Zajac *et al.*, *J. Exp. Med.* **188**, 2205 (1998).
5. V. Appay, D. Sauce, *J. Pathol.* **214**, 231 (2008).
6. J. J. Chang, M. Altfeld, *J. Infect. Dis.* **202** (suppl. 2), S297 (2010).
7. G. d'Ettorre, M. Paiardini, G. Ceccarelli, G. Silvestri, V. Vullo, *AIDS Res. Hum. Retroviruses* **27**, 355 (2011).
8. N. Sevilla *et al.*, *J. Exp. Med.* **192**, 1249 (2000).
9. R. Ahmed, A. Salmi, L. D. Butler, J. M. Chiller, M. B. Oldstone, *J. Exp. Med.* **160**, 521 (1984).
10. M. Salvato, P. Borrow, E. Shimomaye, M. B. Oldstone, *J. Virol.* **65**, 1863 (1991).
11. C. F. Evans, P. Borrow, J. C. de la Torre, M. B. Oldstone, *J. Virol.* **68**, 7367 (1994).
12. B. M. Sullivan *et al.*, *Proc. Natl. Acad. Sci. U.S.A.* **108**, 2969 (2011).
13. A. Berghalter *et al.*, *Proc. Natl. Acad. Sci. U.S.A.* **107**, 21641 (2010).
14. S. Scheu, P. Dresing, R. M. Locksley, *Proc. Natl. Acad. Sci. U.S.A.* **105**, 20416 (2008).
15. M. Macal *et al.*, *Cell Host Microbe* **11**, 617 (2012).
16. K. C. Sheehan *et al.*, *J. Interferon Cytokine Res.* **26**, 804 (2006).
17. N. Sevilla, D. B. McGavern, C. Teng, S. Kunz, M. B. Oldstone, *J. Clin. Invest.* **113**, 737 (2004).
18. M. B. Oldstone, K. P. Campbell, *Virology* **411**, 170 (2011).
19. S. Müller *et al.*, *J. Virol.* **76**, 2375 (2002).
20. D. P. Berger *et al.*, *Virology* **260**, 136 (1999).
21. M. Suresh *et al.*, *J. Virol.* **76**, 3943 (2002).
22. M. Zeng *et al.*, *J. Clin. Invest.* **121**, 998 (2011).
23. M. Zeng *et al.*, *PLoS Pathog.* **8**, e1002437 (2012).
24. B. Hahn, M. J. Trifilo, E. I. Zuniga, M. B. Oldstone, *Immunity* **22**, 247 (2005).
25. D. B. Stetson, R. Medzhitov, *Immunity* **25**, 373 (2006).
26. L. C. Platanias, *Nat. Rev. Immunol.* **5**, 375 (2005).
27. A. Isaacs, J. Lindenmann, *Proc. R. Soc. Lond. B Biol. Sci.* **147**, 258 (1957).
28. J. W. Schoggins, C. M. Rice, *Curr. Opin. Virol.* **1**, 519 (2011).
29. J. W. Schoggins *et al.*, *Nature* **472**, 481 (2011).
30. O. Manches, N. Bhardwaj, *J. Clin. Invest.* **119**, 3512 (2009).
31. B. Jacquelin *et al.*, *J. Clin. Invest.* **119**, 3544 (2009).
32. S. E. Bosinger *et al.*, *J. Clin. Invest.* **119**, 3556 (2009).
33. S. G. Deeks, B. D. Walker, *Immunity* **27**, 406 (2007).
34. A. Sáez-Cirión, G. Pancino, M. Sinet, A. Venet, O. Lambotte, *Trends Immunol.* **28**, 532 (2007).
35. A. I. Su *et al.*, *Proc. Natl. Acad. Sci. U.S.A.* **99**, 15669 (2002).
36. L. G. Guidotti, F. V. Chisari, *Annu. Rev. Pathol.* **1**, 23 (2006).

Acknowledgments: The authors thank D. Fremgen, C. Cubitt, N. Ngo, and S. Rice for technical excellence. Data reported in the manuscript are tabulated in the main paper and in the supplementary materials. This research was supported by NIH grant AI09484 (M.B.A.O.); National Cancer Institute grants NCI CA43059 (R.D.S.) and U54AI057160 to the Midwest Regional Center of Excellence for Biodefense and Emerging Infectious Diseases Research (MRCE) (R.D.S. and M.B.A.O.); grants AI077719 and AI047140 (J.C.d.I.T.), postdoctoral training grants AI007354; and American Heart fellowships 11POST7430106 (J.R.T.), HL007195 (C.N.), and NS041219 (B.M.S.).

Supplementary Materials

www.sciencemag.org/cgi/content/full/340/6129/2071
DC1

Materials and Methods

Figs. S1 to S6

Reference (37)

15 January 2013; accepted 28 February 2013

10.1126/science.1235214

Injectable, Cellular-Scale Optoelectronics with Applications for Wireless Optogenetics

Tae-il Kim,^{1,2*} Jordan G. McCall,^{3,4,5,6*} Yei Hwan Jung,^{1†} Xian Huang,¹ Edward R. Siuda,^{3,4,5,6} Yuhang Li,⁷ Jizhou Song,⁸ Young Min Song,¹ Hsuan An Pao,¹ Rak-Hwan Kim,¹ Chaofeng Lu,⁹ Sung Dan Lee,¹⁰ Il-Sun Song,¹¹ Gunchul Shin,¹ Ream Al-Hasani,^{3,4,5} Stanley Kim,¹ Meng Peun Tan,¹⁰ Yonggang Huang,⁷ Fiorenzo G. Omenetto,^{12,13} John A. Rogers,^{1,10,11,14*†} Michael R. Bruchas^{3,4,5,6*†}

Successful integration of advanced semiconductor devices with biological systems will accelerate basic scientific discoveries and their translation into clinical technologies. In neuroscience generally, and in optogenetics in particular, the ability to insert light sources, detectors, sensors, and other components into precise locations of the deep brain yields versatile and important capabilities. Here, we introduce an injectable class of cellular-scale optoelectronics that offers such features, with examples of unmatched operational modes in optogenetics, including completely wireless and programmed complex behavioral control over freely moving animals. The ability of these ultrathin, mechanically compliant, biocompatible devices to afford minimally invasive operation in the soft tissues of the mammalian brain foreshadow applications in other organ systems, with potential for broad utility in biomedical science and engineering.

Electronic systems that integrate with the body provide powerful diagnostic and therapeutic capabilities for basic research

and clinical medicine. Recent research establishes materials and mechanical constructs for electronic circuits, light-emitting diodes (LEDs),

sensors, and other components that can wrap the soft, external surfaces of the brain, skin, and heart, for diverse functions in analytical measurement, stimulation, and intervention (1–10). A significant constraint in operating these devices, however, follows from their surface-mounted configurations and inability to provide direct interaction into the volumetric depths of the tissues. Passive penetrating electrodes or optical fibers with interconnections to externally located electronic control and/or acquisition systems or light sources can be valuable in many contexts, particularly in neuroscience, engineering, and surgery (7, 10–14). Direct biological integration is limited by challenges from tissue lesions during insertion, persistent irritation, and engineering difficulties in thermal management, encapsulation, scalable interconnection, power delivery, and external control. Many of these issues constrain attempts to insert conventional, bulk LEDs into brain tissue (15) and to use semiconductor nanowire devices as cellular probes or active, in vitro tissue scaffolds (3, 16). In optogenetics, engineering limitations of conventional, tethered fiber optic devices restrict opportunities for in vivo use and widespread biological application. As a solution, we developed mechanically compliant, ultrathin multifunctional optoelectronic systems

¹Department of Materials Science and Engineering, Frederick Seitz Materials Research Laboratory, University of Illinois at Urbana-Champaign, Urbana, IL 61801, USA. ²School of Chemical Engineering, Sungkyunkwan University (SKKU), Suwon 440-746, Korea. ³Department of Anesthesiology, Division of Basic Research, Washington University School of Medicine, St. Louis, MO 63110, USA. ⁴Washington University Pain Center, Washington University School of Medicine, St. Louis, MO 63110, USA. ⁵Department of Anatomy and Neurobiology, Washington University School of Medicine, St. Louis, MO 63110, USA. ⁶Division of Biological and Biomedical Sciences, Washington University School of Medicine, St. Louis, MO 63110, USA. ⁷Department of Civil and Environmental Engineering, Department of Mechanical Engineering, and Institute for Public Health and Medicine, Northwestern University, Evanston, IL 60208, USA. ⁸Department of Mechanical and Aerospace Engineering, University of Miami, Coral Gables, FL 33146, USA. ⁹Soft Matter Research Center and Department of Civil Engineering, Zhejiang University, 38 Zheda Road, Hangzhou 310027, China. ¹⁰Department of Electrical and Computer Engineering, University of Illinois at Urbana-Champaign, Urbana, IL 61802, USA. ¹¹Department of Mechanical Science and Engineering, University of Illinois at Urbana-Champaign, Urbana, IL 61802, USA. ¹²Department of Biomedical Engineering, Tufts University, Medford, MA 02115, USA. ¹³Department of Physics, Tufts University, Medford, MA 02115, USA. ¹⁴Department of Chemistry, University of Illinois at Urbana-Champaign, Urbana, IL 61802, USA.

*These authors contributed equally to this work.

†Present address: Department of Electrical and Computer Engineering, University of Wisconsin-Madison, WI 53706, USA

‡Corresponding author. E-mail: bruchasm@wustl.edu (M.R.B.); jrogers@uiuc.edu (J.A.R.)

that mount on releasable injection needles for insertion into the depths of soft tissue. These wireless devices incorporate cellular-scale components ranging from independently addressable multicolored microscale, inorganic light-emitting diodes (μ -ILEDs) to colocated, precision optical, thermal, and electrophysiological sensors and actuators.

A scanning electron micrograph (SEM) of an isolated gallium nitride (GaN) μ -ILED, a constituent component of these systems, is presented in Fig. 1A, as well as an epifluorescent image of a device among cultured human embryonic kidney (HEK293) cells, to illustrate the similar sizes. Each such “cellular-scale” μ -ILED (6.45 μ m thick, 50 \times 50 μ m²) uses high-quality epitaxial material grown on sapphire, processed to establish contacts (15 \times 15 μ m² square pads in the corners and an L-shaped current spreading layer for the p-type ohmic contact) and then released, to allow transfer printing onto narrow, thin plastic strips. The μ -ILEDs are less than one-thousandth the size of conventional LEDs (typically 100 μ m thick, with lateral dimensions of 1 mm²) and fiber optic probes, as discussed below (17). The small sizes of μ -ILEDs allow for spatially precise, cellular-scale delivery of photons, highly effective thermal management, reduced tissue damage,

and minimized inflammation for prolonged use in vivo.

Combining μ -ILEDs with electronic sensors and actuators yields multifunctional integrated systems that can be configured in single or multilayer formats. The latter option is illustrated in Fig. 1, B and C, in which the sensors and/or actuators include a Pt microelectrode for electrophysiological recording or electrical stimulation (layer no. 1: a 20 \times 20 μ m² exposure defines the active area), a microscale inorganic photodetector (μ -IPD) based on an ultrathin silicon photodiode (layer no. 2: 1.25 μ m thick, 200 \times 200 μ m²), a collection of four μ -ILEDs connected in parallel (layer no. 3), and a precision temperature microsensor or microheater (layer no. 4: Pt serpentine resistor) (more details in figs. S1 to S3) (18). Each layer is processed on separate substrates shaped to match a releasable, photolithographically defined epoxy microneedle (fig. S4). A thin layer (~500 nm) of epoxy joins each of the layers in a precisely aligned, stacked configuration. The microneedle bonds to the bottom layer with a thin, bio-resorbable adhesive based on a film of purified silk fibroin, which enables removal of the microneedle after implantation (Fig. 1D, movie S1, and fig. S5). The microelectrodes measure extracellular voltage signals in the direct vicinity

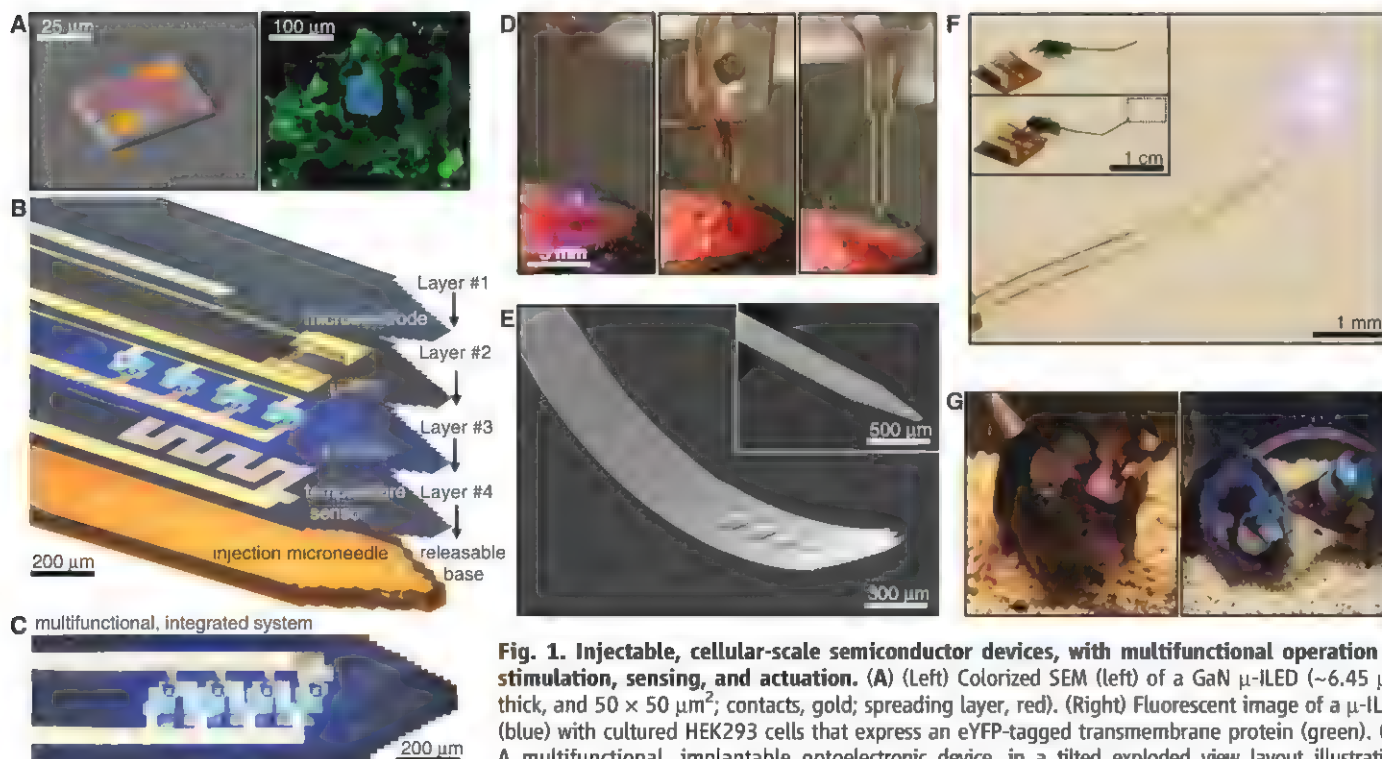


Fig. 1. Injectible, cellular-scale semiconductor devices, with multifunctional operation in stimulation, sensing, and actuation. (A) (Left) Colorized SEM (left) of a GaN μ -ILED (~6.45 μ m thick, and 50 \times 50 μ m²; contacts, gold; spreading layer, red). (Right) Fluorescent image of a μ -ILED (blue) with cultured HEK293 cells that express an eYFP-tagged transmembrane protein (green). (B) A multifunctional, implantable optoelectronic device, in a tilted exploded view layout illustrating various components. The system includes layers for electrophysiological measurement (no. 1: Pt contact pad, microelectrode), optical measurement (no. 2: silicon μ -IPD), optical stimulation (no. 3: μ -ILED array), and temperature sensing (no. 4: serpentine Pt resistor), all bonded to a releasable structural support for injection (microneedle). (C) Top view of the integrated device shown in (B). (D) Process of injection and release of the microneedle. After insertion, artificial cerebrospinal fluid (center) dissolves the external silk-based adhesive. The microneedle is removed (right), leaving only the active device components in the brain. (E) SEM of an injectable array of μ -ILEDs. The total thickness is 8.5 μ m. (Inset) Rigid device before coating with a passivation layer. (F) Integrated system wirelessly powered with RF scavenging. (Insets) A connectorized device unplugged (top) and plugged into (bottom) the wireless power system. (G) Healthy, freely moving mice with lightweight, flexible (left) and rigid (right) wireless systems powering GaN μ -LED arrays in the VTA.

of illumination and can also be used for stimulation (Fig. 2H). The temperature sensors determine the degree of local heating, with a precision approaching ~ 1 mK, and can also be used as microheaters. The μ -IPD can measure the intensity of light from the μ -ILEDs while implanted deep in brain tissue and/or can enable basic spectroscopic evaluations such as absorption, fluorescence, and diffuse scattering (for details, see figs. S6 and S7) (18).

Injection of such flexible devices into the brain follows steps shown in Fig. 1D and movie S1. The injected multifunctional optoelectronic systems have a total thickness of ~ 20 μ m. This exceptionally thin geometry, low bending rigidity, and high degree of mechanical flexibility (Fig. 1, E and F) allow for minimally invasive operation. Wired control schemes use standard transistor-transistor logic (TTL) and are therefore compatible with any readily available electrical commutator. Details on wired powering strategies and demonstration of wired opto-

genetic functionality in rodent behavioral assays are presented in figs. S8, S9, and S10 (18). Implementation of a wireless power module based on radiofrequency (RF) scavenging is shown in Fig. 1F. A custom flexible polyimide film-based lightweight (~ 0.7 g) power scavenger or a rigid printed circuit board-based scavenger (~ 2.0 g) (Fig. 1G and fig. S11) can be temporarily mounted on freely moving animals for short-term experimentation without constraint in natural animal behavior (Fig. 1G). The entire system consists of a wireless power transmitter and RF signal generator; an RF source (910 MHz, power output between 0.02 and 0.1 mW); a power supply; an RF power amplifier (gain of 49 dB at 910 MHz, power output between 1.6 and 7.9 W); and a panel antenna (gain of 13 dBi), as in fig. S11 and fig. S12. The low-frequency signal generator provides user-controlled amplitude modulation for programmed operation. The RF power that reaches the animals, under normal operating conditions at a dis-

tance of ~ 1 m, is between 0.15 and 0.77 mW/cm², which is substantially smaller than the maximum permissible exposure limits (3.03 mW/cm²) for humans in controlled environments (19). Wireless control allows access to complex and ethologically relevant models in diverse environmental settings, including social interactions, home cage behaviors, wheel running, complex maze navigation tasks, and other behavioral outputs (Fig. 1G and fig. S13).

The electrical, optical, and thermal characteristics of the devices when operated in biological environments are important for optogenetics and other biomedical applications. The total optical power density of the four μ -ILEDs in this device as a function of electrical input power is shown in Fig. 2A (more details in figs. S14 and S15) (18). This performance is comparable to similarly designed, state-of-the-art conventional GaN LEDs (17). Many optogenetic constructs can be activated with ~ 1 mW/mm², at wavelengths near 450 nm (13). These conditions are well matched

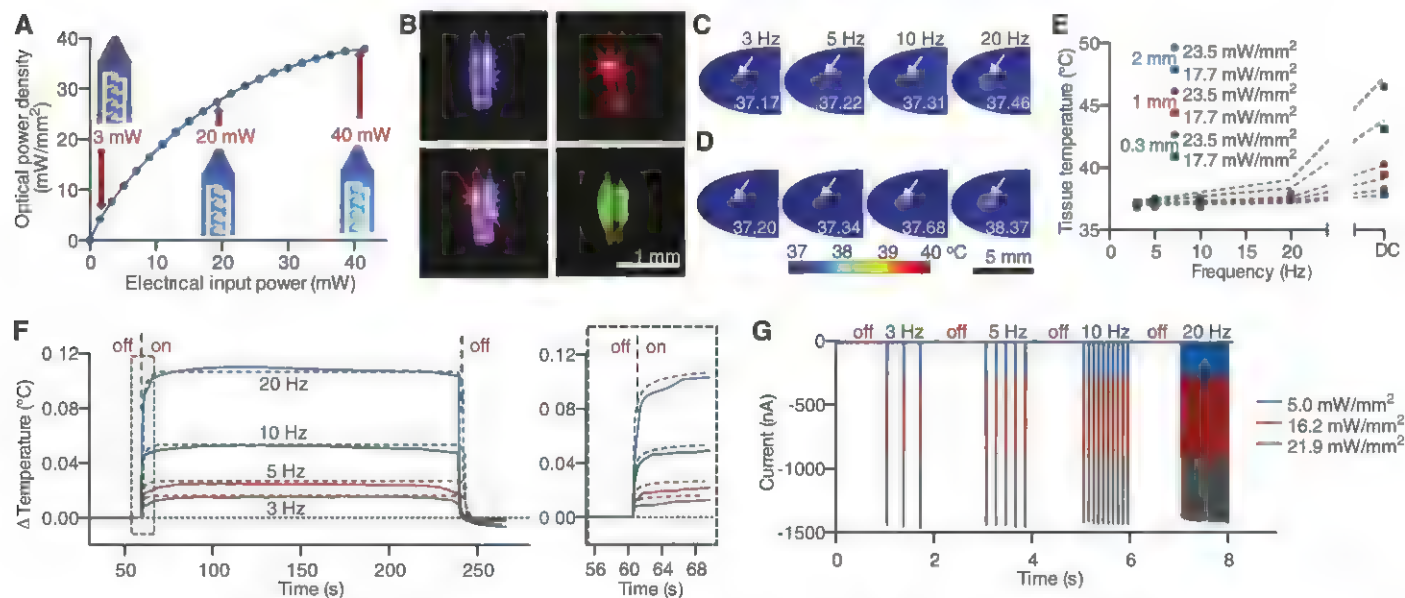


Fig. 2. Optical, thermal, and electrophysiological studies with corresponding theoretical analyses. (A) Total optical power density as a function of electrical input power applied to an array of four GaN μ -ILEDs; optical images show operation at 3, 20, and 40 mW. (B) A single device has one 675-nm GaAs μ -ILED and four 450-nm GaN μ -ILEDs that can be activated independently (top left and top right) or concurrently (bottom left). The same device is coated in a fluorescein sodium salt phosphor for 530-nm light (bottom right). (C) Measured and (D) calculated temperatures in explanted brain tissue near implanted μ -ILEDs at a depth of 0.3 mm and operated at 17.7 mW/mm² of light output power. (E) Temperatures in a system similar to that of (C) and (D), as a function of duty cycle in the operation of the μ -ILEDs and at three different implantation depths (0.3, 1.0, and 2.0 mm) and two different light output powers (17.7 and 23.5 mW/mm²). (F) Change in brain temperature as a function of time, measured using an integrated temperature sensor colocated with an array of four μ -ILEDs in a lightly anesthetized mouse. Results evaluated at a peak input electrical power of 8.65 mW, in 3-, 5-, 10-, and 20-Hz pulses (10-ms duration). The vertical dashed lines indicate onset (at 60 s) and offset (at 240 s) of the μ -ILEDs. Colored dashed lines corre-

spond to theoretical models for the temperature. The right frame shows the time dynamics as the device is powered. (G) Change in photocurrent as a function of time, measured using an integrated μ -IPD, for three different light output powers to an array of μ -ILEDs: 5.0 mW/mm² (blue trace), 16.2 mW/mm² (red trace), and 21.9 mW/mm² (black trace) at different pulse frequencies (10-ms pulses at 3, 5, 10, and 20 Hz). (H) Extracellular voltage trace (5 s) of spontaneous neuronal activity gathered using the integrated Pt micro-electrode. (I) The same data are filtered and sorted using principal components analysis to identify single units.

to the output of the GaN μ -ILEDs. Input power of ~ 1.0 to 1.5 mW (Fig. 2A) is sufficient for both activation of the channelrhodopsin-2 [ChR2 (H134)] ion channel and precise control of intracellular signaling [adenosine 3',5'-monophosphate (cAMP) and extracellular signal-regulated kinase (ERK 1/2)] via an optically sensitive seven-transmembrane domain receptor (OPTO- β 2) (20) (Fig. 3, C and D, and figs. S16 and S17). Wirelessly, at a distance of 1 m, the RF scavenger produces 4.08 mW of electrical power resulting in a 7 mW/mm² optical power density. Other wavelengths are possible using different types of μ -ILEDs, either in multicolored or uniform arrays. An example of the latter, with blue and red (GaAs) μ -ILEDs, and the former, with green devices (produced using fluorescein sodium salt phosphor on a blue GaN μ -ILED), are shown in Fig. 2B.

μ -ILED-induced changes in temperature determined by infrared imaging and by analytical calculation, respectively, are shown in Fig. 2, C and D. The μ -ILEDs were implanted 0.3 mm into an explanted piece of brain tissue held at 37°C. The time-averaged temperatures measured at light-pulse (10-ms) frequencies of 3, 5, 10, and 20 Hz with peak light output of 17.7 mW/mm²

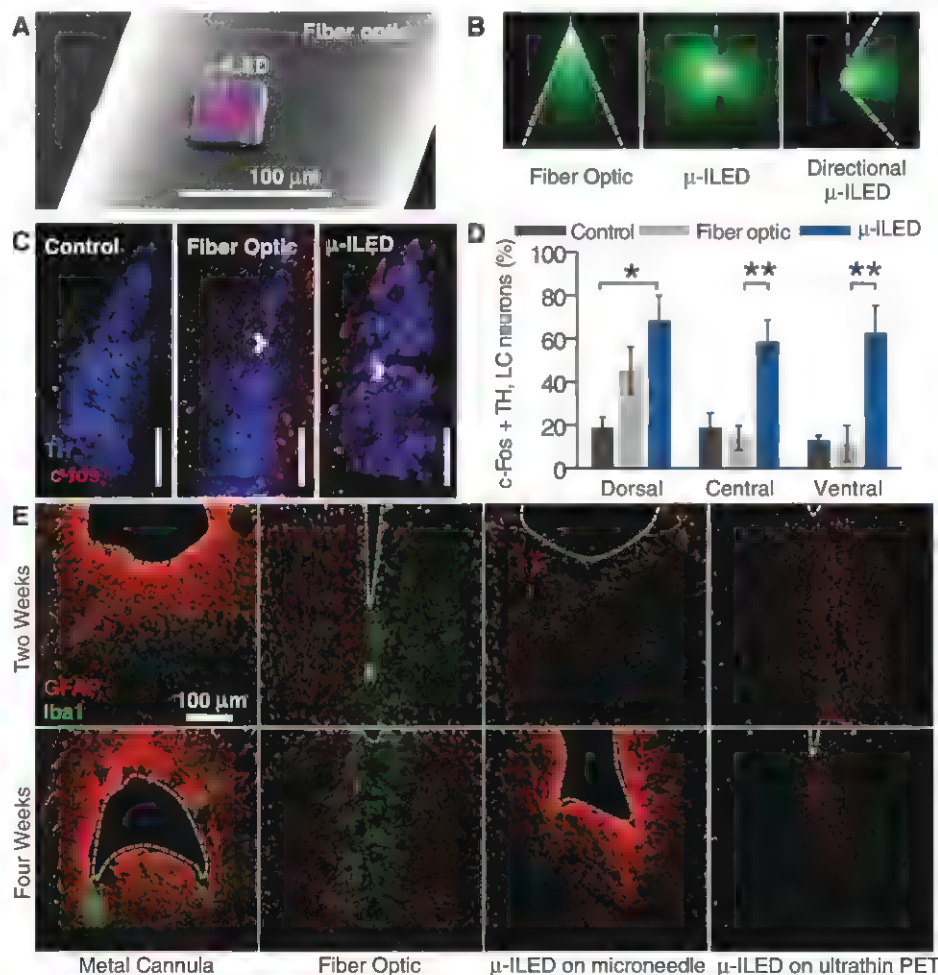
are 37.17°, 37.22°, 37.31°, and 37.46°C, respectively. These results are similar to calculated time-averaged temperatures of 37.20°, 37.34°, 37.68°, and 38.37°C, respectively. Note that the input power used in these tests is 10 times what is necessary to activate many optogenetic constructs (13). The cellular-scale dimensions of the μ -ILEDs enable high rates of passive thermal spreading, and the brain tissue itself operates as an efficient heat sink. The latter is apparent in studies of the dependence of operating temperature on tissue thickness, operating power, and frequency (Fig. 2E). As in Fig. 2D, the experiment and theory agree remarkably well in spite of the indirect correlation between infrared imaging results and temperature at the location of the devices (details appear in figs. S18 and S19) (18). Perfusion in living tissue further increases the efficacy of these biological heat sinks. Changes in temperature measured in vivo using an integrated temperature sensor (fig. S6) compared with calculated results are shown in Fig. 2F. Collectively, these results indicate that changes in temperature associated with operation of μ -ILEDs can be less than 0.10°C for pulse frequencies less than 20 Hz, typical of many neuronal firing rates. These values are much lower than those that

occur in human deep brain stimulation (DBS) regulation, $\sim 2^\circ\text{C}$ (21). Furthermore, in wireless operation, there is no appreciable change in temperature associated with operation at the head stage antenna or the skull (fig. S20).

Other components of this multifunctional platform exhibit similarly good characteristics. To demonstrate operation of the silicon μ -IPD, Fig. 2G shows photocurrents generated by different intensities of light from μ -ILEDs at different pulse frequencies. Finally, the Pt microelectrode has a 400 μm^2 exposure site with ~ 1.0 M Ω impedance at 1 kHz capable of measuring extracellular potentials on the microvolt scale necessary to distinguish individual action potentials (Fig. 2H), as demonstrated with clear clustering in the principal component analysis of spike data (Fig. 2I).

For use in optogenetics, such devices eliminate the need for lasers, bulk LEDs, fiber coupling systems, tethers, and optomechanical hardware used in conventional approaches (fig. S8). Furthermore, the fundamental optics of μ -ILEDs are very different from typical fiber optic implants. Absorbing and reflecting structures around the emissive areas of the μ -ILEDs enable precise delivery of light to cellular subregions. The

Fig. 3. μ -ILED devices improve spatial targeting and reduce gliosis. (A) Colorized SEM (left) of a μ -ILED mounted on a standard 200- μm fiber optic implant. (B) (Left) A dorsal-ventral-oriented light cone (outlined in white) from a 200- μm bare fiber implant (blue dash) emitting 465-nm light in 30 μM fluorescein water. (Center) Nearly omnidirectional light escape from a μ -ILED device (blue dash) with four 450-nm μ -ILEDs. (Right) Lateral light escape (outlined in white) from a modified μ -ILED device (blue dash) to allow unique spatial targeting, including flanking positions along the dorsal-ventral axis of brain loci. (C) Confocal fluorescence images of 30- μm brainstem slices containing the LC show staining for tyrosine hydroxylase (TH) and c-fos in control (left), fiber optic-implanted (center), and μ -ILED device-implanted (right) animals after 1 hour of 3-Hz photostimulation (15-ms pulses, 5-mW output power). Scale bar, 100 μm . (D) Fiber optic and μ -ILED treatments specifically increase coimmunoreactivity. In ventral portions of the LC, the μ -ILED devices express a higher proportion of TH (blue) and c-fos (red) coimmunoreactive neurons than fiber optic or control groups [$n = 3$ slices per brain from three brains for each group; two-way analysis of variance (ANOVA) with Bonferroni post hoc adjustment; all error bars represent means \pm SEM; $*P < 0.05$, $**P < 0.01$]. (E) Confocal fluorescence images of 30- μm striatal slices show staining for astrocytes [glial fibrillary acidic protein (GFAP), red] and activated microglia (Iba1, green) at the ventral tip of each implanted device (dashed outline). Gliosis is smallest with the μ -ILED device at 2 and 4 weeks.



relative size and the different patterns of light emission from μ -ILEDs to fiber optic probes are shown in Fig. 3, A and B. Fiber optics typically approach brain structures dorsally. This approach preferentially illuminates cells in the dorsal portion of the targeted region with greater light intensity near the point of light escape (22) (Fig. 3B, left, and fig. S21). Targeting ventral cell bodies or terminals requires lesion of dorsal regions or the use of substantially greater, and potentially phototoxic (23), amounts of light to the site of interest. Neither option protects the intact architecture of a complete brain locus. Although recent advances have spatially restricted light from implanted fiber optics (24, 25), these approaches require the use of invasive metal cannulae (Fig. 3E) or rely on sophisticated and sensitive optomechanical engineering that may limit their use in awake, behaving animals. The architecture of the μ -ILEDs enables light delivery medial or lateral to the intended target brain region. Native light escape from μ -ILEDs is nearly omnidirectional (Fig. 3B, center) but can be restricted to a wide range of angles with absorbing or reflective structures on the device (Fig. 3B, right).

We implanted both μ -ILEDs and fiber optics into animals expressing Chr2(H134)-eYFP (tagged with enhanced yellow fluorescent protein) in the locus coeruleus (LC) (fig. S21). One hour of

output-matched photostimulation induced c-fos expression (26), a biochemical marker of neuronal activation, in both groups of Chr2(H134)-eYFP-expressing mice that was not seen in green fluorescent protein (GFP)-expressing controls (Fig. 3, C and D). The spatial distribution of c-fos expression, however, differed markedly between the fiber optic and μ -ILED groups. μ -ILED devices produced significantly greater activation in the ventral LC (Fig. 3D).

The physical sizes and mechanical properties of the μ -ILED systems reduce lesioning, neuronal loss, gliosis, and immunoreactivity. Glial responses are biphasic with an early phase featuring widespread activation of astrocytes and microglia and a late, prolonged phase hallmarked by restriction of the gliosis to the area closest to the implanted substrate (27). The μ -ILED devices produced substantially less glial activation and caused smaller lesions than metal cannulae and fiber optics, at both early (2 weeks) and late (4 weeks) phases (Fig. 3E). Furthermore, the brain tolerates the thin, flexible devices better than rigid structures (Fig. 3E), consistent with reports on passive electrode devices (28). Finally, we examined the chronic functionality of the devices and demonstrated that they are well tolerated in freely moving animals with encapsulated sensors and μ -ILEDs, which maintain function over several months (fig. S22).

We next implemented a fully wireless system for dissecting complex neurobiology and behavior. Phasic neuronal firing of ventral tegmental area (VTA)-dopaminergic (VTA-DA) neurons encodes salient stimuli and is sufficient for behavioral conditioning (29–32). We selectively targeted Chr2(H134)-eYFP to VTA-DA neurons (Fig. 4A) and tested whether mice would engage in wireless, optical self-stimulation (20 5-ms pulses every nose poke) of their dopamine reward pathway. To increase the contextual salience of the stimulation and to demonstrate wireless function of the μ -ILED devices, the mice were free to explore a complex environment (fig. S23, A to C). In the absence of physical reward, the same stimulation of VTA-DA neurons that drives a traditional conditioned place preference (fig. S9) (29, 30) is actively sought with a cued nose poke when paired within a discrete environmental context. Chr2(H134)-eYFP mice learned to self-stimulate their dopamine neurons (Fig. 4, B and C) and, furthermore, developed a robust place preference (Fig. 4, D and E) for the environmental context containing the active nose poke for VTA-DA stimulation. Chr2(H134)-eYFP animals showed strong correlation ($r = 0.8620$, $P = 0.0272$) between the number of active nose pokes and the magnitude of conditioned place preference that was absent in eYFP controls (Fig. 4F and fig. S23E).

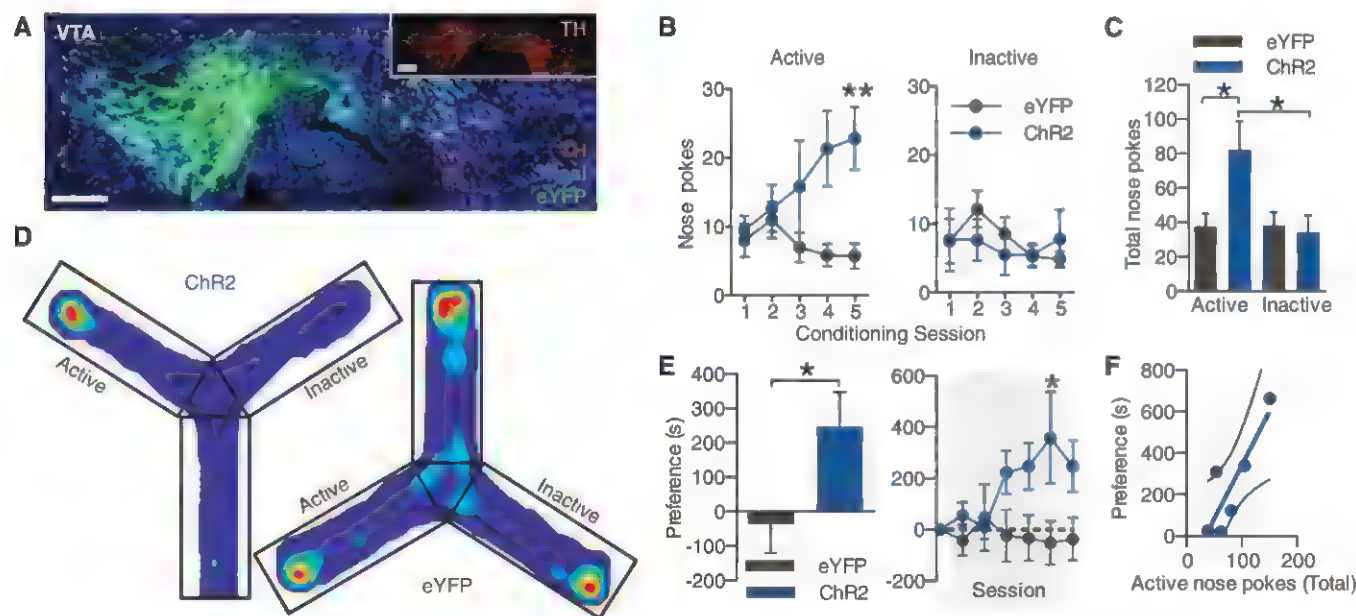


Fig. 4. Wirelessly powered μ -ILED devices operantly drive conditioned place preference. (A) Cell type-specific expression of Chr2(H134)-eYFP (green) in dopaminergic and TH-containing (red) neurons of the VTA. (Inset) For clarity, TH channel alone. All scale bars, 100 μ m. (B) Operant learning curve on the active (left) and inactive (right) nose poke devices over 5 days of 1-hour trials in the Y maze. Each active nose poke drives 1 s of 20-Hz light (5-ms pulses) from the μ -ILED device ($n = 6$ to 8 mice/group; two-way ANOVA with Bonferroni post hoc adjustment; $**P < 0.01$). (C) Mean number of nose pokes \pm SEM across all five conditioning sessions ($*P < 0.05$, one-way ANOVA with Bonferroni post hoc adjustment). (D) Heat maps of activity

during the posttest; hotter colors represent longer duration in a location in that part of the apparatus. (E) (Left) Place preference scores calculated as posttest minus pretest in the active nose poke-paired context. Five days of self-stimulation significantly conditioned a place preference that developed over the course of the training sessions and remained during the posttest (right) ($*P < 0.05$, t test compared with controls; $*P < 0.05$, two-way ANOVA with Bonferroni post hoc adjustment). All error bars represent means \pm SEM. (F) Scatter plot demonstrating positive correlation ($r = 0.8620$, $P = 0.0272$) between posttest preference and total number of active nose pokes during training in the Chr2(H134)-eYFP group.

In addition, we examined the effects of wireless tonic stimulation of VTA-DA neurons on anxiety-like behavior. Tonic stimulation at 5 Hz reduced anxiety-like behavior, whereas phasic activation of VTA-DA neurons did not have an effect on anxiety-like behavior (fig. S24). These findings are consistent with the anxiolytic actions of nicotine on VTA-DA neurons, as well as the behavioral phenotypes seen in the *ClockΔ19* mice that have increased tonic firing of VTA-DA neurons (33, 34), and further establish the utility of wireless optogenetic control in multiple environmental contexts.

These experiments demonstrate that these devices can be readily implemented in optogenetic experiments. Future possible uses are in closed-loop operation, where actuators (e.g., heat, light, and electrical) operate in tandem with sensors (e.g., temperature, light, and potential) for altering light stimulation in response to physiological parameters, such as single-unit activity, pH, blood oxygen or glucose levels, or neurochemical changes associated with neurotransmitter release. Many of the device attributes that make them useful in optogenetics suggest strong potential for broader utility in biology and medicine. The demonstrated compatibility of silicon technology in these injectable, cellular-scale platforms foreshadows sophisticated capabilities in electronic processing and biological interfaces. Biocompatible deep-tissue injection of semiconductor devices and integrated systems, such as those reported here, will accelerate progress in both basic science and translational technologies.

References and Notes

1. D.-H. Kim et al., *Nat. Mater.* **9**, 511 (2010).
2. J. Viventi et al., *Sci. Transl. Med.* **2**, 24ra22 (2010).
3. B. Tian et al., *Science* **329**, 830 (2010).
4. D.-H. Kim et al., *Science* **333**, 838 (2011).
5. Q. Qing et al., *Proc. Natl. Acad. Sci. U.S.A.* **107**, 1882 (2010).
6. T. Sekitani, T. Someya, *MRS Bull.* **37**, 236 (2012).
7. J. Ordóñez, M. Schuettler, C. Boehler, T. Boretius, T. Stieglitz, *MRS Bull.* **37**, 590 (2012).
8. S. C. B. Mannsfeld et al., *Nat. Mater.* **9**, 859 (2010).
9. T. Sekitani et al., *Science* **326**, 1516 (2009).
10. S. Takeuchi, T. Suzuki, K. Mabuchi, H. Fujita, *J. Micromech. Microeng.* **14**, 104 (2004).
11. E. Stark, T. Koos, G. Buzsáki, *J. Neurophysiol.* **108**, 349 (2012).
12. Y.-T. Kim, M. I. Romero-Ortega, *MRS Bull.* **37**, 573 (2012).
13. J. Mattis et al., *Nat. Methods* **18**, 159 (2011).
14. P. Anikeeva et al., *Nat. Neurosci.* **15**, 163 (2011).
15. H. Cao, L. Gu, S. K. Mohanty, J.-C. Chiao, *IEEE Trans. Biomed. Eng.* **60**, 225 (2013).
16. B. Tian et al., *Nat. Mater.* **11**, 986 (2012).
17. T.-I. Kim et al., *Small* **8**, 1643 (2012).
18. Materials and methods are available as supplementary materials on Science Online.
19. Federal Communications Commission (FCC), *Guidelines for Evaluating the Environmental Effects of Radiofrequency Radiation* (FCC publication docket no. 93-62, 1996), http://transition.fcc.gov/Bureaus/Engineering_Technology/Orders/1996/fcc96326.txt.
20. R. D. Airan, K. R. Thompson, L. E. Fenno, H. Bernstein, K. Deisseroth, *Nature* **458**, 1025 (2009).
21. M. M. Elwassif, Q. Kong, M. Vazquez, M. Bikson, *J. Neural Eng.* **3**, 3D6 (2006).
22. A. M. Aravanis et al., *J. Neural Eng.* **4**, S143 (2007).
23. Q. Yizhar, L. E. Fenno, T. J. Davidson, M. Mogri, K. Deisseroth, *Neuron* **71**, 9 (2011).
24. K. M. Tye et al., *Nature* **471**, 358 (2011).
25. A. N. Zorzos, J. Scholvin, E. S. Boyden, C. G. Fonstad, *Opt. Lett.* **37**, 4841 (2012).
26. M. E. Carter et al., *Nat. Neurosci.* **13**, 1526 (2010).
27. D. H. Szarowski et al., *Brain Res.* **983**, 23 (2003).
28. T. D. Y. Kozai, D. R. Kipke, *J. Neurosci. Methods* **184**, 199 (2009).
29. H. C. Tsai et al., *Science* **324**, 1080 (2009).
30. A. R. Adamantidis et al., *J. Neurosci.* **31**, 10829 (2011).
31. I. B. Witten et al., *Neuron* **72**, 721 (2011).
32. K. M. Kim et al., *PLoS ONE* **7**, e33612 (2012).
33. T. M. McGranahan, N. E. Patzlaff, S. R. Grady, S. F. Heinemann, T. K. Booker, *J. Neurosci.* **31**, 10891 (2011).
34. L. Coqje et al., *Neuropsychopharmacology* **36**, 1478 (2011).

Acknowledgments: This work is supported by the NIH Common Fund; National Institute of Neurological Disorders and Stroke, NIH, R01NS081707 (M.R.B., J.A.R.); National Institute on Drug Abuse, NIH, R00DA025182 (M.R.B.);

McDonnell Center for Systems Neuroscience (M.R.B.); National Security Science and Engineering Faculty Fellowship of Energy (J.A.R.); Division of Materials Sciences, U.S. Department of Energy, under award no. DE-FG02-07ER46471 (J.A.R.), and the Materials Research Laboratory and Center for Microanalysis of Materials (DE FG02 07ER46453) (J.A.R.); and the Division of Biology and Biomedical Sciences, Washington University in St. Louis (WUSTL) (J.G.M.). We thank H. Tao (Tufts University) and S. Hwang (University of Illinois at Urbana-Champaign) for their help in preparation of silk solution and valuable discussions; the Bruchas laboratory and the laboratories of R. W. Gereau IV (WUSTL) and G. D. Stuber (University of North Carolina at Chapel Hill) for helpful discussions; K. Deisseroth (Stanford University) for the channelrhodopsin-2 (H134) and OPTO-β2 constructs; G. D. Stuber for the TH-IRES-Cre mice; the WUSTL Bakewell Neuroimaging Laboratory Core; and the WUSTL Hope Center Viral Vector Core.

Supplementary Materials

www.sciencemag.org/cgi/content/full/340/6129/211/DC1
Materials and Methods
Figs. S1 to S24
Table S1
References (35–48)
Movie S1

6 November 2012; accepted 18 February 2013
10.1126/science.1232437

Interactions Between the Nucleus Accumbens and Auditory Cortices Predict Music Reward Value

Valorie N. Salimpoor,^{1,2,3*} Iris van den Bosch,⁴ Natasa Kovacevic,² Anthony Randal McIntosh,² Alain Dagher,¹ Robert J. Zatorre^{1,3}

We used functional magnetic resonance imaging to investigate neural processes when music gains reward value the first time it is heard. The degree of activity in the mesolimbic striatal regions, especially the nucleus accumbens, during music listening was the best predictor of the amount listeners were willing to spend on previously unheard music in an auction paradigm. Importantly, the auditory cortices, amygdala, and ventromedial prefrontal regions showed increased activity during listening conditions requiring valuation, but did not predict reward value, which was instead predicted by increasing functional connectivity of these regions with the nucleus accumbens as the reward value increased. Thus, aesthetic rewards arise from the interaction between mesolimbic reward circuitry and cortical networks involved in perceptual analysis and valuation.

Music is a potent phenomenon, existing in all cultures from prehistory onward (1). How sounds that have no intrinsic reward value can become highly pleasurable remains largely unknown. Prior studies demonstrate that listening to music engages not only the

auditory cortices, but also emotion regions and reward-related mesolimbic circuits (2, 3); studies have also shown that dopamine mediates this response in the striatum (4). These reward circuits reinforce biologically adaptive behaviors, including eating and sex (5, 6), and are shared by most vertebrates. However, appreciation of music is complex and seemingly distinct to humans and is dependent on sociocultural factors, experience, and memory, suggesting an integrative role for cortical processes in interaction with dopamine-reinforcement circuits. Dopamine is involved in incentive salience and reward prediction, leading to expectation and anticipation

¹Montreal Neurological Institute, McGill University, Montreal, Quebec H3A2B4, Canada. ²The Rotman Research Institute, Toronto, Ontario M6A2E1, Canada. ³BRAMS International Laboratory for Brain, Music and Sound Research, Montreal, Quebec, Canada. ⁴Utrecht University, 3508 TC Utrecht, Netherlands

*Corresponding author. E-mail: vsalimpoor@research.baycrest.org

of a desirable item (7–9). The principal affective impact of music is thought to be elicited by the creation of expectancies through temporally rooted phenomena, such as delay, anticipation, and surprise (10). Previously, functional magnetic resonance imaging (fMRI) revealed hemodynamic activity associated with anticipatory periods preceding peak pleasure moments during music listening; this activity took place in the same regions that showed dopamine release using ligand-based positron emission tomography (4). Anticipation may arise from either explicit knowledge of specific music or more implicit schematic expectancies representing rules of how sound patterns are organized (10, 11) based on culture- and person-specific musical knowledge gained through years of exposure to various musical sounds. The former can explain why we enjoy familiar music, but not how previously unheard music can be ap-

preciated. A prediction-error model (12) in which predictions are fulfilled or surpassed, mediated via a dopaminergic response (9), may shape the biological response to music based on schematic expectancies independent of explicit knowledge. To examine this hypothesis, we used new music excerpts to minimize explicit predictions, selected with the help of music-recommendation software designed to reflect individual preferences (see www.zlab.mcgill.ca/science2013/ for a list of music stimuli used in this experiment) (13). To assess reward value objectively, individuals could purchase the music with their own money, as an indication that they wanted to hear it again. To further increase ecological validity, we used an interface and prices similar to those in iTunes. While undergoing fMRI scanning, 19 participants (10 female, 9 male) (table S1) listened to 60 musical excerpts, providing bids of how much they were willing to spend

for each item in an auction paradigm (Fig. 1 and fig. S1) (14).

Whole-brain analysis of hemodynamic activity during the 30-s listening period of excerpts with bids greater than \$0 showed increased activity in the dorsal and ventral striatum, inferior frontal gyrus (IFG), insula, temporal pole, and cerebellum (Fig. 2A and table S2). To examine which of these regions are associated with reward value, we selected the 11 individuals with sufficient bids in all categories (\$0, \$0.99, \$1.29, and \$2) and at least three bids in the most expensive category. Multivariate regression revealed that reward value (amount bid) was most directly related to the degree of activity in the right nucleus accumbens (NAcc) in the ventral striatum, a key region associated with positive prediction error (15, 16); NAcc activity accounted for 33% of the variability in bids. The right caudate, a part of the dorsal

Fig. 1. Experimental paradigm.

(A) Blood-oxygenation-level-dependent (BOLD) activity was collected while participants listened to 60 30-s clips of new music (matched to their preferences by music-recommendation software, such as Pandora and Last.fm). Participants then placed bids with their own money that were used to categorize each excerpt according to desirability (\$0, \$0.99, \$1.29, and \$2) for the purposes of analysis. (B) Contrast analysis revealed regions associated with purchasing (Fig. 2A). (C) Multivariate connectivity methods allowed us to examine neural interactions associated with increased reward value of music (Fig. 3).

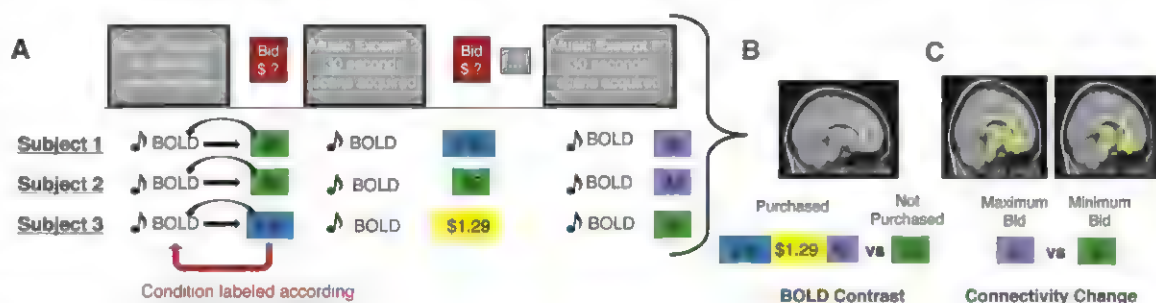


Fig. 2. Neural activity associated with reward value of music. (A) A whole-brain contrast revealed areas, including the dorsal and ventral striatum, that are active during the processing of desirable (bids > \$0) as opposed to undesirable (\$0 bids) music (table S2A). Z, plane of horizontal section (millimeters); t, value of t statistic; X, plane of vertical section (millimeters). (B) Among individuals who made sufficient bids in all categories (13), multiple linear regression allowed us to determine which purchasing-related regions (table S2B) corresponded to increasing reward value. Among the clusters from Fig. 1A, signal change in the right NAcc accounted for 33% of the variability in the amount spent, and the caudate accounted for an additional 10%; other regions did not contribute directly to reward value. Error bars indicate 1 SEM. (C) Average BOLD signal time course for the right NAcc and right caudate during the 30-s excerpts.

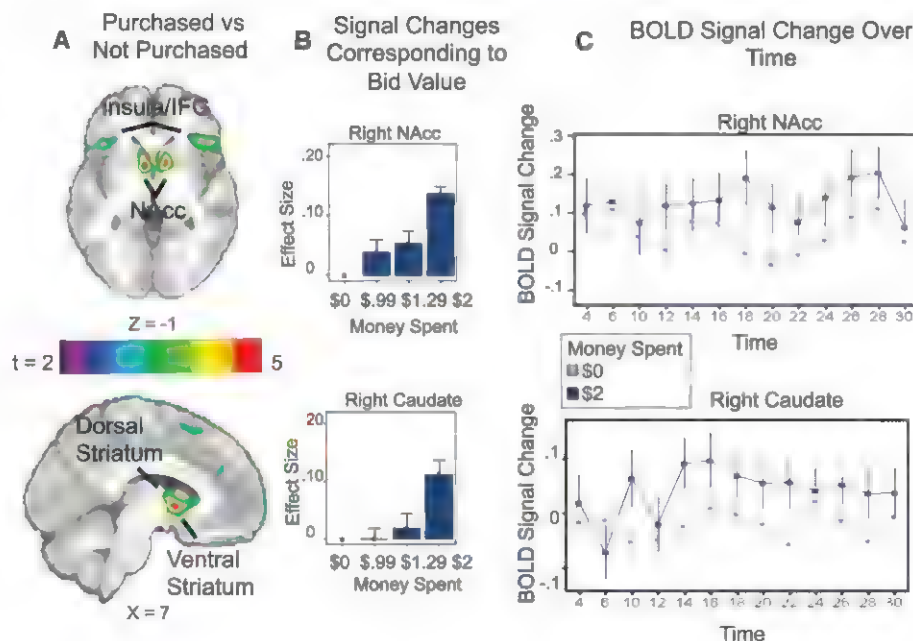
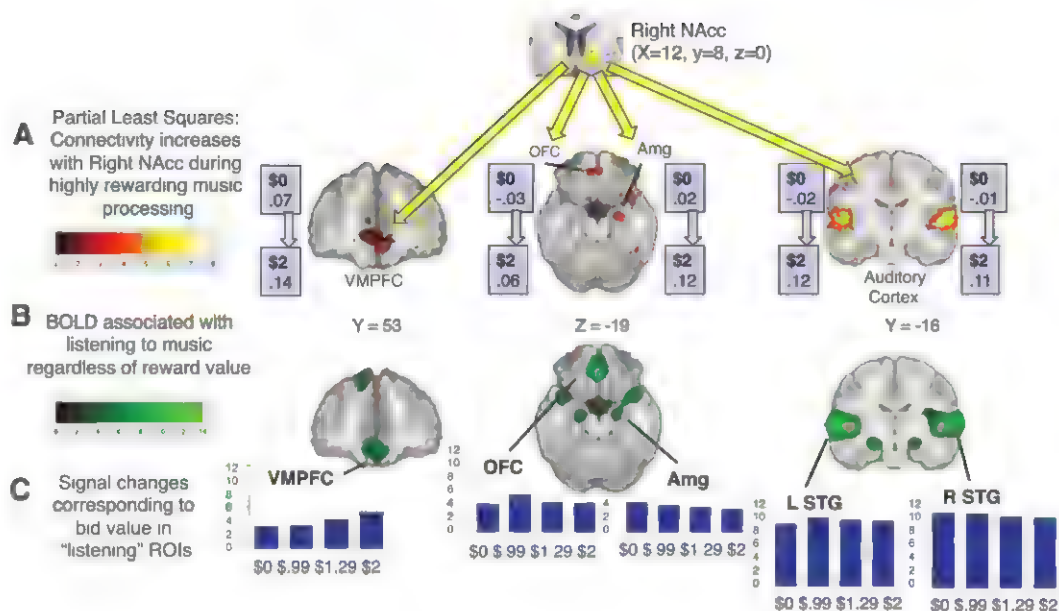


Fig. 3. Changes in NAcc functional connectivity associated with increasing desirability of music. (A) Partial least-squares analysis revealed robust increases in connectivity between the NAcc and other subcortical and cortical regions when individuals hear music they consider highly desirable, compared with music they do not want to hear again (table S3). Here, the boxes show changes in correlation as a function of amount bid between the NAcc and each region. A subset of these regions (A) overlap with areas that are recruited during music listening compared with rest (B). These areas show equally high activity during all music valuation conditions compared with rest (C), but their interactions with the NAcc increase as items become more desirable. Amg, amygdala; ROI, region of interest.



striatum, accounted for a smaller proportion of variability (10%) in bid value, whereas the other clusters (table S1) did not show a significant contribution.

We used partial least-squares analysis (17) to examine how the mesolimbic striatal areas interact with other brain regions as musical sequences gain reward value. The NAcc showed highly robust increases in functional connectivity with large portions of the superior temporal gyrus (STG), encompassing the primary and surrounding auditory cortices bilaterally when individuals listened to items they found most desirable (Fig. 3A). These same auditory regions showed increased activity during music listening as opposed to silence (Fig. 3B) and are involved in perceptual processing of music (18). Increased hemodynamic activity in these regions did not predict reward value (Fig. 3C). However, their degree of functional connectivity with the NAcc established the level of desirability of the music for the individual (Fig. 3A).

Other areas that showed an increase in functional connectivity with the NAcc as music value increased include the ventromedial prefrontal cortex (VMPFC), orbitofrontal cortex (OFC), amygdala, hippocampus, right IFG, anterior cingulate cortex, and clusters in the somatosensory and motor areas (table S3). Although activity in most of these areas was also increased in the maximum reward condition, the VMPFC, OFC, and amygdala demonstrated similar activity in all conditions, regardless of amount bid (Fig. 3C). These regions play a well-established role in emotional processing and value-guided decision-making (19, 20) and are consistently recruited for processing all musical stimuli, which suggests a role for assigning and main-

taining value of musical sound sequences as they are temporally revealed. Importantly, these brain regions show increased connectivity with the NAcc only when the sounds gain reward value for the individual (Fig. 3A). These findings suggest a mechanism for valuation of stimuli with abstract importance.

The right caudate also showed increased connectivity bilaterally with the posterior STG proportionally to bid value, suggesting a role for retrieval of previously stored sound information; other areas showing this trend included the hippocampus and the prefrontal cortex (table S4). Connectivity between the caudate and premotor areas implicated in beat processing (21) also increased during time spent listening to highly desirable sounds.

Our results show that a network of regions—similar to that from studies with other stimuli in tasks involving reward, salience, and purchasing (19, 22)—was recruited during real-time processing of desirable new music, but only the dorsal and ventral striatum demonstrated activity proportional to the reward value of the stimulus. These areas were similar to those that showed dopamine release to familiar, highly pleasant music (4). Thus, the current results show that explicit familiarity is not necessary for activity in dopamine target regions, which may also depend on implicitly formed expectations based on previously acquired musical knowledge. Further, as the temporal unfolding of novel sound sequences gains reward value, highly robust interactions occur between cortical areas that store information about sound relationships and subcortical areas involved in assessing positive prediction errors (19, 23, 24). These results collectively sug-

gest that our appreciation of new music is likely related to (i) highly individualized accumulation of auditory cortical stores based on previous listening experiences, (ii) the corresponding temporal expectations that stem from implicit understanding of the rules of music structure and probabilities of the occurrence of temporal and tonal events, and (iii) the positive prediction errors that result from these expectations. This conclusion is consistent with music-theoretic models that emphasize temporal expectations as one of the main dimensions resulting in the affective impact of music (10, 25). Here, both dorsal and ventral striatal regions were involved in these interactions, whereas in our previous study (4), the two structures were temporally dissociated according to anticipation versus experience of peak pleasure. The present finding is consistent with the idea that during music listening there may be ongoing, possibly overlapping, processes of expectancy and evaluation as musical events unfold, thus giving rise to activity in both striatal regions.

The reward value of music is abstract: It does not involve a tangible substance, but rather a combined sensory and cognitive experience that can influence one's affective state. Our data show robust interactions between sensory and affective systems: The subcortical regions work in concert with the auditory sensory cortices to establish a potentially rewarding stimulus that is experienced for the first time as desirable. The auditory cortices are involved in auditory sensory memory and imagery, extraction of sound relationships, and discrimination and organization of sound patterns (18). These cortical stores may contain templates of previously

heard sounds, making them an ideal location for feedback regarding temporal predictions, which, in combination with the NAcc, can contribute to the rewarding nature of musical sounds. These expectancies need not be confined to harmonic or metrical structure, but may also include other features of musical sounds, including timbre, loudness changes, and perhaps even the integration of verbal content when present. Further support linking musical reward with temporal expectancies and positive prediction errors comes from the finding that highly desirable items are marked by enhanced NAcc connectivity with regions of the IFG that are thought to be involved in harmonic expectancy and processing musical structure (26). As these frontal areas are more generally involved in attentional processes, sequencing, and working memory and are also connected to the STG (27), they are in prime position to integrate auditory information over time and form syntactic predictions. Music processing also involves sensory-motor interactions coupling auditory with premotor and frontal regions, a link that has also been proposed as related to musically elicited emotion (21). In summary, we show that through the temporal dimension, previously neutral cues—tones and other sound sequences that have no inherent reward value—interact with higher-order cognitive brain regions to gain incentive salience, which then influences affective brain regions and impacts behavioral decisions about the value of an abstract stimulus.

References and Notes

1. N. J. Corrad, M. Malina, S. C. Münzel, *Nature* **460**, 737 (2009).
2. A. J. Blood, R. J. Zatorre, *Proc. Natl. Acad. Sci. U.S.A.* **98**, 11818 (2001).
3. S. Koelsch, *Trends Cogn. Sci.* **14**, 131 (2010).
4. V. N. Salimpoor, M. Benovoy, K. Larcher, A. Dagher, R. J. Zatorre, *Nat. Neurosci.* **14**, 257 (2011).
5. M. R. Melis, A. Argiolas, *Neurosci. Biobehav. Rev.* **19**, 19 (1995).
6. K. C. Berridge, C. Y. Ho, J. M. Richard, A. G. DiFeliceantonio, *Brain Res.* **1350**, 43 (2010).
7. D. F. Wong *et al.*, *Neuropsychopharmacology* **31**, 2716 (2006).
8. N. D. Volkow *et al.*, *J. Neurosci.* **26**, 6583 (2006).
9. W. Schultz, P. Dayan, P. R. Montague, *Science* **275**, 1593 (1997).
10. D. Huron, *Sweet Anticipation: Music and the Psychology of Expectation* [Massachusetts Institute of Technology (MIT) Press, Cambridge, MA, 2006].
11. J. Bharucha, in *Musical Perceptions*, R. Aiello, Ed. (Oxford Univ. Press, Oxford, 1994), pp. 213–239.
12. R. S. Sutton, A. G. Barto, *Reinforcement Learning. An Introduction* (MIT Press, Cambridge, MA, 1998).
13. Materials and methods are available as supplementary materials on Science Online.
14. G. M. Becker, M. H. DeGroot, J. Marschak, *Behav. Sci.* **9**, 226 (1964).
15. Y. Niv, J. A. Edlund, P. Dayan, J. P. O'Doherty, *J. Neurosci.* **32**, 551 (2012).
16. K. Kuss *et al.*, *Soc. Cogn. Affect. Neurosci.* **8**, 216 (2013).
17. A. R. McIntosh, W. K. Chau, A. B. Protzner, *Neuroimage* **23**, 764 (2004).
18. R. J. Zatorre, J. M. Zatorre, in *The Human Auditory Cortex*, D. Poeppel *et al.*, Eds., vol. 43 of *Springer Handbook of Auditory Research* series (Springer, New York, 2012), pp. 261–294.
19. J. P. O'Doherty, *Curr. Opin. Neurobiol.* **14**, 769 (2004).
20. M. F. S. Rushworth, M. P. Noonan, E. D. Boorman, M. E. Walton, T. E. Behrens, *Neuron* **70**, 1054 (2011).
21. R. J. Zatorre, J. L. Chen, V. B. Penhune, *Nat. Rev. Neurosci.* **8**, 547 (2007).
22. S. N. Haber, B. Knutson, *Neuropsychopharmacology* **35**, 4 (2010).
23. M. Pessiglione, B. Seymour, G. Flandin, R. J. Dolan, C. D. Frith, *Nature* **442**, 1042 (2006).
24. S. M. McClure, G. S. Berns, P. R. Montague, *Neuron* **38**, 339 (2003).
25. L. B. Meyer, *Emotion and Meaning in Music* (Univ. of Chicago Press, Chicago, 1956).
26. S. Koelsch, *Front. Psychol.* **2**, article 110 (2011).
27. M. Petrides, D. N. Pandya, *Eur. J. Neurosci.* **16**, 291 (2002).

Acknowledgments: Funding for this work was provided via grants from the Canadian Institutes for Health Research and the Canada Fund for Innovation (to R.J.Z.) and awards from the Natural Science and Engineering Research Council (CREATE), Montreal Neurological Institute (MNI), and the Centre for Interdisciplinary Research in Music Media and Technology (to V.N.S.). We thank the staff of the MNI McConnell Brain Imaging Centre. The authors have no conflicts of interest to report.

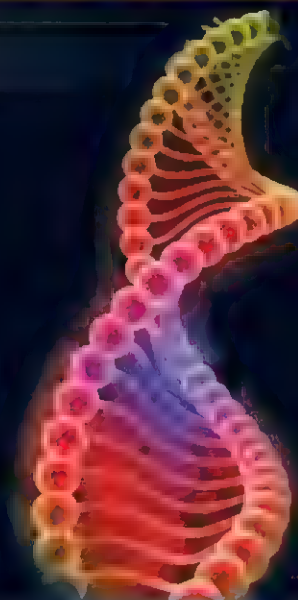
Supplementary Materials

www.sciencemag.org/cgi/content/full/340/6129/216/DC1
Materials and Methods
Figs. S1 and S2
Tables S1 to S5
References

3 October 2012; accepted 8 February 2013
10.1126/science.1231059

An Expanding Color Palette for Biotechnology

Think of any multiplexed biological technique, RT-PCR, DNA sequencing, Flow cytometry, Microscopy. All work on different principles. Yet all have one common factor: fluorescence. The ever-expanding variety of fluorescent molecules, nanoparticles, and proteins has expanded the palette, so to speak, of biological experimentation. The pages of research journals may be filled mostly with reds and greens, but today's researchers have literally dozens of hues available from which to choose. Such variety has expanded the spectrum of applications and instrumentation available to the research community. The future of fluorescence multiplexing has never seemed so, ahem, bright. By Jeffrey M. Perkel



“So while our ability to multiplex hasn’t increased with the new dyes, our sensitivity and ability to make precise measurements has increased in a way that I haven’t seen in 20 years.”

Mario Roederer, senior investigator in the Vaccine Research Center at the National Institute of Allergy and Infectious Diseases (NIAID), knows something of the promise and limitations of fluorescent dyes.

Roederer has been studying T cell responses to infection and vaccines for nearly 20 years, first as a postdoc in Len Herzenberg’s lab at Stanford University and later as a group leader at NIAID. In the early-to-mid-1990s, Roederer says, he and his colleagues in Herzenberg’s lab were using flow cytometry to try to understand the impact of HIV-1 infection on the immune system.

Flow cytometry is the workhorse of immunology labs, enabling researchers to interrogate cells one by one to identify those that do or do not express specific cell surface markers, such as CD3, CD4, and CD8. Using a special kind of flow cytometer called a cell sorter, researchers can even isolate and expand cell populations of interest. The problem was, when Roederer began his postdoc, there simply were not enough usable fluorescent colors available to sift through the dizzying complexity of the human immune system.

“We realized one of our limitations was that we weren’t able to interrogate the immune system sufficiently,” he says.

At the time, flow cytometry was limited by a lack of useful, separable fluorescent labels to four color channels, far too few to delve into immune cell subtypes. By the time Roederer left the lab, however, the number of available channels had risen to 12, the result of improvements in hardware, software, and dye chemistries, and by the early 2000s it was up to 18 thanks to a new class nanoparticulate quantum dots from Quantum Dot (now part of Life Technologies).

Using those 18-color panels, Roederer’s group has been able not only to identify cells of interest, but probe their behavior as well. “You need six or eight colors just to identify the cells,” he explains, “and then you need other colors to see what they are doing.” In one recent paper, Roederer’s lab characterized stem cell-like memory T cells as a subpopulation of CD95⁺, IL-2R[β]⁺, CXCR3⁺, LFA-1⁺ cells within the larger CD45RO⁺, CCR7⁺, CD45RA⁺, CD62L⁺, CD27⁺, CD28⁺, IL-7R[α]⁺ T cell “compartment.”

Today, Roederer’s 18-color panels represent essentially the state-of-the-art in fluorescent flow cytometry (and, for that matter, for fluorescent experiments in general). But the state-of-the-art isn’t static: New fluorescent dyes promise to boost his multiplexing capability to 25- or even 30-plex within the next few years, meaning he and other immunologists will be able to tease apart immune cell responses with ever more sophistication. Yet researchers using other fluorescence techniques are not being left out in the cold: new hardware and reagents are enabling higher levels of multiplexing and greater sensitivity for a range of biological applications.

Brilliant New Dyes

To squeeze more colors from his already strained BD Biosciences LSRII, Roederer is going to need some new fluorophores. Enter Brilliant Violet dyes from Sirigen (acquired by BD Biosciences in August 2012).

Unlike quantum dots, which are nanoparticles, and small molecule organic dyes like Life Technologies’ Alexa Fluors, Sirigen’s fluorophores are actually light harvesting polymers. They rely on the same electrically conductive polymer chemistry that was recognized with the 2000 Nobel Prize in Chemistry, and are used either directly or as “tandems,” in which the polymer non radiatively passes its energy to another dye that shifts its emission further into the red. In this case, the company has over

Upcoming Features

The Microbiome—May 10

Proteomics: MALDI Imaging—May 31

Data Management: Cloud-Based—June 14

the past year and a half developed and released a series of seven violet laser (407 nm) excitable fluorophores, called Brilliant Violet dyes, which emit at wavelengths from 421 nm through 785 nm.

According to Robert Balderas, vice president of biological sciences at BD Biosciences, the Sirigen dyes possess many of the qualities one would want in a good fluorophore. They are photostable and resist quenching, and most importantly, are exceptionally bright, up to 10-times brighter than phycoerythrin (PE), which is one of the brightest dyes available. And that's important because in flow cytometry especially, the trick is coupling dye brightness with target abundance. To label an abundant protein, researchers can use a relatively dim dye, as the sheer number of fluorophores on any given cell will overcome the weak signal. For rare proteins, though, bright dyes are best, and until recently only a few were available. Now, says Roederer, there is at least one more, Brilliant Violet 421; other dyes in the series are almost equally as strong.

"The Sirigen dyes are really remarkable," says Roederer, who had thought with QDots that he had maxed out fluorescence multiplexing with 18 channels. Now he is slowly rotating the Sirigen dyes into his cytometry panels in lieu of QDots, producing panels that are no more complex than before, but that are far brighter and thus more sensitive. "So while our ability to multiplex hasn't increased with the new dyes, our sensitivity and ability to make precise measurements has increased in a way that I haven't seen in 20 years," he says.

Development of new colors, though—for instance, polymers that excite in the ultraviolet or far in the red ends of the spectrum—will increase Roederer's multiplexing ability even more. "I am optimistic in the next five years we could do 25 or even 30 color measurements, which is really fantastic."

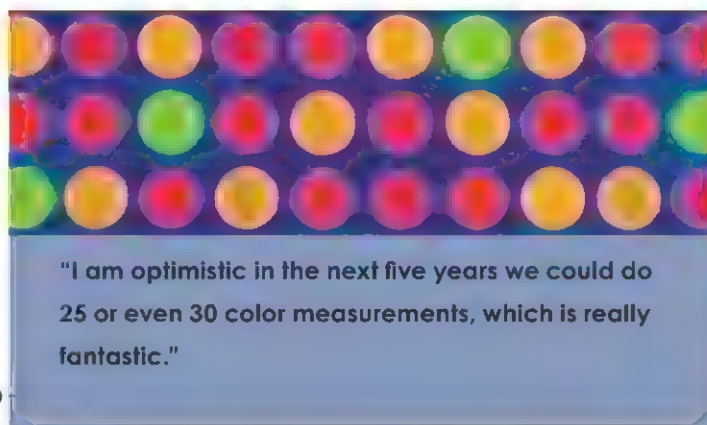
According to Balderas, Sirigen is already hard at work making that expansion happen. And that could significantly alter the flow cytometry market, he says, by allowing the development of multiple colors off individual lasers, while at the same time pushing the envelope on higher-end instrumentation. "If we could build multiple dyes off multiple lasers, imagine what we could do with an instrument that has five lasers."

Bead-Based Megaplexing

Another application for fluorescence multiplexing is analyte quantitation. And no such tool is quite so popular as **Luminex's** xMAP beads.

xMAP beads enable a kind of highly multiplexed, solution-based ELISA. Where an ELISA measures single analytes individually in each well of a microtiter plate, xMAP technology uses fluorescently coded beads to, in essence, pool multiple wells into one and distinguish them optically.

Key to that process are xMAP beads, micrometer-sized polystyrene spheres loaded with varying amounts of two or three fluorescent dyes. The precise amounts of each dye serves as a kind of fluorescent fingerprint for the beads, and Luminex currently supports as many as 500 such fingerprints.



In an xMAP assay, each fingerprint is associated with a specific biomarker. For instance, a panel for assaying immune cell responses in blood sera might have one fingerprint associated with an antibody to IL-2, a second for IL-4, and so on. (A separate set of Luminex beads, called xTAG beads, enable nucleic acid-based assays.) Beads corresponding to the different analytes to be tested are mixed in a single well of a microtiter plate and incubated with the biological sample. The

antibodies capture their specific targets. Then, after washing, a mixture of fluorescently tagged secondary antibodies is added, after which the reaction is read.

In the traditional Luminex workflow, the beads are read on a dedicated instrument, essentially a flow cytometer, that uses lasers to interrogate each bead one by one, first to read its fingerprint—that is, identify the analyte being measured—and then the abundance of antigen it bound. In 2010, however, the company released a new instrument, the MAGPIX, for labs looking for a smaller, less-expensive, and less-multiplexed alternative.

The Luminex MAGPIX is a fluorescence imager that uses paramagnetic microspheres (hence the name) and holds them in place on a solid substrate with a magnet to create a fixed, albeit temporary, solid-phase bead array. (The magnetic beads also simplify sample processing and improve bead recovery, says Jehangir Mistry, head of multiplex and immunoassays at **EMD Millipore**, which markets MILLIPLEX-branded xMAP assays.) The instrument then excites that array with LEDs and captures the resulting fluorescence on a CCD camera.

Unlike the Luminex 200 (which can distinguish up to 100 different bead types) and the FLEXMAP 3D (which can recognize 500), the MAGPIX is limited to 50 different bead fingerprints, says Matthew Grow, director of marketing at Luminex. But that's more than enough for most assays, he notes. In fact, the MAGPIX (along with the Luminex 200) is approved for use in both Canada and Europe with the company's 15-pathogen xTAG Gastrointestinal Pathogen Panel. EMD Millipore's largest panel, says Mistry, is a 42-plex human cytokine and chemokine panel. (Most Luminex assays are actually created and sold by its partners, including EMD Millipore, Bio-Rad Laboratories, R&D Systems, and more than a dozen others. The company recently launched an iPhone application, xMAP Kit Finder, to help researchers identify kits targeting specific biomarkers.)

Bioassays On A View-Master

Quanterix Corporation, a Boston-based firm founded in 2007, has taken an approach not all that different from the MAGPIX to effect highly sensitive multiplexed analyte detection.

Quanterix was founded by **Tufts University** professor David Walt, who also co-founded **illumina**, and that corporate heritage is evident in Quanterix's single-molecule array (Simoa) technology. **continued>**

Before it became known as a sequencing firm, Illumina developed a bead-based microarray called the BeadArray, which blends the bead-based approach of Luminex with planar microarray detection. Similarly, Simoa assays are carried out on small "Simoa Discs," which look like high-tech reboots of the View-Master reels so popular in the 1960s and 1970s. Each disc holds 24 arrays of 216,000 holes on its periphery, with each array corresponding to one well of a microtiter plate. The holes are just large enough to hold the 3 μ m beads Quanterix uses for its antigen-capture assays.

As with xMAP, each bead is fluorescently fingerprinted with one of four dyes, and each has a unique capture antibody on its surface. After incubation with the sample and washing, those beads are incubated with secondary antibodies and then labeled with an enzyme. They are then flowed onto the Simoa Disc, where the beads are captured in wells and then sealed. That step, explains David Duffy, the company's vice president for research, makes the Quanterix system exceptionally sensitive, as the enzyme converts a dark substrate to a fluorescent one in a femtoliter-sized volume, rather than allowing the fluorophores to diffuse into a larger space.

"You go from needing millions of enzymes to a single enzyme generating about 3,000 flours, and you can detect a single protein molecule," Duffy says.

Duffy claims the Quanterix system (called the Simoa HD-1 Analyzer) can detect as little as 0.02 pg/mL of signaling molecules like TNF-alpha, which is one-to-two orders of magnitude better than comparable Luminex assays. The system, which is set to launch in July 2013, can theoretically multiplex up to 12 different analytes. But in practice, he says, the company will focus on panels of five or so targets to speed assay development and minimize antibody cross-reactivity. Initial panels will target applications such as oncology, neurology, and inflammatory and infectious diseases.

Quantifying RNA In Vivo

Another new development in fluorescent multiplexing comes from Chad Mirkin's lab at Northwestern University. Called Nanoflares by Mirkin and commercialized by AuraSense and EMD Millipore (which calls them SmartFlare RNA Detection Probes), the technology enables researchers to quantify RNA as in an RT-PCR assay, but within living cells.

Nanoflares are 13 nm gold particles coated with 20-base oligonucleotides complementary to the RNA of interest—a structure Mirkin calls a



Featured Participants

AuraSense aurasense.com	National Institute of Allergy and Infectious Diseases www.niaid.nih.gov
BD Biosciences www.bdbiosciences.com	Northwestern University www.northwestern.edu
EMD Millipore www.millipore.com	Quanterix www.quanterix.com
Life Technologies www.lifetechnologies.com	
Luminex www.luminexcorp.com	

"spherical nucleic acid." A second, shorter oligonucleotide is bound to the targeting oligo and end-labeled with a fluorophore. Initially that fluor is dark, as gold is an extremely efficient fluorescence quencher. When these constructs encounter a complementary RNA, however, a short "flare" is released, producing a fluorescent signal.

According to Mirkin, the beauty of spherical nucleic acids (which his team first developed some 16 years ago) is that they are naturally and rapidly taken up by cells via scavenger receptors, so no transfection agents are required. When coupled with the Nanoflare design, this property allows researchers to quantify RNAs in living cells, apparently without toxicity.

"One of the real wins in nanoscience has been the discovery that if you take what I think is arguably the world's most important molecule ever synthesized, DNA, and you arrange it in a highly oriented spherical form, you get properties that are radically different, and one

of those is the ability to enter cells," he says.

Mirkin's team published a duplex version of the Nanoflare approach in early 2012, using one color channel to quantify an RNA of interest and the second to measure a housekeeping control. Up to three or four color multiplexing is possible, he says.

According to David Giljohann, chief operating officer and principal scientist at AuraSense, Nanoflares can be used as an alternative (albeit a less sensitive and quantitative one) to RT-PCR, for instance, to monitor transgene expression or siRNA efficacy. Just add the flares to a dish of cells, wait 12 to 16 hours, and measure the results using flow cytometry. EMD Millipore already has over 100 SmartFlare detection probes available, Mistry says, and more are coming.

For cell biologists testing the efficacy of short regulatory RNAs or measuring transgene efficacy, such tools could prove to be a godsend, especially as positive cells can be isolated and put back into culture using cell sorting. That could even benefit immunologists like Roederer, who could, for instance, use the approach to compare immune responses in RNAi-treated and untreated cells.

It truly is a bright time for fluorescence multiplexing.

Jeffrey M. Perkel is a freelance science writer based in Pocatello, Idaho.

DOI: 10.1126/science.opms.p1300074

IMAGE ANALYSIS SYSTEMS

The new PXi Touch range of high-resolution, multi-application image analysis systems is ideal for scientists wanting a rapid touchscreen driven method of accurately imaging chemiluminescent and fluorescent blots, as well as 1-D and 2-D gels stained with any type of visible or fluorescent dye. Each PXi Touch features a camera with a large fixed aperture lens, which enables scientists to quickly capture images without having to adjust the camera's settings. The PXi Touch is available in three versions with a high-resolution four, six, or eight megapixel camera for chemiluminescence and 1-D and 2-D gel applications. To enable researchers to choose the best and safest lighting for their fluorescent gel and blot applications, the PXi Touch fits a number of lighting and filter options, making the system versatile enough to use with Syngene's ultraviolet and blue light transilluminators as well as white, infrared, red, blue, or green epi lighting.

Syngene

For info: +44-(0)-1223-727123 | www.syngene.com/pxi-pxi-touch

**LUMINEX ASSAY ANALYSIS SOFTWARE**

Milliplex Analyst 5.1 is designed for analysis and interpretation of Luminex bead-based assay results. The newly released software includes unique features such as autofit and potency calculation and offers superior quality of data reduction analytics compared with other Luminex software packages. Superior algorithms yield better data at the low- and high-end of the standard curve. The autofit feature saves time by automatically using the best curve fit method for the curve presented. The potency calculation feature compares two or more standard curves, giving researchers a choice when reducing their data. Data acquisition and analysis integrates seamlessly with all Luminex instruments. Milliplex Analyst 5.1 is accessed using a code flash drive making it possible to use the software on multiple systems. More user-friendly plate setup means there are no limitations to where the standard curve can be put on the plate. Other software requires the standard curve to be placed vertically in the first column.

EMD Millipore

For info: 800-645-5476 | www.millipore.com

CONFOCAL IMAGING

The new FluoView FV1200 confocal laser scanning microscope is optimized for live cell imaging. The new system uniquely combines the accuracy of the newly engineered IX83 frame with enhanced fluorescence sensitivity and simultaneous laser stimulation of cells, making it ideal for advanced life science applications such as FRAP, FLIP, and photo-activation. In particular, the new highly reflective, silver-coated galvanometer scanning mirrors and dual channel GaAsP FluoView PMT module both act to maximize light transfer and detection. This allows for reduced laser power, protecting against the effects of photobleaching and phototoxicity. The generation of insightful confocal imaging data from living cells depends on optimally balancing laser power and sensitivity to minimize the effects of phototoxicity and photobleaching. To meet this challenge, the FV1200 is designed to maximize sensitivity via a new dual channel GaAsP FluoView high sensitivity PMT module, which delivers up to 45% quantum efficiency.

Olympus

For info: +49 40 23773 5913 | www.microscopy.olympus.eu

USB FLUORESCENCE CAMERA

The ultrasensitive SPOT Pursuit USB digital camera combines superb image quality with excellent temporal resolution for rapid time-lapse recordings, allowing researchers to document live cells and photobleaching fluorescence specimens with ease. The camera is equipped with a high quantum efficiency CCD sensor and Peltier cooling, which makes it a suitable solution for a range of applications, from simple fluorescence documentation to the demanding process of live cell imaging and ratiometric experiments. The SPOT Pursuit USB live cell imaging camera achieves high-speed acquisition rates of 11 frames per second at full resolution without sacrificing read noise. New images can be captured while the previous image is still being read out. The user-friendly SPOT software included with the camera is compatible with both Windows and Mac. Data is transferred to the computer via the USB 2.0 interface, making it a snap to get up and running quickly.

SPOT Imaging Solutions

For info: 586-731-6000 | www.spotimaging.com/camPRUSB.html

CYANINE DYES

A new range of high-quality cyanine dye products support the demand for fluorescent labeling in biological imaging and molecular diagnostics. In addition to a new range of 3'-CPG solid supports modified with Cyanine 540 and Cyanine 650, Link Technologies now also manufactures and supplies the commonly used phosphoramidites, allowing researchers to source an extended range of cyanine reagents. Until now, 3'-cyanine modification of an oligonucleotide could only be done postsynthetically, normally to an amino-modified oligo, or by the use of a cyanine phosphoramidite onto a universal or modified support that will not interfere with the intended use of the oligo. With the innovative 3'-modified 1,000Å CPG supports, cyanine dyes can be added directly to oligos of interest without additional modification steps. Used as fluorescent markers in oligonucleotide synthesis, dyes are central to numerous detection techniques, such as real time polymerase chain reaction, fluorescence in situ hybridization, SERRS based DNA detection assays, and FRET studies.

Link Technologies

For info: +44 (0) 1698 849911 | www.linktech.co.uk

There's only one Science

Science Careers Advertising

For full advertising details, go to ScienceCareers.org and click For Employers, or call one of our representatives.

Tracy Holmes

Worldwide Associate Director
Science Careers
Phone: +44 (0) 1223 326525

THE AMERICAS

E-mail: advertise@sciencecareers.org
Fax: 202-289-6742

Tina Burks

United States/Canada/South America
Phone: 202-326-6577

Marci Gallun

Sales Administrator
Phone: 202-326-6582

Online Job Posting Questions

Phone: 202-312-6375

EUROPE / INDIA / AUSTRALIA / NEW ZEALAND / REST OF WORLD

E-mail: ads@science-int.co.uk
Fax: +44 (0) 1223 326532

Lucy Nelson

Phone: +44 (0) 1223 326527

Kelly Grace

Phone: +44 (0) 1223 326528

JAPAN

Yuri Kobayashi

Phone: +81-(0)90-9110-1719
E-mail: ykobayas@aaas.org

CHINA / KOREA / SINGAPORE / TAIWAN / THAILAND

Ruolei Wu

Phone: +86-1367-1015-294
E-mail: rwu@aaas.org

All ads submitted for publication must comply with applicable U.S. and non-U.S. laws. *Science* reserves the right to refuse any advertisement at its sole discretion for any reason, including without limitation for offensive language or inappropriate content, and all advertising is subject to publisher approval. *Science* encourages our readers to alert us to any ads that they feel may be discriminatory or offensive.



ScienceCareers.org

DIRECTOR, BIOSCIENCES DIVISION ARGONNE NATIONAL LABORATORY CHICAGO, ILLINOIS

Argonne National Laboratory seeks applications for the position of Director of the Biosciences (BIO) Division. Argonne, located about 25 miles southwest of Chicago, Illinois, is one of the U.S. Department of Energy's largest national laboratories for scientific and engineering research. Argonne is managed by UChicago Argonne, LLC, for the U.S. Department of Energy's Office of Science. Argonne applies a unique mix of world-class science, engineering, and user facilities to deliver innovative research and technologies that address the grand challenges of our time: plentiful and safe energy, a healthy environment, economic competitiveness, and a secure nation.

The mission of the BIO Division is to use state-of-the-art technology to conduct multidisciplinary basic and applied research that will increase our understanding of the fundamental molecular mechanisms of life, with the goal of enabling important advances in energy production and sustainability, environmental protection and remediation, and human health and welfare. Program areas include structural, computational, environmental, and molecular and systems biology.

The BIO Division Director will lead world-class basic and applied research integrating 'multi-omics' with microbial and ecosystem science through pursuit of innovative scientific directions; foster collaborative partnerships with national and international researchers from national laboratories, academia, and industry for the advancement of scientific discovery; manage the division's scientific staff of ~100 members, while promoting innovative research yielding significant scientific contributions and publications; anticipate trends in and needs for biological research in order to develop relevant and effective program strategies; maintain an active role in R&D activities within his/her area of expertise, including publishing scholarly papers in scientific journals and participating in conferences and workshops.

The successful candidate will have a Ph.D. in a relevant discipline; 10+ years of experience in systems biology, synthetic biology, environmental microbiology, or plant biology; a proven record of creating, developing and sustaining research programs with experience in attracting and shaping funding for complex multidisciplinary research operations; and demonstrated leadership abilities. For the appropriate candidate a joint appointment with University of Chicago, Northwestern University, or University of Illinois at Chicago may be possible. For more information about the Biosciences Division or this position please visit our website at <http://www.bio.anl.gov/> or contact search committee chair **Dr. Robin L. Graham** at glocasto@anl.gov. To apply for the position, please submit your CV, including references, and a cover letter describing your research interests and leadership capabilities to: <http://l.usa.gov/XhgiGp>



engineering & public policy

Faculty Openings in EPP at CMU

The Department of Engineering and Public Policy at Carnegie Mellon seeks the following faculty candidates:

- A behavioral decision scientist committed to collaborative research with engineers on energy, environment, telecommunications, and technological innovation.
- Someone with a strong technical background and knowledge of the relevant literatures to address problems in the management of technical innovation and R&D policy from "inside the black box" in energy, manufacturing, or other technical areas
- A senior PhD economist with a technical background to work on problems in technology and policy and occupy the Lester B. Lave chair between EPP and the Tepper School of Business.
- An EE or CS PhD to address both the technical and policy aspects of computer or network security.

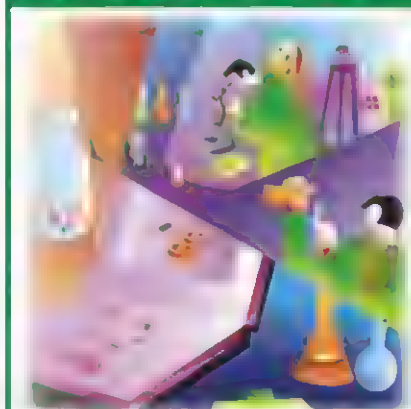
See www.epp.cmu.edu.

Send resume, references, and 2-3 sample publications to **Adam Loucks** (aloucks@andrew.cmu.edu).

Carnegie Mellon is an EEO/AA Employer.

CAREER TRENDS

Running
Your Lab



Download your free copy today at
34.100.1.100/CMU/EEPP/Book111

Science Careers

From the journal *Science* AAAS

Brought to you by the
AAAS/Science Business Office

Academia

Industry

Private Organizations

patients with devices similar to pacemakers that monitor heart rhythm. She hopes her research will launch a career in patient-oriented work for a pharmaceutical or medical device company. Grew appreciates the networking opportunities that come with her training. "It's a chance to get into industry and see what it is like to take something from an idea to real life, to make things better for patients with chronic diseases," she says.

At Medtronic Denmark, **Elisabeth Reimer Rasmussen's** expertise in health economics, policy, and public affairs made her a natural fit to be Grew's industry contact. Although the company was not seeking to host a Ph.D. student with an anthropologist's outlook, Rasmussen says Grew's fresh perspective has already changed thinking about patient satisfaction. And corporations know, says Rasmussen, "If you want to stay ahead, you have to see things in different ways."

Make Connections

Industry and academic scientists whose careers are already under way can connect through initiatives from companies, governments, and private organizations. Industry Fellowships from the Royal Society, the United Kingdom's national academy of science, support open-ended industry-academic collaborations. "The guiding principles of the fellowship are pure, excellent science," says **Joe Sweeney**, professor of catalysis and chemical biology, University of Huddersfield, West Yorkshire, England. Sweeney has a fellowship to work with AstraZeneca, which has its corporate headquarters in London and its research headquarters in Södertälje, Sweden, and he is helping to increase **continued**>

—Elisabeth Reimer
Rasmussen

Alan Palkowitz

Regional Focus: Wales—April 26

Diversity (online only)—June 7

Postdoc – August 23

CREDITS (TOP) © ISTOCKPHOTO.COM; (BOTTOM) ELI LILLY AND COMPANY



“Up front, everyone must appreciate that funding strictly depends on meeting timelines, so goals and expectations must be aligned, with everyone on the same page about priorities, specific aims, and go/no-go decisions.”

—Anthony Coyle

networking and knowledge-sharing among the program's participants. The business exposure is a benefit, he says: “My own university research has improved through what I've learned from industry practices about management, engagement with funding agencies, and identifying translational opportunities.”

On the industry side, Lilly, headquartered in Indianapolis, Indiana, has a program that encourages scientists at the pharmaceutical company to collaborate with university researchers. The Lilly Research Awards Program (LRAP) funds precompetitive research proposals developed jointly by Lilly and university scientists. **James Stevens**, a Lilly distinguished research fellow, says the goals are fostering innovation and cultivating professional relationships. “LRAP allows our scientists to pursue lifelong learning,” he says. “But we also expect returns on investment in innovation and in the development of our scientists.” LRAP allows Lilly scientists to work with academic researchers on high-risk projects. Experiments are conducted at the academic laboratory, and Lilly scientists contribute data analysis, project planning, and other virtual activities.

Open Wide

Also virtual, but more directly targeted to Lilly interests is the Open Innovation Drug Discovery initiatives. **Alan Palkowitz**, Lilly vice president of discovery chemistry and technologies, says open innovation programs are born of the realization, especially by pharmaceutical companies, that “we can't do it alone; our current challenges are too big and complex.”

The program is a global, crowdsourced drug candidate search. Scientists working on molecules with therapeutic potential in specific areas such as anti-angiogenesis send them to Lilly. Company scientists perform high throughput assays and screens and send data to the scientists. “Access to external compounds in exchange for biological data—that's the currency we have developed,” says Palkowitz. “We evaluate the commercial potential of compounds to be optimized into drug candidates. In exchange for the data, Lilly gets first right of access for promising compounds.”

Cultivating long-term relationships is a goal. Palkowitz describes the academic partners as customers as well as collaborators and says Lilly wants the scientists to return to the program as they find new drug candidates. Lilly crafts agreements that ensure confidentiality about the scientists' compounds, offer mutually beneficial intellectual property rights, and allow publication of the data. Says Palkowitz, “This program will live and die

based on the experiences the scientists have, so we put effort into serving their interests, first and foremost.”

While the Lilly model is virtual, Pfizer is investing in an open innovation model based on face-to-face, side-by-side collaborations. The company, which has corporate headquarters in New York, deployed 90 of their own scientists to Centers for Therapeutic Innovations (CTIs) at three U.S. locations so far: San Francisco/San Diego, New York, and Boston. The CTIs have Pfizer laboratory space near academic medical research centers and five-year collaboration agreements with universities.

CTI projects—currently, about 20 are in progress—begin with academic scientists proposing research on protein-based drugs, such as therapeutic antibodies. Accepted proposals, evaluated by a joint industry-academic committee, receive staff funding, supplies, and access to company resources such as antibody libraries and instruments. Pfizer and academic scientists do the research, directed by Pfizer project managers. The endpoint is a proof-of-mechanism clinical trial, after which Pfizer has the first option to develop the potential therapy. Collaboration barriers such as material transfer agreements are removed in advance. Intellectual property arrangements recognize academic interests: at project completion, if Pfizer is not interested, rights to the candidate therapy revert to the university for further study or development.

Stuart A. Aaronson, chair of oncological sciences, Icahn School of Medicine at Mount Sinai in New York City, and **Gadi Bornstein**, Pfizer associate research fellow, are collaborators at the New York-based CTI. Their project is developing therapeutic antibodies against an oncogenic target. “It's been a good experience,” says Aaronson. “We feel like we're moving together to a common goal, and we've had consensus so far on what's important to pursue.” Although they have clear deadlines and deliverables, the academic scientists have not felt limited, says Aaronson. “Everyone appreciates that learning more about the target is helpful to the whole project.” Success depends on this mutual vision and contribution, says Bornstein. “The academic scientists have the biological experience with the target system, and Pfizer has the drug discovery expertise.”

CTI projects have hard deadlines, and they are not basic research projects. The mechanism “doesn't work for everybody in academia and is not a replacement for NIH grants,” says **Anthony Coyle**, Pfizer chief scientific officer, adding that “total transparency” is crucial. “Up front, everyone must appreciate that funding strictly depends on meeting timelines, so goals and expectations must be aligned, with everyone on the same page about priorities, specific aims, and go/no-go decisions. But we work as a team to achieve pre-agreed steps.” In the next year or so, Coyle expects the first clinical trials from CTIs to start, with three to five candidate proteins identified for trials each year, starting in 2013.

Get Everyone Into the Act

Open innovation is now a megamodel, underlying partnerships of companies, universities, government agencies, and philanthropic organizations. The Innovative Medicines Initiative (IMI) is a public-private endeavor based in Belgium with a €2 billion (approximately US\$2.6 billion) budget. Funding comes from the European Commission (EC) and in-kind contributions such as research activities from members of the European Federation of Pharmaceutical Industries and Associations (EFPIA). Governed by EFPIA and EC representatives and guided by scientific advisors and European Union member state representatives, the IMI is accelerating new medicine development. **Michel Goldman**, executive director, says that the IMI was founded in 2008 because European investment in drug development was declining, with severe economic effects: “To the EC and

EFPIA, it was clear that the only way to restore European competitiveness in drug development was through collaboration.”

The IMI funds multinational consortia of companies, universities, hospitals, small businesses, regulatory agencies, and patient organizations. Projects address areas ranging from diabetes to schizophrenia. From the perspective of managing one of the world's largest private-public partnerships, Goldman says that teamwork among diverse entities can happen “if all parties agree to work toward common objectives, and if each partner is given a clear mission and is carefully evaluated to make sure they are adding value.”

The IMI acts as a trusted neutral party that brings businesses, universities, and government agencies together. By cooperating, these diverse entities can take on challenges that are important to all partners, but neglected because they are high risk or have low profit potential, such as developing new antibiotics. Goldman says the IMI also provides a platform for agencies such as the U.S. Food and Drug Administration and the European Medicines Agency to discuss novel regulatory approaches to getting drugs to patients quickly while ensuring safety and efficacy. As part of the IMI's educational mission, it has five programs for training in regulatory science, including programs in pharmacovigilance and new approaches to toxicology.

GlaxoSmithKline, headquartered in London, is participating in IMI antibiotic initiatives. **Andreas Heddini** is a medical advisor with the company, and confirms the importance of the IMI in bringing together parties whose interests don't always align. The IMI is crucial for advancing antibiotic development, says Heddini. “This is a critical area for infectious disease, but it has been neglected for decades. The initiative is great because it has three components: it leads to an increased understanding of resistance mechanisms, brings new candidate drugs forward, and provides a way to share data, including about what does not work.”

Data and knowledge-sharing are also essential to the TB Drug Accelerator program. This tuberculosis initiative is just one of many programs supported by the Bill & Melinda Gates Foundation, a philanthropic organization based in Seattle that invests in global health. The TB Drug Accelerator partners include the U.S. National Institutes of Health, six research institutions, and seven pharmaceutical companies. The Wellcome Trust, a charitable organization based in London, is also a contributor.

A major challenge to fighting tuberculosis is the six-month treatment regimen, says **Ken Duncan**, Gates Foundation deputy director of Global Health Discovery. The TB Drug Accelerator program is seeking medicines that shorten the therapy to a month or less. Companies in the partnership supply compound libraries and drug discovery expertise to the effort, while academic partners contribute knowledge about the disease and facilities for screens and assays. The Foundation, says Duncan, provides financial support and project coordination, setting timelines and milestones and monitoring progress. “Our most important function,” he says, “is integration—bringing everybody together.”

Duncan, who spent 16 years at GlaxoSmithKline working on diseases of the developing world, says companies in the TB Drug Accelerator program have an unusually open agreement. This includes sharing drug candidate structures and positive and negative results. The consortium will put data in the public domain as quickly as possible, to help prevent research redundancy. While the commercial potential might not be immediate, Duncan says the collaboration could yield concrete rewards for the companies, such as new R&D avenues from identification of novel drug targets. In addition, he says, “the scientists get to apply their energy and expertise to help solve a medical problem and have an impact on global health.”

Featured Participants

Bill & Melinda Gates Foundation
www.gatesfoundation.org

GlaxoSmithKline
www.gsk.com

Icahn School of Medicine at Mt. Sinai
www.mssm.edu

Innovative Medicines Initiative (IMI)
www.imi.europa.eu

Lilly
www.lilly.com

Medtronic
www.medtronic.com

Pfizer
www.pfizer.com

University of Copenhagen
www.ku.dk/english

University of Huddersfield
www.hud.ac.uk

WellPoint
www.wellpoint.com

Additional Resources

Danish Industrial PhD Program
scim.ag/Z3JiNU

Marie Curie Initial Training Networks
scim.ag/Y2MxmW

Royal Society Industry Fellowships
scim.ag/WujWao

Where We Go From Here

Patients and patient advocacy groups are now joining private-public partnerships as advisors, connections to trial participants, and conduits for results. Potential users of new therapies can provide valuable insights during development. Patients can also help companies and regulatory agencies explain their products and policies to the general public.

Collaborations among industry, academia, foundations, governments, and end users are becoming more common. The result is a dynamic R&D environment that fits the networked, integrated, and interdisciplinary way people live and work today. Driving open innovation is tight budgets all around. “Everybody is under pressure—academia, pharmaceutical companies—it encourages collaborating effectively,” says Mt. Sinai's Aaronson.

Regardless of partners, collaborative success rests on three principles: a mutual interest in a common, achievable goal; constant communication about expectations, timelines, and rewards; and transparency throughout the project. Joe Sweeney says, “In my experience, almost all roadblocks to collaboration have not been the project but problems with human interactions—a lack of understanding about requirements. It's important to have conversations in which all partners explain what they need from the collaboration: funding, deliverables, publications, patents. A good industry academic partnership is set up from the start as a win-win for all sides.”

Chris Tachibana is a science writer based in Seattle, USA, and Copenhagen, Denmark.

DOI: 10.1126/science.opms.r1300132



“To the EC and EFPIA, it was clear that the only way to restore European competitiveness in drug development was through collaboration.”

—Michel Goldman



Northeast Ohio
MEDICAL UNIVERSITY

Endowed Chair in Microbiology and Immunology

The Department of Integrative Medical Sciences at the Northeast Ohio Medical University (NEOMED) invites applications to fill the newly created Watanakunakorn Chair in Microbiology and Immunology. We are especially interested in applicants whose research programs will complement existing departmental strengths in cardiovascular disease, regenerative medicine, lipid metabolism, liver biology, inflammation and viral pathogenesis as well as enhance and expand existing ties with NEOMED's clinical partners in Northeast Ohio. Applicants will be expected to have an internationally recognized research program in basic, translational or clinical microbiology/immunology/inflammation/infectious disease research; a history of sustained extramural funding; and a commitment to academic excellence in medical and graduate education. Position requirements include a Doctorate (PhD, MD, DVM, or equivalent), a successful history as Principal Investigator of federal research grants, and Associate or Professor level qualifications at an academic medical institution or equivalent. This position will provide the successful candidate with significant laboratory space and research resources, and the opportunity to grow their research at NEOMED through the recruitment of additional junior faculty.

Qualified Candidates should send their CVs along with the names of three references to: **Dr. William P. Lynch, Search Committee Chair, c/o Ms. Karen J. Greene (kjc@neomed.edu)**. Applications will be reviewed beginning **May 1, 2013** and continue until a suitable candidate is recruited.

NEOMED is a thriving freestanding Community-based Medical University committed to excellence in medical education, research, and community outreach. The institution is currently in an active growth phase, which includes new state of the art research facilities and expansion of the comparative medicine unit. Uniquely, NEOMED is located in a semi-rural setting with ready access to outstanding urban, suburban and rural cultural, community and recreational activities, along with a very low cost of living index, maximizing quality of life issues.

NEOMED encourages and welcomes diversity in the workplace and is an Equal Opportunity Employer.

DIRECTOR GENERAL



icipe is an international research centre working on improving the livelihoods of people in the tropics through appropriate technological innovations. Headquartered in Nairobi, Kenya, icipe is mandated to develop eco-friendly pest and vector management technologies that are affordable to resource-limited rural and urban communities. icipe's mandate further extends to the conservation and utilisation of the rich insect biodiversity found in the tropics. icipe is the only international institution in Africa working primarily on arthropods. Consequently, capacity building of individual researchers and institutions is an integral part of all R&D activities at the Centre. For more information visit www.icipe.org

icipe is now seeking a dynamic Director General to provide leadership in all areas of icipe activity, including ensuring relevance to stakeholders and delivering highest quality scientific research and development (R&D) for solving complex problems according to the remit of icipe, as well as significantly increasing financial resources available to the R&D agenda.

To find the full details for this challenging opportunity, please visit: www.icipe.org/index.php/jobs/701-dg.html

Applications should be received at dg.applications@icipe.org before the **31st of May 2013**

icipe is an equal opportunity employer and women are particularly encouraged to apply



PROFESSOR AND VICE-CHAIR FOR RESEARCH

The University of Texas Medical School at Houston is seeking applications and nominations for the position of Professor and Vice-Chair for research of the Department of Orthopedic Surgery. The successful candidate will be an internationally recognized, outstanding scientist with demonstrated success in research, teaching, graduate training and service to the academic community. The Department of Orthopedic Surgery (<http://www.uth.tmc.edu/ortho/>) is one of 24 Departments and 23 Centers in the Medical School, which has \$157 million in research expenditures. The Department has a major clinical program and research interests in sports medicine and trauma. The new Vice-Chair will work directly with the chairman, Dr. Walter Lowe, and will be provided with substantial resources to significantly grow the research effort of the department. The Search Committee is particularly interested in Investigators with research programs in regenerative medicine and/or materials science as they relate to orthopedics. The Medical School is located within the Texas Medical Center, which includes the UT Health Science Center at Houston, Baylor College of Medicine and UT M. D. Anderson Cancer Center

Qualified candidates can apply at <http://jobs.uth.tmc.edu> for the Professor and Vice-Chair – Orthopedic Surgery position, Requisition #130855.

UTHealth is committed to creating a diverse environment and is proud to be an Equal Opportunity Employer.



Research Fellow T Cell Receptor Biology

A postdoctoral position is available immediately to participate in an exciting new area of T cell receptor (TCR) biology involving mechanotransduction. The successful candidate must have a PhD or equivalent and be highly motivated. He/she will work with a team of immunologists and structural biologists seeking to explore the details of how mechanical force upon pMHC ligation signals from the TCR ectodomains through their transmembrane and cytoplasmic tails. The ideal candidate should have excellent skills in biochemistry, molecular biology and T cell functional studies including transfection of T cells, cell growth and functional analysis as well as flow cytometry.

Research Fellow HIV-1 Development

A postdoctoral position is available in the area of HIV vaccine immunology with the goal to modulate B cell selection and ultimately elicit high affinity, broadly neutralizing antibodies. The candidate will study the cellular and molecular mechanisms regulating B cell immune responses including B cell repertoire analysis and CD4 T cell requirements in a murine model. A strong scientific background with emphasis on B cell and molecular immunology is required. The successful candidate must have a PhD or equivalent and be highly motivated.

If interested, please send your CV, a brief summary of research experience and names of three referees to: Ellis Reinherz, MD, Professor of Medicine, Harvard Medical School and the Department of Medical Oncology, Dana-Farber Cancer Institute, 77 Avenue Louis Pasteur, HIM 419, Boston, MA 02215; Email: ellis_reinherz@dfci.harvard.edu.

Dana-Farber Cancer Institute is an Affirmative Action/Equal Opportunity Employer – committed to diversity and inclusion in our workforce



Department of Health and Human Services
National Institutes of Health
National Heart, Lung and Blood Institute
Division of Intramural Research
Center for Human Immunology, Autoimmunity, and Inflammation



CHIEF SCIENTIFIC OFFICER

The NIH Center for Human Immunology, Autoimmunity and Inflammation (CHI) is a trans-NIH initiative that studies the human immune system in health and disease using high-throughput multiplex assays and then develops novel insights into immune system function and disease by analyzing the resulting dense data sets using advanced computational approaches. CHI utilizes an integrated team of scientists to implement this translational systems approach, including clinical, laboratory, and bioinformatics scientists. Projects are developed collaboratively and are chosen for implementation by consensus.

CHI is seeking to recruit a Chief Scientific Officer. This individual will have supervisory roles at both the laboratory and larger project levels. At the research level, s/he will be oversee technical staff responsible for implementing and conducting antigen-specific T and B lymphocyte assays to complement our high throughput technologies, such as microarrays, 15 color flow immunocyte phenotyping, multiplex analysis of serum cytokines and proteins, and SNP genotyping. At the project level s/he will contribute human biologic and immunologic insight to the choice and design of CHI research efforts and through collaboration with members of the bioinformatics group, be responsible for providing ongoing biology-based guidance of the computational analysis and interpretation of data emerging from these projects. These latter efforts will provide continuity of input to supplement that provided by the CHI leadership. The incumbent will thus have substantial responsibility for moving CHI projects forward and a significant voice in the future directions of CHI.

The ideal candidate will have an M.D., D.O., Ph.D., or M.D. Ph.D., and a strong record of accomplishment including publications in human immunology: laboratory, clinical, and translational. The candidate must be an outstanding communicator and be a collaborative team player. Experience combining biologic studies with computational analysis is highly desirable (e.g., hands-on experience with the application of bioinformatics approaches for drawing biological insights from large-scale data sets).

How to Apply: Applicants may be U.S. Citizens, resident aliens, or non-resident aliens holding or eligible for a valid employment visa. Applications must be accepted until the position is filled. Please submit a curriculum vitae and brief statement of how your experience relates to the needed qualifications along with 3 letters of reference to **Neal S. Young, M.D. Director CHI c/o Christen Sandoval Building 15F2 MSC 2664 NIH Bethesda MD 20892**, or electronically to christen.sandoval@nih.gov. Additional information about CHI is available online at <http://www.nhlbi.nih.gov/resources/chi/index.htm>

HHS and NIH are Equal Opportunity Employers.



Department of Health and Human Services
National Institutes of Health
National Heart, Lung, and Blood Institute
Division of Intramural Research
Center for Human Immunology, Autoimmunity, and Inflammation



STAFF SCIENTIST/BIOINFORMATICS ANALYSIS LEAD

The NIH Center for Human Immunology, Autoimmunity and Inflammation (CHI) is a trans-NIH initiative that studies the human immune system in health and disease using high-throughput multiplex assays, and then integrating the dense data sets using advanced computational approaches to obtain biological insights.

CHI is seeking to recruit an individual who will have responsibilities in the broad area of computational analysis of diverse data sets from high-throughput assays, such as microarrays, flow immunocyte phenotyping, multiplex analysis of serum cytokines and proteins as well as SNP genotyping. This position involves close collaboration with multiple experimentalists and principal investigators to answer biological questions of interest by performing quality control and statistical analyses of the data, as well as analyses to integrate these data and other relevant information to interpret the resulting discoveries in the biological context. The Staff Scientist/Bioinformatics Lead position is located in CHI's Bioinformatics Laboratory, and involves supervision of a group of 2-3 who perform the more routine analyses for the CHI. To facilitate efficient data retrieval and data mining, the Bioinformatics Group also has responsibility to build databases and software infrastructure to load, store and organize the diverse data sets, associated metadata, and analysis results. The group also conducts cutting-edge bioinformatics and systems biology research, such as developing novel statistical methods for the analysis and integration of high-dimensional data sets to gain biological insight. Because the computing infrastructure of CHI is by necessity inhomogeneous, the incumbent will likely need to develop or work with custom hard- and software solutions to accomplish these various goals.

The ideal candidate will have a Ph.D. in computational biology, bioinformatics, systems biology, or relevant disciplines and 3+ years of hands-on research experience with the analysis of high-throughput data sets. He/she should possess a sound knowledge of statistics and quantitative modeling and solid computer programming skills with proficiency in Matlab/R, SQL, and at least one scripting language (Perl/Python/Ruby); solid experience with databases design and construction. Proficiency in C++ and/or Java as well as experience with multiple OS platforms (Windows, MAC, Linux) are definite pluses as is experience or training in biological medical science. The incumbent will be supervised by the CHI Associate Director/Head for Computational Systems Biology and work closely with this individual and the Chief Scientific Officer of the CHI in monitoring the day to day work of the computational staff, planning large scale data analyses, and conducting efforts for creative integration of the diverse and dense data arising from CHI investigations.

How to Apply: Applicants may be U.S. Citizens, resident aliens, or non-resident aliens holding or eligible for a valid employment visa. Applications will be accepted until the position is filled. Please submit a curriculum vitae and brief statement of how your experience relates to the needed qualifications along with 3 letters of reference to: **Neal S. Young, M.D. Director CHI c/o Christen Sandoval Building 15F2 MSC 2664 NIH Bethesda MD 20892**, or electronically to christen.sandoval@nih.gov. Additional information about CHI is available online at <http://www.nhlbi.nih.gov/resources/chi/index.htm>

HHS and NIH are Equal Opportunity Employers.

There's only one

DR. SHIRLEY MALCOM



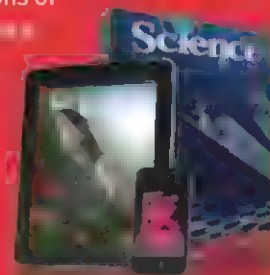
The launch of Sputnik in 1957 seemed even less likely than the launch of the Soviet's Sputnik. But with Sputnik's success, the Space Race officially started and, in an instant, brought a laser-like focus to science education and ways to deliver a proper response. Not long after, Dr. Malcom entered the picture.

Although black schools at the time received fewer dollars per student and did not have sufficient resources to maintain their labs at a level equivalent to the white schools, Dr. Malcom found her way to the University of Washington where she succeeded in obtaining a B.S. in spite of the difficulties of being an African American woman in the field of science. From there she went on to earn a Ph.D. in ecology from Penn State and held a faculty position at the University of North Carolina, Wilmington.

Dr. Malcom has served at the AAAS in multiple capacities, and is presently Head of the Directorate for Education and Human Resources Programs. Nominated by President Clinton to the National Science Board, she also held a position on his Committee of Advisors on Science and Technology. She is currently a member of the Caltech Board of Trustees, a Regent of Morgan State University, and co-chair of the Gender Advisory Board of the UN Commission on Science and Technology for Development. She has held numerous other positions of leadership and is the principal author of the Science Board's report, *Science Education: The Road Ahead*.

Of her active career in science, Dr. Malcom says, "I guess I have become a poster child for taking career advice. But I wouldn't want to say that. I have taken many career steps, but I wouldn't want to say that. I have taken many career steps, but I wouldn't want to say that. And that happens in whatever setting one finds oneself."

All ScienceCareers.org has to offer you is the best career advice, job postings, job alerts, career forum, crafting resumes/CVs, preparing for interviews, forums, job postings, and more — all for free. Visit *Science* today at ScienceCareers.org.



For your career in science, there's only one **Science**



ScienceCareers.org

The American Association for the Advancement of Science seeks an **Associate Editor** to join the dynamic editorial team at *Science Signaling*, the leading weekly research journal and online knowledge environment devoted to cellular signal transduction from the publisher of Science.

Do you prefer reading research and learning new areas of biology to working at the bench focused on a single protein, pathway, or disease? Have you used systems biology approaches to build or analyze cellular regulatory networks? Do you find that your interests lie beyond your current research project? If so, an editorial position at *Science Signaling* may be right for you.

Science Signaling, the leading weekly research journal and online knowledge environment devoted to cellular signal transduction from the publisher of Science, has an open position for a full-time Associate Editor to work in our Washington, DC, USA office. We are looking for a self-motivated scientist with broad interests in the biological sciences and experience with cutting-edge research related to signaling pathways and networks. The primary responsibilities include the selection of original research submissions, managing and updating the Database of Cell Signaling, as well as inviting and editing Perspectives and Reviews. Candidates should have broad knowledge of signaling pathways, have used systems biology approaches to study signaling networks, enjoy reading and learning new topics in biology, and be familiar with databases containing signaling-relevant information.

Major duties and responsibilities:

- Manages the peer review and selection of primary research manuscripts on cell signaling and related systems biology
- Solicits invited content such as Reviews, Perspectives, and Protocols
- Updates the Database of Cell Signaling
- Discusses and makes recommendations regarding manuscripts and journal content with other editorial staff and advisors
- Coordinates special issues
- Edits content and works with authors on revisions and preparation of manuscripts for publication
- Writes short summaries of published papers on a weekly basis
- Fosters contacts and communication with the scientific community through interactions with scientists and travel to scientific meetings

Minimum qualifications:

- Extensive university or college-level training leading to a Ph.D. in the biological sciences, with experience in cell signaling pathways and networks
- Postdoctoral experience resulting in multiple publications in peer-reviewed journals
- Ability to work independently, as well as, constructively as a member of the editorial team
- Excellent written and verbal communication skills
- Previous editorial experience or experience in database curation is a plus

Please visit our job information website <http://www.aaas.org/careercenter/employmentataaas/> to get more information, and to apply to AAAS online.

AAAS is an Equal Opportunity Employer.



北京航空航天大学
BEIHANG UNIVERSITY

Faculty Positions Available in Beihang University, China

Established in 1952, located in Haidian District, Beijing, Beihang University is one of the top research-oriented universities in China, focusing on fundamental cutting edge research and high-level education, covering such diverse fields as science, engineering, technology, humanities, economics, management and law. One of the first universities funded by China's "211" and "985" programs, it has seven national key laboratories and twenty-five provincial and ministerial key laboratories. At present, the university has a total area of two million square meters, and over 3800 faculty and staff.

Beihang University is on a clear path to become a world-class university in many engineering and science disciplines. As part of Beihang's further pursuit for excellence in research and education, we have expanded our global search for the best research talent to join our International Research Institute for Multidisciplinary Science (IRIMS). Five independent international research centers (IRC) were established recently under the name of IRIMS. As the core part of IRIMS, IRCs are devoted to establish a world-class, advanced and multidisciplinary research platform.

Beihang University invites applications for full-time Professors, Associate Professors and excellent scientists. Preference will be given to candidates whose research emphasis demonstrates the potential to complement and advance the IRIMS existing research strengths. Successful candidates will be provided competitive salaries and start-up funds.

Positions Available

- Position offered by the Recruitment Program of Global Experts (1000 Plan Professorship)
- Position offered by the Chang Jiang Scholars Program
- Position offered by the Recruitment Program of Global Young Experts (1000 Plan Professorship for Young Talents)
- Position offered by Beihang University's Zhuoyue Program of Professors
- Position offered by Beihang University's Zhuoyue Program of Associate Professors.

Interested individuals should send curriculum vitae by email to rscreb@buaa.edu.cn, with "Faculty Application from Science" in the title. For more information, please visit the university's Human Resource Department website <http://rsc.buaa.edu.cn/>, or contact us by email rscreb@buaa.edu.cn or by telephone 86-010-82317779.



AAAS is here – helping scientists achieve career success.

Every month, over 400,000 students and scientists visit ScienceCareers.org in search of the information, advice, and opportunities they need to take the next step in their careers.

A complete career resource, free to the public, *Science Careers* offers a suite of tools and services developed specifically for scientists. With hundreds of career development articles, webinars and downloadable booklets filled with practical advice, a community forum providing answers to career questions, and thousands of job listings in academia, government, and industry, *Science Careers* has helped countless individuals prepare themselves for successful careers.

As a AAAS member, your dues help AAAS make this service freely available to the scientific community. If you're not a member, join us. Together we can make a difference.

To learn more, visit aaas.org/plusyou/sciencecareers





Join the Conversation!

Twitter is a great way to connect with AAAS members and staff about the issues that matter to you most. Be a part of the discussion while staying up-to-date on the latest news and information about your personal member benefits.

**Follow us @AAASmember
and join the conversation
with #AAAS**



MemberCentral.aaas.org



BASIC SCIENCE FACULTY COLLEGE OF MEDICINE CENTRAL MICHIGAN UNIVERSITY

Multiple positions; twelve-month Assistant/Associate/Full Professor

The Central Michigan University College of Medicine (CMED) is seeking highly qualified faculty for multiple tenure-track or fixed-term positions in the basic science disciplines. Successful candidates will be expected to develop a vigorous externally funded research program and assume a role in the development and implementation of a highly integrated, cross disciplinary, clinical presentation and inquiry-based medical school curriculum.

Positions will be at the Assistant/Associate/Full Professor rank, depending on credentials, and are available immediately. Start dates are negotiable. CMED will provide a competitive space and start-up package to support the development of an externally funded vigorous research program. Applications are being sought for teaching expertise in all disciplines of the basic biomedical sciences.

Qualifications:

Required: doctoral degree, strong commitment to innovative approaches to education and learning, ability or commitment to facilitate interactive learning in large and small group settings, experience with independent design and conduct of research consistent with discipline(s), strong collaborative and communication skills; and a demonstrated commitment to diversity. Applicants applying for advanced rank should have a demonstrated record of teaching in large and small group settings and/or an extramurally funded research program.

Preferred: Research - while all areas of research will be considered, collaborative opportunities in basic research exist in neuroscience, mitochondrial biology, cancer vaccines, respiratory control and disease, signal transduction, virology, comparative effectiveness, health services, rural medicine, and clinical trials and outcomes. **Teaching** - experience with cross disciplinary teaching; documented experience in patient and/or problem-based medical education; experience with, or a strong knowledge of, pedagogical approaches such as team based learning.

General Information:

Established in 1892, Central Michigan University is one of the nation's 100 largest public universities and the fourth largest in Michigan, with more than 28,000 students in Mount Pleasant, online and at more than 60 locations throughout the United States, Canada and Mexico. CMU offers more than 200 academic programs at the undergraduate through doctoral levels, including several that are nationally recognized. CMU is located in Mount Pleasant, Mich., a classic college town with a blend of natural features, family attractions, small-town life and university culture.

The CMU College of Medicine will welcome its inaugural class in the summer of 2013. The innovative medical school curriculum is being designed to prepare students for practice in mid- to northern Michigan and the Upper Peninsula, with particular attention to primary care needs in the region. The program is housed in a new facility with advanced technology for teaching. For more information, visit <http://www.cmich.edu/med>.

Application Procedure:

Review of applications begins immediately and continues until filled. Applications must be submitted through an on-line process at: www.jobs.cmich.edu. Electronically attach a letter of application, curriculum vitae, evidence of teaching ability if available, statement of teaching philosophy, statement of research/scholarly interest, and a list of three professional references, including phone numbers and email addresses. Questions can be directed to Rebecca Messing, Faculty & Staff Affairs Coordinator, Spenc1rl@cmich.edu, 989-774-7862.

CMU, an AA/EQ Institution, strongly and actively strives to increase diversity within its community (see www.cmich.edu/aaeo).

POSITIONS OPEN

DIRECTOR

Princeton University Department of Chemistry seeks candidates for the position of Director of the new Small Molecule Screening Center.

The director will provide leadership in managing program activities and will be responsible for the overall operations of the screening center by employing a wide range of contemporary high throughput screening assays; performance of all follow-up organic synthesis activities; and, maintenance of the screening center infrastructure.

The successful candidate must hold a Ph.D. in organic synthesis (or related field) and have broad experience and knowledge in medicinal chemistry. The candidate should have current bench skills, demonstrated proficiency in mass spectroscopy technology and analytical chemistry. For further information and to apply online (required) at website: <https://jobs.princeton.edu> (requisition #1300162). Submit a cover letter, curriculum vitae, list of publications and contact information for three references. Princeton University is an Equal Opportunity Employer and complies with applicable EEO and Affirmative Action regulations.

POSTDOCTORAL FELLOW/RESEARCH ASSOCIATE

A postdoctoral/research associate position is available in the Center for Cardiovascular Sciences, Albany Medical College to investigate the functions and mechanisms of cytoskeletal/signaling proteins in respiratory and cardiovascular systems. Highly motivated applicants with Ph.D. degree and experiences in muscle contraction, or molecular biology/techniques, or gene expression are encouraged to apply by sending your application letter, curriculum vitae, and names and contacts of references to **Dr. Dale D. Tang** at e-mail: tangd@mail.amc.edu. An Equal Opportunity/Affirmative Action Employer. Women and Minorities are encouraged to apply.

POSTDOCTORAL FELLOW

Postdoctoral Fellow Positions at UMDNJ-New Jersey Medical School are available to study the molecular and cellular mechanisms underlying chronic pain and opioid tolerance. Strong background and experience in pain biology, electrophysiology, or molecular biology are required. Please send curriculum vitae to **Dr. Yuan-Xiang Tao** at emails: yuanxiangtao@yahoo.com or ytao1@jhmi.edu.

Find
your future
here.



www.ScienceCareers.org

We deliver
customized job alerts.

www.ScienceCareers.org

Download
your free copy
today.

ScienceCareers.org/booklets



From technology specialists to patent attorneys to policy advisers, learn more about the types of careers that scientists can pursue and the skills needed in order to succeed in nonresearch careers.





STAY INFORMED! STAY CONNECTED!

Get more from your AAAS membership

Are you currently registered to receive e-mails from AAAS and *Science*?

E-mail is the primary way that AAAS communicates with our members about AAAS programs, new member benefits, invitations to special events, and, of course, the latest news and research being published in *Science*.

Sign up today to receive e-mails from AAAS and ensure that you are getting the most out of your membership and *Science* subscription.*

To get started visit: promo.aaas.org/stayconnected

You'll need your AAAS Member number. Find it above your name on your *Science* mailing label.

Don't miss a thing. Sign up for e-mail communications from AAAS today!



**Our unparalleled cytokines and growth factors
are just the tip of the iceberg.**



Explore what's beneath the surface with R&D Systems.

Over $\frac{2}{3}$ of our research tools are designed to study intracellular signaling.

Cytokine and growth factor signaling doesn't stop at the cell surface. R&D Systems offers a full line of signal transduction reagents to complement our industry-leading cytokines and growth factors. In the upcoming months we will be adding rich signal transduction content to our website. Follow us on social media to receive updates.

Explore with Us.
RnDSystems



TOCRIS
bioscience

R&D
SYSTEMS®

BostonBiochem®